



University  
of Glasgow

Al-Sharrad, Muayad A. (2013) *Evolving anisotropy in unsaturated soils: experimental investigation and constitutive modelling*. PhD thesis.

<http://theses.gla.ac.uk/3828/>

Copyright and moral rights for this thesis are retained by the author

A copy can be downloaded for personal non-commercial research or study, without prior permission or charge

This thesis cannot be reproduced or quoted extensively from without first obtaining permission in writing from the Author

The content must not be changed in any way or sold commercially in any format or medium without the formal permission of the Author

When referring to this work, full bibliographic details including the author, title, awarding institution and date of the thesis must be given

**EVOLVING ANISOTROPY IN UNSATURATED  
SOILS: EXPERIMENTAL INVESTIGATION AND  
CONSTITUTIVE MODELLING**

by

**Muayad A. Al-Sharrad**

A thesis submitted in fulfilment of the  
requirements for the degree of

Doctor of Philosophy



School of Engineering

December 2012

© Muayad A. Al-Sharrad

## **DECLARATION**

I declare that this thesis is a record of the original work carried out by myself under the supervision of Prof. Domenico Gallipoli and Prof. Simon Wheeler in the School of Engineering at the University of Glasgow, United Kingdom, during the period of September 2008 to December 2012. The copyright of this thesis therefore belongs to the author under the terms of the United Kingdom Copyright acts. Due acknowledgement must always be made of the use of any material contained in, or derived from, this thesis. The thesis has not been presented elsewhere in consideration for a higher degree.

## TABLE OF CONTENTS

Table of Contents	i
List of symbols/abbreviations	vii
Acknowledgments	xviii
Abstract	xix
CHAPTER 1:INTRODUCTION	1
1.1 Anisotropy of soils	1
1.2 Modelling of anisotropy of unsaturated soils	2
1.3 Research objectives	3
1.4 Thesis layout	4
CHAPTER 2: BEHAVIOUR AND MODELLING OF UNSATURATED SOILS AND THE INFLUENCE OF ANISOTROPY	6
2.1 Suction in unsaturated soils	6
2.2 Stress state variables	8
2.3 Aspects of unsaturated soil behaviour	11
2.3.1 Volume change	11
2.3.2 Shear strength	14
2.3.3 Water retention behaviour	15
2.4 Yielding of soils	18
2.4.1 Yielding of saturated soils	18
2.4.2 Yielding of unsaturated soils	20
2.4.3 Empirical and graphical methods for yield identification	22
2.4.4 Influence of anisotropy on yielding	25
2.5 Evolution of soil fabric during hydro-mechanical loading	26
2.5.1 Macropores and micropores	26
2.5.2 Evolution of fabric anisotropy	30
2.6 Shapes and expressions for the yield surface and plastic potential	31
2.6.1 Isotropic yield curve expressions for saturated soils	32

2.6.2	Anisotropic yield curve expressions for saturated soils	34
2.6.3	Yield curve expressions for unsaturated soils	36
2.7	Anisotropic elasto-plastic constitutive models for saturated soils	37
2.7.1	Overview	37
2.7.2	The $S - CLAY1$ model	38
2.8	Elasto-plastic models for unsaturated soils	41
2.8.1	The Barcelona Basic Model ( $BBM$ )	41
2.8.2	Other isotropic models for unsaturated soils	45
2.8.3	Anisotropic elasto-plastic models for unsaturated soils	47
2.9	The coupled mechanical-water retention model of Wheeler et al. (2003a)	49
2.9.1	Elastic behaviour	50
2.9.2	Yield surfaces and flow rules	51
2.9.3	Coupled movements of the yield surfaces	53
2.9.4	Hardening laws	54
2.9.5	Variation of $v$ and $S_r$	55
2.9.6	Critical states	58
CHAPTER 3: EXPERIMENTAL SYSTEMS AND CALIBRATIONS		60
3.1	System 1 and System 2 (unsaturated triaxial cells)	60
3.1.1	Double wall cell	60
3.1.2	Pedestal and top cap	63
3.1.3	Control or measurement of pressure and volume	67
3.1.4	Logging and control system	69
3.1.5	General equipment layout	70
3.1.6	Flushing of diffused air	72
3.2	System 3 (saturated triaxial cell)	74
3.3	Calibrations for System 1 and System 2	76
3.3.1	Pressure transducers	77
3.3.2	Sample volume change gauges	79
3.3.3	Pore water volume change gauges	81
3.3.4	Load cells	83
3.3.5	Axial displacement gauges	83

3.3.6	Apparent volume change	84
3.3.7	Investigation of the accuracy of volume measurements in the double-wall cell	93
3.4	Calibrations for System 3	94
3.4.1	Pressure transducers	94
3.4.2	Pore water volume change gauge	94
3.4.3	Load cell	96
3.4.4	Axial displacement gauge	96
3.4.5	Apparent volume change	96
CHAPTER 4: SAMPLE PREPARATION TECHNIQUE AND TESTING PROCEDURE		98
4.1	Sample preparation	98
4.1.1	Soil type	98
4.1.2	Preparation of Kaolin mix	98
4.1.3	Development of isotropic and anisotropic initial fabrics	99
4.2	Test setup for System 1 and System 2	104
4.2.1	Preparation of de-aired water	104
4.2.2	Saturation of the high air entry filters	104
4.2.3	Sample setup	105
4.3	Test setup for System 3	108
4.4	Data processing	109
4.4.1	Unsaturated testing	109
4.4.2	Saturated testing	112
4.5	Typical test stages	112
CHAPTER 5: EXPERIMENTAL RESULTS AND DISCUSSION		114
5.1	Test series and stress paths	114
5.1.1	Test series to investigate yielding and critical states of as-compacted samples	115
5.1.2	Test series to investigate yielding and critical states of samples with induced anisotropy	117
5.2	Initial sample properties	121
5.3	Compaction stress paths	123
5.4	Initial wetting stages	126

5.4.1	Wetting to $s = 300$ kPa (Test Series A300, B300, Ba300, Bb300, Bc300 & Bd100)	126
5.4.2	Wetting to $s = 100$ kPa (Test Series A100, B100 & Be100)	134
5.4.3	Wetting to saturation (Test Series A0 & B0)	138
5.5	Probing/shearing stages on as-compacted samples	140
5.5.1	Probing/shearing at $s = 300$ kPa (Test Series A300 and B300)	140
5.5.2	Probing/shearing at $s = 100$ kPa (Test Series A100, B100 and Be100)	149
5.5.3	Probing/shearing under saturated conditions (Test Series A0 and B0)	160
5.6	Loading/ unloading and probing/shearing stages on samples with induced anisotropy (Test Series Ba300, Bb300, Bc300 and Bd100)	170
5.6.1	Loading/ unloading stages	170
5.6.2	Probing/ shearing stages	178
CHAPTER 6: INTERPRETATION OF EXPERIMENTAL RESULTS		203
6.1	Elastic constants	203
6.1.1	Elastic indices $\kappa$ and $\kappa_S$	203
6.1.2	Elastic index $\kappa^*$	204
6.1.3	Elastic shear modulus $G$	206
6.2	Isotropic loading of isotropically compacted samples	207
6.2.1	Results in the $v: \ln \bar{p}$ plane	207
6.2.2	Results in the $v: \ln p^*$ plane	207
6.2.3	Unique normal compression isotropic surfaces in $v: \ln p^*: \ln s^*$ and $S_r: \ln p^*: \ln s^*$ spaces	209
6.3	Critical states	212
6.3.1	Investigation of critical states	212
6.3.2	Critical state behaviour in the $q: \bar{p}$ and $v: \ln \bar{p}$ planes	212
6.3.3	Critical state behaviour in the $q: p^*$ and $v: \ln p^*$ planes	219
6.3.4	Unique critical state planar surfaces in $v: \ln p^*: \ln s^*$ and $S_r: \ln p^*: \ln s^*$ spaces	220
6.4	Identifying yield points	223
6.4.1	Bi-linear construction in the $v: \ln \bar{p}$ or $v: \ln p^*$ plane	223
6.4.2	Bi-linear construction in the $v: \bar{p}$ or $v: p^*$ plane	224

6.4.3	Strain energy	226
6.5	Interpretation of the yield points in the $q:p$ and $q:p^*$ planes	227
6.5.1	Yield curves in the $q:p$ plane	228
6.5.2	Yield curves in the $q:p^*$ plane	231
6.6	Experimental flow vectors	233
CHAPTER 7: DEVELOPMENT OF AN ANISOTROPIC MODEL		237
7.1	Overall approach	237
7.2	Elastic behaviour	238
7.3	Yield surfaces	238
7.4	Coupled movements of the yield surfaces	240
7.5	Hardening laws for changes of $p_m^*$ , $s_I^*$ and $s_D^*$	241
7.6	Variation of $v$	242
7.7	Hardening law for changes of $\alpha^*$	242
7.8	Flow rule on $LC$ surface and variation of $m^*$	244
7.8.1	Version 1: associated flow rule and $m^* = f(\alpha^*)$	246
7.8.2	Version 2: $m^* = \text{constant}$ and non-associated flow rule	247
7.9	Critical states	248
7.10	Saturated conditions	249
7.11	Application of the model	252
CHAPTER 8: MODEL SIMULATIONS		253
8.1	Calibration of soil constants other than $\mu$ and $c$	254
8.2	Calculation of initial states	256
8.3	Method of performing simulations	262
8.4	Calibration of soil constants $\mu$ and $c$	268
8.5	Confirmation that constant suction probing tests were acceptable for determining initial size and shape of the $LC$ surface	270
8.6	Simulations of tests on isotropically compacted samples	272
8.6.1	Test Series A100 (all values of $[\Delta q/\Delta \bar{p}]$ )	273
8.6.2	Influence of suction (at one value of $[\Delta q/\Delta \bar{p}]$ )	287
8.7	Simulations of tests on anisotropically compacted samples	288
8.7.1	Influence of the value of $[\Delta q/\Delta \bar{p}]$ and suction	288

8.7.2	Comparison of isotropically and anisotropically compacted samples	291
8.8	Simulating the influence of a previous loading stage	293
8.9	Comparison of Version 1 and Version 2 of the anisotropic model	299
8.9.1	Example simulations	299
8.9.2	Critical state planar surface in $v: \ln p^*: \ln s^*$ space	303
CHAPTER 9: CONCLUSIONS AND RECOMMENDATIONS		305
9.1	Experimental work	305
9.1.1	Experimental equipment	305
9.1.2	Compaction technique	306
9.2	Experimental results	307
9.2.1	Wetting stages	307
9.2.2	Yielding behaviour	307
9.2.3	Critical states	309
9.2.4	Yield curves and plastic flow vectors	310
9.3	Development of a constitutive model for anisotropic unsaturated soils	311
9.3.1	Aspects of the new anisotropic constitutive model	312
9.3.2	Model calibration	313
9.3.3	Performance of Version 1 of the anisotropic model	314
9.3.4	Performance of Version 2 of the anisotropic model	316
9.4	Recommendations for future work	316
9.4.1	Experimental equipment	316
9.4.2	Compaction technique	317
9.4.3	Experimental testing	317
9.4.4	Constitutive modelling	318
REFERENCES		320

## LIST OF SYMBOLS/ABBREVIATIONS

### LIST OF SYMBOLS

$a$	Parameter related to air-entry value of soil (in Brooks & Corey 1964)
$a$	Major axis of the elliptical yield curve (in Cui and Delage, 1996)
$A, B, C$ and $D$	Regression constants to correct raw reading of pressure, volume, etc. transducers of experimental equipment
$B$	Ratio of pore water pressure increase to cell pressure increase for saturated triaxial tests
$b$	Parameter related to the pore-size distribution of the soil (in Brooks & Corey 1964)
$b$	Minor axis of the elliptical yield curve (in Cui and Delage, 1996)
$c$	Constant controlling the current target value for $\alpha^*$
$c'$	Cohesion for saturated conditions
$d\alpha^*$	Increment of inclination of the yield curve in the $q:p^*$ plane
$d\varepsilon_1^p, d\varepsilon_2^p, d\varepsilon_3^p$	Plastic increments of principal strains
$d\varepsilon_{ij}$	Strain increment tensor
$d\varepsilon_s^e$	Elastic shear strain increment
$d\varepsilon_s^p$	Plastic shear strain increment
$d\varepsilon_v^p$	Plastic volumetric strain increment
$d\varepsilon_v^e$	Elastic volumetric strain increment

$dS_r$	Increment of degree of saturation
$dS_r^e$	Elastic increment of degree of saturation
$dS_r^p$	Plastic increment of degree of saturation
$e$	Void ratio
$F$	Parameter controlling the rate of decrease of $m^*$ with increasing $\alpha^*$ (for Version 1 of the proposed anisotropic model)
$f$	Yield surface
$\mathbf{f}$	force
$f(\eta^*)$	Function giving the current target value for $\alpha^*$
$g$	Acceleration due to gravity
$g$	Plastic potential function
$G_s$	Specific gravity of soil particles
$H_0$	Initial height of the sample
$k$	Parameter controls the linear shift of the critical state line with suction in the $q:\bar{p}$ plane (in the model of Alonso et al., 1990)
$K_0$	Coefficient of earth pressure at rest
$k_1$ and $k_2$	Coupling parameters (in the model of Wheeler et al., 2003a)
$L$	Length of stress vector
$M$	Slope of the critical state line in the $q:\bar{p}$ plane
$m$	Aspect ratio of the yield curve in the $q:\bar{p}$ plane

$m$	Parameter related to the asymmetric shape of the retention curve (in Van Genuchten, 1980; Fredlund and Xing, 1994 and Gallipoli et al., 2003a)
$M^*$	Slope of the critical state line in the $q:p^*$ plane
$m^*$	Aspect ratio of the yield curve in the $q:p^*$ plane
$m_0^*$	Value of $m^*$ at $\alpha^* = 0$
$m_{0c}^*$	Value of $m^*$ at $\alpha^* = 0$ for $q/p^* > \alpha^*$
$m_{0e}^*$	Value of $m^*$ at $\alpha^* = 0$ for $q/p^* < \alpha^*$
$M_c$	Slope of the critical state line for triaxial compression in the $q:\bar{p}$ plane (in the model of Wheeler et al., 2003b)
$m_c$	Value of the aspect ratio of the yield curve in the $q:\bar{p}$ plane for $q/(\bar{p} + p_s(s)) > \alpha$
$m_c^*$	Value of the aspect ratio of the yield curve in the $q:p^*$ plane for $q/p^* > \alpha^*$
$M_e$	Slope of the critical state line for triaxial extension in the $q:\bar{p}$ plane (in the model of Wheeler et al., 2003b)
$m_e$	Value of the aspect ratio of the yield curve in the $q:\bar{p}$ plane for $q/(\bar{p} + p_s(s)) < \alpha$
$m_e^*$	Value of the aspect ratio of the yield curve in the $q:p^*$ plane for $q/p^* < \alpha^*$
$M_s$	Mass of the solids within the sample
$M(s)$	Slope of the critical state line, for a given suction $s$ , in the $q:\bar{p}$ plane
$m_w$	Molecular mass of water vapour
$n$	Parameter related to the aspect ratio of the yield curve (in Whittle & Kavvas, 1994 and Taiebat & Dafalias, 2010)
$N$	Specific volume at the intercept of the saturated normal compression line in the $v:\ln p'$ plane (in the model of Wheeler et al., 2003b)

$n$	Porosity
$n$	Parameter related to the slope of the retention curve (in Van Genuchten, 1980; Fredlund and Xing, 1994 and Gallipoli et al., 2003a)
$N^*$	Intercept of the unique isotropic normal compression planar surface in $v: \ln p^*: \ln s^*$ space (in the model of Wheeler et al., 2003a)
$N(0)$	Value of $N(s)$ at zero suction (in the model of Alonso et al., 1990)
$N_s$	Inter-particle force due to meniscus water bridges
$N(s)$	Specific volume on the normal compression line at reference pressure $p^c$ for suction $s$ (in the model of Alonso et al., 1990)
$N_\sigma$	Normal component of inter-particle force due to external stress
$\bar{p}$	Mean net stress
$p$	Mean total stress
$p^*$	Mean Bishop's stress
$p'$	Mean effective stress (for saturated soil)
$\bar{p}_0(0)$	Value of $\bar{p}_0(s)$ at zero suction (in the model of Alonso et al., 1990)
$p'_0$	Intersection of the yield curve of saturated soil with the $p'$ axis
$\bar{p}_0(s)$	Intersection of a constant suction yield curve with the $\bar{p}$ axis (in the model of Alonso et al., 1990)
$p_{atm}$	Atmospheric pressure
$p^c$	Reference pressure (in the model of Alonso et al., 1990)
$p'_c$	Critical state value of the mean effective stress for a given stress state on the yield surface of saturated soil

$\bar{p}_{initial}, q_{initial}$	Initial stress state of a test in the $q: \bar{p}$ plane
$\bar{p}_m(s)$	Size of a constant suction yield curve in the $q: \bar{p}$ plane (in the models of Stropeit et al., 2008 and D'Onza et al., 2011)
$p_m^*$	Size of yield curve in the $q: p^*$ plane
$p'_m$	Size of the yield curve of saturated soil in the $q: p'$ plane
$p_s(s)$	Intersection of the critical state line (and yield curve) with the negative $\bar{p}$ axis for suction $s$ , in the $q: \bar{p}$ plane
$p_x^*$	Dummy variable defines the size of the plastic potential
$q$	Deviator stress
$q_{target}$	Target value of the deviator stress
$R$	Universal gas constant
$r$	Parameter controlling the limiting value of $\lambda(s)$ as suction tends to infinity (in the model of Alonso et al., 1990)
$R_0$	Average radius of the sample after suction equalisation
$R_1$ and $R_2$	Principal radii of curvature of an air-water interface
$s$	Matric suction
$s_0$	Current location of the $SI$ yield surface (in the model of Alonso et al., 1990)
$s^*$	Modified suction
$s_D^*$	Current position of the $SD$ yield surface (in the model of Wheeler et al., 2003a)
$s_i^*$	Initial experimental value of $s^*$
$s_I^*$	Current position of the $SI$ yield surface (in the model of Wheeler et al., 2003a)

$S_r$	Degree of saturation
$S_{r_{after}}$	Experimental degree of saturation at the end of initial wetting stage
$S_r^e$	Effective degree of saturation
$S_{r_{initial}}$	Initial experimental degree of saturation of a compacted sample
$T$	Absolute temperature
$T_s$	Surface tension
$T_\sigma$	Tangential component of inter-particle force due to external stress
$u_a$	Pore air pressure
$u_{a0}$	Initial value of pore air pressure at the beginning of loading after suction equalisation
$u_v$	partial pressure of pore-water vapour
$u_{v0}$	Saturation pressure of water vapour over a flat surface of pure water at the same temperature
$u_w$	Pore water pressure
$v$	Specific volume
$V_0$	Initial volume of the sample
$v_{after}$	Experimental specific volume at the end of initial wetting stage
$v_{cs}(s)$	Critical state value of specific volume for suction $s$
$v_{initial}$	Initial experimental specific volume of a compacted sample
$V_w$	Volume of water within soil sample

$v_w$	Specific water volume
$W$	Work input per unit volume
$w$	Water content
$w_{after}$	Experimental water content at the end of initial wetting stage
$w_{initial}$	Initial experimental water content of a compacted sample
$Y1, Y2, Y3$	Yielding boundaries in stress space where $Y1 < Y2 < Y3$ (in Smith et al., 1992)
$z$	Elevation relative to a reference horizontal datum
$\alpha$	Parameter in non-associated flow rule (in the model of Alonso et al., 1990)
$\alpha$	Parameter controlling the inclination of yield curve in the $q:\bar{p}$ plane
$\alpha$	Parameter related to the air entry value of the soil (in Van Genuchten, 1980; Fredlund and Xing, 1994 and Gallipoli et al., 2003a)
$\alpha^*$	Inclination of yield curve in the $q:p^*$ plane
$\alpha_0^*$	Initial inclination of the yield curve in the $q:p^*$ plane
$\alpha_{cs}$	Critical state inclination of the yield curve in the $q:\bar{p}$ plane (in the model of Wheeler et al., 2003b)
$\alpha_{cs}^*$	Critical state inclination of the yield curve in the $q:p^*$ plane
$\beta$	Parameter controlling the relative effectiveness of $d\varepsilon_s^p$ and $d\varepsilon_v^p$ in determining the overall current target value for $\alpha$ (in the model of Wheeler et al., 2003b)
$\beta$	Parameter giving the rate of change of $\lambda(s)$ with suction (in the model of Alonso et al., 1990)
$\Gamma$	Specific volume at the intercept of the saturated critical state line in the $v:\ln p'$ plane (in the model of Wheeler et al., 2003b)

$\gamma$	Parameter controlling the roundness of the yield curve near to the origin (in Lagioia et al., 1996)
$\Gamma^*(s)$	Specific volume at the intercept of the critical state line in the $v: \ln p^*$ plane for suction $s$
$\Gamma(s)$	Specific volume at the intercept of the critical state line in the $v: \ln \bar{p}$ plane for suction $s$
$[\Delta q / \Delta \bar{p}]$	Constant slope of the stress path in the $q: \bar{p}$ plane
$\Delta H$	Change in sample height since the beginning of loading after suction equalisation
$\delta_{ij}$	Kroneker's delta
$\Delta R$	Average change in sample radius
$\delta S_r$	Increment of degree of saturation
$\Delta V$	Change in sample volume since the beginning of loading after suction equalisation
$\delta \varepsilon_s$	Increment of shear strain
$\delta \varepsilon_v$	Increment of volumetric strain
$\varepsilon_a$	Axial strain
$\varepsilon_r$	Radial strain
$\varepsilon_s$	Shear strain
$\varepsilon_v$	Volumetric strain
$\xi$	Parameter controlling the roundness of the yield curve near to the apex (in Lagioia et al., 1996)
$\eta$	Stress ratio in the $q: \bar{p}$ plane
$\eta^*$	Stress ratio in the $q: p^*$ plane

$\theta$	Inclination of the yield curve (in Cui and Delage, 1996)
$\kappa$	Gradient of elastic compression/swelling line in the $v: \ln \bar{p}$ or $v: \ln p'$ plane
$\kappa^*$	Gradient of elastic compression/swelling line in the $v: \ln p^*$ plane
$\kappa_s$	Gradient of the elastic scanning curves in the $S_r: \ln s^*$ plane (in the model of Wheeler et al., 2003a)
$\kappa_s$	Gradient of elastic shrink/ swelling line in the $v: \ln(s + p_{atm})$ plane (in the model of Alonso et al., 1990)
$\lambda$	Slope of the normal compression line in the $v: \ln p'$ plane for an isotropic soil
$\lambda^*$ and $k_1^*$	Gradients of the unique isotropic normal compression (and critical states) planar surfaces in $v: \ln p^*: \ln s^*$ space (in the model of Wheeler et al., 2003a)
$\lambda(0)$	Gradient of normal compression line for saturated conditions (in the model of Alonso et al., 1990)
$\lambda_s$	Gradient of the elasto-plastic main wetting or main drying curves in the $S_r: \ln s^*$ plane (in the model of Wheeler et al., 2003a)
$\lambda_s$	Gradient of elasto-plastic shrink line in the $v: \ln(s + p_{atm})$ plane (in the model of Alonso et al., 1990)
$\lambda(s)$	Slope of the virgin compression line for suction $s$ in the $v: \ln \bar{p}$ plane (in the model of Alonso et al., 1990)
$\lambda_s^*$ and $k_2^*$	Gradients of the unique isotropic normal compression (and critical states) planar surfaces in $S_r: \ln p^*: \ln s^*$ space (in the model of Wheeler et al., 2003a)
$\mu$	Parameter controlling the rate of evolution of $\alpha$ towards its current target (in the proposed model and in the model of Wheeler et al., 2003b)
$\rho_w$	Density of water
$\sigma'$	Normal effective stress
$\sigma_3$	Cell pressure
$\sigma_{30}$	Cell pressure at the beginning of loading stage (for saturated tests in System 3)

$\sigma_{ij}$	Total stress tensor
$\sigma'_{ij}$	Effective stress tensor
$\sigma_{ij}^*$	“Bishop’s stress” tensor, also known as “average soil skeleton stress” tensor
$\sigma'_v$	Vertical effective stress
$\tau$	Shear strength
$\Phi$ and $\Psi$	Parameters related to the air entry value of the soil (in Gallipoli et al., 2003a)
$\phi'$	Friction angle for saturated conditions
$\phi^b$	Friction angle with respect to suction
$\chi$	Parameter related to degree of saturation
$\chi^*$	Soil constant related to the unique isotropic normal compression planar surface in $S_r: \ln p^*: \ln s^*$ space (in the model of Wheeler et al., 2003a)
$\psi^*(s)$	Slope of the critical state line in the $v: \ln p^*$ plane for suction $s$
$\psi_{ad}$	Adsorption potential
$\psi_{cp}$	Capillary potential
$\psi_{os}$	Osmotic suction
$\psi(s)$	Slope of the critical state line in the $v: \ln \bar{p}$ plane for suction $s$
$\psi_T$	Total suction

**LIST OF ABBREVIATIONS**

<i>ABBM</i>	Model of Stropeit et al. (2008)
<i>ABBM1</i>	Model of D’Onza et al. (2011)
<i>BBM</i>	Barcelona Basic model (by Alonso et al., 1990)
<i>ESEM</i>	Environmental scanning electron microscopy
<i>HAE</i>	High air entry ceramic filter
<i>LC</i>	Loading-Collapse yield curve
<i>LVDT</i>	Linear Variable Displacement Transducer
<i>MCC</i>	Modified Cam Clay model (by Roscoe and Burland,1968)
<i>MIP</i>	mercury intrusion porosimetry
<i>NCL</i>	Normal compression line
<i>PSD</i>	Pore size distribution
<i>RH</i>	Relative humidity
<i>S – CLAY1</i>	Model of Wheeler et al. (2003b)
<i>SD</i>	Suction Decrease yield curve
<i>SEM</i>	Scanning electron microscopy
<i>SI</i>	Suction Increase yield curve

## ACKNOWLEDGMENTS

I gratefully acknowledge the Iraqi Ministry of Higher Education for sponsoring this project which was carried out in the School of Engineering at the University of Glasgow.

I would like to express my heartfelt gratitude to my supervisors, Professor Domenico Gallipoli and Professor Simon Wheeler for their sincere encouragement and thoughtful guidance. Domenico and Simon are ones that you never forget once you meet them and I hope that I can be enthusiastic and energetic as them and I hope that I can in turn pass on the research values and the dreams that they have given to me.

My sincere thanks go to the staff members of the Civil Engineering Department, specially Mr. Stuart McLean and Mr. Tim Montgomery for their technical help, Ms. Barbara Grant, Miss. Amanda Smith and Mrs. Eileen Davies for their administrative help and Mr. Kenneth McColl for his help with computing issues.

Very special thanks to my family. I am grateful to my father, mother and sisters for all the sacrifices that they have made on my behalf. I am indebted to my beloved wife Alaa for her sacrifices and cheering up and for her tireless support. To my beloved son and daughters Zaid, Zainab and Ola, I would like to express my thanks for being such a bundle of joy and happiness. I know it's hard for them, at this age, to imagine their contribution to my doctoral work, but in fact, it is their brilliance that inspired me all the time.

Special thanks also to my lifelong friend Ihsan and his wife Safa for their help especially during the last period of my PhD. Thanks also to all my friends and colleagues from Iraq for support.

## ABSTRACT

This work explores the influence of evolving anisotropy on the stress-strain behaviour of unsaturated soils and proposes a new constitutive elasto-plastic model for unsaturated soils accounting for evolving anisotropy. An extensive campaign of laboratory tests on both isotropically and anisotropically compacted soil samples under a wide range of stress paths was performed. These experimental data were then employed in developing the new model and investigating its performance.

A programme of controlled suction triaxial testing was performed on unsaturated and saturated samples of Speswhite kaolin prepared by two different methods of compaction: isotropic and anisotropic. Tests involved probing stress paths, to investigate the initial forms of the yield surface for isotropically compacted and anisotropically compacted samples at different suction values, and how the yield surface was altered by plastic straining caused by loading stages or by wetting stages with significant collapse-compression. Tests also included shearing to failure, to investigate critical state conditions.

Experimental results were interpreted in terms of mean net stress  $\bar{p}$ , deviator stress  $q$  and suction  $s$  as stress state variables and, alternatively, interpreted in terms of mean Bishop's stress (defined as  $p^* = \bar{p} + S_r s$ ), deviator stress  $q$  and modified suction (defined as  $s^* = ns$ , where  $n$  is the porosity).

The experimental results showed that fabric anisotropy can evolve during plastic straining even for a soil that starts isotropic but is then loaded to anisotropic stress states. Also, the results showed that fabric anisotropy can evolve during wetting stages that involve collapse-compression. Furthermore, the results showed no apparent influence of initial or evolving anisotropy on the critical state, where both the initially isotropic and initially anisotropic samples, loaded at various stress path slopes, showed nearly the same critical states. Critical states can be represented in the  $q:\bar{p}$  plane by a series of parallel lines for different values of suction and the constant suction cross-sections of the yield surface can be represented by distorted ellipses in the  $q:\bar{p}$  plane, intersecting the negative axis at the point of intersection of the corresponding critical state line. Alternatively, critical states can be represented in the  $q:p^*$  plane by a single straight line (for all values of suction) passing through the origin, and constant suction cross-sections of the yield surface can be represented in the  $q:p^*$  plane by distorted

ellipses passing through the origin (suggesting that the yield surface expression is simpler when expressed in terms of  $q, p^*$  and  $s^*$  rather than in terms of  $q, \bar{p}$  and  $s$ ).

A new constitutive model was formulated in terms of Bishop's stresses and modified suction based on the above observations and other considerations such as that representing the coupling between mechanical and water retention behaviour is easier with Bishop's stress than with net stress. The new anisotropic model combines features from the isotropic model for unsaturated soils of Wheeler et al. (2003a) with features for modelling of anisotropy taken from the anisotropic model for saturated soils *S – CLAY1*. The new anisotropic constitutive model was developed solely as a mechanical model, unlike the constitutive model of Wheeler et al. (2003a), which is a combined mechanical and water retention model.

Model simulations of mechanical behaviour with the new anisotropic model were performed by using experimental values of  $S_r$  (with no attempt to predict values of  $S_r$ ), because it was then possible to check whether mechanical aspects of the model were performing well. Model simulations showed that significant improvement in the accuracy of the predicted soil behaviour was achieved by incorporating the role of evolving fabric anisotropy. However, model performance appears more satisfactory in simulating soil behaviour under unsaturated conditions than under saturated conditions. Also, the model is not entirely successful in predicting some aspects of anisotropic soil behaviour such as differences in initial specific volume between isotropically and anisotropically compacted samples.

# 1

## INTRODUCTION

### 1.1 ANISOTROPY OF SOILS

A soil that is anisotropic shows directional dependency of material behaviour. It is well-known that the fabric of soils, that is the arrangement of particles and inter-particle contacts, is often anisotropic due to natural or artificial formation. For instance, normally to lightly overconsolidated natural clays often exhibit anisotropic properties due their depositional history and subsequent consolidation stages. In natural soils, initial anisotropy is induced by deposition under one-dimensional straining and resultant  $K_0$  stress conditions. Initial anisotropy can be subsequently altered by loading stages that produce plastic straining and, hence, a change in the arrangement/orientation of particles and aggregates inside the soil structure. The anisotropy produced by plastic straining after the initial formation process is usually referred to as evolving or induced anisotropy. Therefore, even soils with an initial isotropic fabric can develop an anisotropic fabric if loaded along anisotropic stress paths.

Compaction techniques which involve one-dimensional straining are usually employed in the field and laboratory to produce artificial soil fills. These techniques have been shown to generate a moderately anisotropic fabric because of the particular compaction process. Although both elastic and plastic mechanical aspects of behaviour can show the influence of anisotropy, different aspects of material fabric control the anisotropy of elastic and plastic behaviour.

The influence of soil anisotropy on mechanical behaviour, particularly under saturated conditions, has received significant attention since the 1980s, when experimental and constitutive studies of evolving anisotropy in soils were conducted. One of the clearest indications of anisotropy of mechanical behaviour is the shape of the yield surface in stress space. Any experimental investigation of soil anisotropy usually involves a preliminary identification of the yield surface by means of triaxial tests in which samples are subjected to loading paths radiating, under different stress ratios, from an initial state inside the elastic domain.

Microstructural studies of soil fabric using scanning electron microscopy (*SEM*) and mercury intrusion porosimetry (*MIP*) have provided valuable insight into the loading mechanisms that produce changes of soil fabric and, in particular, of pore size distribution and particles orientation. Researchers are now able to demonstrate the gradual build up or erasure of fabric anisotropy not only from the phenomenological stress-strain behaviour at laboratory sample scale, but also from changes in soil microstructure.

Aspects of unsaturated soil behaviour such as volume change, shear strength and water retention behaviour have been widely investigated in the literature. However, only few studies have been conducted about the influence of anisotropy on mechanical and water retention behaviour of unsaturated soils. For example, little investigation has been carried out about the effects of one-dimensional compaction and the ensuing moderately anisotropic soil fabric on the mechanical behaviour of unsaturated soils.

## **1.2 MODELLING ANISOTROPY OF UNSATURATED SOILS**

A large number of anisotropic elasto-plastic constitutive models for saturated soils have been published in the last three decades accounting for the effect of evolving anisotropy on mechanical behaviour. In most anisotropic saturated models, the yield curve is described in the triaxial stress plane as an inclined ellipse, either rotated or distorted so that it is not symmetrical about the mean stress axis, with evolution of the inclination defined by a constitutive law depending on plastic volumetric and/or shear strains.

Modelling of linear elastic anisotropy requires 5 independent material constants for a cross-anisotropic (transversely isotropic) soil and 21 independent material constants for a generally anisotropic soil (see Graham and Houlsby, 1983). In practical boundary value problems, evolution of anisotropy during plastic straining often means that soils end up developing a general form of anisotropy. Consequently, most anisotropic elasto-plastic models for saturated soils assume isotropic elasticity in order not to add to the already complex description of plastic behaviour.

Modelling anisotropic behaviour in unsaturated soils has not yet received much attention, probably because of its complexity. Nevertheless, proper consideration of the effects of evolving anisotropic fabric on the mechanics of unsaturated soils is necessary. Numerical modelling of boundary value problems involving saturated soils has clearly demonstrated that incorporating anisotropy can be very important in accurately capturing observed field behaviour (Karstunen et al., 2005), and it seems very likely that the same will be true for unsaturated soils.

Significant progress has been made in recent years in the development of isotropic elasto-plastic models for unsaturated soils. Since publication of the Barcelona Basic Model (*BBM*) of Alonso et al. (1990), a large number of elasto-plastic models have been proposed to describe unsaturated soil behaviour. However, most of these models assume material isotropy and the influence of fabric anisotropy is not considered. Most of these models use two independent stress state variables (rather than a single effective stress tensor) to describe unsaturated soil behaviour. In particular, some models use net stresses and matric suction while others use Bishop-type stresses (Bishop, 1959) as the first stress state variable and matric suction or some function of matric suction as the second stress state variable. In the latter approach, both elastic behaviour and shear strength can be related solely to changes of the Bishop-type first stress state variable, and the second stress state variable is only required to define the yield surface (which is expressed in terms of both constitutive variables).

### 1.3 RESEARCH OBJECTIVES

In this work, an attempt is made to explore the influence of evolving anisotropy on the stress-strain behaviour of unsaturated soils. In order to achieve this objective, an extensive campaign of laboratory tests on both isotropically and anisotropically compacted soil samples under a wide range of stress paths was performed. These experimental data were then employed to develop an elasto-plastic model for unsaturated soils accounting for evolving anisotropy.

The objectives of the project can be summarised as follows:

- To set up the necessary laboratory equipment for triaxial testing of unsaturated and saturated samples in triaxial compression and triaxial extension;
- To investigate experimentally the yielding behaviour of isotropically and anisotropically compacted soil samples under different levels of suction;
- To investigate experimentally the effect of plastic straining on changing fabric anisotropy in unsaturated soils and the influence of this evolving anisotropy on yielding behaviour;
- To investigate experimentally the influence of initial and evolving anisotropy on critical states;
- To investigate the advantages and disadvantages of using alternative unsaturated constitutive variables during analysis of yielding and critical states;
- To develop, in the light of the gathered experimental results, an elasto-plastic constitutive model describing the behaviour of unsaturated (and saturated) soils including the effect of evolving anisotropy on stress-strain behaviour;

- To investigate capabilities and limitations of the proposed model via simulation of the behaviour observed during the experiments;
- To propose, if necessary, improvements to the proposed constitutive model in order to enhance predictions.

#### **1.4 THESIS LAYOUT**

The preceding sections of this chapter have discussed the need for taking into account evolving anisotropy in unsaturated soil models and have outlined the objectives of the present project.

Chapter 2 starts by reviewing the fundamental concepts of unsaturated soil mechanics, such as suction and constitutive variables, and by describing volume change, shear strength and water retention of unsaturated soils, including the influence of fabric anisotropy on these aspects of soil behaviour. The next section discusses soil yielding (including some of the common methods for identification of yield points from experimental data) and the changes of soil fabric due to plastic straining. Possible mathematical forms of yield surface and plastic potential are also reviewed. A background review of some elasto-plastic models for saturated and unsaturated soils relevant to this study is also provided.

Chapter 3 describes the laboratory equipment used to undertake the experimental campaign, including a double wall triaxial cell for testing unsaturated soil samples and a conventional triaxial cell for testing saturated soil samples. The calibration of all gauges used for controlling or measuring pressure, volume, displacement, etc. is also described in this chapter.

Chapter 4 describes the method used for compaction of both isotropic and anisotropic soil samples. This chapter also describes the methodology for setting up and performing the tests in the saturated and unsaturated triaxial cells and describes the procedures adopted for processing raw data during tests.

Chapter 5 presents the main body of experimental results. Initially, the properties of all samples after compaction are presented together with a discussion of the stress paths followed in the different test series. The results of suction equalisation stages for all tests are subsequently presented. The later part of the chapter discusses the stress-strain curves of triaxial tests performed to investigate the yielding properties of unsaturated soil samples either in the as-compacted state or after preliminary loading to alter initial anisotropy.

Chapter 6 provides further interpretation of the test results shown in Chapter 5 including a detailed investigation of the shape of the yield surface and critical state behaviour. The selection of soil constants, such as elastic indices and slopes of normal compression and critical state lines is also discussed in detail. Elastic, yielding and critical state behaviour are all interpreted in terms of two alternative sets of constitutive variables highlighting advantages and disadvantages for each set.

Chapter 7 describes the development of a new anisotropic elasto-plastic constitutive model for unsaturated soils. New constitutive relationships describing elastic behaviour, yielding (including hardening laws and flow rules) and critical states are presented.

Chapter 8 investigates the performance of the proposed model by conducting simulations of the tests presented in Chapter 5 and comparing the simulations with the corresponding experimental results. Calibration of soil constants and selection of initial state are also discussed. The methodology followed for performing model simulations is described in detail. A representative set of model simulations, for a wide range of triaxial stress paths, is presented, including simulations of tests on both isotropically and anisotropically compacted samples at different suctions. The capabilities and limitations of the proposed model in predicting the soil response are therefore investigated in this chapter.

Finally, Chapter 9 presents the conclusions drawn from the current project and gives recommendations for future work.

# 2

## BEHAVIOUR AND MODELLING OF UNSATURATED SOILS AND THE INFLUENCE OF ANISOTROPY

### 2.1 SUCTION IN UNSATURATED SOILS

Total soil suction measures the negative thermodynamic potential of soil pore water (expressed in dimensions of pressure) relative to a reference potential of pure water that is free of dissolved solutes and is at the same pressure as the pore air (Lu and Likos, 2004). Under conditions of equilibrium across the air-water interface (no net evaporation or condensation) total suction  $\psi_T$  can be quantitatively described by Kelvin's equation (Sposito 1981) as follows:

$$\psi_T = -\frac{R T \rho_w}{m_w} \ln \left[ \frac{u_v}{u_{v0}} \right] \quad (2.1)$$

where  $R$  is the universal gas constant (8.314 J/mol K),  $T$  is the absolute temperature (K),  $m_w$  is the molecular mass of water vapour (18.016 kg/kmol),  $\rho_w$  is the density of water,  $u_v$  is the partial pressure of pore-water vapour and  $u_{v0}$  is the saturation pressure of water vapour over a flat surface of pure water at the same temperature. The term  $u_v/u_{v0}$  is the relative humidity  $RH$ , which is defined as the ratio of partial pressure of water vapour in the air to the saturation pressure of water vapour at the same temperature. Total suction  $\psi_T$  has a crucial role in governing the flow of liquid water through an unsaturated soil. Flow of liquid water is caused by a gradient in total potential, which is made up of the (negative) total suction and a gravitational term  $\rho_w g z$  (where  $z$  is the elevation relative to a reference horizontal datum).

The total suction  $\psi_T$  can be divided into two of components, namely: matric suction  $s$  and osmotic suction  $\psi_{os}$ :

$$\psi_T = s + \psi_{os} \quad (2.2)$$

According to Baker and Frydman (2009), matric suction is an addition of two energy components (per unit volume), namely capillary potential  $\psi_{cp}$  and adsorption potential

$\psi_{ad}$  which is associated with the adsorbed water film surrounding clay platelets and particles:

$$s = \psi_{cp} + \psi_{ad} \quad (2.3)$$

On the other hand,  $s$  is commonly defined as simply the excess of pore air pressure  $u_a$  over the pore water pressure  $u_w$ :

$$s = u_a - u_w \quad (2.4)$$

Equation 2.4 is considered valid for the case where the capillary potential dominates, however, questions are raised for the validity of this expression when the adsorbed potential is dominant (Baker and Frydman 2009).

Water in an unsaturated soil can exist in different forms: bulk water which fills the water-flooded void spaces; meniscus water which forms “rings” or “bridges” around the inter-particle contacts surrounded by air-filled voids; and adsorbed water which is bound to soil particles by electro-chemical forces and acts as a part of the soil skeleton (Wheeler and Karube, 1996). An idealised picture of the bulk and meniscus water is shown in Figure 2.1.

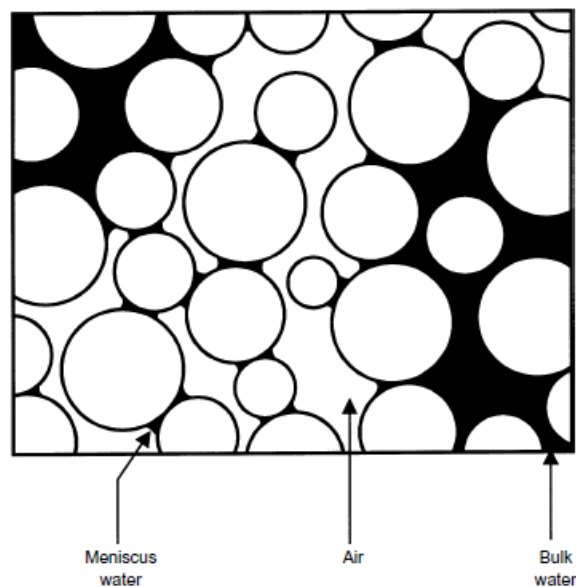


Figure 2.1 Bulk water and meniscus water (Wheeler et al., 2003a)

Matric suction can be related to the surface tension  $T_s$  at the air-water interface and the principal radii of curvature of the interface  $R_1$  and  $R_2$  (see Figure 2.2) by using force equilibrium in the direction perpendicular to the interface to give:

$$s = T_s \left( \frac{1}{R_1} + \frac{1}{R_2} \right) \quad (2.5)$$

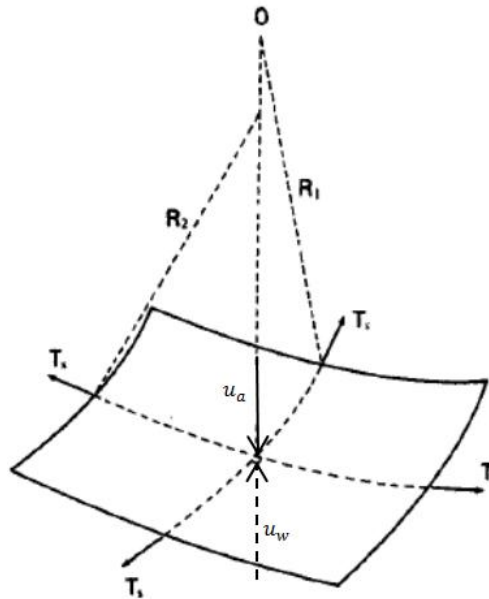


Figure 2.2 Surface tension at an air-water interface (Fredlund and Rahardjo, 1993)

Osmotic suction is related to the concentration of dissolved salts in the pore fluid. According to Blatz et al. (2008), osmotic suction is important in highly plastic clays (due to the clay mineralogy) and when active dissolved salts exist in the pore water.

## 2.2 STRESS STATE VARIABLES

Stress state variables are those variables which are sufficient to characterize completely the mechanical behaviour of the soil. For saturated or dry soils, a single (tensorial) stress state variable is required; the “effective stress” defined by Terzaghi (1936), which takes the form:

$$\sigma'_{ij} = \sigma_{ij} - u\delta_{ij} \quad (2.6)$$

where  $\sigma'_{ij}$  is the effective stress tensor,  $\sigma_{ij}$  is the total stress tensor,  $u$  is the pore pressure and  $\delta_{ij}$  is Kronecker’s delta. Equation 2.6 states that the normal effective stress acting on a given plane is the excess of the corresponding normal total stress over the pore pressure, whereas the effective shear stress on a given plane is equal in value to the corresponding total shear stress. The stress state variable was found to be sufficient to fully describe all the measurable effects of stress changes on the mechanical behaviour of a soil in a saturated or dry state.

For unsaturated soils, early workers investigated the possibility of using of single (tensorial) stress state variable similar to that for saturated soils. One of the earliest and most well-known contributions was by Bishop (1959), who suggested the following general form of the “effective stress” tensor in an unsaturated soil:

$$\sigma'_{ij} = \sigma_{ij} - [\chi u_w + (1 - \chi)u_a] \delta_{ij} \quad (2.7)$$

where  $\chi$  is a parameter which depends on the degree of saturation. Under saturated or dry conditions, the parameter  $\chi$  takes values of 1 and 0 respectively and Equation 2.7 reduces to Equation 2.6. Other researchers including, for example, Croney et al. (1958), Jennings (1960), Aitchison (1961) and Richards (1966), suggested different forms for the effective stress as a unique stress state variable for unsaturated soils. However, the concept of using a single (tensorial) stress state variable (i.e. effective stress) was shown to be insufficient for unsaturated soils. Jennings and Burland (1962) concluded that Equation 2.7 was not sufficient to predict the “collapse compression” sometimes observed during wetting (suction decrease) under a constant total stress. Equation 2.7 will always predict swelling on wetting from an unsaturated state to a saturated state as a result of decrease of effective stress. This deficiency was also acknowledged by other researchers (e.g. Bishop & Blight, 1963; Burland, 1965 and Matyas & Radhakishna, 1968). It was therefore widely accepted that the behaviour of unsaturated soils could not be represented in terms of a single (tensorial) stress state variable.

Bishop & Blight (1963) experimentally examined the use of two stress variables, the net stress tensor  $\sigma_{ij} - u_a \delta_{ij}$  and the scalar matric suction  $u_a - u_w$  by conducting various types of oedometer tests and triaxial tests in which total stresses,  $u_a$  and  $u_w$  were varied. They concluded that net stress and suction are valid stress variables for unsaturated soils. The two independent stress variables of net stress tensor ( $\sigma_{ij} - u_a \delta_{ij}$ ) and the scalar matric suction ( $u_a - u_w$ ) received high attention with the proposition of early elasto-plastic soil models such as, for example, those proposed by Alonso et al. (1990) and Gens & Alonso (1992) in which the authors employed these stress variables to describe the stress state. Various alternative pairs of stress state variables for unsaturated soils are explained in the review articles of Wheeler and Karube (1996) and Gens et al. (2006).

Subsequently, it was realised that employing only matric suction to describe how unsaturated the soil is implies a shortcoming if there is a non-unique relationship between degree of saturation and suction, because of the effects of hydraulic hysteresis (see, for example Wheeler et al. (2003a)). This means that, with a model expressed in terms of net stresses and matric suction, an additional piece of information associated to

the degree of saturation,  $S_r$ , is required in order to give a complete description of soil behaviour. Instead, several authors expressed their constitutive models in terms of two stress state variables, the first of which involves the degree of saturation and is similar to Bishop's effective stress of Equation 2.8, and the second of which is matric suction or some function of matric suction (e.g. Kohgo et al., 1993a; Kohgo et al., 1993b; Bolzon et al., 1996; Loret & Khalili, 2000; Loret & Khalili, 2002; Gallipoli et al., 2003a; Wheeler et al., 2003a; Sheng et al., 2004 and Santagiuliana & Schrefler, 2006).

The work by Wheeler et al. (2003a) is a particular example of the use of two stress state variables where the first is a Bishop's type stress state variable. Wheeler et al. (2003a) defined the first stress variable as a tensor given by:

$$\sigma_{ij}^* = \sigma_{ij} - [S_r u_w + (1 - S_r) u_a] \delta_{ij} = \sigma_{ij} - u_a \delta_{ij} + S_r s \delta_{ij} \quad (2.8)$$

where  $\sigma_{ij}$  is the total stress tensor and  $\delta_{ij}$  is Kroneker's delta.  $\sigma_{ij}^*$  is called the "Bishop's stress" tensor by Wheeler et al. (2003a) and Bolzon et al. (1996) whereas it is called the "average soil skeleton stress" tensor by Jommi (2000) to reflect the effects on the soil skeleton of the total stress, air pressure within the portion of the pores that is air-filled and pore water pressure within the portion of the pores that is water-filled (i.e. the bulk water). Because of the fact that the first stress state variable (i.e. the Bishop's stress tensor) does not account for the additional bonding effects caused by the presence of meniscus water on inter-particle forces (see Section 2.3.1 below), the mechanical behaviour cannot be described solely in terms of this stress variable. The model proposed by Wheeler et al. (2003a) assumes that the yielding behaviour is also influenced by the degree of saturation  $S_r$  (or, more strictly, by plastic change in  $S_r$ ), with changes of  $S_r$  then related to the variation of a second stress state variable referred to as "modified suction",  $s^*$ , given by:

$$s^* = n s \quad (2.9)$$

where  $n$  is the porosity. This choice of  $s^*$  as the second stress state variable was based on the theoretical analysis by Houlsby (1997), which showed that the stress variables  $\sigma_{ij}^*$  and  $s^*$  are work conjugates with the strain increment variables  $d\varepsilon_{ij}$  and  $-dS_r$  respectively. The model proposed by Wheeler et al. (2003a) forms a complete mechanical and water retention model, expressed in terms of the two stress state variables of the Bishop's stress tensor and the scalar modified suction.

Alonso et al. (2010) showed that the term  $S_r s$  in Equation 2.8 becomes unrealistically large for many clayey soils when suction increases to high levels because the soil tends to maintain a relatively high degree of saturation even at high suction values. Instead, Alonso et al. (2010) suggested a ‘microstructurally based effective stress’ based on the idea that a portion of pore water is held by clay minerals and cannot move freely during the process of filling or emptying of the pores. This effective stress tensor is (again) simply the first of two stress state variables and given by:

$$\sigma_{ij}^* = \sigma_{ij} - u_a \delta_{ij} + S_r^e s \delta_{ij} \quad (2.10)$$

where  $S_r^e$  is the effective degree of saturation, which measures the available water that is free to move within the macropores and ranges between 1 for the case where soil is fully saturated and zero when all water is held by the micropores. Hence, to calculate  $S_r^e$ , the volume of water held by the micropores must be known. Alonso et al. (2010) showed that the volume of water in micropores could be determined with different techniques (e.g. porosimetry or from the water retention curve).

## 2.3 ASPECTS OF UNSATURATED SOIL BEHAVIOUR

Researchers in the field of unsaturated soils have made significant progress towards understanding the patterns of unsaturated soils behaviour through investigation of the volume change, shear strength and water retention behaviour of these soils.

### 2.3.1 Volume change

#### Loading/unloading at constant suction

Typically, an unsaturated soil sample shows gradual decrease in its volume when loaded (isotropically or under oedometeric conditions) at a given constant suction. When loading passes a yield stress, irreversible (plastic) volume changes commence due to slippage at inter-particle or inter-aggregate contacts. For identical samples loaded at different suction levels, the yield stress increases with increasing suction. This response can be explained by the role of “meniscus water bridges” at the particle contacts surrounded by air-filled voids as shown in Figure 2.3. As explained by Wheeler and Karube (1996), application of external stress will cause an increase in the tangential forces as well as to the normal forces at the inter-particle contacts, while application of suction within the meniscus water bridges will cause an increase in normal forces only. In Figure 2.3  $N_\sigma$  is the normal component of inter-particle force due to external stress,  $T_\sigma$  is the tangential component of inter-particle force due to external stress and  $N_s$  is the inter-particle force due to the meniscus water bridge. An increase of suction therefore provides additional stabilisation against inter-particle slippage (yielding).

It is generally observed that both the position and the slope of the normal compression line (*NCL*) in a plot of specific volume  $v$  against mean net stress  $\bar{p}$  (where  $\bar{p} = p - u_a$ ), are suction-dependent (see Figure 2.4). For some soils the slope of the *NCL* decreases with increasing suction (see Alonso et al. 1990) whereas for other soils the slope generally increases with increasing suction (e.g. Wheeler and Sivakumar, 1995, as shown in Figure 2.4).

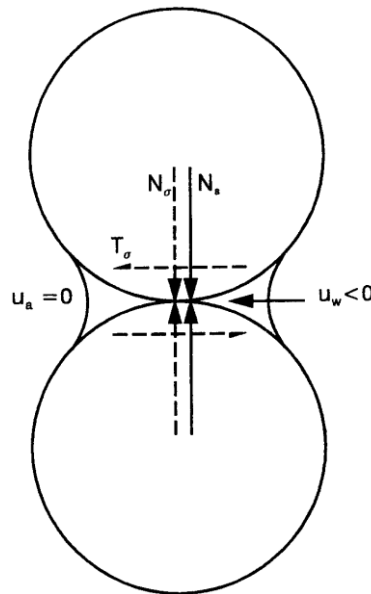


Figure 2.3 Inter-particle forces caused by external stress and meniscus water bridges (Wheeler and Karube, 1996)

Unsaturated soils usually show swelling during unloading stages performed under oedometric conditions or isotropic stress states, see Figure 2.5. Usually, the swelling behaviour is regarded as elastic and linear when the net stress is plotted on a logarithmic scale. The gradients of swelling lines are also generally assumed to be approximately suction-independent as suggested by many researchers (e.g. Alonso et al., 1990; Sivakumar, 1993; and Raveendraraj, 2009).

### Volume change due to wetting or drying at constant net stress

If a wetting stage (reduction of suction) is performed at low value of net stress, the unsaturated soil swells whereas if a wetting stage is performed at a high value of net stress it shows a reduction of volume, commonly termed as collapse compression. During drying (increase in suction), the soil always show a reduction of volume (shrinkage).

Alonso et al. (1987) proposed a yield curve in the  $s:\bar{p}$  plane, known as the Loading-Collapse (*LC*) yield curve, with collapse-compression during wetting stages treated as plastic deformation that results when the stress state reaches the *LC* curve. This idea of

the *LC* yield curve was subsequently employed by Alonso et al. (1990) in developing of the Barcelona Basic model (*BBM*), the first elasto-plastic constitutive model for unsaturated soils. Further explanation of the *BBM* model is provided in Section 2.8.1. Alonso et al. (1990) also proposed that when suction increases beyond the maximum past suction that the soil ever experienced then yielding will take place on a second yield curve referred to as the Suction Increase (*SI*) yield curve.

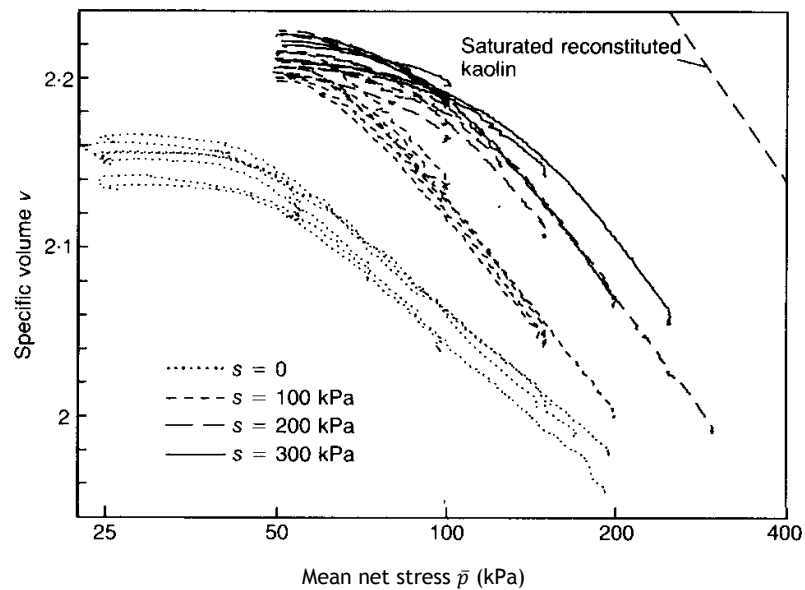


Figure 2.4 Volume change under isotropic loading at constant suction performed on compacted kaolin (Wheeler and Sivakumar, 1995)

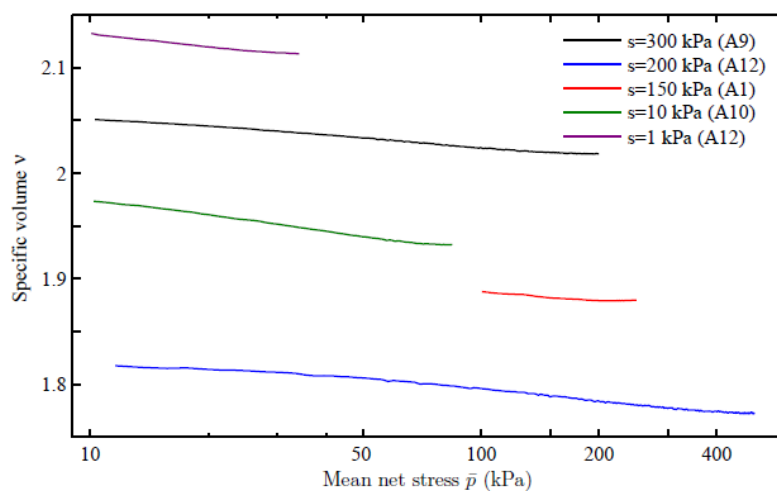


Figure 2.5 Volume change under isotropic unloading at constant suction performed on compacted kaolin (Raveendraraj, 2009)

### 2.3.2 Shear strength

Using net stress and matric suction as the two stress state variables to describe unsaturated soil behaviour, Fredlund et al. (1978) proposed the following expression for shear strength:

$$\tau = c' + (\sigma - u_a) \tan \phi' + (u_a - u_w) \tan \phi^b \quad (2.11)$$

where  $(\sigma - u_a)$  is the normal net stress on the failure plane,  $c'$  and  $\phi'$  are the cohesion intercept and friction angle respectively for saturated conditions and  $\phi^b$  is a friction angle with respect to suction. Equation 2.11 represents a planar failure surface in  $\tau:(\sigma - u_a):(u_a - u_w)$  space that reduces to the conventional Mohr-Coulomb failure envelope (a line in the  $\tau - \sigma'$  plane) under saturated conditions. If  $\phi^b$  is a constant, Equation 2.11 predicts a linear increase of shear strength with suction. Subsequently, many researchers (e.g. Escario and Saez, 1986 and Gan et al., 1988) provided experimental evidence that shear strength increases in a nonlinear fashion with suction. Fredlund et al. (1987) suggested that  $\phi^b$  is equal to  $\phi'$  when soil remains saturated (at low suction below the air entry values) and  $\phi^b$  decreases with increasing suction as soil becomes unsaturated.

Based on the single effective stress approach proposed by Bishop (1959), Bishop and Donald (1961) substituted the Bishop's stress (see Equation 2.7) into the Mohr-Coulomb equation to get the following equation for shear strength of an unsaturated soil:

$$\tau = c' + [(\sigma - u_a) + \chi (u_a - u_w)] \tan \phi' \quad (2.12)$$

Khalili and Khabbaz (1998) and other authors employed a two stress state variable approach, with Bishop's stress as the first stress variable, but agreed that shear strength could be related solely to this first stress variable by Equation 2.12. Khalili and Khabbaz (1998) proposed that  $\chi$  could be calculated from an empirical expression that relates the current soil suction to the air entry value of the soil. Khalili et al. (2004) examined the validity of Equation 2.12 experimentally and found good agreement between measured and predicted shear strength values.

Similarly, Alonso et al. (2010) used a two stress state variable approach for overall behaviour, but with the effective stress given by Equation 2.10 as the first stress state variable, and they suggested that shear strength could be related exclusively to this first stress state variable by:

$$\tau = c' + [(\sigma - u_a) + S_r^e (u_a - u_w)] \tan \phi' \quad (2.13)$$

Alonso et al. (2010) used the information of the water retention curves of different soils to illustrate the capability of Equation 2.13 in predicting reasonably well the shear strength. They showed that the effective degree of saturation  $S_r^e$  could be related to the overall degree of saturation through two material constants.

Vanapalli et al. (1996) proposed an empirical/analytical model to predict shear strength for unsaturated soils by making use of the water retention curve in addition to shear strength parameters for saturated conditions. However, other authors (e.g. Raveendaraj, 2009) have questioned the physical justification for relating shear strength to the water retention behaviour arguing that the physical reasons for an increase of shear strength with increasing suction are not entirely the same as those for a decrease of degree of saturation with increasing suction.

### 2.3.3 Water retention behaviour

The variation of the degree of saturation or water content (volumetric or gravimetric) with suction (matric or total suction) is referred to as a water retention curve or soil-water characteristic curve. This relationship was used first in Soil Science by Buckingham (1907). The main purposes of investigating water retention behaviour from the Soil Science point of view are to predict the water storage capacity of the soil, unsaturated flow and the stability of soil aggregates at different suction levels. From a geotechnical engineering point of view, water retention behaviour is important due to its role in coupled hydro-mechanical boundary value problems. It will also influence mechanical behaviour at the level of an individual point if degree of saturation (rather than simply matric suction) has an influence on mechanical behaviour (e.g. due to the use of a stress state variable such as the Bishop's stress tensor of Equation 2.8).

The central features of water retention behaviour can be summarised as below with help of Figure 2.6.

- On drying from a saturated condition, at a given constant void ratio, degree of saturation stays almost unchanged until a specific value of suction is reached, referred to as the air entry value;
- On drying from a saturated condition, at a given constant void ratio a unique path is followed, referred to as the main drying curve;
- On wetting from a dry condition, at a given constant void ratio, a new unique path is followed referred to as the main wetting path;

- Reversing the direction of suction change shows hysteretic behaviour. Reversing suction from any position on the main drying or main wetting curve results in following new transitory non-unique paths referred to as scanning curves. Scanning curves are fully enclosed by the main drying and main wetting curves.

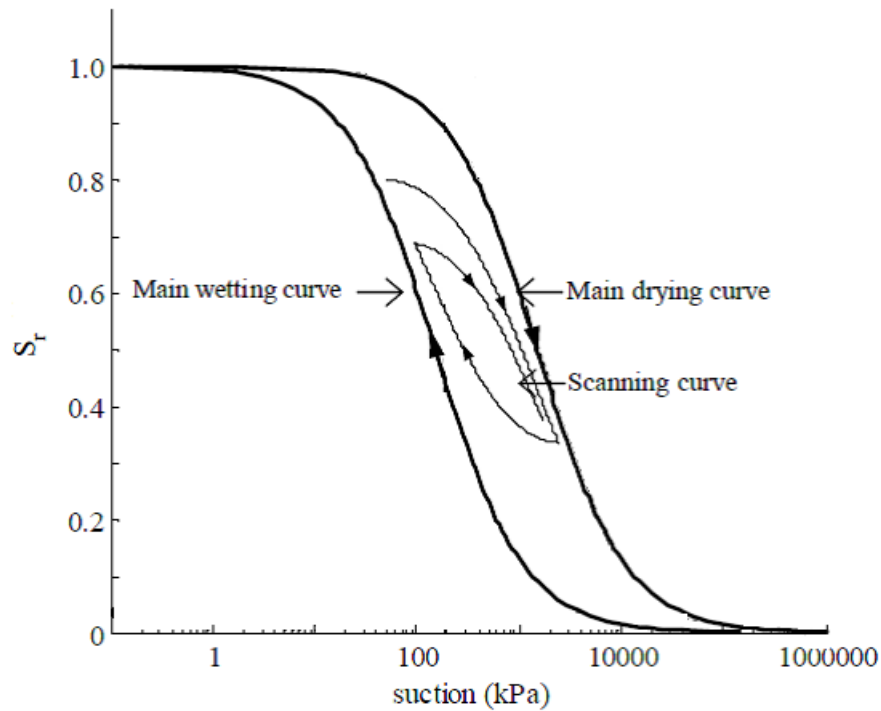


Figure 2.6 Typical water retention behaviour for a fine-grained soil (after Raveendiraraj, 2009)

The water retention behaviour is also influenced by changes of void ratio as a result of changing the dimensions of voids and of connecting passageways. For example, a decrease of void ratio results in shifting the main wetting curve and main drying curve to higher suction levels to reflect the increasing difficulty in flooding or emptying the voids. The effect of void ratio on the water retention behaviour has been studied by many authors (e.g. Gallipoli et al., 2003b).

### Basic expressions for water retention curves

Numerous constitutive expressions to characterise the water retention response have been proposed to date. Most of these expressions approximate the experimental measurements by a power-law variation of degree of saturation or water content with suction. Examples of widely used empirical expressions that describe either the main drying curve or the main wetting curve are shown in this section.

Brooks and Corey (1964) proposed that:

$$S_r = \left(\frac{a}{s}\right)^b \quad \text{for } s \geq a \quad (2.14)$$

where  $a$  is the air entry value of the soil and  $b$  is a parameter related to the pore-size distribution. Equation 2.14 has been validated against experimental data by many authors (e.g. Campbell, 1974). The form of Equation 2.14 is very simple in terms of the required number of fitting parameters, but it does involve a discontinuity of gradient at  $s = a$ , which may not be a good match to experimental behaviour.

Van Genuchten (1980) proposed that:

$$S_r = [1 + (\alpha s)^n]^{-m} \quad (2.15)$$

where  $\alpha$ ,  $n$  and  $m$  are parameters related to the air entry value of the soil, slope of retention curve and asymmetric shape of the curve respectively. Equation 2.15 appears more flexible than Equation 2.14 as it includes one further fitting parameter. Furthermore, Equation 2.15 is a continuous function with no discontinuity of gradient as in Equation 2.14.

Various other authors proposed different expressions for the main drying curve or the main wetting curve. These expressions could be viewed as modified versions of the Van Genuchten (1980) expression. For example, Fredlund and Xing (1994) suggested the following expression based on pore size distribution:

$$S_r = [\ln(e + (\alpha s)^n)]^{-m} \quad (2.16)$$

where  $\alpha$ ,  $n$  and  $m$  are parameters related to the air entry value of the soil, slope of retention curve and asymmetric shape of the curve respectively ( $e$  is the base of natural logarithms). Fredlund and Xing (1994) showed that Equation 2.16 provides a good fit for a wide range of soils over suction values ranging from 0 to 1000 MPa. Features of each individual expression shown above are discussed in detail by Leong and Rahardjo (1997).

### **Expressions accounting for influence of changes of void ratio**

Due to the dependency of degree of saturation on the void ratio (in addition to suction), expressions such as Equations 2.14, 2.15 and 2.16 are not able to predict accurately the water retention behaviour for cases where void ratio is varying. Romero and Vaunat (2000) suggested that the water retention curve at constant void ratio could be fitted by

a modified form of Van Genuchten (1980) expression, but that the values of parameters  $\alpha$ ,  $n$  and  $m$  would be different for different values of void ratio.

Gallipoli et al. (2003a) showed that, for a main wetting curve (or main drying curve), based on analysis of experimental data of triaxial tests on compacted kaolin, the fitting parameters  $n$  and  $m$  in the Van Genuchten (1980) expression of Equation 2.15 could be taken as constants, whereas the parameter  $\alpha$  could be related to void ratio  $e$  by a power law relationship to give:

$$S_r = [1 + (\Phi e^\Psi s)^n]^{-m} \quad (2.17)$$

where  $\Phi$ ,  $\Psi$ ,  $n$  and  $m$  are soil constants.

### **Water retention models accounting for influence of hydraulic hysteresis**

Some authors such as Vaunat et al. (2000) proposed water retention models accounting for the effects of changes of void ratio and hydraulic hysteresis on retention behaviour. In order to capture the influence of void ratio on the retention behaviour, these models must be integrated with an elasto-plastic mechanical model such *BBM*.

Wheeler et al. (2003a) proposed a coupled mechanical and water retention constitutive model. The central feature of the water retention aspects of this model is its capability of reproducing the hydraulic hysteresis and the influence of void ratio on degree of saturation. Variation of degree of saturation is related to variation of the modified suction  $s^*$  (defined in Equation 2.9) and to the occurrence of any plastic volumetric strain. In the absence of plastic volumetric strains, the model assumes that any movement along the main drying or main wetting curves produces an elasto-plastic change in the degree of saturation, with the main drying and main wetting paths represented by two parallel lines with a unique slope  $\lambda_s$  in the  $S_r : \ln s^*$  plane (see Figure 2.7). Scanning curves are represented by straight lines with a unique gradient  $\kappa_s$  and produce only elastic change in the degree of saturation. The model also assumes that plastic volumetric strains cause a lateral shift of the main drying and main wetting curves in the  $S_r : \ln s^*$  plane (hence producing dependency of water retention on changes of void ratio).

## **2.4 YIELDING OF SOILS**

### **2.4.1 Yielding of saturated soils**

Generally, yield stresses are any possible stress combinations that define the limit of the elastic range and beyond which plastic deformation will occur (Yu 2006). Yielding in

saturated soils refers to the occurrence of plastic deformation of the soil fabric under the application of a change of effective stresses. Yielding in soils involves slippage at inter-particle contacts, resulting in a re-organisation of the packing of soil particles, with the possibility of this resulting in a denser or looser packing. Plastic volumetric strains therefore occur in soils (unlike metals), and yielding is often indicated by a significant change in the rate of volumetric straining. Yield stress is also termed “preconsolidation pressure” or “past maximum pressure” in the geotechnical field (Lamb and Whitman 1969). Although the latter terms reflect the influences of previous loading history on stress-strain behaviour of soil, they are less recognised in classical plasticity than yield stress.

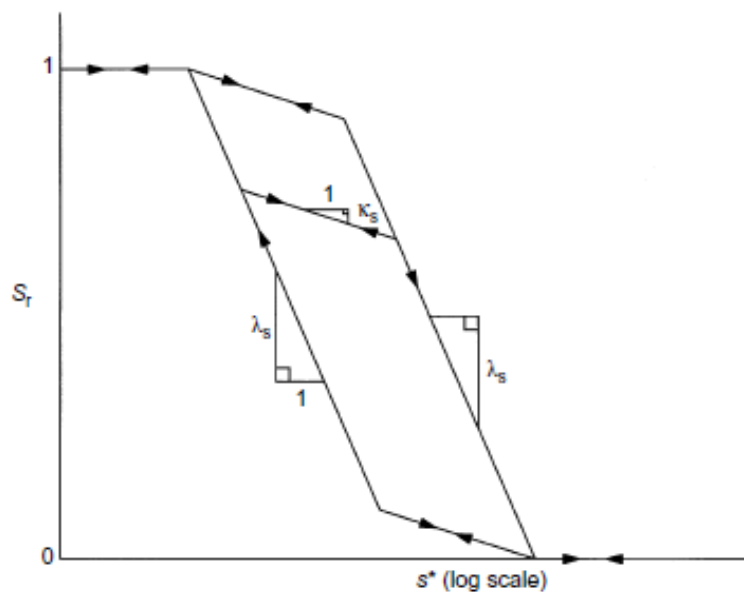


Figure 2.7 Water retention behaviour model (Wheeler et al., 2003a)

Smith et al. (1992) conducted a series of triaxial probing tests on saturated samples of natural Bothkennar clay in order to study the yield behaviour of this clay. The yield stresses were identified from plots in the mean effective stress-volumetric strain plane and in deviator stress-shear strain plane. Smith et al. (1992) considered three boundaries in stress space, based on data from their experimental stress-strain curves, (see Figure 2.8); The first boundary (curve  $Y1$ ) encloses the linear elastic zone, the second boundary (curve  $Y2$ ) encloses the nonlinear elastic zone and the third boundary (curve  $Y3$ ) defines onset of substantial amounts of plastic deformation. As explained in Smith et al. (1992), the size of  $Y1$  is very small so that linear elastic behaviour occurs only for small stress changes (and exceptionally small strains). Once the stress state is between  $Y1$  and  $Y2$  the tangent stiffness reduces rapidly but with fully recoverable strains and hence no slippage at inter-particle contacts is expected to occur. When the stress state is between  $Y2$  and

$Y_3$  very small irrecoverable stains occur. Once the stress state reaches  $Y_3$ , soil particles start to move substantially relative to each other and this produces large irrecoverable strains. On the basis of the above boundaries, it is clear that yielding is not the single clear-cut phenomenon assumed in classical elasto-plastic constitutive models, where it is generally assumed that the yield curve marks a sudden transition from linear (or almost linear) elastic behaviour to the occurrence of substantial plastic strains.

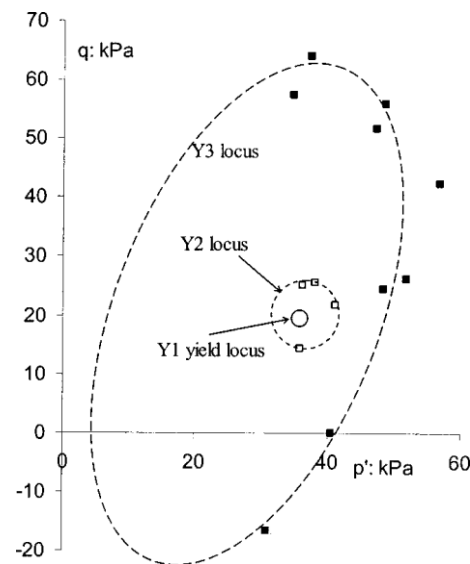
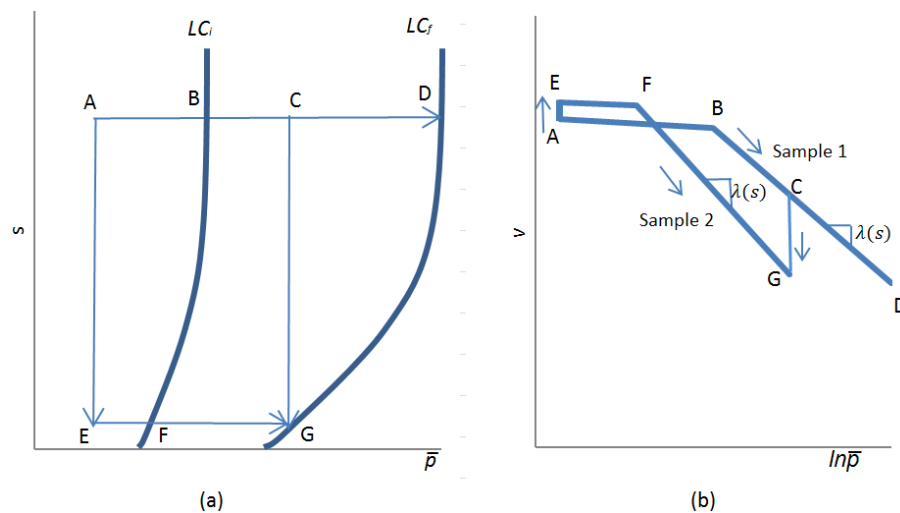


Figure 2.8 Yielding of Bothkennar Clay (yield points were deduced by Muir Wood, 2004, from stress-strain curves in Smith et al., 1992)

#### 2.4.2 Yielding of unsaturated soils

Yielding in an unsaturated soil can be produced by a change of stress state variables. If the net stress tensor and the matric suction are considered to be the stress state variables, then yield behaviour under isotropic stress states can be well explained by using the conceptual  $LC$  curve proposed by Alonso et al. (1987). Consider two identical unsaturated samples (i.e. Sample 1 and Sample 2) both having the same initial stress state given by point  $A$  (inside the elastic domain, see Figure 2.9a). Subsequently, Sample 1 is compressed isotropically at a constant suction to point  $D$  and Sample 2 is wetted to new lower suction value, given by Point  $E$ , then compressed isotropically to Point  $G$ . The compression curves of the two samples would be similar to those shown in Figure 2.9b. Because wetting of Sample 2 is conducted inside the elastic domain, swelling would be expected during wetting as shown by  $A - E$  in Figure 2.9b. The elastic domain is expected to be larger for Sample 1 than that for Sample 2 due to the stabilising effect of meniscus water bridges at the inter-particle contacts as explained earlier. Samples 1 and 2 yield at Points  $B$  and  $F$  respectively on the initial location of the  $LC$  curve (i.e.  $LC_i$ )

which is produced by the previous loading history. Subsequent loading of Samples 1 and 2 to points  $D$  and  $G$  respectively causes plastic compression in the samples and consequently shifts the  $LC$  curve to a new position given by  $LC_f$ . As mentioned previously, the slope of virgin compression line,  $\lambda(s)$ , is suction dependent and therefore different values for  $\lambda(s)$  for Samples 1 and 2 are expected. To illustrate that yielding can occur during wetting, one can imagine that the isotropic stress path of Sample 1 is terminated at Point  $C$  and a wetting stage is commenced along  $C - G$ , see Figure 2.9a. Wetting along  $C - G$  produces substantial plastic “collapse compression” as shown by  $C - G$  in Figure 2.9b. A crucial advance achieved by Alonso et al. (1987) and in the  $BBM$  model by Alonso et al. (1990) was therefore that the occurrence of plastic strains during both loading and wetting were recognised as essentially the same phenomenon, with both represented by yielding on a single yield surface.



**Figure 2.9 Yielding of an unsaturated soil under isotropic stress states: (a) stress paths and  $LC$  yield curve, (b) compression curves (after Alonso et al., 1990)**

Alonso et al. (1990), showed experimental evidence that yielding and the occurrence of plastic volumetric strain could also occur during drying stages (increase of suction). Alonso et al. (1990) represented this within the  $BBM$  by the inclusion of a second yield curve known as the Suction Increase ( $SI$ ) yield curve, see Section 2.8.1). This suggests that yielding on drying should occur at the maximum value of suction previously applied. However, subsequent experimental evidence (as discussed in Wheeler et al., 2003a) showed that yielding on drying can occur at a suction significantly lower than the maximum value of suction previously applied. Wheeler et al. (2003a) captured this aspect of behaviour within their coupled mechanical-water retention model, where the occurrence of plastic strains during loading, wetting and drying are all recognised as a

single phenomenon, corresponding to yielding on a single yield surface (as will be discussed in Section 2.9).

### 2.4.3 Empirical and graphical methods for yield identification

Due to the fact that yield stresses are an important aspect of the stress-strain response of soils, numerous methods have been proposed since the 1930's to determine values of yield stress from experimental test results. Because soil mechanics was initially established based mainly on saturated conditions, the majority of studies concerning yield stress identification assumed that the stress state could be expressed in terms of effective stresses.

Because stress-strain curves typically show non-linear behaviour and a gradual onset of plastic strains (see Section 2.4.1), empirical or semi-empirical methods are usually used to determine yield stresses (Graham et al., 1988). Graphical techniques are widely used for this purpose, although these techniques involve significant amount of judgement and some may involve scale-dependency (Becker et al., 1987 and Grozic et al., 2003).

Yielding for many typical stress paths (isotropic loading, oedometeric loading and triaxial shearing) will generally involve the onset of significant plastic volumetric strains (i.e. plastic changes of specific volume  $v$ ), whereas for some of these stress paths plastic shear strains may not occur or may not be measured. In addition, both pre-yield and post-yield behaviour will often appear more linear when stress is plotted on a logarithmic scale. As a consequence, yield stress identification for saturated soils is often performed using a  $v: \ln p'$  plot (or a  $v: \ln \sigma'_v$  plot for oedometeric loading).

One of the most common methods of determining the yield stress from an experimental  $v: \ln p'$  plot (or a  $v: \ln \sigma'_v$  plot for oedometeric loading) is to idealise pre-yield behaviour by a straight line and post-yield behaviour by a second straight line (a bi-linear approximation) and then to determine the yield stress from the intersection of these two straight lines. This can be difficult, and prone to considerable subjectivity, if the onset of plastic straining is rather gradual and either the pre-yield behaviour or the post-yield behaviour is poorly matched by a linear approximation.

An alternative to the simple intersection point of a bi-linear approximation is the empirical technique that was proposed by Casagrande (1936) to estimate yield stress from oedometer tests. The first step of this technique requires visual detection of the point of maximum curvature on the compression curve in the  $v: \ln \sigma'_v$  plane. Unfortunately, this technique involves a substantial amount of subjectivity and it is also

dependent on the scale selected for plotting of the two axes. In addition, in many cases, the Casagrande technique leads to overestimation of the yield stress compared to other methods. Pacheco Silva (1970) proposed an alternative empirical technique to determine yield stress from the  $v:\ln p'$  plane which does not require detection of the point of maximum curvature in the compression curve. However, the approach was found to overestimate yield stress as in the previous method by Casagrande (1936).

Butterfield (1979) suggested plotting the results of oedometer tests in the  $\ln v:\ln p'$  plane and determining the yield stress from the intersection of a bi-linear approximation. Further empirical methods for determining yield stress from oedometer tests can be found in works such as those by Burland (1990) and Boone (2010).

The ability to detect yield stresses for a wide variety of different stress paths is an issue that arises when analysing experimental results of probing tests (Graham et al., 1982). Graham et al. (1982) presented bi-linear interpretation of experimental data from triaxial tests on various clays in  $v:p'$  and  $q:\varepsilon_a$  planes where  $\varepsilon_a$  is the axial strain. They concluded that using intersection points of bi-linear approximations using linear scales (as an alternative to semi-logarithmic plotting) could reduce subjectivity, however, there are cases in which yielding is not apparent and the procedure may therefore not be universally applicable.

Graham et al. (1983) showed examples of estimating yield stresses of Winnipeg Clay from plots of  $\varepsilon_v:p'$ ,  $q:\varepsilon_s$  and  $L:W$  where  $W$  is the work input to the sample per unit volume and  $L$  is the length of the stress vector:

$$W = \sum(\sigma'_1 \delta \varepsilon_a + 2 \sigma'_3 \delta \varepsilon_r) \quad (2.18)$$

$$L = (\Delta \sigma_1'^2 + \Delta \sigma_3'^2)^{1/2} \quad (2.19)$$

where  $\varepsilon_a$  and  $\varepsilon_r$  are the axial and radial strains respectively. Examples of their results are shown in Figure 2.10.

Inspection of Figure 2.10 suggests that yield stresses are well captured with the bi-linear method in the  $\varepsilon_v:p'$  and  $q:\varepsilon_s$  plots however they are less well captured in the  $L:W$  plot as the plot shows significant curvature (see Sample T202 in Figure 2.10c). On the other hand, the fact that strain energy is a scalar quantity and that the length of the stress vector is independent of stress path direction suggests that the  $L:W$  plot could be more universally applicable than other methods. This could be of importance when

interpreting results of probing tests following a wide variety of stress paths. Further work on using strain energy principles for determining yield stress can be found in Tavenas et al. (1979).

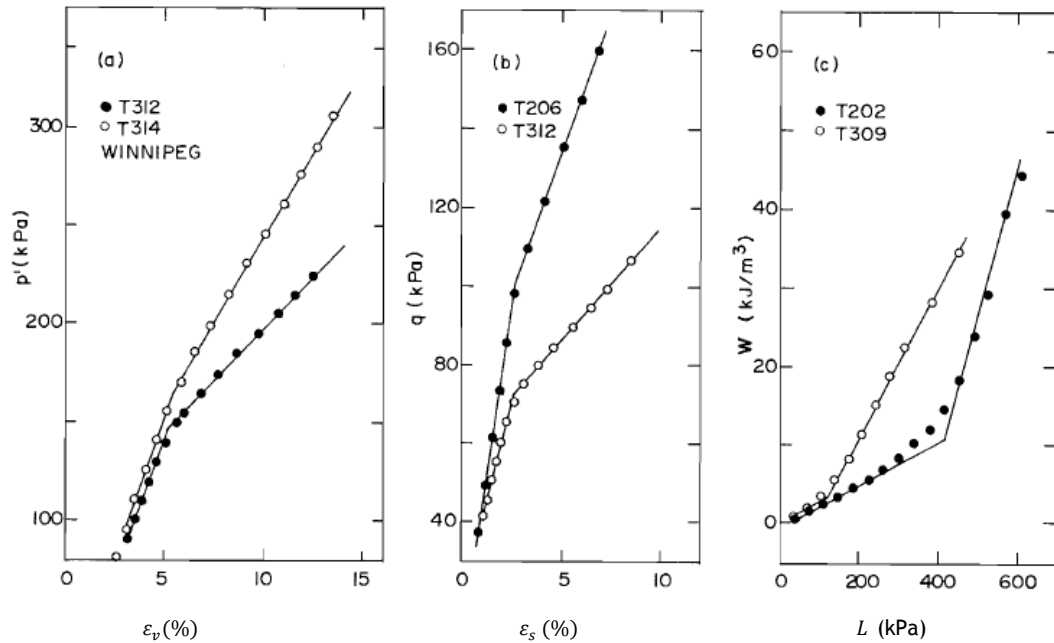


Figure 2.10 Yield stress determination by using bi-linear method in  $\varepsilon_v:p'$ ,  $q:\varepsilon_v$  and  $L:W$  (Graham et al., 1983)

Koskinen et al. (2003) demonstrated that determining yield stress from the intersection point of a bi-linear approximation in the  $v:\ln p'$  plane could be highly inaccurate when substantial change to fabric anisotropy is involved during loading. Instead, they suggested plotting experimental data on a linear scale in  $\varepsilon_v:p'$ ,  $\varepsilon_a:p'$ ,  $q:\varepsilon_v$  and  $q:\varepsilon_a$  planes. The yield stress could then be determined by the intersection of two straight lines best-fitted to the shallowest part of the pre-yield section of the curve and the steepest part of the post-yield section of the curve. It was shown, however, that this four-plot construction is not suitable for any stress path with  $\eta > M$ , where  $\eta = q/p'$  and  $M$  is the slope of critical state line in the  $q:p'$  plane, because the slope of the compression curve in the  $\varepsilon_v:p'$  plane progressively increases until reaching the critical state. Furthermore, for isotropic stress paths ( $q = 0$ ), only two plots exist and, therefore, the four-plot construction cannot be used systematically for a full set of probing experimental tests.

Sultan et al. (2010) determined values of yield stress of saturated Boom clay samples, sheared in a conventional triaxial compression test (at constant radial effective stress), by using the bi-linear method in the  $\varepsilon_v:\ln p'$  plane. They observed that the value of  $\varepsilon_v$  at yielding determined by this method matched reasonably well the corresponding value determined by identifying the yield stress in the  $\varepsilon_v:\varepsilon_a$  plane.

Cui and Delage (1996) conducted suction-controlled triaxial tests on an unsaturated silty soil, including isotropic loading, conventional shearing after isotropic loading and probing at different values of constant stress ratio,  $\eta$  (where  $\eta = q/\bar{p}$  for unsaturated soils). They found that yield stresses could be adequately determined by using the bi-linear method in the  $v:\ln\bar{p}$  plane for both isotropic stress paths and conventional shearing stress paths. However, for probing tests at constant  $\eta$ , the yield point was not clear in the  $v:\ln\bar{p}$  plane compression curves and another yield criterion was suggested by using a plot of total strain increment ratio  $d\varepsilon_v/d\varepsilon_s$  against mean net stress. However, their selection of yield stress from this plot appeared rather surprising, because they selected the yield stress at the level where the large oscillation of the strain increment ratio ceased rather than taking the yield stress at the level where the strain increment ratio showed a significant change of value, which typically marks the onset of large plastic strains (see Figure 2.11). In addition, further subjectivity is required to determine the yield stress with this method as the oscillation occurred gradually.

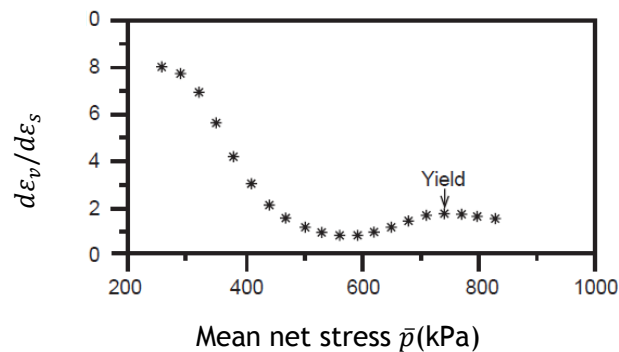


Figure 2.11 Yield stress determination for probing test at constant  $\eta$  and suction,  $s = 1500$  kPa (Cui and Delage, 1996)

#### 2.4.4 Influence of anisotropy on yielding

Anisotropy of stress-strain behaviour is due to anisotropy of the soil fabric, which can change during plastic straining as particles move relative to each other. Hence anisotropy is not fixed but can evolve during plastic straining. The influence of anisotropy can be apparent in both elastic behaviour and plastic behaviour, but it may be different aspects of the fabric that control the anisotropy of elastic behaviour and the anisotropy of plastic behaviour.

According to Graham and Houlsby (1983), a total of 21 independent elastic soil constants are required for fully general anisotropic elastic behaviour but only 5 independent elastic constants are required for cross-anisotropic (transversely isotropic) behaviour. Hence fully general elastic anisotropy is very complicated. Even if a soil starts out as

transversely isotropic, with the same properties in all horizontal directions, unfortunately, evolution of anisotropy during plastic straining will often mean that, for a boundary value problem, the soil develops fully general anisotropy.

Evidence of anisotropy of plastic behaviour is clear from the inclined form of the yield curve as observed in the  $q:p'$  plane for saturated soils (e.g. Graham et al., 1983) and in the  $q:\bar{p}$  plane or  $q:p^*$  plane for unsaturated soils as observed by Cui and Delage (1996) and Della Vecchia et al. (2012) respectively. Evidence of anisotropy also includes anisotropic straining under isotropic loading or wetting paths (e.g. Zakaria et al., 1995). Also, anisotropy seems to influence locations of *NCLs* (see Sivakumar et al., 2010a and 2010b).

## 2.5 EVOLUTION OF SOIL FABRIC DURING HYDRO-MECHANICAL LOADING

Anisotropy of mechanical behaviour is caused by anisotropy of the soil fabric. It is therefore appropriate to review experimental evidence on the fabrics of unsaturated soils and the evolution of soil fabric during plastic straining, caused either by loading (change of net stresses) or by wetting or drying (change of suction). According to Burland (1990), the “structure” of a natural soil consists of “fabric” (which refers to the arrangement of particles and inter-particle contacts) and any ‘bonding’ between particles. In this section, attention is given to the initial soil fabric (caused either by compaction or by natural processes) and the influence of subsequent loading or wetting/drying on the evolution of soil fabric. A substantial number of studies has been conducted dealing with the soil fabric or microstructure in relation to the formation process (i.e. naturally-induced fabric or compaction-induced fabric). Scanning electron microscopy (*SEM*) and mercury intrusion porosimetry (*MIP*) are the most commonly used techniques in geotechnical studies for laboratory examination of soil fabric and microstructure (Delage and Graham, 1996).

### 2.5.1 Macropores and micropores

McGown & Collins (1975) and Collins (1984) (as cited by Alonso et al. 1987), classified the microfabric of expansive and collapsible soils into three types (see Figure 2.12): elementary particle arrangements, particle assemblages (aggregates) and pore spaces (macro or inter-aggregate pores for large pores and micro or intra-aggregate pores for very small pores).

Delage and Lefebvre (1984) used *SEM* and *MIP* in their investigation of the microstructure of Champlain clay in its intact and remoulded states. They investigated also the influence of one-dimensional consolidation on fabric evolution. The results of

*SEM* studies and the plots of pore size distribution (*PSD*) from *MIP* showed clearly that Champlain clay soil had an aggregated structure with both inter-aggregate and intra-aggregate pores (similar to that shown in Figure 2.12b). Although the macroporosity of the intact and remoulded states was different, remoulding did not destroy the aggregates. Delage and Lefebvre (1984) investigated the structure of several samples taken after loading/unloading stages in the oedometer to effective stresses corresponding to the elastic (pre-yield) domain and the plastic (post-yield) domain. The researchers concluded that while the soil is loaded elastically, no significant change to the structure was observed. They observed that at the beginning of virgin loading, plastic compression is characterised by the compression of macropores whereas it characterised by the compression of micropores at very high stresses. This behaviour was also reported by authors such as Griffiths and Joshi (1989). Delage and Lefebvre (1984) observed also that virgin loading caused not only a compression of pores but also distortion of the shape of the pores. They attributed this behaviour to building of fabric anisotropy under one dimensional compression. Interestingly, the *SEM* images showed that with progression of one-dimensional virgin loading, the clay particles become progressively orientated perpendicular to the loading direction, which suggests a continuous change in fabric anisotropy.

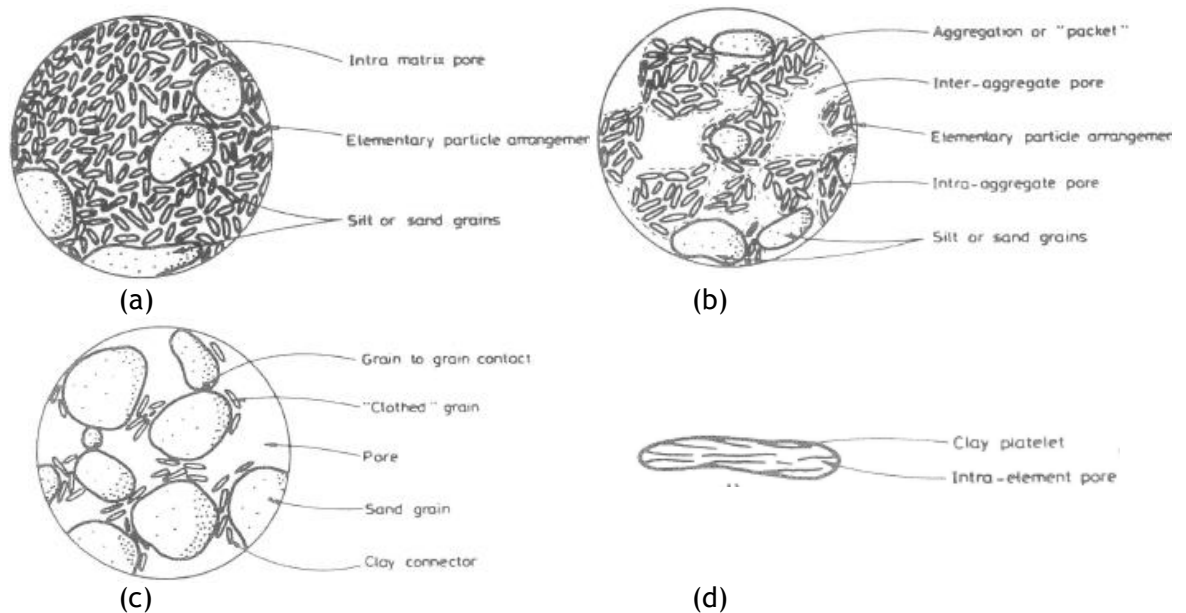


Figure 2.12: Types of microfabric. (a) Elementary particle arrangements of mainly clay platelets and a few isolated silt grains with intra pores, (b) assemblages of elementary particle arrangements with inter and intra pores, (c) sand or silt particles with large inter pores, (d) Elementary particle arrangement in a parallel configuration (Alonso et al. 1987)

Delage et al. (1996) conducted *SEM* and *MIP* studies on three statically compacted samples of Jossigny silt at three points on the Proctor compaction curve corresponding to dry of optimum, optimum water content and wet of optimum. They observed the following (see Figure 2.13):

- On the dry side: aggregated fabric was observed which was made up of silt grains coated by clay particles and the aggregates were separated by large macropores. The fabric was therefore very similar to the plot shown in Figure 2.12b.
- At optimum water content: the fabric had fewer aggregates than on the dry side and silt particles were coated with clay particles. The macro and microporosities were both very small as a result of breaking of the aggregates and this explained the minimum void ratio at the optimum water content.
- On the wet side: clay particles formed a matrix that surrounded silt particles and filled the macropores. The structure was therefore very similar to the plot in Figure 2.12a.

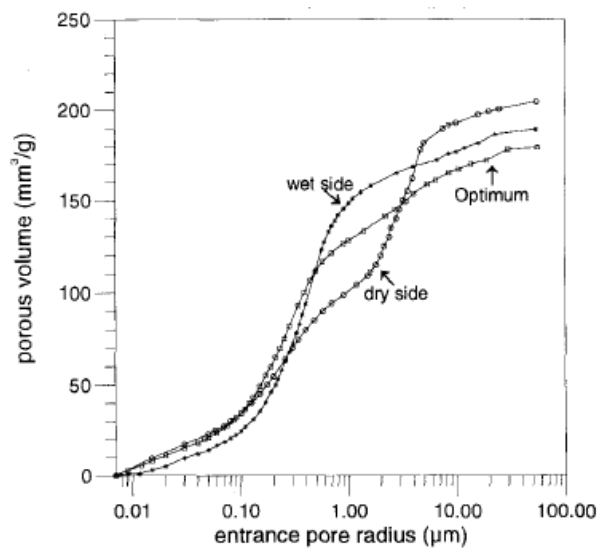


Figure 2.13 *PSD* curves of three samples of Jossigny silt statically compacted on dry side, optimum and wet side of the proctor curve (Delage et al., 1996)

The existence of macro and micropores for the compaction on the dry side of optimum suggests that the *PSD* is bimodal as can be seen in Figure 2.13 where the dry side curve shows two steeper sections.

Hong et al. (2006) investigated changes in the macrostructure and microstructure of natural Diatomite with consolidation pressure by conducting many triaxial tests on saturated samples. The study included performing *SEM* on samples loaded to isotropic stress states corresponding to the pre-yield domain and the post-yield domain (where the

yield stress corresponds to  $Y_3$ , see Figure 2.8). The results of the study showed that the microstructure stayed essentially unchanged inside the  $Y_3$  curve for the elastic domain whereas significant change to microstructure was observed during virgin loading beyond the  $Y_3$  curve. These changes included the compression of micropores as well as macropores and the breakage of diatomite particles. This behaviour agrees well with the proposal of Smith et al. (1992) in the sense that significant slippage and particles movement takes place once the stress state reaches the  $Y_3$  yield curve.

Cuisinier and Laloui (2004) studied the influence of external loads and suction change on soil fabric by conducting several suction-controlled oedometer tests on a compacted sandy silt soil. All tests were started from a saturated condition. The results of the study indicated that during drying significant reduction of the macroporosity component of the total porosity occurred mainly at low suction values during drying under small net stresses. Cuisinier and Laloui (2004) showed that this behaviour is related to reaching the shrinkage limit. They showed that while macropores were reducing in size, micropores, in contrast, showed an increase in size during drying at low suction values in such a way that total porosity could stay constant. The results of loading tests at constant suction confirmed the previously mentioned findings by other authors (e.g. Delage and Lefebvre, 1984) that virgin loading initially causes a progressive decrease in macroporosity then when most of the macropores have disappeared, micropores start to compress.

Monroy et al. (2010) investigated the effect of wetting and loading on soil microstructure by conducting oedometer tests in conventional and osmotic equipment on London clay samples, compacted dry of optimum. The study utilised *MIP* and *ESEM* techniques (where *ESEM* is environmental scanning electron microscopy). A number of samples were wetted from the as-compacted suction,  $s \approx 1000$  kPa, other samples were loaded from the as-compacted suction at constant water content to various stress states corresponding to the elastic domain inside or on the *LC* curve. The initial pore size distribution was shown to be bimodal, as expected for samples compacted dry of optimum water content. It was also shown that wetting from the as-compacted suction under a nominal net stress (7 kPa) only produced a change to the *PSD* from bimodal to unimodal once the suction was less than 40 kPa (see Figure 2.14). These *PSD* curves indicate that the macropores were compressing whereas the micropores were expanding during the wetting process. The results in Figure 2.14 show also that the *PSD* remains the same for very small micropores. Despite the contradicting influence of wetting on macro and micropores, measured volumetric strain indicated an increase in sample volume (i.e. swelling) even when the suction was less than 40 kPa. In addition, the researchers showed that for a sample loaded at constant water content to a stress state close to the

*LC* curve, the *PSD* is still bimodal and only moderate decrease to the dominant macropores size had occurred when compared to the as-compacted sample.

Further work on microstructural changes of fabric anisotropy can be found in Bai and Smart (1997) and Sivakumar et al. (2010a).

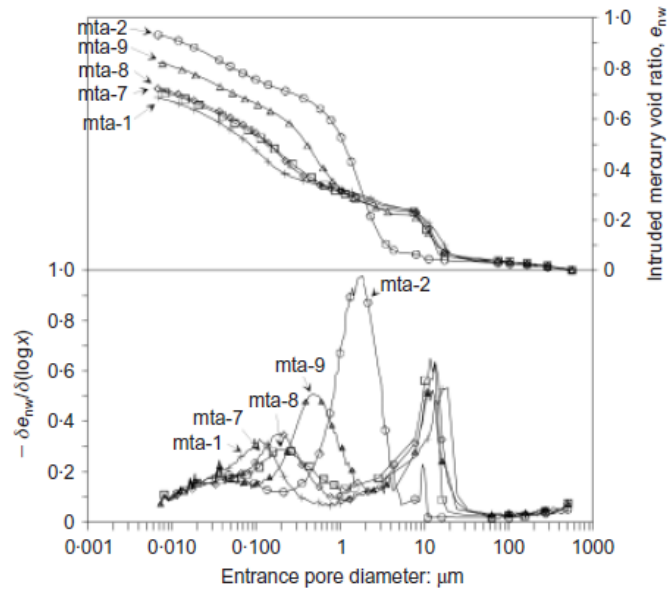


Figure 2.14 *PSD* and density function for reference sample mta-1 ( $s = 1000$  kPa) and samples wetted under nominal net stress to:  $s = 0$  (mta-2),  $s = 470$  kPa (mta-7),  $s = 150$  kPa (mta-8),  $s = 40$  kPa (mta-9) (Monroy et al., 2010)

### 2.5.2 Evolution of fabric anisotropy

Hattab and Fleureau (2011) investigated changes in particle orientation during various levels of plastic straining of one-dimensionally consolidated reconstituted saturated kaolin soil by using the *SEM* technique. The results indicated that one-dimensional consolidation resulted in a preferential orientation of the particles perpendicular to the direction of one-dimensional loading and that the micropores of the initial bimodal fabric was highly affected by the orientation pattern of the particles inside the aggregates. Hattab and Fleureau (2011) attempted to explore the erasure of initial fabric anisotropy by isotropically loading a sample to more than 11 times the initial consolidation pressure. After this isotropic loading to high stress, no preferential orientation of the particles was observed, indicating the erasure of initial fabric anisotropy. *SEM* images taken for samples during various subsequent conventional shear stages on lightly overconsolidated samples showed gradual build-up of fabric anisotropy. Very close to the critical state, the fabric showed clear preferential orientation of particles parallel to the direction of the shear plane, with face-to-face particle arrangement.

Hicher et al. (2000) studied the evolution of fabric anisotropy of saturated kaolin soil and bentonite soil by using *SEM* and *TEM* (transmission electron microscope) techniques. Test samples were prepared from slurry and then one-dimensional and isotropic consolidation tests were performed on these samples. Isotropically consolidated samples showed aggregated fabric of mostly edge-to-face particle associations with no preferential orientation for the kaolin particles (i.e. isotropic fabric). The one-dimensionally consolidated samples showed anisotropic fabric, with mainly face-to-face particle associations, resulting in smaller pore size than those of isotropically consolidated samples (see Figure 2.15).

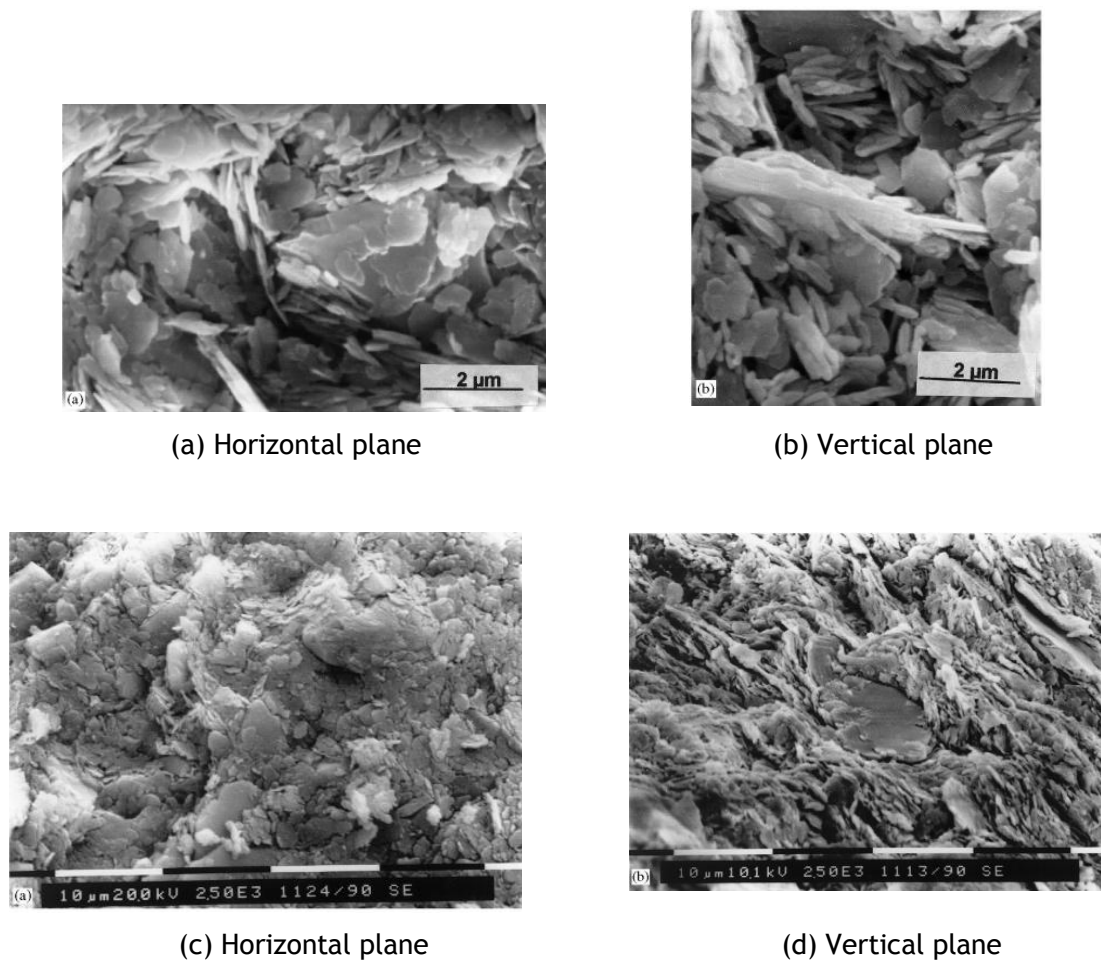


Figure 2.15 *SEM* Images of kaolin consolidated from slurry: (a)(b) isotropic consolidation to 1 MPa, (c)(d) anisotropic consolidation to 6.3 MPa (Hicher et al., 2000)

## 2.6 SHAPES AND EXPRESSIONS FOR THE YIELD SURFACE AND PLASTIC POTENTIAL

In classical plasticity, the yield surface,  $f$ , is a locus of points which separates the elastic region from the elasto-plastic region in stress space, and therefore no plastic deformation is assumed to occur while the stress state is within that locus (Yu 2006). The

plastic potential,  $g$ , is an analytical expression, formulated in terms of stresses, and the direction of the normal to this plastic potential gives the relative magnitudes of plastic strain increments once the stress state is on the yield surface (Lagioia et al., 1996). If the yield surface and potential surface coincide (both have the same analytical expression), the flow vector will be perpendicular to the yield surface and the flow rule is said to be ‘associated’, otherwise the flow rule is said to be “non-associated”. This section discusses some of the various forms of yield surface and plastic potential that have to be used by different authors and compared against experimental data by researchers over the years.

A number of considerations need to be taken into account when developing expressions for the yield surface and plastic potential surface including, for example;

- Each of the two surfaces should preferably be described by using a single function, in order to avoid singularities and numerical difficulties with multi-function surfaces (Taiebat and Dafalias, 2010).
- Even if a single expression is used, the plastic potential has to be smooth, so that derivatives are definite at any point with respect to stress (Jiang and Ling, 2010).
- The expression for the yield surface should be flexible so that a wide range of soils could be fitted, but at the same time the number of fitting parameters should be kept as small as possible. Also, the elastic domain has to be physically acceptable (Jiang and Ling, 2010).
- The formulation should not contravene the principles of thermodynamics; this implies applying some restrictions on the constitutive relations (Collins and Houlsby, 1997). Despite the importance of thermodynamics, most of the well-known classical elasto-plastic models were formulated without referring to thermodynamic constraints.

### 2.6.1 ISOTROPIC YIELD CURVE EXPRESSIONS FOR SATURATED SOILS

One of the simplest shapes for the yield curve employed in saturated elasto-plastic models for triaxial ( $q:p'$ ) stress space is the ellipse (an ellipsoidal surface in principal stress space), as in the Modified Cam Clay model (*MCC*) of Roscoe and Burland (1968). The yield curve, for the simplified triaxial stress space, in this model is given by:

$$f = q^2 - M^2 p' (p'_0 - p') = 0 \quad (2.20)$$

where  $M$  is the aspect ratio of the ellipse (in *MCC* it also represents the critical state stress ratio in the  $q:p'$  plane) and  $p'_0$  is intersection of the yield curve with the  $p'$  axis (i.e. the isotropic yield stress). As can be noticed from Equation 2.20, the ellipse passes through the origin (consistent with the saturation condition) and only one shape parameter is involved (i.e.  $M$ ). The current size of the yield surface is controlled by the value of  $p'_0$ . In addition, as the *MCC* model employs an associated flow rule, the apex of the ellipse (where  $q = Mp'$ ) automatically satisfies the critical state condition of  $d\varepsilon_v^p/d\varepsilon_s^p = 0$ , because at this point  $df/dp' = 0$ .

Equation 2.20 formed the platform for subsequent yield curve expressions that were developed to allow for additional flexibility in fitting various soil states and conditions such as fabric anisotropy (e.g. Dafalias, 1986; Dafalias, 1987; Korhonen & Lojander, 1987 and Wheeler et al., 2003b) and unsaturation (e.g. Alonso et al., 1990 and Raveendraraj, 2009).

Lagioia et al. (1996) proposed a flexible expression for the yield surface and plastic potential for isotropic saturated soils, that allows experimentally observed yield surfaces to be reproduced more accurately than by *MCC*:

$$f \text{ or } g = \frac{p'}{p'_m} - \frac{\left(1 + \frac{\eta/M}{W_2}\right)^{\frac{W_2}{(1-\xi)(W_1-W_2)}}}{\left(1 + \frac{\eta/M}{W_1}\right)^{\frac{W_2}{(1-\xi)(W_1-W_2)}}} = 0 \quad (2.21)$$

where

$$W_{1/2} = \frac{\xi(1-Y)}{2(1-\xi)} \left[ 1 \pm \left( 1 - \frac{4Y(1-\xi)}{\xi(1-Y)^2} \right)^{0.5} \right] \quad (2.22)$$

and  $Y, \xi \neq 1$ . Equation 2.21 was derived by assuming a particular nonlinear variation of plastic strain increment rate,  $d\varepsilon_v^p/d\varepsilon_s^p$ , with stress ratio,  $\eta$ , and then assuming that normality was satisfied at  $\eta = 0$  and  $\eta = M$ . Three geometrical parameters (i.e.  $Y, \xi$  and  $M$ ) control the shape of yield surface while the size is controlled by  $p'_m$ . All of these parameters can be determined by fitting the yield curve against experimental yield points in the  $q:p'$  plane. Variation of  $\xi$  (which controls the roundness near to the tip) or  $Y$  (which controls the roundness near to the origin) could produce a wide range of shapes ranging from 'bullet' shape to 'tear' shape, as demonstrated in Figure 2.16.

### 2.6.2 Anisotropic yield curve expressions for saturated soils

Over the last few decades, several anisotropic elasto-plastic constitutive models for saturated soils have been developed, in which the influence of anisotropy is incorporated in forms such as a rotated ellipse yield curve in the  $q:p'$  plane (e.g. Mouratidis and Magnan, 1983) or a distorted ellipse yield curve in the  $q:p'$  plane (Dafalias, 1986; Banerjee and Yousif, 1986; Wheeler et al., 2003b). A disadvantage of a rotated ellipse yield curve in the  $q:p'$  plane is that the cross-section of the yield surface in the deviatoric plane in principal stress space becomes elliptical rather than circular. In contrast, with a distorted ellipse shape in the  $q:p'$  plane the cross-section of the yield surface in the deviatoric plane remains a circle.

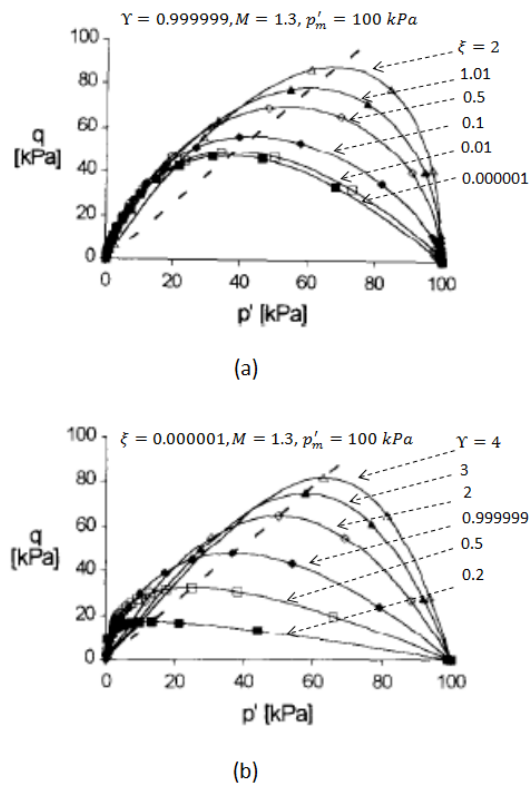


Figure 2.16 Yield surface of Lagioia et al. (1996): (a) influence of  $\xi$  (b) influence of  $Y$

Banerjee and Yousif (1986) proposed a model for anisotropic saturated soils with a yield curve in a form of a distorted ellipse which can be rearranged to:

$$f = (q - \alpha p')^2 - M^2 p' (p'_m - p') = 0 \tag{2.23}$$

where  $\alpha$  and  $p'_m$  define the current inclination and current size of yield curve. Note that this is very similar to the *MCC* yield curve expression of Equation 2.20, the single change being the replacement of  $q$  by  $q - \alpha p'$ . Equation 2.23 suggests that for the case where

$\alpha \neq 0$ , the tangent to the yield curve at the intersection with the critical state line  $q = Mp'$  is not horizontal and a non-associated flow rule is therefore required to satisfy the critical state condition on this line.

Dafalias (1986) introduced two modifications to the *MCC* yield curve expression of Equation 2.20 to incorporate the influence of anisotropy; replacing  $q$  in the first term by  $q - \alpha p'$  and replacing  $M^2$  in the second term by  $(M^2 - \alpha^2)$  which led to the following expression:

$$f = (q - \alpha p')^2 - (M^2 - \alpha^2)p'(p'_m - p') = 0 \quad (2.24)$$

Equation 2.24 describes a distorted ellipse in the  $q:p'$  plane, where the value of  $\alpha$  controls the degree of distortion of the ellipse (see Figure 2.17) and if  $\alpha$  is set to zero, Equation 2.20 is retrieved. A particular feature of Equation 2.24 is that, irrespective of the value of  $\alpha$ , the tangent to the yield curve is always horizontal at the intersection with the critical state line ( $q = Mp'$ ), and hence an associated flow rule can be employed. Inspection of Figure 2.17 shows that if  $\alpha$  is greater than zero when a critical state is achieved at Point  $c$ , then the value of the ratio  $p'_m/p'_c$  will be less than 2 whereas in *MCC* this ratio has a value of 2. This means that the anisotropic models generally predict a smaller spacing, between the normal compression line and the critical state line in the  $v:\ln p'$  plane than is predicted by *MCC*.

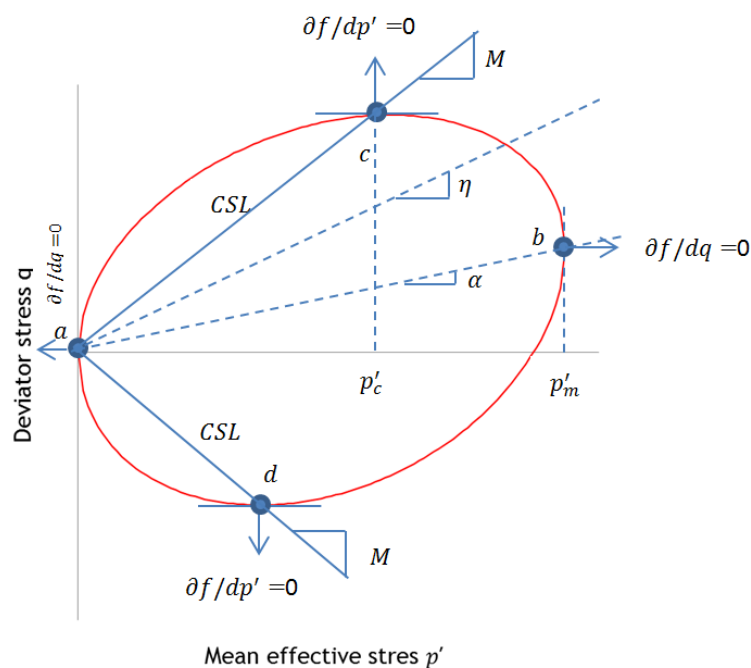


Figure 2.17 Anisotropic yield curve of Dafalias (1986)

In order to introduce flexibility of the aspect ratio of the distorted ellipse, the quantity  $(M^2 - \alpha^2)$  in Equation 2.24 could be substituted by  $(n^2 - \alpha^2)$  as in Whittle and Kavvas (1994) or by  $(n + |\alpha|)^2$  as suggested by Taiebat and Dafalias (2010). The new arbitrary variable,  $n$  can be defined as a function of  $M$  and  $\alpha$ . The advantage of this suggestion is that the slenderness of the ellipse can be controlled in such a way that the elastic domain becomes more realistic.

### 2.6.3 Yield curve expressions for unsaturated soils

In the field of unsaturated soils, researchers attempted to extend the *MCC* yield curve expression to include the effects of unsaturation on the yield behaviour. Alonso et al. (1990) in their *BBM* model, formulated the yield surface expression in terms of mean net stress  $\bar{p}$ , deviator stress  $q$  and suction  $s$ :

$$f = q^2 - M^2(\bar{p} + ks)(\bar{p}_0(s) - \bar{p}) = 0 \quad (2.25)$$

where  $k$  is an additional soil constant. For a given value of  $s$ , Equation 2.25 gives an elliptical yield curve of aspect ratio  $M$  which intersects the positive and negative  $\bar{p}$  axes at  $\bar{p} = \bar{p}_0(s)$  and  $\bar{p} = -ks$  respectively. Equation 2.25 recovers the original form of the *MCC* yield curve expression for the case where  $s = 0$ .

Stropeit et al. (2008) and D'Onza et al. (2010) incorporated anisotropy into the *BBM* yield surface expression of Equation 2.25 by employing a distorted ellipse, similar to that suggested for saturated soils in Equation 2.24. Further details regarding their work will be given in Section 2.8.3.

Cui and Delage (1996) proposed an anisotropic yield surface for unsaturated soil in the  $q:\bar{p}:s$  space, where each constant suction cross section of the yield surface takes the form of a rotated ellipse:

$$f = b^2(\bar{p} \cos \theta + q \sin \theta - c)^2 + a^2(-\bar{p} \sin \theta + q \cos \theta)^2 - a^2b^2 = 0 \quad (2.26)$$

where  $a$  and  $b$  are the major and minor axes of the ellipse respectively and  $c$  and  $\theta$  give the position and inclination of the yield curve respectively. Figure 2.18 shows experimental yield points plotted by Cui and Delage (1996) against their proposed yield curve expression.

Romero and Jommi (2008) and Della Vecchia et al. (2012) presented an anisotropic yield curve for unsaturated soil presented in terms of mean Bishop's stress  $p^*$  (see Equation

2.8) and deviator stress  $q$  (rather than mean net stress  $\bar{p}$  and deviator stress  $q$ ). The yield curve is in the form of a distorted ellipse (equivalent to Equation 2.24):

$$f = (q - \alpha^* p^*)^2 - (M^{*2} - \alpha^{*2}) p^* (p_m^* - p^*) = 0 \quad (2.27)$$

where  $M^*$  is a soil constant and the parameters  $p_m^*$  and  $\alpha^*$  describe the current size and inclination of the yield curve in the  $q:p^*$  plane.

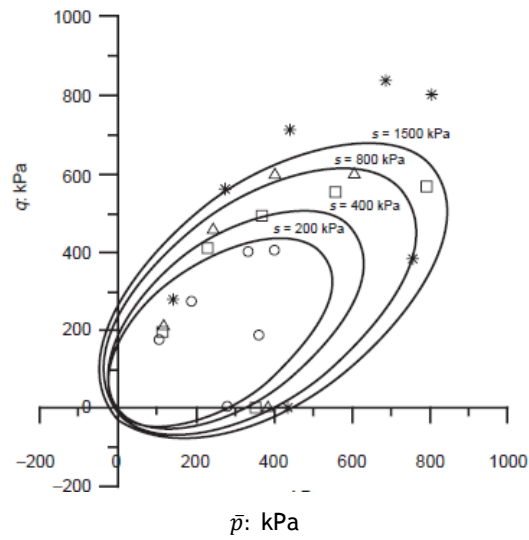


Figure 2.18 Experimental yield points and cross-sections of the yield surface (Cui and Delage, 1996)

## 2.7 ANISOTROPIC ELASTO-PLASTIC CONSTITUTIVE MODELS FOR SATURATED SOILS

### 2.7.1 Overview

The earliest elasto-plastic constitutive models for saturated soils were the isotropic models Original Cam Clay (Roscoe et al., 1958) and Modified Cam Clay (Roscoe and Burland, 1968). These formed the basis for many subsequent proposals for elasto-plastic models for saturated soils, some of which incorporate the influence of soil anisotropy. This section gives a brief overview of these anisotropic elasto-plastic models for saturated soils, and the subsequent section gives a more detailed description of one particular anisotropic model (the  $S - CLAY1$  model of Wheeler et al., 2003b), because features from this model are incorporated within the anisotropic model for unsaturated soils developed in Chapter 7.

Various anisotropic elasto-plastic models for saturated soil can be found in the literature, including, for example, Mouratidis and Magnan (1983), Dafalias (1986), Banerjee and

Yousif (1986), Davies and Newson (1993) and Wheeler et al. (2003b). These models tend to assume that elastic behaviour is isotropic (for simplicity) whereas plastic behaviour is anisotropic (because plastic strains will often dominate, and hence it is important to predict these strains accurately). As mentioned in Section 2.6.2, anisotropy of plastic behaviour is represented by a curve in the  $q:p'$  plane that generally takes the form of either a rotated ellipse or a distorted ellipse.

Early anisotropic elasto-plastic models (e.g. Mouratidis and Magnan, 1983) assumed that anisotropy remains unchanged during plastic straining. However, subsequent models incorporated the crucial feature that anisotropy can evolve during plastic straining (e.g. Dafalias, 1986; Banerjee and Yousif, 1986; Davies and Newson, 1993; Whittle and Kavvas, 1994 and Wheeler et al., 2003b). Some authors (e.g. Dafalias, 1986; Banerjee and Yousif, 1986 and Whittle and Kavvas, 1994) assume that change of anisotropy is caused only by plastic volumetric strains. Wheeler (1997), Karstunen and Wheeler (2002) and Wheeler et al. (2003b) argued that this was unrealistic and that plastic shear strains should also be capable of producing a change of anisotropy. In particular, if a model assumes that changes of anisotropy are produced only by plastic volumetric strains, then it will predict that the influence of initial anisotropy will not be totally erased on shearing to a critical state, and the model will not predict a unique critical state line in the  $v:\ln p'$  plane. Banerjee et al. (1988) made the alternative suggestion that changes of anisotropy are caused only by plastic shear strains, but this too is physically unreasonable. Wheeler et al. (2003b) therefore proposed a more physically realistic relationship, where changes of anisotropy can be caused by both plastic volumetric strains and plastic shear strains.

Some anisotropic elasto-plastic constitutive models for saturated soils are extremely complicated (e.g. Whittle and Kavvas, 1994) as they incorporate other features of behaviour such as a gradual transition from elastic to elasto-plastic behaviour.

### 2.7.2 The $S - CLAY1$ model

The anisotropic elasto-plastic  $S - CLAY1$  was proposed by Wheeler et al. (2003b) to account for the evolving anisotropy of soft saturated clays. The model is described here in some detail, because features from it are used in Chapter 7 for the development of an anisotropic model for unsaturated soils. The model is described here for the simplified case of a cross-anisotropic (transversely isotropic) soil subjected to a triaxial test stress state, with the plane of transverse isotropy of the soil perpendicular to the axis of the triaxial apparatus. In this case the soil remains transversely isotropic, the stress state can be fully expressed in terms of  $q$  and  $p'$  and the soil anisotropy can be fully expressed in

terms of the value of a single scalar quantity  $\alpha$ . A fully generalised tensorial version of the model (accounting for 3D stress states, including rotation of principal stress directions, and evolution of fully generalised soil anisotropy) is presented in Wheeler et al. (2003b).

Isotropic linear elasticity is assumed in *S – CLAY1* (in the interest of simplicity) with the same form as in the *MCC* model:

$$d\varepsilon_v^e = \frac{\kappa dp'}{v p'} \quad \text{and} \quad d\varepsilon_s^e = \frac{dq}{3G} \quad (2.28)$$

where  $d\varepsilon_v^e$  and  $d\varepsilon_s^e$  are the elastic volumetric strain increment and elastic shear strain increment respectively.

The yield curve is assumed to be a distorted ellipse in the  $q:p'$  plane that is identical to that proposed by Dafalias (1986,1987, see Equation 2.24 and Figure 2.17), which can be expressed as:

$$f = (q - \alpha p')^2 - (M^2 - \alpha^2)p'(p'_m - p') = 0 \quad (2.29)$$

$M$  is soil constant, whereas  $p'_m$  and  $\alpha$  are variables (hardening parameters, describing the current size and current inclination of the yield curve). Wheeler et al. (2003b) showed that Lode angle dependency can be incorporated into the model by replacing the critical state ratio,  $M$ , by  $M_c$  (a triaxial compression value) for  $\eta \geq \alpha$  and by  $M_e$  (a triaxial extension value) for  $\eta \leq \alpha$ .

Two hardening laws are incorporated in the *S – CLAY1* model. The change in size of the yield curve is related to increments of plastic volumetric strain  $d\varepsilon_v^p$  by a relationship that is identical to the hardening law in the *MCC* model:

$$dp'_m = \frac{v p'_m d\varepsilon_v^p}{\lambda - \kappa} \quad (2.30)$$

where  $\lambda$  is the slope of the normal compression line in the  $v:\ln p'$  plane for an isotropic soil. The change of  $\alpha$  is related to increments of plastic volumetric strain  $d\varepsilon_v^p$  and plastic shear strain  $d\varepsilon_s^p$  by:

$$d\alpha = \mu[(3\eta/4) - \alpha]d\varepsilon_v^p + \beta[(\eta/3) - \alpha]d\varepsilon_s^p \quad (2.31)$$

Equation 2.31 was proposed on the basis of the results of a series of experimental tests reported by Wheeler et al. (2003b). Inspection of Equation 2.31 shows that (positive) plastic volumetric strains attempt to change the value of  $\alpha$  towards a current target value of  $3\eta/4$ , whereas (positive or negative) plastic shear strains are simultaneously attempting to change the value of  $\alpha$  towards a current target value of  $\eta/3$ .  $\mu$  is a soil constant which controls the rate of evolution of  $\alpha$  towards its current target and  $\beta$  is a second soil constant which controls the relative effectiveness of plastic shear strains and plastic volumetric strains in determining the overall current target value for  $\alpha$ .

Experimental evidence presented by a number of researchers, such as Graham et al. (1983), suggests that an associated flow rule is realistic when combined with an inclined yield surface. The *S – CLAY1* model therefore adopts an associated flow rule which corresponds to:

$$\frac{d\varepsilon_s^p}{d\varepsilon_v^p} = \frac{2(\eta - \alpha)}{M^2 - \eta^2} \quad (2.32)$$

The *S – CLAY1* model predicts that continued isotropic loading ( $\eta = 0$ ) will lead to an isotropic soil ( $\alpha = 0$ ) and that this will correspond to convergence with a unique isotropic normal compression line in the  $v: \ln p'$  plane, defined by:

$$v = N - \lambda \ln p' \quad (2.33)$$

where  $N$  is a soil constant. The model also predicts (through Equations 2.32 and 2.31) that critical states will be achieved at a unique critical state degree of anisotropy  $\alpha_{cs}$  given by:

$$\alpha_{cs} = M/3 \quad (2.34)$$

As a consequence, a unique critical state line is predicted in both the  $q:p'$  plane and the  $v: \ln p'$  plane, defined by

$$q = Mp' \quad (2.35)$$

$$v = \Gamma - \lambda \ln p' \quad (2.36)$$

The predicted spacing between the isotropic normal compression line and the critical state line in the  $v: \ln p'$  plane is smaller than for *MCC* and is given by:

$$N = \Gamma + (\lambda - \kappa) \ln(3/2) \quad (2.37)$$

The *S – CLAY1* model requires the values of seven soil constants, five of which are common with *MCC* ( $\lambda, \kappa, G, M$  and  $\Gamma$  (or  $N$ )) and two more that relate to the evolution of anisotropy ( $\mu$  and  $\beta$ ). Karstunen and Koskinen (2008) showed that the *S – CLAY1* model provides an excellent representation of the stress-strain behaviour of saturated reconstituted clays. Other authors (e.g. Wheeler et al., 2003b) showed that for saturated natural clays *S – CLAY1* performs significantly better than *MCC*, although the fit is not as good as for reconstituted clays, because of the additional influence of destructuration (destruction of inter-particle bonding) in natural clays.

## 2.8 ELASTO-PLASTIC MODELS FOR UNSATURATED SOILS

This section provides a review of elasto-plastic constitutive models for the mechanical behaviour of unsaturated soils. The Barcelona Basic Model (*BBM*) of Alonso et al. (1990) is presented first. The *BBM* is presented in some detail, because it was the first elasto-plastic model for unsaturated soils, it is still the most widely used and it can be considered as the starting point for development of subsequent constitutive models. Also, the *BBM* can be used to illustrate some key issues which apply to all constitutive models for unsaturated soils. Presentation of the *BBM* is followed by a less detailed review of other isotropic constitutive models for unsaturated soils and then a review of the small number of published unsaturated constitutive models that incorporate the influence of evolution of anisotropy.

### 2.8.1 The Barcelona Basic Model (*BBM*)

The *BBM* was proposed by Alonso et al. (1990) after initial development of qualitative ideas of how key features of unsaturated soil behaviour could be represented within an elasto-plastic framework by Alonso et al. (1987). The *BBM* assumes that the net stress tensor and the scalar value of matric suction are the appropriate stress state variables for unsaturated soil (see Section 2.2) and hence for the simplified stress state of the triaxial test, the model is expressed in terms of mean net stress  $\bar{p}$ , deviator stress  $q$  and matric suction  $s$ .

The *BBM* can be regarded as an extension of the *MCC* model to include unsaturated conditions that the former recovers the form of the latter whenever  $s = 0$ , but only when  $s = 0$ . This means that the *BBM* implicitly assumes that the soil is saturated when  $s = 0$

and only when  $s = 0$ , whereas in reality the soil may remain saturated even when a non-zero value of suction is applied (below the air entry value of the soil) and conversely it is possible for a soil to remain unsaturated even at a suction of zero (if there are voids filled with trapped air).

The increments of elastic volumetric strain are given by:

$$d\varepsilon_v^e = \frac{1}{v} \left( \kappa \frac{d\bar{p}}{\bar{p}} + \kappa_s \frac{ds}{(s + p_{atm})} \right) \quad (2.38)$$

where  $p_{atm}$  is atmospheric pressure and  $\kappa$  and  $\kappa_s$  are two elastic soil constants. The term involving  $\kappa$  represents elastic volume changes caused by variation of  $\bar{p}$ , giving elastic unloading/reloading lines of gradient  $\kappa$  in the  $v: \ln \bar{p}$  plot, whereas the term involving  $\kappa_s$  represents elastic volume changes caused by variation of  $s$  (swelling on wetting and shrinkage on drying), giving shrink/swell lines of gradient  $\kappa_s$  in the  $v: \ln(s + p_{atm})$  plot. Atmospheric pressure  $p_{atm}$  was (rather arbitrarily) included in Equation 2.38 in order to avoid infinite elastic volumetric strains as suction tends to zero.

Elastic shear strain increments are given by:

$$d\varepsilon_s^e = \frac{dq}{3G} \quad (2.39)$$

where  $G$  is the elastic shear modulus (a soil constant).

The variation of specific volume with change in mean net stress  $\bar{p}$  during isotropic loading to virgin states follows normal compression lines (*NCLs*) for each value of suction, defined by:

$$v = N(s) - \lambda(s) \ln \frac{\bar{p}}{p^c} \quad (2.40)$$

where  $p^c$  is a reference pressure (a soil constant) and the intercept  $N(s)$  (defined at the reference pressure  $p^c$ ) and gradient  $\lambda(s)$  are both functions of suction. The variation of  $\lambda(s)$  with suction is given by:

$$\lambda(s) = \lambda(0)[(1 - r)\exp(-\beta s) + r] \quad (2.41)$$

where  $\lambda(0)$  (a soil constant) is the slope of the *NCL* for saturated conditions, and  $r$  and  $\beta$  are two further soil constants. The value of  $r$  controls the limiting value of  $\lambda(s)$  as suction tends to infinity (note that when  $s \rightarrow \infty$ ,  $\lambda(s) = r\lambda(0)$ ) and the value of  $\beta$  controls the rate of exponential approach to this limiting value. The variation of  $N(s)$  with suction is assumed as:

$$N(s) = N(0) - \kappa_s \ln \frac{s + p_{atm}}{p_{atm}} \quad (2.42)$$

where  $N(0)$  (a soil constant) is the value of  $N(s)$  at zero suction. The form of Equation 2.42 was assumed by Alonso et al. (1990) in order to produce a relatively simple form for the *LC* yield curve expression (see below).

The increase of isotropic yield stress with increasing suction is described by the concept of the *LC* yield curve, as introduced in Section 2.4.2. Combination of Equations 2.38, 2.40 and 2.42 led to the following expression for the shape of the *LC* yield curve in the *BBM*:

$$\left(\frac{\bar{p}_0(s)}{p^c}\right) = \left(\frac{\bar{p}_0(0)}{p^c}\right)^{\left(\frac{\lambda(0)-\kappa}{\lambda(s)-\kappa}\right)} \quad (2.43)$$

where  $\bar{p}_0(s)$  and  $\bar{p}_0(0)$  are the isotropic yield stress at a given suction and for the saturated condition respectively. The graphical representation of Equation 2.43 is shown in Figure 2.19b.

To incorporate the role of deviator stress  $q$ , the *LC* yield curve is developed to form a *LC* yield surface in  $q:\bar{p}:s$  space. Constant suction cross-sections of the *LC* yield surface are assumed to be elliptical in the  $q:\bar{p}$  plane, as discussed in Section 2.6.3 and shown in Figure 2.19a:

$$q^2 - M^2(\bar{p} + ks)(\bar{p}_0(s) - \bar{p}) = 0 \quad (2.44)$$

where  $M$  and  $k$  are two soil constants.

The hardening law for yielding on the *LC* yield surface is given by:

$$\frac{d\bar{p}_0(0)}{\bar{p}_0(0)} = \frac{v}{\lambda(0) - \kappa} d\varepsilon_v^p \quad (2.45)$$

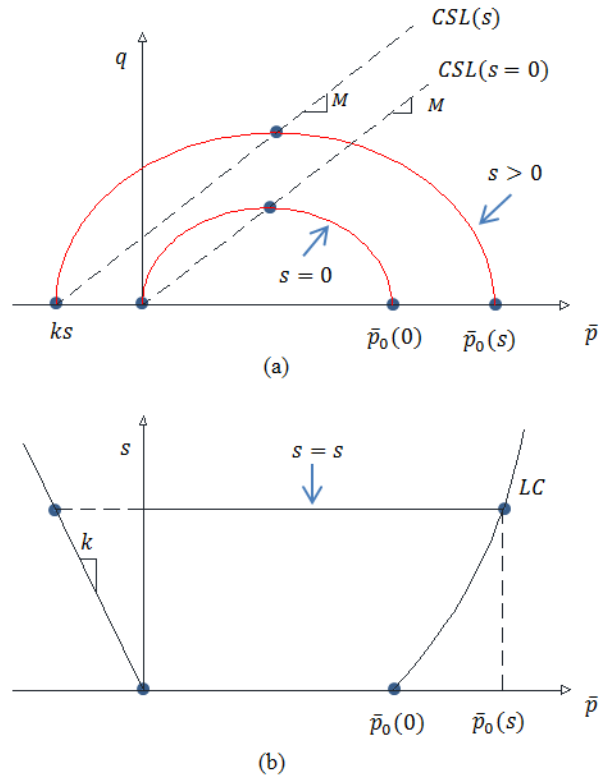


Figure 2.19 *BBM* yield surface: (a) constant suction cross-sections in the  $q: \bar{p}$  plane, (b) in the  $s: \bar{p}$  plane (Alonso et al., 1990)

The *BBM* assumes a non-associated flow rule for yielding on the *LC* yield surface given by:

$$\frac{d\varepsilon_s^p}{d\varepsilon_v^p} = \frac{2q\alpha}{M^2(2\bar{p} + ks - \bar{p}_0)} = \frac{2\bar{\eta}\alpha}{M^2 - \bar{\eta}^2} \quad (2.46)$$

where:

$$\bar{\eta} = \frac{q}{\bar{p} + ks} \quad (2.47)$$

and  $\alpha$  is a constant.  $\alpha = 1$  would correspond to an associated flow rule, but Alonso et al. (1990) suggest a value for  $\alpha$  (which can be expressed in terms of  $M$ ,  $\lambda(0)$  and  $\kappa$ ) selected in order to give zero lateral strain during elasto-plastic loading of a saturated sample at a stress ratio approximating to the normally consolidated  $K_0$  value suggested by Jaky (1948).

As a consequence of the flow rule and the hardening law (Equations 2.46 and 2.45), the *BBM* predicts critical state lines for different values of suction defined in the  $q: \bar{p}$  plane by:

$$q = M\bar{p} + Mks \quad (2.48)$$

Note that *BBM* therefore predicts a linear increase of shear strength with suction (equivalent to the shear strength expression of Fredlund et al. (1978) in Equation 2.11 (but with  $c' = 0$ )), whereas experimental evidence suggests a non-linear increase of shear strength with suction (see Section 2.3.2).

The *BBM* also includes a second yield surface, known as the *SI* yield surface, to represent the possibility of plastic volumetric strains during drying. The *SI* yield surface expression, the hardening law for the *SI* yield surface and the flow rule for yielding on this surface are given by:

$$s = s_0 \quad (2.49)$$

$$\frac{ds_0}{s_0 + p_{atm}} = \frac{v}{\lambda_s - \kappa_s} d\varepsilon_v^p \quad (2.50)$$

$$\frac{d\varepsilon_s^p}{d\varepsilon_v^p} = 0 \quad (2.51)$$

where  $s_0$  is a hardening parameter, describing the current location of the *SI* yield surface, and  $\lambda_s$  is a soil constant.

The *BBM* requires values of eleven soil constants, eight of which describe the isotropic behaviour (i.e.  $\kappa$ ,  $\kappa_s$ ,  $p^c$ ,  $\lambda(0)$ ,  $r$ ,  $\beta$ ,  $N(0)$  and  $\lambda_s$ ) and three more to describe shear behaviour (i.e.  $G$ ,  $k$  and  $M$ ). Detailed discussion about problems and limitations on the use of this model is given by Wheeler et al. (2002). A systematic method for calibrating each parameter is given by Gallipoli et al. (2010).

## 2.8.2 Other isotropic models for unsaturated soils

A large number of isotropic elasto-plastic constitutive models have been proposed for unsaturated soils since the publication of the *BBM*. Some of these models are expressed in terms of net stresses and suction, whereas other models use alternative stress state variables. Reviews of constitutive modelling of unsaturated soils can be found in Wheeler and Karube (1996), Gens et al. (2006) and Sheng et al. (2008).

Wheeler and Sivakumar (1995) proposed a constitutive model which takes similar form to the *BBM* but with some modifications like, for example, the  $\lambda(s)$  and  $N(s)$  are defined

empirically by conducting several suction controlled tests. Chiu and Ng (2003) proposed a constitutive model that enhances prediction of the dilatant behaviour of unsaturated soils by considering the effects of void ratio, stress state and suction. Sheng et al. (2008) proposed a constitutive model for unsaturated soils that focuses on modelling of some unsaturated soil behaviour aspects such as the smooth transition in the compression curves that is normally observed when soil is loaded at constant suction and the change in yield stress with suction. These models are among other models which employ net stresses and suction as stress state variables for unsaturated soils.

Also, some “double structure” elasto-plastic constitutive models employ net stress and suction as stress state variables for unsaturated soils. These models incorporate the influence of microstructure and macrostructure and the coupling between them on yielding behaviour of unsaturated soils. The first elasto-plastic model of this type was presented by Gens and Alonso (1992). Subsequently, this model was further developed by Alonso et al. (1994) and Alonso et al. (1999). Sánchez et al. (2005) presented a “double structure” unsaturated model based on the concept of “generalised plasticity” rather than classical elasto-plasticity. Generalised plasticity can provide a gradual transition from elastic to full elasto-plastic behaviour and can describe the occurrence of some plastic straining during unloading.

Many classical elasto-plastic models for unsaturated soils use alternative stress state variables to net stress and suction (e.g. Kohgo et al., (1993a, 193b); Modaressi, and Abou-Bekr, 1994; Jommi and Di Prisco, 1994; Jommi, 2000; Lloret and Khalili, 2002 and Sheng et al., 2004). Some of these models use Bishop’s stress tensor as the first stress state variable. One of the advantages of some these models is that the first stress state variable is defined in such a way that both elastic behaviour and shear strength can be related solely to changes of this stress variable, and the second stress state variable (typically matric suction or some function of matric suction) is required solely to define the yield surface (which is expressed in terms of both stress variables). In contrast, if the net stress tensor and matric suction are chosen as the stress state variables (as in *BBM*), then elastic strains, shear strength and yielding behaviour all have to be expressed in term of both stress variables.

The fact that, in some of these models expressed in terms of alternative stress state variables, elastic strains and shear strength can be uniquely related to the first stress state variable has sometimes led authors of such models to call their first stress state variable the “effective stress” tensor. However, it is probably best to reserve the term

“effective stress” for the case where all aspects of mechanical behaviour can be related to a single stress tensor.

### 2.8.3 Anisotropic elasto-plastic models for unsaturated soils

Cui and Delage (1996) were the first to propose an anisotropic elasto-plastic model for unsaturated soils. The model was expressed in terms of net stresses and matric suction, and each constant suction cross-section of the yield surface was in the form of a rotated ellipse in the  $q:\bar{p}$  plane (see Equation 2.26 in Section 2.6.3). Based on experimental results from tests on compacted Jossigny silt, they proposed that the inclination  $\theta$  of the rotated elliptical yield curves was independent of the value of suction (see Figure 2.18 in Section 2.6.3). The anisotropic model employed a non-associated flow rule and importantly, did not allow for any evolution of anisotropy during plastic straining ( $\theta$  remained constant). Cui and Delage (1996) demonstrated the performance of their model by comparison of model simulations against the experimental stress-strain curves from tests on compacted Jossigny silt.

Stropeit et al. (2008), proposed an anisotropic elasto-plastic model for unsaturated soils, expressed in terms of net stresses and suction, which models evolving anisotropy through ideas taken from the saturated anisotropic model  $S - CLAY1$  (see Section 2.7.2) and incorporates this within the unsaturated isotropic model  $BBM$  (see Section 2.8.1). The model of Stropeit et al. (2008) was named  $ABBM$ , and a second slightly modified version, known as  $ABBM1$ , was subsequently published by D’Onza et al. (2011).

Both  $ABBM$  and  $ABBM1$  allow for the possibility of a non-linear increase of shear strength with suction, with the critical state lines for different values of suction defined in the  $q:\bar{p}$  plane by:

$$q = M\bar{p} + Mf(s) \quad (2.52)$$

where alternative linear and non-linear functions were proposed for  $f(s)$ .

Both  $ABBM$  and  $ABBM1$  employ a yield surface in the  $q:\bar{p}:s$  space, each constant suction cross-section of the yield surface taking the form of a distorted ellipse (as in the saturated model  $S - CLAY1$ ). For  $ABBM1$ , the distorted elliptical yield curve is given by:

$$f = (q - \alpha\bar{p})^2 - \left( (M^2 - \alpha^2) \left( \bar{p} + \frac{M}{M - \alpha} f(s) \right) \right) (\bar{p}_m(s) - \bar{p}) = 0 \quad (2.53)$$

Equation 2.53 is illustrated in Figure 2.20. For a yield curve at a non-zero value of  $s$ , vertical tangent points occur at Points  $A$  and  $B$ , corresponding to  $\bar{p} = -Mf(s)/(M - \alpha)$  and  $\bar{p} = \bar{p}_m$  respectively. Inspection of Equation 2.52 and Figure 2.20 shows that, whatever the value of  $\alpha$ , Point  $A$  corresponds to the intersection of the critical state line (defined by Equation 2.52) and the “ $\alpha$ -line” passing through the origin and Points  $A$  and  $B$ . This has the effect that in  $ABBM1$  the critical state line always intersects the apex of the yield curve (where the tangent is horizontal), irrespective of the value of  $\alpha$ . In contrast, the earlier version ( $ABBM$ ) of Stropeit et al. (2008) employed a slightly different yield curve expression to Equation 2.53, with the effect that the critical state line only intersects the apex of the yield curve when  $\alpha$  reaches the unique critical state value  $\alpha_{cs}$  (see Equation 2.34). In both  $ABBM$  and  $ABBM1$ , the yield surface is developed into  $q:\bar{p}:s$  space by assuming that  $\bar{p}_m(s)$  varies with suction according to the same function as the  $LC$  yield curve expression in  $BBM$  (see Equation 2.43).

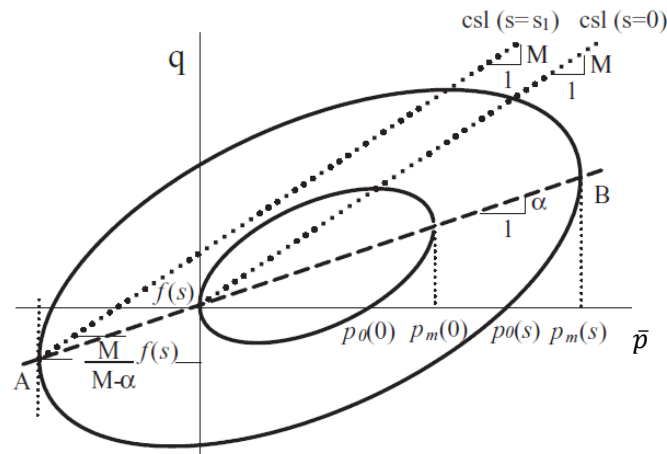


Figure 2.20 Yield curve in the  $q:\bar{p}$  plane of  $ABBM1$  (D’Onza et al., 2011)

In both  $ABBM$  and  $ABBM1$ , the current value of  $\alpha$  is assumed to be independent of suction and the evolution of  $\alpha$  during plastic straining is related to the increments of plastic volumetric strain and plastic shear strain through an expression similar to that in the saturated model  $S - CLAY1$  (see Equation 2.31). Both models employ an associated flow rule (as in  $S - CLAY1$ ).

Stropeit et al. (2008) and D’Onza et al. (2011) demonstrated that  $ABBM$  and  $ABBM1$  both resulted in improved simulations of experimental stress-strain curves when compared with the conventional isotropic model  $BBM$ .

Della Vecchia et al. (2012) proposed a coupled mechanical and water retention constitutive model for unsaturated soil which incorporate the evolution of anisotropy

during plastic straining. The mechanical aspects of the model are expressed in terms of the Bishop's stress tensor (defined in Equation 2.8), which they refer to as the "average skeleton stress". Elastic strains and shear strength are related solely to changes of Bishop's stresses, but the yield surface is expressed in terms of Bishop's stresses and degree of saturation  $S_r$  (rather than suction directly). The variation of  $S_r$  is then related to the variation of suction through the water retention aspects of the model, which incorporate both hydraulic hysteresis and the influence of changes of void ratio on water retention behaviour (including multi-scale coupling between microstructure and macrostructure).

For the stress conditions of the triaxial test, each constant  $S_r$  cross-section of the yield surface proposed by Della Vecchia et al. (2012) takes the form of a distorted ellipse in the  $q:p^*$  plane, of the same form as proposed by Dafalias (1986) for saturated soils (see section 2.6.2) (i.e. the same form as in the saturated model  $S - CLAY1$  (see Equation 2.29). An associated flow rule was applied as in  $S - CLAY1$  (see Equation 2.32), but, unlike  $S - CLAY1$ , the evolution of anisotropy during plastic straining was described by relating changes of  $\alpha$  solely to plastic volumetric strains, with no dependency on plastic shear strains (compare with the  $S - CLAY1$  expression of Equation 2.31). As described in Section 2.7.1, this is physically unrealistic and means that the model does not predict a unique degree of anisotropy at critical states. Hence the model predicts that critical states are influenced by differences in initial anisotropy or by differences of stress path to the critical state, which seems undesirable.

## 2.9 THE COUPLED MECHANICAL-WATER RETENTION MODEL OF WHEELER ET AL. (2003A)

Wheeler et al. (2003a) proposed a combined mechanical and water retention elasto-plastic constitutive model which incorporates coupling in both directions (the influence of plastic changes of degree of saturation on mechanical behaviour and the influence of plastic volumetric strains on water retention behaviour). The model was presented by Wheeler et al. (2003a) solely for the case of isotropic stress states and was subsequently extended by Raveendraraj (2009) to the stress states of the triaxial test, by including the role of deviator stress. The model was generalised to 3D stress states by Lloret et al. (2008) and Lloret (2011). The model is presented here in considerable detail, because it is used in Chapter 7 as the basis for the development of an anisotropic constitutive model for unsaturated soils.

The coupled mechanical-water retention model employs, as stress state variables, the Bishop's stress tensor  $\sigma_{ij}^*$  (defined in Equation 2.8) and the scalar variable modified

suction  $s^*$  (defined in Equation 2.9) (see Section 2.2). For the stress conditions of the triaxial test, this means that the stress state variables are mean Bishop's stress  $p^*$ , deviator stress  $q$  and modified suction  $s^*$ . As shown by Houlsby (1997), the three corresponding work-conjugate strain increment variables are the volumetric strain increment  $d\varepsilon_v$ , shear strain increment  $d\varepsilon_s$  and the decrement of degree of saturation  $-dS_r$  (see Section 2.2).

Development of the model was based on consideration of the physical processes likely to be responsible for the various elastic and plastic components of strains. For the mechanical aspects of the model, elastic volumetric strains and elastic shear strains were considered to be caused by elastic deformation of individual soil particles or aggregates and were therefore considered to be controlled solely by changes of Bishop's stresses. Plastic volumetric strains and plastic shear strains were attributed to slippage at inter-particle or inter-aggregate contacts, and were thus influenced not only by Bishop's stresses but also by the stabilising effect of meniscus water bridges at particle contacts. This stabilising effect was considered to be controlled essentially by the number of contacts affected by meniscus water bridges rather than by the suction within the bridges. The model therefore assumes that the stabilising effect is governed by plastic changes of degree of saturation. For the water retention aspects of the model, elastic changes of degree of saturation were considered to be caused by changes in shape of the air-water interfaces, but without any individual voids flooding or emptying with water. In the model these elastic changes of  $S_r$  are therefore related solely to changes of modified suction  $s^*$ . Plastic changes of  $S_r$  were considered to be caused by individual voids flooding or emptying with water. In the model these plastic changes of  $S_r$  are therefore assumed to be controlled not only by changes of modified suction  $s^*$  but also by changes in the size of voids, as represented by the occurrence of plastic volumetric strains.

### 2.9.1 Elastic behaviour

The increments of elastic volumetric strain, elastic shear strain and elastic change in degree of saturation are given by:

$$d\varepsilon_v^e = \frac{\kappa dp^*}{vp^*} \quad (2.54)$$

$$d\varepsilon_s^e = \frac{dq}{3G} \quad (2.55)$$

$$dS_r^e = \frac{-\kappa_s ds^*}{vs^*} \quad (2.56)$$

The above equations suggest no coupling between the effects of change in  $p^*$  and  $s^*$  on elastic strains, where  $d\varepsilon_v^e$  is solely governed by a change in  $p^*$  whereas  $dS_r^e$  is solely governed by a change in  $s^*$ .

### 2.9.2 Yield surfaces and flow rules

The model includes three yield surfaces in  $q:p^*:s^*$  space, namely the Loading-Collapse (*LC*) surface, the Suction Increase (*SI*) surface and the Suction Decrease (*SD*) surface, see Figure 2.21.

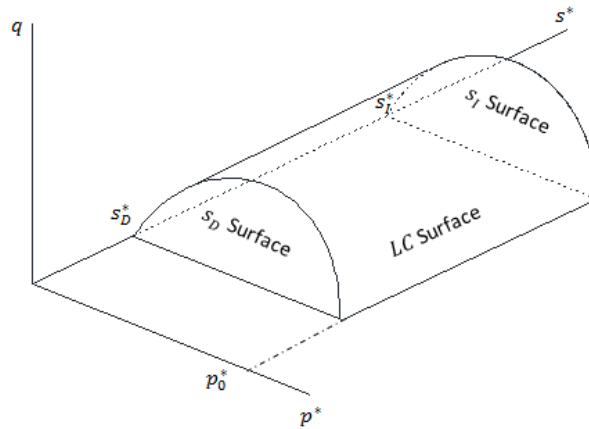


Figure 2.21: Yield surfaces in  $q:p^*:s^*$  space (after Raveendiraraj 2009)

Yielding on the *LC* surface describes the mechanical behaviour and is associated with slippage at inter-particle or inter-aggregate contacts. Plastic volumetric and plastic shear strains occur during yielding on this surface but no plastic changes of degree of saturation occur. Yielding on the *SD* or *SI* surfaces describes the water retention behaviour and is associated with flooding or emptying of voids with water. Plastic changes of degree of saturation occur during yielding on *SD* or *SI* surfaces, but no plastic volumetric strains or plastic shear strains occur.

Raveendiraraj (2009) proposed that cross-sections of the *LC* yield surface in the  $q:p^*$  plane should be elliptical and pass through the origin (equivalent to *MCC* for saturated soils) (see Figure 2.21). The equation of the *LC* yield surface is therefore:

$$f_{LC} = q^2 - M^{*2}p^*(p_0^* - p^*) = 0 \quad (2.57)$$

where  $M^*$  is the aspect ratio of the ellipse (a soil constant) and  $p_0^*$  represents the current size of the ellipse (a hardening parameter). Note that the *LC* yield surface expression of Equation 2.57 includes no dependence on the third stress variable  $s^*$  (i.e. the value of  $p_0^*$

is independent of  $s^*$ ), because the stabilising role of meniscus water bridges is not related directly to  $s^*$  but is instead related to plastic changes of degree of saturation. Modelling of this effect is achieved though the coupled movement of the  $LC$  surface which occurs during yielding on the  $SD$  or  $SI$  surface (described in Section 2.9.3 below).

An associated flow rule is assumed for yielding on the  $LC$  surface, so that when yielding on this surface alone:

$$\frac{d\varepsilon_s^p}{d\varepsilon_v^p} = \frac{2\eta^*}{M^{*2} - \eta^{*2}} \quad (2.58)$$

$$dS_r^p = 0 \quad (2.59)$$

where  $\eta^* = q/p^*$ .

The  $SI$  and  $SD$  yield surfaces are represented by vertical walls in  $q:p^*:s^*$  space (see Figure 2.21), defined by:

$$f_{SI} = s^* - s_I^* = 0 \quad (2.60)$$

$$f_{SD} = s_D^* - s^* = 0 \quad (2.61)$$

where  $s_I^*$  and  $s_D^*$  are the hardening parameters defining the current positions of the  $SI$  and  $SD$  surfaces respectively. Note that the  $SI$  and  $SD$  yield surface expressions of Equations 2.60 and 2.61 include no dependence on the Bishop's stresses  $p^*$  and  $q$ . However, the positions of the  $SI$  and  $SD$  surfaces (and hence the water retention behaviour) is influenced by plastic volumetric strains, through coupled movements of the  $SI$  and  $SD$  surfaces during yielding on the  $LC$  surface (described in Section 2.9.3 below).

Associated flow rules are assumed on both  $SI$  and  $SD$  surfaces, so that when yielding on one of these surfaces alone:

$$d\varepsilon_v^p = d\varepsilon_s^p = 0 \quad (2.62)$$

Also, when yielding on the  $SI$  surface:

$$dS_r^p < 0 \quad (2.63)$$

and when yielding on the  $SD$  surface:

$$dS_r^p > 0 \quad (2.64)$$

### 2.9.3 Coupled movements of the yield surfaces

Yielding on the  $LC$  surface produces plastic volumetric strains. Consequently, this yielding on the  $LC$  surface causes coupled movements of the  $SI$  and  $SD$  surfaces (see Figure 2.22a for the case of isotropic stress states). The coupled movements of  $SI$  and  $SD$  surfaces represents the effect of mechanical loading on decreasing dimensions of voids and passageways which in turn increases the value of modified suction required for flooding or emptying of the voids with water. As a result of the yielding process, the main wetting and main drying curves are shifted to higher values of modified suction (according to the model).

The magnitudes of the coupled movements of the  $SI$  and  $SD$  surfaces are controlled by a coupling parameter  $k_2$ , so that when yielding on the  $LC$  yield surface alone the following coupling relationship holds:

$$\frac{ds_I^*}{s_I^*} = \frac{ds_D^*}{s_D^*} = k_2 \frac{dp_0^*}{p_0^*} \quad (2.65)$$

The effect of this coupling is illustrated (for isotropic stress states) in Figure 2.22a (where  $p^*$  and  $s^*$  are both plotted on logarithmic scales).

Yielding on the  $SI$  or  $SD$  surfaces produces plastic changes of degree of saturation. Consequently, this yielding on the  $SI$  or  $SD$  surface causes coupled movements of the  $LC$  surface (see Figure 2.22b), as a consequence of changes in the number of inter-particle contacts surrounded by meniscus water bridges and hence the stabilising effect of these bridges. These coupled movements of the  $LC$  surface are controlled by a coupling parameter  $k_1$ , so that when yielding on the  $SI$  and  $SD$  surface alone:

$$\frac{dp_0^*}{p_0^*} = k_1 \frac{ds_I^*}{s_I^*} = k_1 \frac{ds_D^*}{s_D^*} \quad (2.66)$$

The effect of this coupling is illustrated (for isotropic stress states) in Figure 2.22b (where  $p^*$  and  $s^*$  are both plotted on logarithmic scales).

Inspection of Equations 2.65 and 2.66 shows that during yielding on any surface the following relationships holds:

$$\frac{ds_I^*}{s_I^*} = \frac{ds_D^*}{s_D^*} \quad (2.67)$$

Hence, the spacing between *SI* and *SD* surfaces is assumed to always remain constant, when  $s^*$  is plotted on a logarithmic scale.

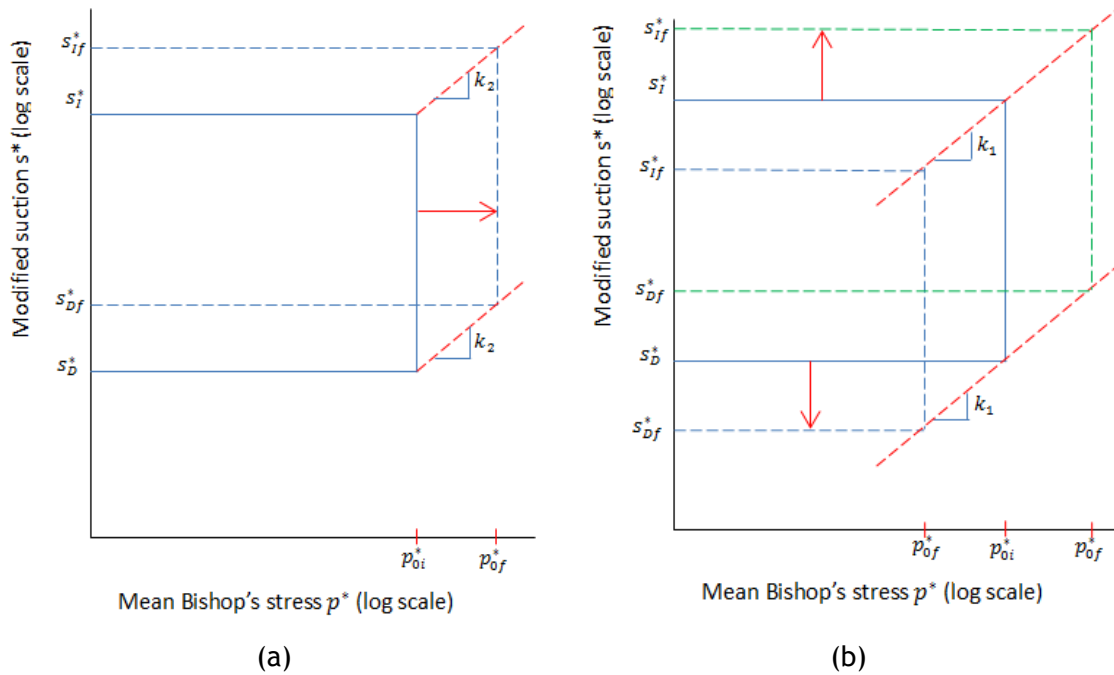


Figure 2.22: Coupled movements of *SI*, *SD* and *LC* yield surfaces for isotropic stress states: (a) yielding on the *LC* yield surface alone, (b) yielding on the *SI* or *SD* yield surface alone (after Wheeler et al., 2003a)

### 2.9.4 Hardening Laws

The full hardening laws allow for the possibilities of yielding on a single yield surface or of yielding simultaneously on two surfaces (when the stress state lies on the edge between *SD* and *LC* surfaces or on the edge between *SI* and *LC* surfaces, see Figure 2.21). These hardening laws are given by:

$$\frac{dp_0^*}{p_0^*} = \frac{v d\varepsilon_v^p}{(\lambda - \kappa)} - \frac{k_1 dS_r^p}{(\lambda_s - \kappa_s)} \quad (2.68)$$

$$\frac{ds_I^*}{s_I^*} = \frac{ds_D^*}{s_D^*} = -\frac{dS_r^p}{(\lambda_s - \kappa_s)} + k_2 \frac{v d\varepsilon_v^p}{(\lambda - \kappa)} \quad (2.69)$$

where  $\lambda$  and  $\lambda_s$  are soil constants.

The special case of the hardening law and coupling relationship when yielding on the *LC* surface alone is recovered by setting  $dS_r^p = 0$  in Equations 2.68 and 2.69. Equation 2.68 then shows (when combined with the elastic volumetric strain from equation 2.54) that yielding on the *LC* surface alone during isotropic loading produces a normal compression line of gradient  $\lambda$  in the  $v:\ln p^*$  plane.  $\lambda$  is also the conventional gradient of the saturated normal compression line in the  $v:\ln p'$  plane.

The special case of the hardening law and coupling relationship when yielding on the *SD* or *SI* surface alone is recovered by setting  $d\varepsilon_v^p = 0$  in Equations 2.69 and 2.68. Equation 2.68 then shows (when combined with the elastic expression of Equation 2.56) that yielding on the *SI* or *SD* surface alone produces a main drying curve or main wetting curve of gradient  $\lambda_s$  in the  $S_r:\ln s^*$  plane (see Figure 2.7). These main drying and main wetting curves are translated in the  $S_r:\ln s^*$  plane by any occurrence of plastic volumetric strains (during yielding on the *LC* surface).

Inspection of Figure 2.7 shows that the model assumes no elastic change in  $S_r$  whenever  $S_r$  is 1 or 0. Raveendraraj (2009) identified a small inconsistency with the Wheeler et al. (2003a) model regarding this assumption. The inconsistency arises when plastic volumetric strains occur at  $S_r = 1$  or 0. The model then predicts irreversible subsequent elastic change in  $S_r$ . The new anisotropic model developed in Chapter 7 does not include the retention aspects of the Wheeler et al. (2003a) model, and this inconsistency therefore does not appear in the current work.

The hardening laws of Equations 2.68 and 2.69 can be combined to give general expressions for the plastic volumetric strain and plastic change in degree of saturation:

$$d\varepsilon_v^p = \frac{(\lambda - \kappa)}{v(1 - k_1 k_2)} \left( \frac{dp_0^*}{p_0^*} - k_1 \frac{dS_D^*}{S_D^*} \right) \quad (2.70)$$

$$dS_r^p = \frac{-(\lambda_s - \kappa_s)}{(1 - k_1 k_2)} \left( \frac{dS_D^*}{S_D^*} - k_2 \frac{dp_0^*}{p_0^*} \right) \quad (2.71)$$

### 2.9.5 Variation of $v$ and $S_r$

Lloret (2011) showed that a wide variety of isotropic stress paths would ultimately arrive at the corner between *LC* and *SD* yield curves, irrespective of the starting position relative to the yield curves. This includes, for example, isotropic loading paths at

constant suction. Lloret (2011) then demonstrated that the model predicts that isotropic stress states at the corner between  $LC$  and  $SD$  yield curves correspond to a unique planar surface in  $v: \ln p^*: \ln s^*$  space and a second unique planar surface in  $S_r: \ln p^*: \ln s^*$  space.

When the stress state remains at the corner between  $LC$  and  $SD$  yield curves (with  $p_0^* = p^*$ ,  $s_D^* = s^*$  and  $q = 0$ ), then the total increments of  $v$  and  $S_r$  can be expressed (by using Equations 2.54, 2.56, 2.70 and 2.71) as:

$$dv = dv^e + dv^p = -\frac{\kappa dp^*}{p^*} - \frac{(\lambda - \kappa)}{(1 - k_1 k_2)} \left( \frac{dp^*}{p^*} - k_1 \frac{ds^*}{s^*} \right) \quad (2.72)$$

$$dS_r = dS_r^e + dS_r^p = -\frac{\kappa_s ds^*}{s^*} - \frac{(\lambda_s - \kappa_s)}{(1 - k_1 k_2)} \left( \frac{ds^*}{s^*} - k_2 \frac{dp^*}{p^*} \right) \quad (2.73)$$

Lloret (2011) showed that a unique expression for  $v$  as a function of  $p^*$  and  $s^*$  is obtained when integrating Equation 2.72:

$$v = N^* - \lambda^* \ln p^* + k_1^* \ln s^* \quad (2.74)$$

where  $N^*$  is a soil constant and:

$$\lambda^* = \frac{(\lambda - \kappa k_1 k_2)}{(1 - k_1 k_2)} \quad (2.75)$$

$$k_1^* = k_1 \frac{(\lambda - \kappa)}{(1 - k_1 k_2)} \quad (2.76)$$

$\lambda^*$  and  $k_1^*$  are the gradients of the unique planar surface in  $v: \ln p^*: \ln s^*$  space. Similarly, a unique expression for  $S_r$  as a function of  $p^*$  and  $s^*$  is obtained when integrating Equation 2.73:

$$S_r = \chi^* - \lambda_s^* \ln s^* + k_2^* \ln p^* \quad (2.77)$$

where  $\chi^*$  is a soil constant and

$$\lambda_s^* = \frac{(\lambda_s - \kappa_s k_1 k_2)}{(1 - k_1 k_2)} \quad (2.78)$$

$$k_2^* = k_2 \frac{(\lambda - \kappa)}{(1 - k_1 k_2)} \quad (2.79)$$

$\lambda_s^*$  and  $k_2^*$  are the gradients of the unique planar surface in  $S_r$ :  $\ln p^*$ :  $\ln s^*$  space.

Equations 2.74 and 2.77 describe the evolution of  $v$  and  $S_r$ , respectively, under isotropic states, provided that the stress state is at the corner between the  $LC$  and  $SD$  yield curves and provided that the soil remains unsaturated. It is worth mentioning that the parameters  $\lambda^*$ ,  $k_1^*$ ,  $\lambda_s^*$  and  $k_2^*$  are given in Equations 2.75, 2.76, 2.78 and 2.79 in terms of the original soil parameters (i.e.  $\lambda$ ,  $\kappa$ ,  $k_1$ ,  $k_2$ ,  $\lambda_s$  and  $\kappa_s$ ), so that no new soil parameters are introduced. The uniqueness of the planar surfaces described by Equations 2.74 and 2.77 was validated by Lloret (2011) against experimental data from isotropic compression tests at different non-zero suction values, performed by Sivakumar (1993). Lloret (2011) also showed that measuring the gradients  $\lambda^*$ ,  $k_1^*$ ,  $\lambda_s^*$  and  $k_2^*$  of these two planar surfaces forms an ideal method for experimental determination of the values of the soil constants  $\lambda_s$ ,  $\kappa_s$ ,  $k_1$  and  $k_2$  if the values of  $\lambda$  and  $\kappa$  are already known from tests on saturated samples.

It is worth mentioning also that these unique relationships do not apply when yielding takes place on the  $LC$ ,  $SI$  or  $SD$  yield curves alone. However in many cases, due to the coupled movements of the curves, the stress state would eventually arrive at the corner between  $LC$  and  $SD$  curves if the stress path was continued indefinitely. It should be noted also that, the unique planar surfaces are valid for the case where  $0 < S_r < 1$  (i.e. while the soil remains unsaturated).

For general stress states, which do not necessarily lie on the  $LC$  and  $SD$  yield surfaces and where the deviator stress  $q$  is not necessarily zero, the values of  $v$  and  $S_r$  can be calculated by considering an elastic stress path starting from a point corresponding to the unique planar surfaces of Equations 2.74 and 2.77 (see Figure 2.23) to give:

$$v = N^* - \lambda^* \ln p_0^* + k_1^* \ln s_D^* + \kappa \ln \left( \frac{p_0^*}{p^*} \right) \quad (2.80)$$

$$S_r = \chi^* - \lambda_s^* \ln s_D^* + k_2^* \ln p_0^* - \kappa_s \ln \left( \frac{s^*}{s_D^*} \right) \quad (2.81)$$

Equations 2.79 and 2.80 provides general expressions for  $v$  and  $S_r$ , valid for any stress state.

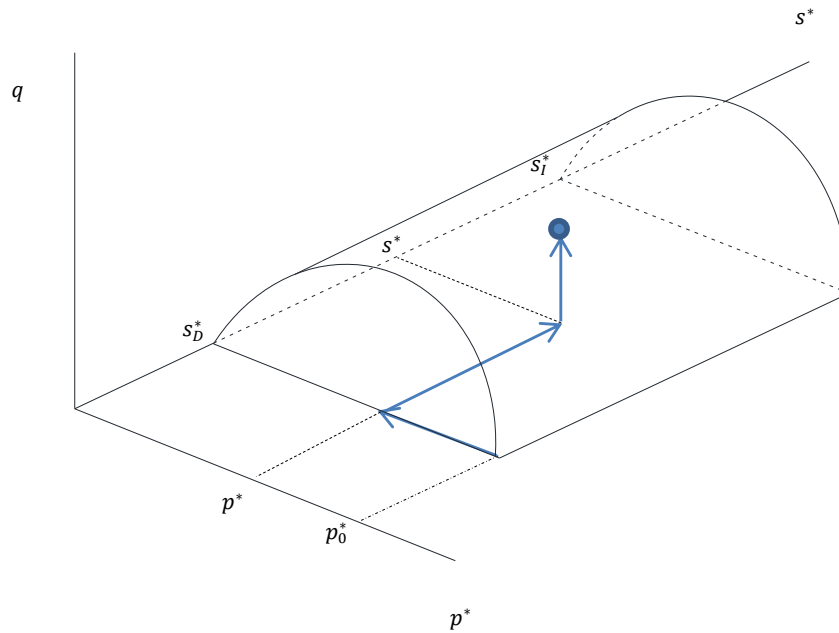


Figure 2.23 Stress path used to calculate  $v$  and  $S_r$  for general stress states

### 2.9.6 Critical states

The definition of critical states implies that a critical state is reached when no further change in  $q, p^*, s^*, S_r$  or  $v$  is taking place with infinite increase in shear strain. The associated flow rule of Equation 2.58 means that the model predicts that critical states will be achieved for stress states that correspond to the apex of the  $LC$  yield surface. This results in a unique critical state line in the  $q:p^*$  plane:

$$q = M^* p^* \quad (2.82)$$

Authors such as Gallipoli et al. (2008) and Raveendiraraj (2009) demonstrated, by comparison with experimental data, that Equation 2.82 is a reasonable approximation for many soils.

The model predicts that critical states must lie at the top of the elliptical cross-section of the  $LC$  yield surface, but they do not necessarily have to also lie on the  $SD$  or  $SI$  surface. However Lloret (2011) demonstrated that a wide variety of shearing stress paths will arrive at the edge between  $LC$  and  $SD$  yield surfaces prior to reaching a critical state, and the critical state will subsequently correspond to a stress state falling on both  $LC$  and  $SD$  surfaces. Lloret (2011) then showed that, for critical states which fall on both  $LC$  and  $SD$  surfaces, the model predicts a unique planar critical state surfaces in both  $v:\ln p^*:\ln s^*$  space and in  $S_r:\ln p^*:\ln s^*$  space.

For stress states at the intersection of the *LC* and *SD* yield surfaces and at the top of the elliptical cross-section of the yield surface,  $s_D^* = s^*$  and  $p_0^* = 2p^*$ . Insertion of these conditions in the general equations for  $v$  and  $S_r$  of Equations 2.74 and 2.77 led Lloret (2011) to the following expressions for the planar critical state surface for  $v$  and  $S_r$ :

$$v = N^* - (\lambda^* - \kappa)\ln 2 - \lambda^* \ln p^* + k_1^* \ln s^* \quad (2.83)$$

$$S_r = \chi^* + k_2^* \ln 2 - \lambda_s^* \ln s^* + k_2^* \ln p^* \quad (2.84)$$

Equation 2.83 represents a critical state planar surface in  $v:\ln p^*:\ln s^*$  space that is parallel to the corresponding isotropic compression surface (see Equation 2.74) with the vertical spacing between the two surfaces given by  $(\lambda^* - \kappa)\ln 2$ . Equation 2.84 defines a critical state planar surface in  $S_r:\ln p^*:\ln s^*$  space that is parallel to the corresponding isotropic compression surface (see Equation 2.77), with the vertical spacing between the two surfaces given by  $k_2^* \ln 2$ .

Lloret (2011) investigated the validity of Equations 2.83 and 2.84 against the experimental data of Sivakumar (1993). He confirmed the existence of such unique critical state planar surfaces in  $v:\ln p^*:\ln s^*$  space and in  $S_r:\ln p^*:\ln s^*$  space and that each surface was parallel to the corresponding normal compression surface. He also showed that the experimental spacing between the critical state and normal compression surfaces for  $S_r$  was well captured by the model, but that the spacing between the critical state and normal compression surfaces for  $v$  was overestimated by the model. The overestimation in the spacing between normal compression surface and the critical state surface observed in  $v:\ln p^*:\ln s^*$  space is inherited from the *MCC* model which serves as the saturated base-model.

The full mechanical and water retention model of Wheeler et al. (2003a), extended to the stress states of the triaxial test by Raveendraraj (2009) and Lloret (2011), includes a total of 10 soil constants:  $\lambda, \kappa, \lambda_s, \kappa_s, k_1, k_2, G, M^*, N^*$  and  $\chi^*$ .

# 3

## EXPERIMENTAL SYSTEMS AND CALIBRATIONS

The experimental investigation was carried out in three independent triaxial systems. System 1 and System 2 were designed to undertake suction controlled unsaturated triaxial compression and extension tests, while System 3 was designed to carry out saturated triaxial compression and extension tests. This chapter describes, in detail, the elements of each system including both the triaxial cell and associated equipment for measuring or controlling pressures, volumes, etc. The calibration of the load/pressure/displacement transducers and of the apparent volume change of both cell and pore water lines is also described in this chapter.

### 3.1 SYSTEM 1 AND SYSTEM 2 (UNSATURATED TRIAXIAL CELLS)

Sivakumar et al. (2006) presented a new version of double wall cell triaxial apparatus with a major improvement of changing the material of the inner cell to high quality glass to eliminate water absorption by the acrylic wall as reported in Wheeler (1986) and Sivakumar (1993). System 1 and System 2 were designed and built by the company V J Tech Ltd and consisted of a double wall triaxial cell (based on the work by Sivakumar et al. (2006)), drainage system, controlling and measuring devices and data acquisition system.

#### 3.1.1 Double wall cell

Figure 3.1 shows a schematic diagram of the double wall cell. The outer cell is a standard acrylic cylinder capable of maintaining a maximum pressure of 1600 kPa. The top cover is made of stiff metal with a hole located at its centre. A hanging screw passes through this hole to provide support to the load cell. Nine outlets in total are located in the base of the outer cell and are equipped with push-in fittings. One of these outlets is for filling and emptying the outer cell, one is for pressurizing the outer cell, four outlets are for pore water drainage to the soil sample, one outlet is for filling, emptying and pressurizing the inner cell, one outlet is for pore air drainage to the soil sample and one outlet is for the temperature probe.

The inner cell is manufactured with a detachable base that is connected to the loading ram by a screw joint. The inner cell base has six outlets with compression fittings, including one outlet to pressurize and measure the water volume changes of the inner cell, one outlet to accommodate the pore air drainage line and four outlets to accommodate the pore water drainage lines.

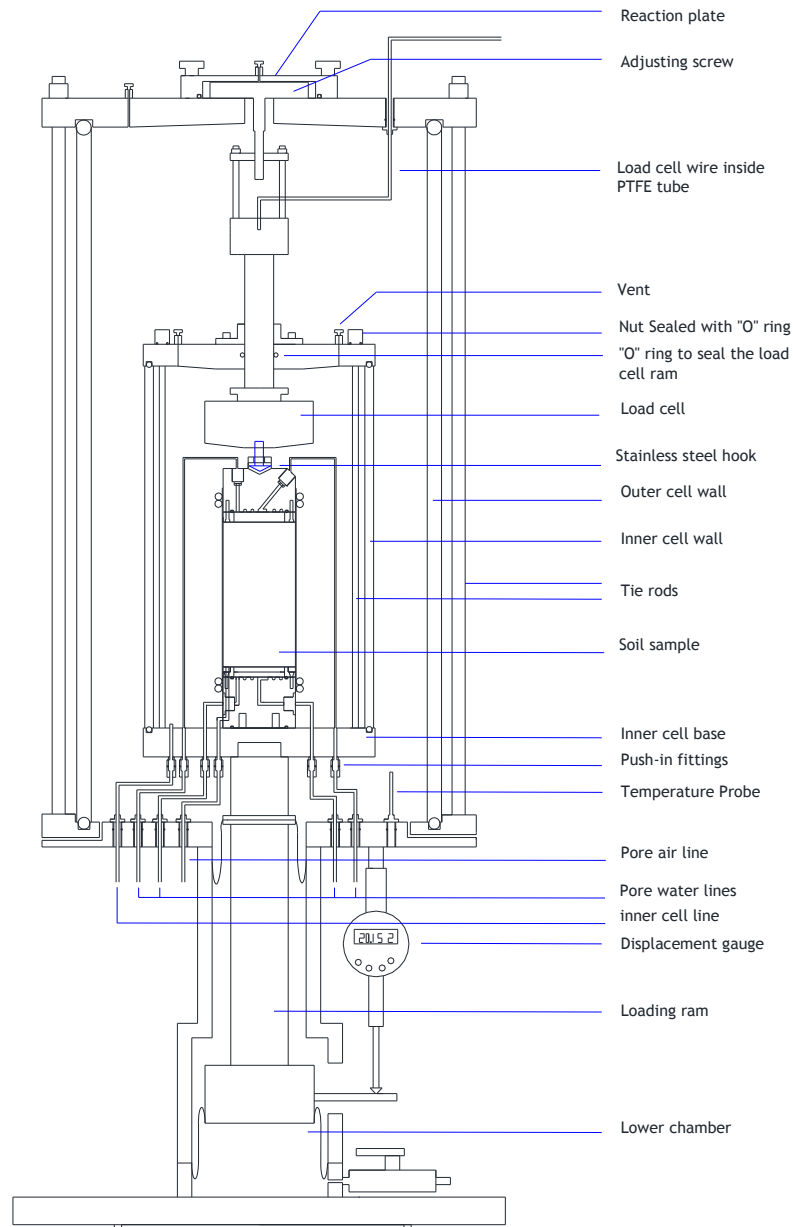


Figure 3.1 Schematic diagram of the double wall cell

The top cap and the base pedestal are each fitted with dual pore water drainage lines through flexible PTFE tubes to allow flushing of any trapped air. The base pedestal is also fitted with a single pore air drainage line. A submersible load cell type STALC3 – 5 kN is

located inside the inner cell and a tight “O” ring is positioned inside the central hole of the top cover around the load cell ram to prevent any water leak between the inner and outer cells during movement of the ram. The load cell electrical wire passes inside the hollow ram then passes through a PTFE tube which has one end connected to the ram and the other end connected to the outer cell cover. In a typical triaxial test, a deviator load or displacement is applied by controlling the pressure in the lower chamber as in standard Bishop-Wesley apparatus. The axial displacement is conventionally measured by a displacement gauge from the change of position of a beam attached to the lower chamber with respect to a reference point attached to the cell.

### **Arrangement for the application of deviator load**

The apparatus was initially designed by VJ Tech for testing soil specimen of 50 mm diameter and 100 mm height in triaxial compression with a maximum travel displacement of only 22 mm. This travel distance was not always sufficient to explore soil behaviour through to critical states. A new part was, therefore, designed during the present project and manufactured by the workshop at the School of Engineering of the University of Glasgow to allow re-setting of the positions of the load cell and the lower chamber during tests.

In this work the original VJ Tech setup shown in Figure 3.1 was only used for tests which involved one or more extension loading stages. In these tests the load cell was initially suspended from the top cover by using the screw shown in Figure 3.1 and there was therefore no initial deviator stress applied to the sample during suction equalization or, if applicable, isotropic compression stages. In this setup it was also not possible to gain additional travel distance by re-setting the position of the load cell and lower chamber during tests.

Figure 3.2 shows the alternative “ball-bearing” arrangement designed in this work as a modification to the original VJ Tech Ltd setup and adopted for those tests which included only triaxial compression loading stages. In this setup, the submerged weight of the load cell is carried by the soil sample (about 12 N or 6 kPa deviator stress for a sample with diameter of 50 mm). In this setup, additional stroke distance can be gained during the test by lowering the load cell and the piston of the lower chamber once travel has run out. This is achieved by manually adjusting the position of the ram via a double-threaded screw while keeping deviator stress constant.

A stiff stainless steel plate, with an opening in the middle to accommodate insertion of the loading cell hook, is screwed to the top cap (see Figure 3.3) to allow application of a

tensile force when required. During assembly of the cell, the small stainless steel hook of the load cell with a truncated end in the shape of arrow-head was slotted through the opening of this plate, then the load cell was rotated by 90 degrees to engage with the top cap. During extension loading, the upper surface of the hook was pulling against the stainless plate (see Figure 3.3a) while during compression loading, the bottom arrow-head surface of the hook was pushing against a central bevel on the top cap (see Figure 3.3b).

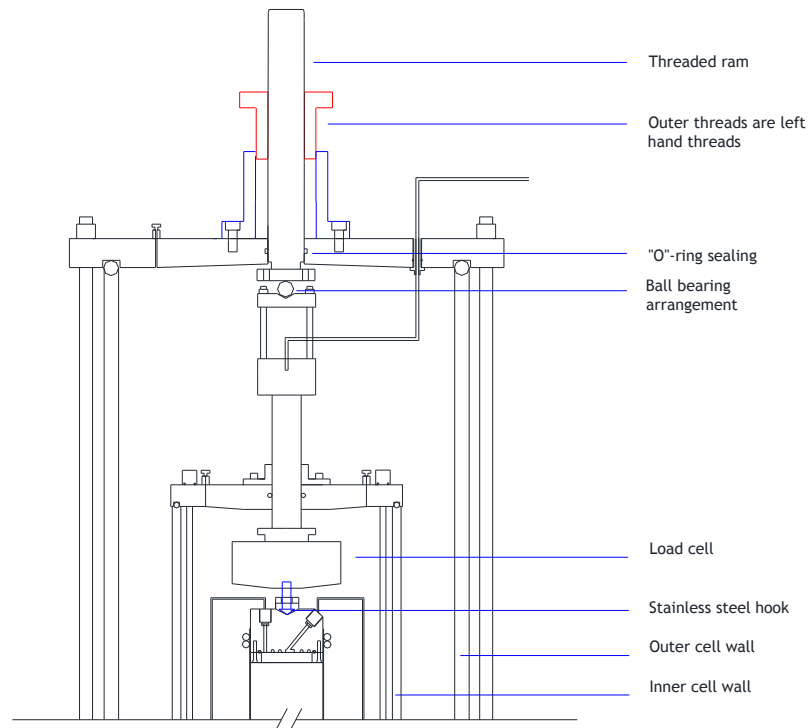


Figure 3.2 Arrangement for triaxial compression tests

### 3.1.2 Pedestal and top cap

The original design by VJ Tech Ltd of the base pedestal and top cap was not suitable for testing unsaturated soil samples. Therefore, these two parts had to be re-designed during this work and sent to VJ Tech for manufacturing.

Figure 3.4 and Figure 3.5 show the layout of the pedestal and top cap respectively, together with their high air entry (*HAE*) ceramic filter holders. Pore air drainage is arranged through the pedestal so that only a short PTFE tube connection was needed (see Figure 3.1) and the amount of diffused air into cell and the effect of tubing compressibility on volume measurement during loading/unloading conditions could therefore be minimized. A spiral flushing groove (2 mm width and 2 mm depth) is used for the pore water drainage connections on both pedestal and top cap. This arrangement

has two advantages; firstly, it increases water conductivity by providing sufficient contact between the high air entry ceramic filter and the water in the drainage lines; secondly, it provides higher efficiency in removing any trapped air beneath the ceramic filter as a single flushing path and no sharp corners are present in the water flow path during flushing.

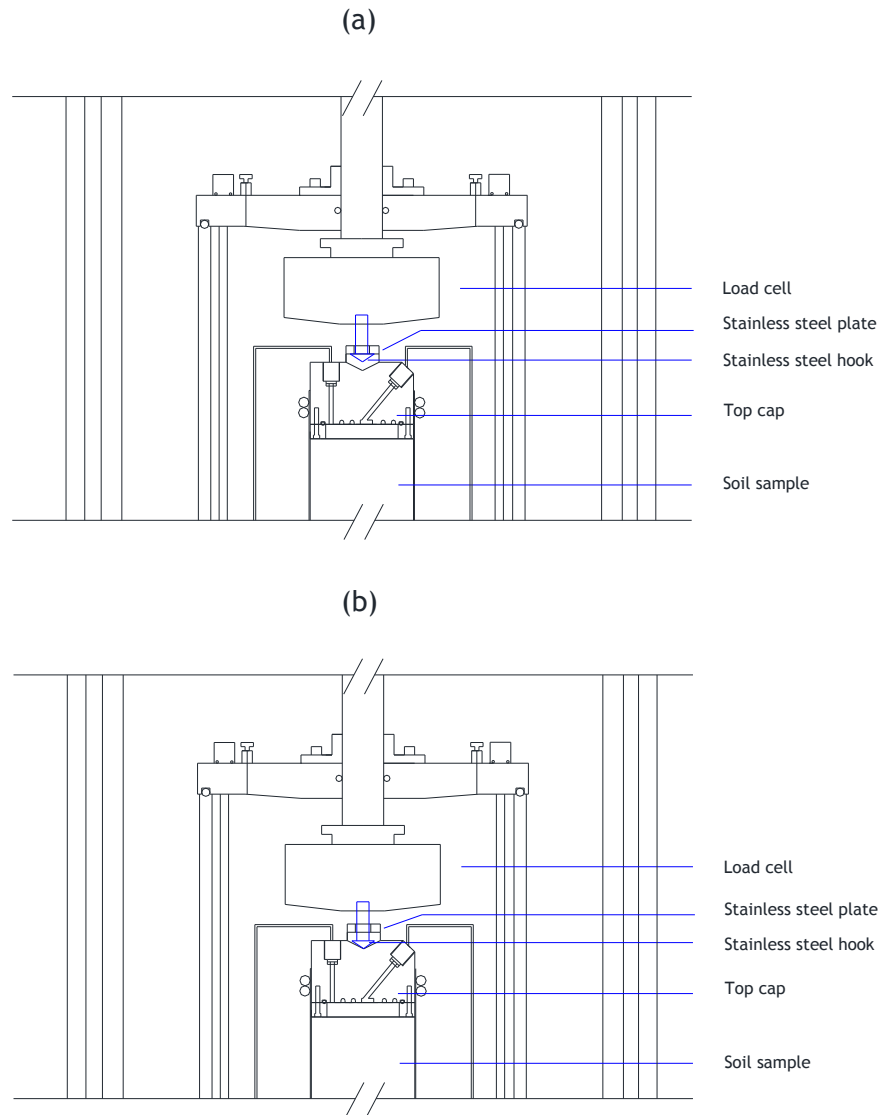


**Figure 3.3 Load cell hook position: (a) triaxial extension (b) triaxial compression**

Both pedestal and top cap were made of stainless steel and stainless steel filter holders were attached to them by means of four 2 mm counter-sunk screws. Figure 3.4 and Figure 3.5 show the filter holders of the pedestal and top cap, respectively. Glued within each filter holder is a 35 mm diameter high air entry ceramic filter with an air entry value of 500 kPa. In order to maintain good distribution of air pressure at the sample base, a porous annulus made of sintered brass (50 mm outer diameter and 40 mm inner

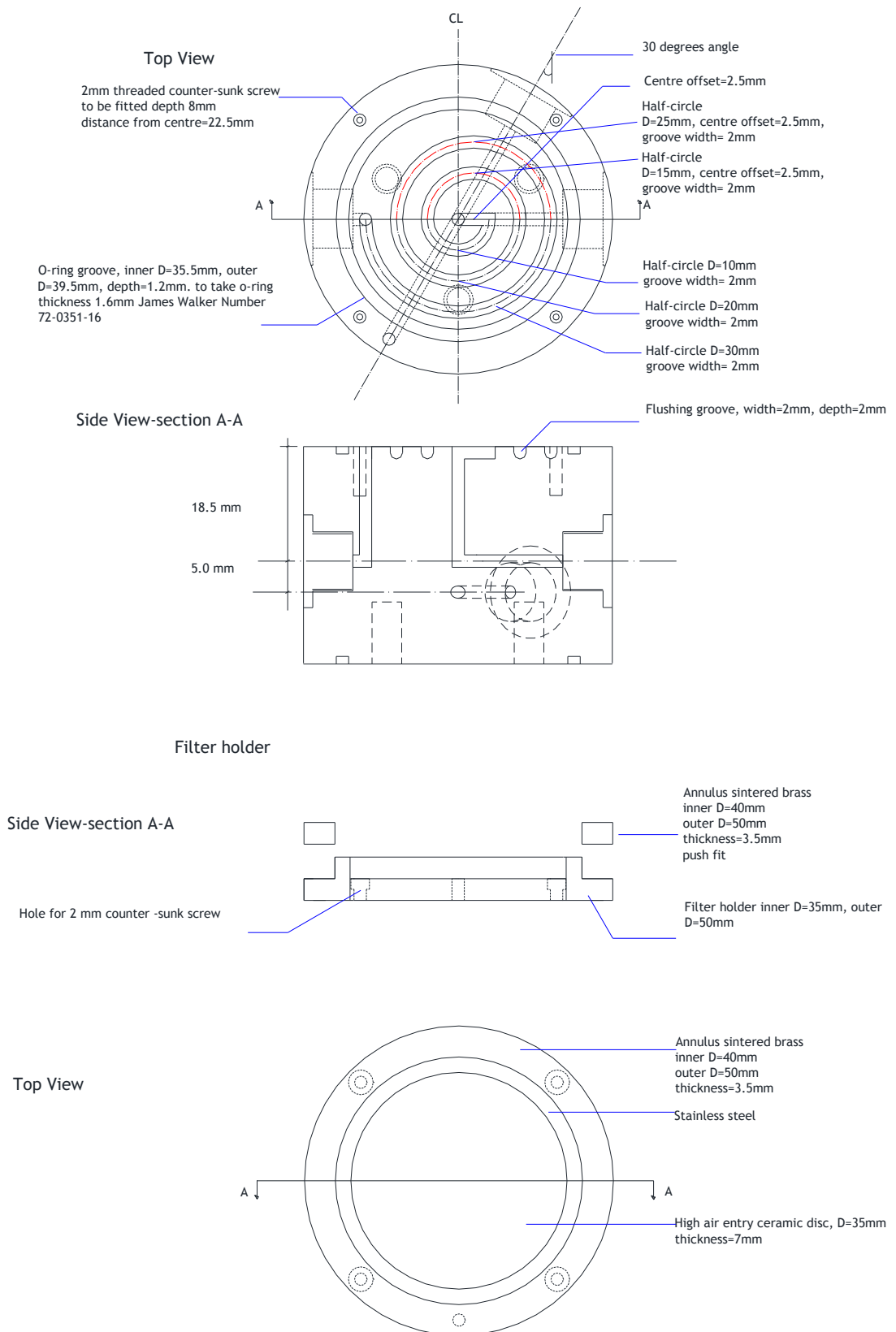


Figure 3.4 Base pedestal design

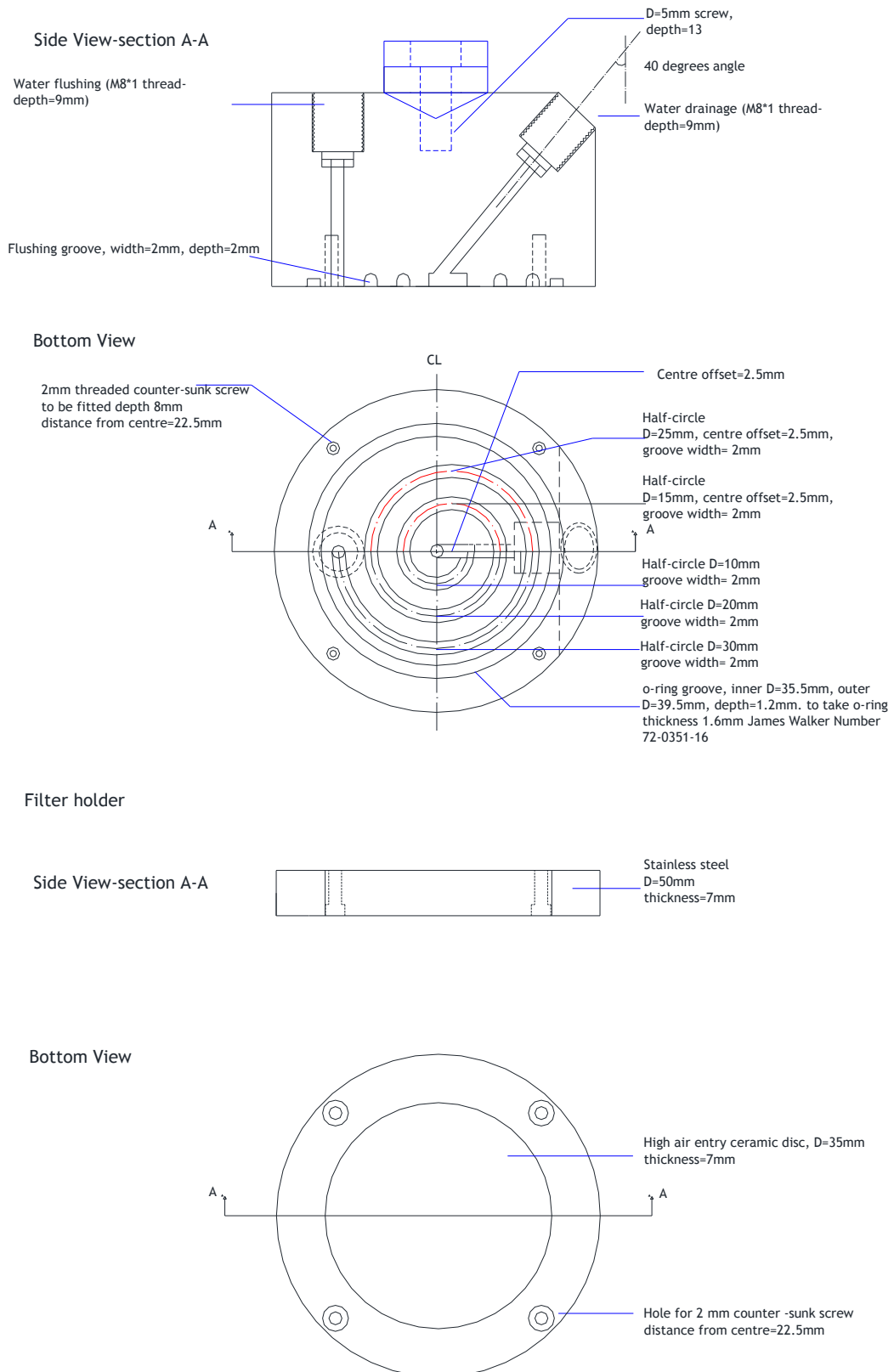


Figure 3.5 Top cap design

diameter) is positioned on a shoulder set within the pedestal filter holder. An “O” ring is placed in a groove between the spiral flushing groove on the pore water drainage lines and the air line outlet in order to prevent any air leak to the water drainage line. The design of top cap filter is the same as the design of pedestal filter with the only exception being the absence of the sintered brass annulus for air drainage.

### 3.1.3 Control or measurement of pressure and volume

#### Sample volume change gauges

A double wall cell is used because it allows measurement of the changes in volume of the soil specimen from the flow of water to or from the inner glass cell. This inner cell does not deform, because the same pressure is applied on both sides of the glass, and it does not adsorb water, being made of glass. In order to measure the inflow or outflow of water to the inner cell, this project made use of Imperial College-type volume gauges manufactured by V J Tech Ltd, shown schematically in Figure 3.6.

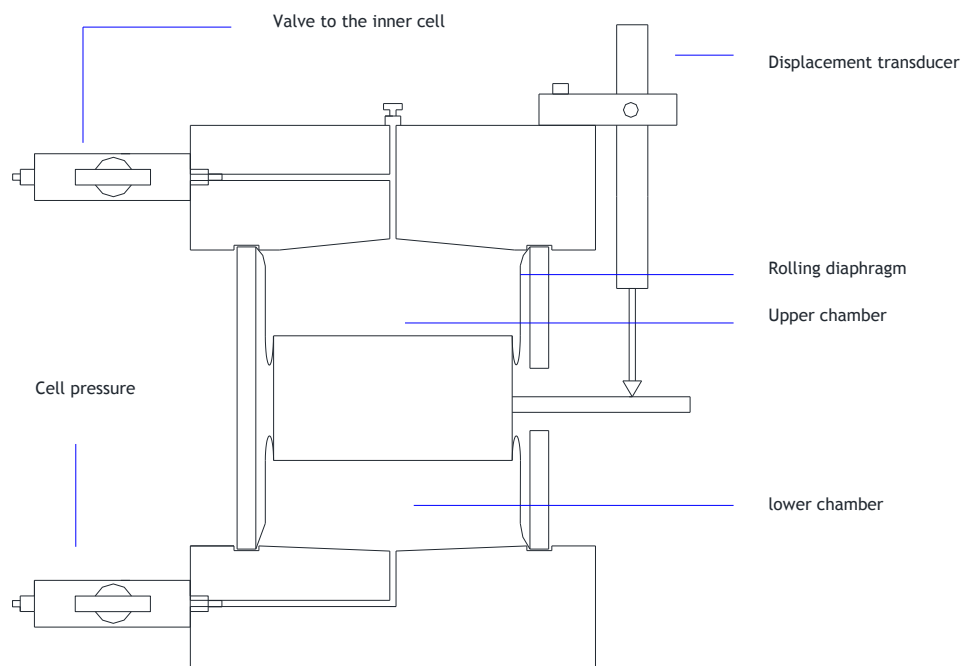


Figure 3.6 Schematic diagram of cell volume gauge

The pressure in the upper chamber of the volume gauge, which is connected to the cell, is maintained by controlling the pressure in the lower chamber of the gauge. The pressure in the upper chamber is transferred to the inner cell through an outlet installed on the top cover of the volume gauge. Any outflow/inflow of water from/into the upper chamber causes upward/downward movement of the piston connecting the two chambers. The movement of the piston is detected by a displacement transducer and

hence the volume change is deduced by converting the travel of the transducer to volume change by applying a suitable calibration. The capacity of this gauge was  $100 \text{ cm}^3$  which was sufficient to perform a full triaxial test without need of re-setting the gauge during the course of the experiment.

### Water pressure controllers

Piston-pumps were used to control cell pressure, pore water pressure and lower chamber pressure. A schematic diagram of this type of device is shown in Figure 3.7. The controller provides a stable pressure source without needing a compressed air line. It works on the principle of pressurising a liquid (de-aired water) inside a cylinder by applying a gradual movement of a piston to get to a target pressure. The pressure inside piston is measured by an integral pressure transducer with a range of  $0 - 3000 \text{ kPa}$ . The piston movement is triggered by an electrical stepper motor and gearbox. The water pressure controllers can also be used to measure volume change, and pore water pressure controller was used to measure pore water volume change. The change of water volume inside the piston is deduced from the number of steps of the stepper motor and, therefore, the accuracy of the measurement is proportional to the size of step. The capacity of cylinder is  $250 \text{ cm}^3$  and that was more than enough to perform full triaxial test without need of re-setting the gauge during the course of the experiment. The cell pressure controller could not be used to measure the volume flow to the inner cell (and hence the sample volume change), because this controller provided the pressure source (and hence water flows) to both inner and outer cells. A separate Imperial College-type volume change gauge (as described previously) therefore had to be used to measure the flow to the inner cell.

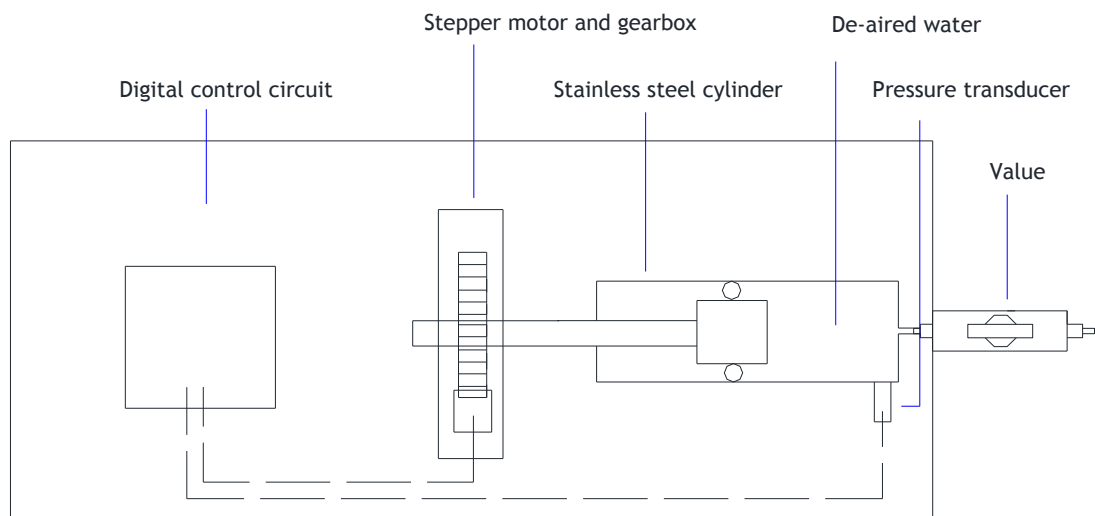


Figure 3.7 Schematic diagram of water pressure controller

### **Air pressure controller**

The pore air pressure line was provided by a pressure regulator that uses a stepper motor to modify the air pressure supplied by an external compressor. The air pressure is measured by an integral pressure transducer with a range of 0 – 3000 kPa. An increased fluctuation of air pressure was initially noticed during periods of humid weather which was avoided by installing an air drying unit on the main air line.

### **Other sensors**

The following additional transducers (shown in Figure 3.1) were also used during the course of the experimental campaign:

- A submersible load cell (5 kN capacity) which was used to measure the deviator force applied to the sample. As confirmed by the manufacturer, this load cell was also capable of measuring a maximum of 1 kN tensile force which was necessary to perform triaxial extension tests.
- A temperature sensor with a precision of 0.1°C which was located on the base of the outer cell and measured the temperature of the water in the outer cell.
- A digital displacement gauge (Mitutoyo ID – 1025) which was used to measure the variation of sample height with a maximum travel distance of 25 mm and a precision of 0.001 mm.

#### **3.1.4 Logging and control system**

All pressure, volume, displacement and load transducers were connected to corresponding input channels of a data logger (Model MPX3000) through a system of data cables and interfaces. The data logger communicated with the software “Clisp Studio” (developed by VJ Tech Ltd).

In the software, a test can be divided into several stages i.e. suction equalisation, loading, wetting, shearing, etc. with different parameters defined for each stage. Parameters could also be defined as “common data” to make them accessible from any stage within a test. “Common data” could be divided into three categories; “Input”, “Measured” and “Calculated”. “Input” category includes, for example, initial sample height, inclination of stress path and initial position of the lower chamber. “Measured” category includes, for example, cell pressure, pore water pressure, air pressure and pore water volume. “Calculated” category includes any derived variables from processing the input and measured data. Due to the existence of specific problems with the logging system when using multistage configuration, it was decided to use single stage

configuration, which implied stopping the current stage while maintaining the loading condition and changing, if necessary, the controlling and the input parameters manually.

The software was set up to control a number of different variables in order to run stress path triaxial tests on unsaturated soil samples. These possible control variables included, for example, mean net stress, deviator stress, suction, axial strain and volumetric strain. Each controller was set to impose the value of a given soil variable by ramping or maintaining the target value of that variable. For each controller, either the pressure or volume channel could be used to control a certain variable. The data could be viewed in either table form or graphical form and it could also be transferred to Excel or Matlab spreadsheets. A typical interface of the Clisp Studio software is shown in Figure 3.8.

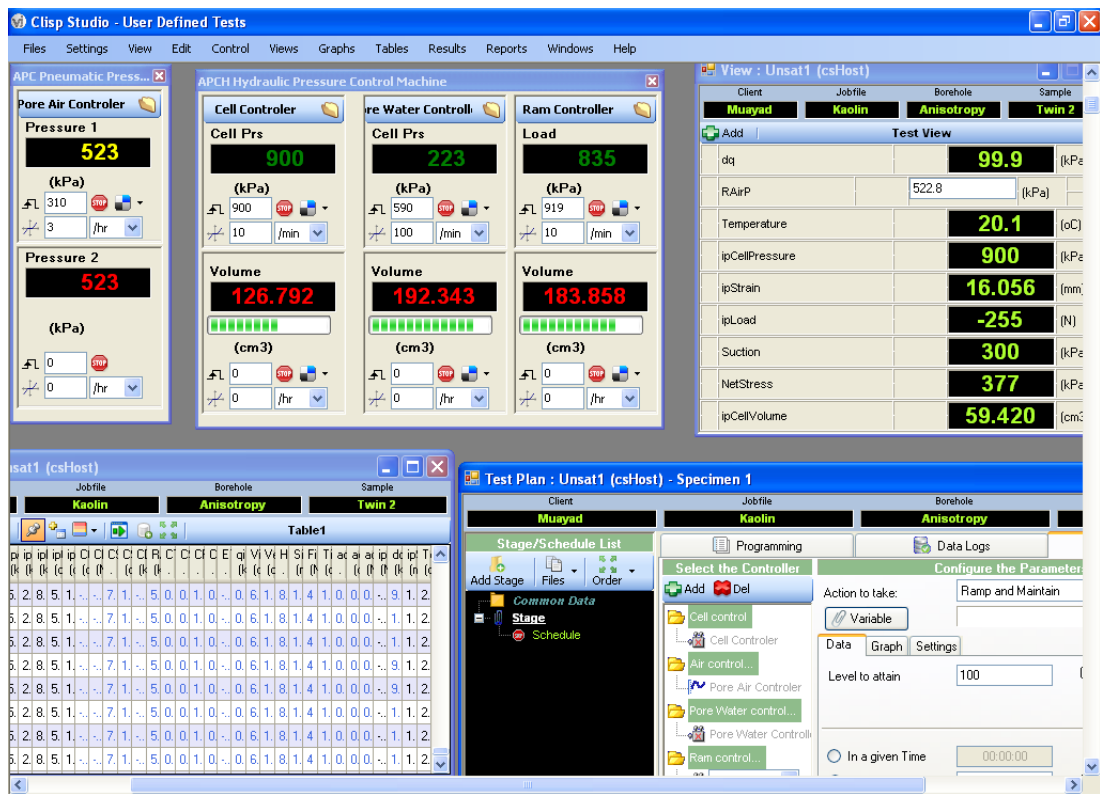


Figure 3.8 Typical interface of Clisp Studio software

### 3.1.5 General equipment layout

A photograph of System 1 and System 2 is shown in Figure 3.9. The schematic layout for System 1 and System 2 is shown in Figure 3.10, including the cell, the control and measurement devices and the data logging unit. Each system has three water pressure/volume controllers to supply pressure to the cell, lower chamber and pore water lines, respectively, as well as one air pressure controller.

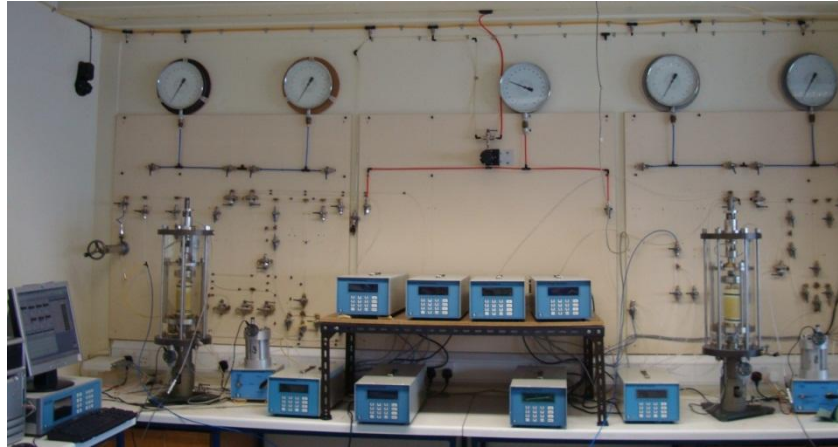


Figure 3.9 Photograph of System 1 and System 2

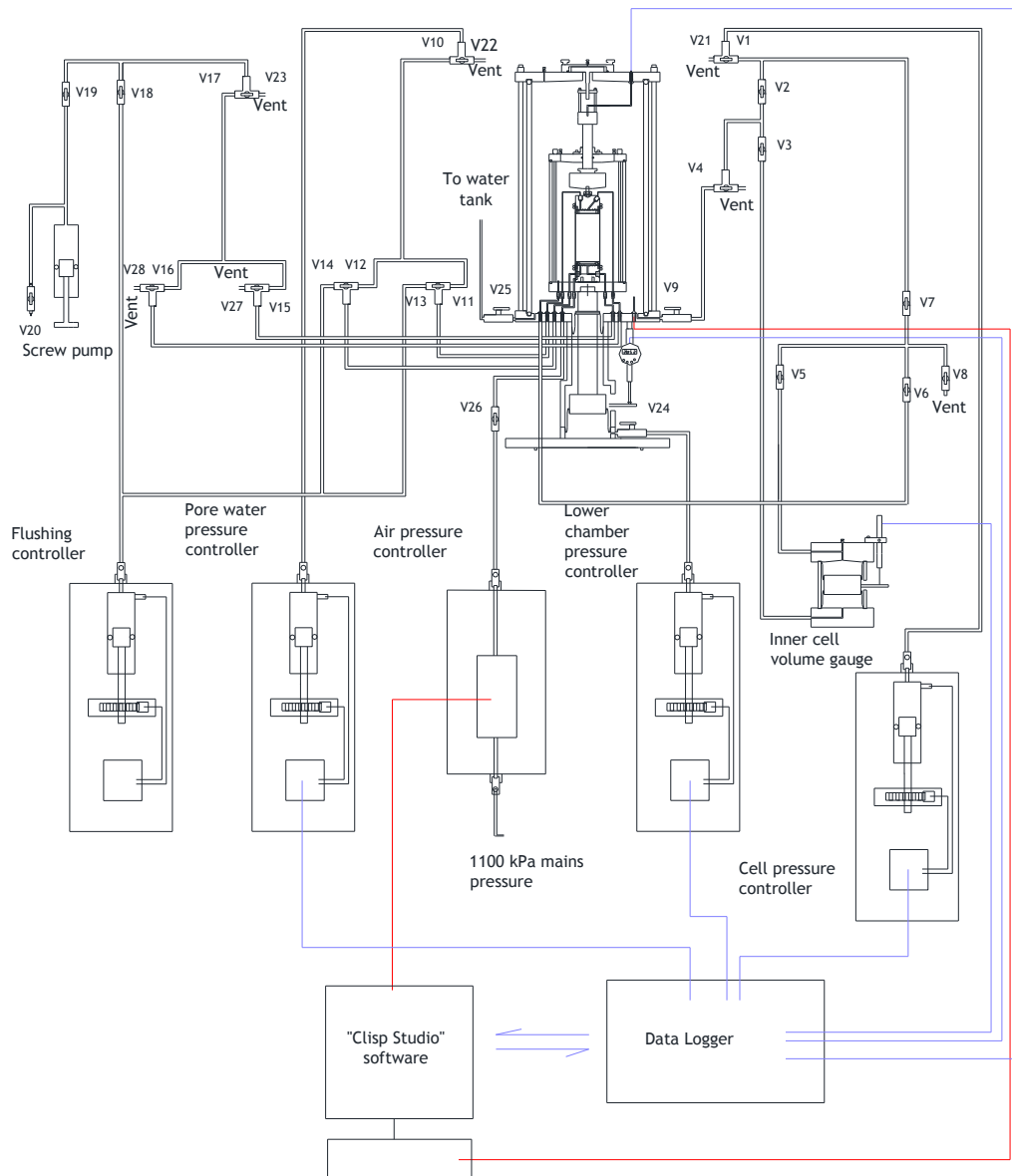


Figure 3.10 Schematic layout of System 1 and System 2

To avoid the risk of breaking the inner glass cell due to a pressure difference across the inner wall, both cells are pressurized by using the same controller. Therefore, the pressure source from the single controller is split in two lines, one going straight to the outer cell and another connected to the lower chamber of the volume gauge whose upper chamber is in turn connected to the inner cell.

The compressed air supplied from a compressor at a pressure of 1600 kPa is first reduced to 1100 kPa by using a manual regulator and then fed to the air pressure controller. The drainage and flushing system was carefully designed to ensure accurate measurements, with connecting PTFE tubes (4 mm outer diameter and 2.5 mm inner diameter) kept as short as possible to reduce errors caused by expansion of the tubes and diffusion of moisture through the tubes walls. One-way and two-way ball valves (manufactured by Legris) were installed on a board and special ferrule were inserted at tube ends to reduce leakage at junctions.

### 3.1.6 Flushing of diffused air

If the pore water drainage system is sealed against air leaks and if the high air entry filters are saturated with de-aired water, then air can only enter the drainage line from the soil sample by diffusion through the saturated high air entry filter. Diffused air can accumulate inside the drainage system causing errors in pore water volume measurements and in the applied suction. The amount of air diffusing through the saturated high air entry filter mainly depends on the applied suction level and it increases with increasing suction. In addition, a reduction of pore water pressure (regardless of whether suction changes or stays constant) can cause air to come out of solution leading to the formation of air bubbles in the drainage system. To remove diffused air from the drainage line, a diffused air flushing system was used as shown in Figure 3.11. At the start of each test, the screw pump was carefully emptied and filled several times with de-aired water to eliminate any trapped air. During the test, valves 10,11 and 12 were open, with pressure applied from the pore water pressure controller. Valves 17,18 and 19 were also open with water pressure equal to the pore water pressure applied from an independent flushing controller, however valves 15 and 16 were closed. Consequently, the de-aired water in the screw pump and in the drainage lines up to valves 13,14,15 and 16 was under pressure at a level imposed by the flushing controller.

The flushing procedure started by closing valve 18 to isolate the screw pump from the flushing controller. Purging of diffused air from the top cap and the pedestal was then performed one at the time. To flush the diffused air in the top cap drainage path, valve

11 was first closed and valves 13 and 15 were subsequently opened. One way flushing was achieved by slowly unscrewing the pump (to avoid a large drop of pore water pressure at the boundaries of the soil sample) to generate water flow from the independent pressure controller to the screw pump. After the end of flushing, valves 13 and 15 were closed and valve 11 was opened again. To flush the diffused air in the pedestal drainage path, valve 12 was first closed and valves 14 and 16 were subsequently opened. A procedure similar to that described for the top cap drainage path was then followed.

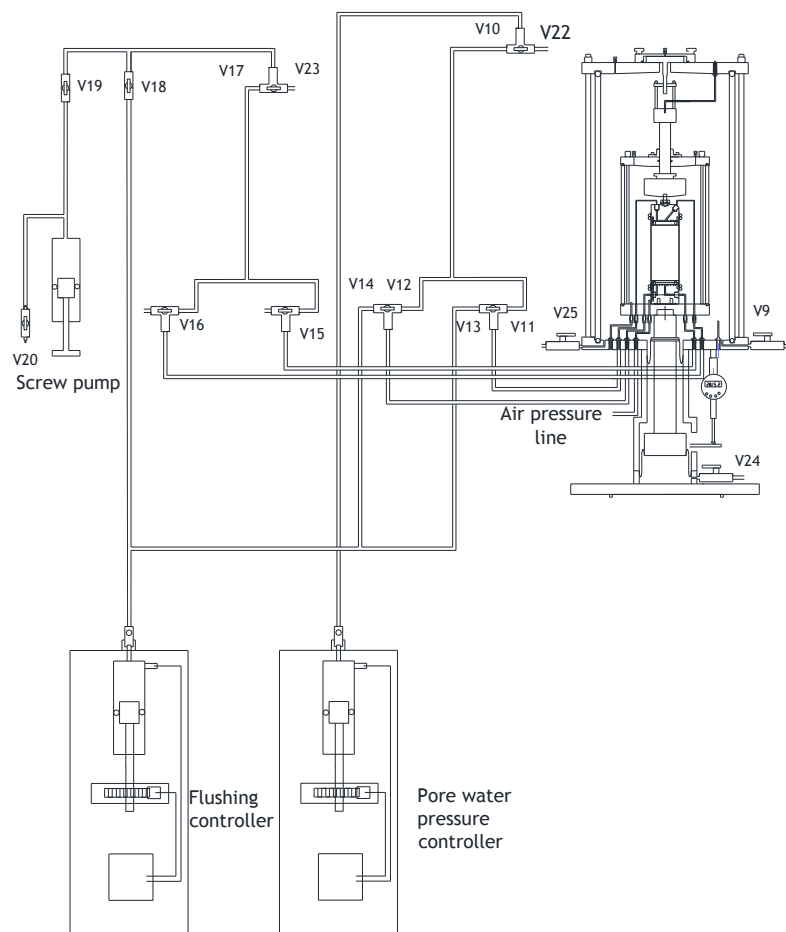


**Figure 3.11 Diffused air flushing system**

Flushing was carried out after each loading, unloading or probing stage in all tests. For tests in which pore water pressure was kept above 200 kPa, no air bubbles were noticed in the transparent drainage tubes during the flushing process. However, isolated air bubbles were observed for tests that involved a decrease of pore water pressure below 200 kPa. In these tests, additional flushing was therefore performed after each 50 kPa drop in pore water pressure. It is worth mentioning that the absence of corners in the spiral drainage groove of both the top cap and the pedestal eliminated the need for

reversing the direction of flow during flushing. No measurement of flushed air volume was conducted, but volume was always small.

### 3.2 SYSTEM 3 (SATURATED TRIAXIAL CELL)

A photograph of System 3 is shown in Figure 3.12 while the layout, including the cell and loading frame, the control and measurement devices and the data logging/control system, is shown schematically in Figure 3.13. A conventional triaxial set-up was employed to carry out saturated tests. The cell, produced by Wykeham Farrance and rated for a maximum pressure of 1000 kPa, was originally designed to perform triaxial tests on 100 mm diameter samples. However, modifications were made to the base of the cell during this work to accommodate 50 mm diameter samples for consistency with the testing of unsaturated samples in System 1 and 2. A submersible load cell type STALC3 – 5 kN was attached to the loading ram to measure the deviator force. A conventional loading frame, produced by Wykeham Farrance, was used to load the sample during shearing at a constant rate of displacement.

During the test, the upper end of the loading ram was attached to the frame through a ball and socket joint, while the cell was attached to the loading frame piston through stiff “U” shape tie rods to reduce system slackness and to allow application of extension loading. Axial displacement of the sample was measured by a 50 mm range displacement transducer attached to the loading frame and positioned on the top cover of the cell. Two-way drainage was arranged from top and bottom of the sample and the pore water volume change was measured by using an Imperial College-type volume gauge, identical to those used in System 1 and System 2.

During the saturation stage, to allow flushing of water through the sample (from the bottom upwards), the top cap drainage line was connected to the atmosphere by means of a two-way valve. A pressure transducer was installed on the drainage line between the volume gauge and the cell, to allow measurement of the  $B$  parameter (the ratio of pore water pressure increase to cell pressure increase under untrained loading). Two GDS-type pressure controllers were used to supply cell pressure and back pressure. The working principle for these controllers is similar to that explained earlier for the pressure controllers of System 1 and System 2.

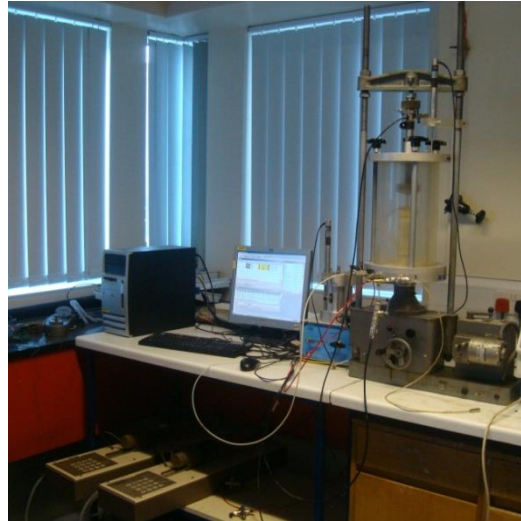


Figure 3.12 Photograph of System 3

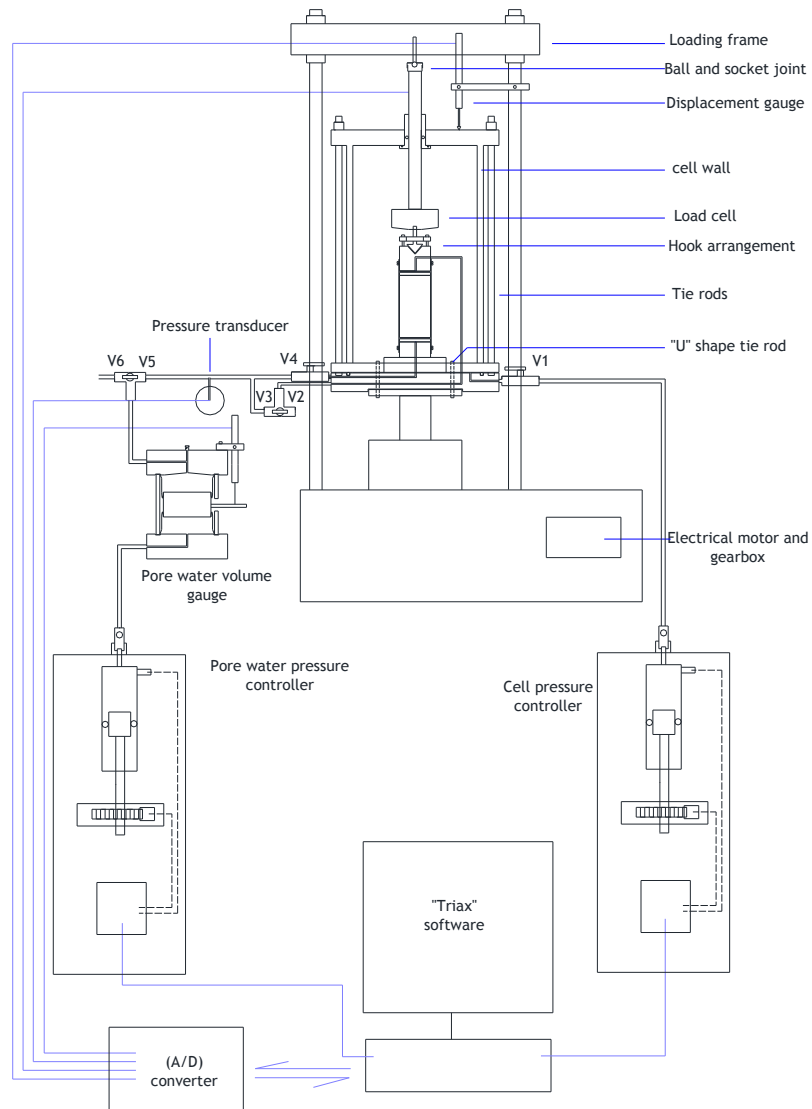


Figure 3.13 Schematic layout of System 3

## Logging and control system

The cell pressure and pore water pressure signals from the transducers embedded in the two pressure controllers were directly converted to a digital form inside the controllers and transferred to the computer through a serial port. Outputs from the other transducers (i.e. displacement, load, pressure and volume gauge transducers) were brought to an analogue/digital converter (Datascan type 7220 MSL) before being transferred to the computer. Input and output was managed by the software “Triax 5.1.8” developed by Toll (2010). A typical interface of the Triax software is shown in Figure 3.14. The calibrated readings from different transducers could be displayed (see “Monitor” window) and logged (see “Scan” window). Controlling parameters could be shown in the “control” box (GDS1 is the pore water pressure and GDS2 is the cell pressure). Output data can be presented in table (see “Scan” window) or graphical forms within the Triax software and/or transferred to Excel or Matlab spreadsheets. For a given test stage, target parameter values are controlled in terms of steps of predefined size. The size of each step is selected so that the oscillation in the reading is kept within the tolerance (usually set to  $\pm 0.5$  kPa for pressure).

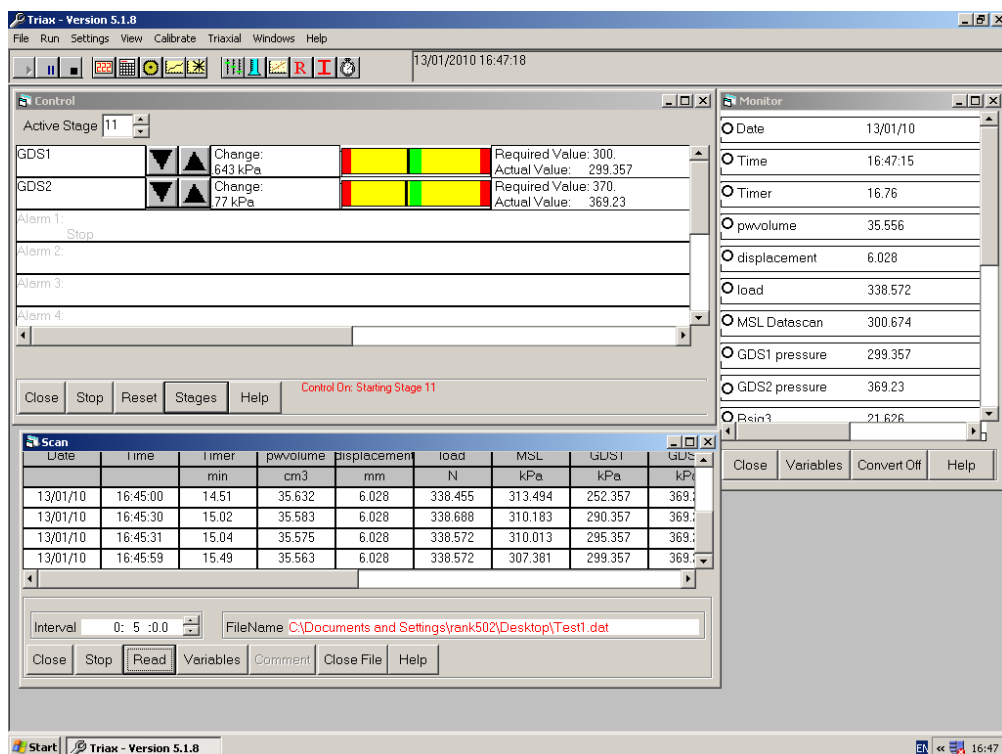


Figure 3.14 Typical interface of Triax software

## 3.3 CALIBRATIONS FOR SYSTEM 1 AND SYSTEM 2

All measurement devices for System 1 and System 2 were already calibrated by the manufacturer in terms of pressure, volume or displacement against measured voltage.

These calibrations were stored in the data logger and pressure/volume controllers and were not visible to the user. Therefore, a decision was made in this work to treat all the readings as raw readings and perform a new calibration of these raw readings of pressure, volume or displacement in order to confirm the accuracy and to identify suitable correction factors if necessary. Generally, all calibrations showed linear relationships between the raw readings and applied values that can be expressed as:

$$\text{Correct value} = A * \text{raw reading} + B \quad (4.1)$$

where,  $A$  and  $B$  are regression constants and their values were found to be different from 1 and 0 respectively, indicating that correction must be applied to the raw readings to obtain the actual values. Values of  $A$  and  $B$  from the calibrations of transducers (including those for System 3) are listed in Table 3.1.

For pressure transducers, ignoring corrections would result in a maximum error of approximately 1.5 kPa in the mean net stress and a maximum error of approximately 3 kPa in suction. For volume transducers ignoring the corrections would result in an error of approximately 0.25 cm<sup>3</sup>. After consultation with the manufacturer VJ Tech Ltd (who advised that pressure control would be more stable when controlled directly from the controller), decided to conduct the tests by using the raw readings of pressure and volume and then apply post-test correction to the results. This decision was also taken after spending significant time, with the help of VJ Tech Ltd, solving a series of other problems with the software, including sudden loss of pressure control and incorrect output readings. For the deviator load, it was straightforward to define the actual deviator load as a new “Calculated” variable (see Section 3.1.4).

### 3.3.1 Pressure transducers

The cell pressure and pore water pressure transducers were calibrated against a standard dead-weight calibration device (see Figure 3.15) which was also used to calibrate load cells. The balance consisted of a screw piston, oil reservoir, dead weights, motorized vertical piston and a loading frame to calibrate load cells. The role of the motor is to reduce side friction by rotating the piston about its vertical axis. The pressure transducer was placed at the same vertical level as the calibration balance and any pressure in the system was released by opening the vent valve. Calibration was conducted by placing standard dead weights on the vertical piston and by screwing the horizontal piston until equilibrium was reached between the oil pressure and the applied weights. The pressure applied to the transducer was then calculated from the dead weight and the vertical piston cross-sectional area.

Table 3.1 Values of  $A$  and  $B$  from the calibrations of the transducers

	Transducer	$A$	$B$
System 1	Cell pressure	1.0017	2.6 kPa
	Pore water pressure	0.9948	7.2 kPa
	Air pressure	1.0019	1.9 kPa
	Inner cell volume	1.0054	0.1619 cm <sup>3</sup>
	Pore water volume	$(-0.00006847u_w - 1.0160)$ (with $u_w$ in kPa)	0
	Axial displacement	1.0001	0.0068 mm
	Load cell	0.9425	41.5 N
System 2	Cell pressure	0.9963	7.8 kPa
	Pore water pressure	1.0050	0.9 kPa
	Air pressure	1.0013	2.9 kPa
	Inner cell volume	1.0039	0.0366 cm <sup>3</sup>
	Pore water volume	$(-0.000013284 u_w - 1.0076)$ (with $u_w$ in kPa)	0
System 3	Axial displacement	1.0001	0.0065 mm
	Load cell	1.0018	8.7 N
	Cell pressure	1.0029	7.7 kPa
	Pore water pressure	1	0
System 3	Pore water volume	0.0000481115 cm <sup>3</sup> /μV	15.5841 cm <sup>3</sup>
	Axial displacement	-0.000011129 mm/μV	29.0444 mm
	Load cell	0.1845 N/μV	37.8662 N

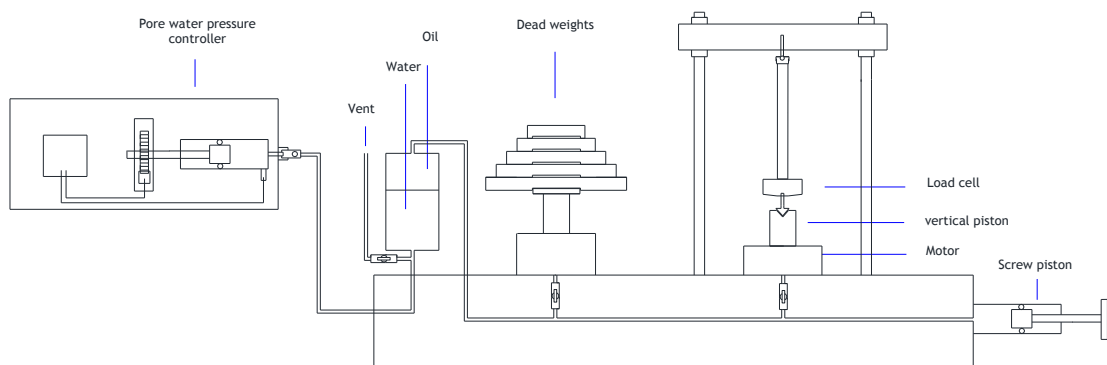


Figure 3.15 Schematic diagram of calibration set-up for pressure transducers and load cells

All pressure transducers were calibrated over the pressure range of 100 – 900 kPa with the plot of applied pressure against raw pressure reading following an approximately linear relationship. Values of  $A$  and  $B$  from the calibration regression of the pressure transducers of System 1 and System 2 are given in Table 3.1. The accuracy of the linear calibration was  $\pm 0.5$  kPa for the pressure range between 100 – 900 kPa. Figure 3.16 shows a typical example of this calibration for the pore water pressure transducer of System 1 together with the best fit line.

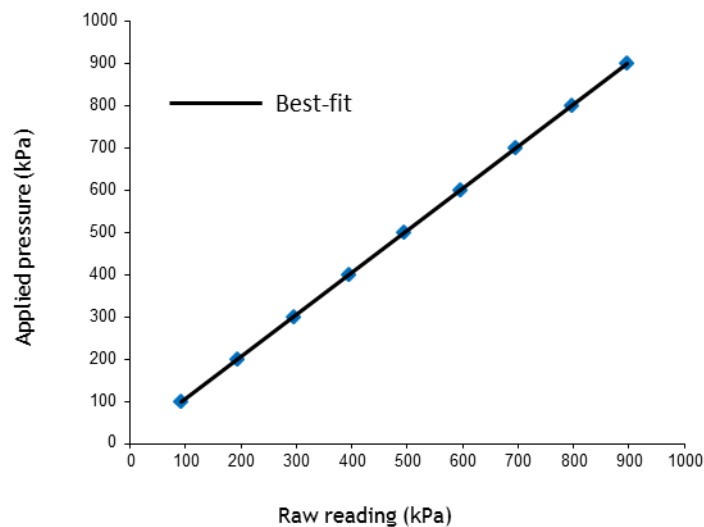


Figure 3.16 Calibration of the pore water pressure transducer of System 1

The air pressure transducer could not come into contact with water and was therefore calibrated against another pre-calibrated transducer. The accuracy of the linear calibration was  $\pm 0.4$  kPa for the pressure range between 100 – 900 kPa.

### 3.3.2 Sample volume change gauges

Figure 3.17 shows the arrangement used to calibrate the sample volume change gauges for System 1 and System 2. The lower chamber of the volume gauge was connected to a water pressure controller while the upper chamber was connected to the internal glass cylinder ( $0.01 \text{ cm}^3$  precision and  $5 \text{ cm}^3$  capacity) of a double-burette. The inner glass cylinder was open at the top and in communication with the outer acrylic cylinder. The double-burette system ensures accurate measurement of water volume change by eliminating the expansion of the inner cylinder. Two immiscible liquids were placed in the double-burette to mark a clear interface which was used to take readings, i.e. paraffin oil at the top and water at the bottom. The outer acrylic cylinder was then connected to a second water pressure controller.

Initially, valves 1,3,4,5,6 and 7 were kept open while valve 2 was kept closed and a line pressure of 900 kPa was applied from both controllers for one day to eliminate effects associated to immediate (or nearly immediate) volume changes. This pressure value is equal to the constant cell pressure value that was applied throughout the experimental programme.

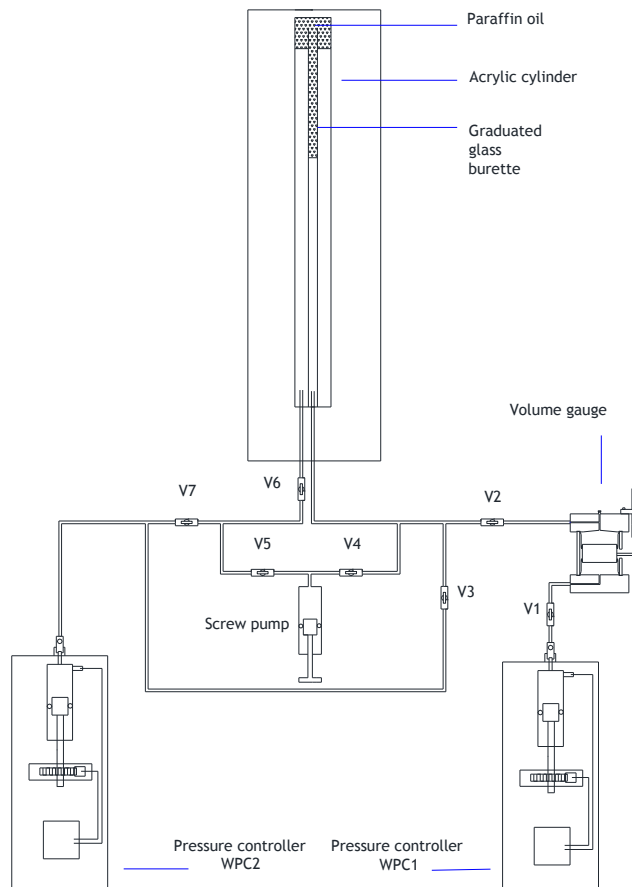


Figure 3.17 Schematic diagram of calibration system for volume gauges

During calibration, a known volume of water was displaced from the glass burette to the upper chamber of the volume gauge by closing valves 3, 4 and 5 and opening valve 2. Water movement to the volume gauge was triggered by a constant pressure difference of 5 kPa, as water pressure was set to 900 kPa inside WPC1 while it was set to 905 kPa inside WPC2. The equivalent increase in water volume in the volume gauge was also recorded. When the oil reached the end of travel inside the burette, valve 2 was closed and valve 3 was opened so that oil moved upwards by gravity until it reached the equilibrium level. To remove any remaining oil on the inner tube's wall, a pressure pulse was applied from the screw pump and this was done by closing valve 3 and subsequently opening valve 4. The position of the oil-water interface in the burette was finely reset

before re-starting calibration by using the screw pump with valves 4 and 7 closed and valves 5, 6 and 3 opened.

Each volume gauge was calibrated for the range 30 – 80 cm<sup>3</sup> and it was found that measured volume varied linearly with applied volume with a maximum error of  $\pm 0.05$  cm<sup>3</sup>. Figure 3.18 shows a typical example of this calibration for the cell volume gauge of System 1 together with the best fit line.

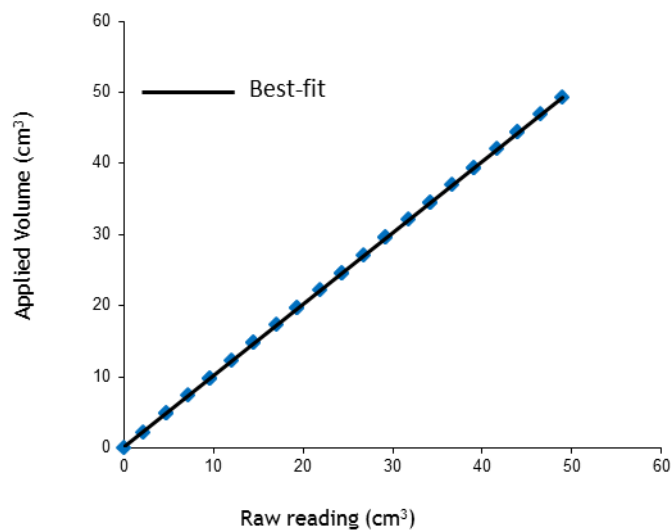


Figure 3.18 Calibration of the inner cell volume gauge of System 1

### 3.3.3 Pore water volume change gauges

It was planned to measure pore water volume change by using the volume gauge of the pore water pressure controller as mentioned earlier. Therefore, it was important to examine the measurement accuracy of this gauge by using the technique mentioned in Section 3.3.2. In this laboratory campaign, the mean net stress and suction were controlled by varying the pore water pressure and pore air pressure while keeping the cell pressure constant. It was therefore important to explore the influence of pressure level on the accuracy of pore water volume measurement (the size of the stainless steel cylinder, see Figure 3.7, was expected to change with pressure). Pore water volume changes during a test are not larger than 50 cm<sup>3</sup>, so it was decided to limit volume measurement, and hence calibration, to the range 240 – 190 cm<sup>3</sup> (instead of the full range of 250 – 0 cm<sup>3</sup>). For this smaller range, the pore water volume gauges of System 1 and System 2 were calibrated under five different pressures (i.e. 100, 200, 400, 600 and 800 kPa respectively). The calibration arrangement was identical to that shown in Figure 3.17 with the exception that the sample volume change gauge was removed from the system (calibration was conducted for WPC1).

Figure 3.19 shows a typical example of this calibration for the pore water volume gauge of System 2 under 800 kPa pressure, together with the best fit line. The raw reading of 240 cm<sup>3</sup> indicates that 10 cm<sup>3</sup> of water was inside the volume gauge while 190 cm<sup>3</sup> indicates that 60 cm<sup>3</sup> of water was inside the volume gauge and the gradient of applied volume change to the raw reading of volume change is therefore negative.

For a given pressure, this calibration showed a linear variation of raw reading of volume against applied volume with a maximum error of  $\pm 0.03$  cm<sup>3</sup>.

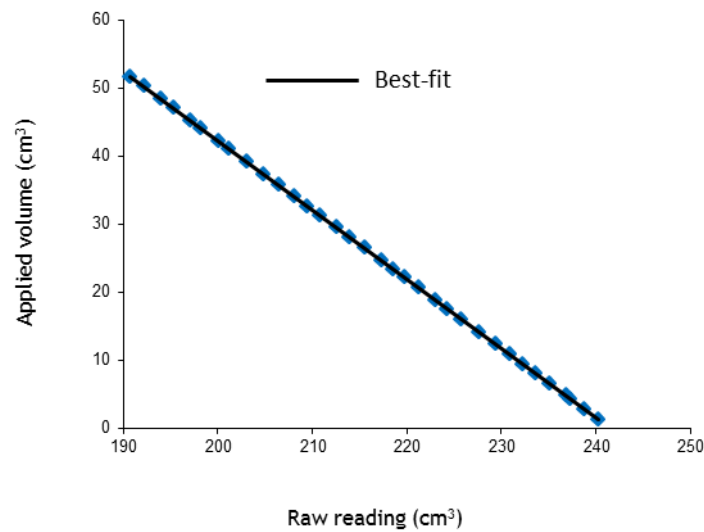
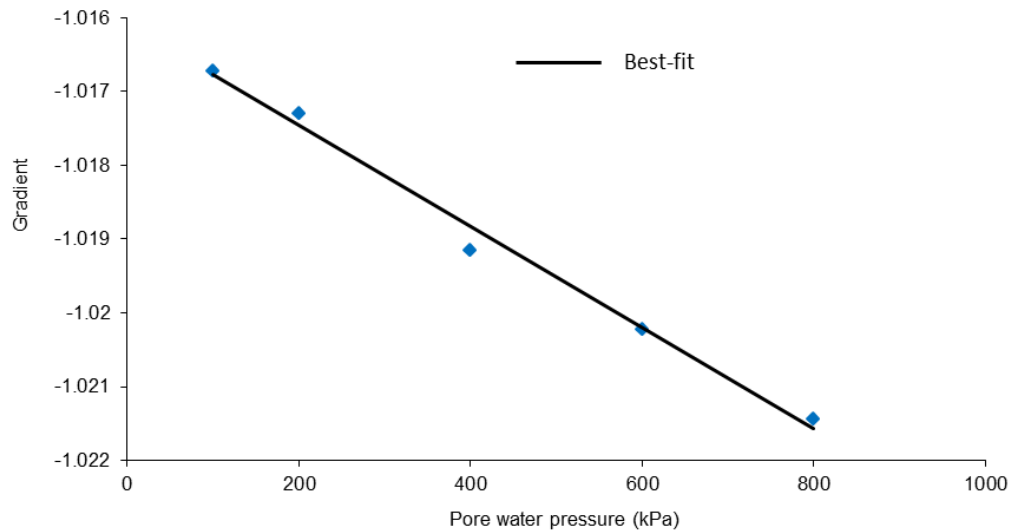


Figure 3.19 Calibration of System 2 pore water volume gauge under 800 kPa

The results also showed a monotonic change of the gradient of the relationship between applied volume changes and raw reading of volume changes with pressure. Ignoring this change would result in an error of 0.25 cm<sup>3</sup> over a range of 50 cm<sup>3</sup> which corresponded to an error about 0.004 in specific water volume ( $v_w = 1 + wG_s$ ), however applying a correction using linear regression reduced the error to less than  $\pm 0.02$  cm<sup>3</sup> over the same range. The variation of the gradient of the applied volume change to the raw reading of volume change with pressure could be expressed as:

$$\text{Gradient (A)} = C * \text{applied pressure} + D \quad (4.2)$$

where  $C$  and  $D$  are regression constants. A typical example of this variation is shown in Figure 3.20 for System 1. Values of  $A$  and  $B$  from the calibration regression of the pore water volume gauges of System 1 and System 2 are given in Table 3.1.



**Figure 3.20** Gradient of the relationship between applied volume and raw reading volume for different values of pressure (System 1)

### 3.3.4 Load cells

The load cells for System 1 and System 2 were calibrated in two stages. In the first stage, each load cell was calibrated over the compression range 200 – 2000 N by using the dead-weight balance system shown in Figure 3.15. In the second stage, each load cell was calibrated over the extension range 0 – 200 N. This was done by hanging the load cell by the ram and hooking to it a known dead weight. The full calibration was obtained by combining the results from the two stages.

The results showed a linear variation of the applied load with raw reading of load with an accuracy of  $\pm 1.5$  N which corresponds to an accuracy of  $\pm 1$  kPa in terms of deviator stress for a 50 mm diameter triaxial sample. Values of  $A$  and  $B$  from the calibration regression for System1 and System 2 are given in Table 3.1. Figure 3.21 shows a typical example of this calibration for the load cell of System 2 together with the best fit line.

### 3.3.5 Axial displacement gauges

The axial displacement gauges were calibrated over the full range of 25 mm using slip gauges of different heights after fixing the displacement gauge to a reference beam. A linear variation of the applied displacement with the measured displacement was found with an accuracy of  $\pm 0.03$  mm. Values of  $A$  and  $B$  from the calibration regression for System1 and System 2 are given in Table 3.1. Typical example of this calibration for the axial displacement gauge of System 1 is shown together with the best fit line in Figure 3.22.

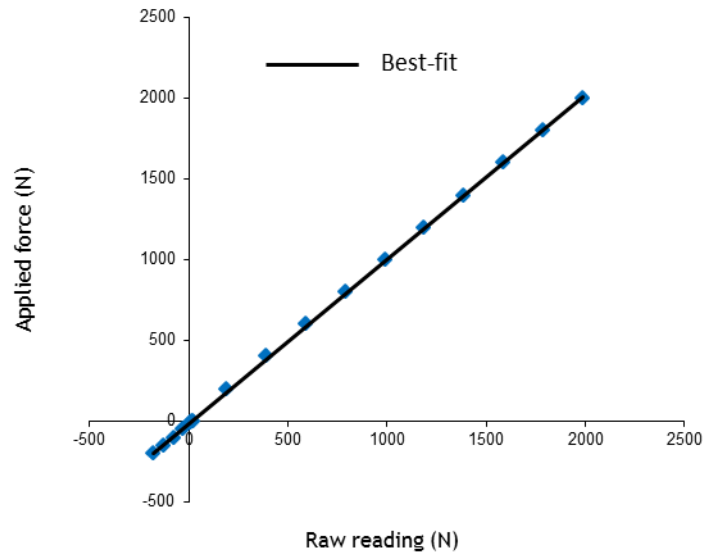


Figure 3.21 Calibration of the load cell of System 2

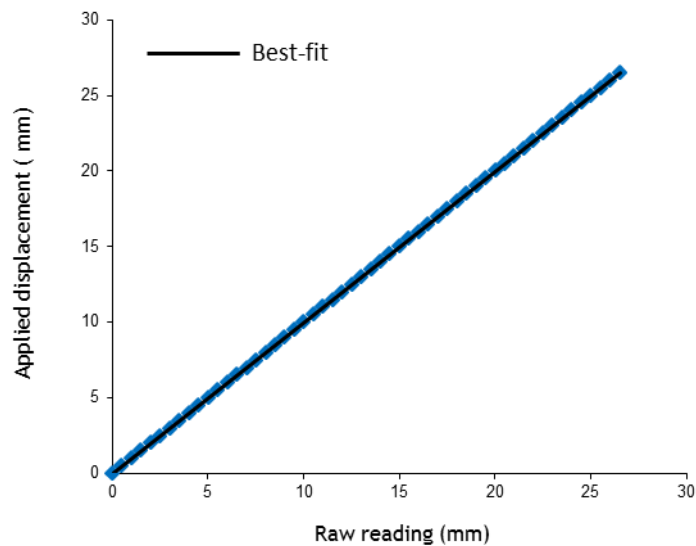


Figure 3.22 Calibration of the axial displacement gauge of System 1

### 3.3.6 Apparent volume change

A double wall triaxial cell was used to ensure accurate measurement of overall sample volume change by measuring water flow into or out of the inner cell. To conduct a suction controlled test by using the axis translation technique, it is possible to set the cell pressure, the pore water pressure or air pressure to a certain value and change the other pressures as required. In this work, the cell pressure was set to a constant value. One reason for this choice was that sample volume changes were measured based on the inflow or outflow of water into/from the inner cell and the accuracy of this measurement was greatly enhanced by eliminating sources of error that were caused by variation of cell pressure.

Volume measurement can be affected by any of the following sources of error:

- 1- Compression of occluded air in the measuring system which increases with the increase in the pressure level. The rate of compressibility is decreasing with increase in the time under a constant pressure.
- 2- Compressibility/expansion of the water and parts of the system such as fittings, “O” rings, etc. which is proportional to the pressure level.
- 3- Diffusion of water through the flexible tubes which increases with increase in pressure difference across the tube’s wall.
- 4- Temperature variation in the testing room which causes oscillations in the volume measurement due to the expansion or contraction of water in the measuring system.
- 5- Movement of the loading ram inside the inner cell.

Moreover, despite the use of a submersible load cell, the measurement of deviator load is more reliable at a constant cell pressure.

Before the tests, the sample volume change measuring system was therefore calibrated for time dependency and temperature variation effects (cell pressure was kept constant during the tests and no calibration for pressure dependency was therefore required). Similarly, it was necessary to calibrate the pore water volume change measuring system for time and pressure dependent effects. No attempt was made to calibrate the pore water volume change measuring system for temperature variation due to unavailability of a temperature probe inside the drainage system.

The above calibration included all parts of System 1 and System 2 that could affect measurement of sample volume change and pore water volume change during an unsaturated triaxial test. During calibration, almost the same arrangement as in a real test was reproduced by removing the high air entry filter holders and attaching acrylic stoppers of the same dimensions to the top cap and pedestal to separate the drainage lines of the inner cell and the pore water drainage lines and by using a dummy brass sample of 50 mm diameter and 100 mm height to substitute the real soil sample. The load cell was kept free to move vertically with the inner cell (with no relative movement) by entirely loosening the screw that connects the load cell to the top cover of the outer cell (see Figure 3.3b). Prior to calibration, all lines were flushed with de-aired water to take out any trapped air in the system. The pore air drainage line between the pedestal and valve 26 (see Figure 3.10) was flushed with de-aired water and the valve was kept close for the entire calibration so that cell pressure was applied to that

line. The sample volume change gauge was flushed several times and filled with de-aired water. The setting up procedure for calibration was similar to that followed for sample setup (as is given in Section 4.2.3). Referring to Figure 3.10, valves 1, 2, 3, 4 and 5 were opened at a line pressure of 10 kPa, then valves 6 and 9 were opened simultaneously to pressurise the outer cell and inner cell respectively. For the pore water drainage system, valve 10 was opened first with a line pressure of 10 kPa then valves 11 and 12 were opened subsequently. Cell pressure and pore water pressure were increased to target values of 900 kPa and 800 kPa respectively at a rate of 30 kPa/minute. Cell pressure was then kept constant over the calibration period. Once the volume change rate was stabilised (usually after 2 – 3 days), the pore water pressure was decreased by step changes to 600, 400, 200 and 100 kPa for System 1 and to 400 and 200 kPa for System 2. The variation of pore water volume was monitored and recorded for a period of 2 – 3 days under each pressure. The pore water pressure was then increased to 200, 400, 600 and 800 kPa for System 1 and to 600 and 800 kPa for System 2 following the same manner described above.

Figure 3.23 and Figure 3.24 shows the variation of the inner cell volume against elapsed time for System 1 and System 2 respectively. Calibration time for System 2 was shorter than that for System 1 due to unplanned power shutdown in the laboratory. The variation of the inner cell volume against time could be separated into two parts; the first part represents the immediate changes in volume due to the application of the cell pressure whereas the second part represents the time dependent change in volume. It could be noticed from Figure 3.23 that the immediate volume change stabilised after approximately one day. In a real test, it was therefore decided to wait one day between pressurization of the cell and the first stage (usually suction equalisation). The apparent fluctuation in the measured volume change reflected the effect of temperature variation on volume measurement. Fluctuation in temperature was more noticeable during the calibration of System 2 due to a fault in the room temperature controller. Generally, the magnitude of the immediate change in the inner cell water volume due to pressure increase was bigger for System 2 than for System 1, though this is not very important as, during a real test, cell pressure is maintained constant. During the course of inner cell volume change calibration, pore water pressure was decreased in step change from 800 to 100 or 200 kPa (as explained previously), though, no evidence of any cell volume change was noticed during this process.

The variation of the pore water volume change against elapsed time is shown in Figure 3.25. The discontinuities in the plot refer to the instantaneous volume changes due to pressure change. On the pore water drainage line the rates of volume change at constant

pressure was changing monotonically from  $-0.008 \text{ cm}^3/\text{day}$  to  $0.008 \text{ cm}^3/\text{day}$  for pore water pressures decrease from 800 kPa to 100 kPa.

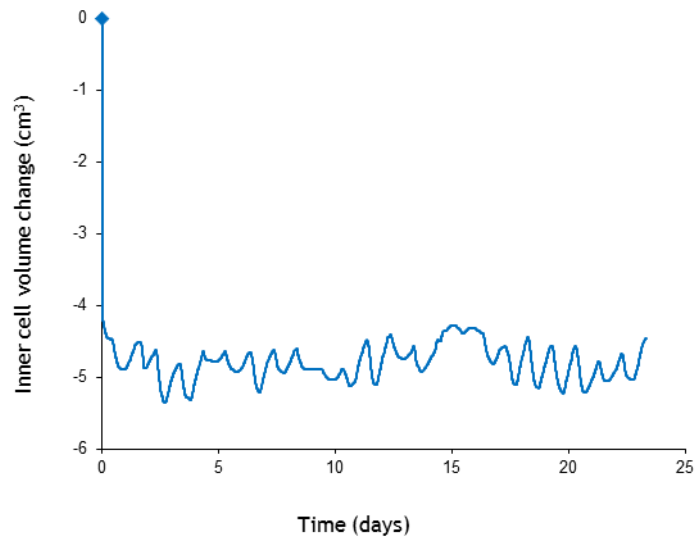


Figure 3.23 Variation of the inner cell volume against elapsed time for System 1

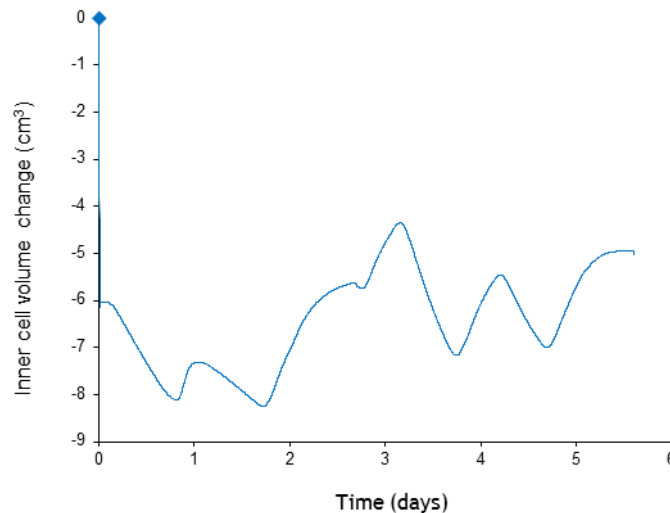


Figure 3.24 Variation of the inner cell volume against elapsed time for System 2

The decrease in the rate of volume change with the decrease in pore water pressure (under a constant cell pressure) can be explained with reference to the water/air diffusion and any creep expansion of the flexible tubes as set out in the next paragraph.

In terms of water diffusion through the PTFE tubes of the pore water drainage, the rate of inward diffusion to the pore water drainage line (from the water in the triaxial cell), for the sections of drainage line inside the cell, is expected to increase with decreasing

pressure in the pore water drainage line. In addition, for the sections of drainage line outside the cell, the rate of outward diffusion from the pore water drainage line (to the atmosphere) is expected to decrease with decreasing pressure in the pore water drainage line. In terms of air diffusion, water inside the drainage tubes and the cell were of the same quality (de-aired), therefore no air diffusion was expected through the tubes inside the cell. On the other hand, air diffusion was expected to occur from the atmosphere to the section of pore water drainage line outside the cell, because the water inside the tube was not air-saturated. In terms of any creep expansion of the PTFE tubes, the drainage tubes inside the cell were expected to contract (external loading condition) whereas the drainage tubes outside the cell are expected to expand (internal loading condition). The positive rate of pore water volume change under 100 kPa, which indicates an increase in the volume of water inside the volume gauge, refers, therefore, to the net effect of these sources. The rate of pore water volume change under a constant pressure during the pressure increase steps was slightly less than the corresponding rate during the pressure decrease steps suggesting that the amount of air that came out of solution in the pressure decrease cycle is less than the original amount of air that went into solution during the first pressure increase.

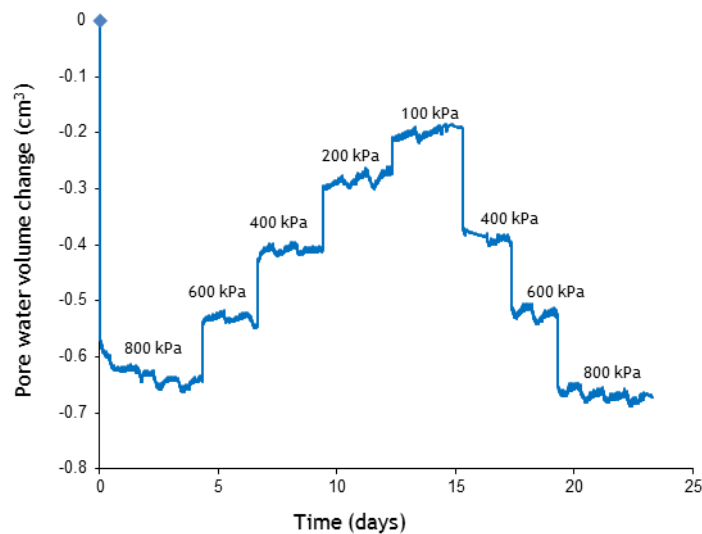


Figure 3.25 Variation of the pore water volume change against elapsed time for System 1

Figure 3.26 shows the immediate changes in pore water volume after a change of pressure for System 1. If the volume change after initial pressurization of the cell is ignored (initial volume change is indeed ignored during a real test as the drainage lines up to valves 11 and 12 (see Figure 3.10) are initially pressurised to 800 kPa), it is then

possible to approximate the volume changes caused by both pressure decrease and increase by a single line.

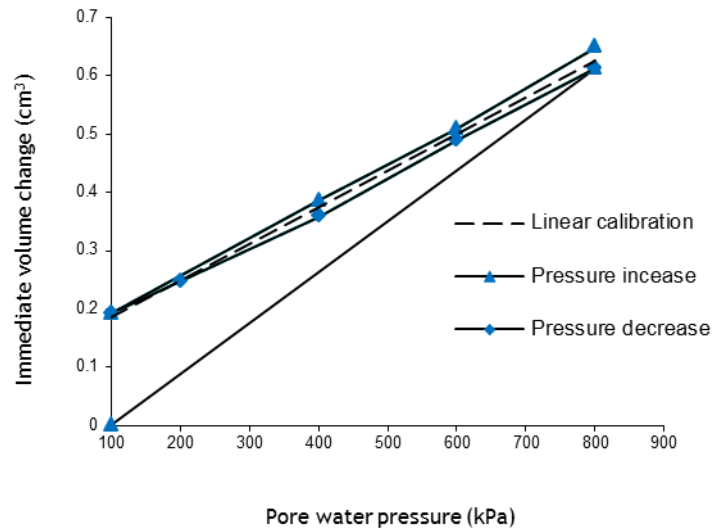


Figure 3.26 Immediate pore water volume change against pore water pressure for System 1

Figure 3.27 shows the changes in pore water volume after changes of pressure for System 2. The rates of volume change at constant pressure were changing monotonically from  $-0.03 \text{ cm}^3/\text{day}$  to  $-0.01 \text{ cm}^3/\text{day}$  for pore water pressures decrease from 800 kPa to 100 kPa. Similar to the observation shown above for System 1, the rate of pore water volume decreases with decreasing pore water pressure under a constant cell pressure. Figure 3.28 shows the variation of the immediate changes of pore water volume against pore water pressure for System 2. Approximating both the pressure decrease and increase by a single line was found adequate.

### Correction for temperature fluctuation

The temperature control unit was set to maintain the temperature of the testing room at  $21^\circ\text{C}$  with a tolerance of  $\pm 0.5^\circ\text{C}$ . As well as normal oscillations, additional fluctuations in room temperature were also observed when a rapid change in temperature occurred outside the room. Figures 3.29 and Figure 3.30 show the variation of the inner cell volume together with temperature variation for System 1 and system 2 respectively. As it can be seen, volume change fluctuations were strongly correlated to temperature fluctuations and a correction for these fluctuations was therefore applied. It was observed that the application of a temperature correction could result in eliminating most of the errors in volume measurement caused by long-term changes in temperature but it could equally produce new small unwanted short-term oscillations in volume measurement (caused by small rapid fluctuation of temperature recorded by the

temperature gauge, which did not reflect the average temperature of the water in the cell) . A correction factor of  $0.75 \text{ cm}^3/\text{°C}$  was found adequate to eliminate most of the effect of changes in temperature for both System 1 and System 2. This correction factor produced about  $\pm 0.1 \text{ cm}^3$  oscillation in the inner cell volume change measurement which corresponded to approximately  $\pm 0.001$  error in the measured specific volume.

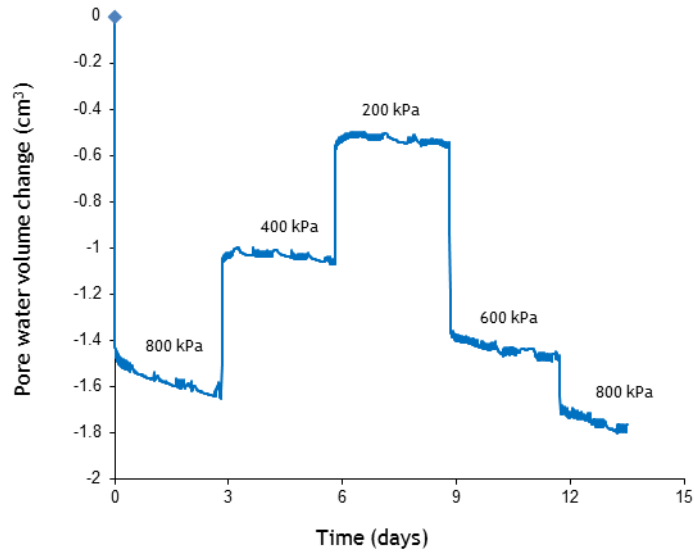


Figure 3.27 Variation of the pore water volume change against elapsed time for System 2

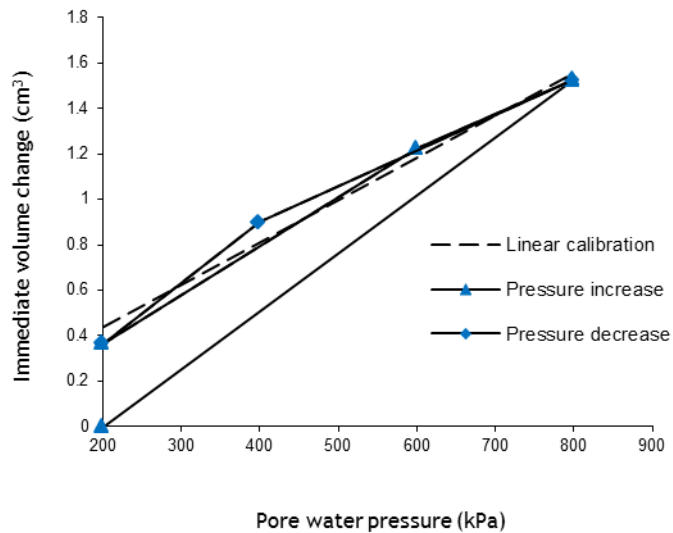


Figure 3.28 Immediate pore water volume change against pore water pressure for System 2

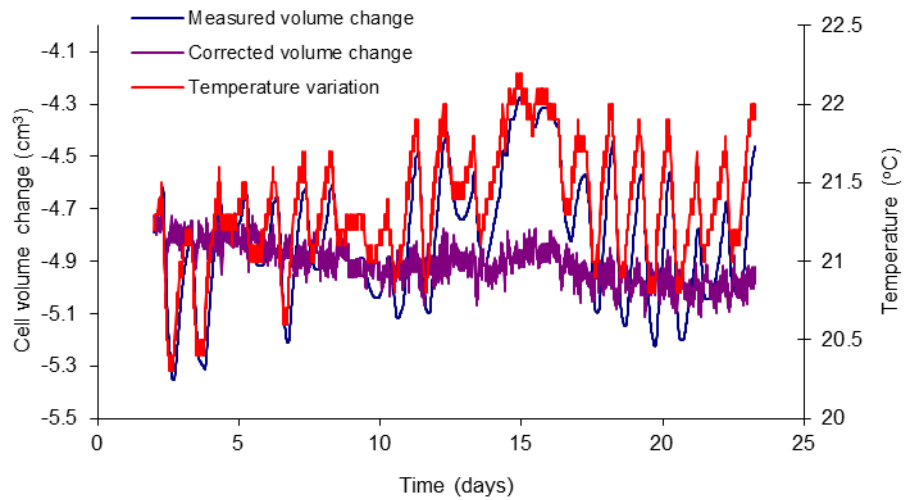


Figure 3.29 Variation of measured and corrected volume change with time for System1

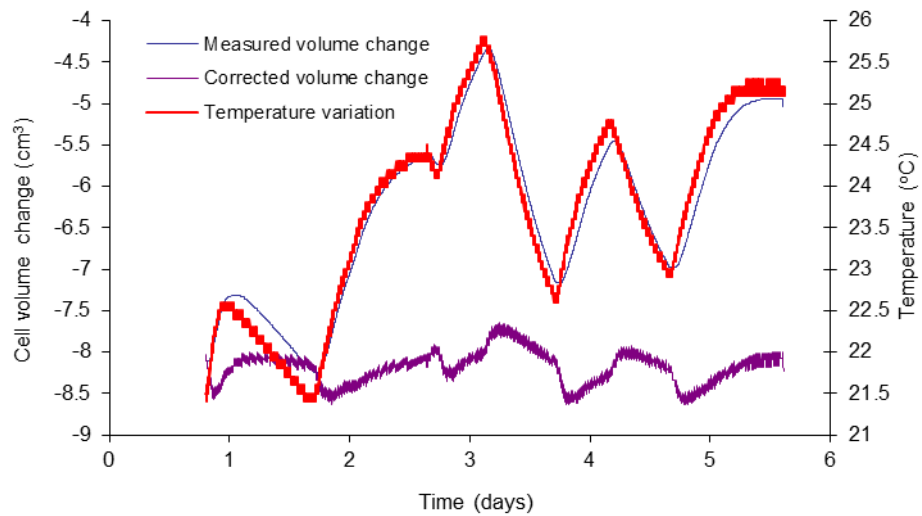


Figure 3.30 Variation of measured and corrected volume change with time for System2

### Calibration for loading ram intrusion in the inner cell

Vertical movement of the loading ram during the application of the deviator stress implied a corresponding increase or decrease in the inner cell water volume due to the intrusion of the loading ram (see Figure 3.1). Calibration for this effect was carried out by increasing the ram displacement at a given rate and measuring the corresponding change in the inner cell water volume. Figure 3.31 and Figure 3.32 show the change in

the inner cell water volume against the axial displacement along with the best fit line for System 1 and System 2 respectively. The calibration factor was  $0.4948 \text{ cm}^3/\text{mm}$  and  $0.5058 \text{ cm}^3/\text{mm}$  for System 1 and System 2 respectively. The accuracy of the linear calibration were found to be  $\pm 0.03 \text{ cm}^3$ .

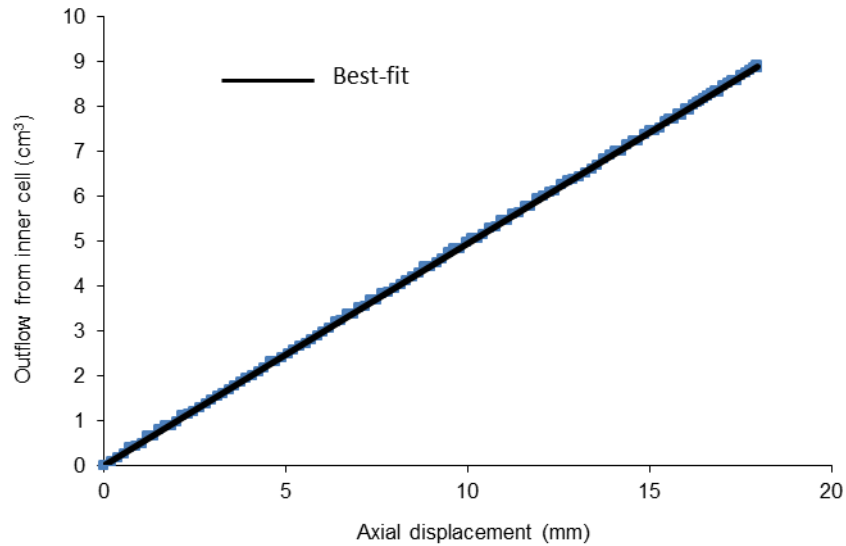


Figure 3.31 Calibration for stroke intrusion for System 1

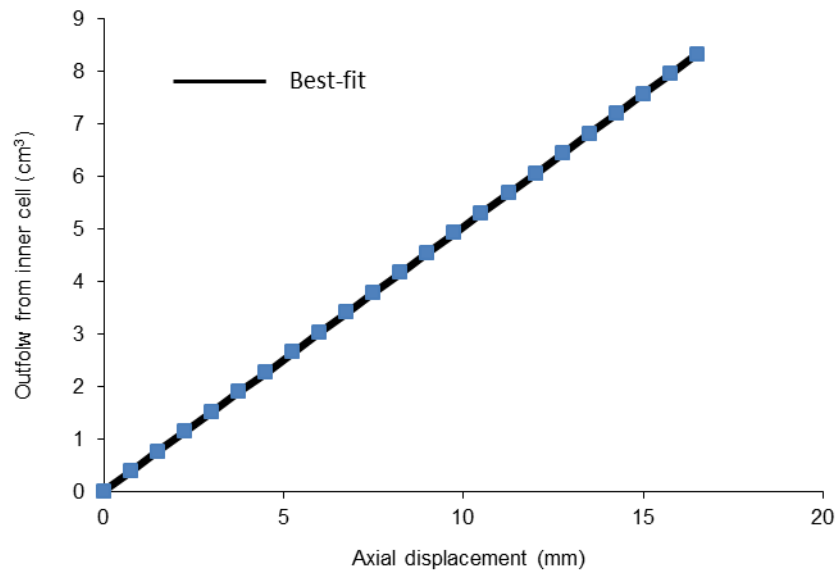


Figure 3.32 Calibration for stroke intrusion for System 2

### 3.3.7 Investigation of the accuracy of volume measurements in the double-wall cell

The accuracy of the sample volume change measurements of System 1 and System 2 was investigated by testing two saturated compacted samples in the double-wall cells and comparing the measured sample volume change using the flow into the inner cell (with the various calibrations and corrections) against measured pore water volume changes. This was done during isotropic loading. The compaction technique was as given in Section 4.1, the sample setup procedure was as given in Section 4.2.3 and the saturation procedure was as given in Section 5.4.3.

Figures 3.33 and 3.34 show the variation of specific volume with mean effective stress during isotropic loading stage of two identical samples tested in System 1 and System 2 (after applying the relevant calibrations). Inspection of these figures indicates excellent matching between the two measurement techniques. In addition, the volume change measurements of both samples were very similar in System 1 and System 2.

This investigation confirms that the testing equipment for the unsaturated tests gave high quality volume change measurements.

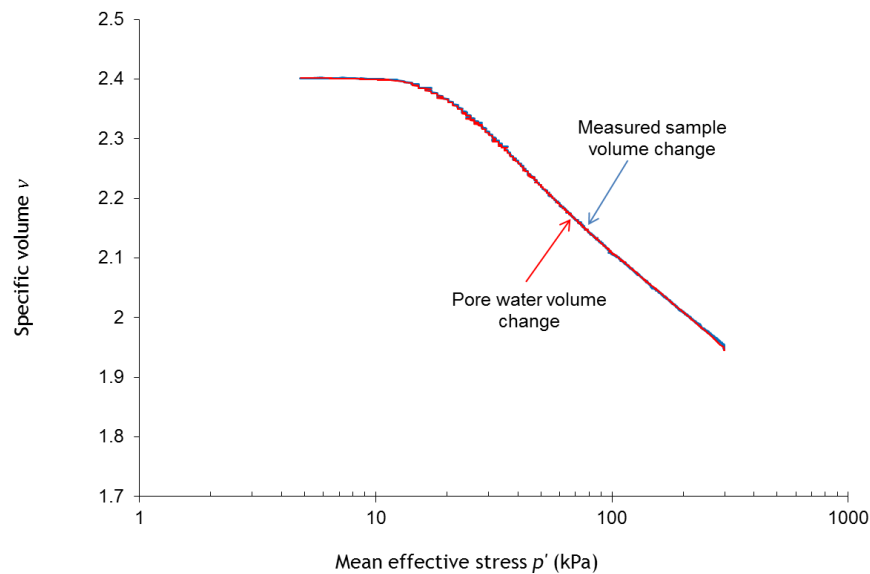


Figure 3.33 Sample volume change and pore water volume change of a saturated sample measured in System 1

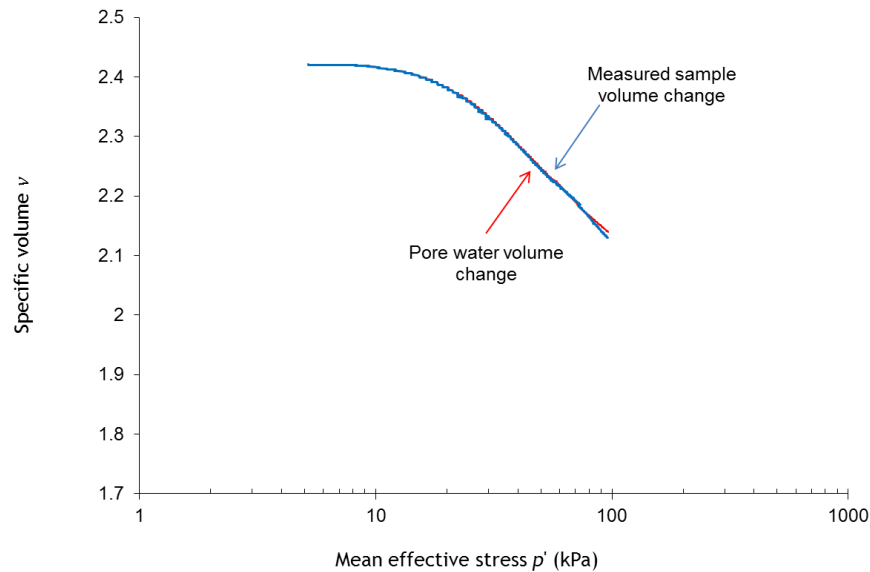


Figure 3.34 Sample volume change and pore water volume change of a saturated sample measured in System 2

### 3.4 CALIBRATIONS FOR SYSTEM 3

In the unsaturated tests, cell pressure was kept constant during the course of the tests and radial net stress was applied by varying pore air and pore water pressures simultaneously at a given rate. This procedure gives the maximum accuracy in terms of sample total volume change measurements. To achieve the same quality of volume change measurement for saturated tests based on measuring the changes in the pore water volume, effective stress should be increased by holding the pore water pressure at a constant value while increasing cell pressure.

#### 3.4.1 Pressure transducers

The pore water pressure controller and cell pressure controller were calibrated using the calibration system shown in Figure 3.15. The calibration procedure was exactly the same as that followed in System 1 and System 2. Accuracy of the linear calibration was found to be  $\pm 0.5$  kPa for the pressure range between 100 – 600 kPa. Values of  $A$  and  $B$  from the calibration regression for the pore water pressure transducer for System 3 are given in Table 3.1. Figure 3.35 shows the calibration result of the cell pressure controller of System 3 together with the best fit line.

#### 3.4.2 Pore water volume change gauge

This volume gauge was calibrated over the range 10 – 95 cm<sup>3</sup> by using the setup shown in 3.17. The calibration procedure was similar to that followed in System 1 and System 2 except that a line pressure of 300 kPa was applied instead of 900 kPa. This volume gauge was fitted with an analogue *LVDT*, rather than a digital one, and a different

logging/software setup was employed compared to the previous two unsaturated systems. Calibration data were therefore plotted in terms of applied volume change against measured voltage and linear calibration with an accuracy of  $\pm 0.15 \text{ cm}^3$  was considered to be adequate. Values of  $A$  and  $B$  from the calibration regression for the pore water volume change gauge for System 3 are given in Table 3.1. Figure 3.36 shows the calibration result together with the best fit line.

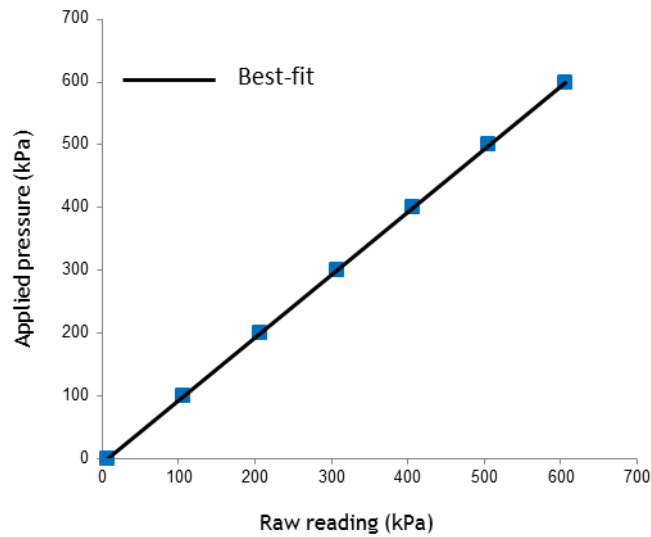


Figure 3.35 Calibration of the cell pressure transducer of System 3

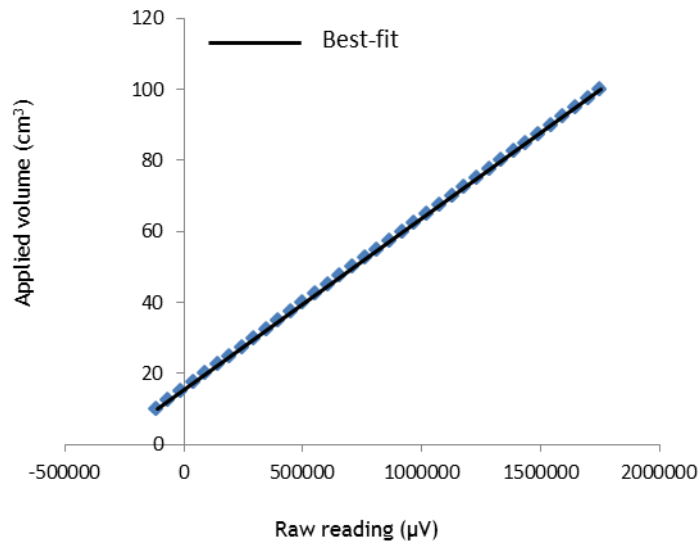


Figure 3.36 Calibration of pore water volume gauge of System 3

### 3.4.3 Load cell

The load cell for System 3 was calibrated using by using the procedure described in Section 3.3.4. The calibration data were plotted in terms of applied load against measured voltage. This gave a linear calibration with accuracy of  $\pm 1$  N. Values of  $A$  and  $B$  from the calibration regression for the load cell of System 3 are given in Table 3.1. The calibration of the load cell of System 3 together with the best fit line is shown in Figure 3.37.

### 3.4.4 Axial displacement gauge

The axial displacement gauge were calibrated over the range 0 – 50 mm using slip gauges as described for System 1 and System 2. Calibration data was plotted in terms of applied displacements against voltage and a linear variation with accuracy of  $\pm 0.04$  mm was found adequate. Values of  $A$  and  $B$  from the calibration regression for the axial displacement gauge for System 3 are given in Table 3.1. Figure 3.38 shows the calibration of the displacement transducer together with the best fit line.

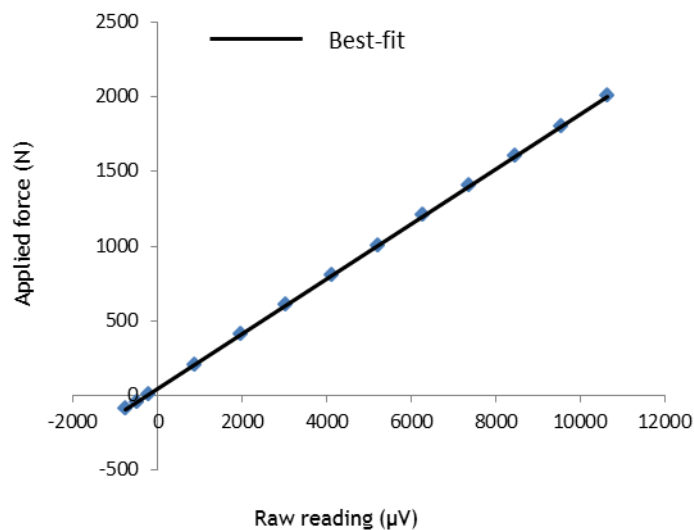


Figure 3.37 Calibration of the load cell of System 3

### 3.4.5 Apparent volume change

The pore water volume measuring system was calibrated for any errors caused by any occluded air, water diffusion from the tubes and expansion of the tubes. The calibration included the volume gauge and the connecting tubes which were outside the triaxial cell (see Figure 3.13). The drainage system was initially flushed with de-aired water to remove air bubbles and the gauge was filled with de-aired water. Then a back pressure of 300 kPa was applied to the lower chamber of the volume gauge and this was

maintained for 14 days. The results showed that the volume change rate was approximately  $-0.02 \text{ cm}^3/\text{day}$ .

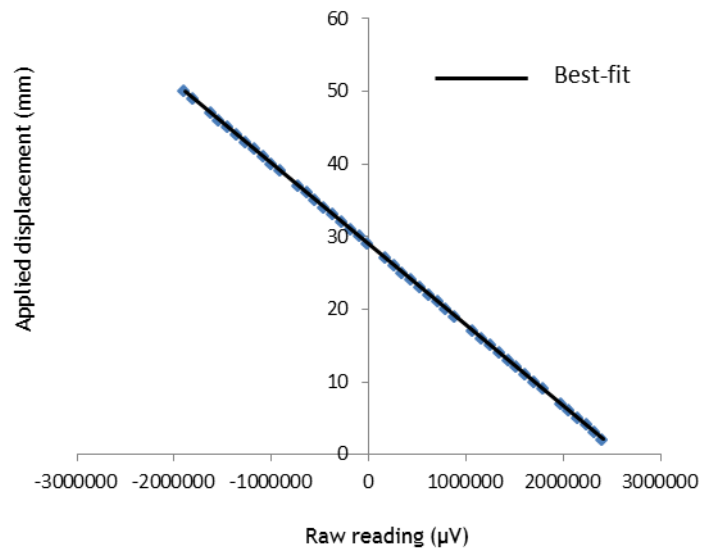


Figure 3.38 Calibration of the displacement transducer for System 3

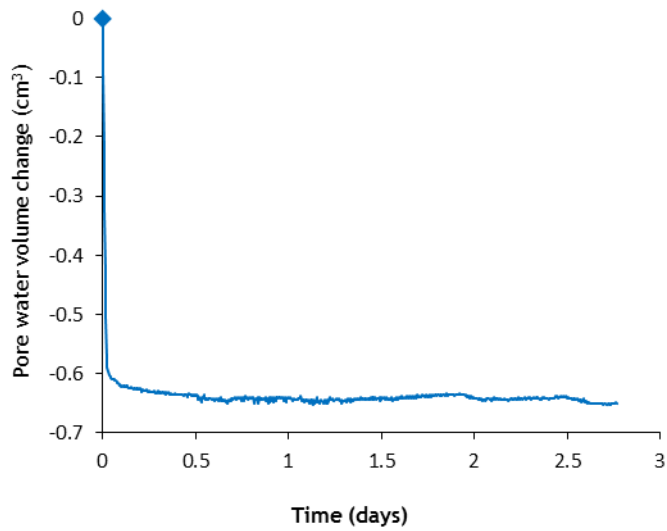


Figure 3.39 Variation of the pore water volume against elapsed time for System 3

# 4

## SAMPLE PREPARATION TECHNIQUE AND TESTING PROCEDURE

This chapter covers three topics, namely the preparation of samples, the test setup and the data processing.

### 4.1 SAMPLE PREPARATION

#### 4.1.1 Soil type

Speswhite Kaolin was selected for the present experimental programme based on the following considerations:

- Kaolin clays do not contain highly expansive clay minerals, thus avoiding the additional complexity that this would introduce.
- The mechanical and water retention behaviour of compacted samples of this material is relatively well known as it has been investigated in depth by many researchers such as, for example Sivakumar (1993), Sharma (1998) and Raveendiraraj (2009).
- The air entry value of compacted kaolin samples is relatively low and hence it is possible to investigate unsaturated soil behaviour over the low suction range 0 – 300 kPa which is convenient for testing.
- Test duration is reasonable as the rate of consolidation is higher for compacted Kaolin than that of most other clays.

#### 4.1.2 Preparation of Kaolin mix

Given that sample diameter for a triaxial test was 50 mm, it was decided to limit the maximum aggregate diameter to 2 mm, to keep the maximum aggregate diameter much smaller than the sample diameter (assuming that the size of aggregates will not change significantly during the compaction process). After several trials of mixing at different water contents, it was concluded that mixing at water contents more than 0.25 was not practical because it was extremely difficult to pass the mix through a sieve with an aperture size of 2 mm. To maintain as much consistency as possible with the work of other researchers (e.g. Sivakumar, 1993 and Raveendiraraj, 2009) who worked on compacted Kaolin, a target water content 0.25 was selected. The mix after sieving was

stored in sealed plastic bags under controlled temperature for one day prior to compaction in order to allow for moisture equalisation.

### 4.1.3 Development of isotropic and anisotropic initial fabrics

The experimental investigation of the anisotropic behavior of unsaturated soils requires a compaction technique that is capable of:

- Producing homogeneous samples in terms of soil fabric.
- Producing samples that are stiff enough for handling and trimming.
- Producing repeatable samples in terms of physical properties (e.g. void ratio, moisture content, etc.).
- Producing samples with both isotropic initial fabric (or with minimal anisotropy) and anisotropic initial fabric.

Many researchers including Sivakumar (1993), Cui and Delage (1996), Sharma (1998), Wheeler and Sivakumar (2000) prepared samples by one-dimensional static compaction inside a stiff-walled compaction mould. The resulting fabric was found to be anisotropic due to the restriction on lateral movement. Because of this, one dimensional compaction was considered unsuitable to produce isotropic samples in the current project. Alternatively, Sivakumar (2005) proposed an isotropic compaction technique in which wet kaolin was placed inside a latex membrane and was compacted inside a large triaxial cell by increasing cell pressure and allowing air to drain out of the soil through the top cap and pedestal of the cell. Sivakumar (2005) concluded that the technique was adequate to produce repeatable and homogenous isotropic samples.

For the current project, a more general compaction technique was proposed by using the basic principle proposed by Sivakumar (2005). The proposed technique allows compaction to be performed along a predefined stress path, by controlling both the radial and deviator stresses.

### Compaction setup

The compacting equipment (see Figure 4.1 and Figure 4.2) consisted of a loading frame, a triaxial cell for 100 mm diameter samples, a cylindrical rubber membrane, a membrane stretcher, two acrylic coarse filters, circular rubber sheets and four “O” rings. The rubber membrane was attached to the pedestal and sealed with two “O” rings then the membrane stretcher was placed and the membrane was folded at the top and bottom of the stretcher. Trapped air between the membrane and the membrane stretcher was removed. A coarse filter was placed on the pedestal and two circular rubber sheets, with

silicon lubricant in between them, were placed on top of the coarse filter to reduce end friction. Small holes were made in the rubber sheets to allow air drainage which was arranged through the base of the cell. The mix was transferred into the membrane by means of a small scoop. Another two circular rubber sheets, with silicon lubricant in between, were then placed on the top surface of the soil. The top cap was then placed and the membrane stretcher was removed. The membrane was then attached to the top cap by using two “O” rings.



Figure 4.1 Components of compaction setup

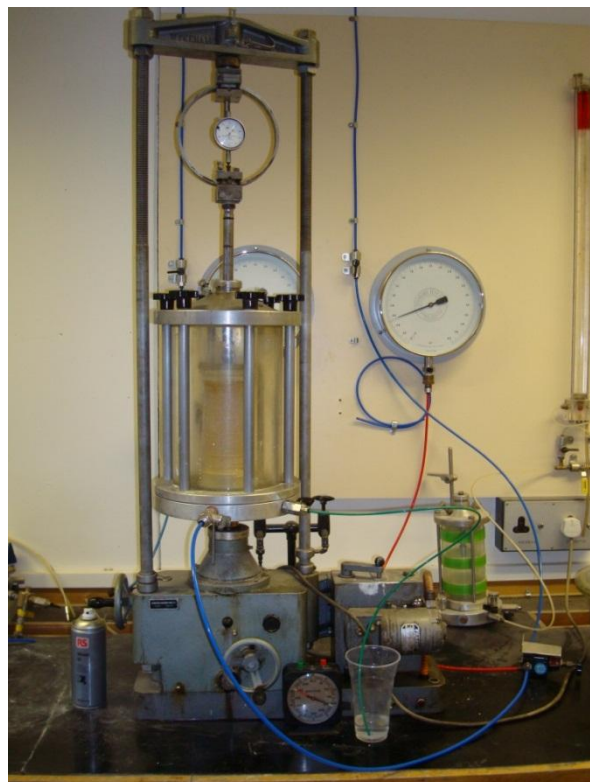


Figure 4.2 Compaction frame

The cell was assembled and transferred to the compaction frame (see Figure 4.2). The cell pressure was applied by means of compressed air while the deviator load was measured externally by a proving ring (corrections were made for the effects of cell pressure increase and loading ram friction). The isotropic compaction was performed by increasing the cell pressure at a constant rate of 3 kPa/minute, while the anisotropic compaction was performed by increasing the axial displacement at a constant rate of 0.75 mm/minute, measuring the deviator load and adjusting the cell pressure accordingly. No water drainage was observed during the compaction process.

After compaction, the cell pressure was removed and the sample was taken out of the cell. A triaxial specimen of 50 mm diameter was cored from the oversized compacted sample. The initial (before compaction) height of the oversized sample, i.e. the height of soil mix placed inside the membrane, was about 200 mm while the final (after compaction) height was about 140 mm. This was sufficient to core a triaxial soil sample of 100 mm in height. The sampler used during coring was a standard oedometer ring (50 mm diameter) which was attached to a cylinder of sufficient height with a diameter slightly bigger than 50 mm to eliminate any friction between the sample and the cylinder wall. The sample was cored vertically by using a compression frame at a rate of 5 mm/minute. This rate was a compromise to keep both sample disturbance and loss of moisture as small as possible. A soil sample of 50 mm in diameter with a larger height than required for triaxial tests was obtained. Subsequently, cored sample was placed in a standard split mould and cut to the required height. Samples that were to be tested in stress path tests involving only triaxial compression stages were trimmed to 100 mm height, whereas samples that were to be tested in stress path tests including triaxial extension stages were trimmed to 75 mm height. This difference was necessary because during testing in triaxial extension there would have been insufficient axial travel for testing of samples with an initial height of 100 mm. Sample height was measured with a standard height gauge of 0.02 mm accuracy. Direct measurement of the sample diameter was difficult, due to the risk of sample damage and the inner diameter of the coring ring was instead measured.

### **Isotropic and anisotropic compaction stress paths**

Figure 4.3 shows the loading paths followed during compaction of both isotropic and anisotropic samples. In both cases the initially loose soil was first loaded isotropically to a mean net stress of 100 kPa and subsequently unloaded to zero stress in order to define an initial reference state common to all samples. The sample was subsequently loaded from this initial reference state either isotropically (method A) or anisotropically at a stress ratio  $\eta \approx 1.2$ , where  $\eta = q/\bar{p}$  (method B) to the same reference mean net stress

$\bar{p} = 250$  kPa. The value of this reference stress was selected as a compromise between two conflicting requirements; to facilitate handling of the sample after compaction (samples compacted to a very low value of mean net stress were fragile and difficult to trim) and to produce samples that would yield at relatively low stress levels. Samples compacted to very high values of mean net stress would have required application of high stresses to yield, which would have caused problems in the subsequent triaxial test programme, where the intension was not only to explore the initial yield behaviour but also to then explore evolution of anisotropy by subjecting the samples to stress paths involving considerable plastic straining. This was only possible if the initial yield stress was relatively low, because of the capacity of the double wall triaxial cell (e.g. a maximum radial net stress of 590 kPa at a suction  $s=300$  kPa).

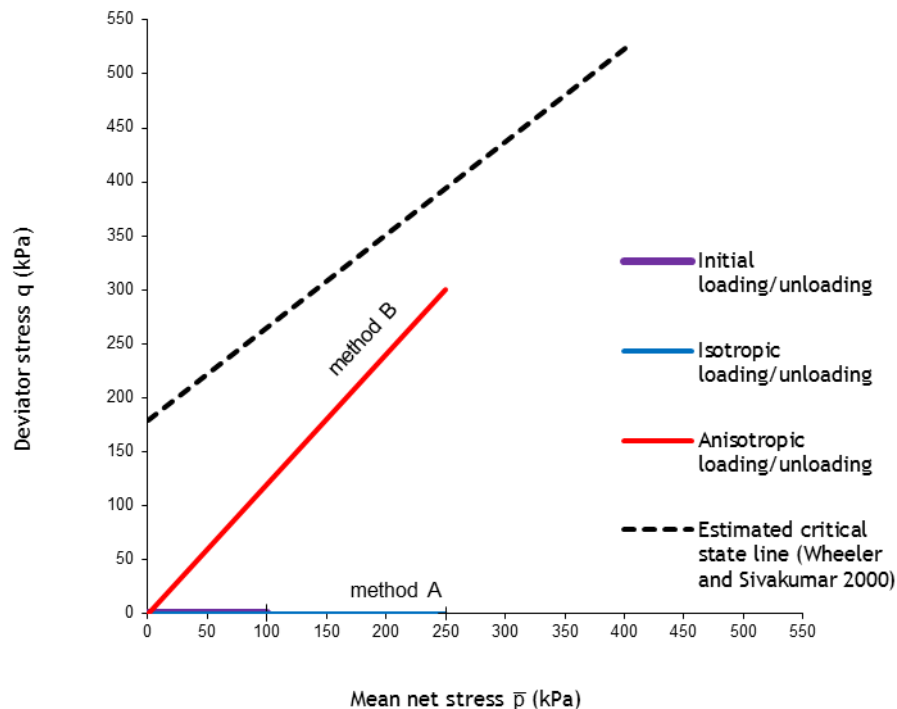


Figure 4.3 Loading paths during compaction and estimated critical state line (at suction corresponding to the end of anisotropic compaction)

At the beginning of this work, the precise position of the critical state line in the  $q:\bar{p}$  plane corresponding to the suction at the end of anisotropic compaction was not known. It was therefore estimated by assuming a gradient and intercept from Wheeler and Sivakumar (2000) corresponding to  $s = 650$  kPa (this is the average suction after anisotropic compaction as measured in this work by using the axis translation technique). The value of the intercept was calculated by quadratic extrapolation of the relationship between cohesion intercept and suction proposed by Wheeler and Sivakumar (2000).

Due to uncertainty about critical state, a relatively small stress ratio  $\eta$  equal to 1.2 was chosen for the anisotropic compaction stress path. In terms of Bishop's stress, the average final stress ratio in the  $q:p^*$  plane at the end of anisotropic compaction was even smaller, i.e.  $\eta^* \approx 0.5$ , as in this case the stress path starts far from the origin at a point with horizontal coordinate  $p^* = \bar{p} + S_r s$  (where  $\bar{p} = 0$  but  $S_r s \neq 0$ ). As a consequence, a moderately anisotropic fabric was expected at the end of anisotropic compaction. Note that there was never any indication of shear planes on the anisotropically compacted samples.

The specific volume of anisotropic samples (i.e. compacted by using method B) was smaller than that of isotropic samples (i.e. compacted by using method A). To investigate the influence of void ratio, a second set of anisotropic samples was prepared by following a path with the same stress ratio of method B but limited to a void ratio equal to that of samples compacted by using method A. This required imposition of a smaller maximum anisotropic stress, which was found by trial and error to be equal to  $\bar{p} = 160$  kPa and  $q = 192$  kPa.

During compaction it was not possible to measure sample volume changes. Therefore it was not possible to measure the average cross-sectional area of the sample and hence to calculate the deviator stress correctly. The cross-sectional area was assumed to be constant and several compaction trials were conducted to find the axial force needed to obtain a stress ratio of  $\eta \approx 1.2$  along the anisotropic compaction path. In the first compaction trial, the cross-sectional area was taken equal to that obtained during isotropic compaction. A suitable combination of deviator force and radial stress was therefore imposed based on the assumed cross-sectional area. However, the measured average cross-sectional area after compaction showed some deviation from the assumed value and, therefore, a new compaction trial was conducted based on the cross-sectional area measured during the first trial (a new combination of deviator load and radial stress was calculated). This procedure was repeated until the difference between measured and assumed cross-sectional area was reasonably small.

Finally, despite the two lubricated sheets, the compacted sample showed the influence of some friction at the ends (i.e. a non-cylindrical sample). Therefore, to minimize fabric heterogeneity, all triaxial samples were cut from the middle section of the oversized sample.

## 4.2 TEST SETUP FOR SYSTEM 1 AND SYSTEM 2

### 4.2.1 Preparation of de-aired water

De-aired water was used in the entire testing system (including the outer cell) to avoid formation of air bubbles and therefore to reduce volume measurement errors and increase stability of pressure control. De-aired water was prepared by using a Nold Deaerator of 8 litres capacity. Given that approximately 12 litres of de-aired water was required to perform a triaxial test, de-airing was done in two stages and water stored in an elevated tank. In each stage the deaerator was filled with tap water and a vacuum of 98 kPa was applied. De-airing was accelerated by a rotating disc that sheared the water during application of vacuum. A de-airing period of 1.5 hours was found sufficient to prepare high quality water. After this, the de-aired water was transferred to the storage tank and kept under vacuum while the second de-airing stage was in progress.

### 4.2.2 Saturation of the high air entry filters

The high air entry ceramic filters of the pedestal and the top cap were saturated inside the cell to avoid potential problems associated to removal and reattachment of filters such as air leaking to the water drainage system. Filters saturation consisted of the following steps (referring to Figure 3.10):

- The drainage system was flushed carefully with de-aired water to remove any trapped air.
- The outer cell was assembled (without the inner glass cell) and filled with de-aired water.
- Valves 3, 5 and 6 were closed while valves 1, 2, 4 and 9 were opened on the cell drainage line. On the pore water drainage system, valves 11 and 12 were closed. A cell pressure of 900 kPa was applied and kept for one day to force any air bubbles in the system to go into solution.
- With pressure of 800 kPa on pore water drainage line, valves 11 and 12 were opened. The pressure on the pore water drainage line was then reduced gradually to 50 kPa. Drainage was therefore allowed from the cell into the pore water drainage line (note that both filters were directly exposed to the cell pressure with the top cap left hanging in the cell during saturation) until the measured coefficient of permeability of the two filters reached a constant value. A typical variation of the measured filter permeability with time is shown in Figure 4.4.
- At the end of the saturation process, the cell pressure was reduced gradually to 60 kPa. Then both the cell pressure and pore water pressure were reduced gradually to 10 kPa.

- The drainage system was flushed again with de-aired water to remove any trapped air that might have formed during flushing of the ceramic filters.

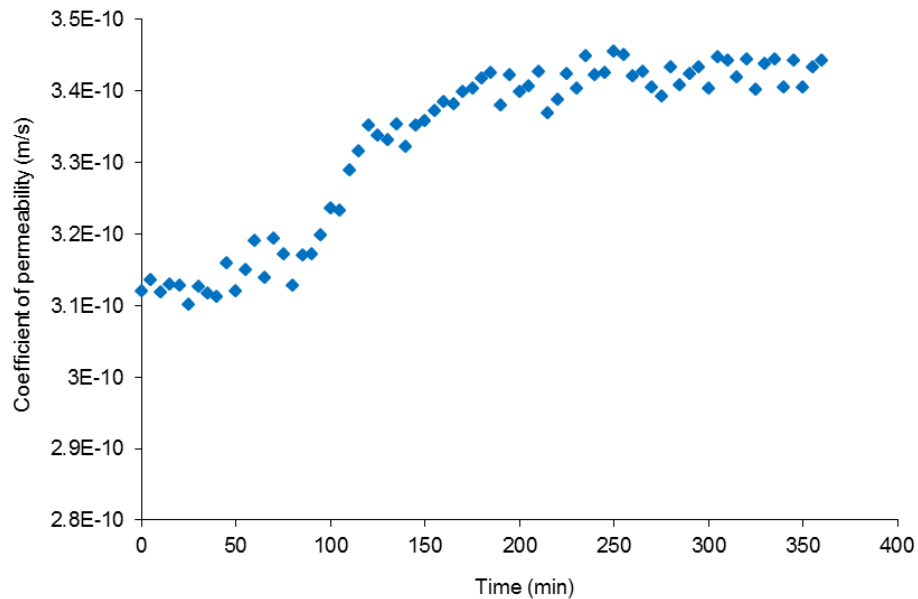


Figure 4.4 Typical variation of filter permeability with time

### 4.2.3 Sample setup

After saturation of the filters, the pore water volume gauge was filled with de-aired water (as discussed in Section 3.3.3). The lower chamber of the gauge was brought to the required position (usually the lowermost position for a triaxial compression test and the uppermost position for a triaxial extension test).

Prior to sample setup, valve 11 (on the top cap drainage line) was closed while valve 12 (on the pedestal drainage line) was kept open (see Figure 3.10). A smear of water was maintained on the pedestal's high air entry filter while the top cap was placed in a small container with shallow water to avoid cavitation and hence filter de-saturation. The sintered brass annulus was placed on the shoulder of the pedestal filter holder. A rubber membrane of suitable length was prepared and examined for any holes. The procedure followed during sample set up can be summarized in the following steps (a schematic representation of each step is shown in Figure 4.5):

- Step 1: the soil sample was placed directly on the high air entry filter of the pedestal. Once the sample was in touch with the high air entry filter, negative pore water pressure began to develop rapidly in the pedestal drainage path. This pressure was recorded by the pressure transducer inside the pore water

controller. The rubber membrane was placed around the sample, by using a membrane stretcher, and sealed with two “O” rings on the pedestal. The top cap was then placed and the membrane was sealed on it with two “O” rings. Valve 11 was then opened (valve 12 was kept open throughout) to monitor the negative pore water pressure developing also in the top cap. Once pore water pressure reached  $-50$  kPa, valve 10 was closed and valve 22 (vent) was subsequently opened for 1 second to release the negative pressure. Valve 10 was then reopened.

- Step 2: The outer cell wall was placed and sealed against the base by using tie rods and two pieces of acrylic. The cell was filled with de-aired water up to a certain level.
- Step 3: The inner glass cell was lowered into position under water to avoid trapping air. The top cover of the inner cell with the attached load cell was then submerged in an inclined position to avoid trapping air in the load cell hole. The top cover was then slowly rotated back into vertical position under water and placed carefully in place. The submerged weight of the load cell during this step was entirely taken by the sample. To allow hooking of the top cap (as described in Section 3.1.1), the load cell was rotated by 90 degrees around its vertical axis. The nuts of the inner cell’s tie rods were turned upside down under water to remove trapped air before screwing them in place. The vent valves of the top cover were kept open during tightening of the nuts to avoid development of any excess cell pressure acting on the sample inside the inner cell.
- Step 4: Water in the outer cell was drained out and the outer cell was subsequently removed (due to space limitation) to adjust the inner cell’s wall (as the wall, sometimes, does not align with the base “O” ring). The vent valves on the top cover were then closed.
- Step 5: The outer cell wall was lowered into position and the top cover was placed and fixed with the nuts. For triaxial extension, the load cell was hooked to the top cover of the outer cell by adjusting the reaction screw as described in Section 3.1.1. A cell pressure of 5 kPa was applied to the inner cell (valves 1, 2, 3, 5 and 6 were opened) before adjusting the reaction screw to avoid development of negative pressures inside the inner cell (during lifting of the load cell). The reaction plate was subsequently attached to the top cover and the outer cell was filled with de-aired water. Valves 4 and 9 were opened to apply a pressure of 5 kPa to the outer cell. Valve 26 was then opened with an air pressure of 1 kPa and the cell pressure was subsequently increased to 11 kPa so that the radial net stress was 10 kPa.

- Step 6: Valves 11 and 12 on the pore water drainage line were closed to avoid the risk of air breaking through the high air entry filters that could be caused by the compressibility of water in the drainage lines or by the expansion of drainage tubes (pore water pressure was not controlled at this stage). The cell pressure and the air pressure were increased to 900 kPa and 890 kPa respectively at a rate of 35 kPa/minute (with the difference maintained at 10 kPa throughout the process).

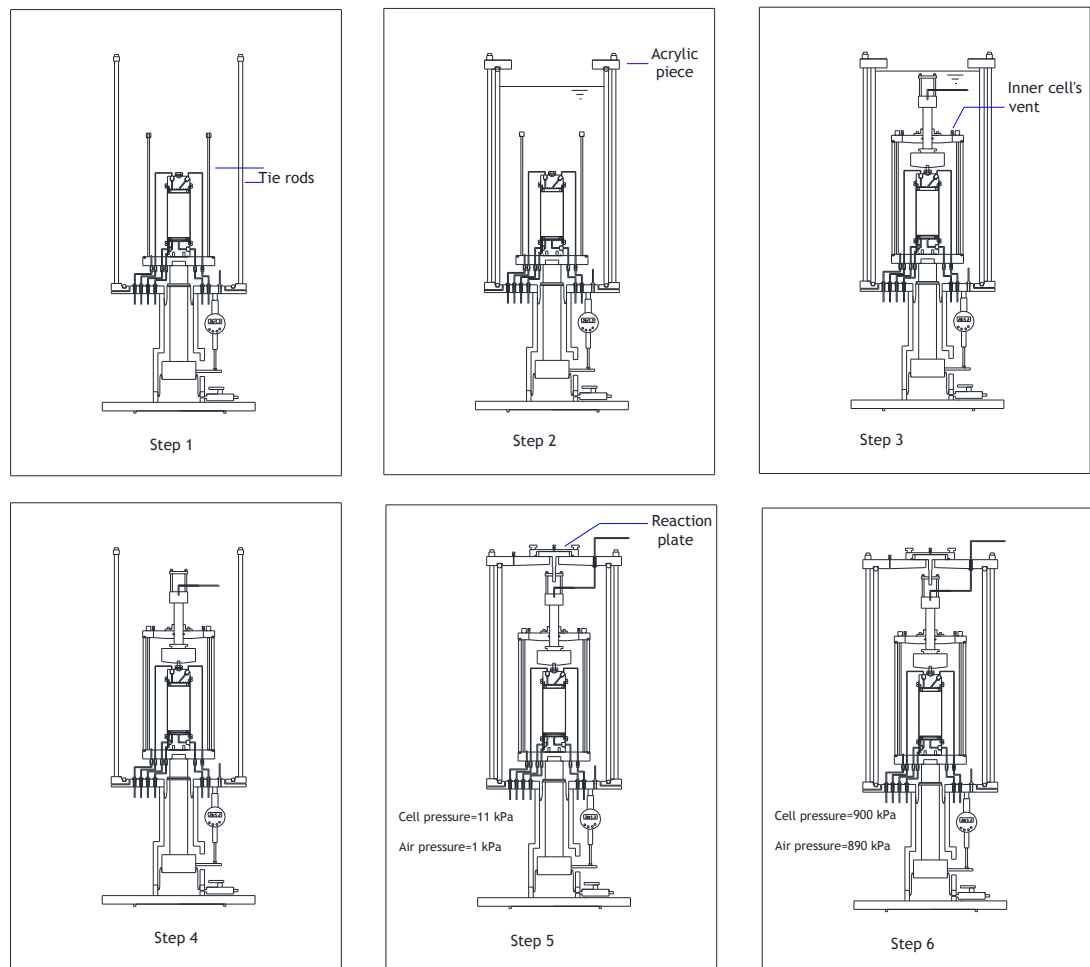


Figure 4.5 Steps of sample setup in System 1 and System 2

### Setting up of saturated samples in System 1 and System 2

Two tests on fully saturated soil samples were conducted in System 1 and System 2 to monitor the volume change during sample saturation and to compare the two techniques for measuring sample volume change during loading (i.e. to compare the changes in the inner cell apparent volume and pore water volume).

The following modifications were made to the drainage system:

- The air drainage line was flushed with de-aired water between the pedestal and valve 26. Valve 26 was kept closed for the whole test period.
- The high air entry filter of the top cap was replaced with a coarse filter. A filter paper disc was also inserted to avoid sample smear into the filter. Air was therefore drained from the top cap (instead of the pedestal as in the original setup) and this was achieved by connecting the air pressure controller to valve 28 (see Figure 3.10) by using a PTFE tube.
- The section of tubing between the pedestal and valve 11 was flushed with de-aired water and the valve was kept close during saturation. The pore water pressure was supplied via valve 12 on the pedestal drainage line.

A sample set up procedure similar to that described for unsaturated samples was followed. Sample saturation was achieved as follows:

- Water was flushed through the sample from the bottom (by opening valve 12) under cell pressure of 900, with an air pressure of 890 kPa on the air drainage line to the top cap and a water pressure of 898 kPa on the drainage line to the pedestal. This step was terminated when water (with no air bubbles) was noticed in the drainage line from the top cap (usually after 5 – 8 days from the start of flushing).
- The remaining air in the top cap was flushed by closing valve 12 (to avoid dropping of pore water pressure at the base of the sample during the flushing) and opening valves 11 with a pore water pressure of 898 kPa. Valve 28 was then closed and kept close over the rest of the test. Valve 12 was then reopened to have the same pore water pressure of 898 kPa at the top and bottom of the sample.
- The pore water pressure was reduced to 895 kPa and maintained at this level for 5 to 10 days to force the remaining air inside the sample to go into solution. It should be noted that no *B*-check was performed in these tests.

### 4.3 TEST SETUP FOR SYSTEM 3

The pedestal pore water drainage lines were flushed with de-aired water. The top cap drainage line was flushed with dry air to facilitate air drainage during sample saturation. Two coarse sintered brass filters of 50 mm diameter were prepared; one was saturated in an ultrasonic water bath whereas the other one was oven-dried. Circular filter papers, “O” rings and a rubber membrane were also prepared before setting up the sample. The procedure followed during sample setting up and saturation is explained in the following steps with reference to Figure 3.13:

- Step 1: Valve 4 (on the pedestal drainage line) was closed. The water saturated coarse filter was placed on the pedestal and the filter paper was placed on the top of it to avoid sample smear into the filter. The sample was placed directly on the filter paper and subsequently another filter paper was placed on the top of the sample before positioning the dry coarse filter. The rubber membrane was placed and sealed with two “O” rings to the pedestal. The top cap was placed and the membrane was sealed also to the top cap with two “O” rings.
- Step 2: The cell wall was placed with care and the hook of the load cell was properly positioned in the bevel of the top cap without displacing the sample. The cell was subsequently transferred to the loading frame and filled with tap water.
- Step 3: Water was flushed through the sample by opening valve 2 (so that the air pressure at the top of the sample was atmospheric), opening valve 1 with a cell pressure of 10 kPa and valves 4 and 5 with a back pressure 8 kPa. Drainage was allowed until clear water (with no air bubbles) flowed from the top cap (usually after 2 – 3 days).
- Step 4: Valves 2 and 4 were closed and valve 3 was opened to apply a back pressure of 8 kPa to the top cap. Once the back pressure in the top cap drainage line reached 8 kPa, valve 4 was opened again (this valve was closed to avoid application of an excess pressure to the base of the sample when the back pressure was less than 8 kPa). The cell pressure was increased to 13 kPa so that the radial effective stress was 5 kPa. The cell pressure and back pressure were increased to 305 kPa and 300 kPa respectively to dissolve the remaining air inside the sample. The pressure was raised at a slow rate (4 kPa/hour) to avoid applying an excess pressure to the soil while the sample was still unsaturated.
- Step 5: Saturation was confirmed by performing a  $B$ -check (where  $B$  is the ratio between the increase in pore pressure and the increase in the cell pressure) by closing valve 5, increasing the cell pressure by 10 kPa and measuring the corresponding increase in pore pressure by using the pressure transducer. The sample was considered saturated if the  $B$  value was above 0.96 (the  $B$  value for this work was found to be between 0.97 and 0.99).

## 4.4 DATA PROCESSING

### 4.4.1 Unsaturated testing

As explained in Chapter 3, variables can be calculated in Clisp studio software from input and measured data as shown below.

$$s = u_a - u_w \quad (4.1)$$

$$q = \frac{f}{(V_0 - \Delta V)} (H_0 - \Delta H) \quad (4.2)$$

where  $V_0$ ,  $\Delta V$ ,  $H_0$  and  $\Delta H$  are the initial sample volume (input variable), the change in sample volume (measured data), the initial height of the sample (input variable) and the change in sample height (measured data) respectively,  $f$  is the deviator force (measured data),  $q$  is the current value of the deviator stress. Values of  $\Delta V$  and  $\Delta H$  are measured from the beginning of loading after suction equalisation.

The current value of  $q$  from Equation 4.2 can be compared with the required current target value of  $q$  in order to follow the described stress path of specified gradient  $[\Delta q/\Delta \bar{p}]$ . This target value of  $q$  can be calculated by starting from the relationship between increments of mean net stress  $\bar{p}$ , deviator stress  $q$  and radial net stress  $\bar{\sigma}_3$ :

$$\Delta \bar{p} = \Delta \bar{\sigma}_3 + \Delta q/3 \quad (4.3)$$

This can be re-arranged to express  $\Delta q$  as a function of  $[\Delta q/\Delta \bar{p}]$  and  $\Delta \bar{\sigma}_3$ :

$$\Delta q = \frac{3[\Delta q/\Delta \bar{p}]}{3 - [\Delta q/\Delta \bar{p}]} \Delta \bar{\sigma}_3 \quad (4.4)$$

If radial net stress is adjusted by varying the pore air pressure while holding the cell pressure constant, then  $\Delta \bar{\sigma}_3 = -\Delta u_a$  and Equation 4.4 then results in the following expression for the target value of  $q$ :

$$q_{target} = q_0 + \frac{3[\Delta q/\Delta \bar{p}]}{3 - [\Delta q/\Delta \bar{p}]} (u_{a0} - u_a) \quad (4.5)$$

where  $q_0$  is the initial value of  $q$  at the start of the test (input variable),  $[\Delta q/\Delta \bar{p}]$  is the required stress path gradient (input variable),  $u_{a0}$  is the initial value of pore air pressure (input variable) and  $u_a$  is the current value of pore air pressure (measured data). In a stress-controlled stage, where radial net stress being increased (or decreased) at a specified rate, the software calculates the current and target values of deviator stress increment from Equations 4.2 and 4.5 respectively, and compares the error to the tolerance ( $\pm 0.5$  kPa). When the error exceeds the tolerance, the deviator force  $f$  is increased/decreased to track the target value of deviator stress by sending a signal to the lower chamber pressure controller. Instead, in a strain-controlled stage when axial

displacement is being increased (or decreased) at a specified rate, the current deviator stress is calculated from Equation 4.2 and is fed into Equation 4.5 to calculate the target air pressure value. The software then compares the error in the current value of the air pressure to the tolerance ( $\pm 0.5$  kPa). When the error exceeds the tolerance, the air pressure is increased/decreased accordingly by sending a signal to the air pressure controller.

After applying the necessary corrections to the raw data obtained from the software, a number of derived variables were calculated by using MS Excel. Values of the specific volume  $v$ , water content  $w$ , degree of saturation  $S_r$ , true axial strain  $\varepsilon_a$ , true radial strain  $\varepsilon_r$ , true volumetric strain  $\varepsilon_v$ , true shear strain  $\varepsilon_s$  and mean Bishop's stress  $p^*$  were calculated after the test as shown below.

$$v = \frac{\rho_w G_s (V_0 - \Delta V)}{M_s} \quad (4.6)$$

$$w = \frac{\rho_w V_w}{M_s} \quad (4.7)$$

$$S_r = \frac{G_s w}{(v - 1)} \quad (4.8)$$

$$\varepsilon_a = -\ln\left(\frac{H_0 - \Delta H}{H_0}\right) \quad (4.9)$$

$$\varepsilon_r = -\ln\left(\frac{R_0 - \Delta R}{R_0}\right) \quad (4.10)$$

$$\varepsilon_v = -\ln\left(\frac{V_0 - \Delta V}{V_0}\right) \quad (4.11)$$

$$\varepsilon_s = \frac{2}{3}(\varepsilon_a - \varepsilon_r) \quad (4.12)$$

$$p^* = \bar{p} + S_r s \quad (4.13)$$

where  $\rho_w$  and  $G_s$  are the density of water and the specific gravity of the solid particles, taken as  $1 \text{ Mg/m}^3$  and 2.6 respectively.  $M_s$  is the mass of the solids within the sample, which was initially calculated approximately from the wet mass and water content after compaction (necessary to perform a stress path test) and subsequently measured more

accurately after oven-drying of the sample at the end of the test.  $V_w$  is the volume of the water in the sample.  $R_0$  is the average radius of the sample after suction equalisation and  $\Delta R$  is the current average change in sample radius (calculated from the average sample cross-section area). The negative signs in Equations 4.9, 4.10 and 4.11 were required because of the use of a standard soil mechanics sign convention of compressive strains as positive.

#### 4.4.2 Saturated testing

In the saturated triaxial system (System 3), the stress path was controlled by increasing axial displacement (see Section 3.2), measuring the deviator stress (Equation 4.2) and adjusting the cell pressure accordingly:

$$\sigma_3 = \sigma_{30} + \frac{3 - [\Delta q / \Delta \bar{p}]}{3[\Delta q / \Delta \bar{p}]} q \quad (4.14)$$

where  $\sigma_{30}$  is the cell pressure at the beginning of loading stage and  $\sigma_3$  is the current cell pressure value. The tolerance in the current cell pressure value was set to  $\pm 0.5$  kPa. Raw data were subsequently corrected and processed in MS Excel to calculate derived variables by using Equations 4.6, 4.9, 4.10, 4.11 and 4.12.

#### 4.5 TYPICAL TEST STAGES

Normally, each stress path test consisted of one or more of the stages described below. For unsaturated tests, the cell pressure was kept constant for the whole test at 900 kPa and the radial net stress was controlled by varying the air pressure (and the pore water pressure simultaneously to control suction as required). For saturated tests, the pore water pressure was held constant and the radial effective stress was controlled by varying cell pressure.

##### Wetting stages for unsaturated tests

The initial suction of the samples, measured by using the axis translation technique, was higher than 300 kPa as will be shown in Section 5.3. Samples were equalised to target suctions of 100 kPa or 300 kPa under a stress state of  $\bar{p} = 12$  kPa and  $q = 6$  kPa for tests that involved only triaxial compression stages and under of stress state of  $\bar{p} = 10$  and  $q = 0$  for tests involving triaxial extension loading (as described in Section 3.1.1). Suction equalisation was achieved by imposing a step change of suction from the initial value to the target one. This target value of suction was maintained for the whole duration of the equalization stage (usually about 3 to 6 days). In all cases, the pore water volume gauge recorded inflow of water to the sample confirming that suction equalisation involved

wetting of the sample. For one series of the tests, additional wetting stages from  $s = 300$  kPa to  $s = 100$  kPa (as will be explained in Section 5.1.2) were conducted under constant net stress.

### Loading stages

The test programme involved probing along a series of loading paths at constant inclinations in the  $q:\bar{p}$  plane under constant suction. Loading started after the wetting stage from the equalization stress state.

For loading stages that did not involve shearing to failure, loading was conducted by varying the radial net stress at a constant rate of 2 kPa/hr and adjusting the deviator stress accordingly. The suitability of this loading rate was confirmed, at the beginning of testing programme, by monitoring volume changes of unsaturated samples over 24 hours rest period after isotropic loading to  $\bar{p} = 300$  kPa at different suction levels. As volume change is smaller during unloading than loading, unloading was conducted by decreasing the radial net stress at a constant rate 4 kPa/hr. For loading stages that involved shearing to failure, axial displacement was varied at a constant rate of 0.2 mm/hr, measuring the deviator stress and adjusting the radial net stress accordingly. This rate of axial displacement gives nearly the same time period for the shearing stages as that for the loading stages conducted by varying the radial net stress. It is worth mentioning that no attempt was made to investigate the influence of increasing or decreasing the constant rates of loading/shear on the measured response of the soil.

For saturated tests, loading started from the stress state after saturation (i.e.  $p' = 5$  kPa and  $q = 0$  kPa). For isotropic stress paths, loading was conducted by increasing the radial effective stress at a constant rate 2 kPa/hr. For other stress paths, loading was conducted by increasing the axial displacement at a constant rate of 0.2 mm/hr, measuring the deviator stress and adjusting the radial effective stress accordingly (by holding pore water pressure constant and varying cell pressure).

### Shear stages

Loading stages with a stress path inclination less than the critical state ratio were followed by a conventional shearing stage which was conducted by increasing the axial displacement at a constant rate of 0.2 mm/hr at constant radial (net or effective) stress. The duration of this shear stage was similar to that of other stages (e.g. wetting and isotropic/anisotropic loading). In most cases, shearing was conducted up to failure in triaxial compression or extension.

# 5

## EXPERIMENTAL RESULTS AND DISCUSSION

This chapter presents results from the laboratory tests conducted during this PhD. Material behaviour under unsaturated and saturated conditions is initially discussed in this chapter and is further analysed in Chapter 6.

### 5.1 TEST SERIES AND STRESS PATHS

The experimental campaign consisted of 11 Test Series with each series involving up to 7 triaxial compression and extension tests. The first objective was to determine yield points and, hence, to define both the initial yield surface induced during compaction and the changes of yield surface produced by plastic loading. The second objective was to examine whether critical states were independent of the evolving anisotropy. Each unsaturated test began with an initial wetting stage to a required suction under a stress state of  $\bar{p} = 12$  kPa and  $q = 6$  kPa (for tests involving shearing in triaxial compression) or a stress state of  $\bar{p} = 10$  kPa and  $q = 0$  (for tests involving shearing in triaxial extension). Each saturated test began instead with a saturation stage under a stress state of  $p' = 5$  kPa and  $q = 0$ .

The wetting/saturation stage was followed by a “probing” stage consisting of loading at constant suction at different constant values of  $[\Delta q/\Delta \bar{p}]$  (in the case of unsaturated tests) or  $[\Delta q/\Delta p']$  (in the case of saturated tests).

All probing stages are delimited in the  $q:\bar{p}$  plane or  $q:p'$  plane by the two lines defined by  $\eta = 3$  and  $\eta = -1.5$  (where  $\eta = q/\bar{p}$  or  $q/p'$ ). This is because loading at  $\eta > 3$  or  $\eta < -1.5$  would involve applying a negative (tensile) radial stress or a negative (tensile) axial stress, respectively.

The name of each test series begins with a letter which is either A if the samples were compacted isotropically or B if the samples were compacted anisotropically. For those test series conducted to investigate the changes of the yield surface induced by plastic loading, the first letter is followed by a second one (either a, b, c, d or e) depending on the particular plastic loading path followed. The first letter/letters is/are followed by a

number indicating the value of constant suction at which all tests in this series were conducted.

The name of each individual test within a given series begins with the series name followed by a number in brackets referring to the constant gradient of the stress path  $[\Delta q/\Delta \bar{p}]$  or  $[\Delta q/\Delta p']$  under which probing was conducted. For instance, A300(1) refers to a test on an isotropically compacted sample, wetted to  $s = 300$  kPa and then probed under constant suction at  $[\Delta q/\Delta \bar{p}] = 1$ .

As mentioned in Section 4.1.3, two different sample heights had to be used for testing samples in triaxial compression and triaxial extension due to the limitation on axial displacement. The initial sample height for tests involving loading stages in triaxial compression only was 100 mm (with initial sample aspect ratio of 2) whereas the initial sample height for tests involving loading stages in triaxial extension was 75 mm (with initial sample aspect ratio of 1.5). However, it was found interesting that as test progresses, the aspect ratio becomes more similar in triaxial compression and triaxial extension, suggesting that having lower initial aspect ratio in triaxial extension than in triaxial compression is rather advantageous.

It is worth mentioning that few tests were repeated in System 1 and System 2 to investigate how repeatable the results are. It was concluded that that testing procedure gives very repeatable results.

### 5.1.1 Test series to investigate yielding and critical states of as-compacted samples

Test Series A300, A100 and A0 were performed on isotropically compacted samples at constant suctions of  $s = 300$  kPa,  $s = 100$  kPa and under saturated conditions respectively, whereas Test Series B300, B100, Be100 and B0 were performed at the same three values of suction but on anisotropically compacted samples.

For the unsaturated Test Series A300, A100, B300 and B100 the slopes of the probing stress paths were identical and equal to  $[\Delta q/\Delta \bar{p}] = 3, 2, 1, 0, -0.5, -1$  and  $-1.5$  (see Figure 5.1).

Probing stages were initiated either from point  $a$  (corresponding to  $\bar{p} = 12$  kPa and  $q = 6$  kPa) or from point  $b$  (corresponding to  $\bar{p} = 10$  kPa and  $q = 0$ ) depending on whether tests involved shearing in triaxial compression or extension, as previously explained. Tests performed at  $[\Delta q/\Delta \bar{p}] = 3, 2, 1, -1$  or  $-1.5$  followed the same probing stress path

until failure occurred. For tests performed at  $[\Delta q/\Delta \bar{p}] = 0$  or  $-0.5$ , the probing stress path was terminated at a radial net stress of 300 kPa (Points *c* and *d* respectively in Figure 5.1) and this was followed by constant suction shearing at  $[\Delta q/\Delta \bar{p}] = 3$ , i.e. under constant radial net stress, to failure in triaxial compression or extension, respectively.

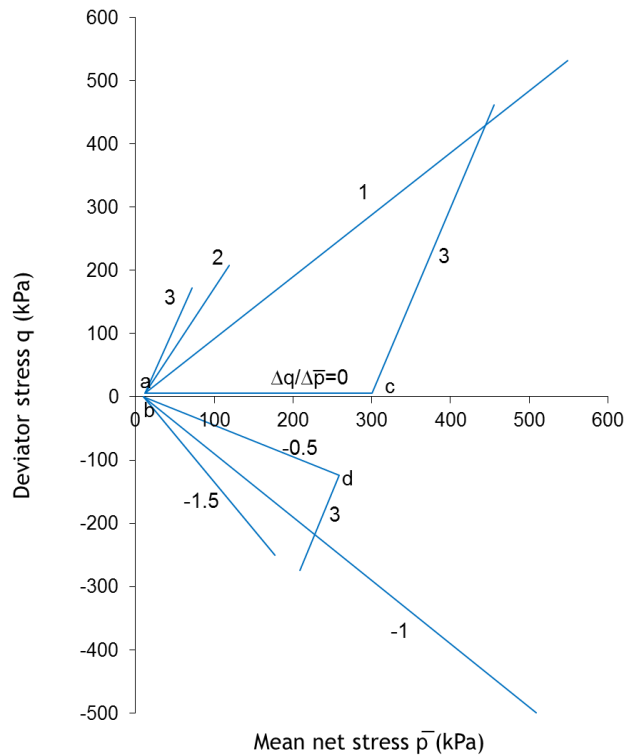


Figure 5.1 Stress paths of Test Series A300, A100, B300 and B100

Test Series Be100 was conducted on anisotropically compacted samples with same initial specific volume as the isotropically compacted samples. The probing stages in this series were performed at  $[\Delta q/\Delta \bar{p}] = 2, 1, 0, -0.5, -1$  and  $-1.5$ .

For the saturated Test Series A0 and B0, the probing stages initiated from point *a* (corresponding to  $p' = 5$  kPa and  $q = 0$ ) and followed similar stress paths as those of the unsaturated tests but this time defined in terms of effective stress, i.e.  $[\Delta q/\Delta p'] = 2, 1, 0.5, 0, -0.5, -1$  and  $-1.5$  (see Figure 5.2).

Unlike the unsaturated Test Series A300, A100, B300, B100, the saturated Test Series A0 and B0 did not include a probing stress path at  $[\Delta q/\Delta p'] = 3$  because this resulted in an almost immediate attainment of critical state. An additional probing stress path at  $[\Delta q/\Delta p'] = 0.5$  was instead performed. Saturated tests performed at  $[\Delta q/\Delta p'] = 0$  were conducted under a nominal deviator stress of 1 kPa in order to track changes of sample

height throughout loading. Tests at  $[\Delta q/\Delta p'] = 2, 1, -1$  or  $-1.5$  followed the same stress path until failure. Instead, for tests at  $[\Delta q/\Delta p'] = 0$ , the probing stage terminated at a radial net stress of 300 kPa (point *c* in Figure 5.2) and was followed by constant radial stress shearing ( $[\Delta q/\Delta p'] = 3$ ) to failure in compression. For  $[\Delta q/\Delta p'] = 0.5$  or  $-0.5$ , the probing stage terminated at a mean effective stress  $p' = 150$  kPa (Points *b* and *d* respectively in Figure 5.2), and was followed by constant radial net stress shearing  $[\Delta q/\Delta p'] = 3$  to failure in compression or extension respectively.

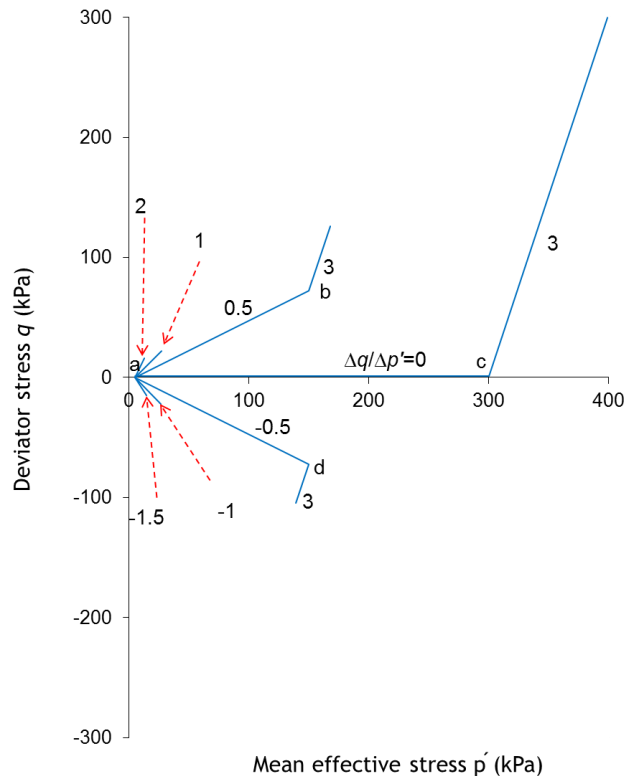


Figure 5.2 Stress paths of Test Series A0 and B0

### 5.1.2 Test series to investigate yielding and critical states of samples with induced anisotropy

Four further Test Series were performed on anisotropically compacted samples. Each of them involved an initial loading and unloading stages at a given stress ratio followed by probing/shearing stress paths of the same types as described in the previous section.

In Test Series Ba300, 6 anisotropically compacted samples were all loaded initially at a stress ratio  $[\Delta q/\Delta \bar{p}] = 1.2$  to a final mean net stress  $\bar{p} = 200$  kPa (see loading paths *a – b* in Figures 5.3) corresponding to about 1.7 times the yield stress measured from the closest probing stress path in Test Series B300. Loading to a mean net stress higher than this would have brought the samples very close to critical state which was not desirable.

Test Series Ba300 was conducted to investigate the expansion of the yield surface caused by loading along nearly the same stress path as followed during compaction.

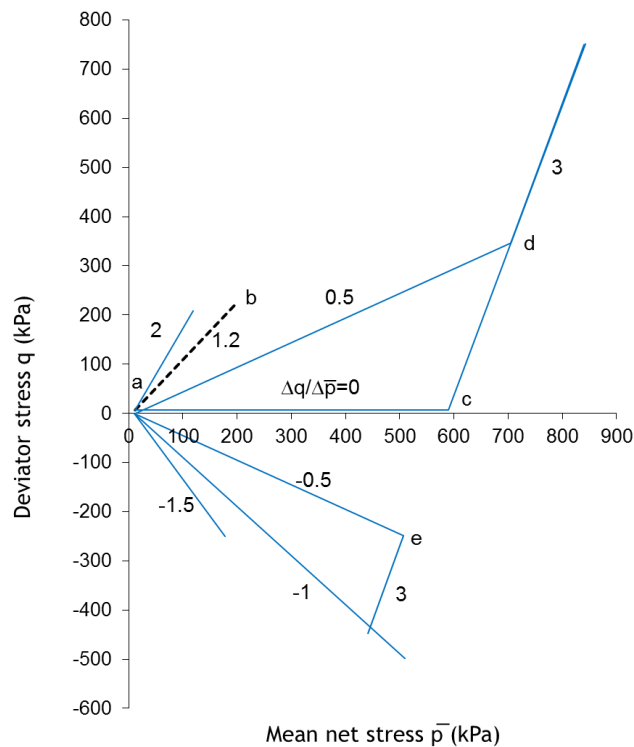


Figure 5.3 Stress paths of Test Series Ba300

In Test Series Bb300 (5 tests) and Bc300 (5 tests) the initial loading stages involved loading at  $[\Delta q/\Delta \bar{p}] = 0$  and  $-1$  respectively, to a final mean net stress  $\bar{p} = 200$  kPa (see loading paths  $a - b$  in Figures 5.4 and 5.5 respectively). These tests were conducted to investigate expansion of the yield surface during loading along very different stress paths to those followed during previous compaction. In all tests within Series Ba300, Bb300 and Bc300, the initial loading stage was followed by unloading to the initial stress state by going back along the same stress path in the  $q: \bar{p}$  plane.

Test Series Ba300 included 6 tests with probing paths at  $[\Delta q/\Delta \bar{p}] = 2, 0.5, 0, -0.5, -1$  and  $-1.5$  (see Figure 5.3). Test Series Bb300 included 5 tests with probing paths at  $[\Delta q/\Delta \bar{p}] = 1.2, 0.5, -0.5, -1$  and  $-1.5$  (see Figure 5.4). Test Series Bc300 included 5 tests with probing paths at  $[\Delta q/\Delta \bar{p}] = 1.2, 0.5, 0, -0.5$  and  $-1.5$  (see Figure 5.5). Tests at  $[\Delta q/\Delta \bar{p}] = 2, 1.2, -1$  or  $-1.5$  continued along the same stress path until shear failure. For tests at  $[\Delta q/\Delta \bar{p}] = 0, 0.5$  or  $-0.5$ , probing terminated at a radial net stress of 590 kPa (Points  $c, d$  or  $e$  in Figures 5.3, 5.4 and 5.5) and was followed by constant suction shearing at constant radial net stress (i.e.  $[\Delta q/\Delta \bar{p}] = 3$ ) until failure was attained in either compression or extension.

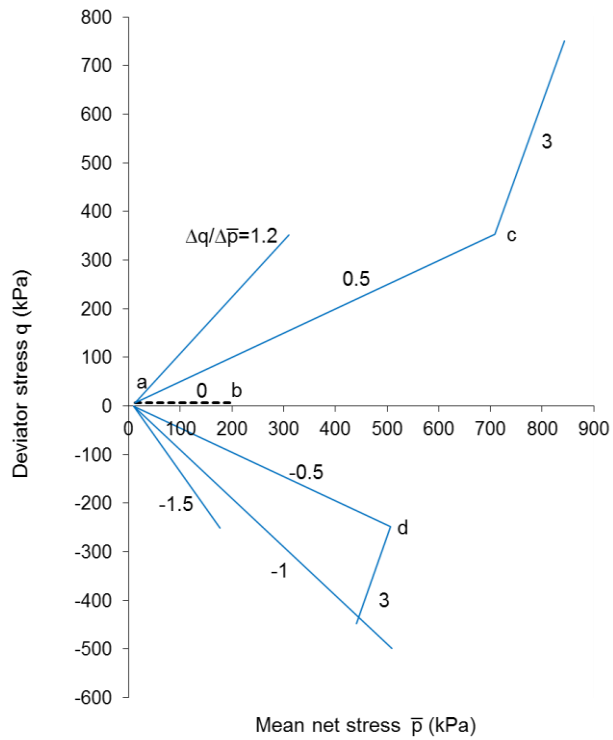


Figure 5.4 Stress paths of Test Series Bb300

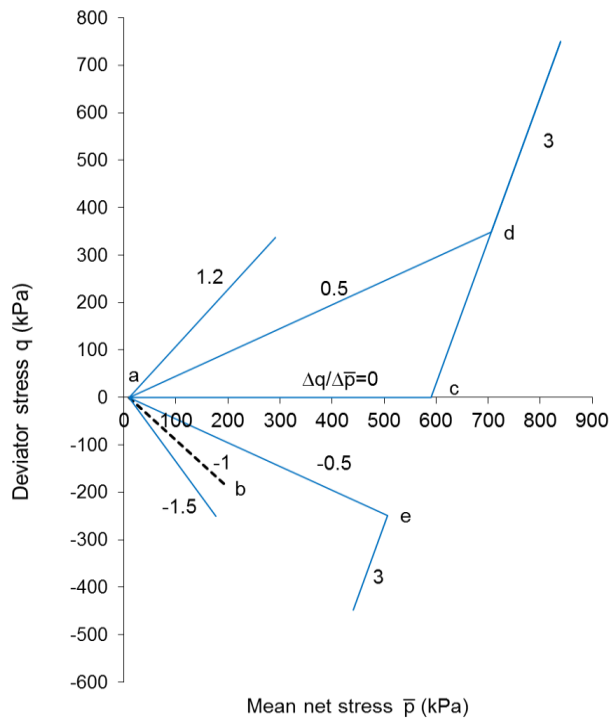


Figure 5.5 Stress paths of Test Series Bc300

In order to examine the effect of wetting-induced plastic collapse-compression on the evolution of the yield locus for anisotropically compacted samples, Test Series Bd100 was conducted. Figures 5.6 and 5.7 show the loading, wetting and unloading stages of Test Series Bd100. Samples were initially wetted to a suction  $s = 300$  kPa, as explained

earlier. Subsequently they were loaded at  $[\Delta q/\Delta \bar{p}] = 0$  to  $\bar{p} = 90$  kPa under constant suction  $[\Delta q/\Delta \bar{p}] = 0$  (see path  $a-b$ ) at which point the soil was about to yield. Then, they were wetted to  $s = 100$  kPa (see path  $b-c$ ), by imposing a step change of suction from 300 kPa to 100 kPa at the top and bottom boundaries of the sample. This was followed by unloading to  $d$ , at the net stress state imposed during the initial wetting. The subsequent probing/shearing stages for this series (see Figure 5.7) were identical to those in Test Series Bb300.

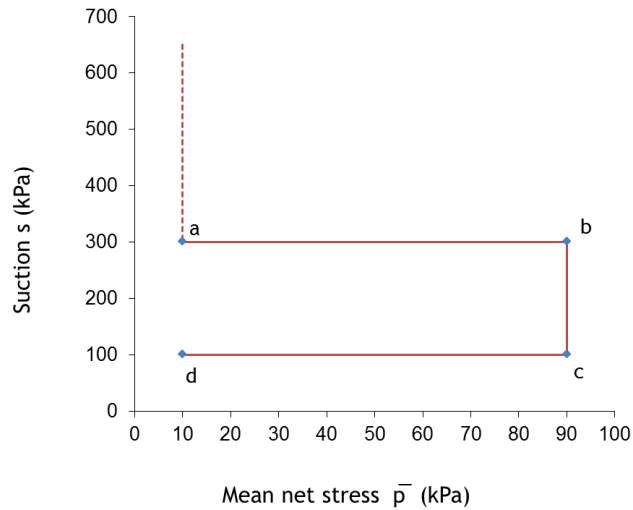


Figure 5.6 Loading, wetting and unloading stages in Test Series Bd100

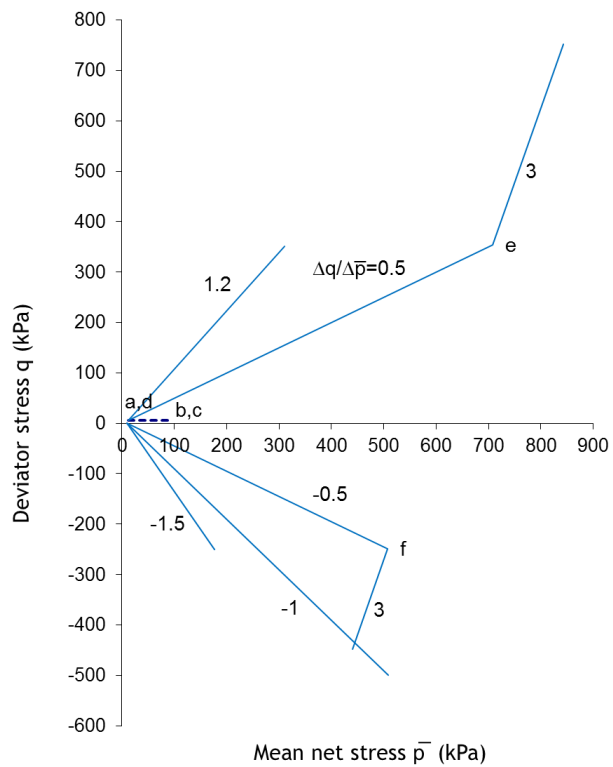


Figure 5.7 Stress paths of Test Series Bd100

In addition to the tests campaign described in Sections 5.1.1 and 5.1.2, three supplementary tests were performed (i.e. Tests A200(0), A0(sat1) and A0(sat2)).

Test A200(0) was performed on an isotropically compacted sample wetted to  $s = 200$  kPa and loaded subsequently at  $[\Delta q/\Delta \bar{p}] = 0$ , from an initial stress state of  $\bar{p} = 10$  kPa and  $q = 0$  to  $\bar{p} = 300$  kPa. The result of this test was used together with the results of Tests A300(0) and A100(0) in plotting the isotropic normal compression planar surface (see Section 6.2.3) that was used subsequently in performing model simulations with the proposed anisotropic model in Chapter 8.

Tests A0(sat1) and A0(sat2) were performed on isotropically compacted samples in System 1 and System 2 respectively after applying some modifications to the equipment (see Section 4.2.3). These tests involved isotropic loading from an initial stress state of  $p' = 5$  kPa and  $q = 1$  kPa to  $p' = 300$  kPa and 100 kPa respectively then unloading to the initial state. The sample of Test A0(sat1) was subsequently re-loaded isotropically to  $p' = 150$  kPa then sheared at constant  $p'$  to a final  $q$  value of 75 kPa. The sample of Test A0(sat2) was subsequently re-loaded isotropically to  $p' = 100$  kPa then sheared at constant  $p'$  to a  $q$  value of 60 kPa then unloaded at constant  $p'$  to  $q = 1$  kPa. The purposes of Tests A0(sat1) and A0(sat2) were:

- to compare sample volume change measured by using the overall change of sample size to that measured from the pore water volume change (see Section 3.3.7);
- to obtain values for the elastic soil constants  $\kappa$  and  $G$  under saturated condition.

## 5.2 INITIAL SAMPLE PROPERTIES

The details of all tests are given in Table 5.1. In this table:  $\bar{p}_{initial}$ ,  $q_{initial}$  and  $s$  refer to the mean net stress, deviator stress and suction, respectively, at which equalization during the initial wetting stage took place;  $w_{initial}$ ,  $v_{initial}$  and  $S_{r_{initial}}$  refer to the initial (after compaction) water content, specific volume and degree of saturation, respectively;  $w_{after}$ ,  $v_{after}$  and  $S_{r_{after}}$  refer to the water content, specific volume and degree of saturation, respectively, at the end of the initial wetting stage.

The after-compaction values of water content, specific volume and degree of saturation for the isotropically compacted samples were  $0.2470 \pm 0.0020$ ,  $2.318 \pm 0.015$  and  $0.4868 \pm 0.0050$  respectively while, for the anisotropically compacted samples, they were  $0.2474 \pm 0.0020$ ,  $2.169 \pm 0.016$  and  $0.5501 \pm 0.0040$ , respectively. These data show

a relatively small scatter and, therefore, a good repeatability of the compaction techniques.

Table 5.1 Properties of samples before and after the initial wetting stage

Series	Test code	$\bar{p}_{initial}$		$s$	$w_{initial}$	$w_{after}$	$v_{initial}$	$v_{after}$	$S_{r_{initial}}$	$S_{r_{after}}$
		kPa	$q_{initial}$							
A300	A300(3)	12	6	300	0.2485	0.2905	2.335	2.364	0.4838	0.5535
	A300(2)	12	6	300	0.2458	0.2817	2.327	2.353	0.4814	0.5413
	A300(1)	12	6	300	0.2464	0.2779	2.333	2.351	0.4803	0.5348
	A300(0)	12	6	300	0.2444	0.2738	2.317	2.338	0.4825	0.5320
	A300(-0.5)	10	0	300	0.2483	0.2810	2.312	2.336	0.4921	0.5467
	A300(-1)	10	0	300	0.2470	0.2765	2.309	2.324	0.4904	0.5427
	A300(-1.5)	10	0	300	0.2493	0.2874	2.318	2.349	0.4918	0.5537
A100	A100(3)	12	6	100	0.2494	0.3594	2.361	2.390	0.4764	0.6719
	A100(2)	12	6	100	0.2474	0.3677	2.323	2.357	0.4860	0.7044
	A100(1)	12	6	100	0.2473	0.3589	2.328	2.373	0.4841	0.679
	A100(0)	12	6	100	0.2465	0.3698	2.314	2.352	0.4879	0.7108
	A100(-0.5)	10	0	100	0.2469	0.3597	2.307	2.348	0.4908	0.6936
	A100(-1)	10	0	100	0.2473	0.3641	2.300	2.344	0.4949	0.7041
	A100(-1.5)	10	0	100	0.2474	0.3679	2.301	2.362	0.4911	0.7023
A0	A0(2)			0	0.2462		2.303	2.403	0.4912	
	A0(1)			0	0.2482		2.321	2.421	0.4883	
	A0(0.5)			0	0.2462		2.302	2.402	0.4916	
	A0(0)			0	0.2452		2.310	2.410	0.4865	
	A0(-0.5)			0	0.2479		2.320	2.420	0.4882	
	A0(-1)			0	0.2475		2.316	2.416	0.4888	
	A0(-1.5)			0	0.2471		2.330	2.430	0.4829	
	A0(sat1)			0	0.2451		2.301	2.402	0.4898	
A0(sat2)			0	0.2467		2.302	2.422	0.4924		
B300	B100(3)	12	6	300	0.2446	0.2778	2.166	2.180	0.5454	0.6118
	B300(2)	12	6	300	0.2446	0.2771	2.177	2.189	0.5402	0.6058
	B300(1)	12	6	300	0.2456	0.2780	2.175	2.190	0.5433	0.6074
	B300(0)	12	6	300	0.2452	0.2763	2.173	2.180	0.5435	0.6083
	B300(-0.5)	10	0	300	0.2477	0.2767	2.162	2.182	0.5539	0.6086
	B300(-1)	10	0	300	0.2490	0.2775	2.172	2.190	0.5523	0.6064
B100	B300(-1.5)	10	0	300	0.2460	0.2841	2.174	2.200	0.5448	0.6161
	B100(3)	12	6	100	0.2461	0.3646	2.163	2.211	0.5499	0.7823
	B100(2)	12	6	100	0.2476	0.3663	2.168	2.213	0.5510	0.7847
	B100(1)	12	6	100	0.2504	0.3628	2.178	2.218	0.5525	0.7740
	B100(0)	12	6	100	0.2479	0.3657	2.167	2.201	0.5524	0.7913
	B100(-0.5)	10	0	100	0.2485	0.3559	2.166	2.211	0.5537	0.7639
	B100(-1)	10	0	100	0.2489	0.3585	2.177	2.217	0.5498	0.7657
B100(-1.5)	10	0	100	0.2477	0.3546	2.189	2.231	0.5415	0.7489	
Be100	Be100(2)	12	6	100	0.2464	0.3665	2.307	2.343	0.4901	0.7090
	Be100(1)	12	6	100	0.2460	0.3671	2.320	2.353	0.4846	0.7051

Table 5.1 Continued

Series	Test code	$\bar{p}_{initial}$	$q_{initial}$	$s$	$w_{initial}$	$w_{after}$	$v_{initial}$	$v_{after}$	$S_{r_{initial}}$	$S_{r_{after}}$
		kPa								
	Be100(0)	12	6	100	0.2451	0.3584	2.352	2.387	0.4712	0.6715
	Be100(-0.5)	10	0	100	0.2475	0.3704	2.306	2.378	0.4926	0.6985
	Be100(-1)	10	0	100	0.2469	0.3654	2.298	2.348	0.4944	0.7046
	Be100(-1.5)	10	0	100	0.2471	0.3670	2.335	2.368	0.4813	0.6971
	B0(2)			0	0.2487		2.171	2.271	0.5521	
	B0(1)			0	0.2468		2.175	2.275	0.5457	
	B0(0.5)			0	0.2476		2.158	2.258	0.5558	
B0	B0(0)			0	0.2443		2.167	2.267	0.5443	
	B0(-0.5)			0	0.2470		2.184	2.284	0.5420	
	B0(-1)			0	0.2495		2.186	2.286	0.5468	
	B0(-1.5)			0	0.2476		2.173	2.273	0.5485	
	Ba300(2)	12	6	300	0.2490	0.2833	2.157	2.184	0.5593	0.6218
	Ba300(0.5)	12	6	300	0.2481	0.2835	2.162	2.191	0.5550	0.6188
Ba300	Ba300(0)	12	6	300	0.2465	0.2826	2.171	2.194	0.5474	0.6155
	Ba300(-0.5)	10	0	300	0.2490	0.2782	2.167	2.184	0.5547	0.6108
	Ba300(-1)	10	0	300	0.2490	0.2849	2.173	2.203	0.5520	0.6156
	Ba300(-1.5)	10	0	300	0.2455	0.2819	2.157	2.167	0.5515	0.6277
	Bb300(1.2)	12	6	300	0.2494	0.2882	2.157	2.189	0.5601	0.6301
	Bb300(0.5)	12	6	300	0.2476	0.2911	2.169	2.185	0.5504	0.6385
Bb300	Bb300(-0.5)	10	0	300	0.2498	0.2796	2.170	2.184	0.5557	0.6140
	Bb300(-1)	10	0	300	0.2481	0.2747	2.167	2.180	0.5527	0.6051
	Bb300(-1.5)	10	0	300	0.2480	0.2874	2.152	2.183	0.5594	0.6315
	Bc300(1.2)	10	0	300	0.2469	0.2715	2.182	2.198	0.5429	0.5890
	Bc300(0.5)	10	0	300	0.2457	0.2770	2.171	2.185	0.5452	0.6076
Bc300	Bc300(0)	10	0	300	0.2492	0.2866	2.183	2.196	0.5475	0.6227
	Bc300(-0.5)	10	0	300	0.2454	0.2692	2.178	2.186	0.5415	0.5902
	Bc300(-1.5)	10	0	300	0.2482	0.2823	2.162	2.179	0.5554	0.6223
	Bd300(1.2)	12	6	300	0.2473	0.2771	2.154	2.167	0.5568	0.6171
	Bd300(0.5)	12	6	300	0.2451	0.2797	2.162	2.178	0.5480	0.6171
Bd100	Bd300(-0.5)	10	0	300	0.2480	0.2832	2.160	2.185	0.5556	0.6213
	Bd300(-1)	10	0	300	0.2477	0.2815	2.160	2.182	0.5552	0.6192
	Bd300(-1.5)	10	0	300	0.2469	0.2764	2.168	2.176	0.5492	0.6108

### 5.3 COMPACTION STRESS PATHS

The stress paths imposed during both isotropic and anisotropic compaction (see Section 4.1.3) were replicated on two different samples inside System 1 (i.e. the double walled triaxial cell) to obtain some insight into the behaviour of the soil during compaction. Both samples were initially isotropically loaded to  $\bar{p} = 100$  kPa by using the setup shown in Figure 4.2. A second loading, either isotropic or anisotropic, was conducted in System 1 under constant water content by holding cell pressure at 900 kPa and decreasing air

pressure at a rate of 4 kPa/hr. The pore water pressure and the sample volume change were recorded during this process.

Figure 5.8 shows the stress paths followed during the second loading in the  $q:\bar{p}$  plane ( $a-b-c$ ) and  $q:p^*$  plane ( $a^*-b^*-c^*$ ) for both the isotropically and anisotropically compacted samples. At the start of the second loading (i.e. after the first isotropic loading) suction was higher for the isotropically compacted sample A than for the anisotropically compacted sample B by  $\approx 40$  kPa although the same procedure was followed during preparation and first loading of both samples (see point  $a$  in Figure 5.9). The slope of the anisotropic loading path is smaller in the  $q:p^*$  plane ( $a^*-b^*$ ) than in the  $q:\bar{p}$  plane ( $a-b$ ) which is attributed to the increase in the value of the product  $S_r s$  during loading. The increase in the term  $S_r s$  is attributed to the compression of large voids during compaction which resulted in a considerable increase of degree of saturation (see points  $a'$  and  $b'$  in Figure 5.9). Conversely, suction decreased slightly during loading, which is expected as the sample was getting denser.

Inspection of Figure 5.8 shows that the unloading stress path  $b^*-c^*$  in the  $q:p^*$  plane deviates from the loading stress path  $a^*-b^*$ , which is due to the irreversible change of degree of saturation during loading (see point  $c'$  in Figure 5.9). If the stress path during anisotropic compaction is interpreted in terms of Bishop stresses, the value of  $\eta^*$  at the end of loading (where  $\eta^* = q/p^*$ ) is only  $\approx 0.5$ , which suggests that the initial isotropic fabric, created during the isotropic first loading stage, would only be altered to a moderately anisotropic state during the subsequent anisotropic loading.

Figure 5.10 shows the compression curves of the isotropically and anisotropically compacted samples in the  $v:\ln\bar{p}$  and in  $v:\ln p^*$  planes. The yield stress is higher for sample A than for sample B which agrees with the fact that sample A had a higher suction than sample B and was isotropically compressed, unlike sample B which was anisotropically compressed. Although both samples were compacted to the same mean net stress (i.e.  $\bar{p} = 250$  kPa), the specific volume after unloading (point  $c$ ) was significantly less for sample B than for sample A. This behaviour could be attributed to the reorientation of aggregates or particles during anisotropic loading which resulted in a denser packing. This reorientation is not expected to occur during isotropic loading of a sample with an initial isotropic fabric.

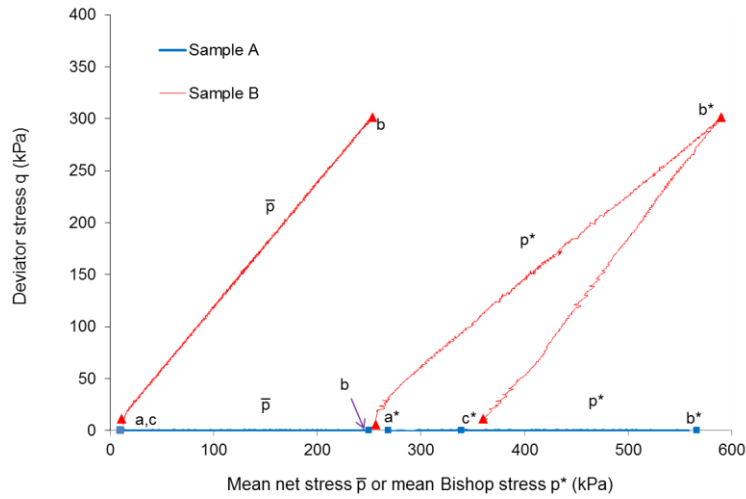


Figure 5.8 Stress paths followed during isotropic (sample A) and anisotropic (sample B) compaction

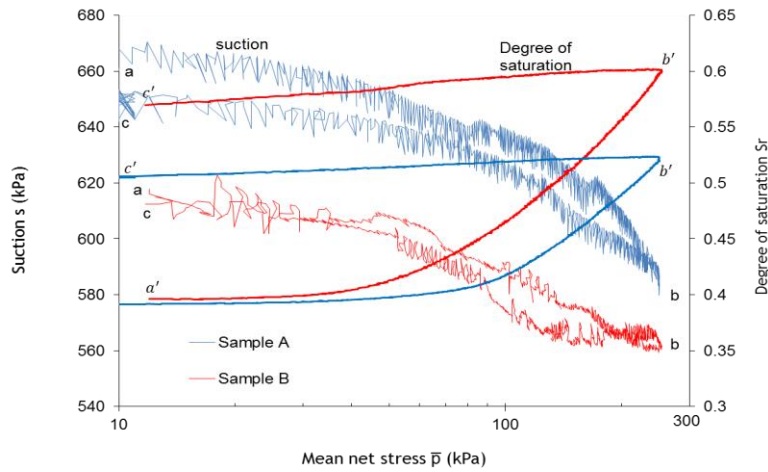


Figure 5.9 Variation of suction and degree of saturation with mean net stress during isotropic (sample A) and anisotropic (sample B) compaction

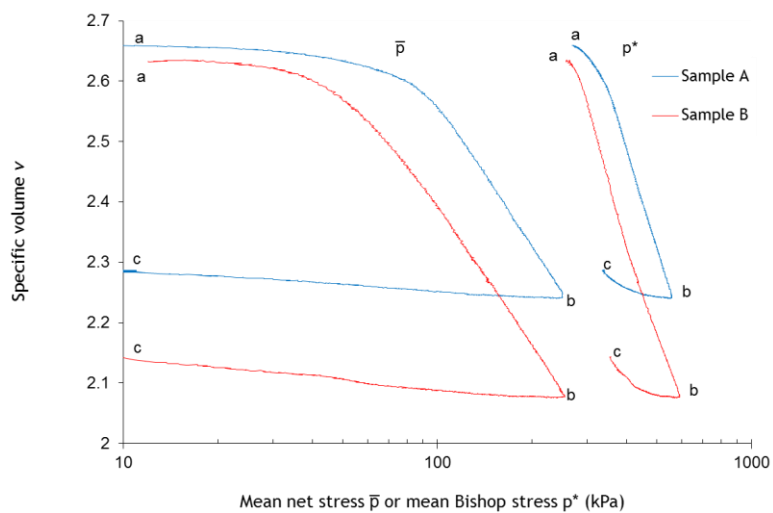


Figure 5.10 Compression behaviour in terms of both net stress and Bishop stress during isotropic (sample A) and anisotropic (sample B) compaction

## 5.4 INITIAL WETTING STAGES

As shown in Table 5.1, unsaturated samples which were to be subsequently loaded only in triaxial compression were wetted under  $\bar{p} = 12$  kPa and  $q = 6$  kPa whereas unsaturated samples which were to be subsequently loaded in triaxial extension were wetted under  $\bar{p} = 10$  kPa and  $q = 0$  (see Section 5.1). Figure 5.9 indicates that, after compaction, suction was generally greater than 600 kPa which suggests that all samples were wetted during equalisation to  $s = 300$ ,  $s = 100$  kPa or to saturation.

### 5.4.1 Wetting to $s = 300$ kPa (Test Series A300, B300, Ba300, Bb300, Bc300 & Bd100)

Figures 5.11 to 5.15 show the increase in water content, specific volume and degree of saturation against time during the initial wetting stages for all Test Series conducted at  $s = 300$  kPa (i.e. A300, B300, Ba300, Bb300 and Bc300). The results of the initial wetting stage in Test Series Bd100 (at  $s = 300$  kPa) are shown in Figure 5.16. During the initial wetting stage all samples showed an increase in water content confirming that the suction value after compaction was higher than 300 kPa. All figures indicate that  $v$  increased during wetting, with no sign of collapse compression. The large oscillations in specific volume (for example, see Figures 5.11b) are mainly attributable to the effect of temperature variation on instrumentation, which cannot be completely eliminated by calibration. Oscillations are less obvious in the plots of degree of saturation, confirming that changes of degree of saturation are dominated by the increase in water content rather than by the variation of specific volume. Further inspection of Figures 5.11 to 5.16 indicates that both specific volume and specific water volume ( $v_w = 1 + w G_s$ ) stabilised, in the majority of tests, after 3 days (when the rate of change of both these quantities fell below 0.001 per day). These observations were helpful in deciding the duration of the initial wetting stage.

Inspection of Figure 5.11a shows that the average increase in water content for the isotropically compacted samples was 0.034. Despite the anisotropically compacted samples have an initial specific volume significantly lower than the isotropically compacted samples (see Table 5.1), the average increase in water content of these samples (see Figures 5.12a, 5.13a, 5.14a, 5.15a and 5.16a) was 0.033 which is very similar to the isotropically compacted samples. This might indicate that material fabric and particle orientation do not have a significant influence on water retention behaviour when analysed in terms of water content rather than degree of saturation (further support to this hypothesis will be given later in this chapter).

The isotropically compacted samples showed an average increase in specific volume of about 0.023 (see Figure 5.11b) which is higher than that of anisotropically compacted samples, which had an average increase in specific volume of 0.018 (see Figures 5.12b, 5.13b, 5.14b, 5.15b and 5.16b). The difference could be explained by considering that anisotropic samples show a more interlocked fabric than isotropic samples due to the occurrence of aggregate/particle reorientation during anisotropic compaction.

The average increase in degree of saturation for isotropically compacted samples was 0.057 (see Figure 5.11c), slightly less than the average increase for anisotropically compacted samples which was 0.064 (see Figures 5.12c, 5.13c, 5.14c and 5.16c). This is consistent with the smaller increase in pore volume of the anisotropically compacted samples compared to the isotropically compacted samples (recall that both the isotropically and anisotropically compacted samples experienced approximately the same increase in water content).

No effect of the initial stress condition (i.e.  $\bar{p} = 12$  kPa and  $q = 6$  kPa for the tests only loaded subsequently in triaxial compression or  $\bar{p} = 10$  kPa and  $q = 0$  kPa for tests subsequently loaded in triaxial extension) on soil behaviour during equalization could be clearly observed, indicating that these effects were sufficiently small to be hidden by the data scatter. The rate of increase of water content was unusually slow for some samples (see, for example, Bb300(0.5) in Figure 5.14). This might have been due to initial poor contact between the sample and the high air entry filter. Although the initial sample height was different for tests loaded only in triaxial compression (100 mm) or loaded in triaxial extension (75 mm), no apparent effects of sample height on changes of water content, specific volume and degree of saturation during equalization were observed.

The average values of water content, specific volume and degree of saturation at the end of wetting were  $0.2812 \pm 0.0060$ ,  $2.345 \pm 0.008$  and  $0.5435 \pm 0.0100$ , respectively, for the isotropically compacted samples while they were  $0.2802 \pm 0.0080$ ,  $2.185 \pm 0.010$  and  $0.6146 \pm 0.0100$ , respectively, for the anisotropically compacted samples (see Table 5.1). The difference between the initial specific volume of isotropic and anisotropic samples reduced slightly after wetting. However, the difference between the degree of saturation, or water content, of isotropic and anisotropic samples was slightly bigger after wetting than immediately after compaction.

Data scatter is relatively small and its influence on subsequent loading stages is limited, as it will be shown in the next sections.

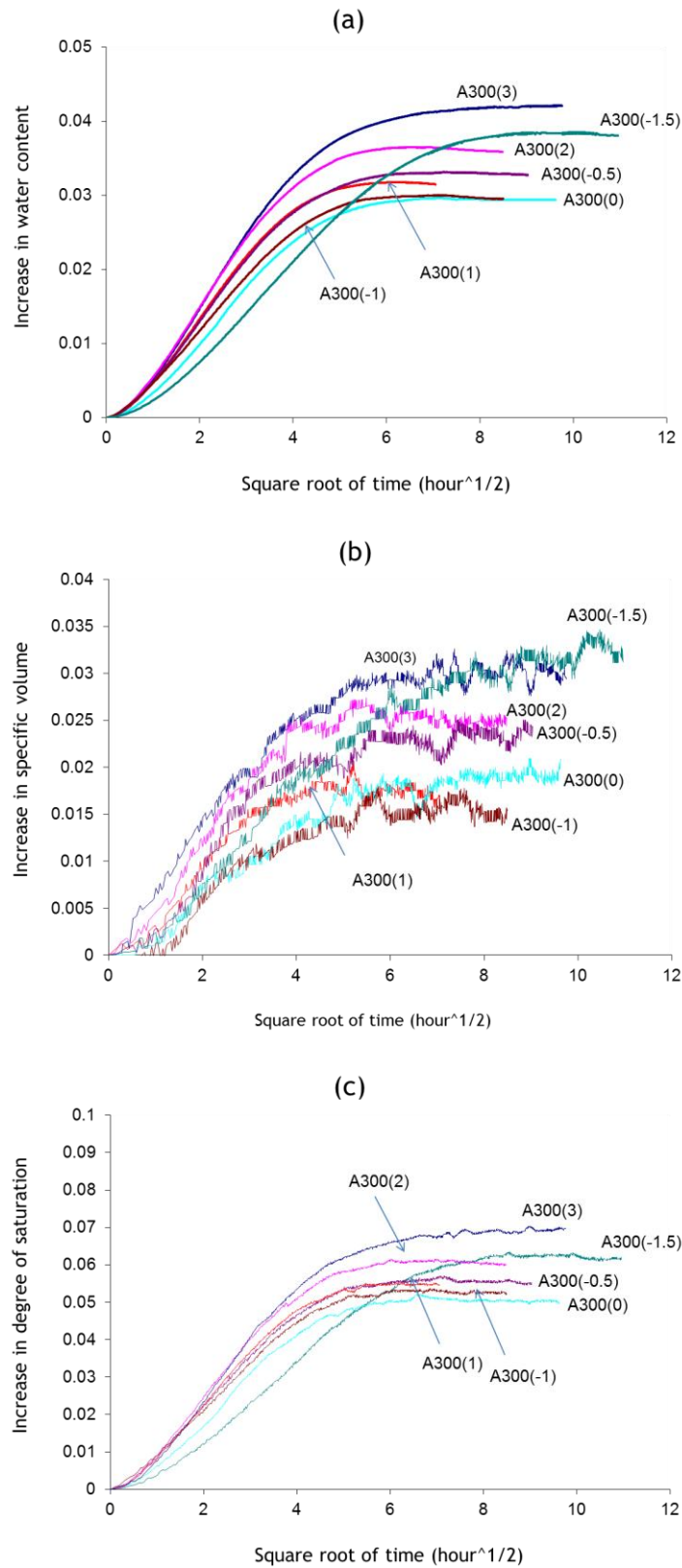


Figure 5.11 Wetting stage of Test Series A300: (a) increase in water content, (b) increase in specific volume, (c) increase in degree of saturation

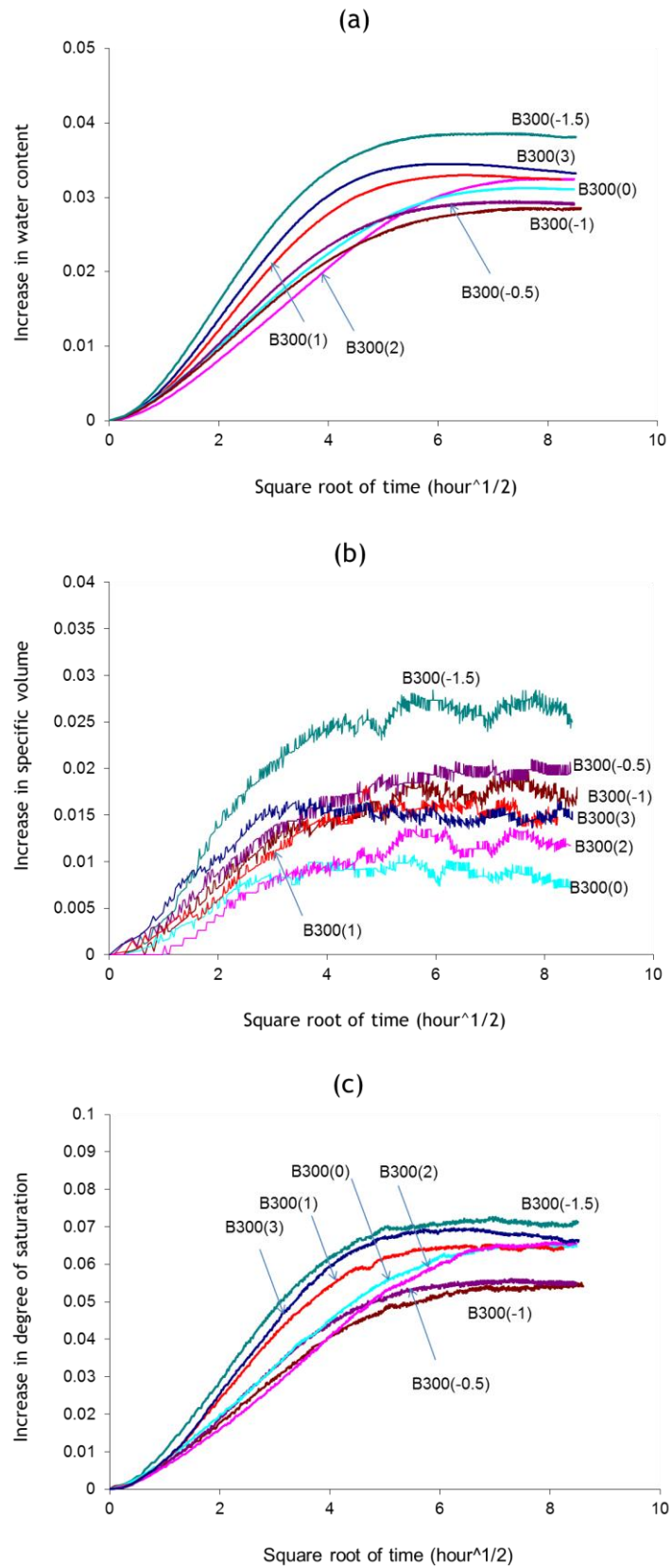


Figure 5.12 Wetting stage of Test Series B300: (a) increase in water content, (b) increase in specific volume, (c) increase in degree of saturation

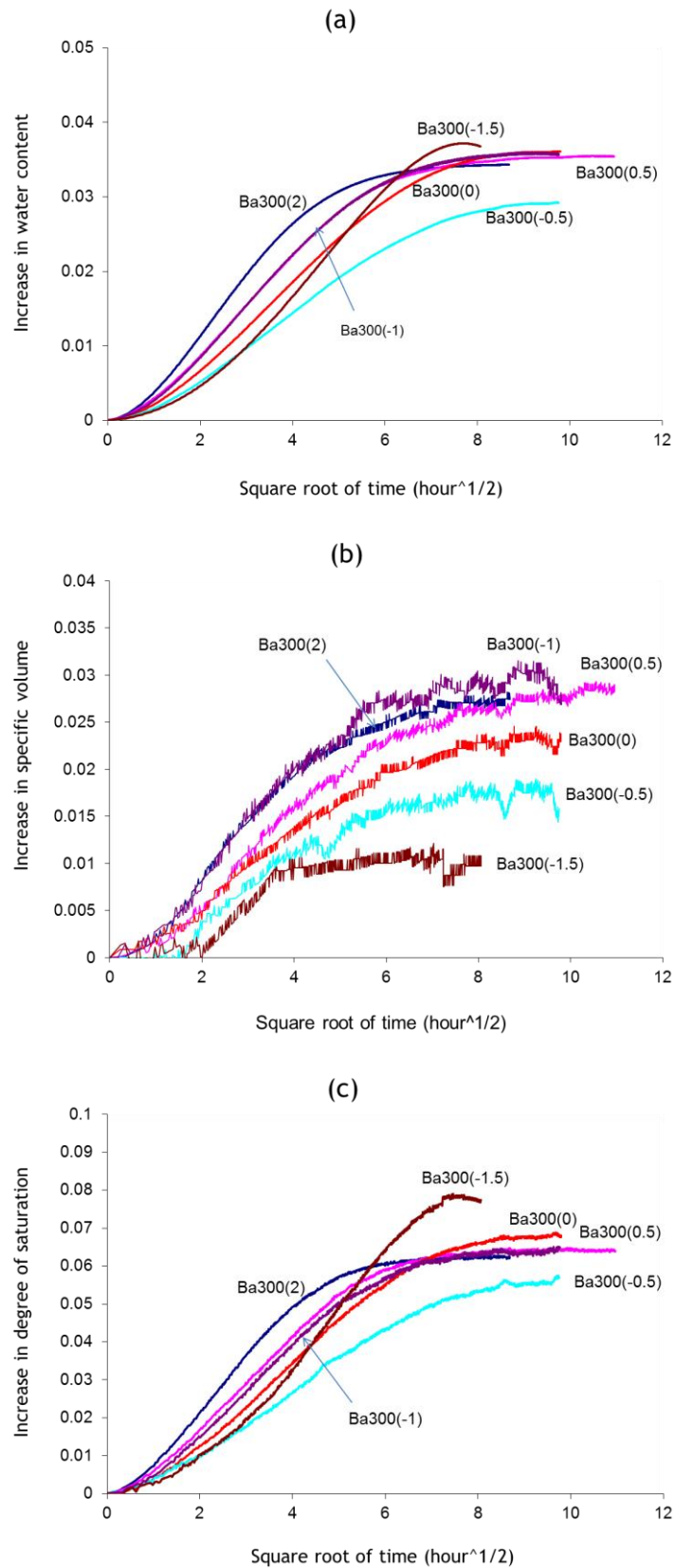


Figure 5.13 Wetting stage of Test Series Ba300: (a) increase in water content, (b) increase in specific volume, (c) increase in degree of saturation

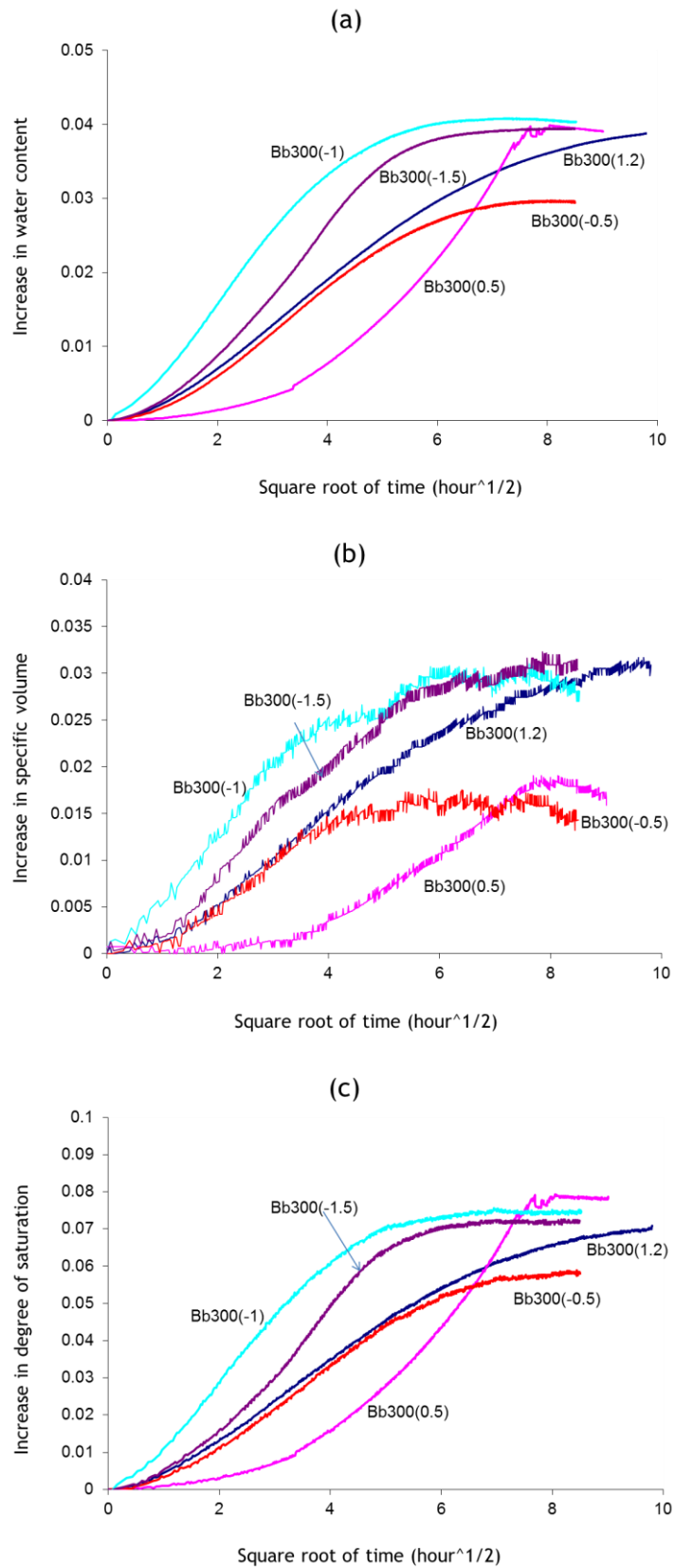


Figure 5.14 Wetting stage of Test Series Bb300: (a) increase in water content, (b) increase in specific volume, (c) increase in degree of saturation

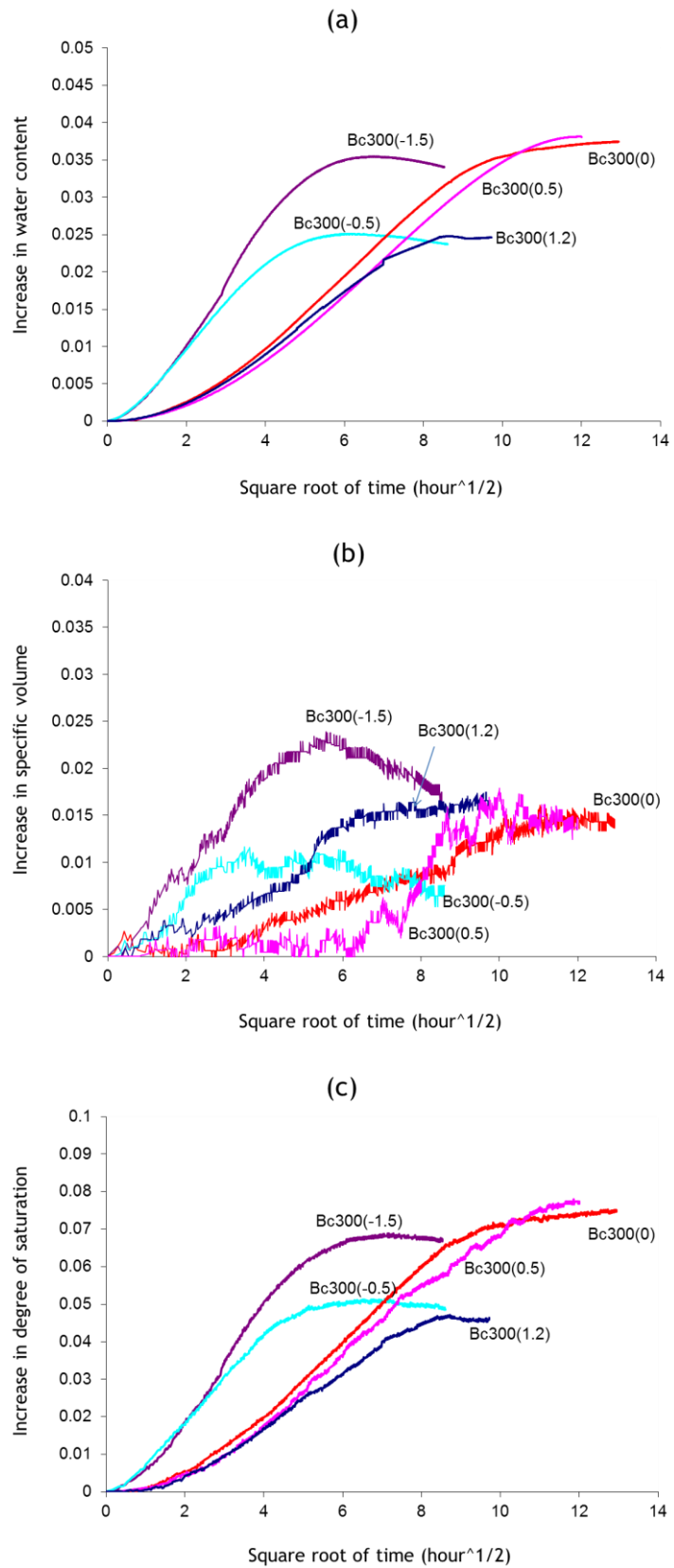


Figure 5.15 Wetting stage of Test Series Bc300: (a) increase in water content, (b) increase in specific volume, (c) increase in degree of saturation

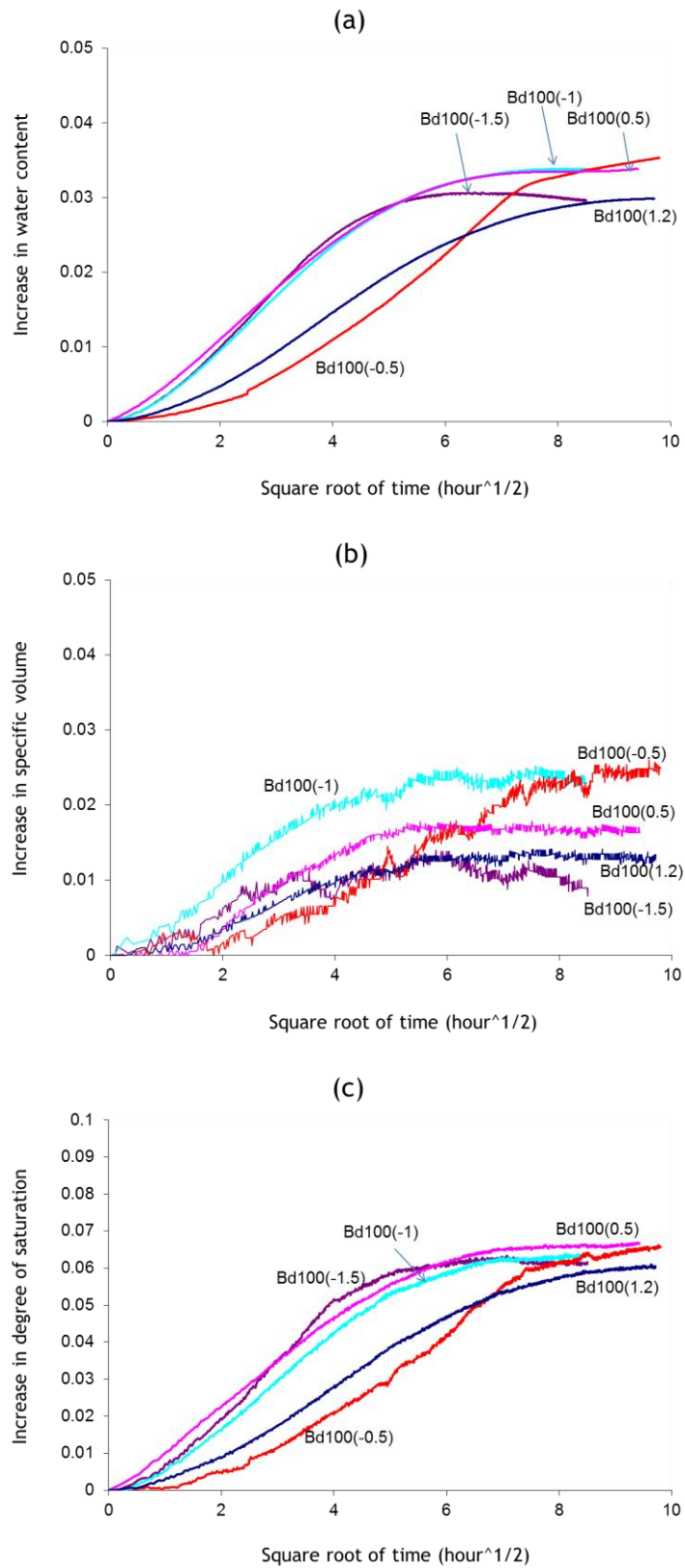


Figure 5.16 Wetting stage of Test Series Bd300: (a) increase in water content, (b) increase in specific volume, (c) increase in degree of saturation

### 5.4.2 Wetting to $s = 100$ kPa (Test Series A100, B100 & Be100)

Figures 5.17, 5.18 and 5.19 show the increase in water content, specific volume and degree of saturation against time during the initial wetting stage for all test series conducted at  $s = 100$  kPa. All samples showed a significant increase in water content (about three times the increase in water content observed during the initial wetting stage of tests conducted at  $s = 300$  kPa). Specific volume increased during wetting, with no sign of collapse compression.

Similar to the samples wetted to  $s = 300$  kPa, the specific volume and specific water volume stabilised, in the majority of tests, after 3 days (after this time, the daily change of both these quantities became less than 0.001).

Inspection of Figures 5.17a, 5.18a and 5.19a suggests that the average increase in water content was about 0.1164, 0.1130 and 0.1193 for Test Series A100, B100 and Be100 respectively. The similar increase in water content for samples with different degrees of anisotropy (also noticed during wetting to  $s = 300$  kPa) supports the hypothesis that water retention behaviour, if described in terms of water content rather than degree of saturation, is independent of material fabric (at least for suctions of 100 kPa and greater).

The average increase in specific volume was 0.0417, 0.0420 and 0.0430 for Test Series A100, B100 and Be100 respectively (see Figures 5.17b, 5.18b and Figure 5.19b) suggesting that the anisotropic samples swelled slightly more than the isotropic samples. This is, to some extent, contradicting what was observed during wetting to  $s = 300$  kPa. However, given that data scatter is relatively high compared to the average increase in  $v$ , it is not possible to conclude with any confidence that anisotropy affects swelling behaviour.

The average increase in degree of saturation was 0.2078, 0.2228 and 0.2119 for Test Series A100, B100 and Be100 respectively (see Figures 5.17c, 5.18c and 5.19c). The average increase in degree of saturation of isotropically compacted samples was less than that of anisotropically compacted samples which is in agreement with the observation for the Test Series at  $s = 300$  kPa. Finally, consistent with expected soil behaviour, the increase of degree of saturation during wetting to  $s = 100$  kPa is significantly bigger than the increase in degree of saturation during wetting to  $s = 300$  kPa. The average values of water content, specific volume and degree of saturation after wetting to  $s = 100$  kPa were  $0.3639 \pm 0.0060$ ,  $2.360 \pm 0.016$  and  $0.6951 \pm 0.0140$  respectively for Test Series A100 whereas they were  $0.3612 \pm 0.0060$ ,  $2.214 \pm 0.007$  and  $0.7729 \pm 0.0150$  respectively

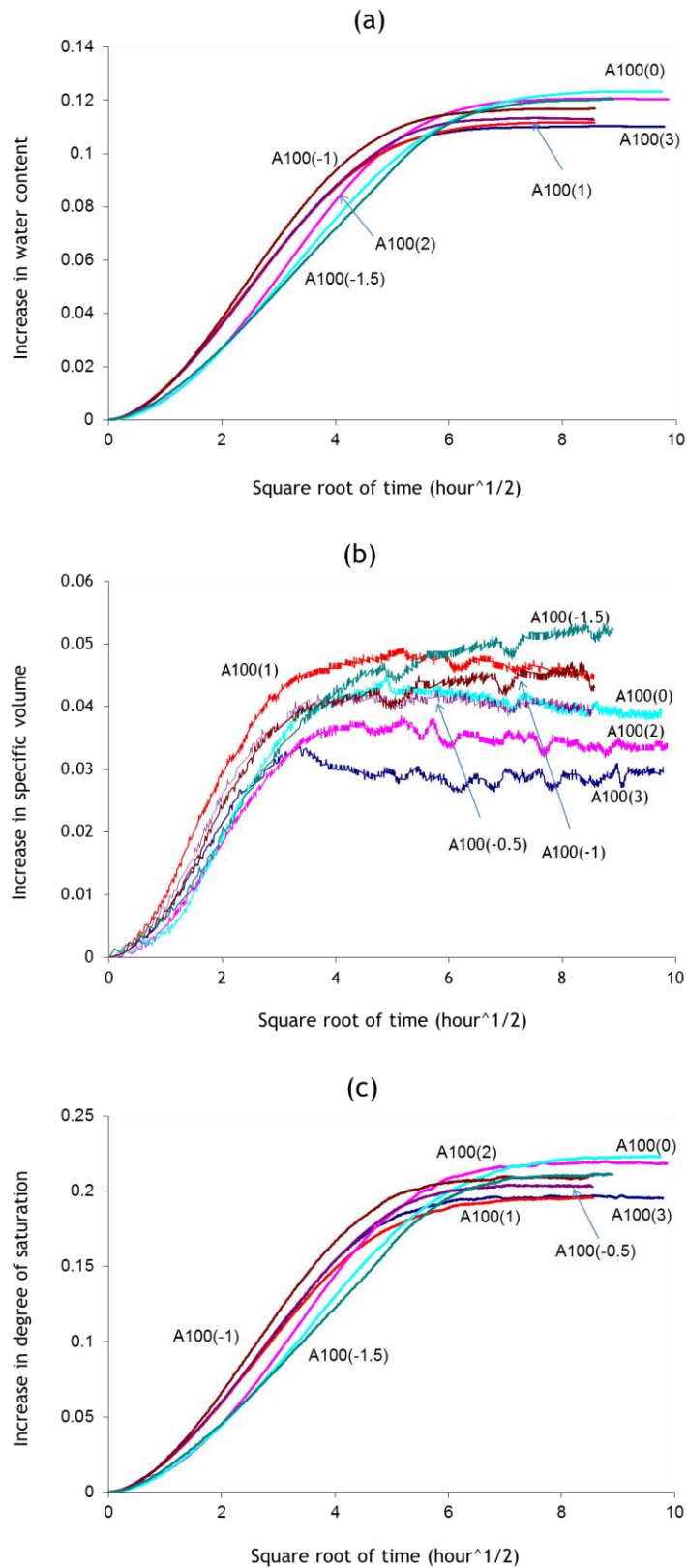


Figure 5.17 Wetting stage of Test Series A100: (a) increase in water content, (b) increase in specific volume, (c) increase in degree of saturation

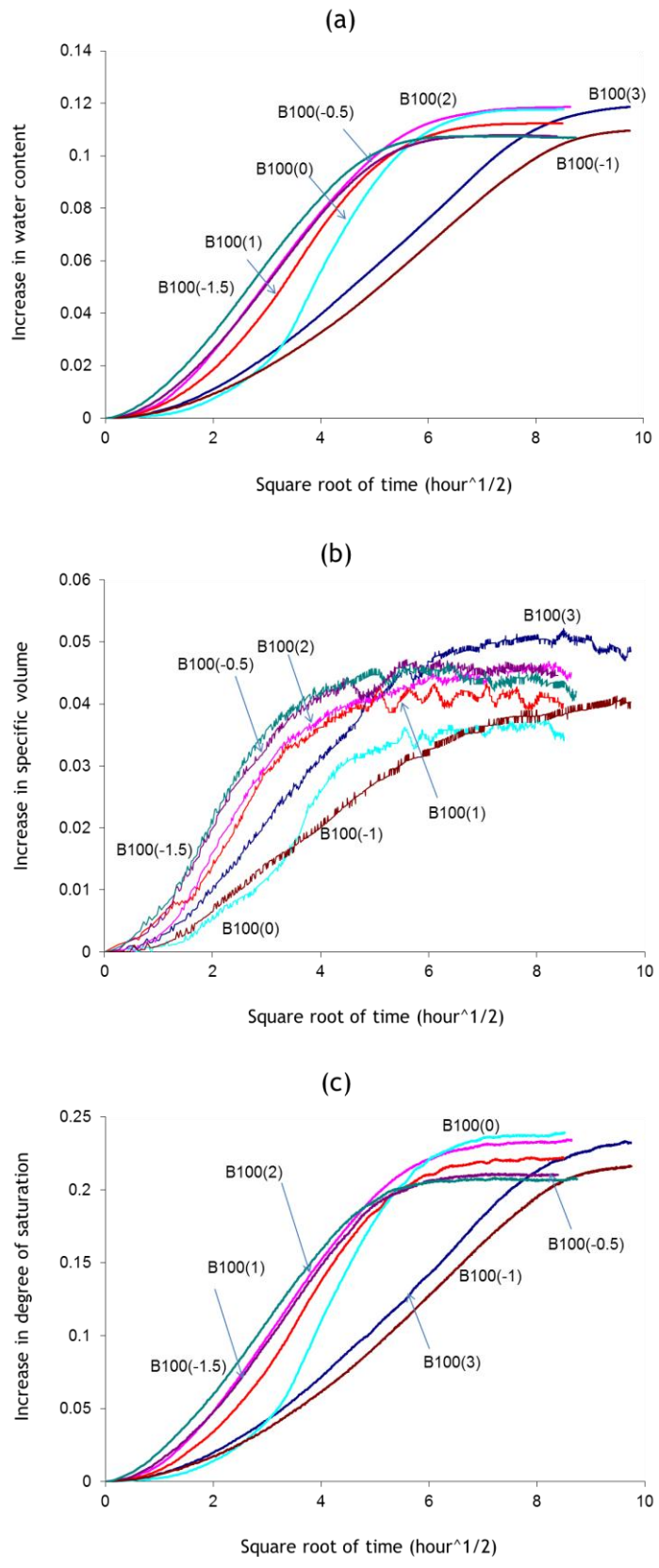


Figure 5.18 Wetting stage of Test Series B100: (a) increase in water content, (b) increase in specific volume, (c) increase in degree of saturation

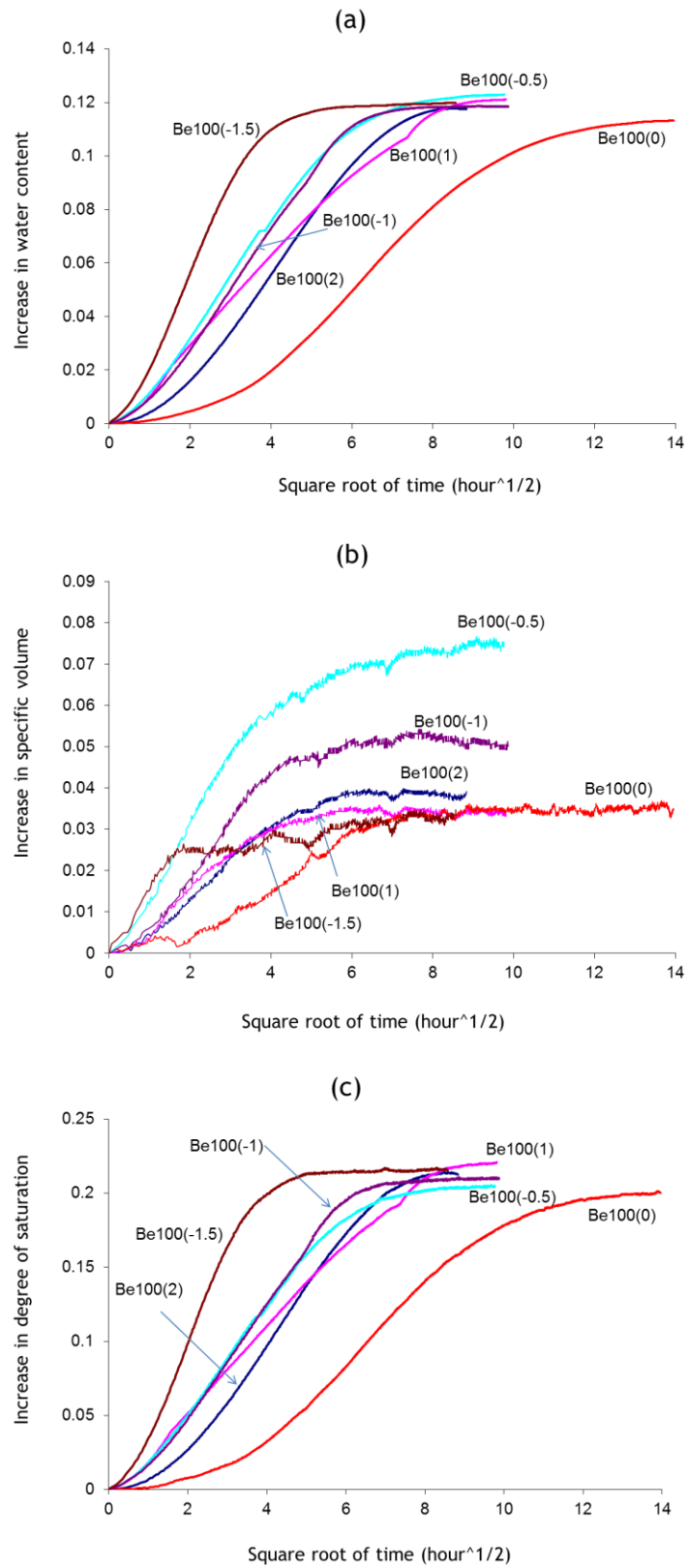


Figure 5.19 Wetting stage of Test Series Be100: (a) increase in water content, (b) increase in specific volume, (c) increase in degree of saturation

for Test Series B100 and  $0.3658 \pm 0.0050$ ,  $2.362 \pm 0.019$  and  $0.6976 \pm 0.0100$  respectively for Test Series Be100.

As intended, the values of water content, specific volume and degree of saturation of Test Series Be100 were noticeably closer to those of Test Series A100 than to those of Test Series B100.

As mentioned earlier, the specific volume varied by  $\approx \pm 0.010$  and  $\approx \pm 0.019$  after wetting to  $s = 300$  kPa and  $s = 100$  kPa respectively. Similarly, the degree of saturation varied by  $\approx \pm 0.0100$  and  $\approx \pm 0.0150$  after wetting to  $s = 300$  kPa and  $s = 100$  kPa respectively. This variation has of course no effect on compression curves when these are presented in terms of mean net stress,  $\bar{p}$ , however it has an effect when compression curves are presented in terms of mean Bishop's stress,  $p^*$  ( $p^* = \bar{p} + S_r s$ ). The resulting variation of Bishop's stress is about  $\pm 2$  kPa and  $\pm 1$  kPa for  $s = 300$  kPa and  $s = 100$  kPa respectively, which might produce a small horizontal shift of the compression curves in the  $v:\ln p^*$  plane. Because of this, yield stresses measured in terms of mean net stress are slightly more accurate than those measured in terms of Bishop's stress. Note however that, after wetting to  $s = 300$  kPa, the values of mean Bishop's stress are  $p^* \approx 175$  kPa and  $p^* \approx 200$  kPa for the isotropically and anisotropically compacted samples respectively while, after wetting to  $s = 100$  kPa, the values of mean Bishop's stress are  $p^* \approx 80$  kPa and  $p^* \approx 90$  kPa, for isotropically and anisotropically compacted samples respectively. The above variation would therefore account for about  $\approx 1.5\%$  of the relevant stress levels, which is relatively small.

### 5.4.3 Wetting to saturation (Test Series A0 & B0)

System 3 (used for testing saturated soil samples) did not allow measurement of sample volume changes during the saturation process. Because of this, two isotropically compacted samples, namely A0(sat1) and A0(sat2), were saturated and tested under saturated conditions in System 1 and System 2 respectively. Samples A0(sat1) and A0(sat2) were saturated in two stages (see Section 4.2.3), using the same procedure as for the tests performed in System 3 (see Section 4.3). In the first stage water was flushed through the sample to force air out from large voids, while in the second stage the remaining air bubbles were forced into solution through back-pressurization.

During saturation of samples A0(sat1) and A0(sat2), the sample volume changes were recorded by measuring the volume of water flowing in or out of the inner cell. The pore water volume change was not measured because, during the initial flushing, water had drained from the sample into the air drainage line.

Generally, sample volume continuously increased, with no sign of wetting-induced collapse-compression during saturation. Figure 5.20 shows the increase in specific volume against the square root of time for samples A0(sat1) and A0(sat2). In Figure 5.20, point *a* corresponds to the start of the second stage of the saturation process, after which a substantial increase in specific volume, accompanied by a large water inflow, was recorded for sample A0(sat2) whereas only a modest increase of specific volume, with a small water inflow, took place in sample A0(sat1). The increase in specific volume during the second stage is due to two reasons; firstly, an elastic unloading of 5 kPa (see Section 4.2.3) and, secondly, the disappearance of water menisci at inter-particle contacts in those voids that were not fully saturated at the end of the initial flushing.

Based on the above tests, the values of specific volume after-saturation (see the column  $v_{after}$  in Table 5.1) of Test Series A0 and B0 were assumed to be the initial specific volume (see the column  $v_{initial}$  in Table 5.1) plus a constant increase of 0.1 which is the appropriate increase in specific volume taken from Figure 5.20.

Finally, the amount of sample swelling during wetting increased with decreasing applied suction (i.e.  $s = 300$  kPa, 100 kPa or 0 kPa) with no evidence of any wetting-induced collapse-compression. This fits the expected behaviour of compacted Kaolin during wetting at low mean net stress. The fact that samples swelled more during wetting to lower suction values could be explained by the greater reduction of suction during wetting paths that remained inside the *LC* yield curve, as first proposed by Alonso et al. (1990).

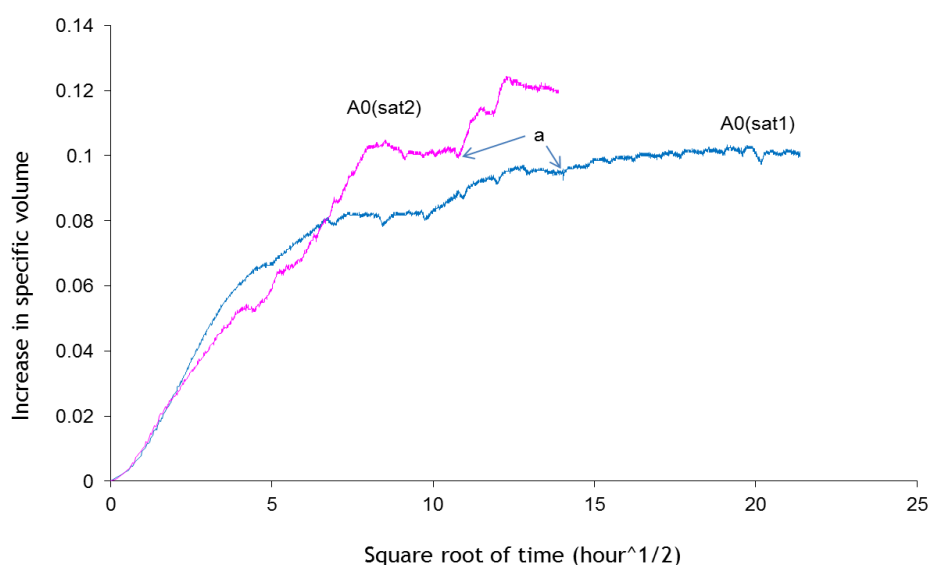


Figure 5.20 Increase in specific volume of samples A0(sat1) and A0(sat2) during saturation

## 5.5 PROBING/SHEARING STAGES ON AS-COMPACTED SAMPLES

To investigate the influence of fabric anisotropy on unsaturated soil behaviour, several isotropically and anisotropically compacted samples were loaded along stress paths with different slopes in the  $q:\bar{p}$  under constant suction.

### 5.5.1 Probing/shearing at $s = 300$ kPa (Test Series A300 and B300)

Figures 5.21 to 5.27 show the results from tests performed at  $s = 300$  kPa on isotropically compacted samples (i.e. Test Series A300) and anisotropically compacted samples (i.e. Test Series B300).

Comparison of results in the  $q:\varepsilon_s$  plane suggests that, initially, both isotropically and anisotropically compacted samples show similar stiffness. However, as loading progresses at  $[\Delta q/\Delta \bar{p}] = 3, 2, 1, -1$  and  $-1.5$  (see Figures 5.21a, 5.22a, 5.23a, 5.26a and Figure 5.27a respectively), the response is less stiff for the isotropically compacted samples than for the anisotropically compacted samples. This might be partly attributed to the lower initial void ratio of the anisotropic samples compared to isotropic samples and partly to the effect of particle orientation on the mobilized shear strength at a given strain level.

Inspection of Figure 5.24a indicates that isotropic probing at  $[\Delta q/\Delta \bar{p}] = 0$  produced a small positive shear strain in the isotropically compacted sample due to the existence of a small initial positive deviator stress and the non-inclined yield locus. Conversely, isotropic probing at  $[\Delta q/\Delta \bar{p}] = 0$  caused a small negative shear strain in the anisotropically compacted sample due to the inclined yield locus. The response of the anisotropically compacted sample B300(0) during subsequent shearing to failure was very similar to the response of the isotropically compacted sample A300(0) (see Figure 5.24a), suggesting that the previous isotropic probing erased any initial anisotropy in the sample. The behaviour of samples A300(-0.5) and B300(-0.5) was also very similar during both probing and shearing to failure (see Figure 5.25a).

Figures 5.21a to 5.27a show that all samples attained a peak value of strength followed by a sharp reduction of deviator stress  $q$ . This is attributed to the occurrence of strain localization, as confirmed by the visual observation of shear bands at the end of the tests. For tests at  $[\Delta q/\Delta \bar{p}] = 0, -0.5$  and  $-1$ , both anisotropically and isotropically compacted samples attained very similar values of peak deviator stresses (see Figures 5.24a, 5.25a and Figure 5.26a respectively) whereas, for tests at  $[\Delta q/\Delta \bar{p}] = 3, 2$  and  $-1.5$ , the value of peak deviator stress was noticeably larger ( $\approx 15 - 50\%$ ) for the anisotropically compacted samples than for the isotropically compacted samples (see Figures 5.21a, 5.22a and Figure 5.27a respectively).

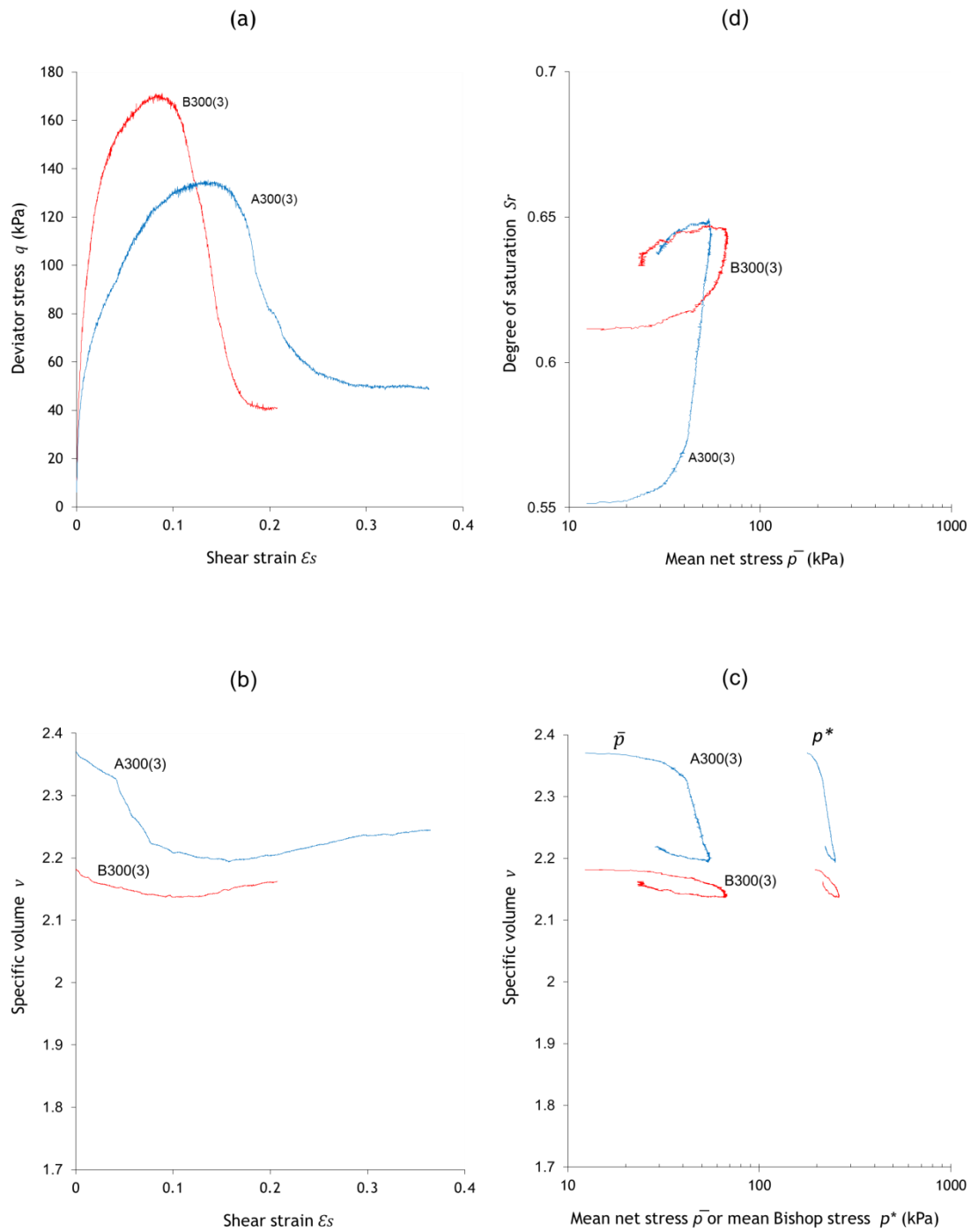


Figure 5.21 Results of Tests A300(3) and B300(3) in: (a)  $q: \epsilon_s$  plane, (b)  $v: \epsilon_s$  plane, (c)  $v: \ln \bar{p}$  or  $v: \ln p^*$  plane (d)  $S_r: \ln \bar{p}$  plane

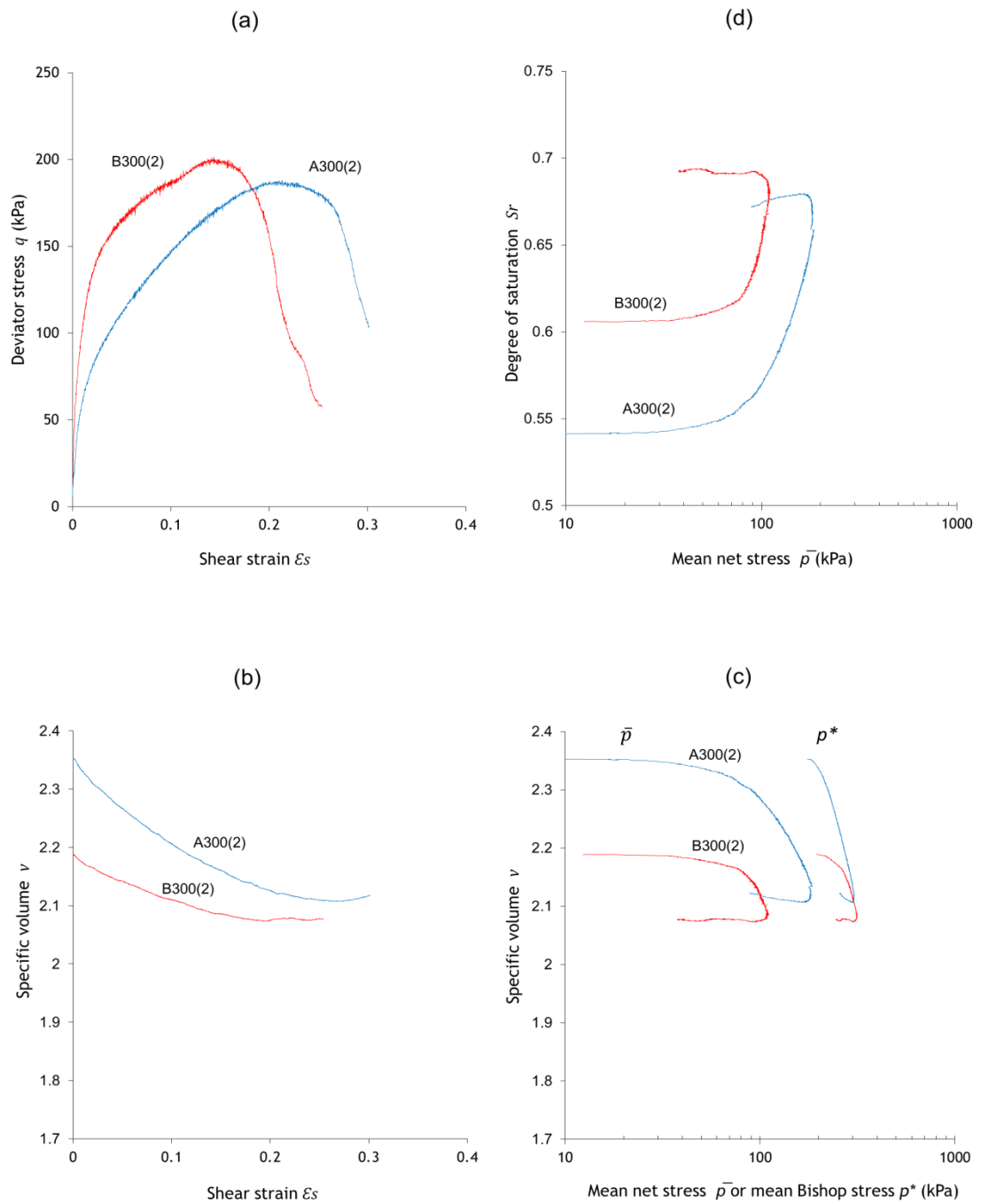


Figure 5.22 Results of Tests A300(2) and B300(2) in: (a)  $q: \epsilon_s$  plane, (b)  $v: \epsilon_s$  plane, (c)  $v: \ln \bar{p}$  or  $v: \ln p^*$  plane (d)  $S_r: \ln \bar{p}$  plane

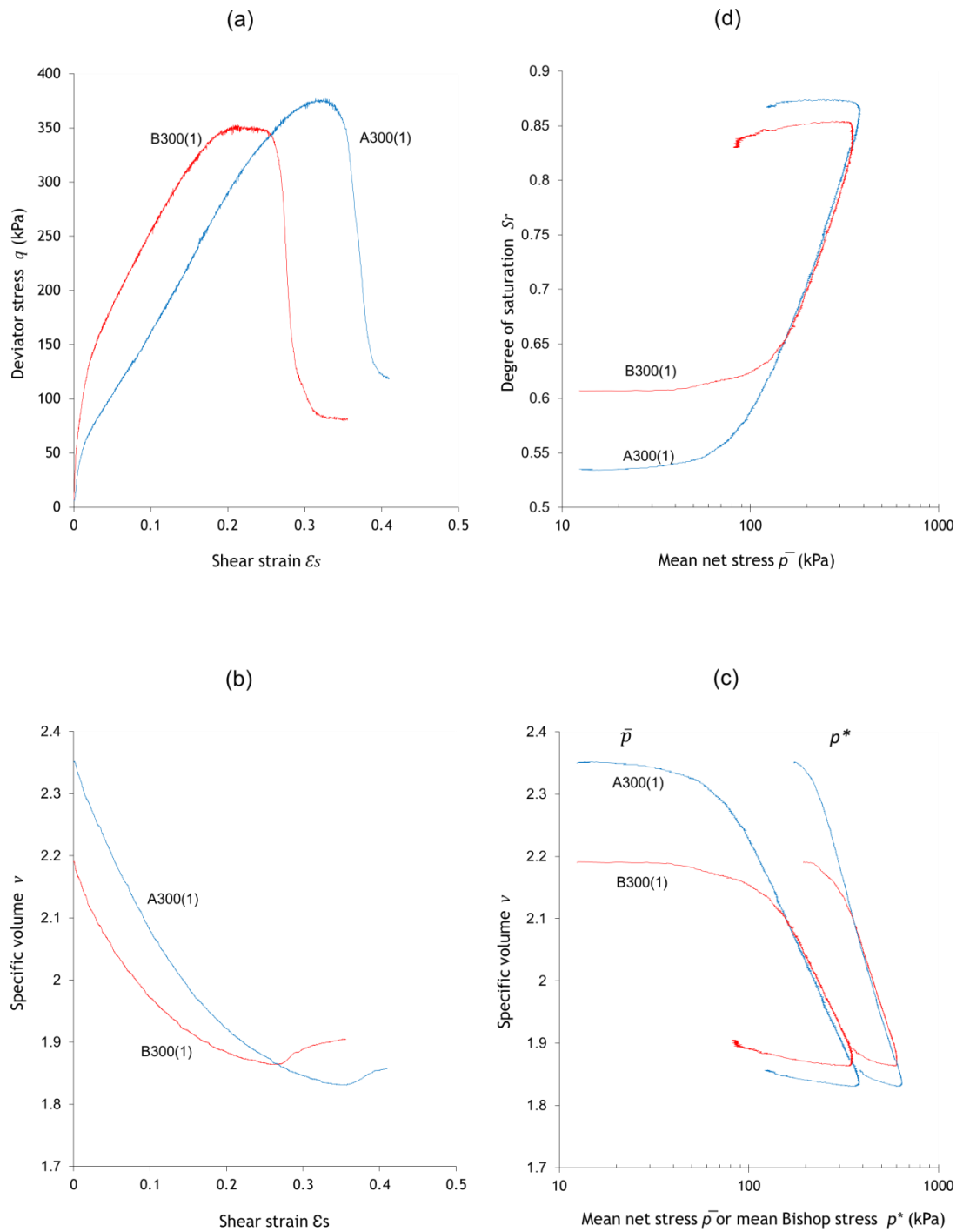


Figure 5.23 Results of Tests A300(1) and B300(1) in: (a)  $q: \epsilon_s$  plane, (b)  $v: \epsilon_s$  plane, (c)  $v: \ln \bar{p}$  or  $v: \ln p^*$  plane (d)  $S_r: \ln \bar{p}$  plane

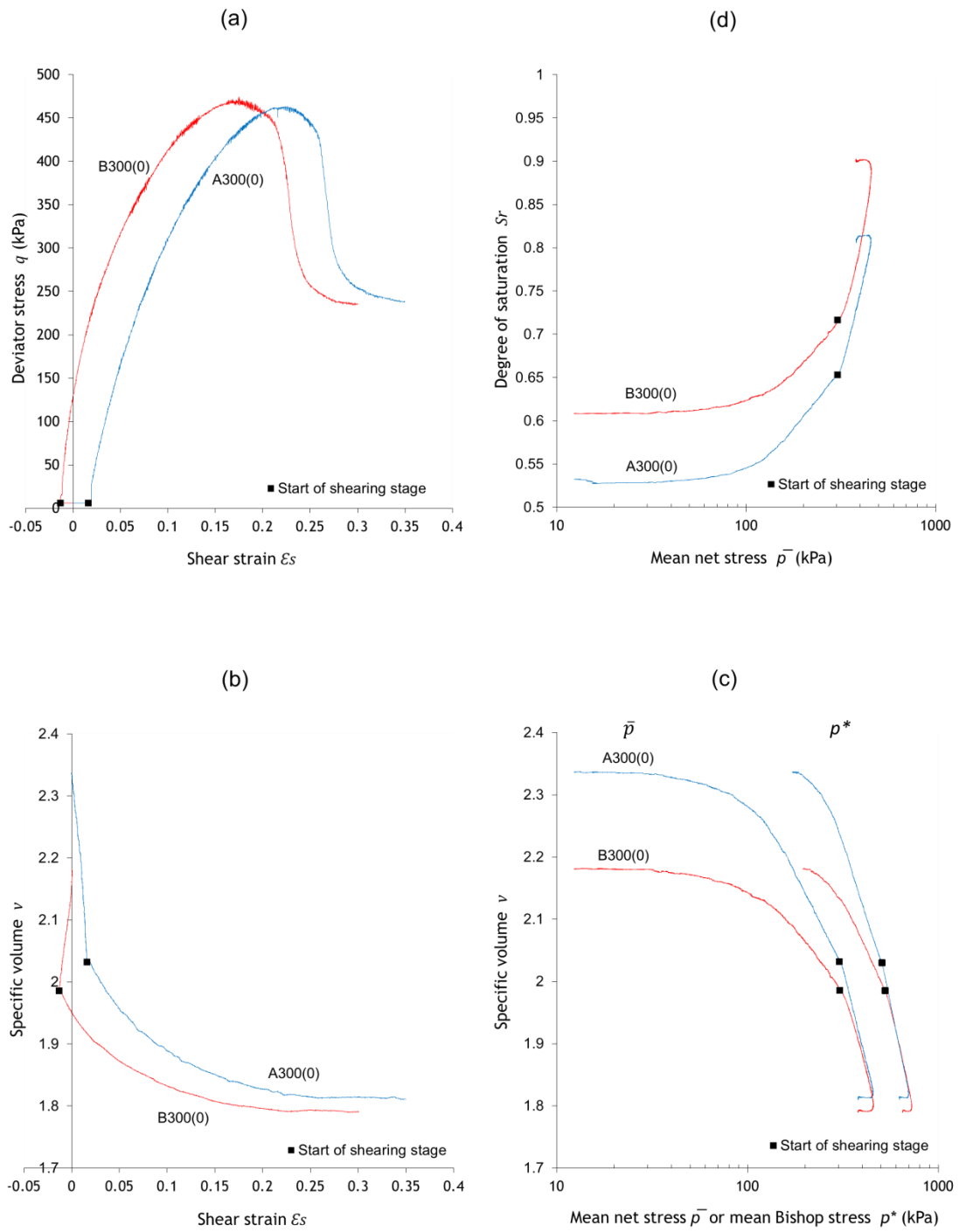


Figure 5.24 Results of Tests A300(0) and B300(0) in: (a)  $q: \epsilon_s$  plane, (b)  $v: \epsilon_s$  plane, (c)  $v: \ln \bar{p}$  or  $v: \ln p^*$  plane (d)  $S_r: \ln \bar{p}$  plane

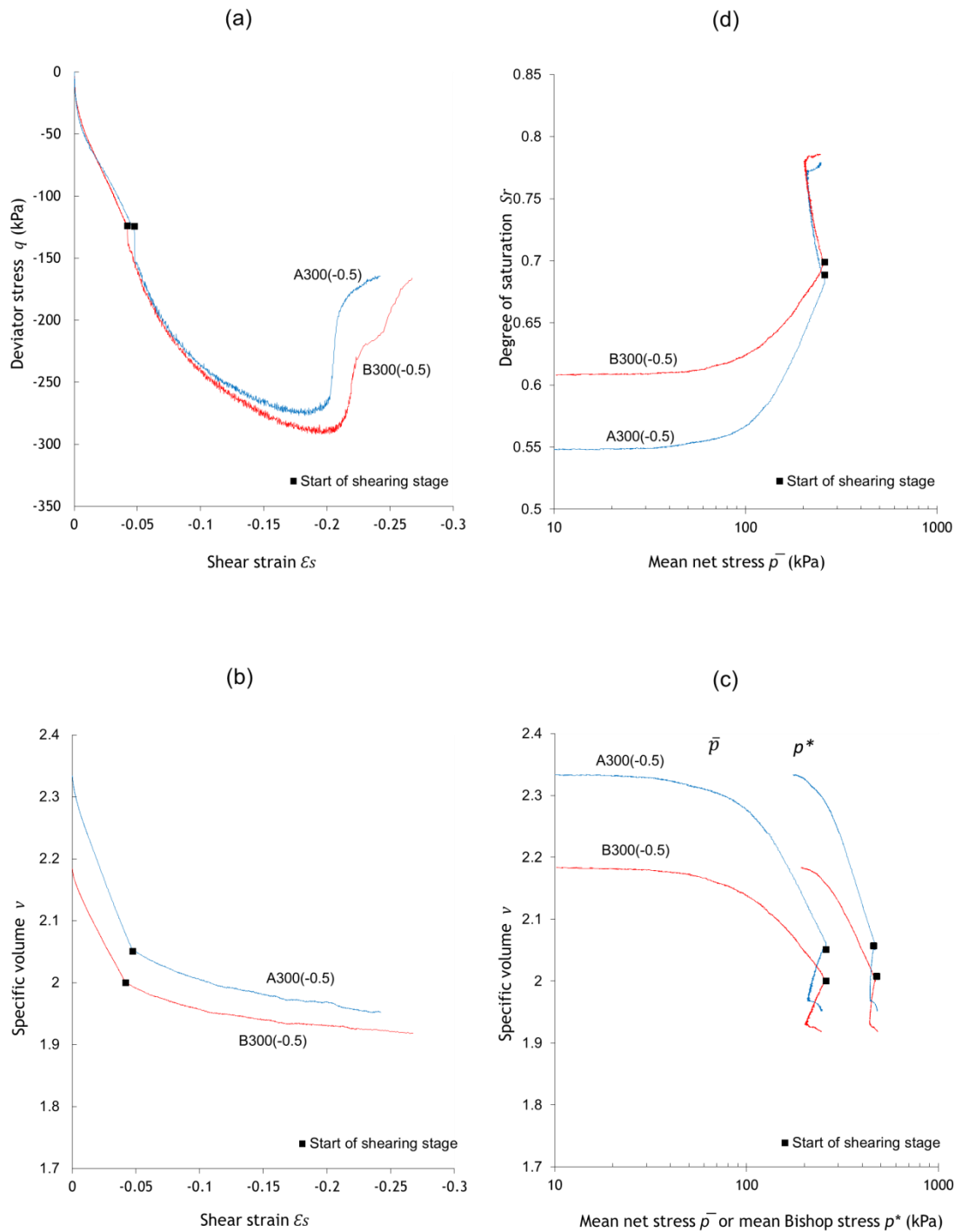


Figure 5.25 Results of Tests A300(-0.5) and B300(-0.5) in: (a)  $q: \epsilon_s$  plane, (b)  $v: \epsilon_s$  plane, (c)  $v: \ln \bar{p}$  or  $v: \ln p^*$  plane (d)  $S_r: \ln \bar{p}$  plane

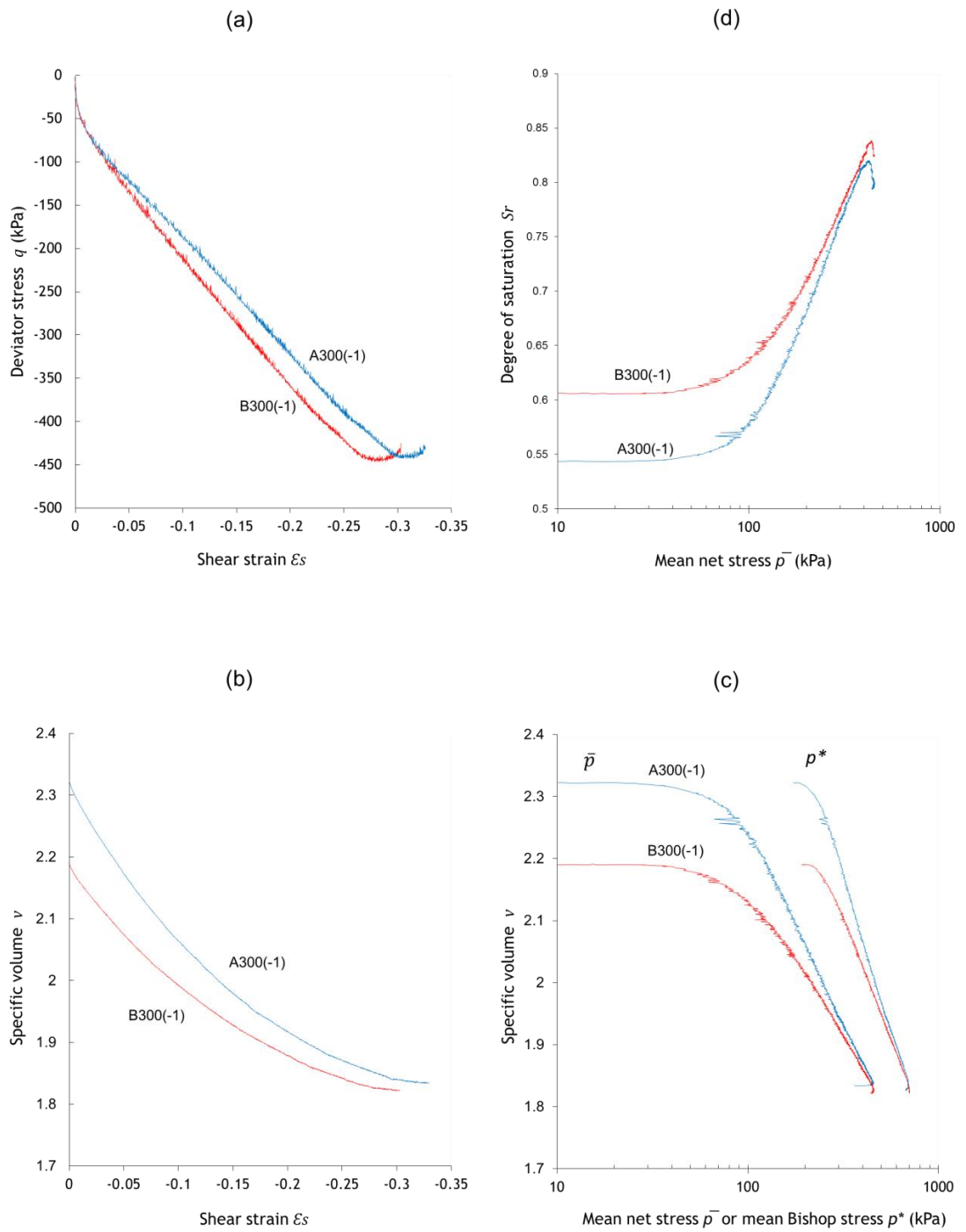


Figure 5.26 Results of Tests A300(-1) and B300(-1) in: (a)  $q: \epsilon_s$  plane, (b)  $v: \epsilon_s$  plane, (c)  $v: \ln \bar{p}$  or  $v: \ln p^*$  plane (d)  $S_r: \ln \bar{p}$  plane

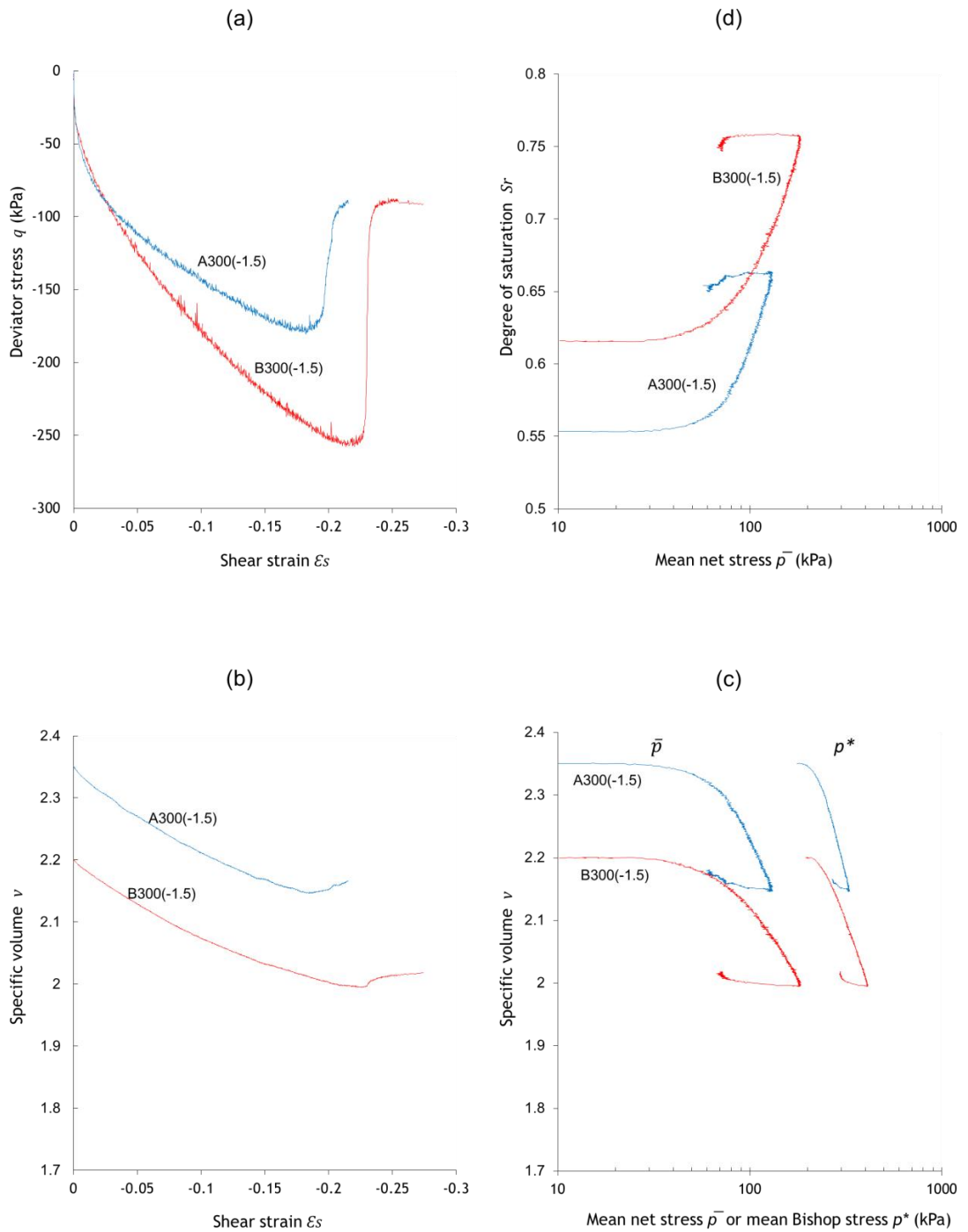


Figure 5.27 Results of Tests A300(-1.5) and B300(-1.5) in: (a)  $q: \epsilon_s$  plane, (b)  $v: \epsilon_s$  plane, (c)  $v: \ln \bar{p}$  or  $v: \ln p^*$  plane (d)  $S_r: \ln \bar{p}$  plane

Conversely, for the test at  $\Delta q/\Delta\bar{p} = 1$ , the peak deviator stress of the anisotropically compacted sample was  $\approx 15\%$  smaller than that of the isotropically compacted sample (see Figure 5.23a). No clear pattern of variation of peak deviator stress with initial anisotropy therefore emerges. Further inspection of shear plots shows that the amount of shear strain at peak deviator stress for tests at  $[\Delta q/\Delta\bar{p}] = 3, 2, 1, 0$  and  $-1$  was less in the anisotropically compacted samples than in the isotropically compacted samples. However, at  $[\Delta q/\Delta\bar{p}] = -1.5$ , the shear strain at peak deviator stress is higher for the anisotropically compacted sample than for the isotropically compacted sample indicating that the brittleness of the initially anisotropic material decreases as particles and aggregates progressively lose their initial orientation.

The results in the  $v:\varepsilon_s$  plane (see Figures 5.21b to 5.27b) indicate that the soil behaviour was contractant in all tests and that the specific volume had nearly stopped changing by the time the peak deviator stress was reached. With the only exception of sample B300(1), the values of specific volume of the anisotropically compacted samples at peak strength were smaller than the corresponding values of the isotropically compacted samples. Apart from sample B300(-1.5), the difference in specific volume between isotropic and anisotropic samples declined with increasing shear strains. Such behaviour indicates that accumulation of plastic strains erases the memory of the initial soil fabric (i.e. initial void ratio and anisotropy) and soil behaviour becomes controlled only by the recent stress history during the test. After the formation of a shear plane, measurements of deviator stress and volume changes become, however, inaccurate as the sample is physically split into two parts.

Figures 5.21c to 5.27c show the conventional semi-logarithmic plots of specific volume against mean net stress  $\bar{p}$  or mean Bishop's stress  $p^*$ . The initial value of specific volume was noticeably lower for the anisotropically compacted samples than for the isotropically compacted ones. This suggests that a substantial rearrangement and reorientation of soil particles and aggregates occurred during anisotropic compaction, which resulted not only in distortion/rotation but also expansion of the initial yield surface compared to isotropically compacted samples (this will be further discussed in Chapter 6). As loading progresses, the compression curves of both isotropically and anisotropically compacted samples show a tendency to converge towards a single line. This observation is very clear for probing at  $[\Delta q/\Delta\bar{p}] = 1, 0, -0.5$  and  $-1$  (see Figures 5.23c, 5.24d, 5.25c and 5.26c) suggesting that the soil fabric tends towards a form of anisotropy controlled by the recent stress history alone and independent of the initial (i.e. compaction-induced) soil fabric.

For all tests, the specific water volume  $v_w$  slightly decreased by about 0.003, during initial elastic loading (no figures shown). After yielding, the variation of  $v_w$  depends on the stress path slope,  $[\Delta q/\Delta \bar{p}]$ , with a modest increase of  $\approx 0.02$  for tests at  $[\Delta q/\Delta \bar{p}] = 3, 2, 1$  and  $-1.5$  and two modest decreases of  $\approx 0.02$  and again  $\approx 0.02$  during probing and shearing respectively, for tests at  $[\Delta q/\Delta \bar{p}] = 0$  and  $-0.5$ . It is worth mentioning that the variation of  $v_w$  does not appear to be affected by the initial sample anisotropy.

Inspection of Figures 5.21d to 5.27d shows that  $S_r$  increased in a very consistent way in spite of the almost negligible variation of  $v_w$ , which demonstrates that the variation of  $S_r$  is dominated by changes in specific volume. The initial difference in  $S_r$  between isotropically and anisotropically compacted samples declined as loading progressed, which is consistent with the behaviour in the compression plane.

### 5.5.2 Probing/shearing at $s = 100$ kPa (Test Series A100, B100 and Be100)

Figures 5.28 to 5.34 show results from tests at  $s = 100$  kPa, namely from tests on initially isotropic samples (i.e. Test Series A100), initially anisotropic samples compacted to  $\bar{p} = 250$  kPa (i.e. Test Series B100) and initially anisotropic samples compacted to  $\bar{p} = 160$  kPa (i.e. Test Series Be100).

#### Test Series A100 and B100

The volumetric and shear behaviour was considerably less stiff for Test Series A100 and B100 than for Test Series A300 and B300, confirming the stabilising/stiffening effects of suction.

The plots in the  $q:\varepsilon_s$  plane (Figures 5.28a to 5.34a) show that the anisotropic samples B100(3), B100(2), B100(1), B100(-1) and B100(-1.5) produced a stiffer response than the corresponding isotropic samples A100(3), A100(2), A100(1), A100(-1) and A100(-1.5). Generally, for a given probing stress ratio  $[\Delta q/\Delta \bar{p}]$ , the patterns of variation of deviator stress with shear strain at  $s = 100$  kPa are similar to those observed at  $s = 300$  kPa (see Figures 5.21a to 5.27a). During probing, sample A100(0) developed a small positive shear strain whereas sample B100(0) developed a small negative shear strain, similar to samples A300(0) and B300(0) respectively. In addition, samples A100(-0.5) and B100(-0.5) showed very similar responses during probing and subsequent shearing which was, once again, consistent with the previous comparison between tests A300(-0.5) and B300(-0.5) (see Figure 5.25).

As in Test Series A300 and B300, no pattern emerges when comparing the peak deviator stress of isotropically and anisotropically compacted samples. Tests at  $[\Delta q/\Delta \bar{p}] = 2$  and

–1.5 show values of peak deviator stress that are  $\approx 13\%$  greater for the anisotropically compacted samples compared to the isotropically compacted samples (see Figures 5.29a and 5.34a respectively) whereas the peak deviator stress of the anisotropically compacted sample at  $[\Delta q/\Delta \bar{p}] = 1$  was  $\approx 52\%$  smaller than that of the isotropically compacted sample (see Figures 5.23). Finally, tests at  $[\Delta q/\Delta \bar{p}] = 3, 0, -0.5$  and  $-1$  show very similar peak deviator stress (see Figures 5.28a, 5.31a, 5.32a and Figure 5.23a respectively) for both anisotropically and isotropically compacted samples.

The amount of shear strain at peak deviator stress for tests at  $[\Delta q/\Delta \bar{p}] = 3, 1, 0$  and  $-1$ , but not for tests at  $[\Delta q/\Delta \bar{p}] = -1.5$ , was less in the anisotropically compacted samples than in the isotropically compacted ones. This behaviour is in agreement with the observation for tests at  $s = 300$  kPa.

Inspection of results in the  $v: \varepsilon_s$  plane highlights similar features as already observed in Test Series A300 and B300 (see Figures 5.28b to 5.34b and Figures 5.21b to 5.27b respectively). The behaviour was contractant in all tests and specific volume had nearly stopped changing by the time the peak deviator stress was reached. With the only exception of sample B100(1), the specific volume at peak deviator stress was less for the anisotropically compacted samples than for the isotropically compacted samples. Moreover, apart from sample B100(-1.5), the difference in specific volume between isotropic and the anisotropic samples declined as loading progressed. For any given  $[\Delta q/\Delta \bar{p}]$ , the difference in  $v$  between isotropically and anisotropically compacted samples at peak strength is smaller for  $s = 100$  kPa than for  $s = 300$  kPa.

Further inspection of  $q: \varepsilon_s$  plots of Test Series A300, B300, A100 and B100 indicates that peak strength decreases significantly as suction decreases from  $s = 300$  kPa to  $s = 100$  kPa for both isotropically and anisotropically compacted samples. No consistent trend of variation of shear strain at peak deviator stress with suction could be observed as this stays almost unchanged for tests at  $[\Delta q/\Delta \bar{p}] = 1, 0$  and  $-0.5$  but it decreases or increases for other tests.

Figures 5.28c to 5.34c show the variation of specific volume in the  $v: \ln \bar{p}$  or  $v: \ln p^*$  planes. Although the initial (i.e. after compaction) values of specific volume varied quite randomly from one sample to another (see Table 5.1), the values of specific volume at the beginning of probing (i.e. after the initial wetting stage) were always greater in Test Series A100 and B100 than in Test Series A300 and B300. This observation is consistent with the expectation that, at low mean net stresses, wetting to lower suction levels induces greater swelling.

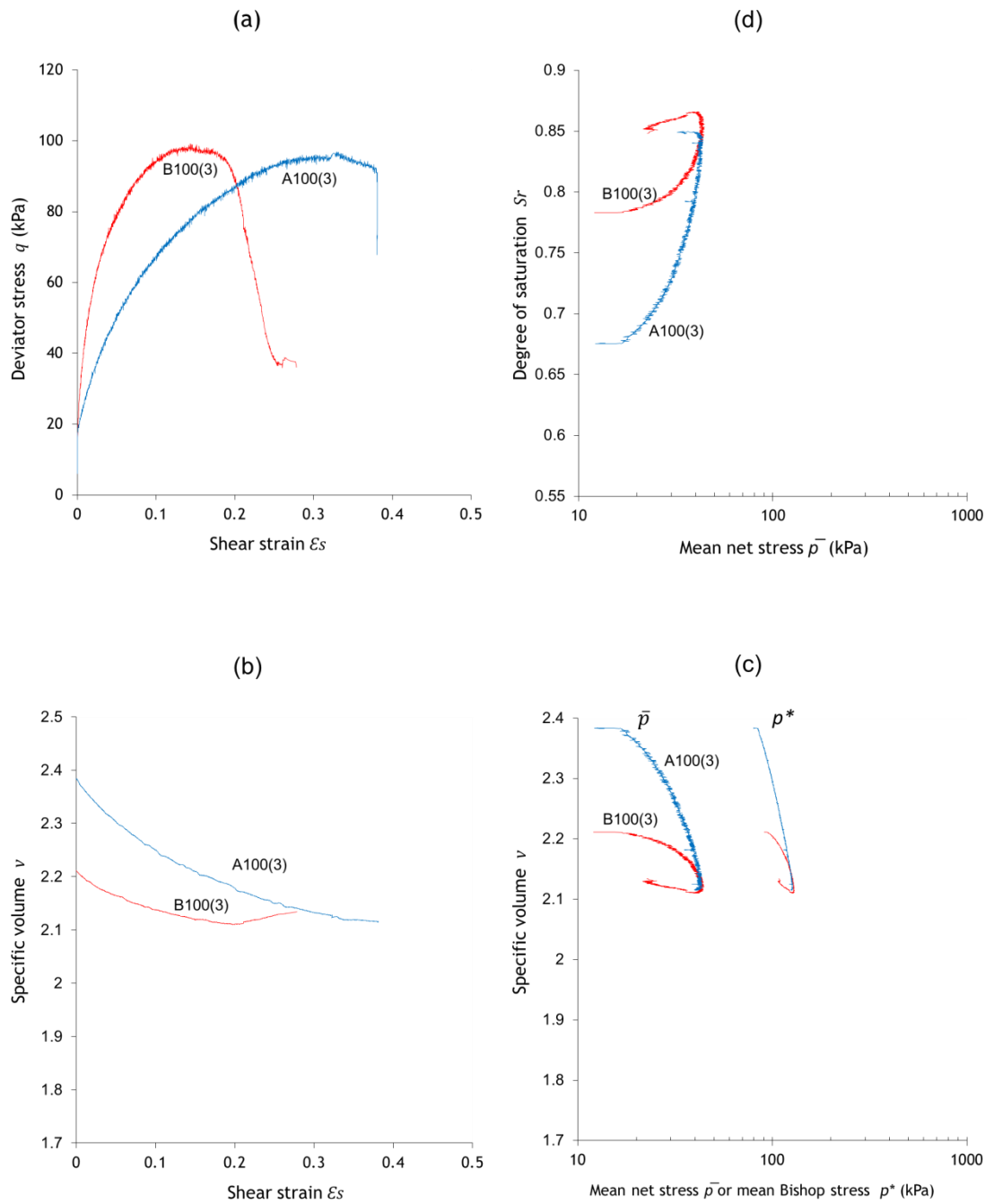


Figure 5.28 Results of Tests A100(3) and B100(3) in: (a)  $q: \epsilon_s$  plane, (b)  $v: \epsilon_s$  plane, (c)  $v: \ln \bar{p}$  or  $v: \ln p^*$  plane (d)  $S_r: \ln \bar{p}$  plane

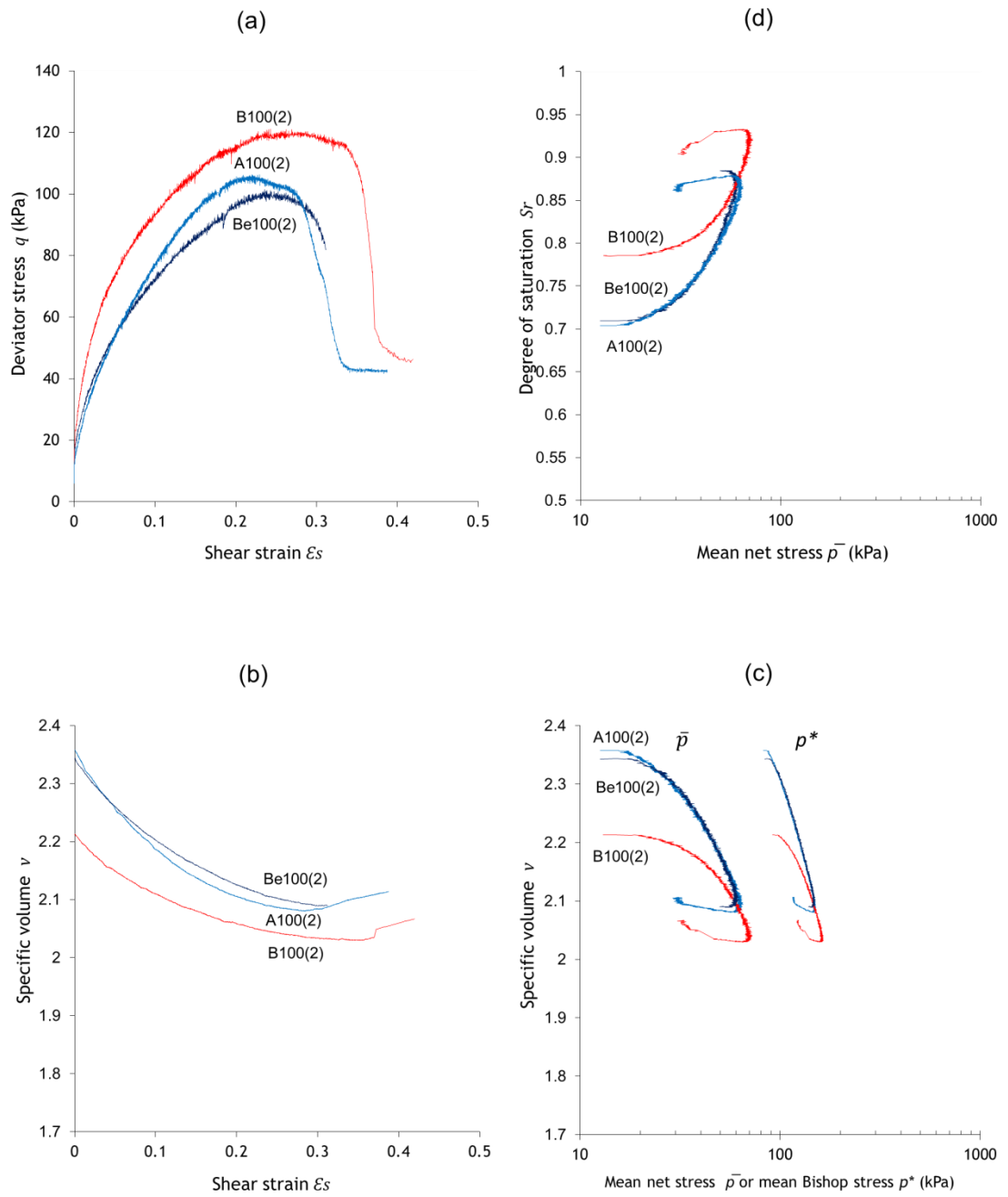


Figure 5.29 Results of Tests A100(2), B100(2) and Be100(2) in: (a)  $q: \epsilon_s$  plane, (b)  $v: \epsilon_s$  plane, (c)  $v: \ln \bar{p}$  or  $v: \ln p^*$  plane (d)  $S_r: \ln \bar{p}$  plane

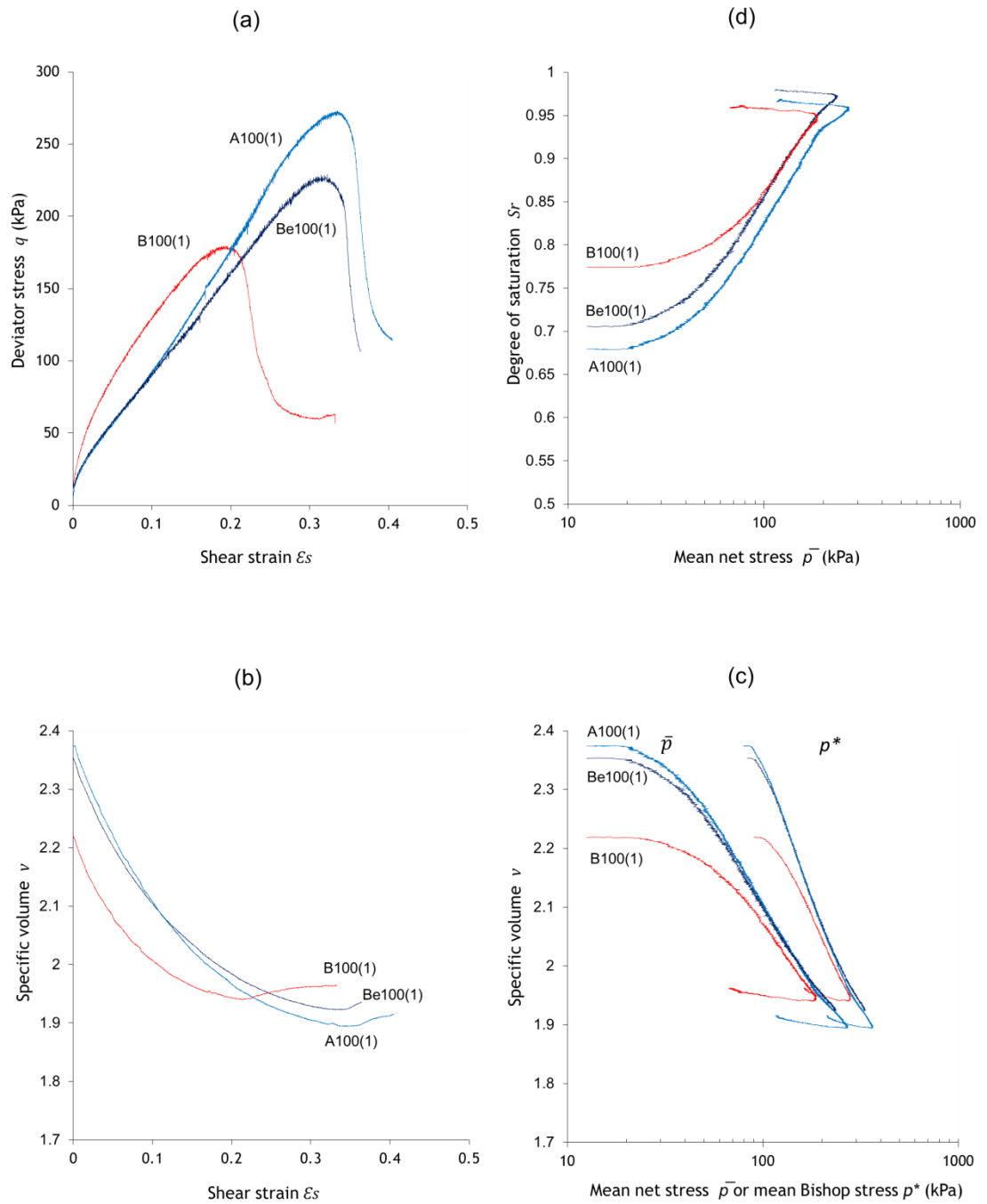


Figure 5.30 Results of Tests A100(1), B100(1) and Be100(1) in: (a)  $q: \epsilon_s$  plane, (b)  $v: \epsilon_s$  plane, (c)  $v: \ln \bar{p}$  or  $v: \ln p^*$  plane (d)  $S_r: \ln \bar{p}$  plane

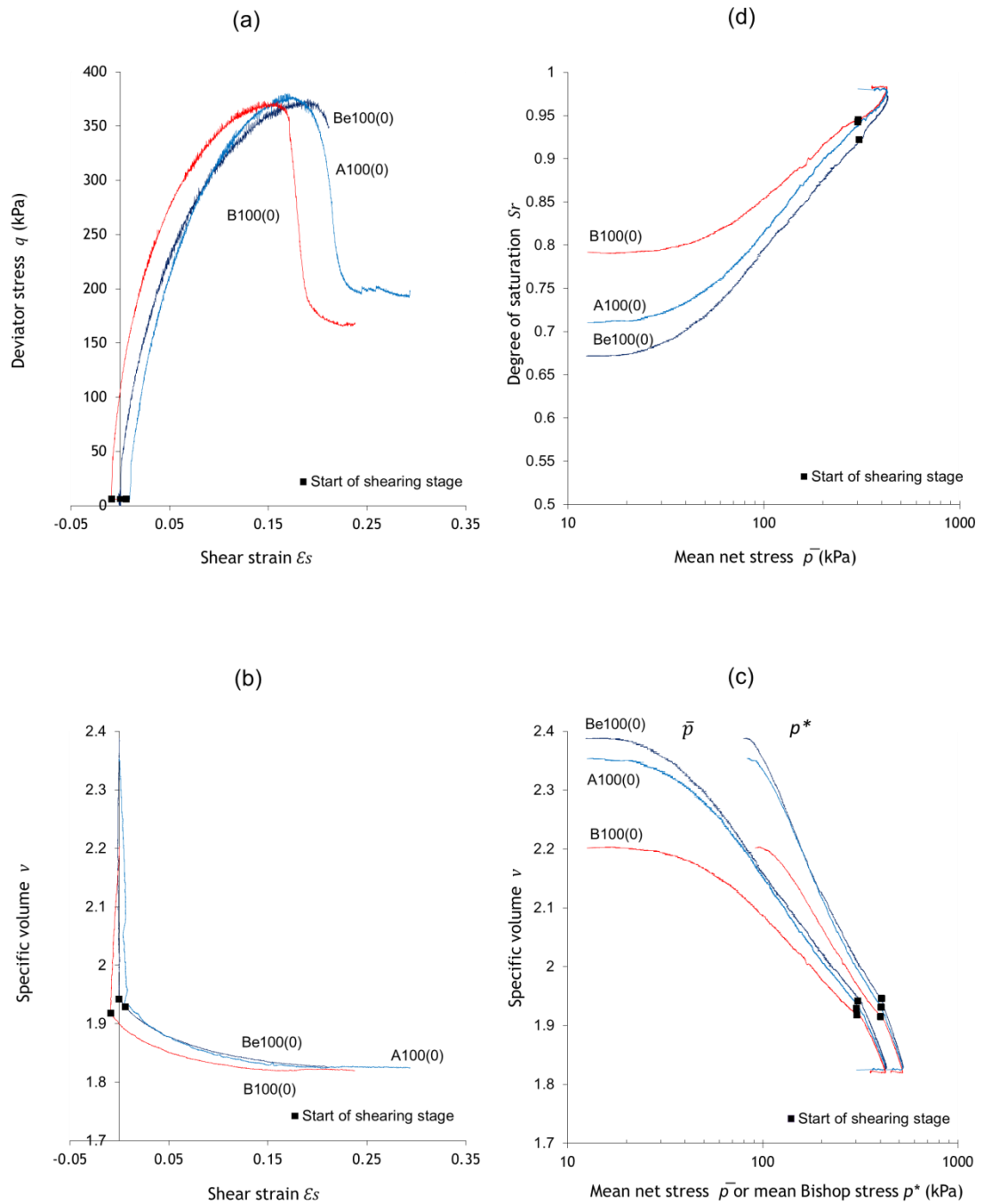


Figure 5.31 Results of Tests A100(0), B100(0) and Be100(0) in: (a)  $q: \epsilon_s$  plane, (b)  $v: \epsilon_s$  plane, (c)  $v: \ln \bar{p}$  or  $v: \ln p^*$  plane (d)  $S_r: \ln \bar{p}$  plane

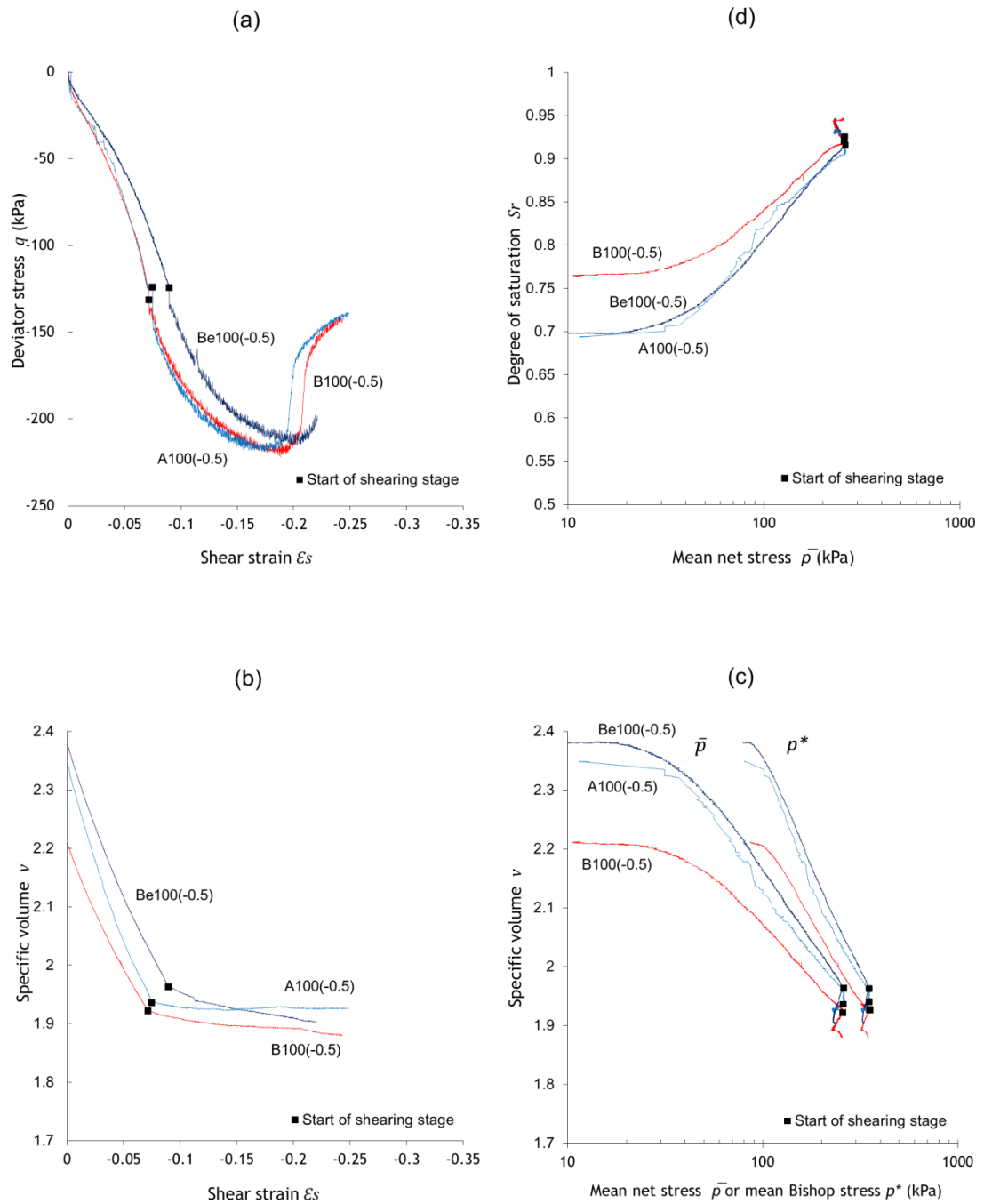


Figure 5.32 Results of Tests A100(-0.5), B100(-0.5) and Be100(-0.5) in: (a)  $q: \epsilon_s$  plane, (b)  $v: \epsilon_s$  plane, (c)  $v: \ln \bar{p}$  or  $v: \ln p^*$  plane (d)  $S_r: \ln \bar{p}$  plane

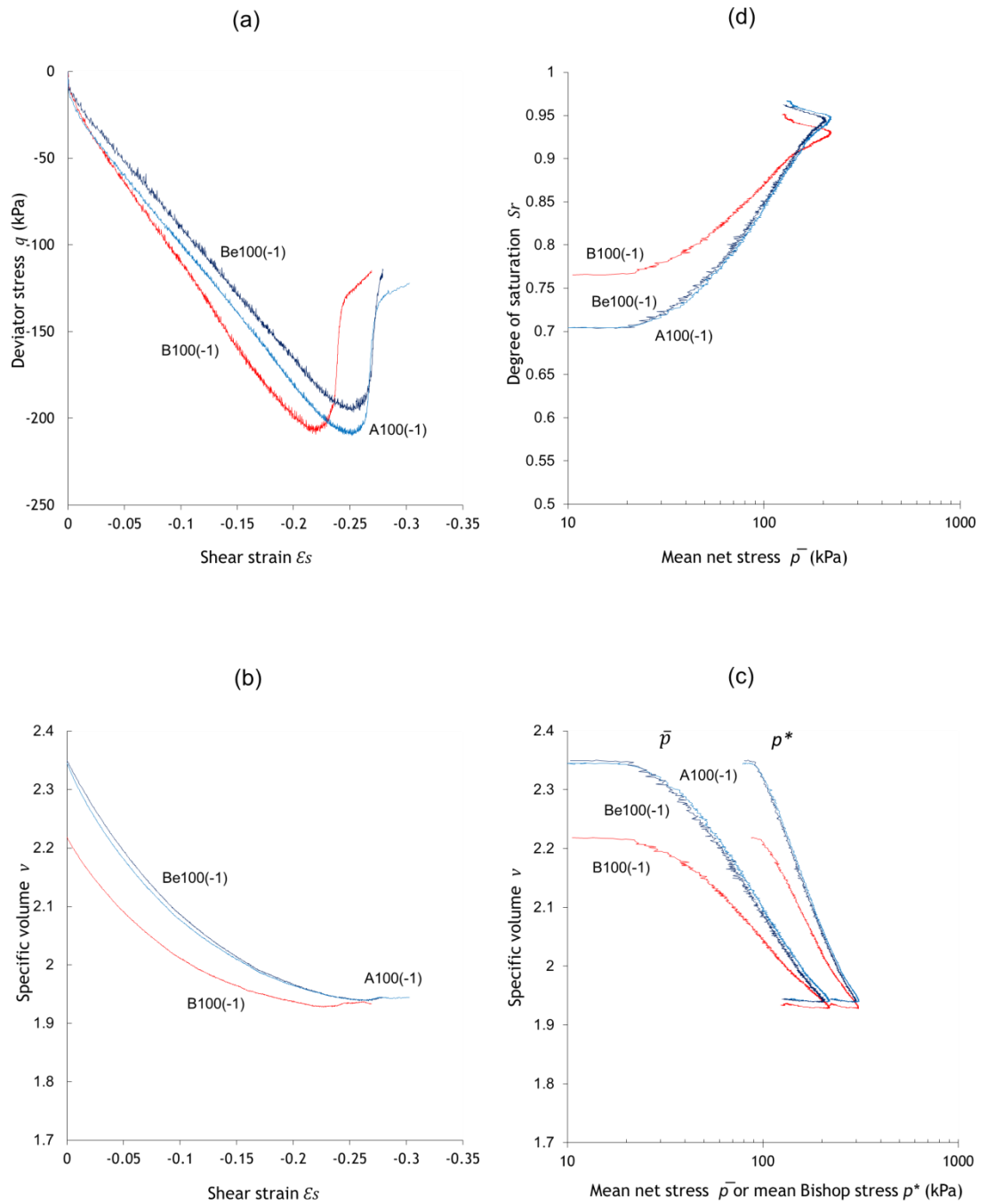


Figure 5.33 Results of Tests A100(-1), B100(-1) and Be100(-1) in: (a)  $q$ :  $\epsilon_s$  plane, (b)  $v$ :  $\epsilon_s$  plane, (c)  $v$ :  $\ln \bar{p}$  or  $v$ :  $\ln p^*$  plane (d)  $S_r$ :  $\ln \bar{p}$  plane

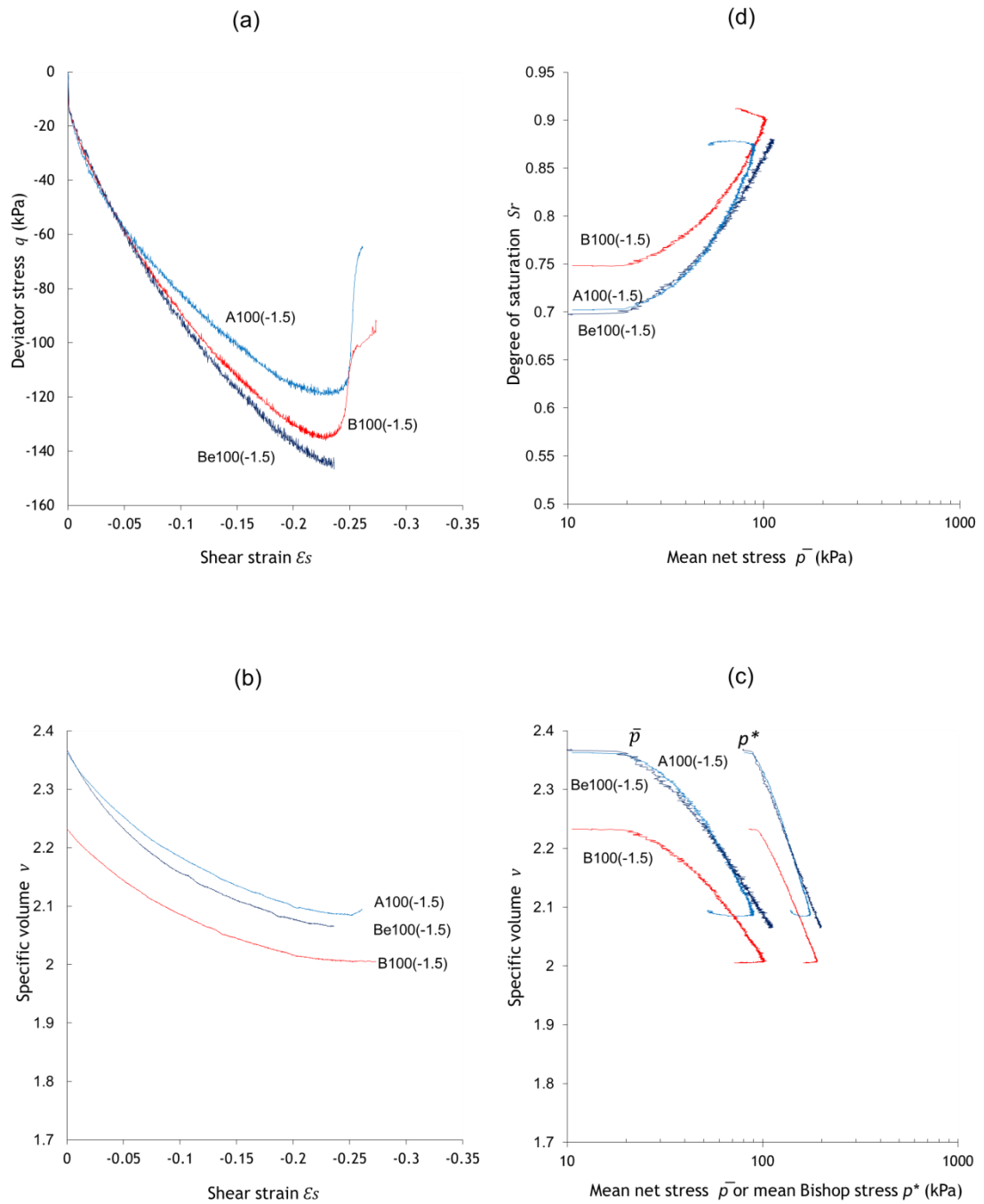


Figure 5.34 Results of Tests A100(-1.5), B100(-1.5) and Be100(-1.5) in: (a)  $q$ :  $\epsilon_s$  plane, (b)  $v$ :  $\epsilon_s$  plane, (c)  $v$ :  $\ln \bar{p}$  or  $v$ :  $\ln p^*$  plane (d)  $S_r$ :  $\ln \bar{p}$  plane

As in Test Series A300 and B300, the compression curves of isotropically and anisotropically compacted samples tend to merge as loading progresses during the probing stage. This observation, which is particularly clear for tests at  $[\Delta q/\Delta \bar{p}] = 1, 0, -0.5$  and  $-1$  (see Figures 5.30c, 5.31c, 5.32c and 5.33c), suggests that, regardless of the initial sample properties, the soil fabric tends to converge towards a unique configuration during loading at constant  $[\Delta q/\Delta \bar{p}]$ , as already observed for tests at  $s = 300$  kPa.

Further evidence of fabric evolution during loading is provided by inspection of the shearing plots of samples A100(1), A100(-0.5) and B100(-0.5) (see Figures 5.30a and Figure 5.32a). These plots show an increase in soil stiffness as shearing progresses, which is attributed to the on-going reorientation of soil particles/aggregates that increases the level of granular interlocking and hence the mobilized shear strength.

Investigation of Figures 5.21c to 5.27c and Figures 5.28c to 5.34c, shows that the pre-yield portions of the compression curves all have very similar gradients regardless of suction value and amount of anisotropy. The value of the yield stress is smaller at  $s = 100$  kPa than at  $s = 300$  kPa, which is expected as increasing values of suction produce greater stabilization of inter-aggregates contacts. The same figures also show that the compression curves of the anisotropically compacted samples present a more gradual change in slope, i.e. a gentler curvature, at yielding than the isotropically compacted samples. This is partly attributed to the larger rotation of the yield curve and partly to the denser packing (requiring larger energy to yield) of anisotropically compacted samples compared to isotropically compacted ones. For any given test series and regardless of the suction value, the slope of the post-yield portions of compression lines shows, to some extent, a dependency on the stress path ratio  $[\Delta q/\Delta \bar{p}]$ . This slope is smallest for  $[\Delta q/\Delta \bar{p}] = 0$  and increases when the ratio  $[\Delta q/\Delta \bar{p}]$  is greater or smaller than zero.

Figures 5.28d to 5.34d depict the variation of degree of saturation caused by changes of both specific water volume and specific volume during probing/shearing. No increase in specific water volume  $v_w$  was observed during loading at low values of mean net stress, i.e. 10 – 20 kPa (no figures shown). During loading to larger stresses, the specific water volume increased monotonically by up to  $\approx 0.02$  for samples A100(3), B100(3) and B100(2) whereas it decreased monotonically by approximately the same amount for samples A100(2), A100(-1.5) and B100(-1.5). For tests at  $[\Delta q/\Delta \bar{p}] = 1, 0, -0.5$  and  $-1$ , a more substantial decrease in specific water volume was observed ( $\approx 0.05 - 0.08$  during

probing and  $\approx 0.07$  during shearing). In addition, the variation of specific water volume does not appear to be affected by fabric anisotropy.

Figures 5.28d to 5.34d show a substantial increase of degree of saturation ( $\approx 0.1 - 0.3$ ). Given the relatively small increase (or even decrease) of specific water volume (as previously discussed), this increase of degree of saturation is mainly caused by the reduction of specific volume during probing/shearing. For tests at  $[\Delta q/\Delta \bar{p}] = 1, 0, -0.5$  and  $-1$ , the degree of saturation became close to 1 ( $S_r \approx 0.95 - 0.97$ ) as loading progressed, indicating that samples had become nearly saturated when peak strength was attained. Furthermore, the corresponding compression curves (see Figures 5.30d, 5.31d, 5.32d and 5.33d) show a consistent tendency to become flatter as the degree of saturation attains values close to 1.

### Test Series Be100

The results of Test Series Be100 are plotted in Figures 5.28 to 5.34 together with the results of Test Series A100 and B100. Samples of Test Series Be100 were compacted at  $[\Delta q/\Delta \bar{p}] = 1.2$  to a smaller value of mean net stress compared to other anisotropically compacted samples, i.e.  $\bar{p} = 160$  kPa instead of 250 kPa, which gave an initial specific volume similar to that of Test Series A100.

Figures 5.29a to 5.34a indicate no consistent pattern for the relative position of the shearing curves of Test Series Be100, A100 and B100. The modestly anisotropic fabric of Test Series Be100 would be expected to show an intermediate response between Test Series A100 and B100.

During isotropic loading of sample Be100(0), the shear strain was almost zero indicating that the positive shear strain caused by the imposed small positive deviator stress is compensated by the negative shear strain caused by the moderate rotation of the yield locus (associated to a small fabric anisotropy). This fits very well with the response of the anisotropic and isotropic samples, B100(0) and A100(0), which showed a small negative shear strain and a small positive shear strain, respectively, during isotropic loading.

Inspection of the shear stages of tests subjected to probing stress paths of  $[\Delta q/\Delta \bar{p}] = 0$  and  $-0.5$  shows similar values of peak strength regardless of anisotropy. However, inspection of the other probing stages shows great discrepancy with respect to the position of peak deviator stress relative to those of Test Series A100 and B100. This

observation will be further discussed in Section 6.3 when discussing critical state behaviour.

In the  $v: \varepsilon_s$  plane (see Figures 5.28b to 5.34b), the behaviour of Test Series Be100 and A100 was very similar confirming the modest anisotropy of the former samples. Because of the same reason, the compression and degree of saturation curves (see Figures 5.28c to 5.34c and Figures 5.28d to 5.34d respectively) of Test Series Be100 and A100 were also very similar.

The results of Test Series Be100 adds further weight to the conclusion that the differences in peak deviator stress between isotropically and anisotropically compacted samples do not follow a particular trend of behaviour but are caused by lack of sample repeatability. Lack of sample repeatability will have the largest effect on measured peak strength for shallow shearing paths that approach the critical state line at a very acute angle (i.e. stress paths that are sub-parallel to the critical state line).

### 5.5.3 Probing/shearing under saturated conditions (Test Series A0 and B0)

Figures 5.35 to 5.41 show the results from saturated tests on isotropically and anisotropically compacted samples. In this case, because the soil is saturated, compression curves are plotted in terms of mean effective stress  $p'$  instead of mean net stress  $\bar{p}$ . Unlike the unsaturated Test Series, the saturated Test Series A0 and B0 were conducted inside a conventional triaxial cell (i.e. System 3 described in Section 3.2). Any potential inconsistency of behaviour between these two saturated test series and other unsaturated ones could therefore be partly attributed to the use of a different experimental setup.

Figures 5.35a to 5.41a show the variation of deviator stress with shear strain during saturated probing at different values of  $[\Delta q/\Delta \bar{p}]$ . Generally, material response was substantially less stiff under saturated conditions than unsaturated conditions, which was expected due to the loss of the stabilizing capillary menisci. Most of the features of soil behaviour already observed for Test Series at  $s = 300$  kPa and  $s = 100$  kPa were also observed during saturated tests. In particular, tests at  $[\Delta q/\Delta \bar{p}] = 2, 0.5, 0, -1$  and  $-1.5$  showed a stiffer response for anisotropically compacted samples than for isotropically compacted ones. Moreover, during isotropic probing, sample B0(0) showed a small negative shear strain whereas sample A0(0) showed a small positive shear strain, which is consistent with the behaviour of sample pairs B300(0)/A300(0) and B100(0)/A100(0) as previously discussed. In addition, the evolution of shear strains in samples A0(1), A0(0.5) and A0(-0.5) takes the same pattern of variation as that of samples A100(1), A100(-0.5),

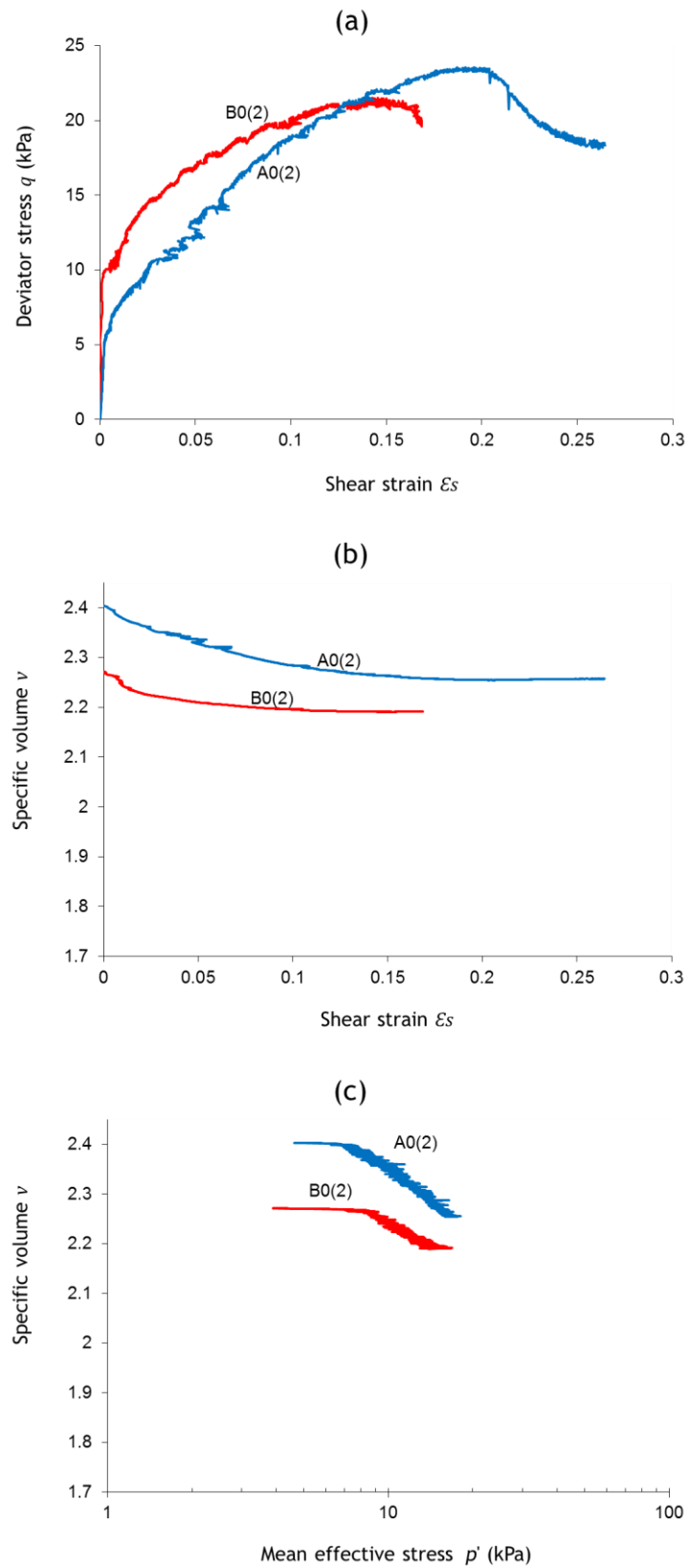


Figure 5.35 Results of Tests A0(2) and B0(2) in: (a)  $q$ :  $\epsilon_s$  plane, (b)  $v$ :  $\epsilon_s$  plane, (c)  $v$ :  $\ln p'$  plane

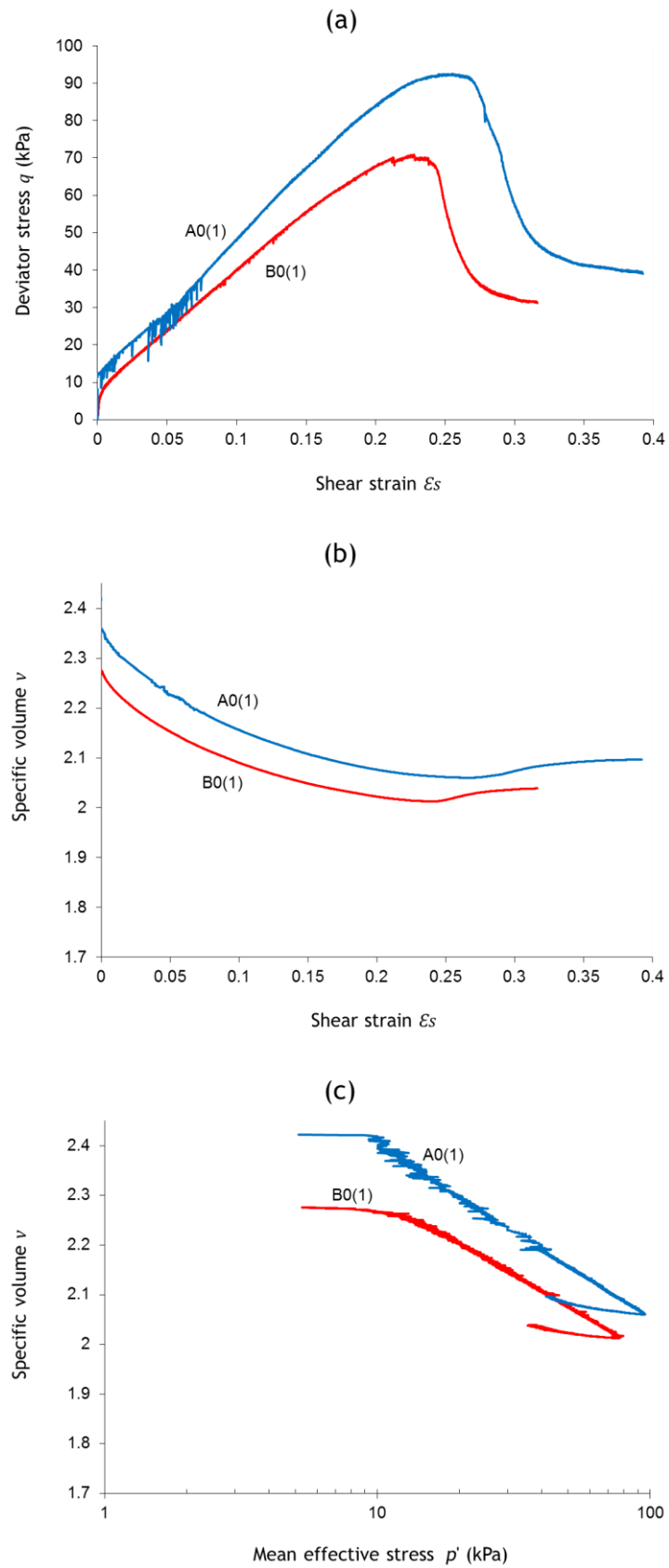


Figure 5.36 Results of Tests A0(1) and B0(1) in: (a)  $q: \epsilon_s$  plane, (b)  $v: \epsilon_s$  plane, (c)  $v: \ln p'$  plane

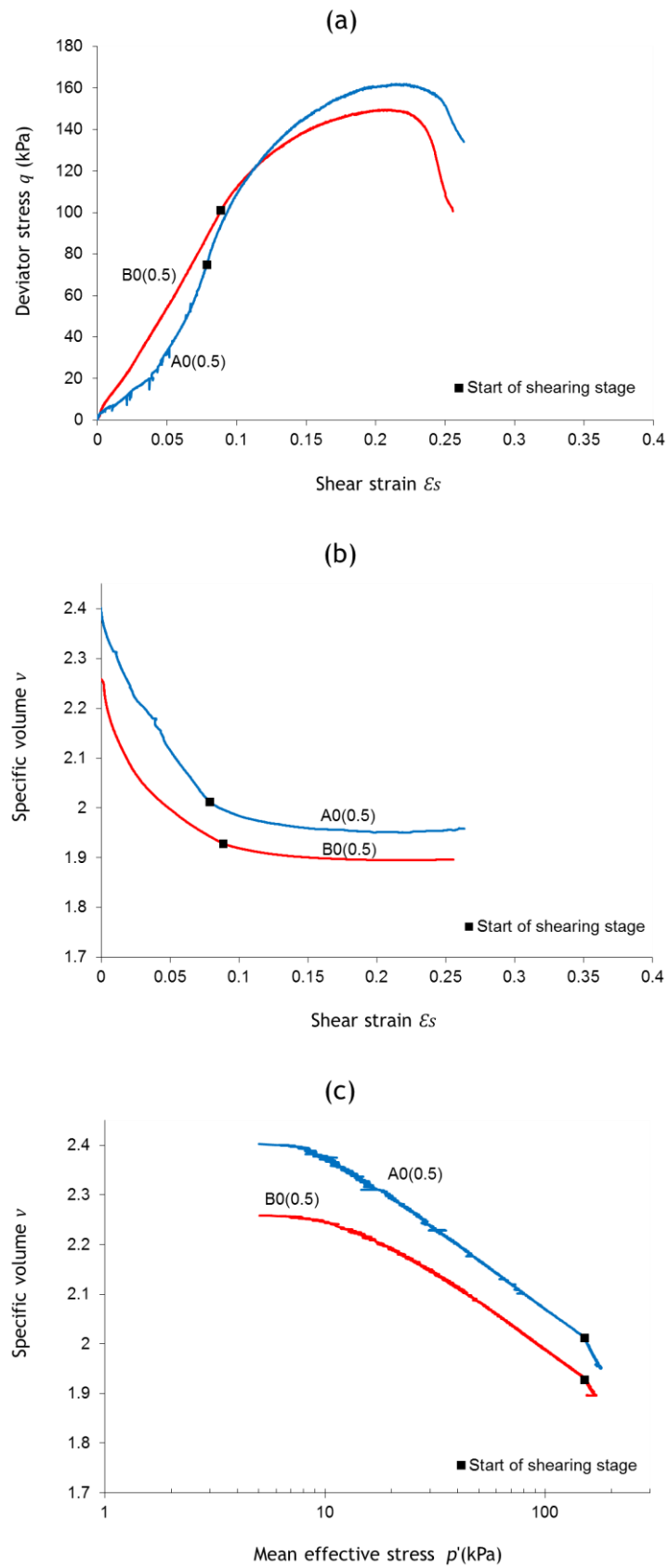


Figure 5.37 Results of Tests A0(0.5) and B0(0.5) in: (a)  $q: \epsilon_s$  plane, (b)  $v: \epsilon_s$  plane, (c)  $v: \ln p'$  plane

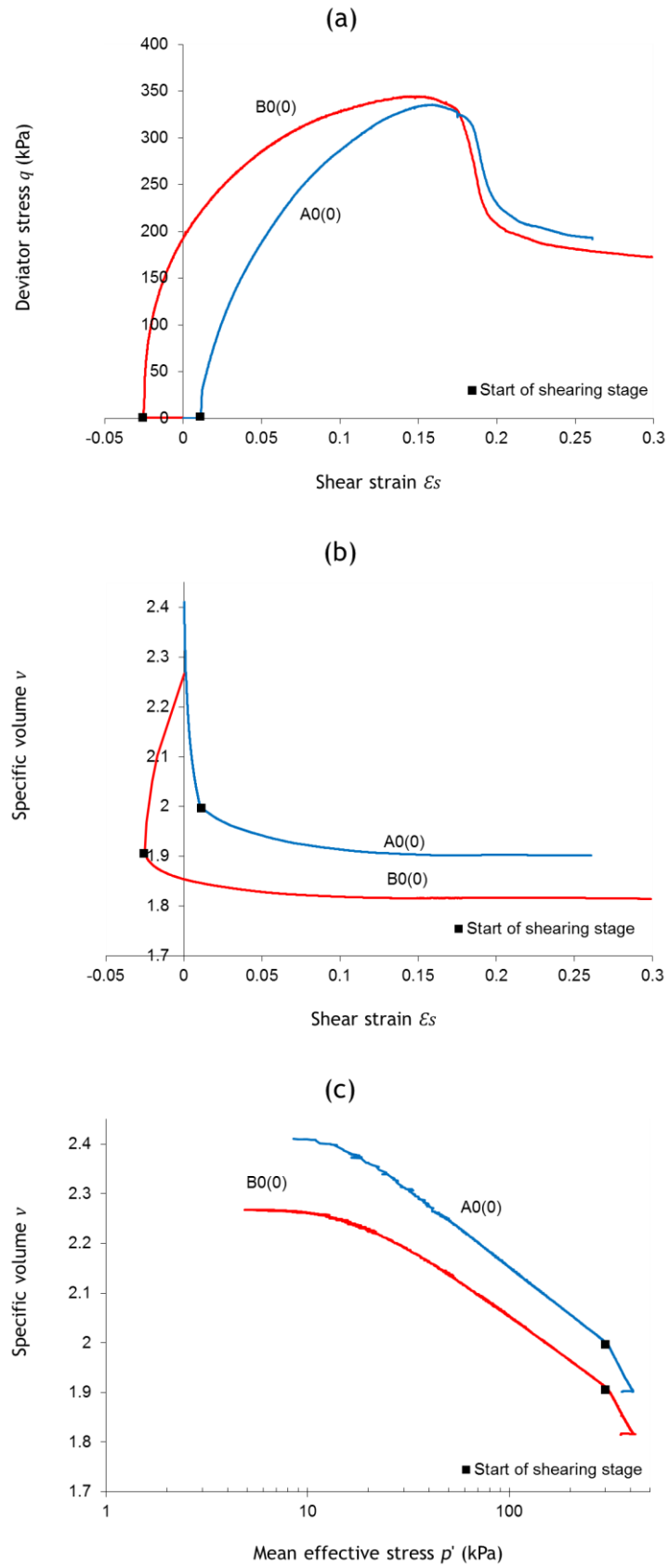


Figure 5.38 Results of Tests A0(0) and B0(0) in: (a)  $q: \epsilon_s$  plane, (b)  $v: \epsilon_s$  plane, (c)  $v: \ln p'$  plane

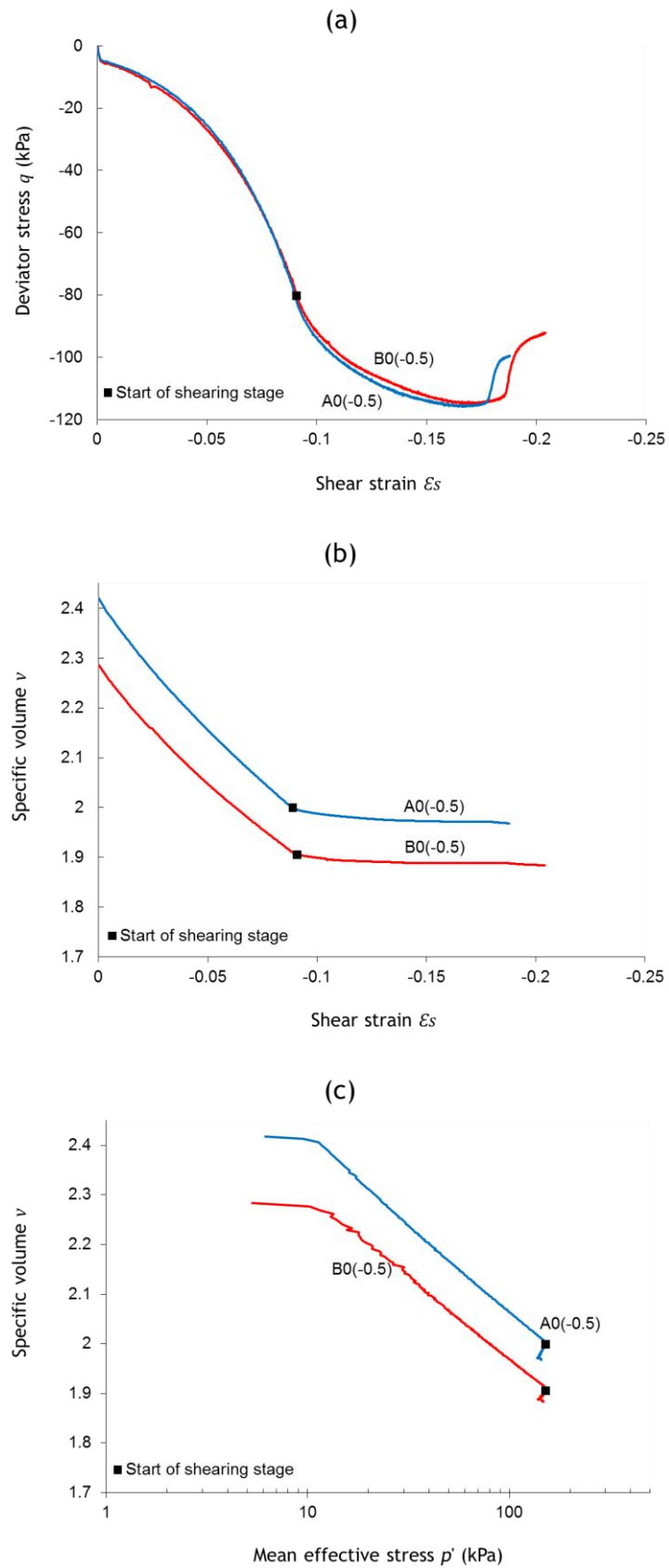


Figure 5.39 Results of Tests A0(-0.5) and B0(-0.5) in: (a)  $q: \epsilon_s$  plane, (b)  $v: \epsilon_s$  plane, (c)  $v: \ln p'$  plane

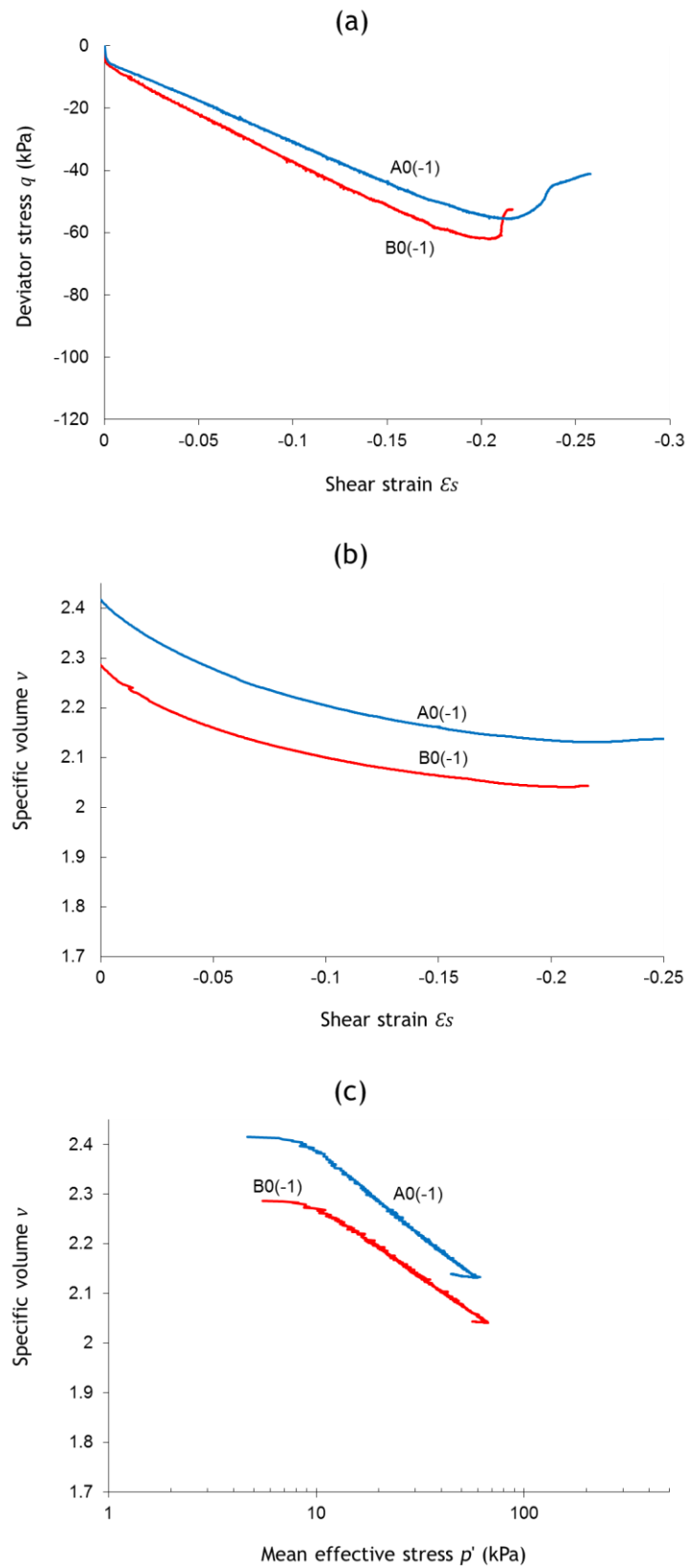


Figure 5.40 Results of Tests A0(-1) and B0(-1) in: (a)  $q: \epsilon_s$  plane, (b)  $v: \epsilon_s$  plane, (c)  $v: \ln p'$  plane

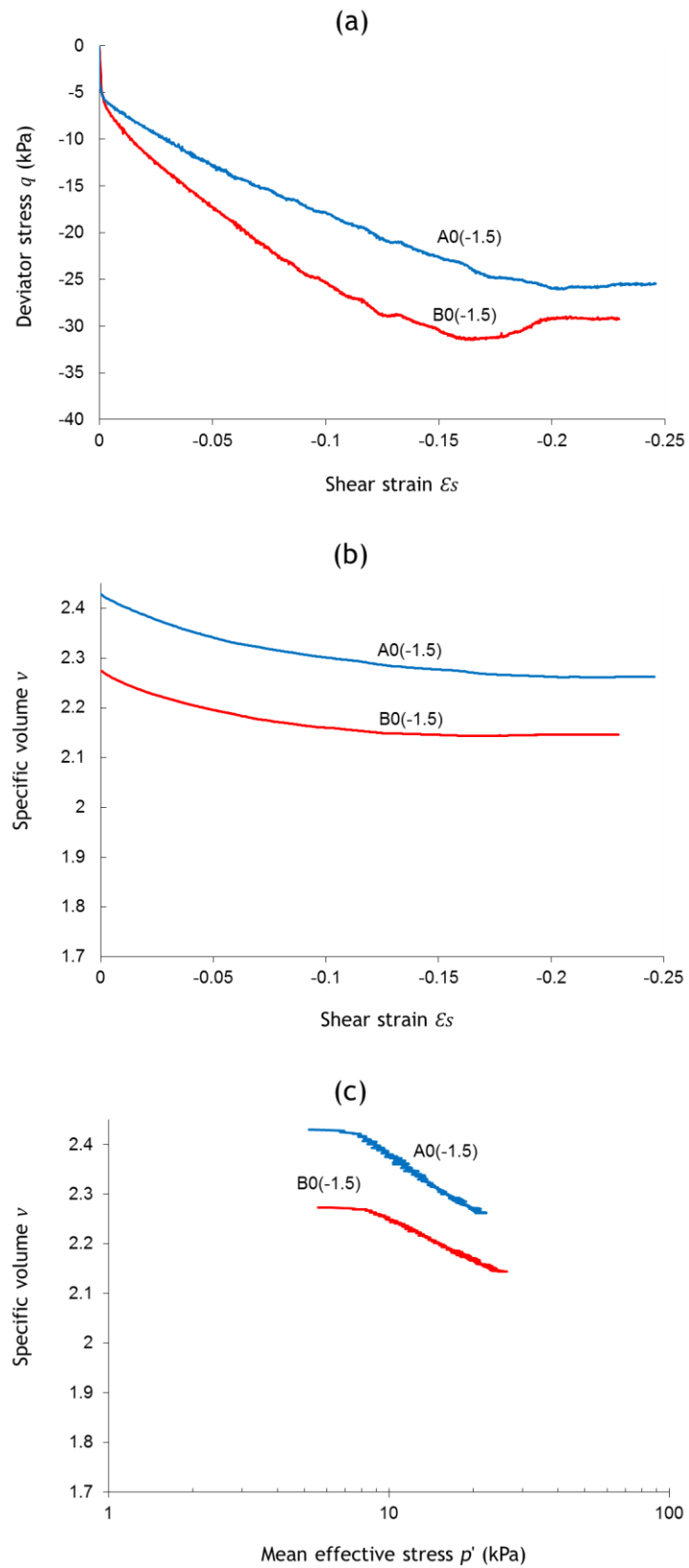


Figure 5.41 Results of Tests A0(-1.5) and B0(-1.5) in: (a)  $q: \epsilon_s$  plane, (b)  $v: \epsilon_s$  plane, (c)  $v: \ln p'$  plane

B100(-0.5) and Be100(-0.5) (see Figures 5.30 and 5.32) which was associated to evolution of fabric anisotropy with progression of loading.

Furthermore, the very similar peak deviator stress attained during shearing of the two sample pairs A0(0)/B0(0) and A0(-0.5)/B0(-0.5) provides further evidence that differences in strength between isotropically and anisotropically compacted soil are mainly due to lack of sample repeatability (which is amplified when samples are sheared along paths which are sub-parallel to the critical state line in the  $q:\bar{p}$  plane) rather than to intrinsic material properties.

Results in the  $v:\varepsilon_s$  plane (see Figures 5.35b to 5.41b) show that soil behaviour was always contractant but, unlike tests at  $s = 300$  kPa and  $s = 100$  kPa, the difference in specific volume between isotropically and anisotropically compacted samples remained unchanged throughout shearing. The same plots also show that specific volume has almost stopped changing by the time peak strength was reached. All samples also showed a sudden post peak reduction of shear strength due to strain localisation.

Figures 5.35c to 5.41c show the plots of specific volume against mean effective stress  $p'$ . The initially flat portion of the compression curve corresponds to elastic loading inside the yield surface and is substantially shorter compared to the Test Series at  $s = 300$  kPa and  $s = 100$  kPa. This is because yielding occurs at lower stress levels for saturated samples than for unsaturated samples because of the absence of stabilising inter-particle capillary menisci under saturated conditions. Unlike Test Series at  $s = 300$  kPa and  $s = 100$  kPa, the difference between compression curves of isotropically and anisotropically compacted samples tested at the same  $[\Delta q/\Delta \bar{p}]$  declines only slightly as loading progresses. Furthermore, the slopes of the post-yield portions of the compression curves were clearly smaller for saturated samples compared to samples tested at  $s = 300$  kPa and  $s = 100$  kPa, indicating a decreasing pattern of the post-yield compression slopes with decreasing suction.

To further investigate the effect of suction on stress-strain behaviour, Figures 5.42 and 5.43 show results from the tests performed on isotropically and anisotropically compacted samples, respectively, under different suctions at  $[\Delta q/\Delta \bar{p}] = 0$ . Figures 5.42a and 5.43a show that the shear strain measured at peak deviator stress was highest at  $s = 300$  kPa whereas it was lowest for saturated samples. Figures 5.42b and 5.43b indicate that the gradient of the post-yield compression lines decreased as suction decreased. Figure 5.42b also indicates that the two saturated compression curves A0(0)

and A0(sat1) (from tests conducted in System 3 and System1, respectively) did not match very well, which could be attributed to the different equipment used.

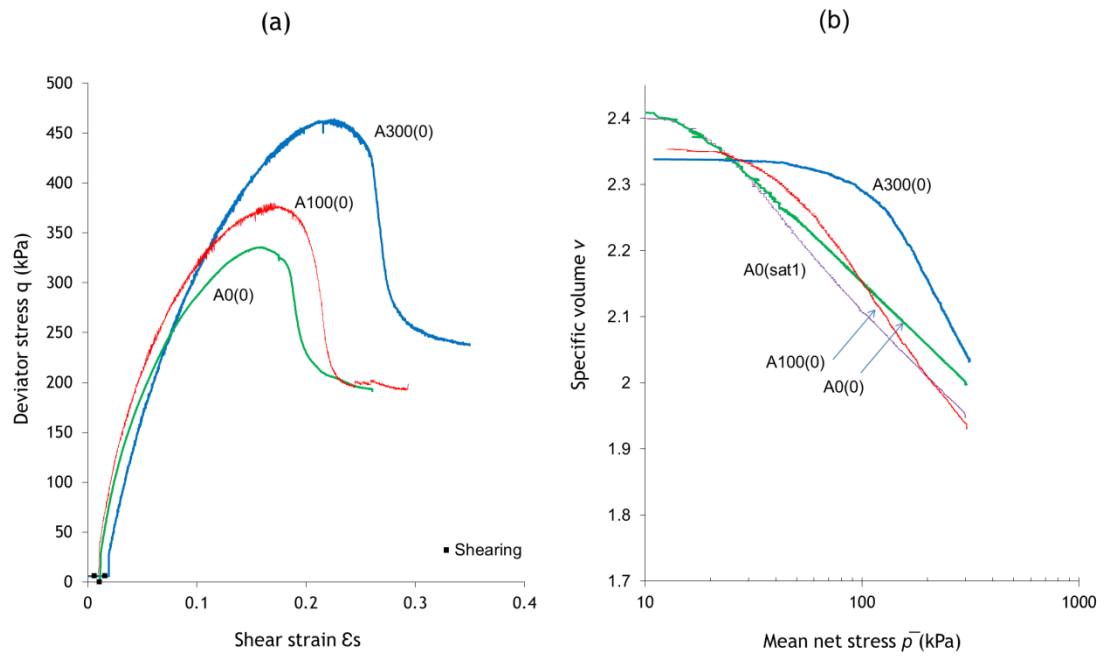


Figure 5.42 Results of tests at  $[\Delta q/\Delta \bar{p}] = 0$  on isotropically compacted samples under different suctions in: (a)  $q: \epsilon_s$  plane, (b)  $v: \ln \bar{p}$  plane

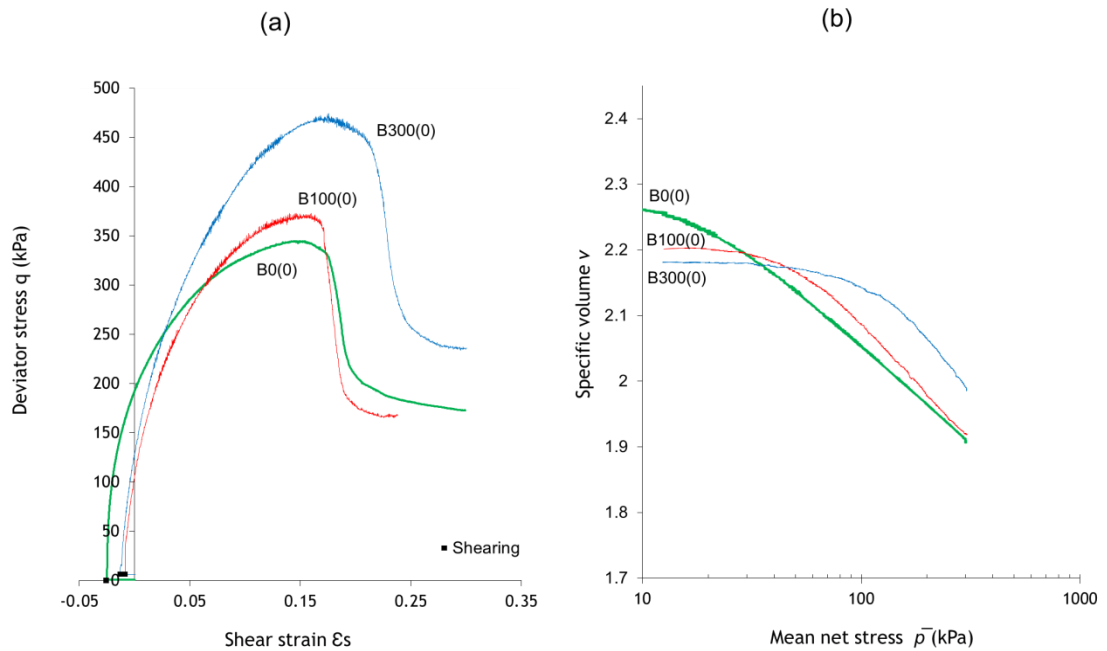


Figure 5.43 Results of tests at  $[\Delta q/\Delta \bar{p}] = 0$  on anisotropically compacted samples under different suctions in: (a)  $q: \epsilon_s$  plane, (b)  $v: \ln \bar{p}$  plane

## 5.6 LOADING/ UNLOADING AND PROBING/SHEARING STAGES ON SAMPLES WITH INDUCED ANISOTROPY (TEST SERIES Ba300, Bb300, Bc300 AND Bd100)

Further to the work described in Section 5.5, four additional Test Series, namely Ba300, Bb300, Bc300 and Bd100, were conducted on anisotropically compacted samples. The objective was to explore the change in the form of the yield surface, and hence the change in the degree of anisotropy with respect to the as-compacted state, produced by previous plastic straining along a given loading path stage and to investigate whether this change of anisotropy had any influence on critical states.

### 5.6.1 Loading/ unloading stages

In Test Series Ba300, Bb300 and Bc300 samples were loaded at  $[\Delta q/\Delta \bar{p}] = 1.2, 0$  and  $-1$ , respectively to mean net stress  $\bar{p} = 200$  kPa and then unloaded back on the same stress path in the  $q:\bar{p}$  plane to the initial stress state (stress path  $a - b - c$  in Figures 5.3, 5.4 and Figure 5.5 respectively).

#### Series Ba300

Figure 5.44 shows results from the loading/unloading stages of Test Series Ba300, where all tests were following precisely the same stress path. Inspection of the  $q:\varepsilon_s$  plots indicates a consistent variation of deviator stress with shear strain with a scatter band that was getting larger for  $q > 200$  kPa (see Figure 5.44a).

The loading curves in the  $q:\varepsilon_s$  plane, see Figure 5.44a, showed an initial part with a similar gradient to that of the unloading curves and a subsequent part with a gradient significantly less than that of the unloading curves. This is consistent with the fact that samples were originally compacted at  $[\Delta q/\Delta \bar{p}] = 1.2$  then subsequently loaded/unloaded at the same value of the  $[\Delta q/\Delta \bar{p}]$ . Yield stresses during loading could therefore be easily identified, in this case, on the basis of the above change of gradient as negligible changes of soil fabric (and, hence, rotation of the yield locus) would be expected during plastic behaviour. Furthermore, unloading paths are remarkably parallel indicating high repeatability of soil behaviour.

Plots of specific volume against shear strain (see Figure 5.44b) show that only a small portion of shear strains was reversible upon unloading, which is consistent with the yielding behaviour described above. Also, the figure shows that, despite the scatter in shear strain, all samples showed very similar values of specific volume by the end of the unloading stage.

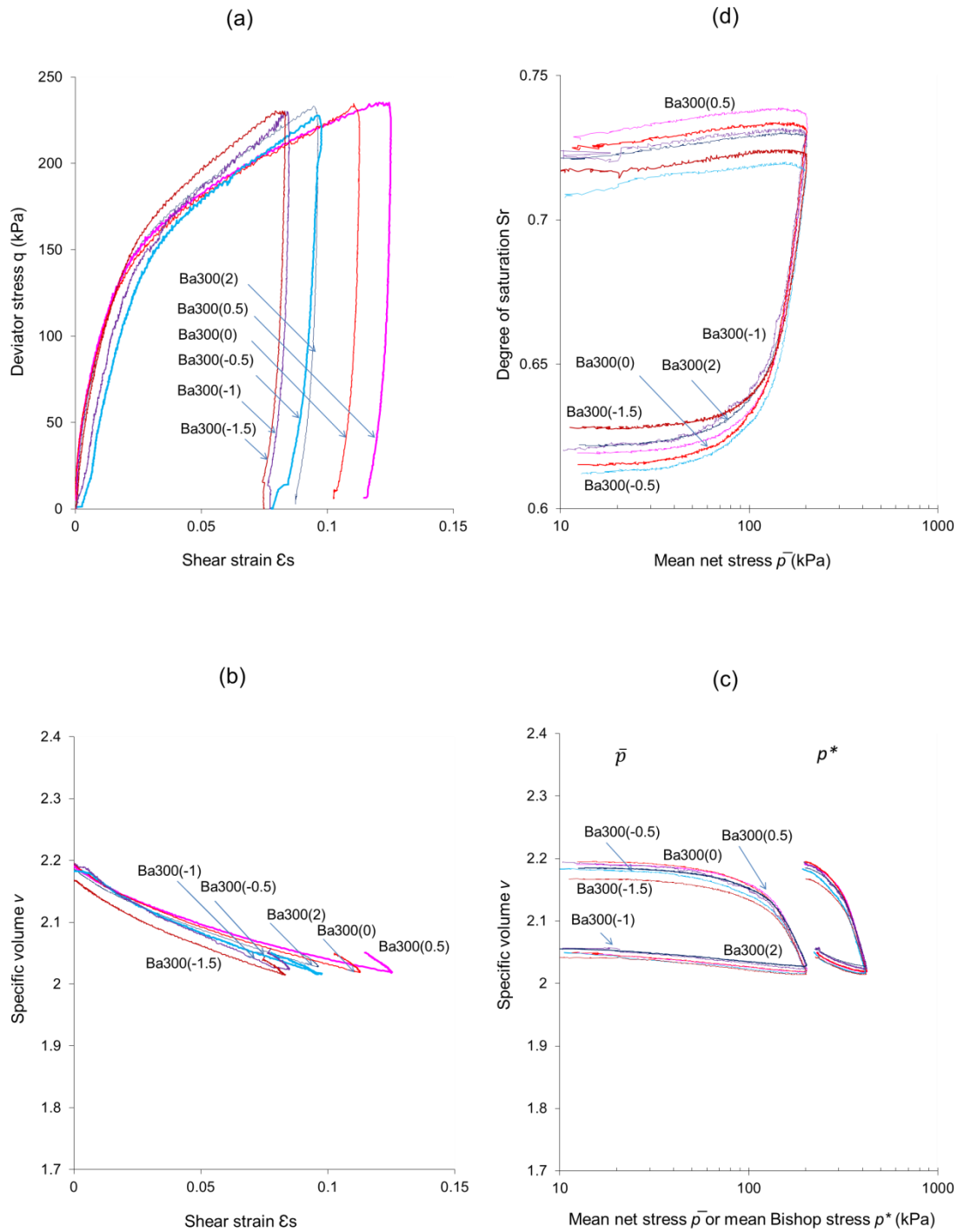


Figure 5.44 Results of loading/unloading stages of Test Series Ba300 in: (a)  $q: \epsilon_s$  plane, (b)  $v: \epsilon_s$  plane, (c)  $v: \ln \bar{p}$  or  $v: \ln p^*$  plane (d)  $S_r: \ln \bar{p}$  plane

Plots of the compression curves in the  $v: \ln \bar{p}$  plane (see Figure 5.44c) show that, despite same scatter in the initial specific volume, all compression curves converge to nearly a single line with progression of loading. The marked change in the gradient of these curves, interpreted as yielding, coincides with the marked change in the gradient of the shear plots described above. The unloading curves fell in a very narrow band with a small linear increase (in a semi-logarithmic plot) of specific volume with decreasing mean net stress. The scatter in specific volume inherited from the end of the wetting stage decreased after the loading/unloading stage which gave a very repeatable starting point for the subsequent probing.

The variation of degree of saturation with mean net stress is shown in Figure 5.44d. The plots show an increase in degree of saturation of  $\approx 0.10$  as a consequence of a marked decrease in specific volume. Monitoring of the pore water volume indicated that a small amount of water flowed into the sample (corresponding to an increase of  $\approx 0.02$  in specific water volume). Interestingly, during unloading, only a small decrease ( $\approx 0.01$ ) of degree of saturation was observed indicating that the change in degree of saturation is mainly dictated by the change in void ratio. Compression curves in the  $v: \ln p^*$  plane (see Figure 5.44c) were also very consistent.

### Series Bb300

Figure 5.45 shows results from the loading/unloading stages of Test Series Bb300 (performed at  $[\Delta q/\Delta \bar{p}] = 0$ ). Figure 5.45a shows that only a very small amount of negative shear strains (less than 0.01) was recorded during the “nearly” isotropic loading/unloading. This behaviour, which reflects erasure of fabric anisotropy with plastic straining, matches very well the behaviour of samples B100(0), Be100(0) and B300(0) discussed in Section 5.5. The slight increase of shear strain in the positive range ( $\approx 0.001$ ) at the beginning of loading, can be attributed to the application of a small positive deviator stress ( $q = 6.5$  kPa for Samples Bb300(1.2) and Bb300(0.5),  $q = 2$  kPa for Samples Bb300(-0.5) Bb300(-1) and  $q = 1$  kPa for Sample Bb300(-1.5)). The differences in shear strain could be attributed to the difference in magnitude of deviator stress as well as to a small lack of sample repeatability.

The plots of specific volume against shear strain (see Figure 5.45b) show that, during unloading, all samples showed a small gradual increase in specific volume. Samples Bb300(1.2), Bb300(0.5) and Bb300(-1) showed a further reduction in shear strain during unloading ( $\approx 0.002$ ). This behaviour could be interpreted as a delayed response to the particle rearrangement process that was taking place during previous isotropic loading. It is worth mentioning that no direct measurements of radial strains were conducted during

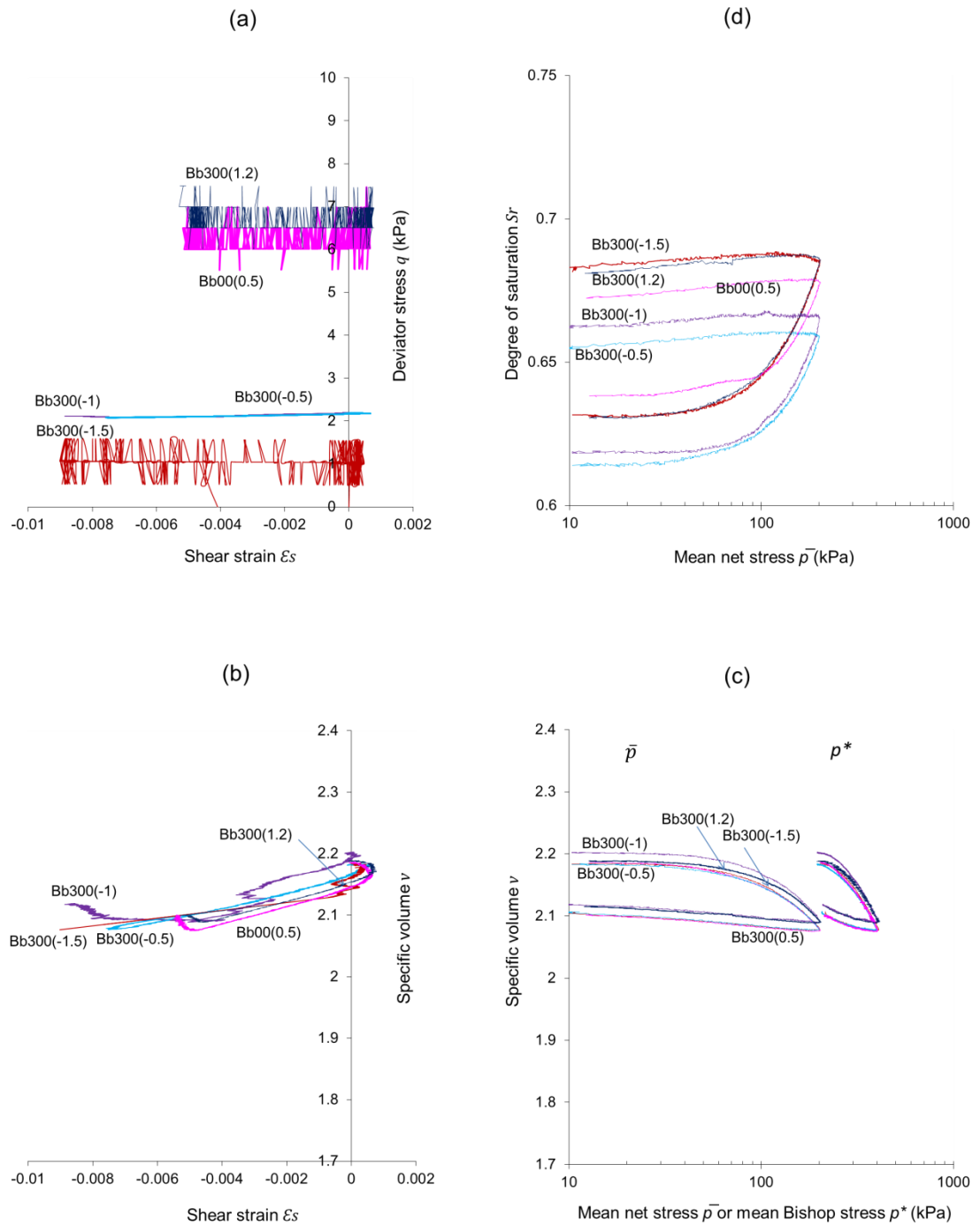


Figure 5.45 Results of loading/unloading stages of Test Series Bb300 in the: (a)  $q: \epsilon_s$  plane, (b)  $v: \epsilon_s$  plane, (c)  $v: \ln \bar{p}$  or  $v: \ln p^*$  plane (d)  $S_r: \ln \bar{p}$  plane

tests (only axial and volumetric strains were recorded). Therefore measurements of shear strains less than 0.002 should not be considered as very reliable.

Plots of specific volume against  $\ln \bar{p}$  or  $\ln p^*$  (see Figure 5.45c) show that the observed decrease in soil stiffness during loading took place very gradually. This response is attributed to the progressive rearrangement of soil fabric which involves a decrease in voids size by slippage at the inter-particle contacts and reorientation of particles and aggregates. Even though both Test Series Ba300 and Bb300 were loaded to the same final value of  $\bar{p}$ , the plastic decrease in specific volume in Test Series Bb300 was  $\approx 0.08$  which was markedly less than that of Test Series Ba300 ( $\approx 0.14$ ). The slopes of pre-yield portions of the compression curves agreed very well with the slopes of unloading portions. Both of these slopes were very similar to those in Test Series Ba300 as will be further discussed in Chapter 6.

Figure 5.45d shows that degree of saturation increased by approximately the same amount ( $\approx 0.05$ ) for all samples which was significantly less than the increase recorded in Test Series Ba300. This is, however, expected in the light of the observation that samples in Test Series Bb300 recorded a smaller reduction of void ratio during compression than samples in Test Series Ba300. As in Test Series Ba300, compression curves in the  $v: \ln p^*$  plane (see Figure 5.45c) were very consistent.

### Series Bc300

Figure 5.46 shows results from the loading/unloading stages of Test Series Bc300 (performed at  $[\Delta q/\Delta \bar{p}] = -1$ ). Inspection of the shear plots indicates a consistent variation of the deviator stress with shear strain with a scatter band that gets larger with progression of loading (see Figure 5.46a). The very first portion of the loading curves showed a stiff response (corresponding to elastic behaviour) followed by a shallow curvature and a final straight part. In terms of the yielding pattern of these loading curves, the transition into the plastic region occurred very gradually and this is attributable to the high level of fabric rearrangement that was taking place during loading. With respect to the unloading behaviour, Figure 5.46a shows a band of parallel curves with slightly higher stiffness at the beginning of the unloading.

In the  $q: \varepsilon_s$  plane (see Figure 5.46a) all curves fell in a narrow band with a scatter of  $\approx 0.03$  in the final shear strain value. As in Test Series Ba300, significant shear strain developed during loading and only a small portion of that strain was recovered during unloading, which is consistent with plastic behaviour.

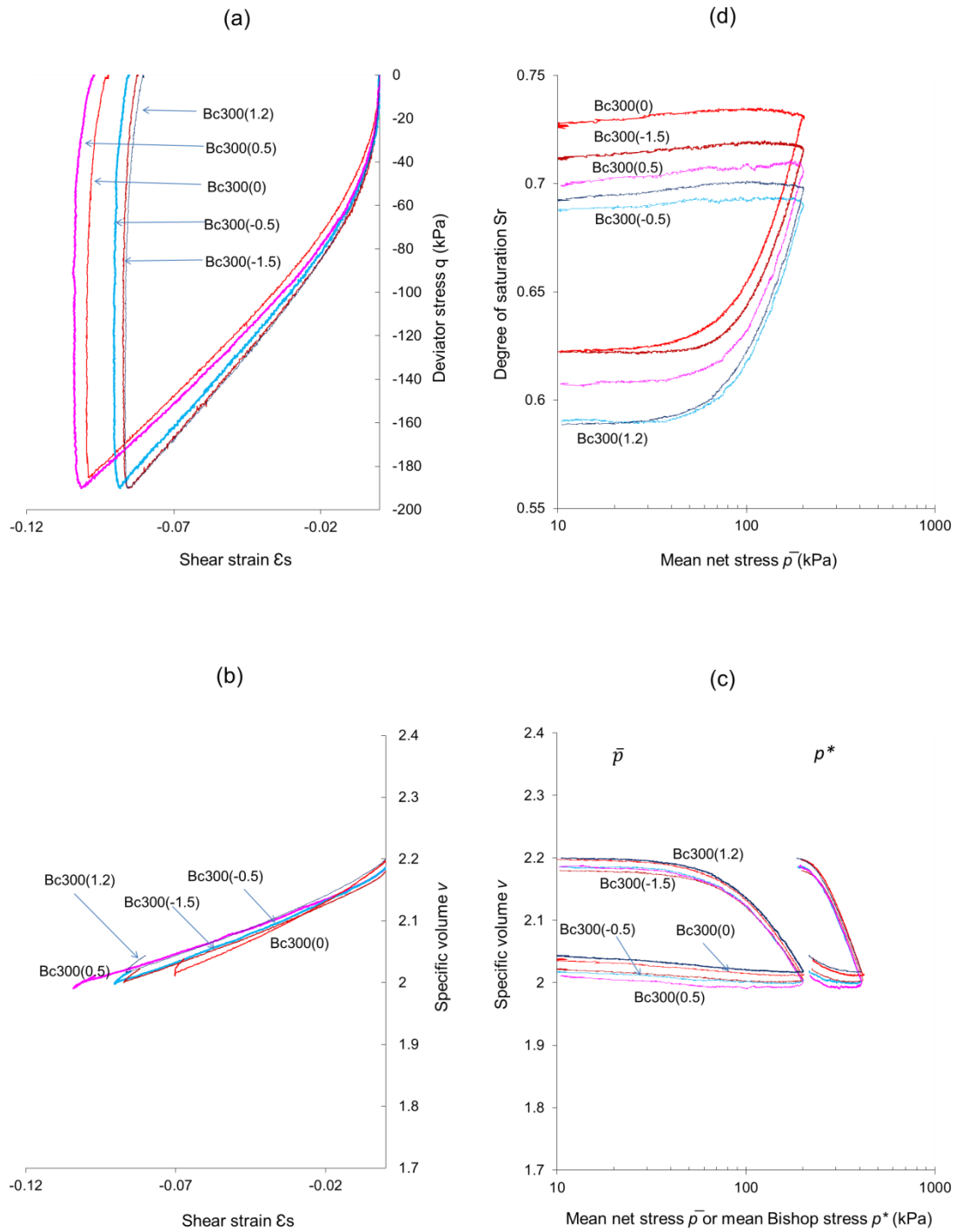


Figure 5.46 Results of loading/unloading stages of Test Series Bc300 in: (a)  $q: \epsilon_s$  plane, (b)  $v: \epsilon_s$  plane, (c)  $v: \ln \bar{p}$  or  $v: \ln p^*$  plane (d)  $S_r: \ln \bar{p}$  plane

The plots of  $v:\varepsilon_s$  in Figure 5.46b indicate that all samples achieved nearly the same amount of change of specific volume during the process of loading and unloading, indicating the repeatability of the behaviour in spite of small differences in the initial specific volume.

The compression behaviour (see Figure 5.46c) was consistent for all the curves. However, the scatter band became slightly bigger during the unloading stages. The compression plot shows a marked change in the slope of the compression curves that is interpreted as yielding. In terms of the plastic decrease in specific volume, Test Series Bc300 showed a change of specific volume of  $\approx 0.16$  by the end of unloading. This amount was only slightly greater than that for Test Series Ba300 but was substantially greater than that in Test Series Bb300. During unloading, all curves run parallel with a slope that was similar to the slope of the pre-yield portion of the loading curves, confirming that elastic behaviour is less sensitive to a change of fabric anisotropy.

The increase in degree of saturation was  $\approx 0.08$  (see Figure 5.46d) and was consistent among all samples in the series. Monitoring of the pore water volume suggested that water flowed out of the sample, which corresponded to a decrease of  $\approx 0.02$  in specific water volume.

### Series Bd100

As previously mentioned, this test series analysed the effect of wetting-induced collapse-compression on the yield surface produced by anisotropic compaction and on critical states. Results from all test stages, for all samples in the series, are shown in Figure 5.47. The behaviour during initial isotropic loading to  $\bar{p} = 90$  kPa is very similar to that of Test Series Bb300 indicating a high level of sample repeatability. The small reduction in specific volume during this initial compression stage (see Figure 5.47c) shows only a slight change in stiffness consistent with elastic behaviour. Correspondingly, the increase in degree of saturation was very modest (see Figure 5.47d). The plots in the  $v:\varepsilon_s$  plane (see Figure 5.47b) show minor initial positive values of shear strains, which became almost zero by the end of the isotropic loading.

The initial isotropic loading stage was followed by a wetting stage to  $s = 100$  kPa, under constant  $\bar{p} = 90$  kPa. This was achieved by a step change of suction at the samples boundary as described in Section 4.5. The variation of water content, specific volume and degree of saturation with time is shown in Figure 5.48. The inflow of water has, in the most cases, ceased after two days (see Figure 5.48a). Figures 5.47c and 5.48b indicate that only collapse compression occurred during wetting. The occurrence of

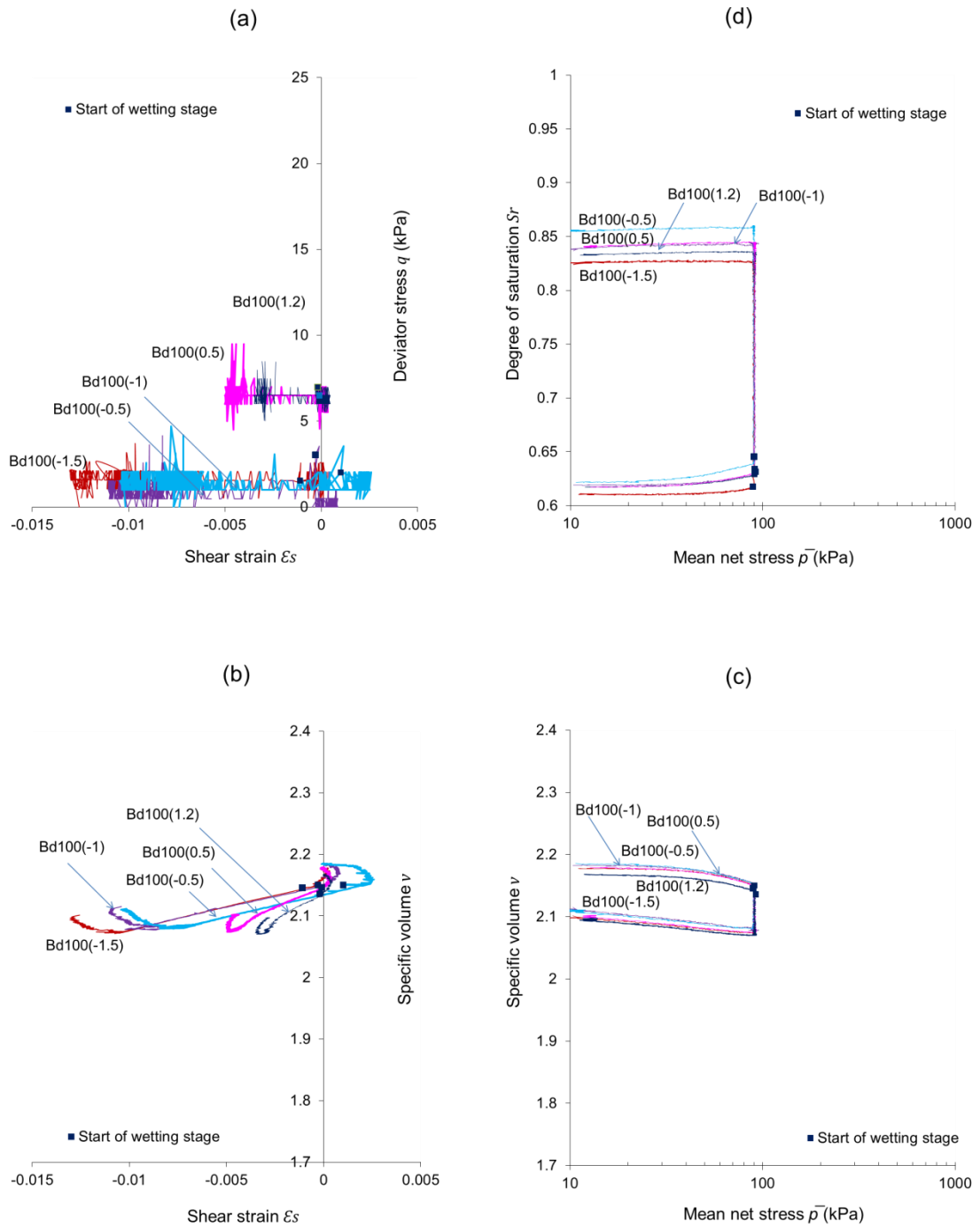


Figure 5.47 Results of loading/wetting/unloading stages of Test Series Bd100 in: (a)  $q: \varepsilon_s$  plane, (b)  $v: \varepsilon_s$  plane, (c)  $v: \ln \bar{p}$  or  $v: \ln p^*$  plane (d)  $S_r: \ln \bar{p}$  plane

collapse compression immediately after the start of wetting indicates that the stress state is just on the yield surface at the end of the previous elastic loading. The specific volume at the end of wetting was very similar to that attained during isotropic loading of the unsaturated sample B100(0) to  $\bar{p} = 90$  kPa (see Figure 5.31c).

The  $q:\varepsilon_s$  and  $v:\varepsilon_s$  plots (see Figures 4.47a and 4.47b) show that, although the mean net stress was kept constant, the samples showed a small negative shear strain during wetting. Once again, the amount of shear strains developed during wetting was approximately of the same magnitude to that in Sample B100(0) (during isotropic loading to  $\bar{p} = 90$  kPa). All of this confirms that reducing suction to 100 kPa under constant stresses has similar effects to those observed during application of the same load under unsaturated conditions.

Furthermore, by the end of unloading, the total reduction in specific volume and the amount of shear strains were very similar to those in Test Series Bb300. This similarity is helpful in comparing yield patterns during subsequent probing/shearing stages at these two constant suctions. As expected, the samples behaved linearly during unloading in the  $v:\ln\bar{p}$  plane, with similar slopes as observed in the unloading stages of previous tests. This confirms that the effect of anisotropy and suction on elastic behaviour is only minor (see Section 6.1 for further discussion of this aspect). Inspection of Figure 5.48 shows that, by the time the inflow of water ceased, the specific volume was still showing a small gradual decrease with time, which could be attributed to delayed fabric rearrangement.

Finally, the large increase in the degree of saturation of  $\approx 0.22$  (see Figure 5.47d and Figure 4.48c) is consistent with both the observed flow of water into the sample and the decrease in pore volume during wetting.

## 5.6.2 Probing/ shearing stages

Results from the probing/shearing stages of Test Series Ba300, Bb300, Bc300 and Bd100 are presented in this section, grouped according to the slope of the probing stress path (i.e.  $[\Delta q/\Delta\bar{p}] = 2, 1.2, 0.5, 0, -0.5, -1$  or  $-1.5$ ). To aid clarity, compression curves are presented only in the  $v:\ln\bar{p}$  plane in this sub-section.

### Probing at $[\Delta q/\Delta\bar{p}] = 2$

During performance of Test Series Ba300, it was thought that probing at  $[\Delta q/\Delta\bar{p}] = 2$  could add more information in terms of yielding. However, it was subsequently found

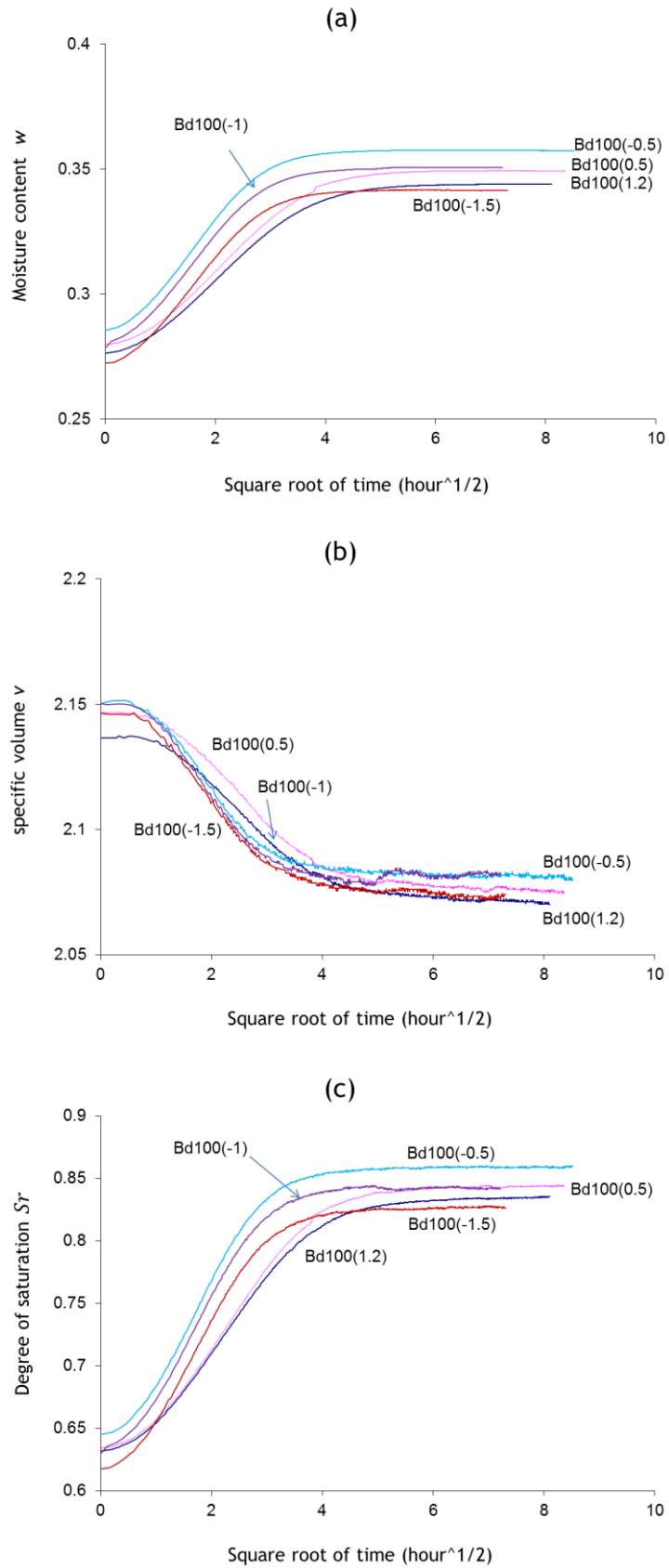


Figure 5.48 Results of wetting stages of Test Series Bd100 in: (a) water content-square root of time plane; (b) specific volume-square root of time plane; (c) degree of saturation-square root of time plane

that the sample reached peak deviator stress almost elastically along this probing path, and then failed due to strain localisation (as confirmed by visual inspection of the shear band at the end of the test). Consequently, all other tests at  $[\Delta q/\Delta \bar{p}] = 2$  planned for subsequent test series were cancelled. Figure 5.49 compares the results of Test Ba300(2) (including the initial loading/unloading stage) with those of Test B300(2). Figure 5.49a indicates that Sample Ba300(2) showed a slightly stiffer response and higher peak deviator stress than B300(2), which is expected as the former had denser packing.

During probing in Test Ba300(2), there was a very slight decrease in specific volume (see Figures 5.49b and 5.49c) and the soil response was mainly elastic. It could be noticed that both samples reached the peak strength at nearly the same total shear strain. Although both samples started from very similar values of specific volume, they reached the steady state at very different values of specific volume. As already mentioned, unfortunately no useful information could be inferred in terms of the yield stresses from Test Ba300(2). The plot of the degree of saturation (see Figure 5.49d) shows that significant water flow into the sample took place beyond peak. This was probably an effect of strain localisation and the degree of saturation measured after this point was, consequently, considered unreliable.

### Probing at $[\Delta q/\Delta \bar{p}] = 1.2$

Three probing tests were conducted at  $[\Delta q/\Delta \bar{p}] = 1.2$  (i.e. Bb300(1.2), Bc300(1.2) and Bd100(1.2)). Figure 5.50 illustrates the results of Tests Bb300(1.2) and Bc300(1.2) along with the loading stage of a single test from Test Series Ba300 (which was also performed at  $[\Delta q/\Delta \bar{p}] = 1.2$ ). Figure 5.50b shows that the probing stages in Tests Bb300(1.2) and Bc300(1.2) start from very different values of specific volume and shear strains which must be taken into consideration while interpreting the results. Generally, Sample Bb300(1.2) showed a very similar response to that observed during the loading stage of Series Ba300 (Figure 5.50a) indicating that only a moderate change in fabric anisotropy took place during the previous isotropic loading stage of Bb300(1.2). The change in gradient of the shear curves in Figures 5.50a (associated with yielding) is more evident in Sample Bb300(1.2) than in Sample Bc300(1.2). At  $[\Delta q/\Delta \bar{p}] = 1.2$ , Sample Bc300(1.2) is expected to exhibit greater rearrangement of soil fabric (associated to hardening due to changes of anisotropy) than sample Bb300(1.2) and therefore less clear yield patterns. Sample Bc300(1.2) could have a peak deviator stress twice as much as that of Sample Bb300(1.2) (bearing in mind that this sample was not yet at peak by the end of the probing stage, due to equipment limitation). This could be attributed to the difference in void ratio between these two samples at the beginning of probing.

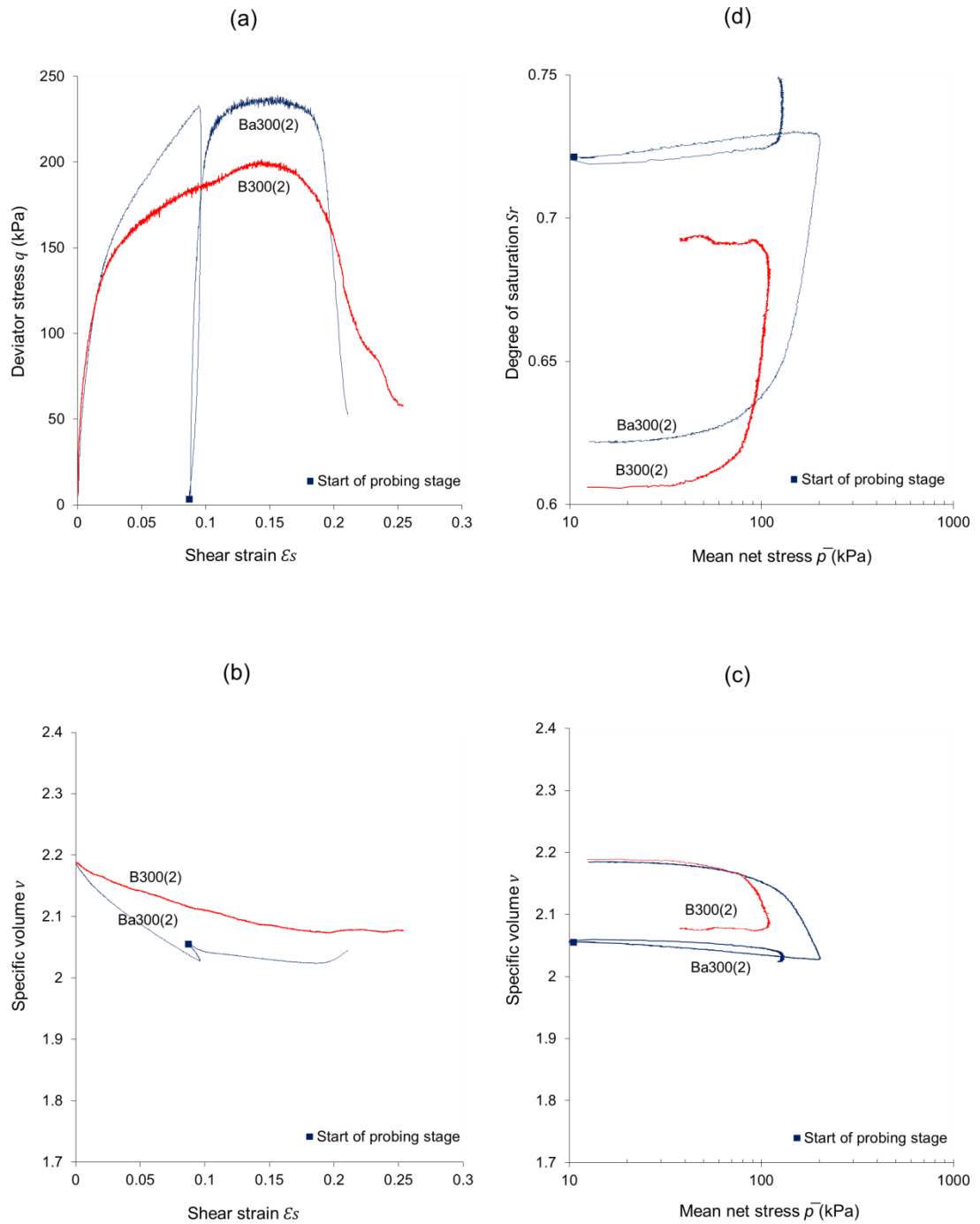


Figure 5.49 Results of the probing stages of Tests Ba300(2) and B300(2) in: (a)  $q$ :  $\epsilon_s$  plane, (b)  $v$ :  $\epsilon_s$  plane, (c)  $v$ :  $\ln \bar{p}$  plane (d)  $S_r$ :  $\ln \bar{p}$  plane

Plots in the  $v:\varepsilon_s$  plane in Figure 5.50b show that the variations of specific volume of Samples Bb300(1.2) and Bc300(1.2) did not tend to converge during probing. This suggests that probing at  $[\Delta q/\Delta \bar{p}] = 1.2$  up to failure was not enough to erase the effects of previous history, which seems to contradict the uniqueness of behaviour at critical states.

In the compression plane (see Figure 5.50c), the compression curves of Samples Bb300(1.2) and Bc300(1.2) showed a small hysteric response over the pre-yield portion of probing which is consistent with the expected elastic response during reloading. Furthermore, the slopes of the pre-yield portion of probing were very similar confirming the assumption that fabric anisotropy does not affect elastic behaviour. Sample Bb300(1.2) showed a slightly sharper change in stiffness than sample Bc300(1.2) during probing. This fits with the idea that, in the former case, fabric anisotropy at the start of probing is closer to the target fabric anisotropy that stress state is attempting to achieve (hence less hardening due to change of anisotropy is expected to occur during probing).

Furthermore, the stress at which the change in soil stiffness occurs is much less than the maximum stress that the sample has experienced during the loading stage (i.e.  $\bar{p} = 90$  kPa). This observation fits with the classical assumption of an elliptical shape of the yield surface. Inspection of Figure 5.50c suggests that samples Bb300(1.2), Bc300 (1.2) and Ba300 tend to converge towards a single compression curve. This could illustrate the role of plastic strains in altering fabric anisotropy in such a way that produces unique fabric arrangement with the progression of loading. But then, it would be difficult to illustrate the substantial difference in soil stiffness among these samples observed in the  $q:\varepsilon_s$  plane (see Figure 5.50a) if unique fabric arrangement is achieved.

Plots of the degree of saturation (see Figure 5.50d) show that Samples Bb300(1.2) and Bc300(1.2) exhibited the same increase in degree of saturation ( $\approx 0.13$ ) during probing (note that both the samples showed small decreases in specific water volume  $\approx 0.01$ ) which is consistent with the decrease of voids size. Figure 5.50d also shows that the hysteric response observed in the compression plots (see Figure 5.50c) also exists in the degree of saturation plots, which confirms once again the strong link between the variation of voids size and degree of saturation.

Figure 5.51 shows the results of Tests Bd100(1.2) and Bb300(1.2). Apart from the stabilising effect of meniscus water at the higher suction, the pattern of evolution of the shear strains (see Figure 5.51a) was very similar for both these tests. This indicates that,

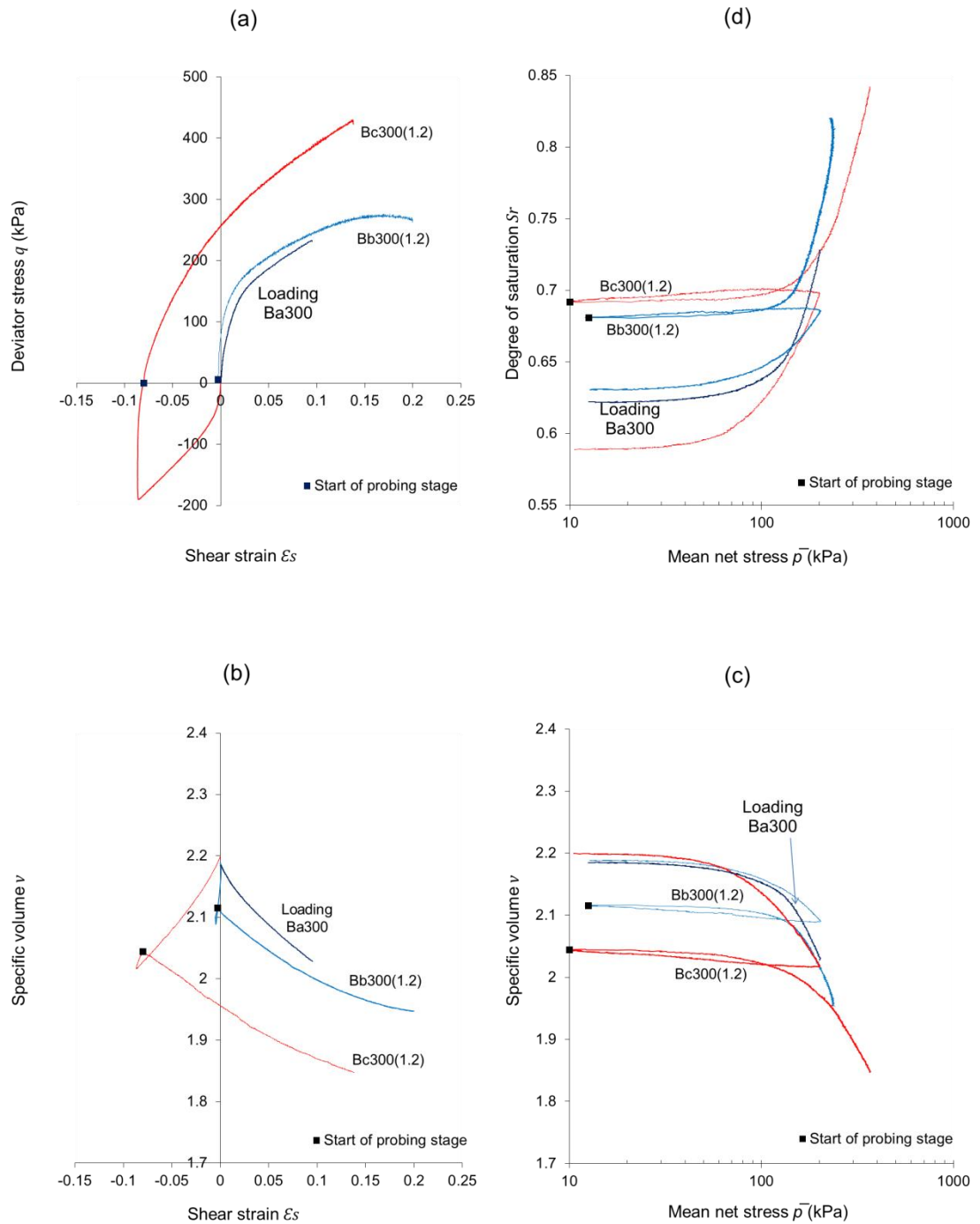


Figure 5.50 Results of the probing stages of Test Bb300(1.2) and Bc300(1.2) in: (a)  $q: \epsilon_s$  plane, (b)  $v: \epsilon_s$  plane, (c)  $v: \ln \bar{p}$  plane (d)  $S_r: \ln \bar{p}$  plane

by the end of the unloading stage, both samples have the same fabric which, in turn, confirms that the new mechanical properties produced by plastic collapse-compression during wetting under constant isotropic stress condition were very similar to those produced by isotropic loading at  $s = 300$  kPa. Further confirmation of this can be obtained by inspection of Figure 5.51b where the pattern of the variation of specific volume was very similar for both samples. However, no test was conducted to investigate what would happen to the soil fabric if wetting was conducted under an anisotropic stress state.

Figure 5.51c shows that, for Sample Bd100(1.2), the mean net stress at which a sharp decrease in soil stiffness occurs, approximately coincides with that observed in the  $q:\varepsilon_s$  plane (see Figure 5.51a). The gradient of the post-yield compression curve is smaller for Sample Bd100(1.2) than for Sample Bb300(1.2). This is similar to what observed when comparing the post-yield gradients of corresponding tests in Test Series B100 and B300 or A100 and A300.

Finally, investigation of Figure 5.51d shows that a significant increase in the degree of saturation ( $\approx 0.12$ ) occurred during probing for both samples.

### Probing at $[\Delta q/\Delta \bar{p}] = 0.5$

Four probing tests were conducted at  $[\Delta q/\Delta \bar{p}] = 0.5$  (i.e. Ba300(0.5), Bb300(0.5), Bc300(0.5) and Bd100(0.5)). Figure 5.52 illustrates the results of Tests Ba300(0.5), Bb300(0.5) and Bc300(0.5). The shear stage of Sample Bc300(0.5) was not completed due to equipment limitations on axial displacement. Visual inspection (through the transparent cells wall) showed buckling of Sample Ba300(0.5) during the shear stage which might be attributed to the fact that the sample was not perfectly centred during mounting or to an irregular strain distribution across the sample (possibly due to poor sample homogeneity). The results of the shear stage of this test were, therefore, considered highly unreliable.

Figure 5.52a shows that the change in shear strain during probing was highest in Sample Bc300(0.5) whereas it was lowest in Sample Ba300(0.5). Samples Ba300(0.5) and Bb300(0.5) showed a noticeable change in shear stiffness, during probing at  $q = 175$  kPa and  $q = 80$  kPa, respectively, whereas there was no such obvious change in shear stiffness for Sample Bc300(0.5). Moreover, Samples Bb300(0.5) and Bc300(0.5) subsequently showed slight increase in the slope of the continuous shear curve which cannot be seen in Sample Ba300(0.5). The decrease of pores size during probing loading is accompanied by a distortion of the pore shape caused by reorientation of particles and

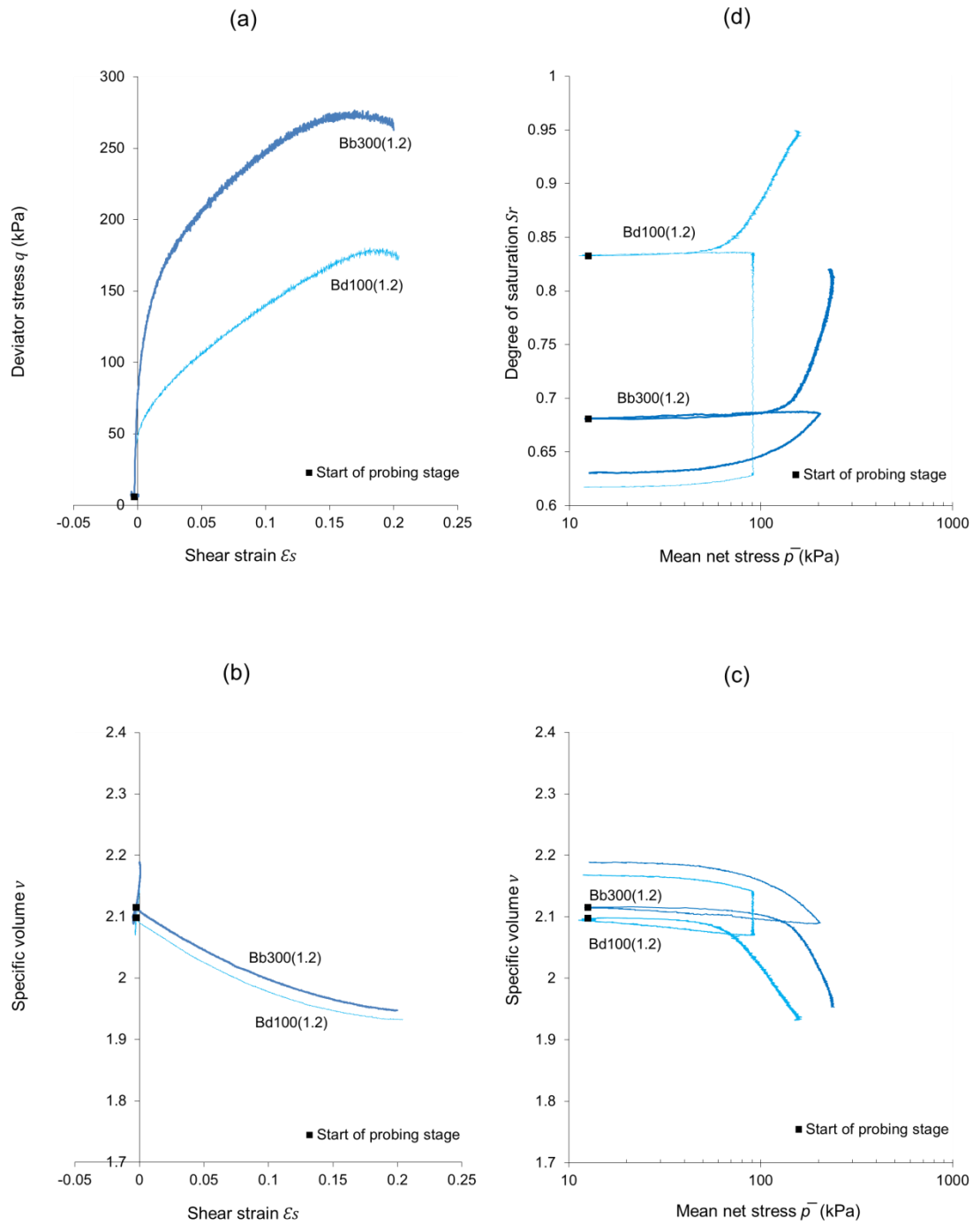


Figure 5.51 Results of the probing stages of Tests Bd100(1.2) and Bb300(1.2) in: (a)  $q: \epsilon_s$  plane, (b)  $v: \epsilon_s$  plane, (c)  $v: \ln \bar{p}$  plane (d)  $S_r: \ln \bar{p}$  plane

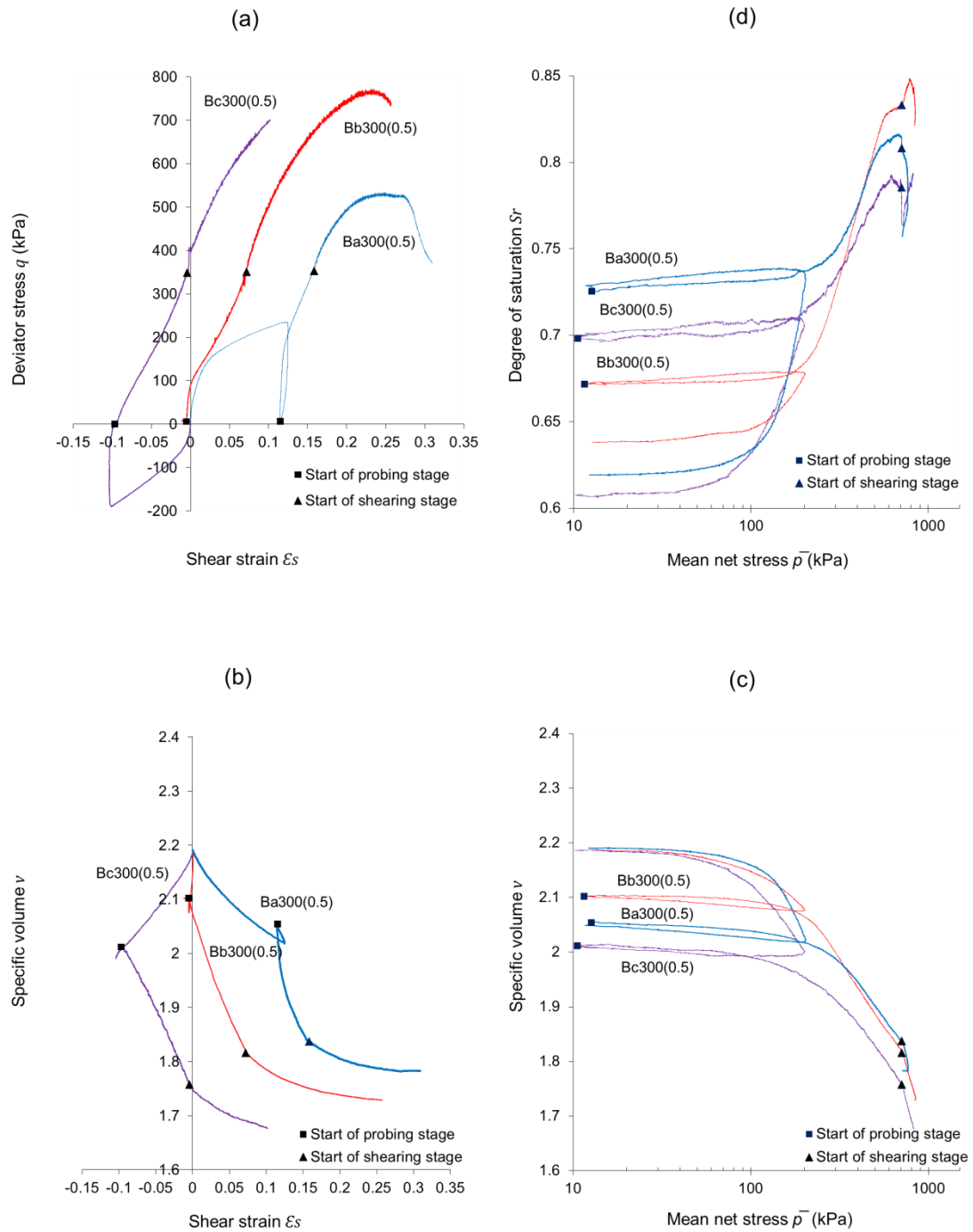


Figure 5.52 Results of the probing/shearing stages of Tests Ba300(0.5), Bb300(0.5) and Bc300(0.5) in: (a)  $q: \epsilon_s$  plane, (b)  $v: \epsilon_s$  plane, (c)  $v: \ln \bar{p}$  plane (d)  $S_r: \ln \bar{p}$  plane

aggregates. The amount of reorientation depends on the difference between the initial soil fabric, at the start of probing, and the target soil fabric, controlled by the imposed stress path. Results for Samples Bb300(0.5) and Bc300(0.5) suggests an increase in soil stiffness after yielding which results from an increase in interlocking among aggregates that mobilises higher shear strength.

Inspection of the  $q:\varepsilon_s$  plots (see Figure 5.52b) shows that values of the specific volume at peak deviator stress (recall that Test Bc300(0.5) was stopped before reaching peak strength) were very different. This means that, for this particular stress path slope of  $[\Delta q/\Delta \bar{p}] = 0.5$ , probing to  $\bar{p} = 590$  kPa was not enough to fully erase the fabric anisotropy developed during the previous loading stage. Further inspection also indicates that the specific volume of Samples Ba300(0.5) and Bb300(0.5) had almost stabilized as these samples approached peak deviator stress.

The yield stresses of Samples Ba300(0.5) and Bb300(0.5) can be easily identified by the sharp change of soil stiffness in the compression plane (see Figure 5.52c). However, no sharp change in stiffness could be noticed for Sample Bc300(0.5). The above observation is also in good agreement with the behaviour observed in the  $q:\varepsilon_s$  plane (see Figure 5.52a).

Inspection of Figure 5.52d indicates that, during probing, Tests Ba300(0.5), Bb300(0.5) and Bc300(0.5) showed an increase in degree of saturation of  $\approx 0.08$ ,  $0.16$  and  $0.09$ , respectively. The largest increase was in Sample Bb300(0.5), which corresponded to the largest decrease in specific volume during probing. Significant outflow of water was recorded from the samples during probing (corresponding to a decrease in specific water volume of  $0.16$ ,  $0.14$  and  $0.08$  for Samples Ba300(0.5), Bb300(0.5) and Bc300(0.5) respectively). Indeed, the degree of saturation of Samples Ba300(0.5) and Bc300(0.5) was decreasing during the late stages of probing and this decrease continued during the subsequent shear stage. This response suggests that, during the late stages of probing and subsequent shearing, water outflow had a dominating effect on the variation of degree of saturation compared to the corresponding decrease of pore volume.

Figure 5.53 compares the results from Tests Bd100(0.5) and Bb300(0.5). The  $q:\varepsilon_s$  curve of Test Bd100(0.5) shows a marked stiffening of the soil response during probing, which confirms the observation already made for Samples Bb300(0.5) and Bc300(0.5). Similarly, the compression curve (see Figure 5.53c) showed a corresponding increase in stiffness at  $\bar{p} \approx 250$  kPa.

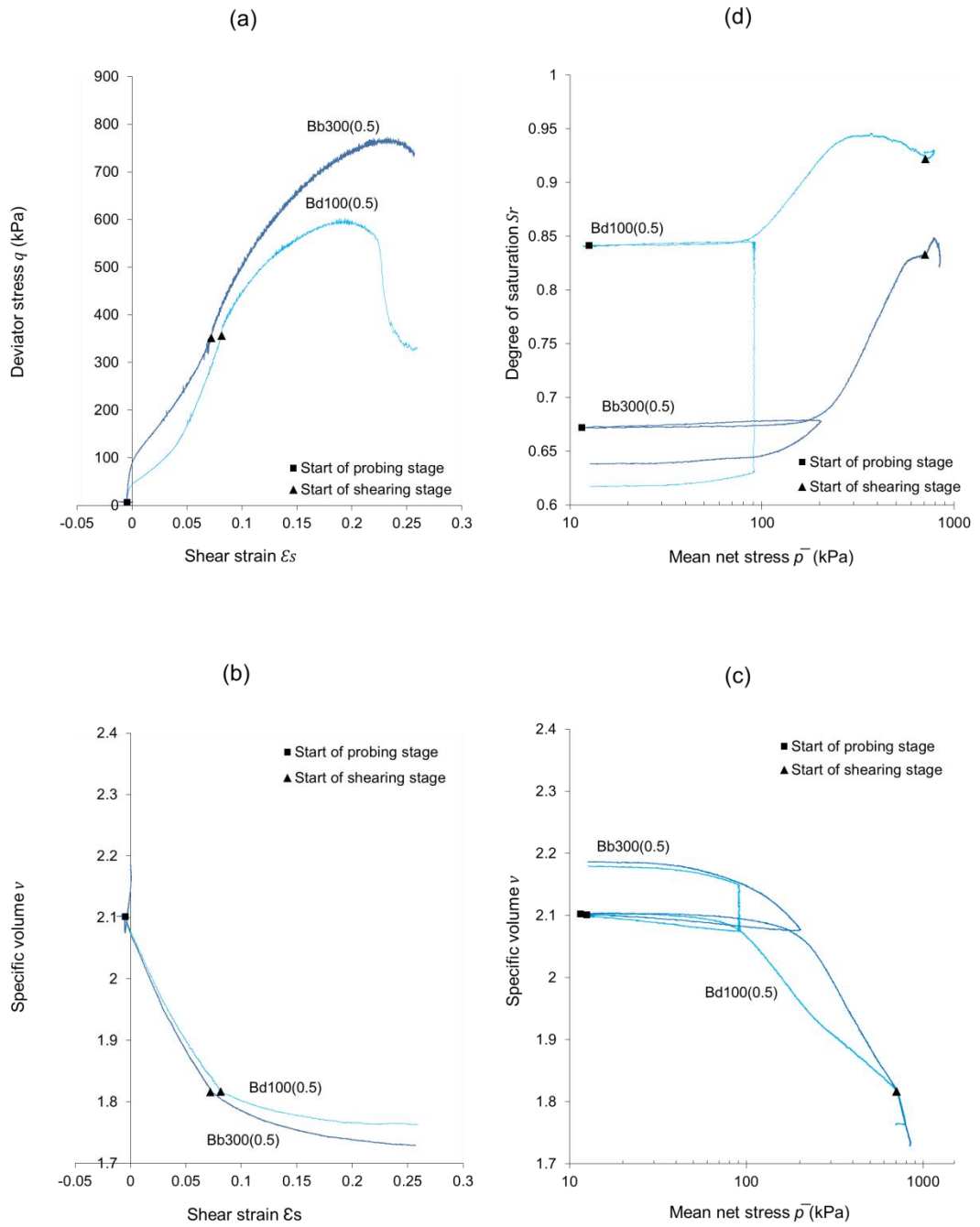


Figure 5.53 Results of the probing/shearing stages of Tests Bd100(0.5) and Bb300(0.5) in: (a)  $q: \epsilon_s$  plane, (b)  $v: \epsilon_s$  plane, (c)  $v: \ln \bar{p}$  plane (d)  $S_r: \ln \bar{p}$  plane

Further inspection of Figure 5.53 suggests that, by the end of probing, the soil fabric was very similar (in both samples) corresponding to very similar values of shear and volumetric strains. Also, at peak deviator stress, the value of specific volume seemed to have stabilized with loading.

Inspection of the plot in Figure 5.53d shows that, for Test Bd100(0.5), the degree of saturation gradually increased during probing by  $\approx 0.09$  to  $\bar{p} \approx 250$  kPa but then gradually decreased by  $\approx 0.02$  to  $\bar{p} \approx 590$  kPa. This later decrease in degree of saturation coincides with the stiffening of the corresponding curve in the compression plane and with a decrease in specific water volume of  $\approx 0.17$ .

### Probing at $[\Delta q/\Delta \bar{p}] = 0$

Two tests were conducted at  $[\Delta q/\Delta \bar{p}] = 0$  (i.e. Ba300(0) and Bc300(0)). Figure 5.54 illustrates the results from these two tests, together with the results of Test B300(0). It is worth mentioning that no shear stage was conducted for Test Bc300(0), due to equipment limitation on axial displacement.

Figure 5.54a shows that, during probing at  $[\Delta q/\Delta \bar{p}] = 0$ , the shear strains changed from  $\approx 0.10$  to  $\approx 0.08$  in Test Ba300(0). This small negative increase in shear strain was similar to that observed in Test B300(0), suggesting that the previous loading/unloading at  $[\Delta q/\Delta \bar{p}] = 1.2$  in Test Ba300(0) had not significantly altered the anisotropy of the fabric. In contrast, during the probing stage of Test Bc300(0) there was a positive increment of shear strain (from  $\approx -0.09$  to  $\approx -0.08$ ). This indicates that, as expected, the previous loading/unloading at  $[\Delta q/\Delta \bar{p}] = -1$  in Test Bc300(0) had significantly altered the anisotropy of the fabric. During shearing, Sample Ba300(0) showed a substantially stiffer response than sample B300(0) (see Figure 5.54a). This is because the void ratio of sample Ba300(0) was substantially lower than that of Sample B300(0), consistent with the fact that shearing started at  $\bar{p} = 590$  kPa for Samples Ba300(0) and at  $\bar{p} = 300$  kPa for Sample B300(0). The peak deviator stress of Sample Ba300(0) was therefore significantly higher than that of Sample B300(0) (see Figure 5.54b). Similarly, at peak strength, the specific volume was lower for Sample Ba300(0) than for Sample B300(0). Note that, in both cases, by the time samples were at peak strength, the specific volume was only slightly decreasing with increasing shear strains (see Figure 5.54b).

Compression behaviour during probing was very similar for Tests Ba300(0) and Bc300(0), as shown in Figure 5.54c. The gradient of the post-yield portion of these compression curves was very similar, and only slightly different from that of Test B300(0), confirming erasure of any anisotropic fabric developed during the previous loading/unloading stages.

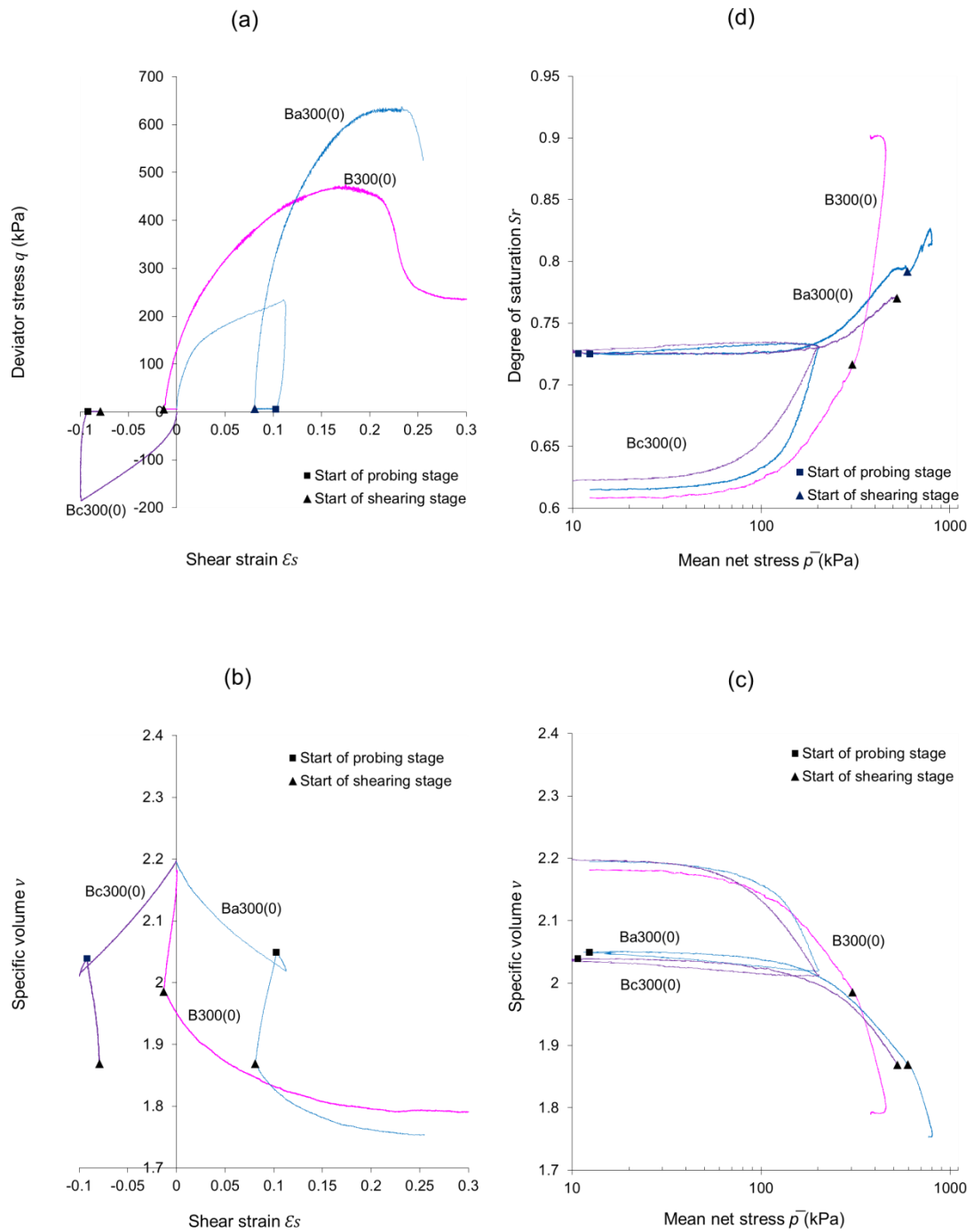


Figure 5.54 Results of the probing/shearing stages of Tests Ba300(0), Bc300(0) and B300(0) in: (a)  $q$ :  $\epsilon_s$  plane, (b)  $v$ :  $\epsilon_s$  plane, (c)  $v$ :  $\ln \bar{p}$  plane (d)  $S_r$ :  $\ln \bar{p}$  plane

Inspection of Figure 5.54d indicates an increase in degree of saturation during probing of  $\approx 0.05$  and  $\approx 0.07$  for Samples Ba300(0) and Bc300(0), respectively. During shearing of Sample Ba300(0), the degree of saturation increased by  $\approx 0.03$ . The specific water volume decreased by  $\approx 0.08$  during probing of Samples Ba300(0) and Bc300(0), and  $\approx 0.08$  during shearing of Sample Ba300(0).

### Probing at $[\Delta q/\Delta \bar{p}] = -0.5$

The results from three tests conducted at  $[\Delta q/\Delta \bar{p}] = -0.5$  (i.e. Ba300(-0.5), Bb300(-0.5) and Bc300(-0.5)) are plotted in Figure 5.55 together with the results of Test B300(-0.5). Results in the  $q:\varepsilon_s$  plane (see Figure 5.55a) indicate that, at the beginning of probing, Sample Ba300(-0.5) showed a less stiff response than other samples. Identification of the yield stress is easier in Samples Bb300(-0.5) and Bc300(-0.5) than in Sample Ba300(-0.5) due to the existence of a clear change of gradient of the stress-strain curves at  $q \approx 120$  kPa and  $q \approx 60$  kPa, respectively. This behaviour indicates that, after yielding, the reorientation of particles and aggregates was larger in Sample Ba300(-0.5) than in Samples Bb300(-0.5) and Bc300(-0.5), due to the greater difference between initial and target soil fabrics. Samples Bb300(-0.5) and Bc300(-0.5) showed a slight stiffening of the response with progression of probing. This behaviour was repeatedly reported for samples loaded at low slopes of  $[\Delta q/\Delta \bar{p}] = 0.5$  and  $[\Delta q/\Delta \bar{p}] = -0.5$ , especially when a significant difference exists between the slopes of the loading and probing paths. In this case, significant hardening due to changes of anisotropy (i.e. rearrangement of particles and aggregates) must occur during probing in order to move towards a different target fabric anisotropy, which can cause fabric interlocking and, hence, an increase in mobilised shear strength.

At the beginning of the shear stage, a very stiff response was observed. This was followed by a gradual decrease in stiffness as shearing progressed. The initial stiff response is associated to a marked change of stress path (e.g. from  $[\Delta q/\Delta \bar{p}] = -0.5$  to  $[\Delta q/\Delta \bar{p}] = 3$ ) which might initially result in elastic behaviour (as the stress path moves inside the yield surface before yielding again on a different position). During shearing, the shape of the stress-strain curves was similar in all the tests, with equal values of peak deviator stress and rather large changes of shear strains at failure. Figure 5.55b shows that specific volume stopped changing at peak strength for Samples Ba300(-0.5) and Bb300(-0.5). In contrast, the specific volume of Sample Bc300(-0.5) was still steadily decreasing.

In the  $v:\ln \bar{p}$  plane (see Figure 5.55c), the transition from the elastic to the elasto-plastic behaviour took place more gradually in Sample Ba300(-0.5) than in Samples Bb300(-0.5) and Bc300(-0.5). This behaviour is consistent with that observed in the  $q:\varepsilon_s$  plane (see

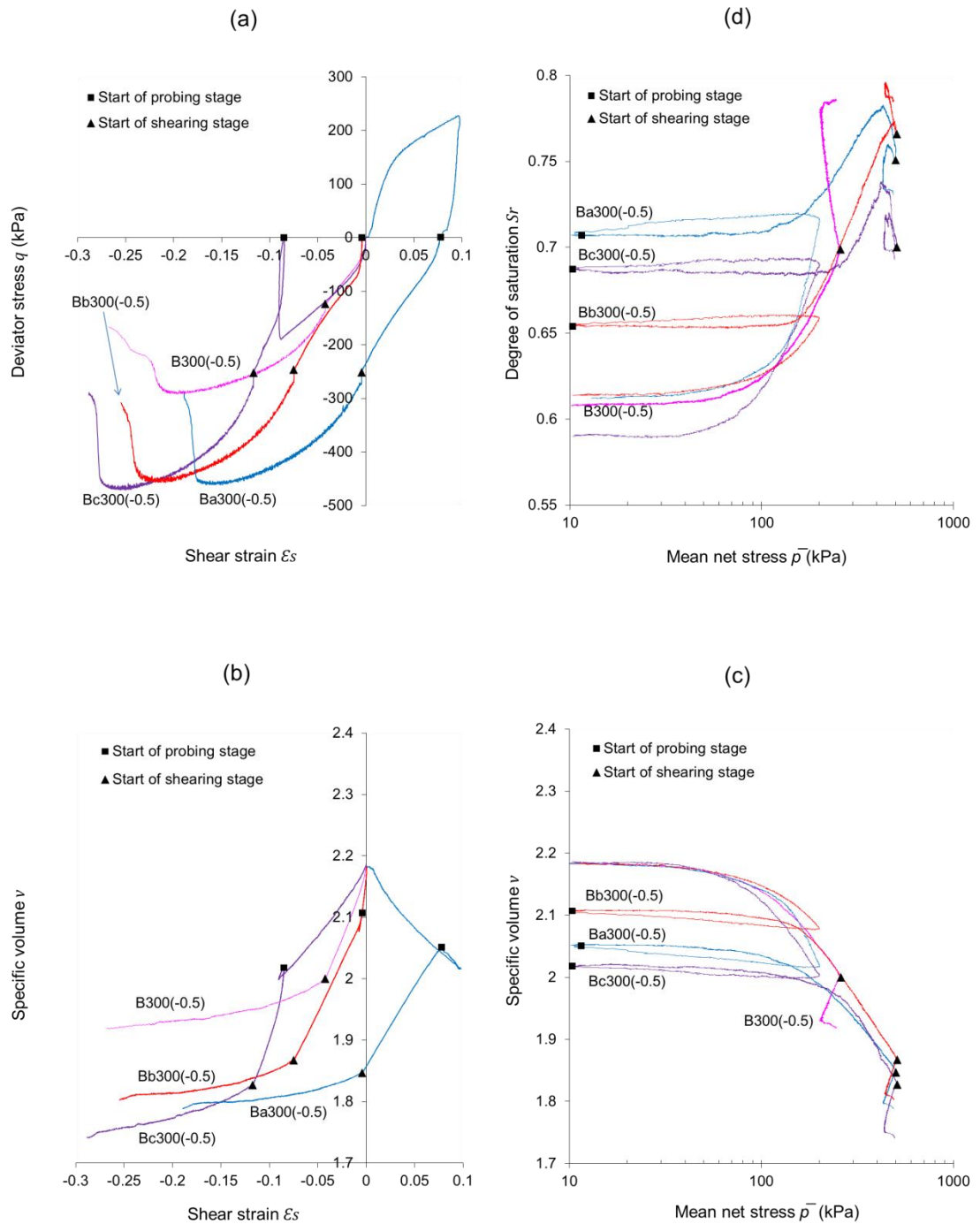


Figure 5.55 Results of the probing/shearing stages of Tests Ba300(-0.5), Bb300(-0.5), Bc300(-0.5) and B300(-0.5) in: (a)  $q: \epsilon_s$  plane, (b)  $v: \epsilon_s$  plane, (c)  $v: \ln \bar{p}$  plane (d)  $S_r: \ln \bar{p}$  plane

Figure 5.55a) and might be explained by the same physical argument used during interpretation of those stress-strain curves. The slopes of the post-yield portions of the compression curves were very similar and their positions were fairly close. The overlap of the compression curves of Samples B300(-0.5) and Bb300(-0.5) suggests that, despite the initial difference in anisotropy, both samples developed the same fabric arrangement under subsequent probing.

Figure 5.55d shows that, during the probing, Samples Ba300(-0.5), Bb300(-0.5) and Bc300(-0.5) exhibited an initial increase in degree of saturation of  $\approx 0.08$ ,  $0.12$  and  $0.04$  respectively, followed by a decrease of  $\approx 0.03$  at relatively high mean net stress. On the other hand, the specific water volume continuously decreased during probing and shearing in all samples by  $\approx 0.12$ . The initial increase in degree of saturation was therefore directly related to the decrease in pore volume and the later drop in degree of saturation could be attributed to the stiffening of the compression curves. The discrepancy in the variation of degree of saturation among samples during shearing could be related to the lower value of pore water pressure which triggered air bubbles out of solution as explained previously.

The results from Test Bd100(-0.5) are plotted in Figure 5.56 along with the results from Tests B100(-0.5) and Bb300(-0.5). The stiffer part of the stress-strain curve at the beginning of probing was smaller in Sample Bd100(-0.5) than in Test Bb300(-0.5) (see Figure 5.56a), which is consistent with the increase in stiffness/strength observed at larger suction levels. The shape of shear curve of Sample Bd100(-0.5) was very similar to that of Sample B100(-0.5) suggesting that the change of fabric anisotropy during wetting was only moderate. The initial stiff response was followed by a clear reduction of stiffness at  $\varepsilon_s \approx 0.01$ . The shape of the shear curves of Samples Bd100(-0.5) and Bb300(-0.5) indicates a significant increase in soil stiffness during probing. As mentioned earlier, this increase is attributed to a combination of a decrease in voids size caused by slippage at inter-particles contacts and a rotation of particles/aggregates produced by the difference between the current and target levels of anisotropy.

The increase in soil stiffness was more apparent in Sample Bd100(-0.5) than in Sample Bb300(-0.5), which suggests that the existence of fewer voids affected by meniscus water (at lower suction) facilitates the evolution of soil fabric. Inspection of behaviour during shearing suggests that the soil initially behaved elastically (corresponding to a stress path taking place inside the yield surface). Shearing of Samples B300(-0.5) and Bd100(-0.5) started from a radial net stress of 300 kPa and 590 kPa respectively so that the same response would not be expected during the shearing stage.

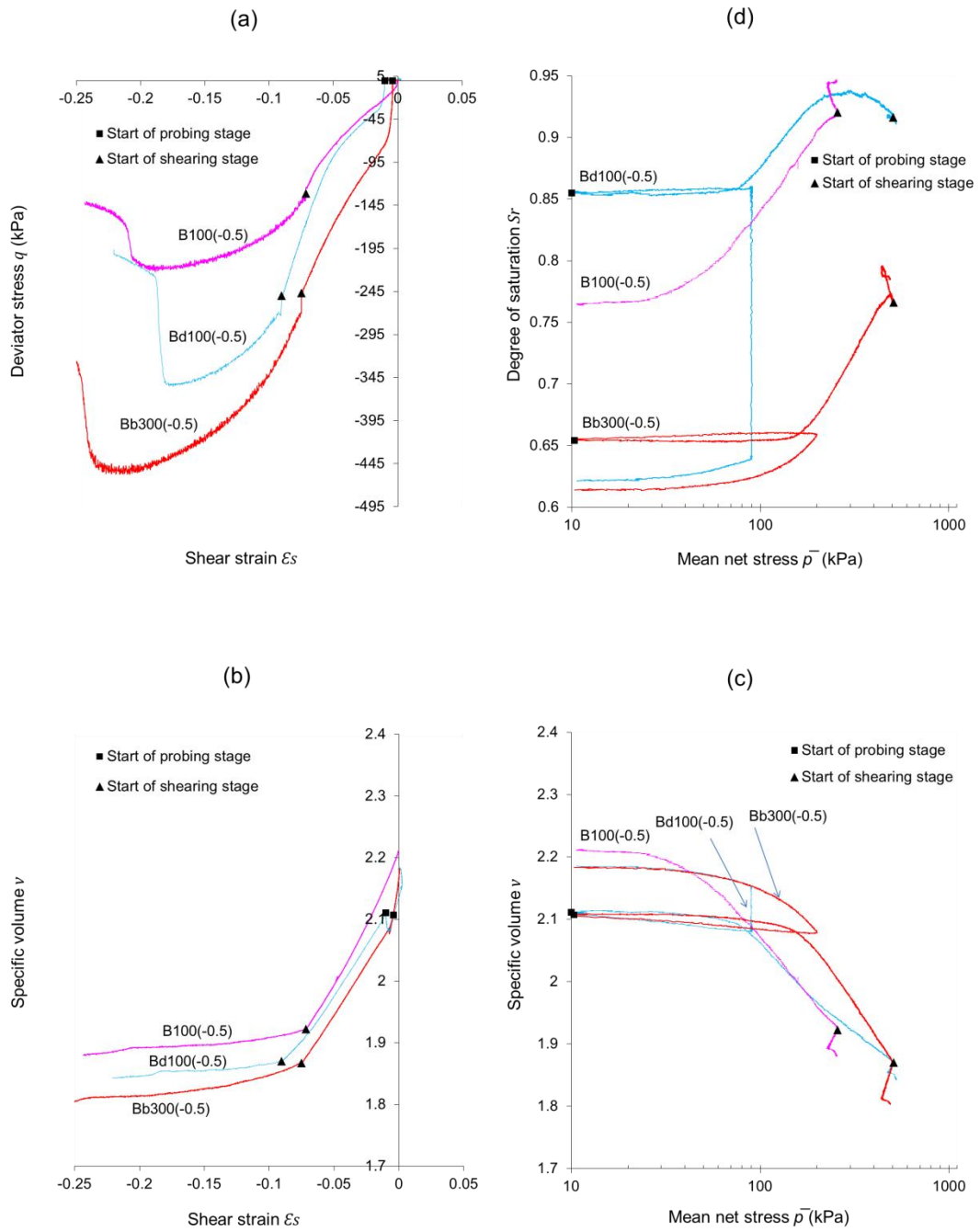


Figure 5.56 Results of the probing/shearing stages of Tests Bd100(-0.5), B100(-0.5) and Bb300(-0.5) in: (a)  $q: \epsilon_s$  plane, (b)  $v: \epsilon_s$  plane, (c)  $v: \ln \bar{p}$  plane (d)  $S_r: \ln \bar{p}$  plane

Figure 5.56b shows that Samples Bd100(-0.5) and Bb300(-0.5) achieved almost the same specific volume by the end of the probing stage. Also, in both cases, the variation of specific volume had almost become negligible by the time the peak deviator stress was reached.

Figure 5.56c indicates that the initial elastic loading of Samples Bd100(-0.5) and Bb300(-0.5) produced almost identical response, confirming good repeatability of tests. With progression of plastic straining, the compression curves of Samples Bd100(-0.5) and B100(-0.5) tended to merge which indicates that, by the end of probing, the fabric of both samples had become similar. The later increase in stiffness (indicated by the flattening of the compression curve) approximately coincides with the attainment of very large values of degree of saturation (see Figure 5.56d) and with the stiffening of the shear curve (see Figure 5.56a).

Inspection of Figure 5.56d shows that, during probing, the degree of saturation of Sample Bd100(-0.5) initially increased to  $\approx 0.93$  but then gradually decreased back to 0.91. At the same time, a significant outflow of water was taking place from the sample (corresponding to a change of specific water volume of  $\approx -0.15$ ). This outflow was expected as the probing stage began at a relatively high degree of saturation ( $\approx 0.86$ ). As previously mentioned, the inversion of the trend of variation in degree of saturation in Test Bd100(-0.5) coincided with a stiffening of the corresponding compression curve.

### Probing at $[\Delta q/\Delta \bar{p}] = -1$

The results from two tests conducted at  $[\Delta q/\Delta \bar{p}] = -1$  (i.e. Ba300(-1) and Bb300(-1)) are plotted in Figure 5.57, together with the results of Test B300(-1). Figure 5.57a shows that identification of yielding is less clear in Test Ba300(-1) than in Test Bb300(-1) which suggests that a greater amount of fabric rearrangement took place after yielding in Test Ba300(-1) than in Test Bb300(-1) (in the latter test part of the compaction-induced fabric anisotropy was already erased by the initial isotropic loading).

Despite the different void ratios of Samples Ba300(-1) and B300(-1), their post-yield curves have similar slopes (see Figure 5.57c), suggesting similar changes of fabric anisotropy for both samples. All samples exhibited very similar values of deviator stress and specific volume at peak strength. In addition, although specific volume was still decreasing by the time peak deviator stress was attained, the rate of decrease had already become very small (see Figure 5.57b).

Figure 5.57c shows, once again, that during probing the identification of the yield stress is clearer in Sample Bb300(-1) than in Sample Ba300(-1) and that the sharp changes in stiffness of Sample Bb300(-1) occur almost at the same point as in the shear plot (see Figure 5.57a). Furthermore, the tendency of all compression curves to converge in a single line shows that the memory of the initial fabric had been almost entirely erased and anisotropy was only controlled by the current stress state.

Figure 5.57d indicates that degree of saturation continuously increased with progression of probing. A small water outflow from the sample was recorded (corresponding to a change of specific water volume of  $\approx -0.05$ ) which can be explained by the relatively high degree of saturation at the beginning of probing ( $\approx 0.72$  and  $0.66$  for Samples Ba300(-1) and Bb300(-1) respectively).

The results from Test Bd100(-1) are plotted in Figure 5.58 along with the results from Tests B100(-1) and Bb300(-1). Similar to Test Bb300(-1), Test Bd100(-1) showed an initial stiff response followed by a noticeable reduction in stiffness after yielding (see Figure 5.58a). Despite the different loading history of Tests Bd100(-1) and B100(-1), both samples showed very similar behaviour with progression of plastic straining, achieving the same value of peak deviator stress, although at slightly different shear strains. Similarly, inspection of results in the compression plane (see Figure 5.58c) shows that, during probing, the response of Samples Bd100(-1) and B100(-1) overlap over a large pressure range confirming that any memory of the fabric at the start of probing was erased by subsequent plastic deformation. The two curves start overlapping shortly after yielding, which may suggest that wetting has caused only a moderate change to the compaction-induced fabric anisotropy.

Figure 5.58d shows that degree of saturation increased during probing and the curves for Tests Bd100(-1) and B100(-1) merged at the same stress level at which compression curves also merged. Specific water volume exhibited a very similar decrease of  $\approx -0.06$  in both samples.

### Probing at $[\Delta q/\Delta \bar{p}] = -1.5$

The results from three tests conducted at  $[\Delta q/\Delta \bar{p}] = -1.5$  (i.e. Ba300(-1.5), Bb300(-1.5) and Bc300(-1.5)) are plotted in Figure 5.59, together with the results of Test B300(-1.5). Figure 5.59a shows that Sample Bc300(-1.5) had a stiff initial response followed by a sharp decrease in stiffness after yielding. The sharpness of the transition from elastic to elasto-plastic behaviour is explained by the fact that the probing slope of  $[\Delta q/\Delta \bar{p}] = -1.5$  was relatively similar to the previous loading/unloading slope of  $[\Delta q/\Delta \bar{p}] = -1$ .

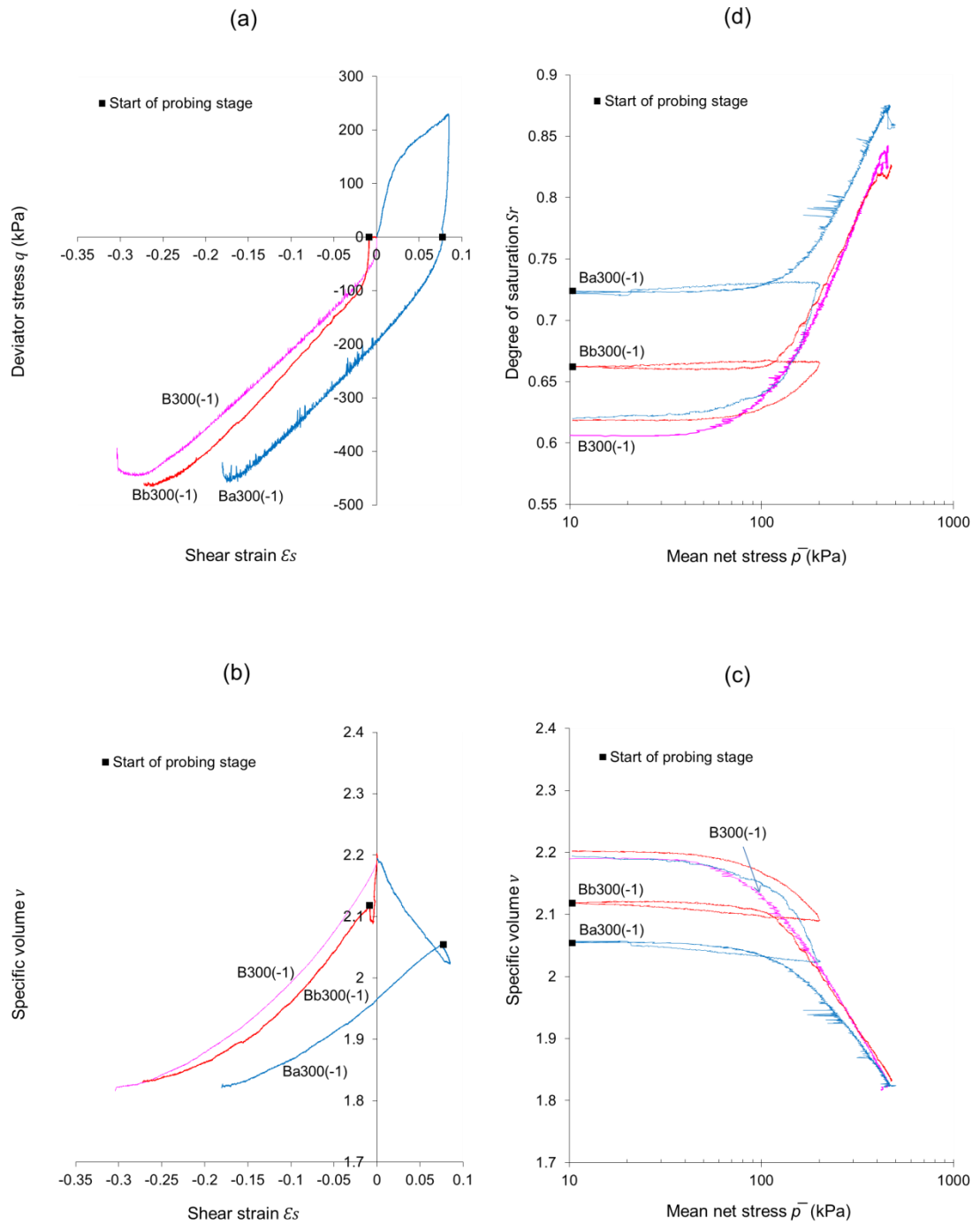


Figure 5.57 Results of the probing stages of Tests Ba300(-1), Bb300(-1) and B300(-1) in: (a)  $q: \epsilon_s$  plane, (b)  $v: \epsilon_s$  plane, (c)  $v: \ln \bar{p}$  plane (d)  $S_r: \ln \bar{p}$  plane

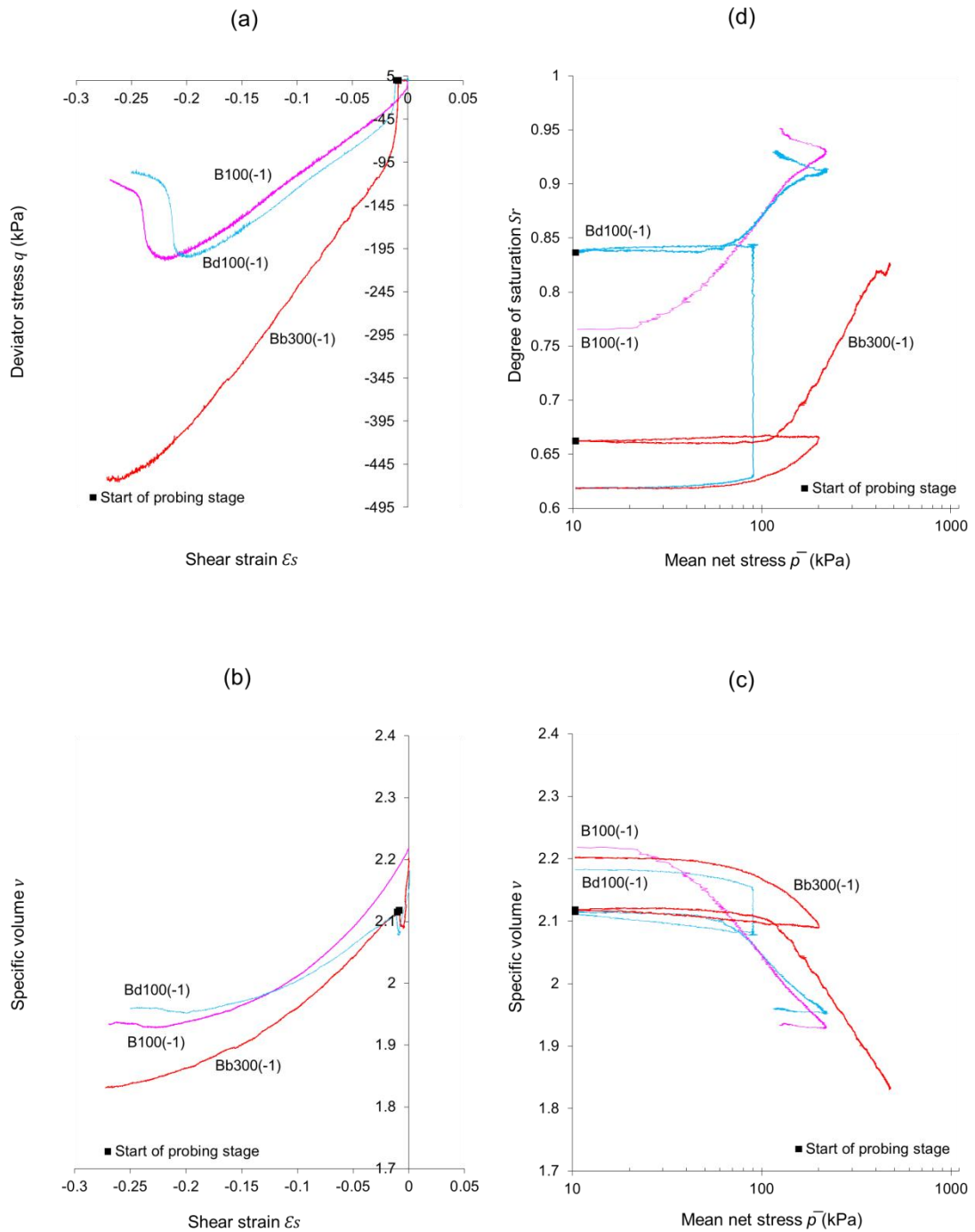


Figure 5.58 Results of the probing stages of Tests Bd100(-1), B100(-1) and Bb300(-1) in: (a)  $q: \epsilon_s$  plane, (b)  $v: \epsilon_s$  plane, (c)  $v: \ln \bar{p}$  plane (d)  $S_r: \ln \bar{p}$  plane

Consequently, only a small degree of particle/aggregate reorientation took place during probing.

Identification of the yield point became considerably more difficult when plastic straining was accompanied by rearrangement/reorientation of particles and aggregates as was the case for Tests Ba300(-1.5) and Bb300(-1.5). Nevertheless, regardless of loading history, all shear curves tended to follow a similar shape with progression of plastic straining. Samples B300(-1.5) and Bb300(-1.5) showed very similar peak strength but smaller than that of Sample Bc300(-1.5). Although Test Ba300(-1.5) was stopped before failure, the shear plot suggests that the expected peak strength would have been noticeably higher than for the other tests.

The variation of specific volume against shear strain (see Figure 5.59b) indicates that different samples arrived at peak strength with different values of specific volume. At peak deviator stress, the specific volume of Samples Bb300(-1.5) and Bc300(-1.5) decreased very slightly with increasing shear strain, whereas for Sample Ba300(-1.5) it remained practically constant.

Figure 5.59c shows that the elastic parts of the compression curves (during unloading and re-loading) were very similar for all samples regardless of the initial differences in specific volume and anisotropy. During probing, the post-yield parts of the compression curves tended to merge into a single line indicating erasure of any anisotropic memory and the attainment of a unique fabric for all tests.

Sample Bc300(-1.5) expressed the clearest yielding, denoted by a sharp change in stiffness. This discontinuity became less obvious in Samples Bb300(-1.5) and Ba300(-1.5) which demonstrates, once more, the influence of substantial rearrangement/rotation of particles and aggregates in these tests where the probing stress path was very different to the previous loading/unloading stress path.

Figure 5.59d shows a very similar increase of degree of saturation of  $\approx 0.10$  for Samples Ba300(-1.5) and Bb300(-1.5) during probing but only  $\approx 0.05$  for Sample Bc300(-1.5). This increase in degree of saturation is consistent with the corresponding decrease in specific volume, given that only a small change in pore water volume was recorded in all tests (corresponding to a change of specific water volume of  $\approx \pm 0.01$ ).

The results of Test Bd100(-1.5) are plotted together with the results of Tests B100(-1.5) and Bb300(-1.5) in Figure 5.60. As expected, the pattern of behaviour of Sample Bd100(-

1.5) is very similar to that of Sample Bb300(-1.5), confirming that both loading and wetting (under isotropic stress states) produce similar erasure of compaction-induced fabric anisotropy. The plastic response of Sample Bd100(-1.5) was clearly stiffer than that of Sample B100(-1.5) with  $\approx 10\%$  bigger peak deviator stress. This is in contrast to the good agreement of the peak strength recorded for Samples Bb300(-1.5) and B300(-1.5) in Figure 5.60a.

Figure 5.60b indicates that, for Sample Bd100(-1.5), the change of specific volume had almost stopped by the time the sample was at the peak strength. The value of the specific volume of Samples Bd100(-1.5) and B100(-1.5) in Figure 5.60b were clearly different at peak strength.

The compression plot of Sample Bd100(-1.5) (see Figure 5.60c) showed a clear change in the compression curve at the onset of yielding. The post-yield response is linear in the  $v: \ln \bar{p}$  plot and it appears that Samples B100(-1.5) and Bd100(-1.5) tend to merge in a single curve at high mean net stresses. The post-yield curve of Sample Bd100(-1.5) was very similar to that of Sample Bb300(-1.5), in contrast with the general observation that the post-yield slope of compression curves tends to be smaller at lower suction values.

Figure 5.60d indicates an increase in degree of saturation of  $\approx 0.10$  during probing of Sample Bd100(-1.5). Despite the high value of degree of saturation, a small amount of water flowed out from the sample during probing (corresponding to a change in specific water volume of  $\approx -0.01$ ).

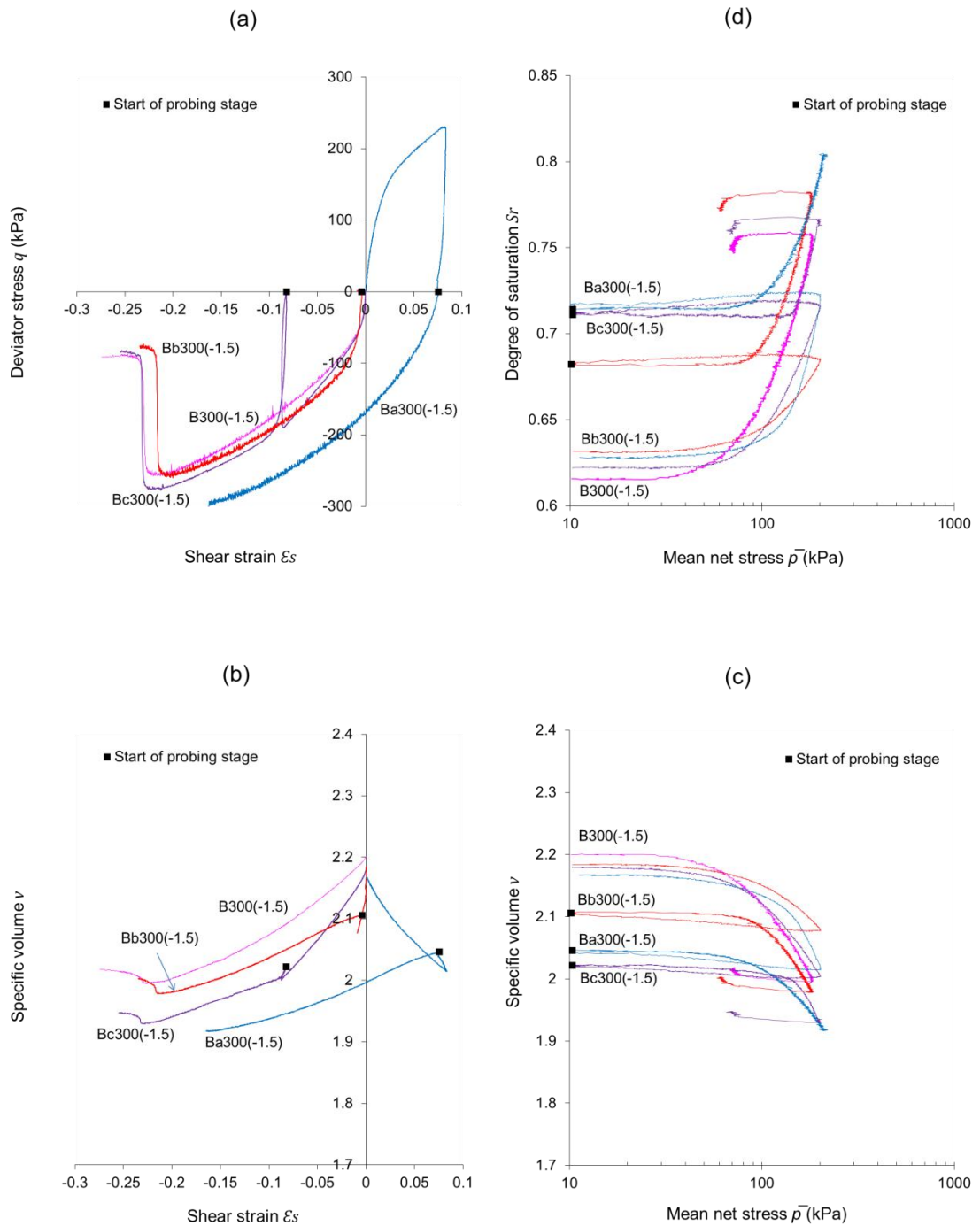


Figure 5.59 Results of the probing stages of Tests Ba300(-1.5), Bb300(-1.5), Bc300(-1.5) and B300(1.5) in: (a)  $q: \epsilon_s$  plane, (b)  $v: \epsilon_s$  plane, (c)  $v: \ln \bar{p}$  plane (d)  $S_r: \ln \bar{p}$  plane

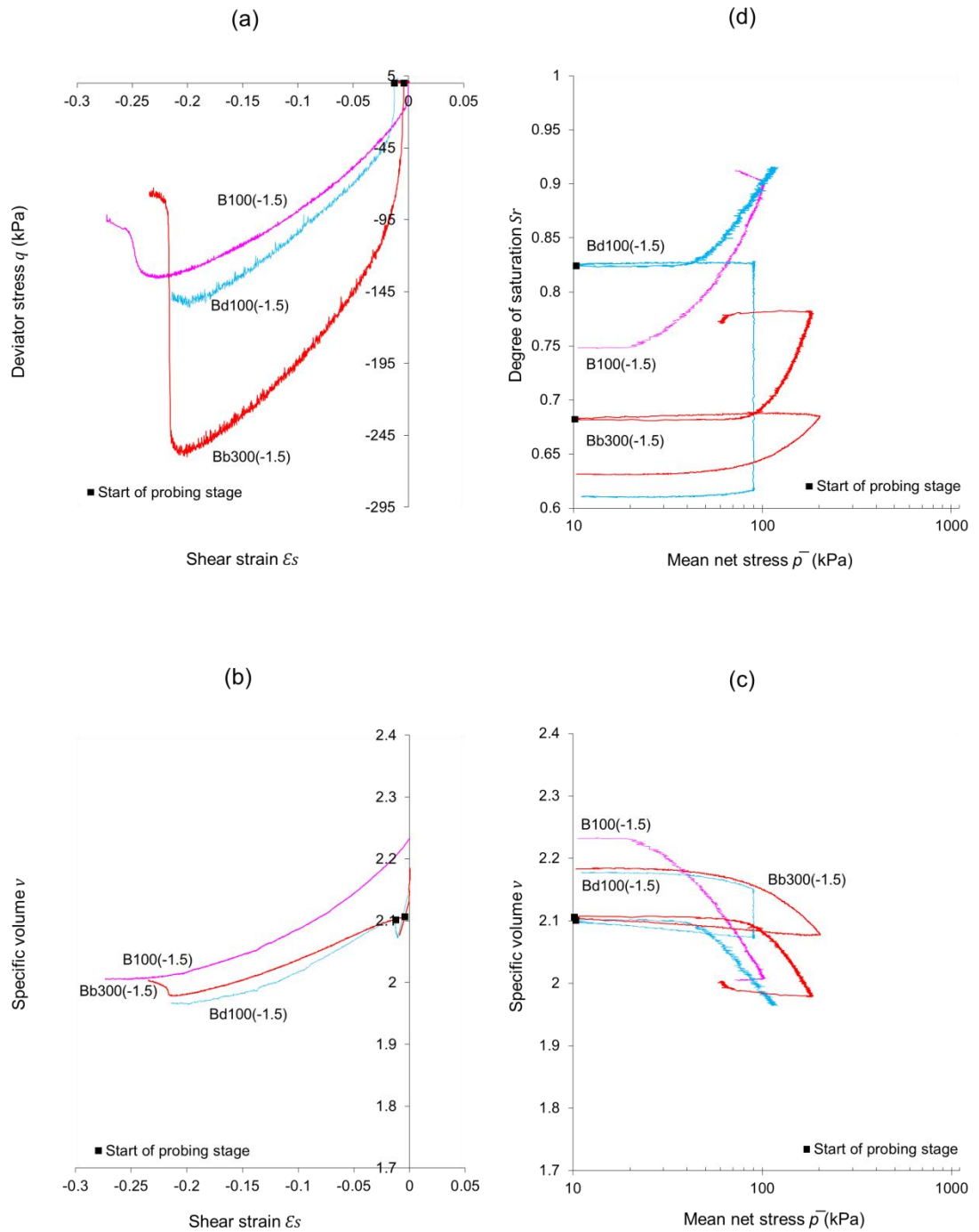


Figure 5.60 Results of the probing stages of Tests Bd100(-1.5), B100(-1.5) and Bc300(-1.5) in: (a)  $q: \epsilon_s$  plane, (b)  $v: \epsilon_s$  plane, (c)  $v: \ln \bar{p}$  plane (d)  $S_r: \ln \bar{p}$  plane

# 6

## INTERPRETATION OF EXPERIMENTAL RESULTS

This chapter includes a detailed interpretation of elastic behaviour, yielding behaviour (including a study of the shape of the yield surface), isotropic compression behaviour and critical state for the tests presented in Chapter 5.

### 6.1 ELASTIC CONSTANTS

This section involves determination of elastic constants from unloading and wetting stages of the tests presented in Chapter 5.

#### 6.1.1 Elastic indices $\kappa$ and $\kappa_s$

The soil constants  $\kappa$  and  $\kappa_s$  describe elastic compression/swelling of an unsaturated soil subjected to loading/unloading and wetting/drying, respectively, for a model formulated in terms of net stress  $\bar{p}$  and suction  $s$  (see Section 2.2 and Section 2.8.1 on the *BBM*).

Figure 6.1a includes the unloading portions of the loading/unloading stages of Test Series Ba300, Bb300, Bc300 and Bd100 and of Tests A200(0), A0(sat1) and A0(sat2) in the  $v: \ln \bar{p}$  plane (mean net stress  $\bar{p}$  reduces to mean effective stress  $p'$  under saturated conditions). The behaviour is almost linear and each of the unloading curves can be fitted adequately by a line of a gradient  $\kappa$ . Figure 6.1a indicates that the unloading curves of the saturated tests are steeper than those of the unsaturated tests when plotted in the  $v: \ln \bar{p}$  plane, suggesting a dependency of elastic volume changes on whether the sample is saturated or unsaturated. Table 6.1 shows the average values of  $\kappa$  for each test series. The results suggest that  $\kappa$  is independent of fabric anisotropy and that, apart from the saturated condition,  $\kappa$  is also independent of suction. The overall average value of  $\kappa$  (allowing for the number of tests in each test series) was 0.012 (see Table 6.1).

Given that no experimental wetting/drying cycles were conducted in this work to investigate the elastic behaviour,  $\kappa_s$  was determined by using the initial wetting stages under constant  $\bar{p}$  (no apparent collapse compression was observed during these wetting stages). The average  $v$  values were calculated from tests on isotropically and anisotropically compacted samples wetted to  $s = 300$  kPa and  $s = 100$  kPa. The value of

$\kappa_s$  was then obtained from an integrated form of Equation 2.38 by considering a wetting path from  $s = 300$  kPa to  $s = 100$  kPa. The values of  $\kappa_s$  are shown in Table 6.1. The overall average value of  $\kappa_s$  (allowing for the number of tests in each group) was 0.004 (see Table 6.1). With the limited experimental data used to obtain  $\kappa_s$  it is difficult to conclude with any confidence if anisotropy has a role on the elastic swelling/shrinkage caused by suction changes.

### 6.1.2 Elastic index $\kappa^*$

For a model formulated in terms of Bishop's stress and suction (or some function of suction), it is usually assumed that elastic volume changes are related solely to Bishop's stress.

Figure 6.1b shows the unloading portions of the loading/unloading stages of Test Series Ba300, Bb300, Bc300 and Bd100 and of Tests A200(0), A0(sat1) and A0(sat2) plotted in the  $v:\ln p^*$  plane (mean Bishop's stress  $p^*$  reduces to mean effective stress  $p'$  under saturated conditions). The behaviour is non-linear and each of the unloading curves can be fitted by a line of gradient  $\kappa^*$  as a reasonable approximation. In contrast to the plots in the  $v:\ln \bar{p}$  plane, the plots in the  $v:\ln p^*$  plane show that unloading curves of saturated tests have a similar gradient to the unsaturated ones, suggesting that suction has no influence on the elastic volume changes of an unsaturated soil when interpreted in terms of Bishop's stress. Table 6.1 shows the average values of  $\kappa^*$  from the unloading stages of the different test series. The results suggest that  $\kappa^*$  is independent of fabric anisotropy and suction although the value of  $\kappa^*$  is slightly smaller for saturated tests than for unsaturated ones.

The elastic soil constant  $\kappa^*$  can be alternatively obtained from the wetting stages. The average  $v$  and  $p^*$  values are calculated from tests on isotropically and anisotropically compacted samples wetted to  $s = 300$  kPa and  $s = 100$  kPa and  $\kappa^*$  is calculated from an integrated form of Equation 2.54 by considering a wetting path (involving a decrease of  $p^*$ ) from  $s = 300$  kPa to  $s = 100$  kPa. The values of  $\kappa^*$  calculated from the wetting stages are shown in Table 6.1. The overall averages of  $\kappa^*$  (allowing for the number of tests in each group) were 0.043 and 0.032 calculated from the unloading and wetting stages respectively (see Table 6.1). Comparing average  $\kappa^*$  values obtained by both methods shows that  $\kappa^*$  is smaller when obtained from wetting stages rather than unloading stages, although the differences are probably within the range of scatter of either methods. Generally, the selection of  $\kappa^*$  from wetting stages is less reliable than the selection from unloading stages, due to the fact that amount of volume change is based on the

difference between two points (at two different suction values) and each of those points represents the average of many samples.

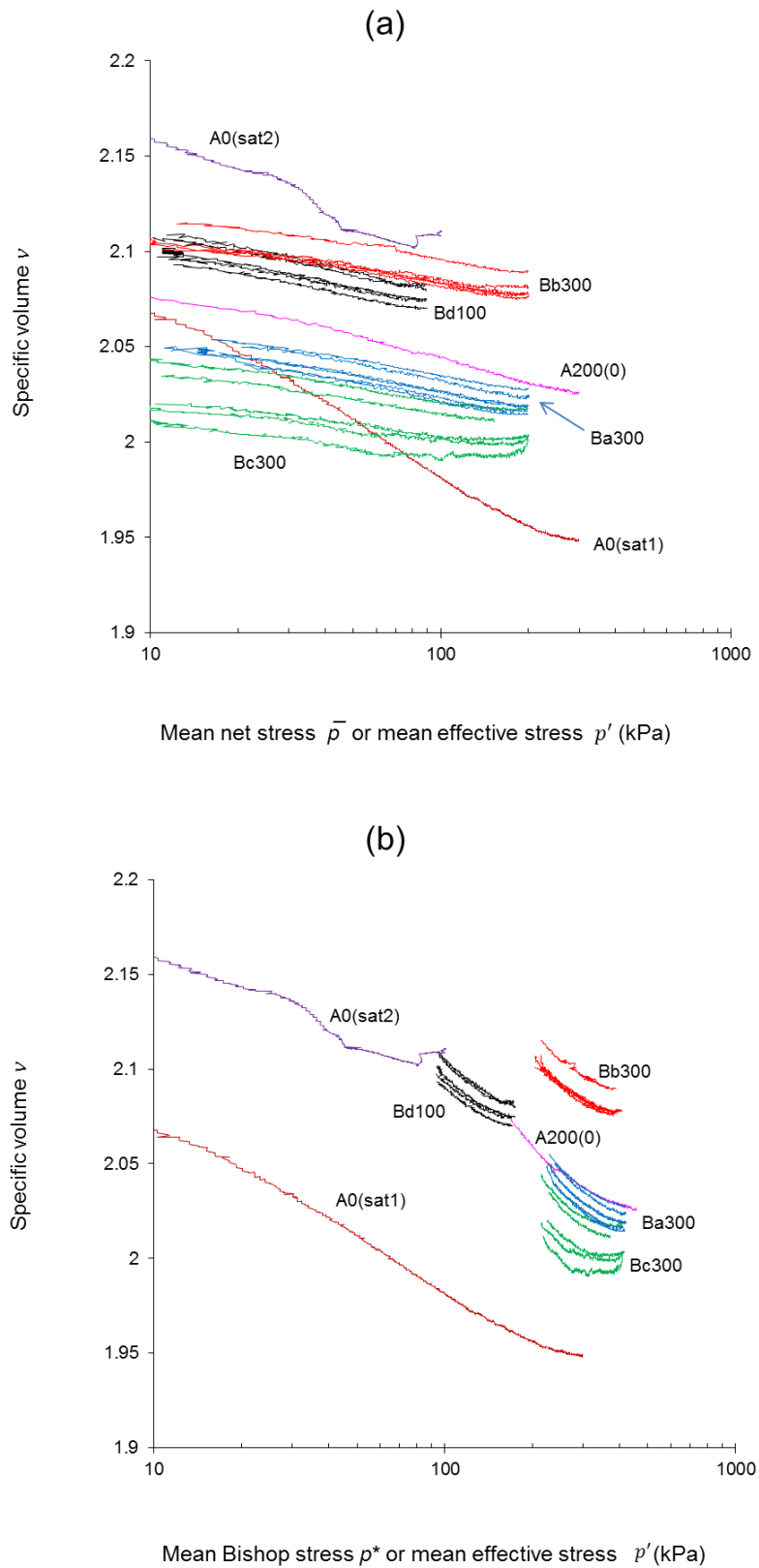


Figure 6.1 Swelling lines during unloading stages: (a) in  $v: \ln \bar{p}$  plane, (b) in  $v: \ln p^*$  plane

Table 6.1 Average values of elastic soil constants

Test or Test Series	$v: \ln \bar{p}$ plane	$v: \ln(s + p_{atm})$ plane	$v: \ln p^*$ plane		$q: \varepsilon_s$ plane
	$\kappa$	$\kappa_s$	$\kappa^*$ (unloading)	$\kappa^*$ (wetting)	$G$ (kPa)
A100	–	0.003	–	0.020	–
A300	–		–		–
B100	–	0.005	–	0.037	–
B300	–		–		–
Ba300	0.012		0.046		9199
Bb300	0.010		0.042		–
Bc300	0.009	0.043	9915		
Bd100	0.013	0.041	–		
A200(0)	0.017	–	0.045	–	–
A0(sat1) and A0(sat2)	0.033	–	0.033	–	11990
Average	0.012	0.004	0.043	0.032	9960

### 6.1.3 Elastic Shear modulus $G$

Due to the uncertainty of the stress state at which yielding occurs, the initial portions of the loading curves are not used for obtaining elastic shear modulus  $G$  and, instead, the unloading stages of Test Series Ba300, Bc300, Test A0(sat1) and Test A0(sat2) are used (note that the unloading stages of Test Series Bb300 and Bd100 were conducted under isotropic conditions and, for this reason, are not included). The unloading stages of these tests are plotted in the  $q: \varepsilon_s$  plane in Figure 6.2. Some tests showed a small continuous increase of shear strain at the beginning of unloading, attributed to delayed straining from the previous loading stage, and therefore the portion of the curve with delayed positive shear strain is disregarded. Figure 6.2 shows clearly that the behaviour during unloading is non-linear and the selection of  $G$  modulus value is crucially dependent on method of interpretation. For the elasto-plastic constitutive modelling for unsaturated soils (as will be presented in Chapter 7) a constant shear modulus value is required. The shear modulus was therefore obtained, as a crude approximation, by best fitting the  $q: \varepsilon_s$  curves by minimising the sum of squared errors in deviator stress. The average  $G$  values are shown in Table 6.1. The average value of 9960 kPa (weight was given to the number of tests in each series) was used for the model simulations with the new anisotropic model presented in Chapter 8.

It is worth mentioning that another method was also considered for selecting the value of the elastic shear modulus  $G$ , which involved fixing the first unloading point in the  $q: \varepsilon_s$  plane and doing a best fit over the subsequent unloading range. However, this method cannot be used systematically due to the observed delayed response in some cases, which results in unrealistic values of shear modulus.

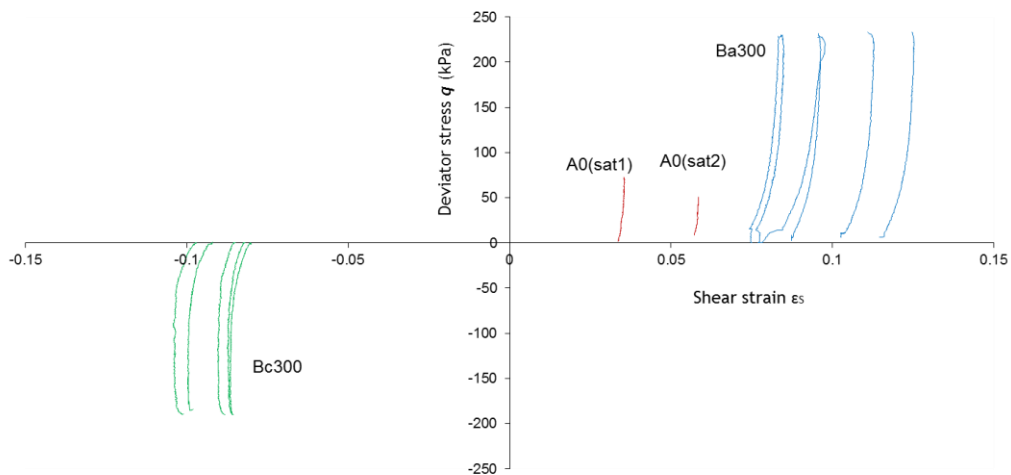


Figure 6.2 Unloading stages in  $q: \varepsilon_s$  plane

## 6.2 ISOTROPIC LOADING OF ISOTROPICALLY COMPACTED SAMPLES

### 6.2.1 Results in the $v: \ln \bar{p}$ plane

Figure 6.3a shows the isotropic compression curves for isotropically compacted samples in the  $v: \ln \bar{p}$  plane for different suction values. Yielding starts earlier in tests performed at lower suction values, due to the smaller stabilising effect exerted by the fewer meniscus water bridges at inter-particle contacts. The post-yield compression curves were fitted by straight lines in the  $v: \ln \bar{p}$  plane and the variation with suction of the gradient and intercept (measured at  $\bar{p} = 1$  kPa) of these normal compression lines (NCLs) are shown in Figure 6.4. Both the gradient and intercept increase with increasing suction and tend to level off at high suction. This is because, the effect of meniscus water bridges on mechanical behaviour tends to be less sensitive to suction variations at lower degrees of saturation.

### 6.2.2 Results in the $v: \ln p^*$ plane

Figure 6.3b shows the isotropic compression curves for the same tests in the  $v: \ln p^*$  plane. For a given value of  $\bar{p}$ , the compression curves at suctions greater than zero are shifted horizontally by different amounts, depending on the product of suction and degree of saturation ( $p^* = \bar{p} + S_r s$ ). Therefore, the post-yield compression curves have

gradients in the  $v: \ln p^*$  plane that differ from those in the  $v: \ln \bar{p}$  plane. The variation with suction of the gradient and intercept of the normal compression lines in the  $v: \ln p^*$  plane is shown in Figure 6.5. Inspection of Figure 6.5 indicates that the gradient and intercept of these normal compression lines increase monotonically with increasing suction with, again, a tendency to become constant at high suction values.

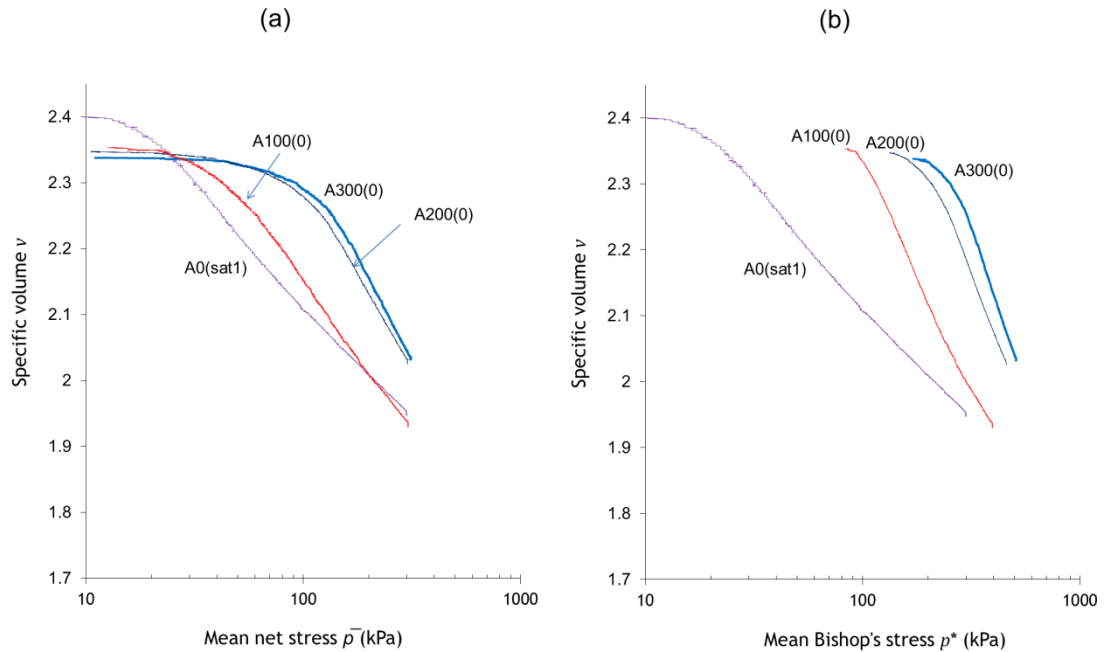


Figure 6.3 Isotropic loading at constant suction of isotropically compacted samples: (a)  $v: \ln \bar{p}$  plane, (b)  $v: \ln p^*$  plane

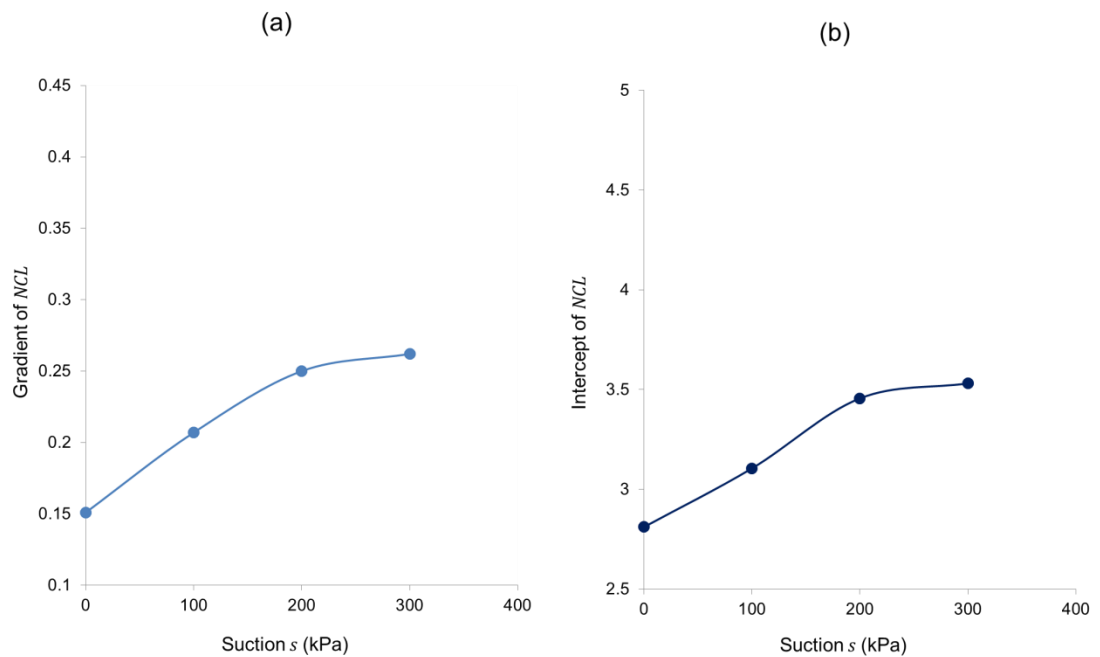


Figure 6.4 Gradient and intercept of constant suction  $NCLs$  in the  $v: \ln \bar{p}$  plane

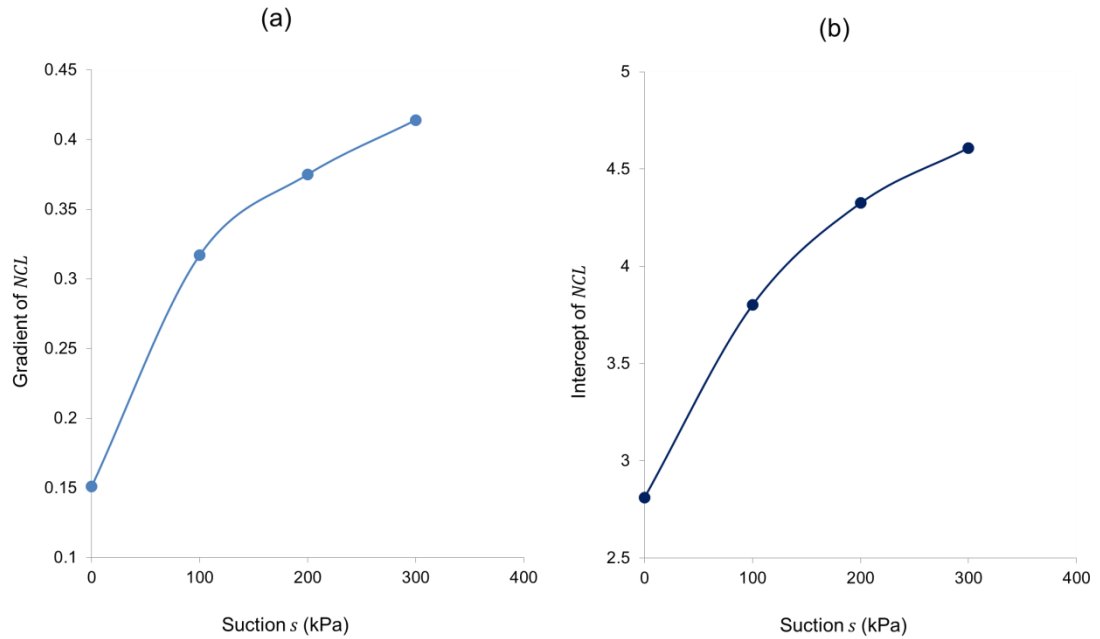


Figure 6.5 Gradient and intercept of constant suction  $NCLs$  in the  $v: \ln p^*$  plane

### 6.2.3 Unique normal compression isotropic surfaces in $v: \ln p^*: \ln s^*$ and $S_r: \ln p^*: \ln s^*$ spaces

The existence of unique isotropic normal compression planar surfaces in the  $v: \ln p^*: \ln s^*$  and  $S_r: \ln p^*: \ln s^*$  spaces for soils under unsaturated conditions and at the corner between  $LC$  and  $SD$  yield surfaces, as predicted by the model of Wheeler et al. (2003a) (see Section 2.9.5), is investigated experimentally. The post-yield portions of the isotropic loading tests on the unsaturated isotropically compacted Samples A300(0), A200(0) and A100(0) are fitted to a pair of planar surfaces in the  $v: \ln p^*: \ln s^*$  and  $S_r: \ln p^*: \ln s^*$  spaces, see Figures 6.6 and 6.7.

During plastic behaviour significant changes in both  $v$  and  $S_r$  were observed (see, for example, Figures 5.24 and 5.31) and it is therefore reasonable to assume that, in the model of Wheeler et al. (2003a) (see Section 2.9), the stress state lies at the corner between the  $LC$  and  $SD$  yield surfaces and that simultaneous yielding takes place on the two surfaces.

Because tests were conducted by controlling  $\bar{p}$  and  $s$  (rather than  $p^*$  and  $s^*$ ), a subset of data points had to be selected to ensure a proper fitting of soil behaviour in  $v: \ln p^*: \ln s^*$  space and  $S_r: \ln p^*: \ln s^*$  space. A constant number of equally spaced experimental points on the  $\ln p^*$  axis is therefore selected from the full range of data for a given constant-suction compression curve. Then the selected experimental data are fitted by planar surfaces in the semi-logarithmic space by using least-squares nonlinear regression.

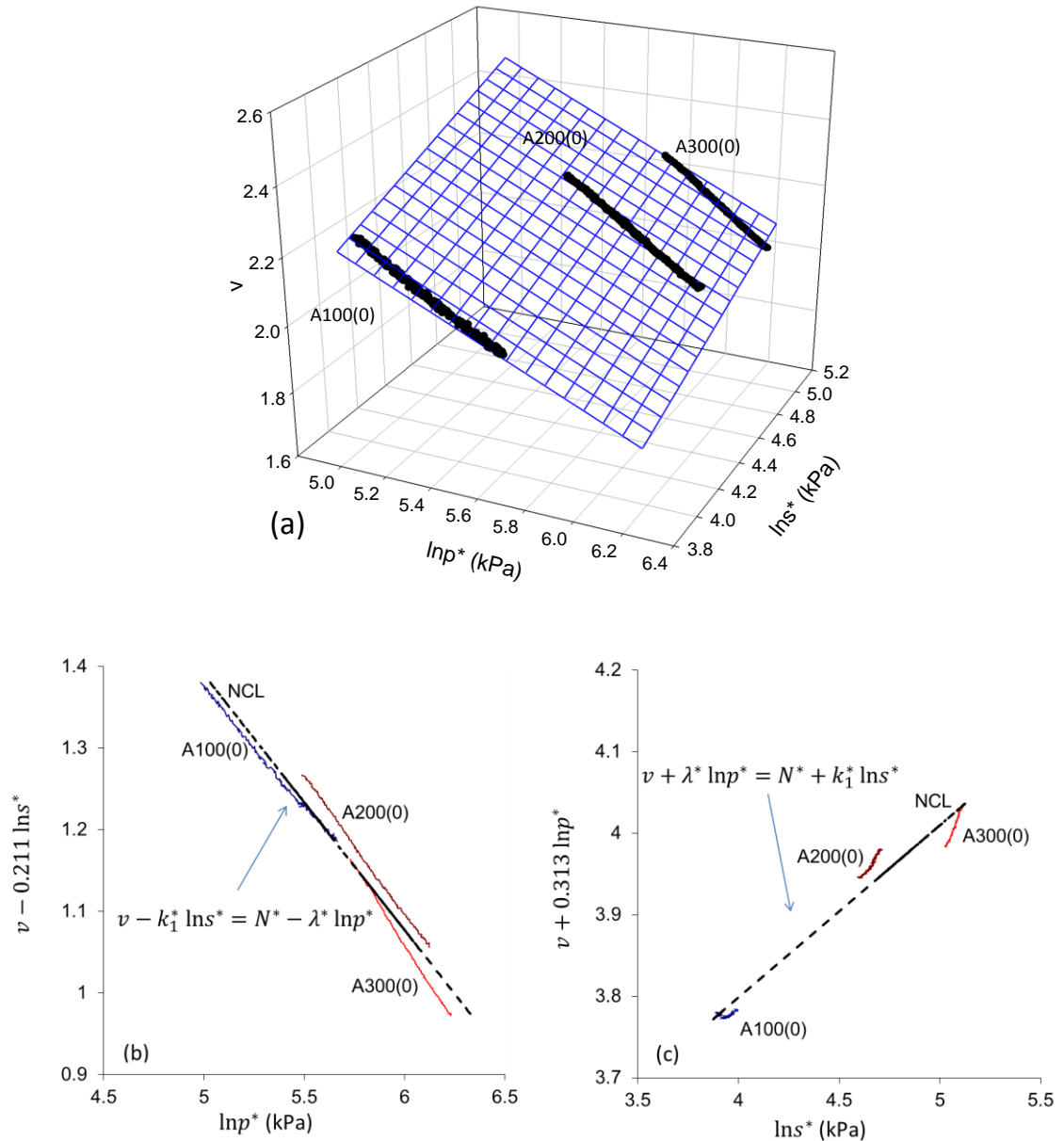


Figure 6.6 Experimental isotropic normal compression behaviour in the  $v: \ln p^*: \ln s^*$  space: (a) three-dimensional view, (b) (c) orthogonal two-dimensional views

The equations of these two planar surfaces are:

$$v = 2.953 - 0.313 \ln p^* + 0.211 \ln s^* \tag{6.1}$$

$$S_r = 1.165 + 0.156 \ln p^* - 0.293 \ln s^* \tag{6.2}$$

The intercept and gradients of Equation 6.1 correspond to the parameters  $N^*$ ,  $\lambda^*$  and  $k_1^*$  (see Equation 2.74) and the intercept and gradients of Equation 6.2 correspond to the parameters  $\chi^*$ ,  $k_2^*$  and  $\lambda_s^*$  (see Equation 2.77). The values of these parameters are summarised in Table 6.2.

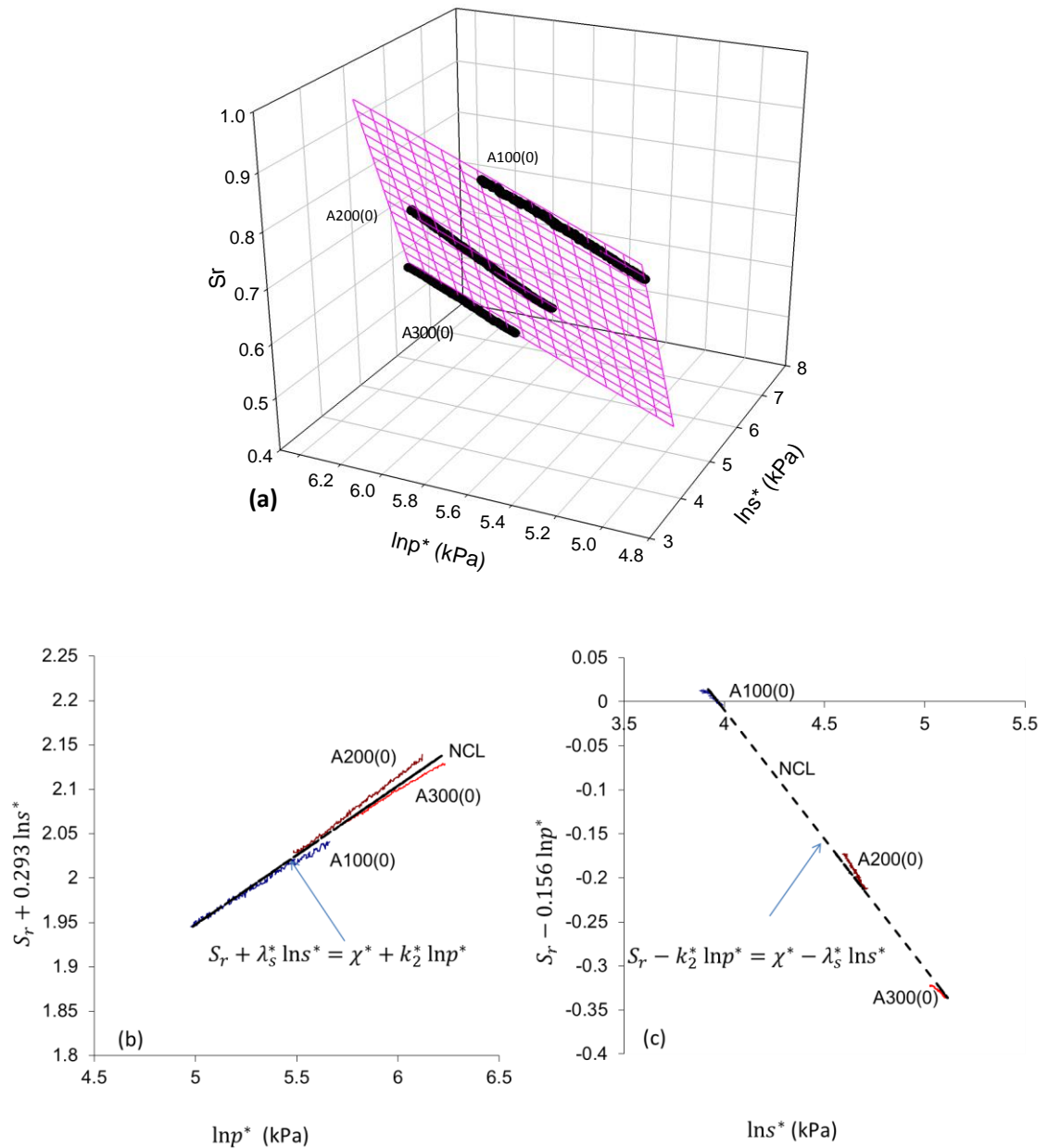


**Figure 6.7** Experimental isotropic normal compression behaviour in the  $v: \ln p^*: \ln s^*$  space: (a) three-dimensional view, (b) (c) orthogonal two-dimensional views

The above normal compression planar surfaces in the  $v: \ln p^*: \ln s^*$  space and  $S_r: \ln p^*: \ln s^*$  space are shown in Figures 6.6 and 6.7, respectively, together with their orthogonal two-dimensional views (in each view the planar surface is collapsed to a straight line).

Despite the small mismatches observed in Figures 6.6 and 6.7, each curve is nearly parallel to the isotropic normal compression surface, which provides further confirmation of the existence of these unique surfaces in both the  $v: \ln p^*: \ln s^*$  and  $S_r: \ln p^*: \ln s^*$  spaces as predicted by the model of Wheeler et al. (2003a) and as initially postulated by Lloret (2011) (see Section 2.9.5).

Table 6.2 Gradients and intercepts of normal compression surfaces in the  $v:\ln p^*:\ln s^*$  and  $S_r:\ln p^*:\ln s^*$  spaces

Planar surface in $v:\ln p^*:\ln s^*$ space			Planar surface in $S_r:\ln p^*:\ln s^*$ space		
$N^*$	$\lambda^*$	$k_1^*$	$\chi^*$	$\lambda_s^*$	$k_2^*$
2.953	0.313	0.211	1.165	0.293	0.156

### 6.3 CRITICAL STATES

#### 6.3.1 Investigation of the critical state

Critical state conditions occur when specific volume, deviator stress and mean net stress reach steady state, i.e. they do not change, under continuous shearing. As pointed out in Sections 5.5 and 5.6, in the majority of tests, specific volume remained virtually constant during shearing by the time the peak deviator stress was reached. While the assumption of critical state in correspondence of peak strength is reasonable for the majority of tests, it however implies an overestimation of the critical state values of  $q$  and  $\bar{p}$  in those tests in which softening is expected. In these latter tests, the occurrence of strain localisation associated to the sharp drop in deviator stress, implies that the post peak part of the shearing curve cannot be accurately measured. In the current work, the peak deviator stress is assumed to coincide with critical state in all tests and the validity of this assumption is investigated in subsequent sections by comparing the measured critical states to the conventionally assumed linear relationship in the  $q:\bar{p}$ ,  $v:\ln \bar{p}$ ,  $q:p^*$ , and  $v:\ln p^*$  planes.

#### 6.3.2 Critical state behaviour on the $q:\bar{p}$ and $v:\ln \bar{p}$ planes

Figure 6.8a shows experimental points from all test series in the  $q:\bar{p}$  plane. In order to facilitate interpretation, experimental data for samples sheared at the same suction and with the same initial anisotropy are analysed in the following. Critical state points in triaxial compression and extension can be adequately fitted by a straight line defined by:

$$q = \pm M(s)(\bar{p} + p_s(s)) \quad (6.3)$$

where  $M(s)$  and  $p_s(s)$  are the slope and the intersection (with the negative  $\bar{p}$  axis) of the critical state line in the  $q:\bar{p}$  plane. Both these parameters are initially assumed free to vary with suction, initial anisotropy and type of test (i.e. triaxial compression or triaxial extension). The resulting values of  $M(s)$  and  $p_s(s)$  are listed in Table 6.3. Because each test series consisted of only 3 – 4 tests in triaxial compression and 3 tests in triaxial extension, the value of these parameters is rather sensitive to data scatter.

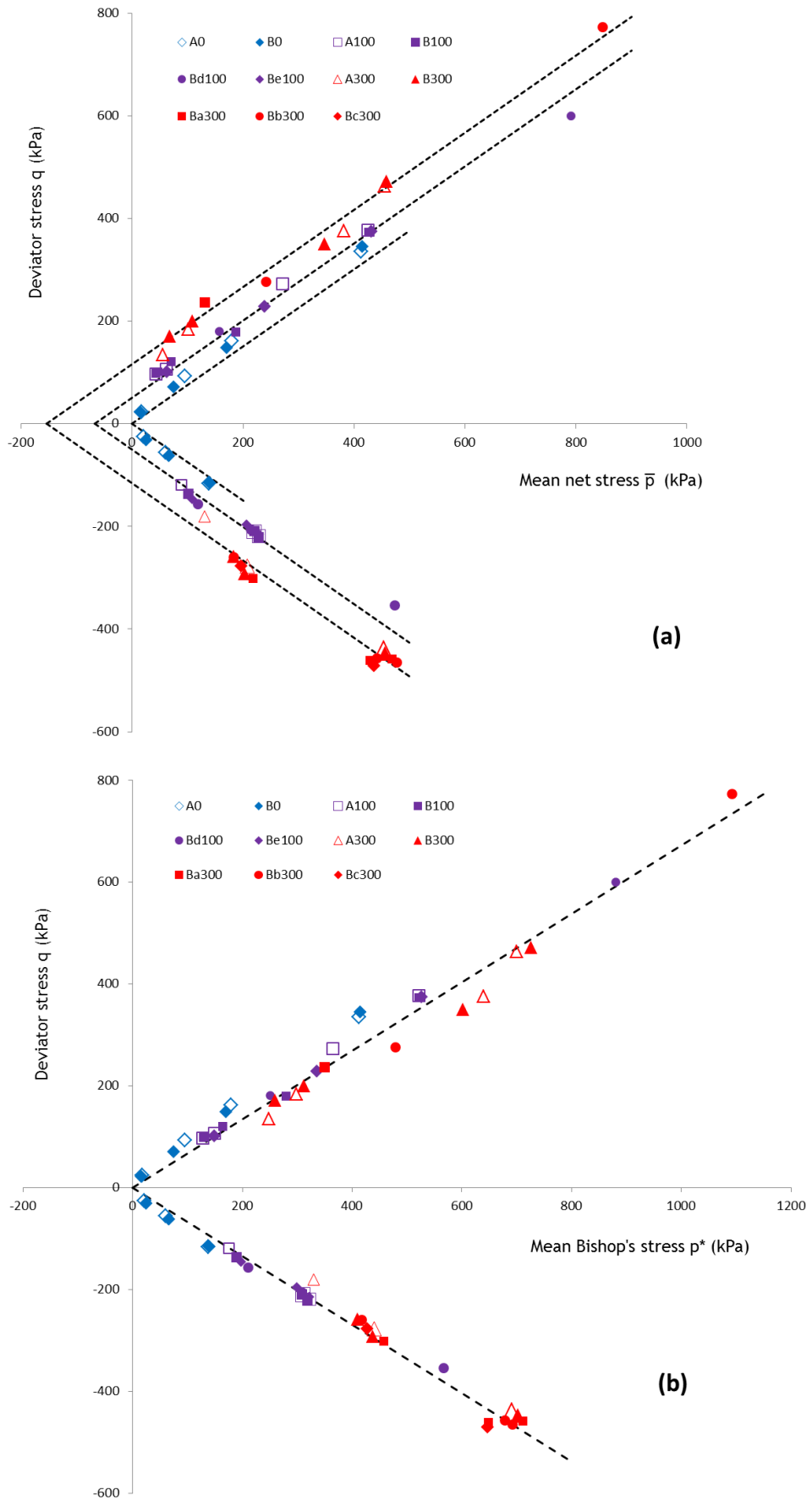


Figure 6.8 Critical state lines in the: (a)  $q$ :  $\bar{p}$  plane, (b)  $q$ :  $p^*$  plane

Table 6.3 Values of  $M(s)$  and  $p_s(s)$ 

Test Series	Triaxial compression		Triaxial extension	
	$M(s)$	$p_s(s)$ , kPa	$M(s)$	$p_s(s)$ , kPa
A0	0.783	19.73	0.769	12.32
B0	0.808	11.95	0.728	18.21
A100	0.744	86.09	0.708	79.08
B100 & Bd100	0.676	69.83	0.572	84.52
Be100	0.741	72.79	0.550	156.56
A300	0.780	122.67	0.776	122.64
B300, Ba300, Bb300 & Bc300	0.767	147.08	0.710	195.19

Inspection of Table 6.3 shows that the value of  $M(s)$  changes with suction in a rather irregular fashion for both isotropically and anisotropically compacted samples, while the value of  $p_s(s)$  increases in a non-linear fashion with suction for both isotropically and anisotropically compacted samples. Unexpectedly, the best fit values of  $p_s(s)$  for A0 and B0 are noticeably different from zero. However, forcing the value of  $p_s(s)$  equal to zero would result in higher values of  $M(s)$  (0.835 and 0.859 for Test Series A0 and 0.840 and 0.853 for Test Series B0 in triaxial compression and extension respectively).

The values of  $M(s)$ , in most cases, are slightly less in triaxial extension than in triaxial compression, which might suggest material behaviour is Lode angle dependent. The values of  $p_s(s)$  in triaxial compression and extension are very similar in some test series (for example, Test Series A300 and A100) but very different in other test series (for example, Test Series Be100), which might be attributed to the influence of data scatter on parameter values.

With respect to the effect of initial anisotropy on critical state, isotropically compacted samples show slightly higher values of  $M(s)$  than anisotropically compacted samples (in both triaxial compression and triaxial extension), with the exception of triaxial compression in Test Series A0. No consistent pattern of variation of  $p_s(s)$  with initial anisotropy is observed at different suctions. In triaxial compression, the value of  $p_s(s)$  is bigger for Test Series A0 than test series B0, though the opposite is true for Test Series A300 and B300/Ba300/Bb300/Bc300. In triaxial extension, the value of  $p_s(s)$  is always bigger for anisotropically compacted samples than for isotropically compacted samples. In triaxial compression, the values of  $M(s)$  and  $p_s(s)$  for Test Series Be100 agree relatively well with those for Test Series A100 and B100/Bd100. However, in triaxial

extension, the values of  $M(s)$  and  $p_s(s)$  are respectively smaller and bigger for Test Series Be100 compared to Test Series A100 and B100/Bd100.

Despite the apparent discrepancies in the values of critical state parameters, Figure 6.8a shows no clear influence of anisotropy on critical state, with results from tests on anisotropically compacted samples falling within the same scatter band as those on isotropically compacted samples performed at the same suction.

The number of critical state parameters can be reduced by assuming that the critical state ratio  $M$  does not change with anisotropy and suction and that the intercept  $p_s(s)$  changes only with suction but not anisotropy. The best fit values of  $M$  and  $p_s(s)$  in triaxial compression and extension are therefore obtained by least-squares fitting of all experimental data with the following expression:

$$q = a M_c [c \bar{p} + d(\bar{p} + p_{sc}(100)) + e (\bar{p} + p_{sc}(300))] - b M_e [c \bar{p} + d (\bar{p} + p_{se}(100)) + e (\bar{p} + p_{se}(300))] \quad (6.4)$$

where  $a$  and  $b$  are equal to 1 for triaxial compression and extension respectively, or equal to zero otherwise,  $c$ ,  $d$  and  $e$  are constants equal to 1 for tests at  $s = 0, 100$  and  $300$  kPa respectively or equal to zero otherwise,  $p_{sc}(100)$  and  $p_{sc}(300)$  are the best-fit values of  $p_s(s)$  at  $s = 300$  kPa and  $s = 100$  kPa respectively in triaxial compression (note that the intercept is set to zero for critical states at  $s = 0$ ),  $p_{se}(100)$  and  $p_{se}(300)$  are the best-fit values of  $p_s(s)$  at  $s = 300$  kPa and  $s = 100$  kPa respectively in triaxial extension. Equation 6.4 gives a set of parallel lines (one line for each value of suction) of unique gradient in triaxial compression and gives another set of parallel lines of different unique gradient in triaxial extension. The values of  $M$ ,  $p_s(100)$  and  $p_s(300)$  are listed in Table 6.4 (Columns 1 and 2). Comparing critical state values in Tables 3 and 4 shows that the new values of  $M$  agree well with the average values of  $M(s)$  while the values of  $p_s(s)$  do not agree with the average ones at a given suction.

A further reduction in the number of parameters can be achieved by imposing an equal value of  $p_s(s)$  in triaxial compression and extension. This is done by fitting all experimental points with the following expression via the least-squares method:

$$q = a M_c [c \bar{p} + d(\bar{p} + p_s(100)) + e (\bar{p} + p_s(300))] - b M_e [c \bar{p} + d (\bar{p} + p_s(100)) + e (\bar{p} + p_s(300))] \quad (6.5)$$

where  $a$  and  $b$  are equal to 1 for triaxial compression and extension respectively, or equal to zero otherwise. Similarly, the constants  $c$ ,  $d$  and  $e$  are equal to 1 for  $s = 0, 100$  and  $300$  kPa respectively, or equal to zero otherwise. The parameters  $M_c$  and  $M_e$  are the critical state ratios in compression and extension, while the parameters  $p_s(100)$  and  $p_s(300)$  are the best-fit values of  $p_s(s)$  at  $s = 300$  kPa and  $s = 100$  kPa for both triaxial compression and extension. The results of this fitting are shown in Table 6.4 (Columns 3 and 4 for triaxial compression and extension, respectively).

**Table 6.4 Values of  $M_c$ ,  $M_e$ ,  $p_{sc}(100)$ ,  $p_{se}(100)$ ,  $p_{sc}(300)$  and  $p_{se}(300)$**

Parameter	1	2	3	4	5
	Compression	Extension	Compression	Extension	Compression and extension
$M_c$ or $M_e$	0.761	0.713	0.753	0.750	0.752
$p_{sc}(100)$					
or	67.89	76.15		66.84	66.86
$p_{se}(100)$					
$p_{sc}(300)$					
or	143.90	185.31		154.89	154.14
$p_{se}(300)$					

Because the values of  $M_c$  and  $M_e$  are very similar in Table 6.4, it might be convenient to use a unique value of  $M$  for both triaxial compression and triaxial extension. The convenience of this suggestion depends on the modelling approach. Based on Mohr-Coulomb failure criterion, the assumption of unique failure friction angle value ( $\phi'$ , see Equation 2.11) implies that the critical state ratio is lower in triaxial extension than in triaxial compression (the failure envelope is represented by an irregular hexagon in the deviatoric plane). Alternatively, in Drucker-Prager modelling approach the failure envelope is represented by a circle in the deviatoric plane which is equivalent to assuming a constant critical state ratio in triaxial compression and triaxial extension, but now friction angle is not constant (bigger in triaxial extension than in triaxial compression).

Following the latter approach, the parameters  $M_c$  and  $M_e$  in Equation 6.5 are replaced by a single parameter  $M$  and the critical state relationship in the  $q:\bar{p}$  plane is written as:

$$q = \pm M [c \bar{p} + d(\bar{p} + p_s(100)) + e (\bar{p} + p_s(300))] \tag{6.6}$$

The critical state lines obtained from Equation 6.6 are plotted, together with the experimental points of all test series, in Figure 6.8a. Experimental data are well-matched at  $s = 300$  kPa and  $s = 100$  kPa but, at  $s = 0$ , they lie above the corresponding critical state lines (a consequence of the assumption of a zero intercept at  $s = 0$ ). In general, a unique critical state seems to be attained in the  $q: \bar{p}$  plane for a given value of suction, which gives further justification to the proposal that the critical state is independent of initial fabric anisotropy.

Figure 6.9 (a, b and c) shows critical state data in the  $v: \ln \bar{p}$  plane for  $s = 300$  kPa, 100 kPa and zero, respectively, together with their best fit lines. The figure also shows the positions of the normal compression lines (*NCLs*) of Tests A300(0), A100(0) and A0(0).

Again, no clear influence of initial anisotropy is observed at critical state for unsaturated tests, i.e. both anisotropically and isotropically compacted samples, tested at the same suction, fall within the same scatter band. Conversely, under saturated conditions, anisotropically compacted samples show smaller values of specific volume at critical state than isotropically compacted samples.

The fitting equation for critical state lines (*CSLs*) in the  $v: \ln \bar{p}$  plane is expressed as:

$$v_{cs} = \Gamma(s) - \psi(s) \ln \bar{p} \quad (6.7)$$

where  $\Gamma(s)$  and  $\psi(s)$  are the intercept and slope of the critical state line at a given  $s$ . The best-fit values of  $\Gamma(s)$  and  $\psi(s)$  are listed in Table 6.5, which shows that the slope of the *CSLs* decreases with decreasing suction in agreement with the decrease of slope of normal compression lines (*NCLs*) with decreasing suction (see Figure 6.4). However, the slopes of constant-suction *CSLs* are clearly less than the slopes of the corresponding *NCLs* (see Figure 6.9).

**Table 6.5** Values of  $\Gamma(s)$  and  $\psi(s)$

$s$ , kPa	$\psi(s)$	$\Gamma(s)$
300	0.187	2.961
100	0.128	2.614
0	0.123	2.575

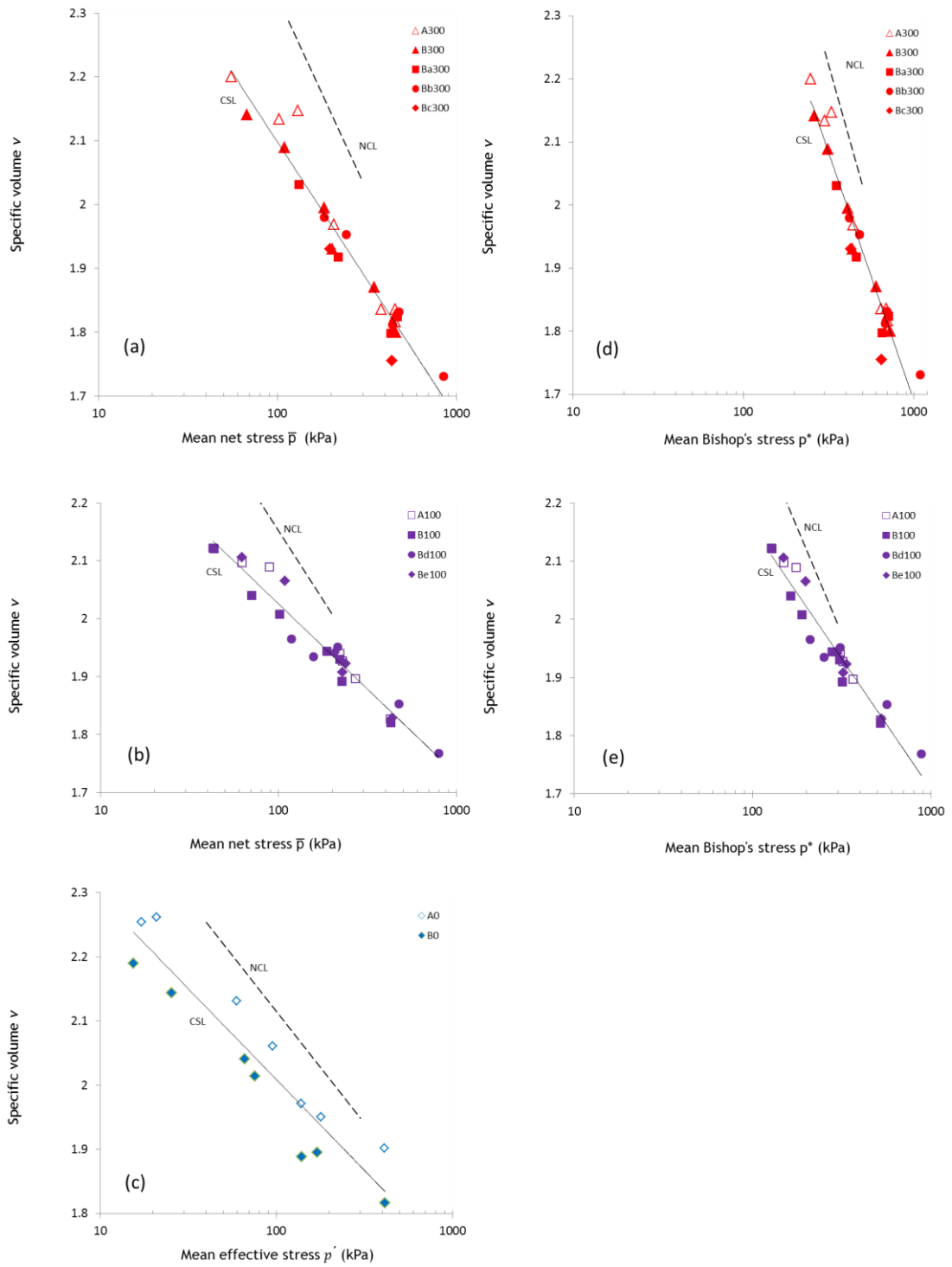


Figure 6.9 Critical state lines in the: (a)  $v: \ln \bar{p}$  plane ( $s = 300$  kPa), (b)  $v: \ln \bar{p}$  plane ( $s = 100$  kPa), (c)  $v: \ln \bar{p}$  plane ( $s = 0$ ), (d)  $v: \ln p^*$  plane ( $s = 300$  kPa), (e)  $v: \ln p^*$  plane ( $s = 100$  kPa)

### 6.3.3 Critical state behaviour in the $q:p^*$ and $v:\ln p^*$ planes

Figure 6.8b shows experimental data from all test series in the  $q:p^*$  plane. Inspection of Figure 6.8b indicates that each set of compression or extension data can be adequately fitted by a linear expression passing through the origin:

$$q = \pm M^* p^* \quad (6.8)$$

where  $M^*$  is the critical state ratio in triaxial compression and extension. The results of this fitting are given in Table 6.6, which provides the values of  $M^*$  obtained for samples with different levels of initial anisotropy (Columns 1 and 2 refer to triaxial compression and extension, respectively). The values of  $M^*$  are slightly smaller in triaxial extension than compression, which agrees well with the observation in the  $q:\bar{p}$  plane, but they appear unaffected by initial anisotropy.

A further fitting exercise is performed by imposing a single slope for the critical state line in triaxial compression and extension. The corresponding value of  $M^*$  is again given in Table 6.6 and the interpolation is graphically demonstrated in Figure 6.8b. Inspection of triaxial compression data in Figure 6.8b does show a slight dependency on suction, with data points for  $s = 0$  generally falling towards the top of the scatter band and data points at  $s = 300$  kPa generally falling towards the bottom of the scatter band.

Table 6.6 Values of  $M^*$

Test Series	1	2	3
	Triaxial compression	Triaxial extension	Compression and extension
A0, A100 & A300	0.676	0.642	
B0, B100, B300, Ba300, Bb300, Bc300 & Bd10	0.679	0.667	0.672
Be100	0.701	0.674	

Inspection of Figures 6.8a and 6.8b indicates that data scatter about the best-fit line is virtually the same in the  $q:\bar{p}$  and  $q:p^*$  planes but the  $q:p^*$  plane allows interpolation of all data by a single critical state line passing through the origin.

Critical state data points in the  $v:\ln p^*$  plane are plotted in Figures 6.9d and 6.9e for tests at  $s = 300$  kPa and  $s = 100$  kPa respectively, together with the corresponding normal compression lines from Tests A300 and A100. Experimental data at each suction can be adequately fitted by the following equation:

$$v_{cs} = \Gamma^*(s) - \psi^*(s)\ln p^* \quad (6.9)$$

where  $\Gamma^*(s)$  and  $\psi^*(s)$  are the intercept and slope of critical state line in the  $v:\ln p^*$  plane. The values of the  $\Gamma^*(s)$  and  $\psi^*(s)$  are listed in Table 6.7. Critical state lines appear independent of initial anisotropy. The slopes vary with suction and are smaller than the slopes of the corresponding normal compression lines, similar to what had been observed in the  $v:\ln \bar{p}$  plane.

**Table 6.7 Values of  $\Gamma^*(s)$  and  $\psi^*(s)$**

$s$ , kPa	$\psi^*(s)$	$\Gamma^*(s)$
300	0.341	4.046
100	0.196	3.058
0	0.123	2.575

In summary, the results of this section and Section 6.3.2 confirm that critical state behaviour is unique and independent of initial anisotropy. By using Bishop's stress, all data points can be interpolated by a single critical state line passing through the origin in the  $q:p^*$  plane. This result, which is in agreement with previous research published, for example, by Gallipoli et al. (2008), is particularly helpful when developing constitutive models, as will be further discussed Chapter 7.

### 6.3.4 Unique critical state planar surfaces in $v:\ln p^*:\ln s^*$ and $S_r:\ln p^*:\ln s^*$ spaces

Figures 6.10 and 6.11 show unsaturated critical state data points fitted to a pair of planar surfaces in the  $v:\ln p^*:\ln s^*$  and  $S_r:\ln p^*:\ln s^*$  spaces, respectively. The purpose of these plots is to investigate the existence of unique critical state planar surfaces in the  $v:\ln p^*:\ln s^*$  and  $S_r:\ln p^*:\ln s^*$  spaces, similar to the unique normal compression planar surfaces presented in Section 6.2.3, and to see whether these critical state surfaces are parallel to the normal compression surfaces (as predicted by the model of Wheeler et al. (2003a), see Section 2.9.6). It is important to emphasise that degree of saturation was always less than 1 in all unsaturated tests (see Sections 5.5 and 5.6) and that, if experimental results are interpreted in the model framework of Wheeler et al. (2003a), the stress state should arrive during probing/shearing at the intersection between the  $LC$  and  $SD$  yield surfaces (see Section 2.9.3), which implies simultaneous yielding on both these surfaces. According to the model of Wheeler et al. (2003a), these conditions must

be satisfied in order for the soil state to lie on the unique critical state planar surfaces (see Section 2.9.6).

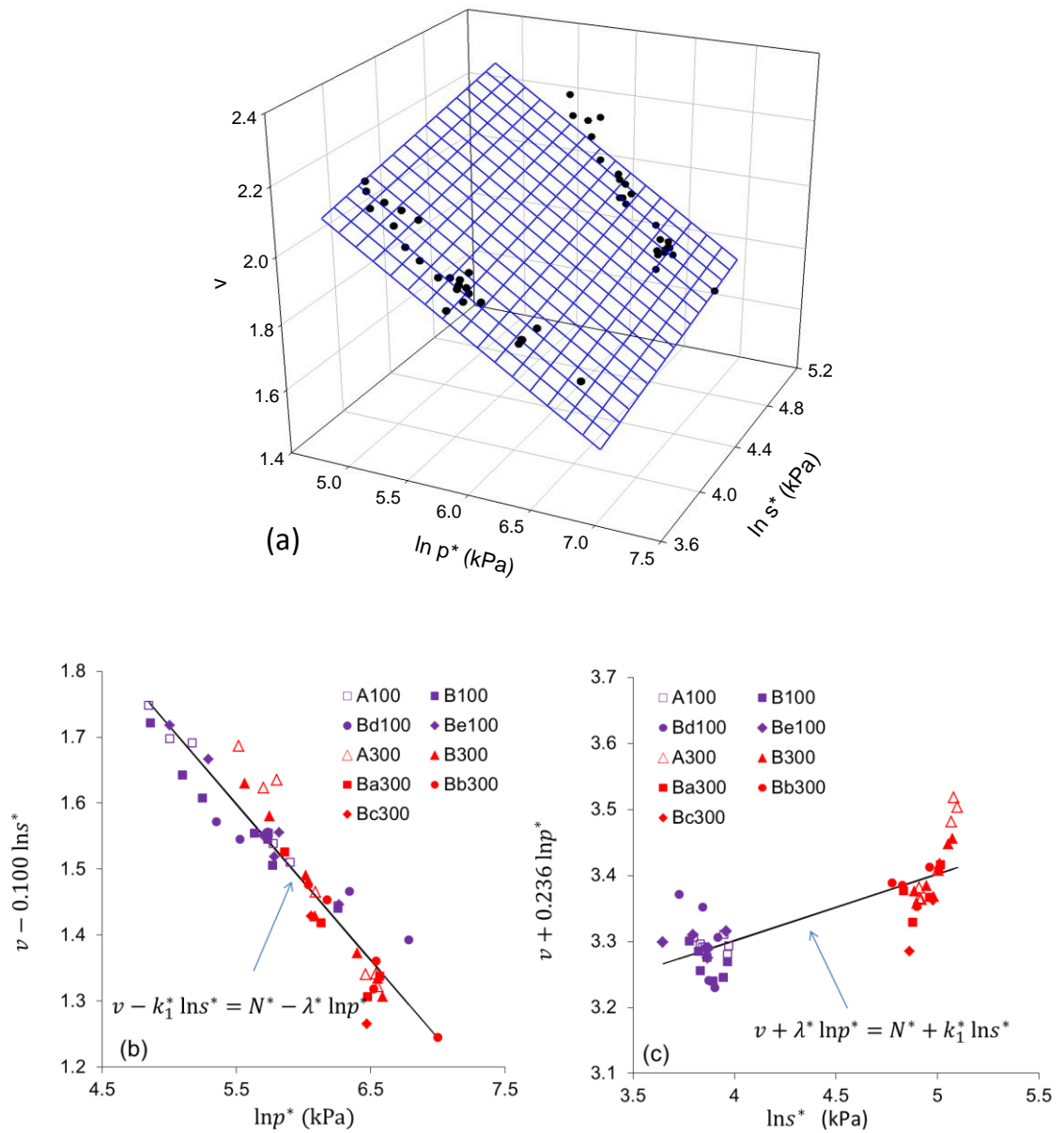


Figure 6.10 Experimental critical state behaviour in the  $v:\ln p^*:\ln s^*$  space: (a) three-dimensional view, (b) (c) orthogonal two-dimensional views

Inspection of Figure 6.10 shows that critical state data are generally well captured by a planar surface in the  $v:\ln p^*:\ln s^*$  space. Figure 6.11 shows significant scatter of critical state data in the  $S_r:\ln p^*:\ln s^*$  space, but no trend with suction. Moreover, Figures 6.10 and 6.11 show no effect of initial anisotropy at critical state. The equations of the two critical state planar surfaces are:

$$v = 2.898 - 0.236 \ln p^* + 0.100 \ln s^* \tag{6.10}$$

$$S_r = 1.200 + 0.070 \ln p^* - 0.177 \ln s^* \tag{6.11}$$

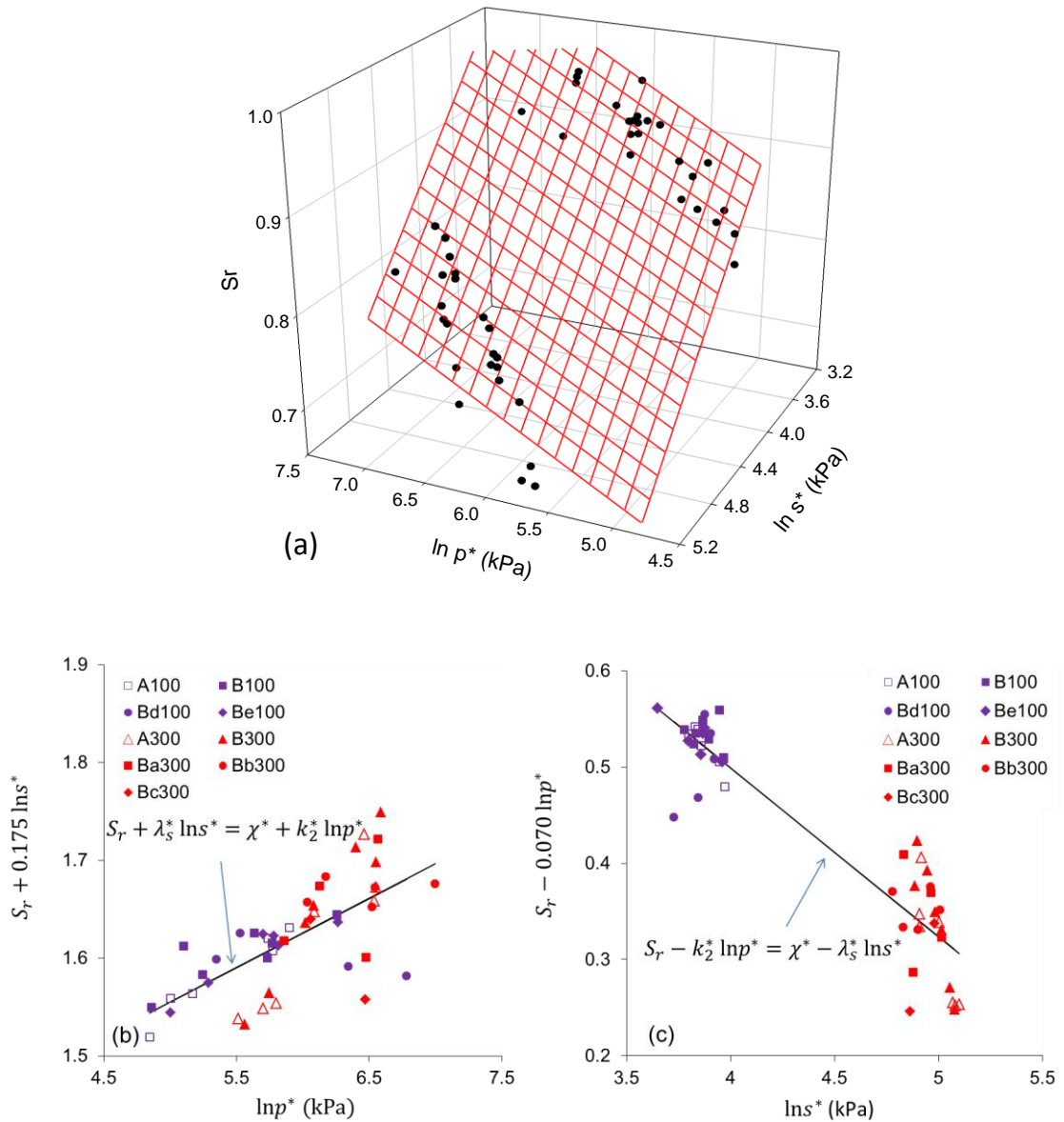


Figure 6.11 Experimental critical state behaviour in the  $S_r$ : $\ln p^*$ : $\ln s^*$  space: (a) three-dimensional view, (b) (c) orthogonal two-dimensional views

The gradients of Equation 6.10 correspond, in the model proposed by Wheeler et al. (2003a), to the parameters  $\lambda^*$  and  $k_1^*$  (see Equation 2.83) while the gradients of Equation 6.11 correspond to the parameters  $k_2^*$  and  $\lambda_s^*$  (see Equation 2.84). The values of the fitting parameters are summarised in Table 6.8 where  $\Gamma^*$  and  $\Psi^*$  are the intercepts of the critical state planar surfaces in  $v$ : $\ln p^*$ : $\ln s^*$  and  $S_r$ : $\ln p^*$ : $\ln s^*$  spaces, respectively.

Inspection of Tables 6.8 and 6.2 shows that values of  $\lambda^*$  and  $k_1^*$  obtained from the critical state surface in  $v$ : $\ln p^*$ : $\ln s^*$  space are significantly smaller than those obtained from the corresponding normal compression surface. Similarly, the values of  $\lambda_s^*$  and  $k_2^*$  obtained

from the critical state surface in  $S_r: \ln p^*: \ln s^*$  space are significantly smaller than those obtained from the corresponding normal compression surface.

**Table 6.8** Gradients and intercepts of critical state planar surfaces in the  $v: \ln p^*: \ln s^*$  and  $S_r: \ln p^*: \ln s^*$  spaces

Planar surface in $v: \ln p^*: \ln s^*$ space			Planar surface in $S_r: \ln p^*: \ln s^*$ space		
$\Gamma^*$	$\lambda^*$	$k_1^*$	$\Psi^*$	$\lambda_s^*$	$k_2^*$
2.898	0.236	0.100	1.200	0.175	0.070

## 6.4 IDENTIFYING YIELD POINTS

Because soil yielding takes place gradually during loading, various authors have suggested different methods to infer the values of yield stresses from experimental data (see Section 2.4.3). In this work, several techniques are investigated to identify yielding, as outlined in the following sections.

### 6.4.1 Bi-linear construction in the $v: \ln \bar{p}$ or $v: \ln p^*$ plane

As discussed in Section 2.4.3, the identification of yield stresses in the  $v: \ln \bar{p}$  or  $v: \ln p^*$  planes is generally prone to subjectivity. To reduce this subjectivity, a bi-linear construction in the  $v: \ln \bar{p}$  or  $v: \ln p^*$  plane is utilised in this work as follows:

- The stress or specific volume axes are generally plotted over the same range of values to maintain consistency among plots.
- A straight line with gradient equal to the elastic index  $\kappa = 0.012$  or  $\kappa^* = 0.043$  (see Table 6.1) is plotted from the first elastic point of the experimental curve in the  $v: \ln \bar{p}$  or  $v: \ln p^*$  plane, respectively (for saturated tests the elastic index  $\kappa^* = 0.043$  is used).
- The post-yield portion of the compression curve in the  $v: \ln \bar{p}$  or  $v: \ln p^*$  plane (taken as the latest and steepest linear part) is then best fitted with a straight line. Any lower gradient part of the compression curve at high mean net stresses or high saturation is excluded from the fitting. Equally, any steep part of the compression curve near critical states for tests conducted at  $[\Delta q / \Delta \bar{p}] > M$  (see, for example, A100(2) and B100(2) in Figure 5.29) is excluded from this fitting.
- The yield stress is found from the intersection of the above two straight lines.

Typical examples of this construction are shown in Figure 6.12. Inspection of this figure shows that, in general, the elastic line falls below the experimental curve and that yield stresses are moderately overestimated compared with a typical subjective judgement.

Further inspection of Figure 6.12 shows that the bi-linear construction gives a reasonable idealisation of compression behaviour for both isotropic and anisotropic samples in both saturated and unsaturated conditions. This method appears therefore suitable for identifying yield stresses, regardless of suction level and evolving anisotropy, in both the  $v: \ln p^*$  plane and in the  $v: \ln \bar{p}$  plane.

Figure 6.12f shows the application of this method on samples with loading and probing stages (i.e. Ba300(0.5) and Bb300(0.5)) and it is evident that the method gives reasonable estimation of yield stresses.

Figures 6.12b and 6.12e exemplify cases where some subjectivity had to be exercised in defining the post-yield portion of the compression curve. In Test A100(2), the gradient of the post-yield curve tends to increase as loading progresses and becomes very steep when critical state is approached. Similarly, in Tests A100(0) and B100(0), the slope of the compression curves tend to reduce at high net stresses as the degree of saturation approaches unity. In all these cases, the fit of the post-yield curve must ignore the latest part of the compression curve which is truncated just before the above increase or decrease of gradient occurs.

Finally, it is worth mentioning that the Casagrande (1936) method was not considered in the present work to identify yielding as this method involves a larger degree of subjectivity and usually predicts higher yield stresses than the current method (see Section 2.4.3 for additional details).

#### 6.4.2 Bi-linear construction in the $v: \bar{p}$ or $v: p^*$ plane

Yielding can be alternatively identified by means of a bi-linear construction on compression curves plotted in the  $v: \bar{p}$  plane or  $v: p^*$  plane. The principle of this construction is similar to that outlined in the previous section, with the only difference that the change in stiffness is now identified on a linear plot rather than a semi-logarithmic one. The yield stress is obtained from the intersection of two straight lines tangent to the shallowest section of the pre-yield part of the compression curve and to the steepest section of the post-yield part of the compression curve (corresponds to an inflection point).

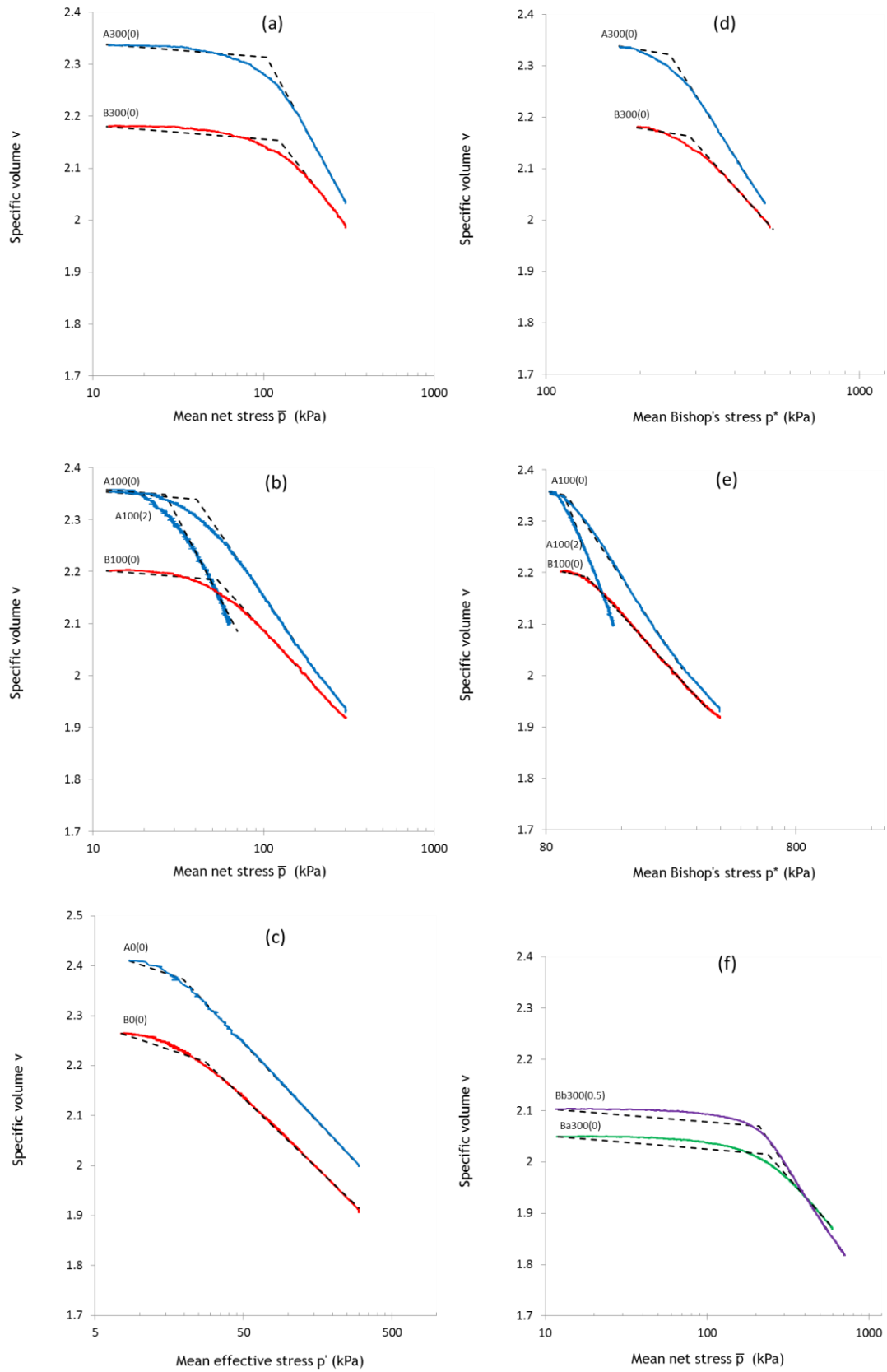


Figure 6.12 Examples of bi-linear construction in the  $v: \ln \bar{p}$  and  $v: \ln p^*$  planes

Figure 6.13 shows examples of the construction in the  $v:\bar{p}$  plane (no example is shown in the  $v:p^*$  plane as the procedure would look exactly the same). Tests A100(0), B100(0) and Bb300(0.5) show a marked change in compressibility and the proposed bi-linear construction captures well the corresponding yield stresses (see Figure 6.13). In contrast, Tests Ba300(0) and Bc300(0) show a more gradual change of compressibility and the proposed bi-linear construction does not provide an accurate identification of yield stresses. Because of this greater level of subjectivity compared to the bi-linear construction in the semi-logarithmic plane, identifying yield points from a bi-linear construction in the linear  $v:\bar{p}$  or  $v:p^*$  planes has been discarded in the current work.

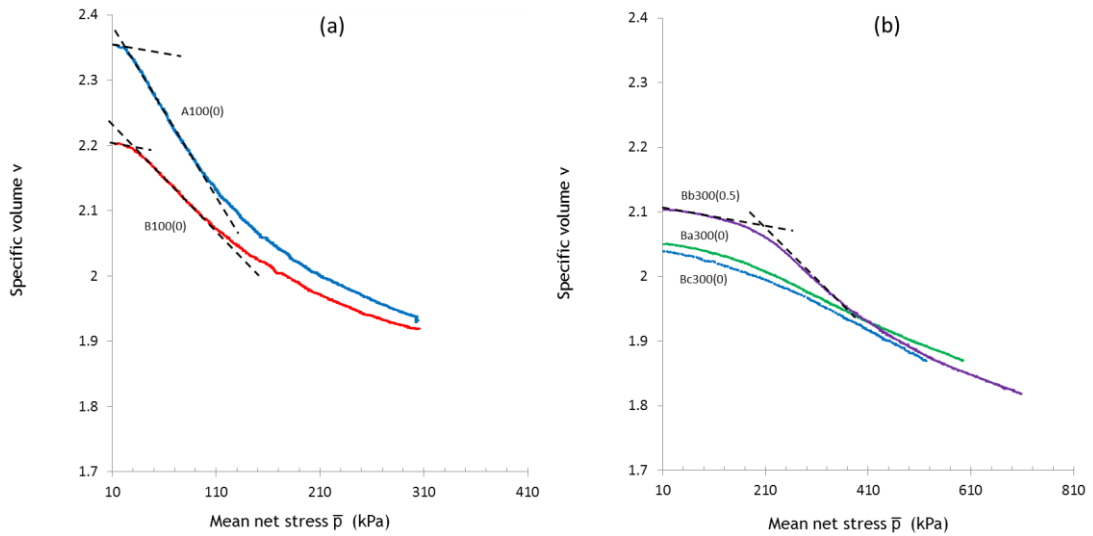


Figure 6.13 Examples of bi-linear construction in the  $v:\bar{p}$  plane

### 6.4.3 Strain energy

A further method for identifying yield stresses is based on the calculation during the test of the input energy per unit volume,  $W$ , as:

$$W = \sum (p^* \delta \varepsilon_v + q \delta \varepsilon_s + s^* \delta S_r) \quad (6.12)$$

The summation in Equation 6.12 is extended over the number of increments of volumetric strain, shear strain and degree of saturation ( $\delta \varepsilon_v$ ,  $\delta \varepsilon_s$ ,  $\delta S_r$ ) in which the test is subdivided. The corresponding values of mean Bishop's stress, deviator stress and modified suction ( $p^*$ ,  $q$ ,  $s^*$ ) are measured at the middle of each increment. The input energy is then plotted against the length of the stress vector increment  $L$  defined as:

$$L = [(p^* - p_0^*)^2 + (q - q_0)^2 + (s^* - s_0^*)^2]^{1/2} \quad (6.13)$$

where  $p_0^*$ ,  $q_0$  and  $s_0^*$  are the mean Bishop's stress, deviator stress and modified suction at the beginning of loading. Figure 6.14 shows typical plots of input energy against stress vector increment length, for Tests A100(0) and A300(1), using linear and semi-logarithmic scales. For Test A100(0), the linear scale plot shows a change in gradient at  $W \approx 0.5 \text{ kJ/m}^3$ , which corresponds to  $\bar{p} \approx 23 \text{ kPa}$ . However, in the semi-logarithmic scale, the input energy during the test increases rather gradually, which makes the identification of the yield point more difficult. The input energy curve of Test A300(1) does not indicate any sharp change of gradient, either in the linear or in the semi-logarithmic scales, so in this case the yield stress can only be obtained indirectly by applying, for example, a bi-linear construction to the input energy curve. However it is less laborious to apply directly a bi-linear construction directly to the original compression curve in the  $v: \ln \bar{p}$  or  $v: \ln p^*$  plane than to the derived input energy curve.

In conclusion, the bi-linear construction in the  $v: \ln \bar{p}$  or  $v: \ln p^*$  plane provides a more systematic and an easier method of identifying yield stresses than other common alternatives and has therefore been used in all tests of the present work.

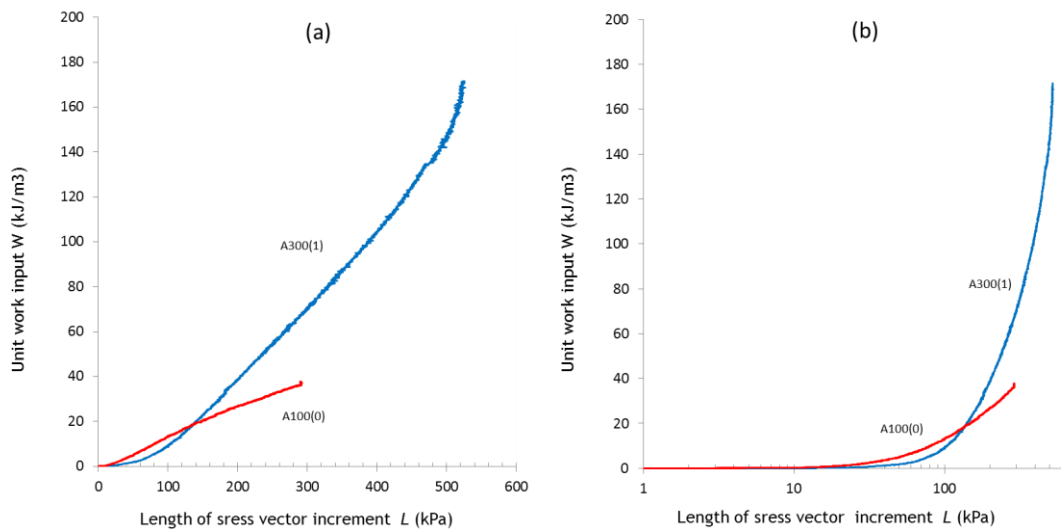


Figure 6.14 Examples of absorbed energy plots in the: (a)  $W:L$  plane, (b)  $W:\ln L$  plane

### 6.5 INTERPRETATION OF YIELD POINTS IN THE $q:\bar{p}$ AND $q:p^*$ PLANES

As previously mentioned, yield points are obtained in this work by applying a bi-linear construction to the compression curves in the  $v: \ln \bar{p}$  or  $v: \ln p^*$  plane (see Section 6.4). Some of these yield points are used to explore the initial yield curves (after compaction), which are shown in the  $q:\bar{p}$  plane in Figures 6.15a, 6.15c and 6.15e and in the  $q:p^*$  plane in Figures 6.15b, 6.15d and 6.15f. Other yield points are used to explore the

evolved yield curves (changed by a loading stage), which are shown in the  $q:\bar{p}$  plane in Figures 6.16a, 6.16c and 6.16e and in the  $q:p^*$  plane in Figures 6.16b, 6.16d and 6.16f.

### 6.5.1 Yield curves in the $q:\bar{p}$ plane

Figures 6.15a and 6.15b show the constant suction cross-sections of the initial yield surface of the isotropically compacted samples (measured from Test Series A0, A100 and A300) while Figures 6.15c and 6.15d show the constant suction cross-sections of the initial yield surface of the anisotropically compacted samples (measured from Test Series B0, B100 and B300). Figures 6.15e and 6.15f show a constant suction cross-section of the initial yield surface for Test Series Be100. Figure 6.16 shows that, for the anisotropically compacted samples, the cross-section of the initial yield surface at  $s = 300$  kPa evolves (in both size and orientation) during loading stages at  $[\Delta q/\Delta \bar{p}] = 1.2$  (Test Series Ba300),  $[\Delta q/\Delta \bar{p}] = 0$  (Test Series Bb300 and Bd100) and  $[\Delta q/\Delta \bar{p}] = -1$  (Test Series Bc300).

Each set of yield points defining a constant suction cross-section of the yield surface is fitted in the  $q:\bar{p}$  plane by the following distorted ellipse (see Figures 6.15a, 6.15c, 6.15e, 6.16a and 6.16c and 6.16e):

$$f = \left( q - \alpha(\bar{p} + p_s(s)) \right)^2 - m^2 (\bar{p} + p_s(s)) (\bar{p}_m - \bar{p}) = 0 \quad (6.14)$$

where  $p_s(s)$  (i.e. the intersect of the distorted ellipse with the negative  $\bar{p}$  axis) is taken from the critical state line at suction  $s$  (see column 5 in Table 6.4),  $m$  is the aspect ratio while  $\bar{p}_m$  and  $\alpha$  define the current size and inclination of the yield curve. Alternative forms of distorted or rotated elliptical curves were considered, including those proposed by Stropeit et al. (2008) and D'Onza et al. (2010) (see Section 2.8.3), but Equation 6.14 was found to give the most satisfactory match. It was found that good matching could be achieved with the aspect ratio  $m$  and inclination  $\alpha$  assumed constant for all constant suction cross-sections of a given yield surface. The three yield curves obtained from Test Series A0, A100 and A300 (or the three yield curves obtained from Test Series B0, B100 and B300) therefore have different sizes but the same inclination. This assumption is supported by the experimental observation that samples with the same fabric anisotropy show similar behaviour at different suction levels (see Sections 5.5 and 5.6).

As a subsequent refinement of fitting, different values of aspect ratio  $m$  were set for the upper and lower sections of the curve, i.e. the sections above and below the vertical tangent points, so that  $m = m_c$  for  $q/(\bar{p} + p_s(s)) > \alpha$  and  $m = m_e$  for  $q/(\bar{p} + p_s(s)) < \alpha$ .

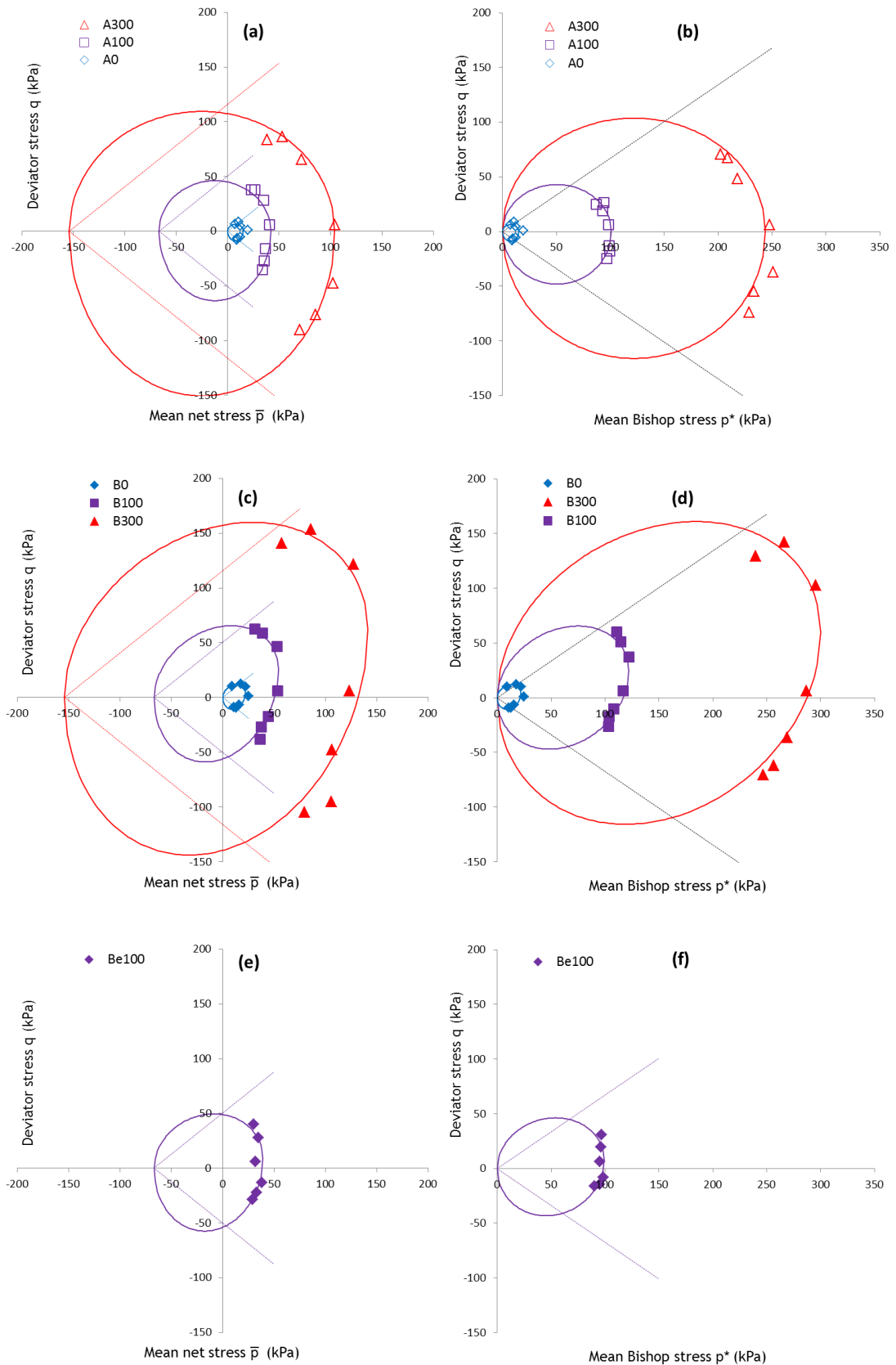


Figure 6.15 Constant suction cross-sections of initial yield surfaces in the  $q$ : $\bar{p}$  and  $q$ : $p^*$  planes for: (a)(b) isotropically compacted samples; (c)(d) anisotropically compacted samples; (e)(f) anisotropically compacted samples at higher void ratio (Test Series Be100)

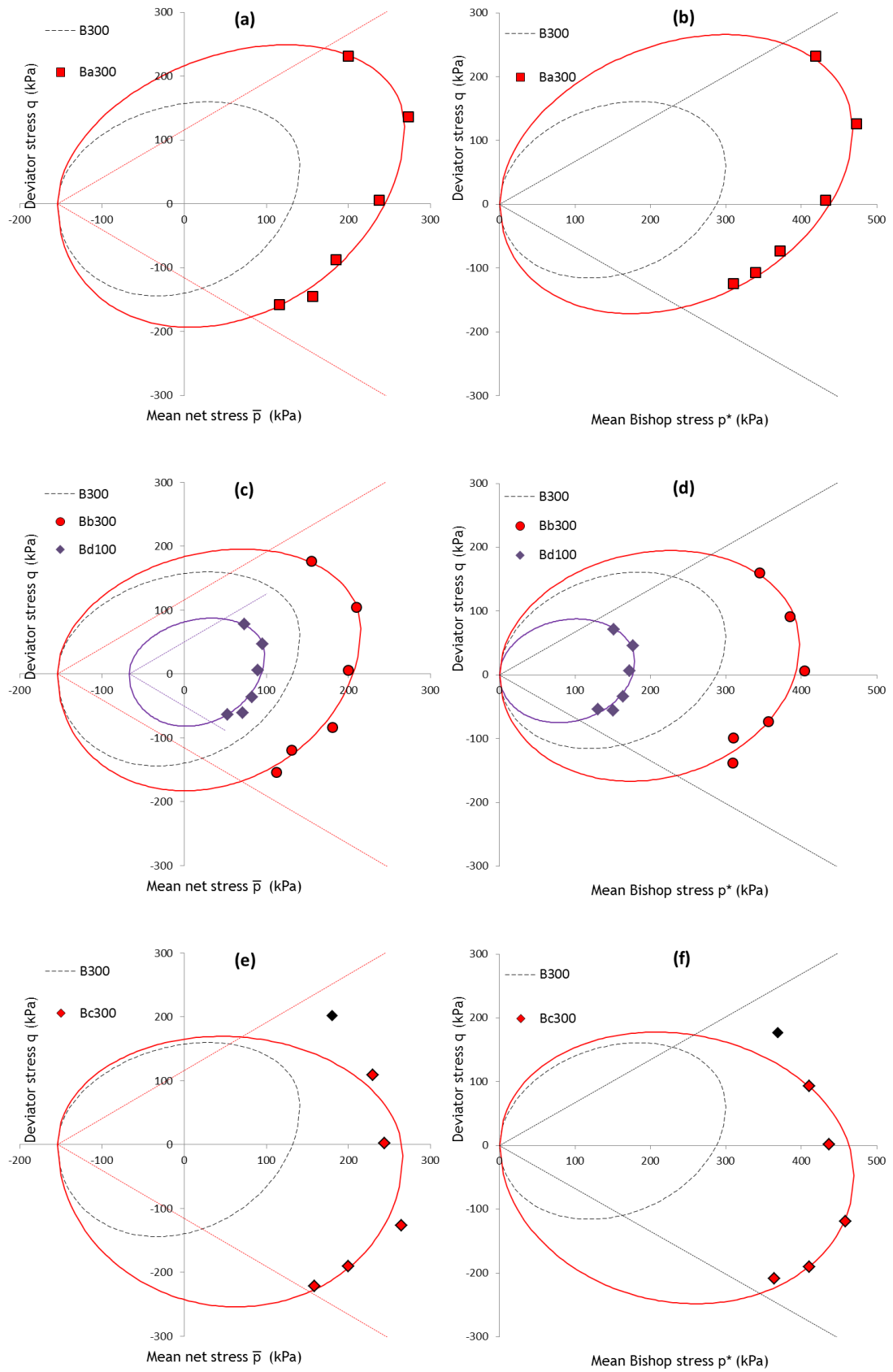


Figure 6.16 Constant suction cross-sections of yield surfaces in the  $q:\bar{p}$  and  $q:p^*$  planes for anisotropically compacted samples loaded at: (a)(b)  $[\Delta q/\Delta \bar{p}] = 1.2$ ; (c)(d)  $[\Delta q/\Delta \bar{p}] = 0$ ; (e)(f)  $[\Delta q/\Delta \bar{p}] = -1$

It was found that the same values of  $m_c$  and  $m_e$  ( $m_c = 0.85$  and  $m_e = 1.17$ ) can be used for all constant suction cross-sections of the yield surfaces, although these values differ from the critical state stress ratio  $M = 0.752$  (see Table 6.4). The value of  $\alpha$  was set to zero for all constant suction cross-sections of the initial yield surface for the isotropically compacted samples (see Figure 6.15a), to reflect the isotropy of the soil fabric. Similarly, a single value of  $\alpha = 0.21$  was found to fit all three constant suction cross-sections of the initial yield surface for the anisotropically compacted samples (Figure 6.15c). For Test Series Be100 (see Figure 6.15e), a smaller value of  $\alpha = 0.08$  was found to provide the best fit to the data as these samples have a smaller degree of initial anisotropy than the anisotropic samples in Figure 6.15c.

Figures 6.16a, 6.16c and 6.16e show that the loading stages in Test Series Ba300, Bb300 and Bc300 increase or decrease the inclination of the yield curve from an initial value of  $\alpha = 0.21$  to final values of  $\alpha = 0.29$ ,  $\alpha = 0.19$  and  $\alpha = -0.04$  respectively. The experimental yield points of Test Series Bd100 (see Figure 6.16c) can also be adequately fitted with a value of  $\alpha = 0.19$  (as in Test Series Bb300) which reflects the similarity of loading history between these two test series, as already pointed out in Section 5.6. One yield point (corresponding to Test Bc300(1.2) and marked as black in Figure 6.16e) was considered unreliable due to bulging of the sample during probing.

### 6.5.2 Yield curves in the $q:p^*$ plane

Figures 6.15b, 6.15d, 6.15f, 6.16b, 6.16d and 6.16f show that each constant suction yield curve can be fitted in the  $q:p^*$  plane by the following distorted ellipse passing through the origin:

$$f = (q - \alpha^* p^*)^2 - m^{*2} p^* (p_m^* - p^*) = 0 \quad (6.15)$$

where  $m^*$  is the aspect ratio while  $p_m^*$  and  $\alpha^*$  are the current size and inclination of the distorted ellipse. As in the  $q:\bar{p}$  plane, different values of  $m^*$  are selected for the upper and lower sections of each constant suction yield curve (i.e. the sections above and below the vertical tangent points), so that  $m^* = m_c^*$  for  $q/p^* > \alpha^*$  and  $m^* = m_e^*$  for  $q/p^* < \alpha^*$ . Similar to the fitting in the  $q:\bar{p}$  plane, the same values of  $m_c^*$  and  $m_e^*$  (i.e.  $m_c^* = 0.85$ ,  $m_e^* = 0.95$ ) can be used for all constant suction cross-sections. Again, these values of  $m_c^*$  and  $m_e^*$  are significantly greater than the critical state stress ratio  $M^* = 0.672$  (see Table 6.6). The value of  $\alpha^*$  was set to zero for all three constant suction cross-sections of the initial yield surface for the isotropically compacted samples (see Figure 6.15b). Similarly, it was found that a single value of  $\alpha^* = 0.20$  could be used for all three constant suction cross-sections of the initial yield surface for the anisotropically

compacted samples (Figure 6.15d). For Test Series Be100 (see Figure 6.15f), a smaller value of  $\alpha^* = 0.08$  was found adequate which is, again, consistent with the fact that these samples have a smaller initial anisotropy than the anisotropic samples in Figure 6.15d.

The loading stages in Test Series Ba300, Bb300 and Bc300 increase or decrease the initial inclination of the yield curve in the  $q:p^*$  plane from an initial value of  $\alpha^* = 0.20$  to final values of  $\alpha^* = 0.25$ ,  $\alpha^* = 0.12$  and  $\alpha^* = -0.10$  respectively (see Figures 6.16b, 6.16d and 6.16f). The experimental yield points of Test Series Bd100 (see Figure 6.16d) can also be adequately fitted with a value of  $\alpha^* = 0.12$  (as in Test Series Bb300) confirming once again the similarity between these two test series.

Table 6.9 Yield curve parameters in the  $q:\bar{p}$  and  $q:p^*$  planes

Test series	$q:\bar{p}$ plane				$q:p^*$ plane			
	$m_c$	$m_e$	$\alpha$	$\bar{p}_m$ (kPa)	$m_c^*$	$m_e^*$	$\alpha^*$	$p_m^*$ (kPa)
A300			0	104			0	244
A100			0	42			0	101
A0			0	15			0	16
B300			0.21	141			0.20	300
B100			0.21	54			0.20	122
B0	0.85	1.17	0.21	22	0.85	0.95	0.20	23
Be100			0.08	39			0.08	99
Ba300			0.29	268			0.25	468
Bb300			0.19	215			0.12	398
Bc300			-0.04	266			-0.10	470
Bd100			0.19	98			0.12	179

The values of  $m_c$ ,  $m_e$ ,  $\alpha$ ,  $\bar{p}_m$ ,  $m_c^*$ ,  $m_e^*$ ,  $\alpha^*$  and  $p_m^*$  are summarised for all test series in Table 6.9. The values of  $\bar{p}_m$  and  $p_m^*$  are substantially bigger for the anisotropic yield curves than for the corresponding isotropic yield curves, due to the lower initial values of specific volume of the anisotropic samples compared to the isotropic samples (see Table 5.1). Similarly, the values of  $\bar{p}_m$  and  $p_m^*$  are much higher for Test Series Ba300 and Bc300

than for Test Series Bb300, although all samples in these test series were initially loaded to the same value of  $\bar{p}$ .

In conclusion, the process of anisotropic compaction employed in the present work generates a moderately anisotropic fabric (as indicated by the small values of  $\alpha = 0.21$  and  $\alpha^* = 0.20$  in the  $q:\bar{p}$  and  $q:p^*$  planes respectively). This is due to the relatively small value of the Bishop's stress ratio at the end of compaction ( $\eta^* = q/p^* \approx 0.5$ ), as shown in Figures 5.8 and 5.9, and to the large suction which stabilizes inter-particle contacts during compaction. Finally, although the samples in Test Series Ba300 are loaded at the same net stress ratio as during anisotropic compaction (i.e.  $[\Delta q/\Delta \bar{p}] = 1.2$ ), the resulting values of  $\alpha$  and  $\alpha^*$  are bigger compared to those of Test Series B300 ( $\alpha = 0.29$  against  $\alpha = 0.21$  and  $\alpha^* = 0.25$  against  $\alpha^* = 0.20$ ). This is again explained by the larger value of the Bishop's stress ratio at the end of the loading stage in series Ba300 ( $\eta^* = q/p^* \approx 0.55$ ) than at the end of compaction in Test Series B300 ( $\eta^* = q/p^* \approx 0.5$ ).

## 6.6 EXPERIMENTAL FLOW VECTORS

Due to the difficulty in separating the elastic and plastic components of strains (and because the elastic strain components tend to be significantly smaller than the plastic strain components) experimental flow vectors are here calculated in terms of total strains instead of plastic strains. In particular, the total shear strain  $\varepsilon_s$  is plotted against the total volumetric strain  $\varepsilon_v$  over a mean net stress increment of 10 kPa (which is small enough to give a linear relationship between the two) starting from the yield points obtained in Section 6.4. The best-fit line to this curve is then calculated and its gradient is taken as the gradient of the plastic flow vector. If the curve shows a marked non-linearity in the  $\varepsilon_s:\varepsilon_v$  plane, the stress increment is gradually reduced until a linear relationship is obtained. A typical determination of the experimental flow vector is shown in Figure 6.17 for Test A100(1).

The experimental flow vectors determined in this way were superimposed on the corresponding yield curves in the  $q:\bar{p}$  or  $q:p^*$  planes (see Figures 6.18 and 6.19).

During isotropic stress paths, the gradient of the experimental flow vector at yield is positive for Test Series A300, A100 and A0 (see Figures 6.18a and 6.18b) but it is negative for Test Series B300, B100 and B0 (see Figures 6.18c and 6.18d) and is almost zero for Test Series Be100 (see Figures 6.18e and 6.18f). These observations agree very well with the distorted elliptical shape of the constant suction yield curves of the isotropically and anisotropically compacted samples. Normality of the plastic flow vector to yield curves (suggesting an associated flow rule) is evident in some cases (e.g. Test Series Ba300,

Bb300 and Bd100 in Figures 6.19a, 6.19b, 6.19c and 6.19d) but is less evident in other cases (e.g. Test Series A0, A100 and Be100 in Figures 6.18a, 6.18b, 6.18e and 6.18f).

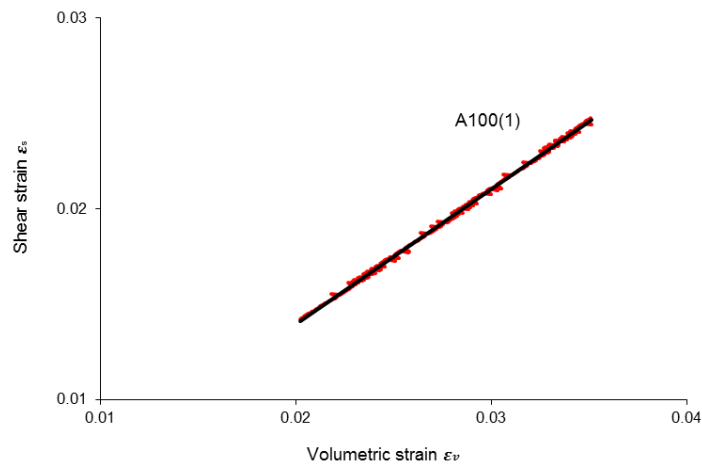


**Figure 6.17** Typical  $\varepsilon_s : \varepsilon_v$  plot to identify plastic flow vector gradient at yielding

As discussed in Sections 5.5 and 5.6, the experiments generally showed a contractant response during plastic loading. This is expected when yielding takes place on the “wet” side of the yield curve and it is indeed consistent with the gradient of the experimental plastic flow vectors in Figures 6.18 and 6.19. However, in the saturated Test (B0(2)), contractant behaviour was also observed while yielding on the “dry” side of the yield curve in both the  $q : \bar{p}$  and  $q : p^*$  planes (see Figures 6.15c and 6.15d respectively). This apparently unexpected behaviour could be a consequence of forcing the saturated critical state line to pass through the origin.

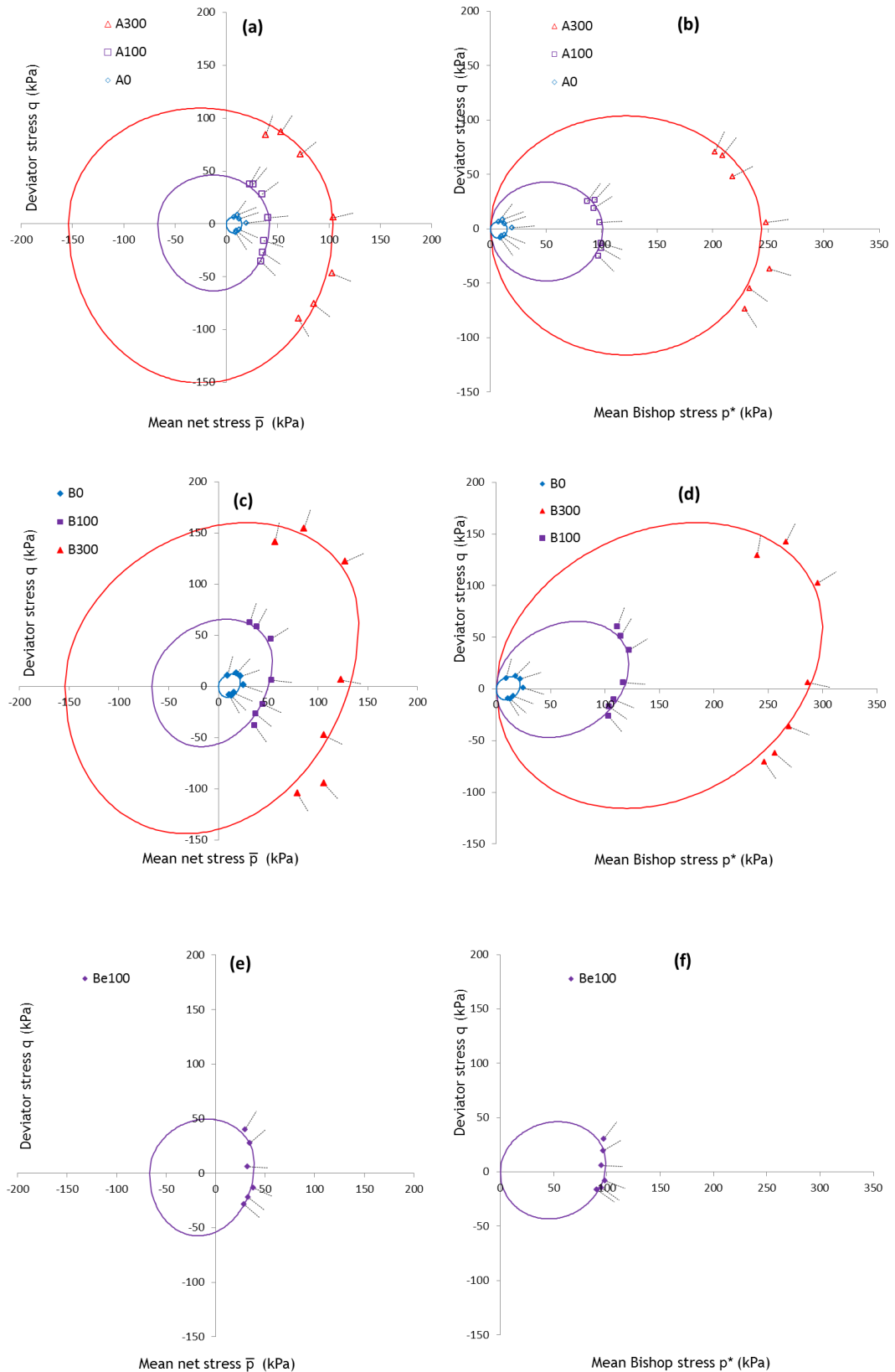


Figure 6.18 Plastic flow vectors superimposed on constant suction cross-sections of initial yield surfaces in the  $q$ : $\bar{p}$  and  $q$ : $p^*$  planes for: (a)(b) isotropically compacted samples; (c)(d) anisotropically compacted samples; (e)(f) anisotropically compacted samples at higher void ratio (Test Series Be100)

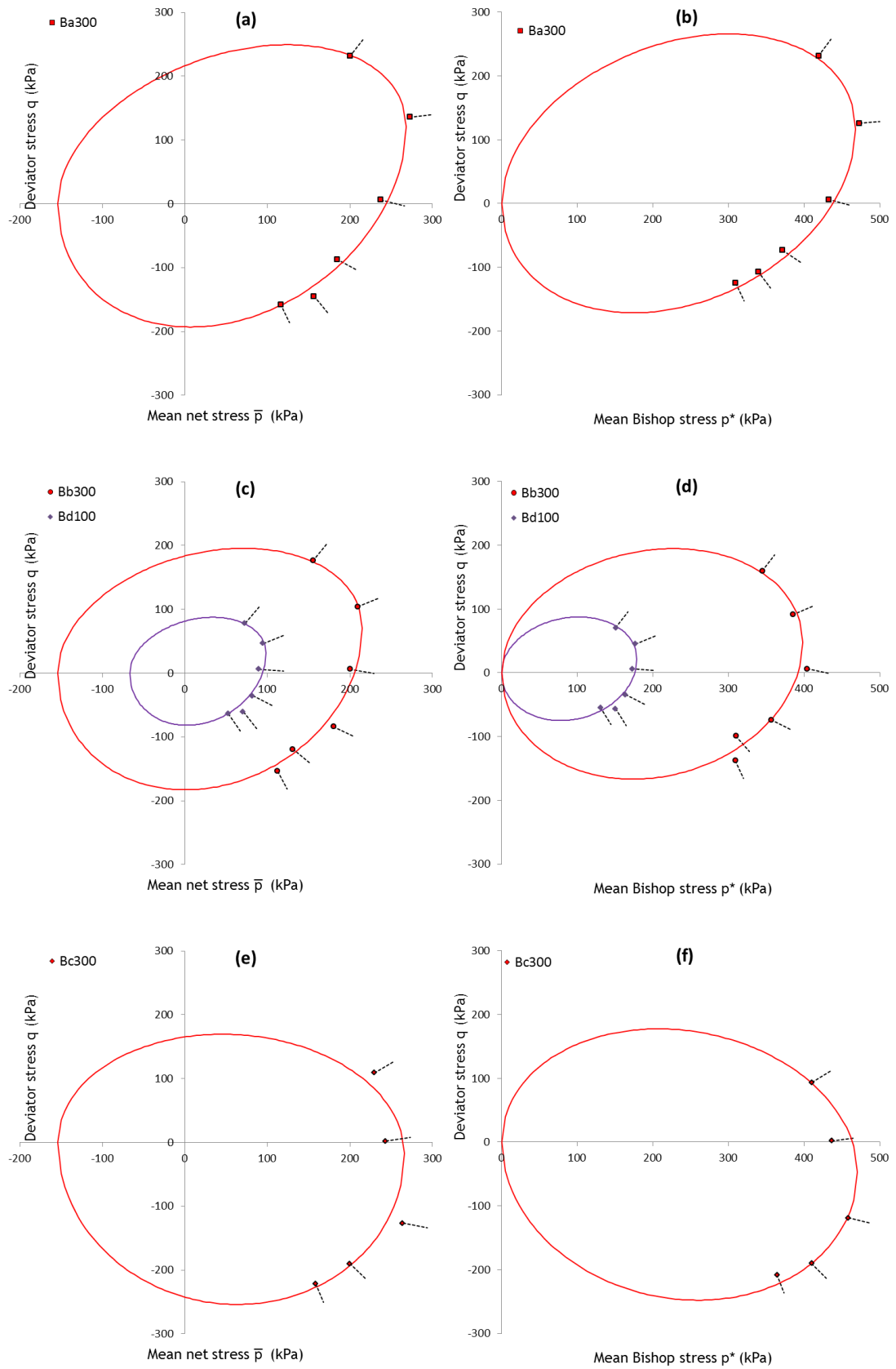


Figure 6.19 Plastic flow vectors superimposed on constant suction cross-sections of yield surfaces in the  $q:\bar{p}$  and  $q:p^*$  planes for anisotropically compacted samples loaded at: (a)(b)  $[\Delta q/\Delta \bar{p}] = 1.2$ ; (c)(d)  $[\Delta q/\Delta \bar{p}] = 0$ ; (e)(f)  $[\Delta q/\Delta \bar{p}] = -1$

## DEVELOPMENT OF AN ANISOTROPIC MODEL

### 7.1 OVERALL APPROACH

This chapter describes the development of a new anisotropic elasto-plastic constitutive model for unsaturated soils. The model combines features from the isotropic model for unsaturated soils of Wheeler et al. (2003a) (described in Section 2.9) with features for modelling of anisotropy taken from the anisotropic model for saturated soils *S – CLAY1* (described in Section 2.7.2).

The approach followed in developing the constitutive model employs Bishop's stresses and modified suction (rather than net stresses and suction) as stress state variables, for the following reasons:

- It is proposed that elastic strains can be related solely to changes of Bishop's stresses (no need to include separately elastic volume changes caused by changes of suction. The experimental evidence from this study is however rather inconclusive on this point (some differences were noticed in the values of  $\kappa^*$  calculated from wetting and unloading stages, see Section 6.1.2);
- Shear strength can, as a reasonable approximation, be uniquely related to Bishop's stress (see Section 6.3.3);
- Yield curves (at constant values of  $s$ ) are simpler in the  $q:p^*$  plane (as they always pass through the origin) than in the  $q:\bar{p}$  plane (see Section 6.5);
- Representing the coupling between mechanical and water retention behaviour is easier with Bishop's stress than with net stress (e.g. see the model of Wheeler et al., 2003a, in Section 2.9).

The constitutive modelling work focused on developing an anisotropic version of the mechanical aspects of the Wheeler et al. (2003a) model i.e. modelling of water retention behaviour was not included. To conduct model simulations of mechanical behaviour with the anisotropic model developed here, so that these could be compared with the experimental results (see Sections 8.6 to 8.9 of the next chapter), experimental values of  $S_r$  were used in the simulations instead of predicted values of  $S_r$  (a detailed description

of the procedure employed is given in Section 8.3). This is because it was then possible to check whether mechanical aspects of the model were performing well. In contrast, if mechanical behaviour was badly predicted with a full combined mechanical and water retention model, it would be unclear whether the fault was with the mechanical aspects of the model or because  $S_r$  was badly predicted by the water retention aspects of the model. It was also clear that the water retention modelling in the Wheeler et al. (2003a) model was relatively crude (e.g. see Figure 2.7) and therefore unlikely to give very precise values of  $S_r$  for the full range of stress paths.

The mechanical model developed in this chapter requires values of  $S_r$ . Therefore for it to be a fully predictive model it would either have to be combined with a separate water retention model or it would subsequently have to be developed to a combined mechanical-water retention model (like Wheeler et al. 2003a) by adding the retention aspects.

## 7.2 ELASTIC BEHAVIOUR

Elastic volumetric and shear strains are given by the same equations as in the extended version of Wheeler et al (2003a) model (see Equations 2.54 and 2.55):

$$d\varepsilon_v^e = \frac{\kappa^* dp^*}{vp^*} \quad (7.1)$$

$$d\varepsilon_s^e = \frac{dq}{3G} \quad (7.2)$$

Unlike the Wheeler et al. (2003a) model, there is no expression for elastic increments of degree of saturation in the anisotropic model developed here, because water retention aspects are not fully developed.

## 7.3 YIELD SURFACES

The model includes three yield surfaces in  $q:p^*:s^*$  space, like the Wheeler et al. (2003a) model: the Loading Collapse (*LC*) yield surface to represent mechanical behaviour (onset of plastic volumetric strains and plastic shear strains) and the *SI* and *SD* yield surfaces to represent water retention behaviour (onset of plastic changes of degree of saturation) (see Figure 7.1). Although the model is limited to prediction of mechanical behaviour, the *SI* and *SD* yield surfaces are still required, because yielding on these surfaces causes coupled movements of the *LC* surface.

Based on the experimental evidence presented in Section 6.5.2, each cross-section of the *LC* yield surface in the  $q:p^*$  plane is in the form of a distorted ellipse (see Figure 7.2), defined by:

$$f_{LC} = (q - \alpha^* p^*)^2 - m^{*2} p^* (p_m^* - p^*) = 0 \tag{7.3}$$

where  $\alpha^*$  and  $p_m^*$  are the hardening parameters defining current anisotropy and current size of yield surface.  $m^*$  is the aspect ratio, which can take a triaxial compression value  $m_c^*$  for  $\eta^* \geq \alpha^*$  and a triaxial extension value  $m_e^*$  for  $\eta^* \leq \alpha^*$  (where  $\eta^* = q/p^*$ ) (see experimental evidence in Section 6.5.2). Experimental evidence in Section 6.5.2 suggests that  $m_c^*$  and  $m_e^*$  are both greater than the critical state stress ratio  $M^*$ , hence it is clear that  $m^*$  cannot take the form  $(M^{*2} - \alpha^{*2})^{1/2}$  that would correspond to the Dafalias (1986) yield curve expression employed in the *S – CLAY1* model (see Equation 2.29). In Section 7.8 below two possibilities are considered: either that  $m^*$  is a constant (this requires a non-associated flow rule in order for the model to predict critical states for  $q = M^* p^*$ ) or that  $m^*$  varies with  $\alpha^*$  (such that an associated flow rule can be employed).

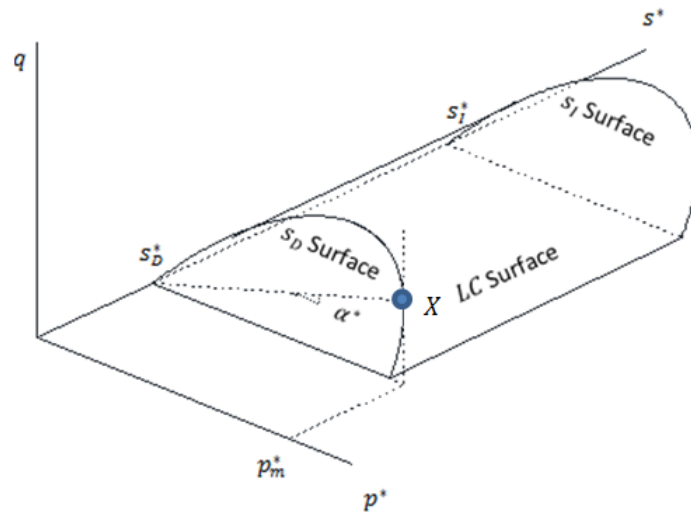


Figure 7.1 Yield surfaces in  $q:p^*:s^*$  space

Yielding on the *LC* yield surface corresponds to the onset of plastic volumetric strains and plastic shear strains, but consideration of the flow rule on this yield surface is delayed until Section 7.8 below.

The *SI* and *SD* yield surfaces are represented by vertical walls in the  $q:p^*:s^*$  space, as in the model of Wheeler et al. (2003a), defined by:

$$f_{SI} = s^* - s_I^* = 0 \quad (7.4)$$

$$f_{SD} = s_D^* - s^* = 0 \quad (7.5)$$

where  $s_I^*$  and  $s_D^*$  are the hardening parameters defining the current positions of the  $SI$  and  $SD$  surfaces respectively (see Figure 7.1).

The flow rule for yielding on both  $SI$  and  $SD$  surfaces is simply:

$$d\varepsilon_v^p = d\varepsilon_s^p = 0 \quad (7.6)$$

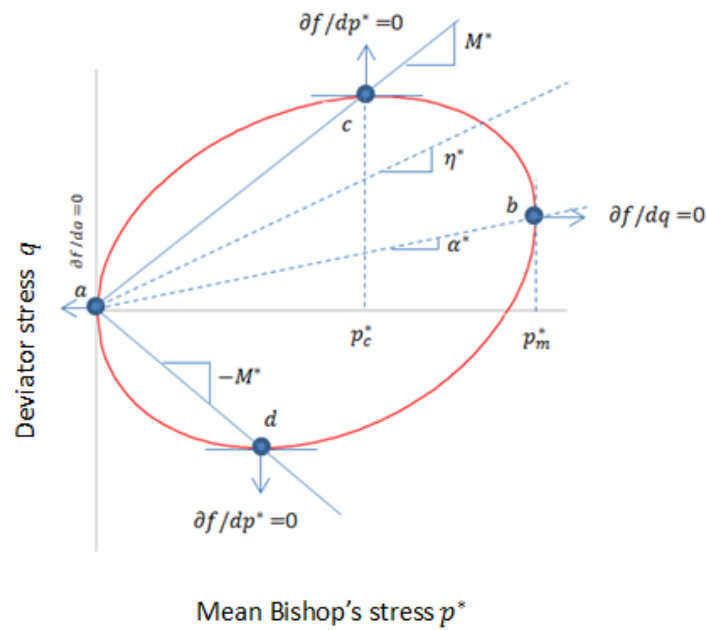


Figure 7.2 Cross-section of the  $LC$  yield surface (at the critical state) in the  $q:p^*$  plane

#### 7.4 COUPLED MOVEMENTS OF THE YIELD SURFACES

When yielding on the  $LC$  surface alone, coupled movements of the  $SI$  and  $SD$  yield surfaces occur, governed by the same coupling relationship as in the Wheeler et al. (2003a) model:

$$\frac{ds_I^*}{s_I^*} = \frac{ds_D^*}{s_D^*} = k_2 \frac{dp_m^*}{p_m^*} \quad (7.7)$$

where  $k_2$  is a coupling parameter.

Similarly, when yielding on the  $SI$  or  $SD$  surface alone, coupled movements of the  $LC$  surface occur, governed by the same coupling relationship as in the Wheeler et al. (2003a) model:

$$\frac{dp_m^*}{p_m^*} = k_1 \frac{ds_I^*}{s_I^*} = k_1 \frac{ds_D^*}{s_D^*} \quad (7.8)$$

Note that Equations 7.7 and 7.8 imply that during yielding on any yield surface:

$$\frac{ds_I^*}{s_I^*} = \frac{ds_D^*}{s_D^*} \quad (7.9)$$

### 7.5 HARDENING LAWS FOR CHANGES OF $p_m^*$ , $s_I^*$ AND $s_D^*$

The hardening law during yielding on the  $LC$  yield surface alone is the same as in the model of Wheeler et al. (2003a) (with  $p_0^*$  replaced by  $p_m^*$ ):

$$\frac{dp_m^*}{p_m^*} = \frac{v d\varepsilon_v^p}{(\lambda - \kappa^*)} \quad (7.10)$$

where  $\lambda$  (a soil constant) is the gradient of the saturated normal compression line in the  $v: \ln p'$  plane followed by an isotropic sample ( $\alpha^* = 0$ ) during isotropic loading.

Following the same logic as in the development of the model of Wheeler et al. (2003a) (see Equation 2.70), allowing for the coupled movements of the yield surfaces, the general hardening law linking plastic volumetric strains to the movements of the surfaces is:

$$d\varepsilon_v^p = \frac{(\lambda - \kappa^*)}{v(1 - k_1 k_2)} \left( \frac{dp_m^*}{p_m^*} - k_1 \frac{ds_D^*}{s_D^*} \right) \quad (7.11)$$

Equation 7.11 is a general hardening law, applicable to yielding on the  $LC$  surface alone, the  $SI$  or  $SD$  surface alone or on two surfaces simultaneously. During yielding on the  $SI$  or  $SD$  yield surface alone, the flow rule of Equation 7.6 applies ( $d\varepsilon_v^p = 0$ ) and Equation 7.11 converts to the coupling relationship of Equation 7.8. During yielding on the  $LC$  yield surface alone, the coupling relationship of Equation 7.7 applies, and Equation 7.11 converts to the special case of the hardening law given in Equation 7.10. Unlike the complete mechanical-water retention model of Wheeler et al. (2003a), in the new anisotropic mechanical model no statement is made linking plastic changes of  $S_r$  to the movements of the yield surfaces.

## 7.6 VARIATION OF $v$

For the special case when the soil state remains on the edge between  $LC$  and  $SD$  yield surfaces at the point where the tangent to the  $LC$  surface is vertical i.e. point  $X$  in Figure 7.1 ( $p^* = p_m^*$ ,  $\eta^* = \alpha^*$  and  $s^* = s_D^*$ ), the total increments of specific volume  $v$  can be expressed (by using Equations 7.1 and 7.11) as:

$$dv = dv^e + dv^p = -\frac{\kappa^* dp^*}{p^*} - \frac{(\lambda - \kappa^*)}{(1 - k_1 k_2)} \left( \frac{dp^*}{p^*} - k_1 \frac{ds^*}{s^*} \right) \quad (7.12)$$

As presented by Lloret (2011), Equation 7.12 can be integrated to show that points such as  $X$  lie on a unique planar surface in the  $v: \ln p^*: \ln s^*$  space (of the same form as Equation 2.74 for the Wheeler et al., 2003a, model):

$$v = N^* - \lambda^* \ln p^* + k_1^* \ln s^* \quad (7.13)$$

where  $N^*$  is a soil constant and:

$$\lambda^* = \frac{(\lambda - \kappa^* k_1 k_2)}{(1 - k_1 k_2)} \quad (7.14)$$

$$k_1^* = k_1 \frac{(\lambda - \kappa^*)}{(1 - k_1 k_2)} \quad (7.15)$$

In particular, the planar surface described by Equation 7.13 applies to isotropic samples ( $\alpha^* = 0$ ) subjected to isotropic compression ( $\eta^* = 0$ ) if the soil state lies on both  $LC$  and  $SD$  yield surfaces. For general stress states, which do not necessarily lie on the  $LC$  and  $SD$  surfaces, the value of  $v$  can be calculated by considering an elastic path starting from Point  $X$  (see Figure 7.1). This results in the following general expression for  $v$ :

$$v = N^* - \lambda^* \ln p_m^* + k_1^* \ln s_D^* + \kappa^* \ln \left( \frac{p_m^*}{p^*} \right) \quad (7.16)$$

## 7.7 HARDENING LAW FOR CHANGES OF $\alpha^*$

Wheeler (1997) and Wheeler et al. (2003b) argued convincingly in the development of the  $S - CLAY1$  anisotropic model for saturated soils that evolution of anisotropy  $\alpha$  must depend upon both plastic volumetric strains and plastic shear strains. However, they did not provide convincing arguments for the specific form of hardening law describing the variation of  $\alpha$  within  $S - CLAY1$  (see Equation 2.31), where plastic volumetric strains and plastic shear strains are each attempting to change  $\alpha$  towards a different instantaneous

target value ( $3\eta/4$  and  $\eta/3$  respectively). Therefore, an alternative hardening law for the variation of  $\alpha^*$  is proposed here, which is considered to be more logical. This takes the form:

$$d\alpha^* = \mu[f(\eta^*) - \alpha^*] \left[ (d\varepsilon_v^p)^2 + \frac{9}{2}(d\varepsilon_s^p)^2 \right]^{1/2} \quad (7.17)$$

where  $\mu$  is a soil constant.  $f(\eta^*)$  is a function of  $\eta^*$ , which represents the current target value for  $\alpha^*$ , with both plastic volumetric strains and plastic shear strains attempting to change  $\alpha^*$  towards this current target value. The particular manner in which plastic volumetric strain increments and plastic shear strain increments are combined in Equation 7.17 has been selected because this relates to the length of the plastic strain increment vector in principal strain space:

$$\left[ (d\varepsilon_v^p)^2 + \frac{9}{2}(d\varepsilon_s^p)^2 \right]^{1/2} = \sqrt{3} \left[ (d\varepsilon_1^p)^2 + (d\varepsilon_2^p)^2 + (d\varepsilon_3^p)^2 \right]^{1/2} \quad (7.18)$$

The function  $f(\eta^*)$  which represent the target value for  $\alpha^*$  in Equation 7.17, could be selected as a continuous non-linear function of  $\eta^*$ . This would resemble the overall target value for  $\alpha$  predicted by the *S – CLAY1* model for constant  $\eta$  stress paths (see Figure 7.3). However, in the interests of simplicity, a simple tri-linear relationship for  $f(\eta^*)$  has been employed at this stage:

$$f(\eta^*) = \begin{cases} -cM^* & \text{for } \eta^* \leq -M^* \\ c\eta^* & \text{for } -M^* < \eta^* < M^* \\ cM^* & \text{for } \eta^* \geq M^* \end{cases} \quad (7.19)$$

where  $M^*$  is the critical state stress ratio (a soil constant) and  $c$  is a further soil constant. The variation of  $f(\eta^*)$  with  $\eta^*$  described by Equation 7.19 is illustrated in Figure 7.4.

Equation 7.17 predicts a unique value of  $\alpha^*$  at critical states (i.e. a unique degree of anisotropy at critical states). Given that critical states correspond to  $\eta^* = \pm M^*$  and at critical states plastic shear strains can increase indefinitely, Equations 7.17 and 7.19 predict a critical state value of  $\alpha^*$  given by:

$$\alpha_{cs}^* = \pm cM^* \quad (7.20)$$

where the positive and negative signs in Equation 7.20 correspond to triaxial compression and triaxial extension respectively.

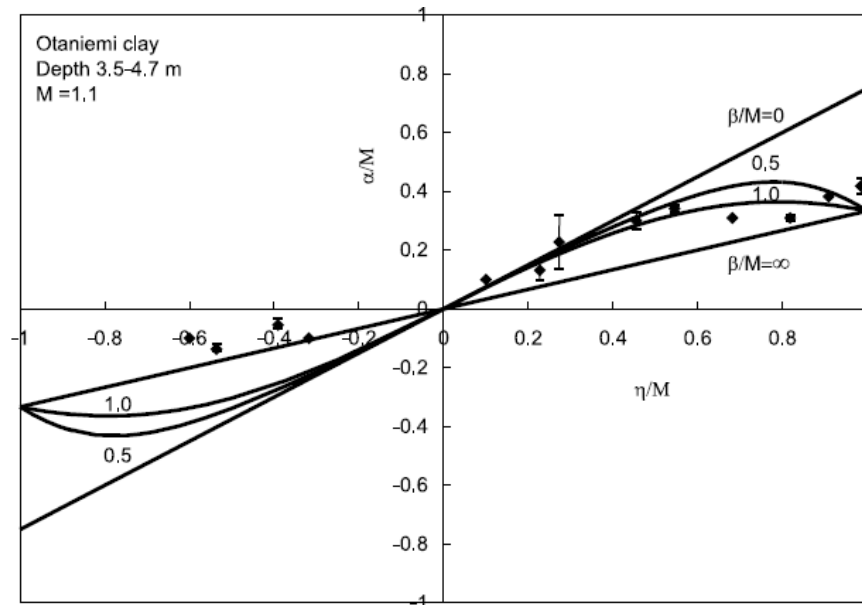


Figure 7.3 Non-linear variation of target value of  $\alpha$  for constant  $\eta$  stress paths in the *S – CLAY1* model (Wheeler et al. 2003b)

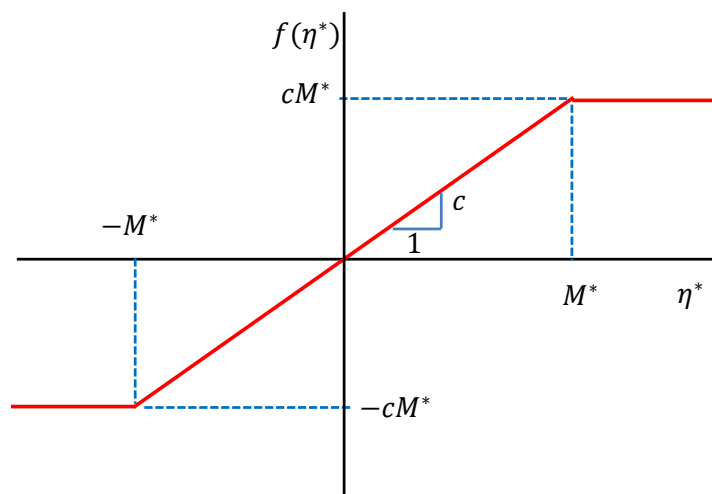


Figure 7.4: Tri-linear variation of  $f(\eta^*)$  with  $\eta^*$

### 7.8 FLOW RULE ON *LC* SURFACE AND VARIATION OF $m^*$

Figure 7.5 shows experimental data points (taken from Section 6.5.2) showing the observed variation of the aspect ratio  $m^*$  of the *LC* yield surface (see Equation 7.3), for both the triaxial compression and triaxial extension sections of the yield surface ( $m_c^*$  and  $m_e^*$  respectively), where  $m_c^*$  applies for  $\eta^* \geq \alpha^*$  and  $m_e^*$  applies for  $\eta^* \leq \alpha^*$ . The experimental data points indicate that  $m_c^*$  is essentially constant at a value of 0.85 for  $\alpha^*$  ranging from  $-0.10$  to  $+0.25$ . Similarly, the experimental data points indicate that  $m_e^*$

is essentially constant at a value of 0.95 for  $\alpha^*$  ranging from  $-0.10$  to  $+0.25$  (see Table 6.9 in Section 6.5.2).

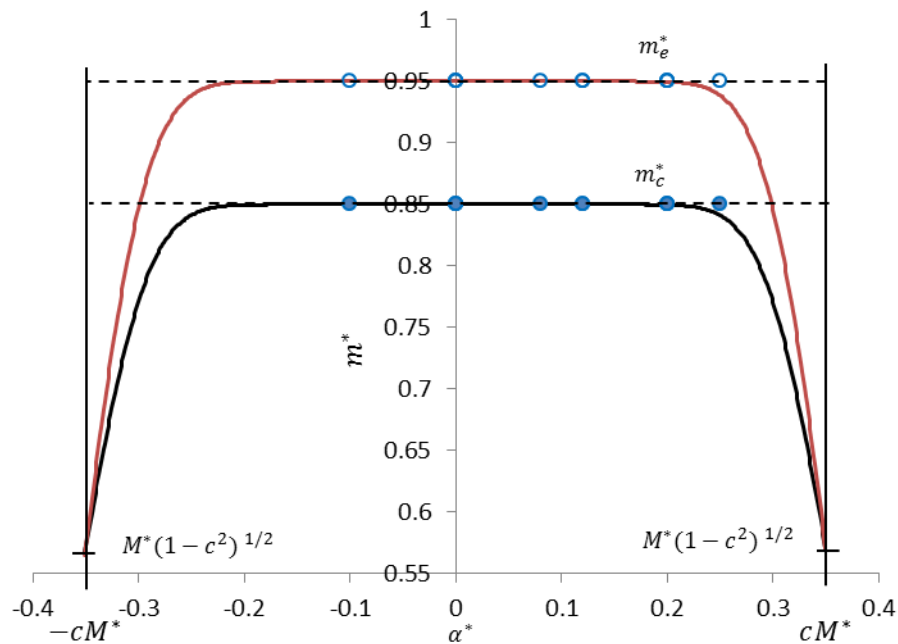


Figure 7.5 Variation of  $m^*$  with  $\alpha^*$

The solid lines and dashed lines in Figure 7.5 illustrate two alternative possibilities for the variation of  $m_c^*$  and  $m_e^*$  over the full range of  $\alpha^*$  predicted by the model (from  $\alpha^* = -cM^*$  to  $\alpha^* = +cM^*$ , see Figure 7.4). The solid lines show  $m_c^*$  and  $m_e^*$  both decreasing at extreme values of  $\alpha^*$ , both reaching a value of  $M^*(1-c^2)^{1/2}$  at the critical state condition ( $\alpha^* = \pm cM^*$ ). This would mean that when a critical state is reached (but only for this condition) the yield curve shape would correspond to the Dafalias (1986) expression assumed in the *S-CLAY1* model (Equation 2.29) and for this condition the yield curve would have a horizontal tangent at  $\eta^* = M^*$ . The model could thus employ an associated flow rule and correctly predict the occurrence of critical states at the desired stress state of  $q = M^*p^*$ . The dashed lines in Figure 7.5 show an alternative scenario, where  $m_c^*$  and  $m_e^*$  each remains constant over the full range of  $\alpha^*$ . In this case, a non-associated flow rule would be required in order for the model to predict the occurrence of critical states at the desired stress state of  $q = M^*p^*$ . Two alternative versions of the model are therefore developed. Version 1 employs an associated flow rule and hence has to allow for variation of  $m_c^*$  and  $m_e^*$  with  $\alpha^*$  (the solid lines in Figure 7.5). Version 2 assumes that  $m_c^*$  and  $m_e^*$  both remain constant over the full range of  $\alpha^*$  (the dashed lines in Figure 7.5) and hence has to employ a non-associated flow rule.

### 7.8.1 Version 1: associated flow rule and $m^* = f(\alpha^*)$

Application of an associated flow rule to the *LC* yield surface expression of Equation 7.3 results in the following relationship:

$$\frac{d\varepsilon_s^p}{d\varepsilon_v^p} = \frac{2(\eta^* - \alpha^*)}{(m^{*2} + \alpha^{*2} - \eta^{*2})} \quad (7.21)$$

If the critical state is to be predicted at  $\eta^* = \pm M^*$ , and at these states the values of  $\alpha^*$  is given by  $\alpha^* = \pm cM^*$  (see Equation 7.20), inspection of Equation 7.21 shows that at this value of  $\alpha^*$  the aspect ratio  $m^*$  must have a value of  $M^*(1 - c^2)^{1/2}$ .

If  $m_c^*$  and  $m_e^*$  are each assumed to be continuous functions of  $\alpha^*$  (over the range  $-cM^* \leq \alpha^* < cM^*$ ), what is required for each is a function that remains approximately constant for  $\alpha^*$  values between  $-0.25$  and  $+0.25$  but then decreases sharply towards a limiting value of  $M^*(1 - c^2)^{1/2}$  as  $\alpha^*$  approaches  $-cM^*$  or  $cM^*$  (see Figure 7.5). The function selected to provide this variation is:

$$m^{*2} = [m_0^{*2} - M^{*2}(1 - c^2)] \tanh \frac{F(cM^* - |\alpha^*|)}{|\alpha^*|} + M^{*2}(1 - c^2) \quad (7.22)$$

where  $m_0^*$  and  $F$  are soil constants.  $m_0^*$  represents the value of  $m^*$  at  $\alpha^* = 0$ . This takes two different values ( $m_{0c}^*$  and  $m_{0e}^*$ ), depending on whether Equation 7.22 is being used to predict  $m_c^*$  or  $m_e^*$ . Figure 7.6 shows the variation of  $m^*$  with  $\alpha^*$  predicted by Equation 7.22 for the case  $m_0^* = 0.85$ ,  $M^* = 0.672$  and  $c = 0.52$ .

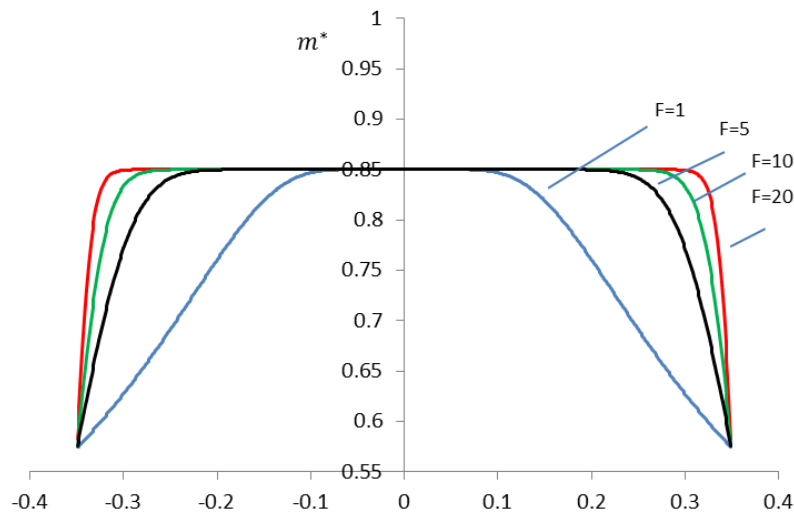


Figure 7.6 Variation of  $m^*$  with  $\alpha^*$  for different  $F$  values

### 7.8.2 VERSION 2: $m^* = \text{CONSTANT AND NON-ASSOCIATED FLOW RULE}$

The second version of the model assumes that  $m_c^*$  and  $m_e^*$  are both constant, independent of the value of  $\alpha^*$ :

$$m^* = m_0^* \quad (7.23)$$

where  $m_0^*$  takes two different values ( $m_{0c}^*$  and  $m_{0e}^*$ ), depending upon whether Equation 7.23 is being used to predict  $m_c^*$  or  $m_e^*$ . If the aspect ratio  $m^*$  of the *LC* yield surface is assumed constant (Equation 7.23), then a non-associated flow rule is required in order to predict critical states for  $\eta^* = M^*$ . The proposed version of non-associated flow rule is:

$$\frac{d\varepsilon_s^p}{d\varepsilon_v^e} = \frac{2(\eta^* - \alpha^*)}{(M^{*2} - \eta^{*2})} \quad (7.24)$$

Equation 7.24 is equivalent to the flow rule assumed in *S-CLAY1* model (see Equation 2.32). This means that Version 2 of the model, assumes a plastic potential that has the same shape as the yield curve in the *S-CLAY1* model. The equation of the plastic potential is thus given by:

$$g_{LC} = (q - \alpha^* p^*)^2 - (M^{*2} - \alpha^{*2}) p^* (p_x^* - p^*) = 0 \quad (7.25)$$

where  $p_x^*$  is a dummy variable defining the current size of the plastic potential so that it passes through the current stress point. The plastic potential described by Equation 7.25 always has a horizontal tangent at  $\eta^* = M^*$  (irrespective of the value of  $\alpha^*$ ). Figure 7.7 shows the plastic potential and yield surface for Version 2 of the model, defined respectively by Equation 7.25 and by Equations 7.3 and 7.23.

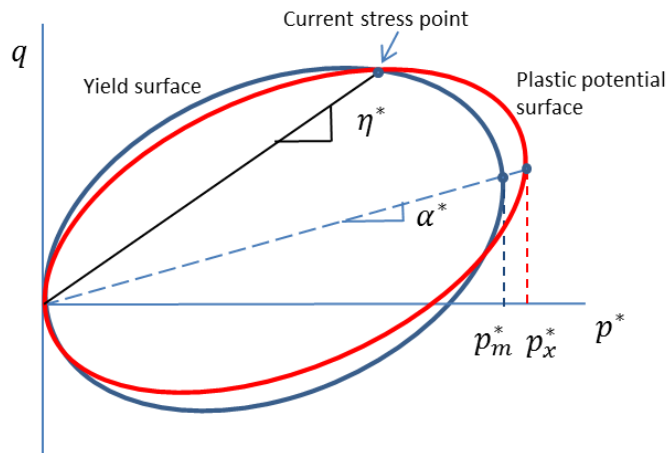


Figure 7.7 Yield surface and plastic potential surface for Version 2 of the model

## 7.9 CRITICAL STATES

Both versions of the model predict a unique critical state line in the  $q:p^*$  plane, defined by:

$$q = M^*p^* \quad (7.26)$$

Critical states must lie on the  $LC$  yield surface but do not have to lie on the edge between  $LC$  and  $SD$  yield surfaces. However, the coupled movements of the yield surfaces during shearing to a critical state will mean that it is very common for the soil state to be on this edge when a critical state is achieved (see the explanation given for the model of Wheeler et al., 2003a, in Section 2.9.6). For critical states that lie on the edge between  $LC$  and  $SD$  surfaces, both versions of the model predict a unique critical state planar surface in  $v:\ln p^*:\ln s^*$  space (similar to the model of Wheeler et al., 2003a).

Figure 7.8 shows the form of the  $LC$  yield curve (in the  $q:p^*$  plane) for Version 1 and Version 2 of the model, when a critical state is achieved (with the same value of  $p_m^*$  for both curves). This shows that the stress ratio  $p_m^*/p^*$  at critical states takes different values for the two versions of the model, because of the difference in aspect ratio of the yield curve. For Version 1 of the model, at critical states ( $\eta^* = M^*$ ,  $\alpha^* = cM^*$  and  $m^* = M^*(1 - c^2)^{1/2}$ ), the yield curve expression (Equation 7.3) gives:

$$\frac{p_m^*}{p^*} = \frac{2}{1 + c} \quad (7.27)$$

In contrast, for Version 2 of the model, at critical states ( $\eta^* = M^*$ ,  $\alpha^* = cM^*$  and  $m^* = m_0^*$ ), the yield curve expression (Equation 7.3) gives:

$$\frac{p_m^*}{p^*} = \frac{(1 - c)^2 M^{*2}}{m_0^{*2}} + 1 \quad (7.28)$$

Insertion of  $s_D^* = s^*$  and the critical state expression for  $p_m^*/p^*$  from Equation 7.27 in the general expression for  $v$  of Equation 7.16 means that the unique critical state planar surface predicted by Version 1 of the model (for critical states at the edge between the  $LC$  and  $SD$  surfaces) is given by:

$$v = N^* - (\lambda^* - \kappa^*) \ln \left( \frac{2}{1 + c} \right) - \lambda^* \ln p^* + k_1^* \ln s^* \quad (7.29)$$

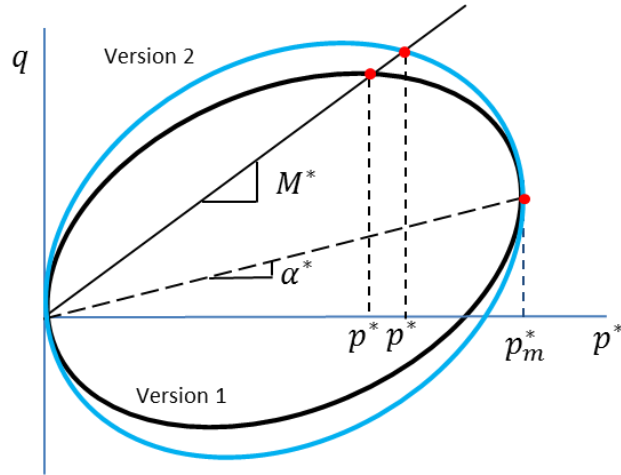


Figure 7.8 The  $LC$  yield curve for Version 1 and Version 2 of the model

Similarly, insertion of  $s_D^* = s^*$  and the critical state expression for  $p_m^*/p^*$  from Equation 7.28 in the general expression for  $v$  of Equation 7.16 means that the unique critical state planar surface predicted by Version 2 of the model (for critical states at the edge between  $LC$  and  $SD$  surfaces) is given by:

$$v = N^* - (\lambda^* - \kappa^*) \ln \left( \frac{(1-c)^2 M^{*2}}{m_0^{*2}} + 1 \right) - \lambda^* \ln p^* + k_1^* \ln s^* \quad (7.30)$$

Equations 7.29 and 7.30 show that both versions of the model predict a unique critical state planar surface in  $v:\ln p^*:\ln s^*$  space that is parallel to the corresponding unique isotropic normal compression surface (for an isotropic soil) (see Equation 7.13). Both versions of the anisotropic model predict a vertical spacing between the two surfaces that is smaller than the spacing predicted by the isotropic model of Wheeler et al. (2003a) (see Equation 2.83), and the two versions of the anisotropic model predict slightly different spacing to each other.

## 7.10 SATURATED CONDITIONS

To describe saturated behaviour ( $S_r = 1$ ), mean Bishop's stress  $p^*$  is substituted by mean effective stress  $p'$  in all model expressions (remembering that  $p^* = \bar{p} + S_r s = p'$  when  $S_r = 1$ ). Model expressions describing elastic behaviour under unsaturated conditions (see Equations 7.1 and 7.2) therefore still apply under saturated conditions. The  $LC$  yield surface expression given by Equation 7.3 still applies (given that  $p^* = p'$  when  $S_r = 1$ ), remembering that the yield curves always pass through the origin in the  $q:p^*$  plane regardless of suction. The hardening law for changes of size of the  $LC$  yield surface when yielding on the  $LC$  surface alone, given by Equation 7.10, also applies to saturated conditions. The hardening law for change of  $\alpha^*$  given by Equation 7.17 is also valid for

saturated conditions (with  $f(\eta^*)$  still given by Equation 7.19, remembering that  $\eta^* = q/p^* = q/p' = \eta$  when  $S_r = 1$ ).

For Version 1 of the model, the associated flow rule of Equation 7.21 still applies for saturated conditions (remember that  $\eta^* = \eta$  when  $S_r = 1$ ). The aspect ratio of the yield curve for the different sections of the curve,  $m_c^*$  and  $m_e^*$  (which apply for  $\eta^* \geq \alpha^*$  and  $\eta^* \leq \alpha^*$  respectively), each varies with  $\alpha^*$  according to Equation 7.22. For Version 2 of the model, the non-associated flow rule of Equation 7.24 still applies with the  $m_c^*$  and  $m_e^*$  each now constant at  $m_{0c}^*$  and  $m_{0e}^*$  respectively.

For isotropic soil ( $\alpha^* = 0$ ), the variation of  $v$  during virgin isotropic loading under saturated conditions is described by the following expression of the isotropic normal compression line in the  $v: \ln p^*$  plane (remembering that  $p^* = p'$  for  $S_r = 1$ ):

$$v = N - \lambda \ln p^* \quad (7.31)$$

where  $N$  and  $\lambda$  are the intercept and gradient of the saturated isotropic normal compression line.

For general stress states, the variation of  $v$  under saturated conditions is described by the following expression:

$$v = N - \lambda \ln p_m^* + \kappa^* \ln \left( \frac{p_m^*}{p^*} \right) \quad (7.32)$$

Equation 7.31 defines a planar surface, for isotropic saturated conditions in the  $v: \ln p^*: \ln s^*$  space, that has zero gradient along the  $\ln s^*$  axis (see Figure 7.9).

The line of intersection of the isotropic normal compression planar surfaces for saturated and unsaturated conditions defines a line referred to as the “line of saturation”. An expression for the “line of saturation” can be obtained by equating Equation 7.13 (defining the unsaturated planar surface in  $v: \ln p^*: \ln s^*$  space) and Equation 7.31 (defining the saturated planar surface in  $v: \ln p^*: \ln s^*$  space), which leads to:

$$\ln s^* = \frac{N - N^* + (\lambda^* - \lambda) \ln p^*}{k_1^*} \quad (7.33)$$

Inserting the definition of  $\lambda^*$  and  $k_1^*$  from Equations 7.14 and 7.15 respectively, Equation 7.33 can be simplified to:

$$\ln s^* = \frac{N - N^*}{k_1^*} + k_2 \ln p^* \quad (7.34)$$

If an unsaturated isotropic soil ( $\alpha^* = 0$ ) was subjected to a stress path involving isotropic stress states and simultaneous yielding on the *LC* and *SD* surfaces, a fully saturated condition ( $S_r = 1$ ) would be reached on the “line of saturation” defined by Equation 7.34 and subsequent changes of specific volume would then be obtained from the expressions for a saturated soil. Similarly, during virgin isotropic loading of an isotropic saturated soil, de-saturation would occur on the “line of saturation” defined by 7.34 and subsequent changes of specific volume would then be obtained from the expressions for unsaturated behaviour. It is important to note that the “line of saturation” defined by Equation 7.34 is not a universal relationship for the boundary between saturated and unsaturated conditions; it applies only for the special case of an isotropic soil ( $\alpha^* = 0$ ), subjected to isotropic loading, with the soil state on both *LC* and *SD* yield surfaces.

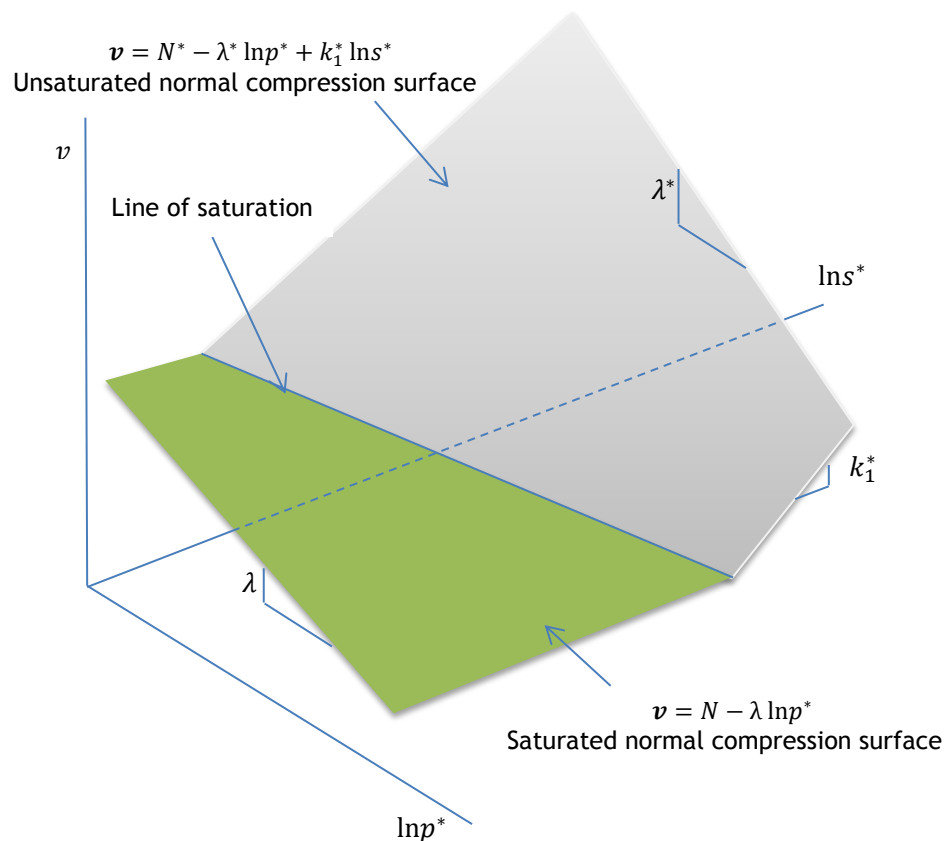


Figure 7.9 Saturated and unsaturated isotropic normal compression planar surfaces in the  $v: \ln p^*: \ln s^*$  space

### 7.11 APPLICATION OF THE MODEL

Version 1 of the anisotropic model involves 13 soil constants:  $\kappa^*$ ,  $G$ ,  $\lambda$ ,  $k_1$ ,  $k_2$ ,  $N$ ,  $N^*$ ,  $M^*$ ,  $\mu$ ,  $c$ ,  $m_{0c}^*$ ,  $m_{0e}^*$  and  $F$ . Version 2 of the model involves one fewer soil constants, because the parameter  $F$  is omitted.

In addition, for both versions of the model, specification of the initial state requires initial values of the stresses  $q$ ,  $p^*$  and  $s^*$  and initial values of the hardening parameters  $p_m^*$ ,  $s_D^*$ ,  $s_I^*$  and  $\alpha_0^*$ , defining the initial positions of the three yield surfaces and the initial inclination of the  $LC$  surface. For many simulations, the  $SI$  yield surface will not be reached, and the initial value of  $s_I^*$  is then not required.

The model (Version 1 or Version 2) can be used to predict the soil response for any stress path that is specified in terms of  $q$ ,  $p^*$  and  $s^*$ . However, if the model is to be used to predict the soil response for a stress path specified in terms of conventional stresses  $q$ ,  $\bar{p}$  and  $s$ , it must either be combined with a separate water retention model (in order to predict the variation of  $S_r$ , which is required to calculate values of  $p^*$ ) or experimental values of  $S_r$  must be used. In the latter case, the model cannot be used for true Class  $A$  predictions. This is the approach taken in Chapter 8 for comparing model simulations with experimental results.

# 8

## MODEL SIMULATIONS

This chapter investigates the performance of the new anisotropic model developed in Chapter 7 by performing simulations of the experimental tests presented in Chapter 5. Sections 8.1 to 8.4 describe how the simulations were performed, including the calibration of the various model constants and the initial states, and simulations are then compared with experimental results in Sections 8.6 to 8.9.

The majority of the simulations were performed with Version 1 of the model (see Chapter 7) but some comparisons between Version 1 and Version 2 are presented in Section 8.9. A limited selection of tests was simulated both with Version 1 of the anisotropic model and with an isotropic variant of Version 1 of the model (see Section 8.6). This was to investigate whether the incorporation of anisotropy in the model resulted in a significant improvement in the accuracy of the simulations.

In performing all model simulations, experimental values of degree of saturation  $S_r$  were employed, so that stress paths could be specified in terms of mean Bishop's stress  $p^*$ , defined by:

$$p^* = \bar{p} + S_r s \quad (8.1)$$

For each stage of every individual test, the experimental values of  $S_r$  were plotted against mean net stress  $\bar{p}$ , and the data for each stage were then fitted by a suitable polynomial expression relating  $S_r$  to  $\bar{p}$ . This fitted expression for the individual test stage (rather than raw experimental values of  $S_r$ ) was then used to give the values of  $S_r$  at any point in a test, in order to calculate the corresponding value of  $p^*$  (from Equation 8.1) for use in model simulations. Figure 8.1 shows an example of the experimental values of  $S_r$  from an individual test (Test A300(0)), together with the two polynomial expressions fitted separately to the two different stages of this test (the probing stage at  $[\Delta q/\Delta \bar{p}] = 0$  and the subsequent shearing stage at  $[\Delta q/\Delta \bar{p}] = 3$ ). This shows that the fitted curves and the raw experimental data are almost indistinguishable. Use of experimental values of  $S_r$  in the model simulations in this way is equivalent to investigating how well the new anisotropic mechanical model would represent the experimentally observed mechanical

behaviour if it was combined with a water retention model which perfectly captured the observed variation of  $S_r$ .

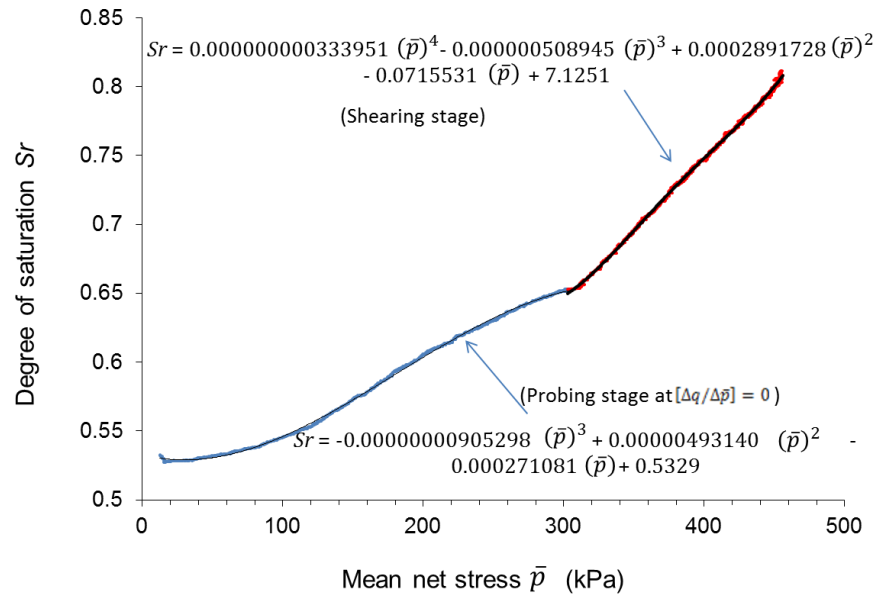


Figure 8.1 Typical fitting of the experimental values of  $S_r$  from Test A300(0)

### 8.1 CALIBRATION OF SOIL CONSTANTS OTHER THAN $\mu$ AND $c$

Referring to Section 7.11, values of 13 soil constants must be specified in order to conduct model simulations with Version 1 of the model or values of 12 soil constants must be specified in order to conduct model simulations with Version 2 of the model (the parameter  $F$  is omitted). Values of soil constants other than  $\mu$  and  $c$  were determined based on the interpretation of experimental results presented in Chapter 6 and these are briefly summarised in this section. The values of the final soil constants  $\mu$  and  $c$  (which control the variation of  $\alpha^*$  during plastic straining, see Section 7.7) were determined by fitting model simulations to experimental results, and this procedure is presented in Section 8.4.

Values of the 13 soil constants in Version 1 of the model and the 12 soil constants in Version 2 are given in Table 8.1.

The value of elastic shear modulus  $G$  was obtained by best-fitting the unloading portions of stress-strain curves in the  $q: \varepsilon_s$  plane and the average value of  $G$  obtained in this way was 9960 kPa (see Section 6.1.3). The value of elastic swelling index  $\kappa^*$  was obtained as the average of slopes of unloading portions of compression curves in the  $v: \ln p^*$  plane and was 0.043 (see Section 6.1.2).

Values of the gradient  $\lambda$  and intercept  $N$  of the saturated isotropic compression line in the  $v:\ln p'$  plane were 0.151 and 2.811 respectively (see Section 6.2.1). Values of the intercept  $N^*$  and gradients  $\lambda^*$  and  $k_1^*$  of the isotropic normal compression planar surface in  $v:\ln p^*:\ln s^*$  space were obtained from best-fitting experimental compression data of isotropic loading of isotropically compacted samples under unsaturated conditions (see Section 6.2.3). The value of the intercept  $N^*$  was 2.953 and the values of the gradients  $\lambda^*$  and  $k_1^*$  were 0.313 and 0.211 respectively. The values of the soil constants  $k_1$  and  $k_2$  were then obtained by rearranging Equations 7.14 and 7.15 to give:

$$k_1 = k_1^*/(\lambda^* - \kappa^*) \quad (8.2)$$

$$k_2 = (\lambda^* - \lambda)/k_1^* \quad (8.3)$$

This led to values of 0.783 and 0.764 for  $k_1$  and  $k_2$  respectively.

**Table 8.1** Values of model constants

Soil constant	Value
$G$	9960 kPa
$\kappa^*$	0.043
$\lambda$	0.151
$N$	2.811
$N^*$	2.953
$k_1$	0.783
$k_2$	0.764
$M^*$	0.672
$m_{0c}^*$	0.85
$m_{0e}^*$	0.95
$F$ (Version 1)	5
$\mu$ (Version 1)	10.4
$c$ (Version 1)	0.52
$\mu$ (Version 2)	7.45
$c$ (Version 2)	0.43

The value of the critical state stress ratio  $M^*$  in the  $q:p^*$  plane was found to be the same in both triaxial compression and triaxial extension and was 0.672 (see Section 6.3.3). The aspect ratio of the  $LC$  yield surface for isotropic conditions ( $\alpha^* = 0$ ) was  $m_{0c}^* = 0.85$  for the triaxial compression section of the surface and  $m_{0e}^* = 0.95$  for the triaxial extension section of the surface (see Section 6.5.2). Finally, a value of  $F = 5$  was selected in Version 1 of the model in order to ensure that the values of  $m_{0c}^*$  and  $m_{0e}^*$  remained almost constant for values of  $\alpha^*$  between about  $-0.25$  and  $+0.25$  (see Figure 7.6 in Section 7.8.1).

For simulations with the isotropic variant of Version 1 of the model, the hardening law for changes of  $\alpha^*$  was de-activated in the simulation code (by setting the hardening parameter  $\mu$  and the initial value of  $\alpha^*$  to zero). Also, in order for the isotropic variant of the model to predict critical states for  $q = M^*p^*$ , the aspect ratio of the  $LC$  yield surface for both triaxial compression and triaxial extension sections of the surface ( $m_{0c}^*$  and  $m_{0e}^*$ ) had to be equal to  $M^*$  (as in the isotropic model of Wheeler et al., 2003a). In this case, the soil constants  $F$  and  $c$  were no longer required.

It is worth mentioning that no sensitivity analysis was carried out in terms of the impact of changing any of the model parameters on model predictions and that is because the current study focuses mainly on qualitative improvement of model predictions by incorporating the influence of evolving anisotropy.

## 8.2 CALCULATION OF INITIAL STATES

Initial states for all tests on isotropically compacted samples were determined in an internally consistent fashion. In particular the initial value of  $p_m^*$  for all tests on isotropically compacted samples conducted at a suction of 300 kPa (Test Series A300) was selected on the basis of experimental evidence, but the initial value of  $p_m^*$  for the corresponding tests conducted at suction of 100 kPa and zero (Test Series A100 and A0) were then calculated in a consistent fashion by calculating how much coupled inward movement of the  $LC$  yield surface would be predicted by the model during wetting from  $s = 300$  kPa to  $s = 100$  kPa and  $s = 0$ . Similarly, for tests on anisotropically compacted samples, the initial value of  $p_m^*$  for Test Series B300 was based on experimental evidence, but then initial values of  $p_m^*$  for Test Series B100 and B0 were determined by calculating how much coupled inward movement of the  $LC$  yield surface would be predicted during wetting to  $s = 100$  kPa and  $s = 0$ .

In every individual test the initial values of  $\bar{p}$ ,  $q$  and  $s$  were known (see Table 8.2). the initial value of  $S_r$  was then taken from the fitted polynomial expression for the

individual test (rather than the raw experimental data point), hence allowing the initial value of mean Bishop's stress  $p^*$  to be calculated from Equation 8.1 for each individual test (see Table 8.2). Due to the dependency of  $p^*$  on the experimental value of  $S_r$ , initial values of  $p^*$  within a given test series varied by  $\pm 1.5$  kPa for tests at  $s = 100$  kPa and by  $\pm 3$  kPa for tests at  $s = 300$  kPa.

**Table 8.2 Initial states for model simulations with anisotropic model (Version 1 and Version 2)**

Test Series	$s$ (kPa)	$\bar{p}$ (kPa)	$q$ (kPa)	$S_r$	$p^*$ (kPa)	$v$	$s^*$ (kPa)	$p_m^*$ (kPa)	$s_D^*$ (kPa)	$\alpha^*$
A300	300	12 or 10	6 or 0	0.530 <sup>1</sup>	171.10 <sup>1</sup>	2.336 <sup>1</sup>	171.59 <sup>1</sup>	244	171.59 <sup>1</sup>	0
A100	100	12 or 10	6 or 0	0.697 <sup>1</sup>	82.77 <sup>1</sup>	2.368 <sup>1</sup>	57.76 <sup>1</sup>	104	57.76 <sup>1</sup>	0
A0	0	5	0	1	5	2.488	0	10.4	0	0
B300	300	12 or 10	6 or 0	0.609 <sup>1</sup>	194.74 <sup>1</sup>	2.270 <sup>1</sup>	167.86 <sup>1</sup>	300	167.86 <sup>1</sup>	0.20
B100	100	12 or 10	6 or 0	0.778 <sup>1</sup>	90.82 <sup>1</sup>	2.303 <sup>1</sup>	56.59 <sup>1</sup>	128	56.59 <sup>1</sup>	0.20
B0	0	5	0	1	5	2.428	0	18.2	0	0.20

<sup>1</sup> Values shown are for Tests A300(0), A100(0), B300(0) and B100(0), values for other tests in A300, A100, B300 and B100 varied slightly because individual values of  $S_r$  were used.

In order to calculate the initial value of modified suction  $s^*$  for each individual test, the initial value of porosity had to be predicted. This meant predicting the initial value of specific volume  $v$  for the individual test, by making use of the general expression for  $v$  of Equation 7.16:

$$v = N^* - \lambda^* \ln p_m^* + k_1^* \ln s_D^* + \kappa^* \ln \left( \frac{p_m^*}{p^*} \right) \quad (8.4)$$

However, inspection of Equation 8.4 shows that this requires initial values for the hardening parameters  $p_m^*$  and  $s_D^*$  (giving the initial positions of the *LC* and *SD* yield surfaces respectively). For the initial value of  $s_D^*$ , it was assumed that the initial state in all tests was on the *SD* yield surface ( $s_D^* = s^*$ ), because of the prior wetting from the much higher post-compaction value of suction. This was supported by significant experimental increases of  $S_r$  during initial wetting to  $s = 300$  kPa,  $s = 100$  kPa or  $s = 0$ . Equation 8.4 could then be expressed as:

$$v = N^* - \lambda^* \ln p_m^* + k_1^* \ln \left[ \frac{s(v-1)}{v} \right] + \kappa^* \ln \left( \frac{p_m^*}{p^*} \right) \quad (8.5)$$

Given that initial values of  $s$  and  $p^*$  were known for each test, Equation 8.5 could be solved for the initial value of  $v$  if the initial value of  $p_m^*$  was known. Alternatively, if the initial value of  $v$  was known, Equation 8.5 could be solved for the initial value of  $p_m^*$ .

For tests within Series A300 the initial value  $p_m^*$  was taken as 244 kPa (see Table 8.2) based on the experimental evidence presented in Section 6.5.2. Equation 8.5 was then solved for the initial value of  $v$  for each test in Series A300. This required an iterative procedure, because  $v$  appears on both sides of Equation 8.5. This was done using a standard solution routine available in Matlab, and led to an initial value of  $v$  of approximately 2.336 (see Table 8.2). Predicted initial values of  $v$  varied slightly between the individual tests within Test Series A300 (by less than  $\pm 0.001$ ), because of the slight variation in the initial values of  $S_r$  between tests.

For tests within Series A100, the initial value of  $v$  in each test was calculated by considering a previous wetting path from a suction of 300 kPa (at a state corresponding to the initial state for Test A300(0) i.e.  $p^* = 171.1$  kPa, see Table 8.2). Considering that only elastic changes of  $v$  would occur along this wetting path (which remained inside the  $LC$  yield surface), this led to the following expression for the initial value of  $v$  for each test within Test Series A100:

$$v = 2.336 + \kappa^* \ln\left(\frac{171.1}{p^*}\right) \quad (8.6)$$

Equation 8.6 led to initial values of  $v$  for all tests in Series A100 of 2.368 (see Table 8.2), with slight variation between individual tests (less than  $\pm 0.001$ ) because of the slight variation of initial values of  $S_r$  between tests. This initial value of  $v$  was then inserted back into Equation 8.5, in order to calculate the corresponding initial value of the hardening parameter  $p_m^*$ . This led to an initial value of  $p_m^*$  of 104 kPa (see Table 8.2). A single initial value of  $p_m^*$  was used for all tests in Series A100. The reduction of the initial value of  $p_m^*$  from 244 kPa in Test Series A300 to 104 kPa in Test Series A100 represented the coupled inward movement of the  $LC$  yield surface caused by yielding on the  $SD$  surface during wetting from  $s = 300$  kPa ( $s^* = 171.59$  kPa) to  $s = 100$  kPa ( $s^* = 57.76$  kPa). Integration of the coupling relationship for yielding on the  $SD$  surface alone (Equation 7.8) during wetting from  $s^* = 171.59$  kPa to  $s^* = 57.76$  kPa confirmed this coupled inward movement of the  $LC$  surface from  $p_m^* = 244$  kPa to  $p_m^* = 104$  kPa.

For tests within Series A0 the initial value of  $v$  was calculated from Equation 8.6, using a  $p^*$  value of 5 kPa (see Table 8.2). This led to an initial value of  $v$  of 2.488 for all tests in

Series A0. The corresponding initial value of  $p_m^*$  was then calculated by inserting this initial value of  $v$  in the general expression for the specific volume of a saturated soil:

$$v = N - \lambda \ln p_m^* + \kappa^* \ln \left( \frac{p_m^*}{p^*} \right) \quad (8.7)$$

where  $N$  and  $\lambda$  are the intercept and gradient of the saturated isotropic normal compression line (see Section 7.10). This led to an initial value of  $p_m^*$  of 10.4 kPa for all tests in Series A0 (see Table 8.2). The reduction of the initial value of  $p_m^*$  from 244 kPa in Test Series A300 to 10.4 kPa in Test Series A0 represented the coupled inward movement of the  $LC$  yield surface caused by yielding on the  $SD$  surface during wetting from  $s = 300$  kPa ( $s^* = 171.59$  kPa) to the point where the soil became fully saturated (at a non-zero value of suction). Further reduction of suction from this point to  $s = 0$  corresponded simply to elastic swelling of a saturated soil (due to a decrease of effective stress), with no further change of  $p_m^*$ . A subsequent check (involving integration of Equation 7.8) confirmed that the reduction of  $p_m^*$  from 244 kPa to 10.4 kPa was consistent with the coupled inward movement of the  $LC$  yield surface produced during wetting from  $s^* = 171.59$  kPa to the point where the soil became fully saturated, when the corner between the  $SD$  and  $LC$  yield curves reached the “line of saturation” described in Section 7.10.

Similar procedures were used to determine the initial states for the model simulations of tests on anisotropic compacted samples. For tests within Series B300, the initial value of  $p_m^*$  was taken as 300 kPa (see Table 8.2) based on the experimental evidence presented in Section 6.5.2. This led (from Equation 8.5) to a corresponding initial value of  $v$  of 2.270 ( $\pm 0.001$ ), as shown in Table 8.2. For tests in Series B100 and B0, the initial value of  $v$  was calculated by considering the elastic change of  $v$  starting from the initial state of Test B300(0):

$$v = 2.270 + \kappa^* \ln \left( \frac{194.7}{p^*} \right) \quad (8.8)$$

This led to initial value of  $v$  of 2.303 ( $\pm 0.001$ ) in Test Series B100 and 2.428 in Test Series B0. Finally, the initial value of  $p_m^*$  in Series B100 was back calculated from Equation 8.5 as 128 kPa and the initial value of  $p_m^*$  in Series B0 was back calculated from Equation 8.7 as 18.2 kPa (see Table 8.2).

The initial value of  $\alpha^*$  was taken as zero for all tests in Series A300, A100 and A0, whereas the initial value of  $\alpha^*$  was taken as 0.20 for all tests in Series B300, B100 and B0. These values were based on the experimental evidence presented in Section 6.5.2.

Table 8.3 shows the initial values of  $p_m^*$  selected or calculated for use in the model simulations and compares these with the corresponding experimental values (from Section 6.5.2). For Series A300 the initial value of  $p_m^*$  used in the model simulations (244 kPa) was specifically selected to match the corresponding experimental value. For Test Series A100 the initial value of  $p_m^*$  predicted by the model (104 kPa) was in close agreement with the experimental value (101 kPa), indicating excellent model performance in predicting the coupled inward movement of the *LC* yield surface while the soil remained unsaturated. However, for Test Series A0 the initial value of  $p_m^*$  predicted by the model (10.4 kPa) was significantly lower than the experimentally observed value (16 kPa), indicating that the model was less successful in predicting the transition from unsaturated to saturated conditions. The initial values of  $p_m^*$  for the tests on anisotropically compacted samples show a similar pattern. For Test Series B300 the initial value of  $p_m^*$  (300 kPa) was selected to match the corresponding experimental value, for Test Series B100 the value predicted by the model (128 kPa) was a good match to the experimental value (122 kPa), whereas for Test Series B0 the value predicted by the model (18.2 kPa) was significantly lower than experimental value (23 kPa).

**Table 8.3** Experimental and model predicted initial values of  $p_m^*$  and  $\nu$  for the anisotropic model (Version 1 and Version 2)

Test Series	$p_m^*$ (kPa)		$\nu$	
	Experimental	Model predicted	Experimental	Model predicted
A300	244	244 (Input value)	2.345	2.336
A100	101	104	2.360	2.369
A0	16	10.4	2.414	2.488
B300	300	300 (Input value)	2.185	2.270
B100	122	128	2.214	2.304
B0	23	18.2	2.273	2.428

Table 8.3 also shows the initial values of  $\nu$  predicted by the model and compares these with the corresponding experimental values (from Section 5.4). The initial values of  $\nu$

predicted for the unsaturated tests on isotropically compacted samples (Test Series A300 and A100) show excellent agreement with the corresponding experimental values. This makes sense, given that the corresponding values of  $p_m^*$  showed a good match and that the experimental data from some of the tests (A300(0) and A100(0)) were used to determine the unique isotropic normal compression planar surface in  $v:\ln p^*:\ln s^*$  space (which provides the link between  $v$  and  $p_m^*$ ). The predicted initial value of  $v$  for Test Series A0 shows a less good match to the corresponding experimental value (see Table 8.3). For this saturated test series, the initial value of  $v$  is over-predicted because of the under-prediction of the initial value of  $p_m^*$ .

Inspection of Table 8.3 shows that the predicted initial values of  $v$  for the unsaturated tests on anisotropically compacted samples (Test Series B300 and B100) significantly overestimate the corresponding experimental values. This indicates that the model is unable to correctly predict or explain the large difference in initial  $v$  value between isotropically compacted and anisotropically compacted samples. The initial values of  $p_m^*$  for the unsaturated tests on anisotropically compacted samples are slightly greater than the corresponding initial values of  $p_m^*$  for tests on isotropically compacted samples, and hence the model predicts slightly lower initial values of  $v$  for the anisotropically compacted samples than for the isotropically compacted samples. However, the experimental results show that the initial values of  $v$  for the unsaturated tests on anisotropically compacted samples are substantially lower than the corresponding values for the tests on isotropically compacted samples. Clearly, the effects of a change from isotropic compaction to anisotropic compaction are not being completely captured by the model. The over-estimation of the initial value of  $v$  for anisotropically compacted samples is exacerbated in the saturated tests (Test Series B0), (see Table 8.3), because the initial value of  $p_m^*$  is also significantly under-predicted.

For the model simulations with the isotropic variant of Version 1 of the model, slightly different assumed initial states were used, as shown in Table 8.4. The initial value of  $\alpha^*$  was obviously zero for all tests in the simulations performed with this isotropic variant of the model. However, it was also appropriate to re-calibrate the initial values of  $p_m^*$  for Test Series A300 and B300 by fitting revised yield curves to the experimental data presented in Section 6.5.2. Revised yield curves were obviously necessary in Test Series B300 because the assumed initial value of  $\alpha^*$  was now zero instead of 0.20. However, revised yield curves were fitted for both Test Series A300 and Test Series B300, because the aspect ratio of the yield curve had to be different for this isotropic variant of the model ( $m_{0c}^* = m_{0e}^* = M^*$  for this isotropic variant, as described in Section 8.1). Re-fitting yield curves with these conditions to the experimental data resulted in initial values of

$p_m^*$  of 255 kPa in Test Series A300 and 320 kPa for Test Series B300 (see Table 8.4). This, then produced slight changes to the initial values of  $p_m^*$  for all remaining tests and to the initial values of  $v$  for all tests (compare Table 8.4 with Table 8.2).

**Table 8.4 Initial states for model simulations with isotropic variant of Version 1 of the model**

Test Series	$s$ (kPa)	$\bar{p}$ (kPa)	$q$ (kPa)	$S_r$	$p^*$ (kPa)	$v$	$s^*$ (kPa)	$p_m^*$ (kPa)	$s_D^*$ (kPa)	$\alpha^*$
A300	300	12 or 10	6 or 0	0.530 <sup>1</sup>	171.10 <sup>1</sup>	2.323 <sup>1</sup>	170.85 <sup>1</sup>	255	170.85 <sup>1</sup>	0
A100	100	12 or 10	6 or 0	0.697 <sup>1</sup>	82.77 <sup>1</sup>	2.355 <sup>1</sup>	57.54 <sup>1</sup>	108.7	57.54 <sup>1</sup>	0
A0	0	5	0	1	5	2.475	0	11.7	0	0
B300	300	12 or 10	6 or 0	0.609 <sup>1</sup>	194.74 <sup>1</sup>	2.251 <sup>1</sup>	166.72 <sup>1</sup>	320	166.72 <sup>1</sup>	0
B100	100	12 or 10	6 or 0	0.778 <sup>1</sup>	90.82 <sup>1</sup>	2.284 <sup>1</sup>	56.23 <sup>1</sup>	136.6	56.23 <sup>1</sup>	0
B0	0	5	0	1	5	2.409	0	21.6	0	0

<sup>1</sup> Values shown are for Tests A300(0), A100(0), B300(0) and B100(0), values for other tests in A300, A100, B300 and B100 varied slightly because individual values of  $S_r$  were used.

### 8.3 METHOD OF PERFORMING SIMULATIONS

A simulation code was developed in Matlab in order to perform model simulations of the experimental tests presented in Chapter 5. Simulations involved an incremental procedure for each test stage. For test stages which did not finish at a critical state, defined increments of mean net stress ( $\Delta\bar{p}$ ) were normally applied ( $\Delta\bar{p} = 1$  kPa), to a defined final value of  $\bar{p}$  (i.e. stress-controlled simulation). In a small number of cases, where a wetting or drying stage was being simulated, defined increments of suction ( $\Delta s$ ) were applied to a defined final value of  $s$ , instead of increments of  $\bar{p}$ . For test stages which finished at a critical state, defined increments of shear strain ( $\Delta\varepsilon_s$ ) were applied (typically  $\Delta\varepsilon_s = 0.001$ ) to a defined (very large) final value of  $\varepsilon_s$  (i.e. a strain-controlled simulation). It is worth mentioning that different values for the increments  $\Delta\bar{p}$  and  $\Delta\varepsilon_s$  were investigated and the increments of  $\Delta\bar{p} = 1$  kPa and  $\Delta\varepsilon_s = 0.001$  were considered adequate for the current simulation work.

Figure 8.2 shows a flow chart of the simulation code. For each increment of stress or strain, there are four possibilities:

- (a) Elastic behaviour;
- (b) Yielding on  $SD$  yield surface alone;
- (c) Yielding on  $LC$  yield surface alone;

(d) Yielding on both *SD* and *LC* yield surfaces

The simulation code considers each of these possibilities in turn, until it finds the one that is correct (see Figure 8.2). In each case, the relevant set of equations is solved, and then the calculated state at the end of the increment is checked against an appropriate set of conditions to see if it is acceptable and consistent. If the conditions are satisfied, the simulation code stores the calculated values, updates all relevant variables and moves on to the next increment. However, if the conditions are not satisfied, the code moves on to the next of the four possibilities in sequence.

For each of the four possible cases, a set of 17 simultaneous equations is solved for 17 unknown quantities, using a standard Matlab routine. The relevant equations for unsaturated tests with Version 1 of the model are shown in Tables 8.5 and 8.6. In these tables  $x(i)$  represents the unknown value of variable  $x$  at the end of the current increment,  $x(i-1)$  represents the known value of variable  $x$  at the start of the current increment and  $\Delta x(i)$  represents the unknown increment of variable  $x$  over the current increment.

Tables 8.5 and 8.6 involve 17 unknown quantities. For both stress-controlled simulations (where increments of  $\bar{p}$  are applied, i.e.  $\bar{p}(i)$  is known) and strain-controlled simulations (where increments of shear strain are applied, i.e.  $\Delta \varepsilon_s(i)$  is known),  $s$  is generally constant (i.e. known) and  $[\Delta q/\Delta \bar{p}]$  is specified (i.e. known). The 17 unknown quantities in the 17 simultaneous equations are:  $p^*(i)$ ,  $S_r(i)$ ,  $q(i)$ ,  $s^*(i)$ ,  $v(i)$ ,  $\eta^*(i)$ ,  $\Delta \varepsilon_v^e(i)$ ,  $\Delta \varepsilon_s^e(i)$ ,  $p_m^*(i)$ ,  $s_D^*(i)$ ,  $\Delta \varepsilon_v^p(i)$ ,  $\Delta \varepsilon_s^p(i)$ ,  $\alpha^*(i)$ ,  $m^*(i)$ ,  $\Delta \alpha^*(i)$  and either  $\Delta \varepsilon_s(i)$  (for a stress-controlled simulation, when  $\bar{p}(i)$  is a known quantity) or  $\bar{p}(i)$  (for a strain-controlled simulation, when  $\Delta \varepsilon_s(i)$  is a known quantity). 17 equations are therefore required, in order to solve for these 17 unknowns. 15 of these 17 equations are common to all four of the possible cases discussed above (see Table 8.5). The final 2 equations differ, depending on which of the four cases is being considered (see Table 8.6).

It is worth mentioning a few comments about the 15 common equations shown in Table 8.5. Firstly, Equation 4 in the table represents the polynomial expression (of first to fourth order) relating  $S_r$  to  $\bar{p}$ , determined by fitting the experimental variation of  $S_r$  observed in the individual test stage, as described at the start of this chapter. Secondly, whereas the elastic volumetric strain increment is calculated from the change of  $p^*$  over the increment in the expected fashion (see Equation 6 in Table 8.5), the plastic volumetric strain is not calculated from direct application of the relevant hardening law,

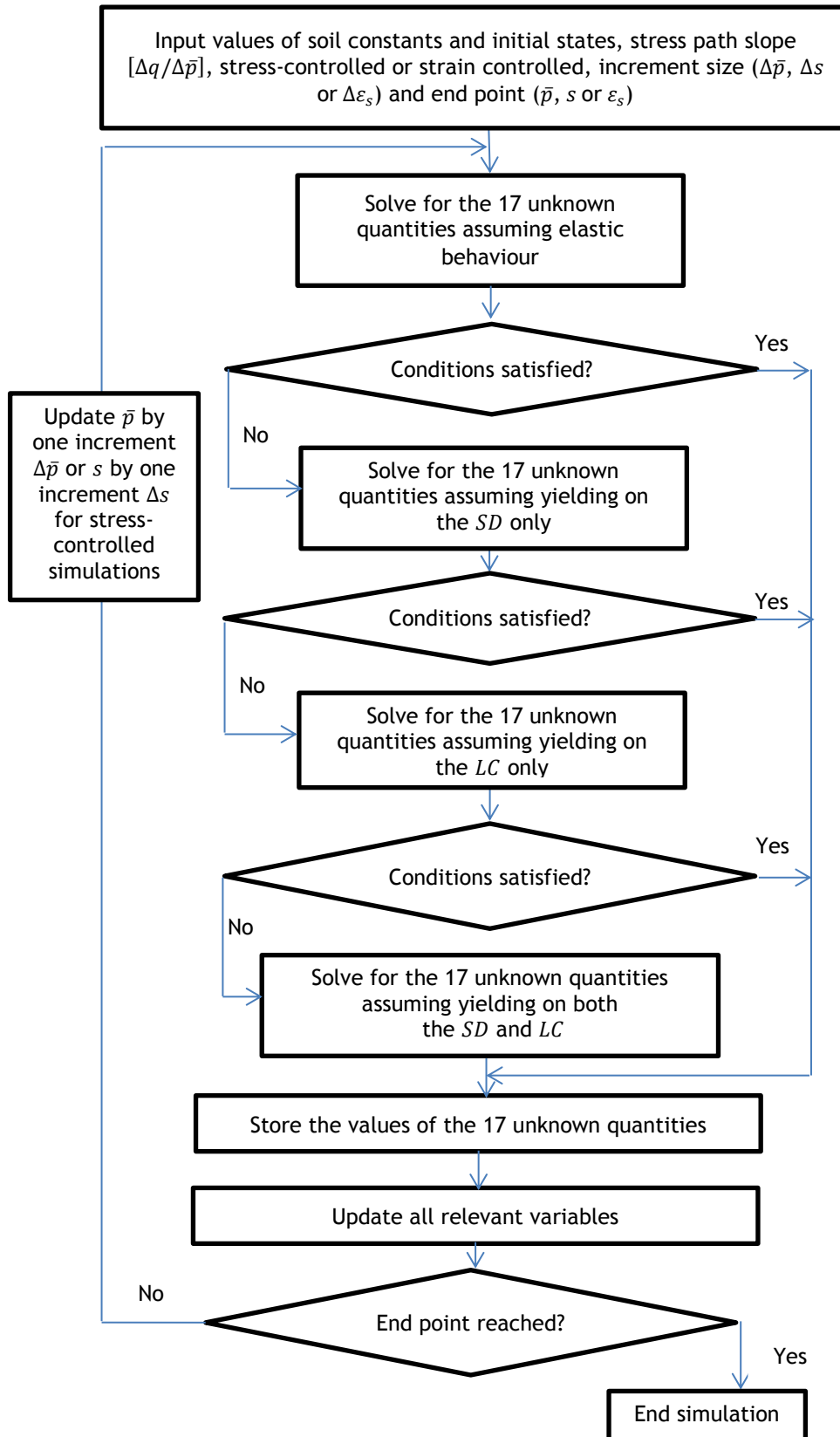


Figure 8.2 Flow chart for the model simulation of a single test stage

Table 8.5 Simulation equations used in all four cases (model Version 1)

$$p^*(i) = \bar{p}(i) + S_r(i) s \quad (1)$$

$$q(i) = \left[ \frac{\Delta q}{\Delta \bar{p}} \right] (\bar{p}(i) - \bar{p}_{initial}) + q_{initial} \quad (2)$$

$$s^*(i) = s \left( \frac{v(i) - 1}{v(i)} \right) \quad (3)$$

$$S_r(i) = f(\bar{p}(i)) \quad (4)$$

$$\eta^*(i) = \frac{q(i)}{p^*(i)} \quad (5)$$

$$\Delta \varepsilon_v^e(i) = \frac{\kappa^* \ln \left[ \frac{p^*(i)}{p^*(i-1)} \right]}{v(i)} \quad (6)$$

$$\Delta \varepsilon_s^e(i) = \frac{[q(i) - q(i-1)]}{3G} \quad (7)$$

$$v(i) = N^* - \lambda^* \ln p_m^*(i) + k_1^* \ln s_D^*(i) + \kappa^* \ln \left( \frac{p_m^*(i)}{p^*(i)} \right) \quad (8)$$

$$\Delta \varepsilon_v(i) = \frac{v(i-1) - v(i)}{v(i)} \quad (9)$$

$$\Delta \varepsilon_v^p(i) = \Delta \varepsilon_v(i) - \Delta \varepsilon_v^e(i) \quad (10)$$

$$\Delta \varepsilon_s^p(i) = \frac{2 \Delta \varepsilon_v^p(i) (\eta^*(i) - \alpha^*(i))}{(m^{*2}(i) + \alpha^{*2}(i) - \eta^{*2}(i))} \quad (11)$$

$$\Delta \varepsilon_s(i) = \Delta \varepsilon_s^e(i) + \Delta \varepsilon_s^p(i) \quad (12)$$

$$\Delta \alpha^*(i) = \mu [f(\eta^*(i)) - \alpha^*(i)] \left[ (\Delta \varepsilon_v^p(i))^2 + \frac{9}{2} (\Delta \varepsilon_s^p(i))^2 \right]^{1/2} \quad (13)$$

where

$$f(\eta^*) = \begin{cases} -cM^* & \text{for } \eta^*(i) \leq -M^* \\ c\eta^*(i) & \text{for } -M^* < \eta^*(i) < M^* \\ cM^* & \text{for } \eta^*(i) \geq M^* \end{cases}$$

$$\alpha^*(i) = \alpha^*(i-1) + \Delta \alpha^*(i) \quad (14)$$

$$m^{*2}(i) = m_0^{*2} - M^{*2}(1 - c^2) \tanh \frac{F(cM^* - |\alpha^*(i)|)}{|\alpha^*(i)|} + M^{*2}(1 - c^2) \quad (15)$$

where  $m_0^* = m_{0c}^*$  for  $\eta^*(i) \geq \alpha^*(i)$  and  $m_0^* = m_{0e}^*$  for  $\eta^*(i) < \alpha^*(i)$

Table 8.6 Final two simulation equations for each of the four cases

(a) <u>Elastic behaviour</u>	
$p_m^*(i) = p_m^*(i - 1)$	(16a)
$s_D^*(i) = s_D^*(i - 1)$	(17a)
(b) <u>Yielding on <math>SD</math> surface alone</u>	
$\ln\left(\frac{p_m^*(i)}{p_m^*(i - 1)}\right) = k_1 \ln\left(\frac{s_D^*(i)}{s_D^*(i - 1)}\right)$	(16b)
$s_D^*(i) = s^*$	(17b)
(c) <u>Yielding on <math>LC</math> surface alone</u>	
$[q(i) - \alpha^*(i) p^*(i)]^2 = m^{*2}(i) p^{*2}(i) \left(\frac{p_m^*(i)}{p^*(i)} - 1\right)$	(16c)
$\ln\left(\frac{s_D^*(i)}{s_D^*(i - 1)}\right) = k_2 \ln\left(\frac{p_m^*(i)}{p_m^*(i - 1)}\right)$	(17c)
(d) <u>Yielding on both <math>SD</math> and <math>LC</math> surfaces</u>	
$[q(i) - \alpha^*(i) p^*(i)]^2 = m^{*2}(i) p^{*2}(i) \left(\frac{p_m^*(i)}{p^*(i)} - 1\right)$	(16d)
$s_D^*(i) = s^*(i)$	(17d)

as might be expected. Instead, the value of  $v$  at the end of the increment is calculated from the general expression for  $v$  (see Equation 8 in the table) and then this is used to calculate the total volumetric strain increment (Equation 9 in the table) and finally the plastic volumetric strain increment is calculated by subtracting the elastic volumetric strain increment (Equation 10 in the table). This produces the same results as applying the relevant hardening law directly, but is considered less susceptible to accumulation of numerical errors over successive increments.

For the case of an elastic increment, Equations 16a and 17a in Table 8.6 simply state that there is no movement of either yield surface over the increment. For the case of an increment involving yielding on the  $SD$  surface only, Equation 16b relates the coupled movement of the  $LC$  surface to the movement of the  $SD$  surface, and Equation 17b states that the stress state at the end of the increment must be on the  $SD$  surface. For the case of yielding on the  $LC$  surface alone, Equation 16c states that the stress state at the end of the increment must be on the  $LC$  surface, and Equation 17c relates the coupled

movement of the  $SD$  surface to the movement of the  $LC$  surface. For the case of yielding on both  $LC$  and  $SD$  surfaces, Equations 16d and 17d state that the stress state at the end of the increment must lie on both surfaces.

For simulations performed with Version 2 of the anisotropic model, the only changes required to the equations shown in Tables 8.5 and 8.6 were to the flow rule on the  $LC$  surface (see Equation 11 in Table 8.5) and the expression for the aspect ratio  $m^*$  of the  $LC$  yield surface (see Equation 15 in Table 8.5). These changes arise from Equations 7.24 and 7.23 respectively in Section 7.8.2. As shown in Figure 8.2, after solving for the 17 unknown quantities the simulation code checks whether appropriate conditions were satisfied and hence whether the correct assumption had been made about the form of behaviour within the increment (i.e. elastic, yielding on the  $SD$  surface alone, yielding on the  $LC$  surface alone). These conditions are set out in Table 8.7.

In Table 8.7,  $p_{eq}^*$  gives the size of an equivalent curve passing through the current stress point (of the same shape as the current cross-section of the  $LC$  yield surface), defined by:

$$p_{eq}^* = \left( \frac{[q - \alpha^* p^*]^2}{m^{*2} p^*} + 1 \right) p^* \tag{8.9}$$

Table 8.7 Conditions checks for each of the four cases

Case	Conditions to be satisfied
Elastic behaviour	$p_{eq}^*(i) \leq p_m^*(i)$ $s^*(i) \geq s_D^*(i)$
Yielding on $SD$ surface alone	$p_{eq}^*(i) \leq p_m^*(i)$ $\Delta s_D^*(i) < 0$
Yielding on $LC$ surface alone	$s^*(i) \geq s_D^*(i)$ $ \Delta \varepsilon_s^p(i) + (\eta^*(i) - \alpha^*(i))  =  \Delta \varepsilon_s^p(i)  +  (\eta^*(i) - \alpha^*(i)) $

Hence, the two conditions shown in Table 8.7 for the elastic case are checks that the stress state at the end of the increment does not lie outside either the  $LC$  surface or the  $SD$  surface. For yielding on the  $SD$  surface alone, the first condition is a check that the stress state at the end of the increment is not outside the  $LC$  surface (Equation 17b in Table 8.6 has already imposed that the stress state at the end of the increment is on the

$SD$  surface). The second condition is a check that the calculated movement of the  $SD$  surface is of the correct sign. For yielding on the  $LC$  surface alone, the first condition is a check that the stress state at the end of increment is not outside the  $SD$  surface (Equation 16c in Table 8.6 has already imposed that the stress state at the end of increment is on the  $LC$  surface). The second condition is a check that the signs of  $\Delta\varepsilon_s^p$  and  $\Delta\varepsilon_v^p$  are individually correct (rather than that simply the ratio  $\Delta\varepsilon_s^p/\Delta\varepsilon_v^p$  is correct). This is achieved by checking that  $\Delta\varepsilon_s^p$  is positive for  $\eta^* > \alpha^*$  and that  $\Delta\varepsilon_s^p$  is negative for  $\eta^* < \alpha^*$  (by checking that  $\Delta\varepsilon_s^p$  and  $(\eta^* - \alpha^*)$  are of the same sign).

For simulations of saturated tests (Test Series A0 and B0), a simplified version of the simulation code was employed, with appropriate equations in Table 8.5, 8.6 and 8.7 either modified or omitted. In particular only two possible cases (rather than four) had to be considered for the simulation of saturated tests:

- (a) Elastic behaviour;
- (b) Yielding on  $LC$  yield surface.

#### 8.4 CALIBRATION OF SOIL CONSTANTS $\mu$ AND $c$

The first model simulations were performed to calibrate the values of the two final soil constants  $\mu$  and  $c$ , which control the hardening for changes of  $\alpha^*$  (see Equation 7.17). This was done by running model simulations of the initial loading stages of Test Series Ba300 (conducted at  $[\Delta q/\Delta\bar{p}] = 1.2$ ), Bb300 (conducted at  $[\Delta q/\Delta\bar{p}] = 0$ ) and Bc300 (conducted at  $[\Delta q/\Delta\bar{p}] = -1$ ) with different values of  $\mu$  and  $c$ . The objective of these simulations was to find a combination of  $\mu$  and  $c$  that gave the best estimate of the final inclination  $\alpha^*$  of the  $LC$  yield curve in the  $q:p^*$  plane for Test Series Ba300, Bb300 and Bc300. In all three of these cases the initial value of  $\alpha^*$  was 0.20 whereas the value of  $\alpha^*$  at the end of the initial loading stage had changed to 0.25 in Test Series Ba300, 0.12 in Test Series Bb300 and  $-0.10$  in Test Series Bc300 (see Section 6.5.2). It is worth mentioning that experimental results of Test Series Bd100 were not used in the calibration of  $\mu$  and  $c$  and, instead, they were used independently to investigate model performance when plastic straining was caused by a reduction of suction, as will be shown in Section 8.8.

In performing these model simulations of the initial loading stage in a given test series, the fitted polynomial expression for  $S_r$  (see Equation 4 in Table 8.5) was based on the average for all the experimental curves in the given test series. An example is presented in Figure 8.3 for Test Series Ba300.

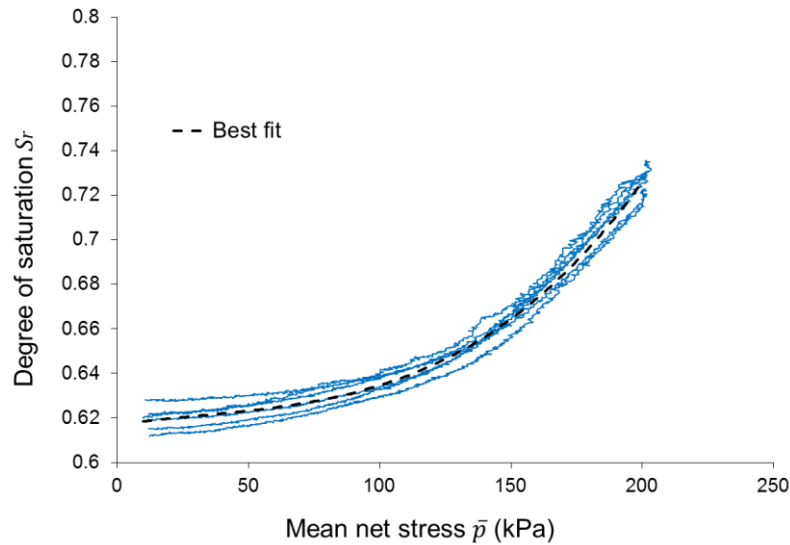


**Figure 8.3** Best fitting of experimental  $S_r$  data for the initial loading stages of Test Series Ba300

The method used to calibrate the values of  $\mu$  and  $c$  for Version 1 of the model is presented first. Inspection of Equations 7.17 and 7.19 show that the change of  $\alpha^*$  is not affected by the soil constant  $c$  for the case where  $\eta^*$  is zero and hence tests of this type are ideal for calibrating for the soil constant  $\mu$ . Values of  $\eta^*$  were very small in Test Series Bb300 (remember that the initial loading stages were conducted at  $[\Delta q/\Delta \bar{p}] = 0$  but under a small constant value of  $q = 6$  kPa in Tests Bb300(1.2) and Bb300(0.5) and under a constant value of  $q = 0$  in Tests Bb300(-0.5), Bb300(-1) and Bb300(-1.5), see Section 5.1.2). For the case where  $q = 6$  kPa,  $c$  contributes slightly to the predicted change of  $\alpha^*$ , but the influence of  $c$  is extremely small (because the value of  $\eta^*$  never exceeded 0.03). For the first simulation, the value of  $c$  was assumed at 0.55 (note that in the  $S-CLAY1$  model of Wheeler et al. 2003b, the equivalent value for  $c$  essentially varies between  $1/3$  and  $3/4$ , see Section 2.7.2). Model simulations were performed for several different values of  $\mu$  for the two cases of  $q = 6$  kPa (relevant to two tests) and  $q = 0$  (relevant to three tests). Figure 8.4a shows the variation with  $\mu$  of the predicted final value of  $\alpha^*$  at the end of initial loading stage (for simulations performed at the two different values of  $q$ ). The experimental results showed a final value of  $\alpha^*$  of 0.12, and inspection of Figure 8.4a shows that, in order to correctly predict this final value of  $\alpha^*$ , a  $\mu$  value of 11 was required for tests with  $q = 6$  kPa and a  $\mu$  value of 9.8 was required for tests with  $q = 0$ . An average value of  $\mu = 10.4$  was therefore provisionally calculated.

Subsequently, the value of  $\mu = 10.4$  was used when calibrating the value of the final model parameter  $c$  by performing simulations of the initial loading stages of Test Series Ba300 and Bc300. Again model simulations were performed for each test series using

several different values of  $c$ . For Test Series Ba300 the initial loading stages were as a stress ratio  $[\Delta q/\Delta \bar{p}] = 1.2$  from an initial stress state of either  $q = 6$  kPa (Tests Ba300(0.5) and Ba300(0)) or  $q = 0$  (Tests Ba300(-0.5), Ba300(-1) and Ba300(-1.5)). For Test Series Bc300 initial loading stages were at  $[\Delta q/\Delta \bar{p}] = -1$ , starting from an initial stress state with  $q = 0$  in all cases. The experimental results showed values of  $\alpha^*$  at the end of the initial loading stage of 0.25 for Test Series Ba300 and  $-0.10$  for Test Series Bc300 (see Section 6.5.2). Inspection of Figures 8.4b and 8.4c shows that these experimental values were matched by the model predictions with  $\mu = 0.52$  (Test Series Ba300 with  $q_{initial} = 6$  kPa),  $\mu = 0.54$  (Test Series Ba300 with  $q_{initial} = 0$ ) or  $\mu = 0.50$  (Test Series Bc300). An average value of  $c = 0.52$  was therefore selected.

As a final check, the selected values of  $c$  and  $\mu$  (0.52 and 10.4 respectively) were used to simulate again the initial loading stage of Test Series Bb300. It was found that the modest change in the value of  $c$  (from the initial guess of  $c = 0.55$  shown in Figure 8.4a to the final value of  $c = 0.52$ ) had an insignificant effect on the predicted final value of  $\alpha^*$  (as expected, because the value of  $\eta^*$  was so low in this stage). The values of  $\mu = 10.4$  and  $c = 0.52$  were therefore considered satisfactory and were employed in all subsequent model simulations with Version 1 of the model (see Table 8.1).

For Version 2 of the model, revised values of  $\mu$  and  $c$  were obtained by following the same procedure as for Version 1 (remembering that initial states and model equations are slightly different for Version 2, see Sections 8.2 and 8.3). This led to slightly different values of  $\mu = 7.45$  and  $c = 0.43$  (see Table 8.1).

## 8.5 CONFIRMATION THAT CONSTANT SUCTION PROBING TESTS WERE ACCEPTABLE FOR DETERMINING INITIAL SIZE AND SHAPE OF THE *LC* SURFACE

In Section 6.5.2, results from sets of constant suction probing stages on isotropically compacted samples (Test Series A300, A100 and A0) and on anisotropically compacted samples (Test Series B300, B100 and B0) were used to investigate the initial size and shape of the *LC* yield curve in the  $q:p^*$  plane (i.e. values of  $p_m^*$ ,  $\alpha^*$ ,  $m_c^*$  and  $m_e^*$ ) following wetting to different initial states. These experimental results were subsequently used in Section 8.1 for the selection of values for model constants  $m_{0c}^*$  and  $m_{0e}^*$ , and in Section 8.2 for the selection of initial values of  $p_m^*$  and  $\alpha^*$  for model simulations.

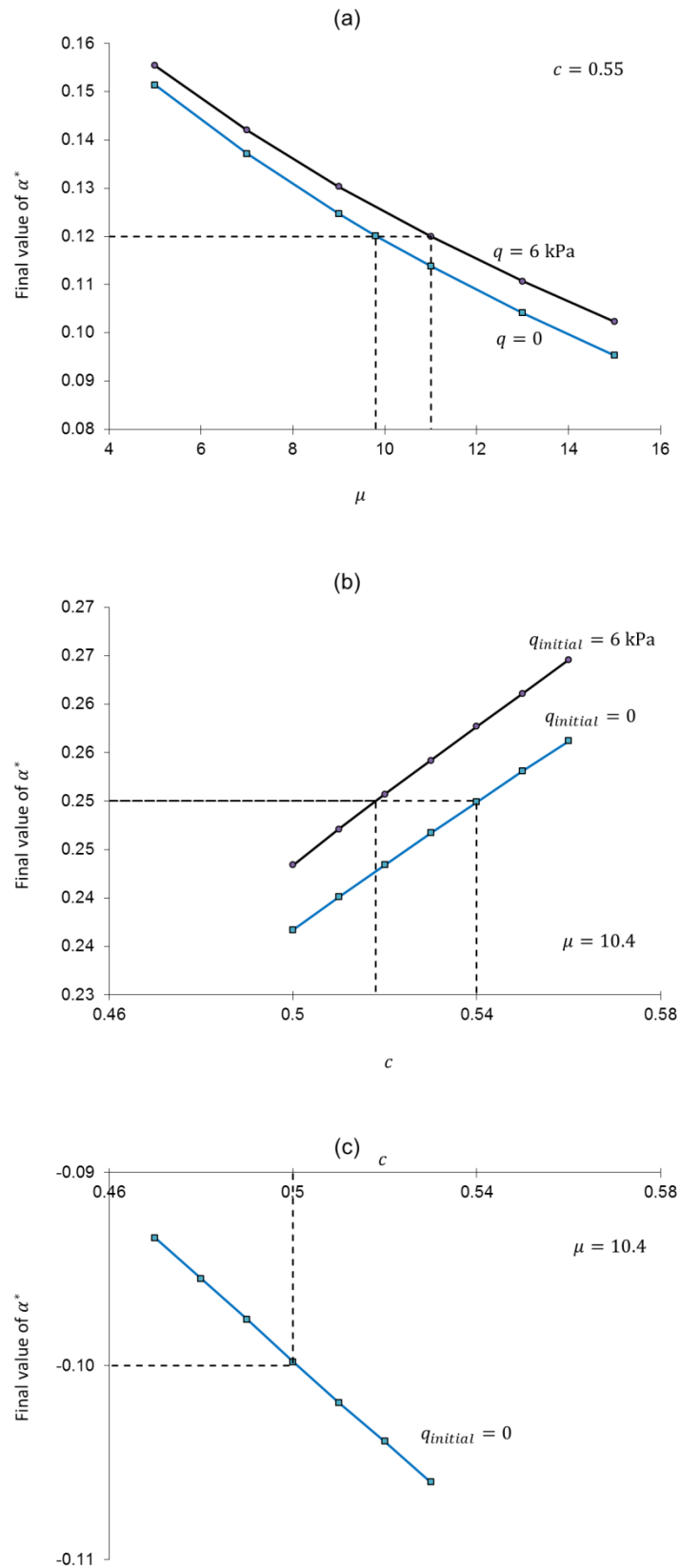


Figure 8.4 Calibration of  $\mu$  and  $c$ : (a) from loading stages of Test Series Bb300, (b) from loading stages of Test Series Ba300, (c) from loading stages of Test Series Bc300

The constitutive model presented in Chapter 7 suggests that all these probing stages commenced at stress states on the  $SD$  yield surface, because of the prior wetting from the higher as-compacted suction to the suction value of 300 kPa, 100 kPa or zero. The model then predicts small amounts of yielding on the  $SD$  surface from the outset of each probing stage, because of the small decrease of  $s^*$  as porosity decreased (due to elastic compression). This small amount of yielding on the  $SD$  surface results in the prediction of a small coupled inward movement of the  $LC$  surface. This means that the model predicts that, in each probing stage, the  $LC$  yield surface would have moved slightly inwards before the yield point on this surface was reached, and the magnitude of this inward movement of the surface prior to arriving at the yield point would be different for each probing stage. As a consequence, it was strictly incorrect to simply join the various experimental yield points within a single test series in order to define the initial form of the  $LC$  yield curve in the  $q:p^*$  plane.

Model simulations of the various probing stages were used to investigate whether the coupled inward movements of the  $LC$  yield surface prior to arriving at the  $LC$  surface were sufficiently small to be considered insignificant. The simulations demonstrated that the decrease of  $p_m^*$  due to coupled inward movements of the  $LC$  surface prior to arriving at the  $LC$  surface were typically less than 1 kPa (e.g. 0.90 kPa and 0.25 kPa in Tests A300(0) and A100(0) respectively and 0.47 kPa and 0.15 kPa in Tests A300(2) and A100(2) respectively). This was within the precision with which yield points could be experimentally determined (see Section 6.5.2). Hence it was confirmed that it was acceptable to use the constant suction probing tests for the determination of the initial size and shape of the  $LC$  yield surface, even though these probing tests commenced on the  $SD$  yield surface.

## 8.6 SIMULATIONS OF TESTS ON ISOTROPICALLY COMPACTED SAMPLES

Model simulations of selected tests on isotropically compacted samples from Test Series A300, A100 and A0 are shown in this section, together with the corresponding experimental results, in order to investigate the capabilities of the new anisotropic model. This is followed by Section 8.7, which shows simulations of selected tests on anisotropically compacted samples from Test Series B300, B100 and B0. Section 8.7 includes an examination of whether the new anisotropic model is able to capture observed differences in behaviour between isotropically compacted and anisotropically compacted samples. Section 8.8 shows simulations of selected tests incorporating a previous loading or wetting stage (from Test Series Ba300, Bb300, Bc300 and Bd100). The test simulations presented in Sections 8.6, 8.7 and 8.8 employ Version 1 of the new anisotropic model (involving an associated flow rule and values of  $m_c^*$  and  $m_e^*$  that vary

with  $\alpha^*$ ), whereas Section 8.9 includes some comparisons of simulations with both Version 1 and Version 2 of the model (involving a non-associated flow rule and constant values of  $m_c^*$  and  $m_e^*$ ), in order to compare the performance of the two versions.

### 8.6.1 Test Series A100 (all values of $[\Delta q/\Delta \bar{p}]$ )

Model simulations (using Version 1 of the new anisotropic model) are compared with the corresponding experimental results for the full set of 7 tests within Test Series A100 ( $s = 100$  kPa), in order to explore the model performance over a wide range of stress path directions. Also shown for comparison are simulations with the isotropic variant of the model (with the soil constant  $\mu$  and the initial value of  $\alpha^*$  both set to zero), in order to investigate whether incorporation of anisotropy in the model results in significant improvement in the accuracy of the model simulations (even for tests on samples that are initially isotropic).

Figure 8.5 shows the model simulations and experimental results for Test A100(0). This test involved an initial probing stage at  $[\Delta q/\Delta \bar{p}] = 0$ , followed by conventional shearing at  $[\Delta q/\Delta \bar{p}] = 3$ .

Inspection of Figure 8.5a and 8.5b shows that the anisotropic model accurately predicts the small positive value of shear strain observed during the initial probing stage at  $[\Delta q/\Delta \bar{p}] = 0$  (i.e. prior to the start of the shearing stage), whereas the isotropic model over-predicts the shear strain during the probing stage. Inspection of Figure 8.5b and 8.5c shows that the volumetric strain during the initial probing stage (i.e. prior to the start of the shearing stage) is well captured by both anisotropic and isotropic models. Figure 8.5c shows that both anisotropic and isotropic model predict well the gradient of the *NCL*, which is expected as the isotropic normal compression surface in  $v:\ln p^*:\ln s^*$  space was fitted through experimental data points from isotropic normal compression probing stages on isotropic unsaturated samples (see Section 6.2.3).

Figures 8.5b and 8.5c show that both anisotropic model and isotropic model over-predict the volumetric strain observed during the shearing stage. However, this over-prediction of volumetric strain during the shearing stage is much less severe for the anisotropic model than for the isotropic model.

For the shearing stage of the test, the experimental curve in Figure 8.5a shows a dramatic post-peak reduction in deviator stress, and similar behaviour is observed in all other tests. This can be attributed to post-peak strain localisation. The model simulations

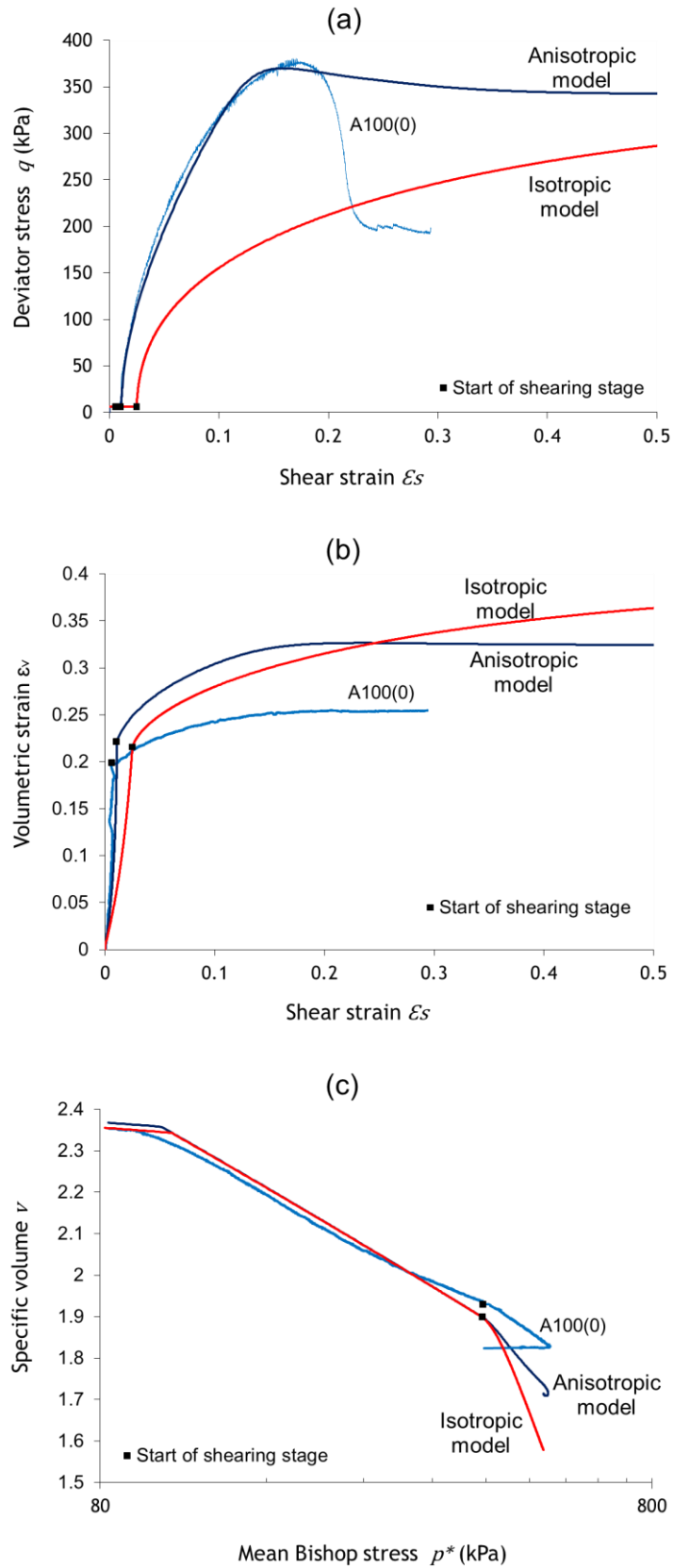


Figure 8.5 Model simulations and experimental results for Test A100(0)

cannot, of course, account for such strain localisation effects, and therefore when comparing model simulations and experimental results, this part of the experimental  $q:\varepsilon_s$  curve should be ignored.

Both anisotropic and isotropic model simulations in Figure 8.5 predict the same critical state value of deviator stress  $q$ , but this is not reached until extremely large values of shear strain for the isotropic model ( $\approx 300\%$ ). The anisotropic model predicts a peak in the  $q:\varepsilon_s$  curve and then a modest post-peak reduction of  $q$  to a critical state, whereas the isotropic model predicts a monotonic increase of  $q$  to the critical state. The peak deviator stress predicted by the anisotropic model is an excellent match to the peak deviator stress observed in the experimental results, whereas the match to the peak value of  $q$  is less good for the isotropic model.

Figure 8.5a shows that the development of shear strain during the shearing stage and prior to reaching peak deviator stress is very well predicted by the anisotropic model. This suggests that the associated flow rule is performing well when combined with an anisotropic yield curve (where  $\alpha^*$  can increase from zero during the shearing stage). In contrast, the isotropic model grossly over-predicts the generation of shear strain during the shearing stage. This indicates that the combination of an associated flow rule with an isotropic yield curve (with  $\alpha^*$  remaining at zero) does not work well (compounded by the fact that plastic volumetric strains have already been significantly over-predicted by the isotropic model).

Overall, it is clear from Figure 8.5 that the anisotropic model provides a significantly better match to the experimental results of Test A100(0) than the isotropic model. Figures 8.6, 8.7 and 8.8 show the model simulations and experimental results for Tests A100(1), A100(2) and A100(3) respectively. These three tests involved probing stages in triaxial compression continued right through to critical states, with  $[\Delta q/\Delta \bar{p}] = 1, 2$  and  $3$  respectively.

Inspection of Figures 8.6b and 8.6c shows that the anisotropic model gives better predictions of the volumetric strains than the isotropic model at  $[\Delta q/\Delta \bar{p}] = 1$ . However, inspection of Figures 8.7b, 8.7c, 8.8b and 8.8c shows that, at  $[\Delta q/\Delta \bar{p}] = 2$  or  $3$ , although the anisotropic model provides better modelling of volumetric strains in the early part of shearing, the isotropic model predicts the final values of volumetric strains better than the anisotropic model.

Anisotropic and isotropic model simulations in Figures 8.6a, 8.7a and 8.8a predict the same critical state value of deviator stress  $q$  for a given value of  $[\Delta q/\Delta \bar{p}]$ , but again this is not reached until extremely large values of shear strain for the isotropic model. At high  $[\Delta q/\Delta \bar{p}]$  values (i.e. 2 or 3) the anisotropic model predicts a peak in the  $q:\varepsilon_s$  curve followed by a modest post-peak reduction of  $q$ , whereas at  $[\Delta q/\Delta \bar{p}] = 1$  the anisotropic model predicts a monotonic increase of  $q$  to a critical state. In contrast, the isotropic model predicts a monotonic increase of  $q$  to the critical state in all three tests. The peak value of  $q$  is reasonably well predicted by the anisotropic model with the exception of Test A100(1), where the peak value of  $q$  is significantly under-predicted by the anisotropic model. This is attributed to the fact that with  $[\Delta q/\Delta \bar{p}] = 1$  the stress path is approaching the critical state line at a very acute angle in the  $q:p^*$  plane, and a small error in the predicted position of the critical state line can result in a large error in the predicted critical state value of  $q$ . Figures 8.6a, 8.7a and 8.8a show that the isotropic model significantly under-predicted the peak value of  $q$  at all three values of  $[\Delta q/\Delta \bar{p}]$ .

Figures 8.6a, 8.7a and 8.8a show clearly that the anisotropic model captures reasonably well the evolution of shear strains prior to reaching peak deviator stress, whereas the isotropic model considerably over-predicts the evolution of shear strain. This confirms that the associated flow rule is performing well when combined with a yield curve with evolving anisotropy but that the combination of an associated flow rule with an isotropic yield curve does not work well, as already observed in the discussion of Figure 8.5.

Figures 8.9, 8.10 and 8.11 show the model simulations and experimental results for Tests A100(-0.5), A100(-1) and A100(-1.5), which all involved testing in triaxial extension. Test A100(-0.5) involved a probing stage at  $[\Delta q/\Delta \bar{p}] = -0.5$  followed by shearing to a critical state in triaxial extension at  $[\Delta q/\Delta \bar{p}] = 3$ . Tests A100(-1) and A100(-1.5) involved probing stages in triaxial extension continued right through to critical states, at  $[\Delta q/\Delta \bar{p}] = -1$  and  $-1.5$  respectively.

Figure 8.9b and 8.9c show that the anisotropic model gives slightly better prediction of the final volumetric strain than the isotropic model during the probing stage at  $[\Delta q/\Delta \bar{p}] = -0.5$ , and the anisotropic model gives significantly better prediction of the volumetric strain observed during the subsequent shearing stage than the isotropic model (although even the anisotropic model does over-predict the final volumetric strain during the shearing stage). Figures 8.10c and 8.11c show that the anisotropic model captured well the final volumetric strains the stress path at  $[\Delta q/\Delta \bar{p}] = -1$  and  $-1.5$ , whereas the isotropic model always over-predicts the final volumetric strain.

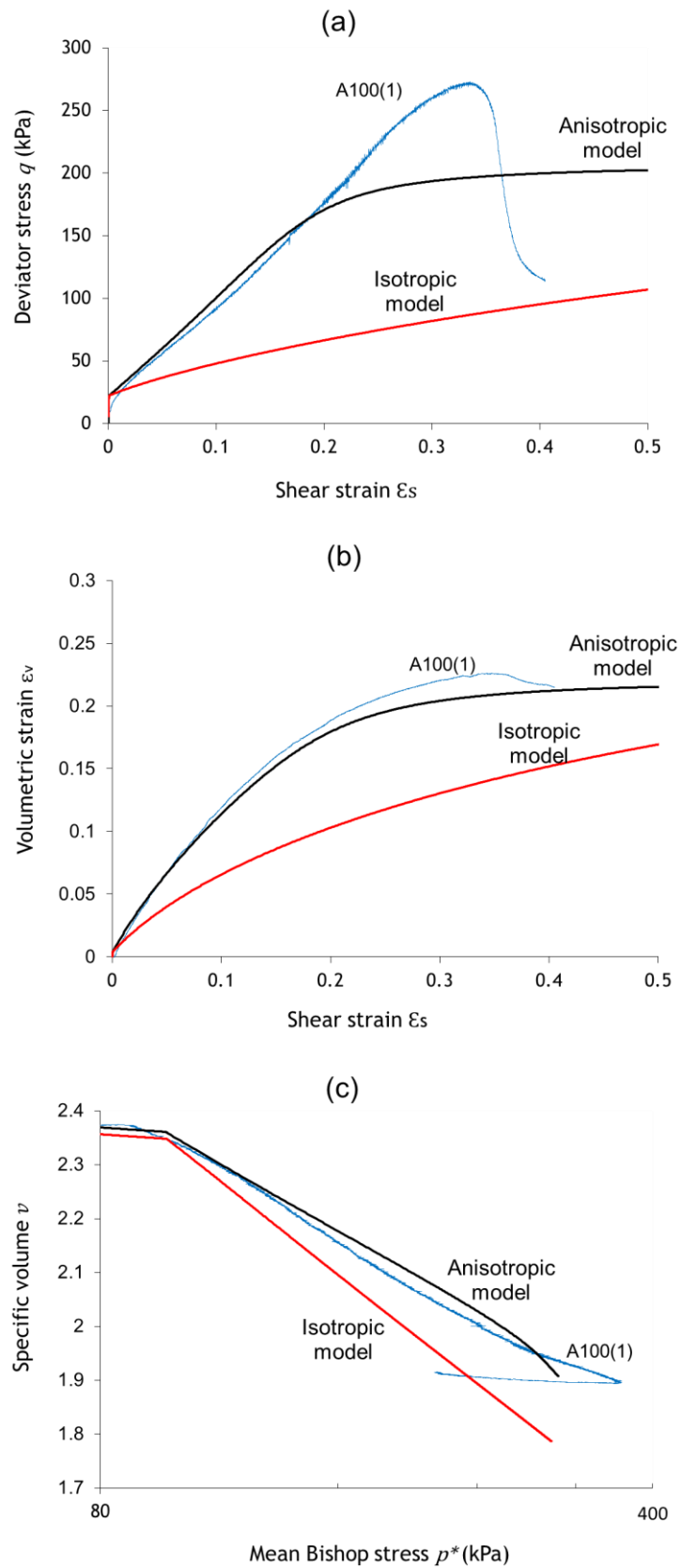


Figure 8.6 Model simulations and experimental results for Test A100(1)

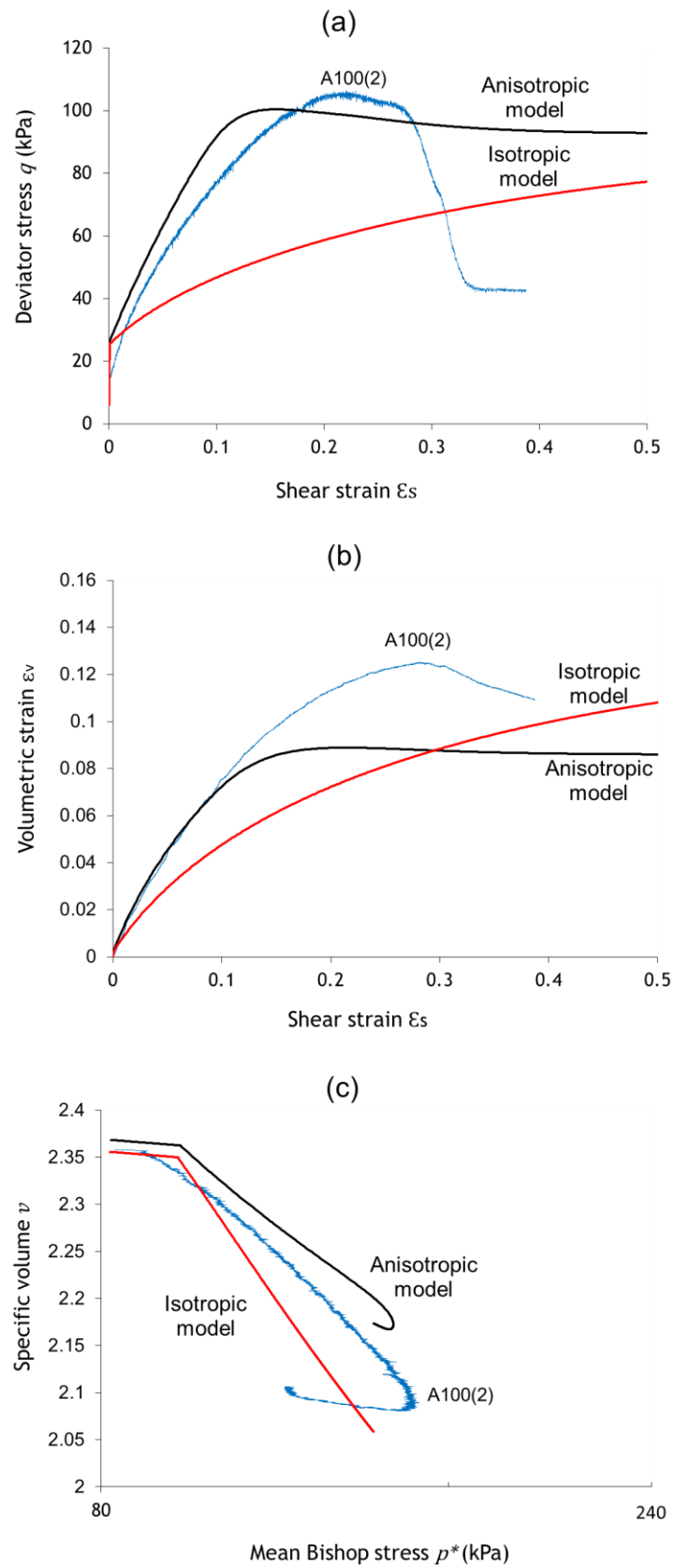


Figure 8.7 Model simulations and experimental results for Test A100(2)

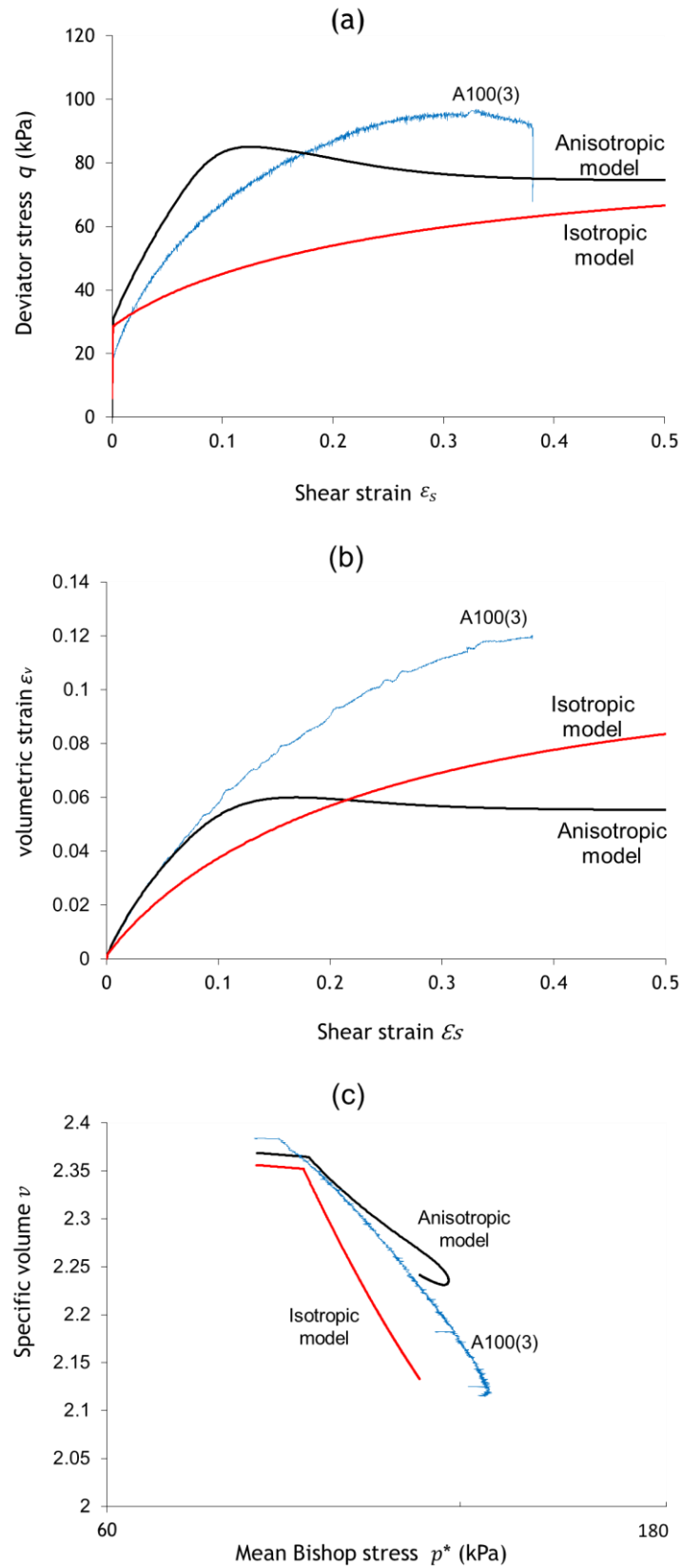


Figure 8.8 Model simulations and experimental results for Test A100(3)

Anisotropic and isotropic model simulations in Figures 8.9a, 8.10a and 8.11a predict the same critical state value of deviator stress  $q$  for a given value of  $[\Delta q/\Delta \bar{p}]$ , but this is not reached until extremely large values of shear strain for the isotropic model (e.g.  $> 300\%$  in A100(-1)). The anisotropic model predicts a peak in the  $q:\varepsilon_s$  curves of A100(-0.5) (i.e. during the shearing stage at  $[\Delta q/\Delta \bar{p}] = 3$ ) and Test A100(-1.5) and then a modest post-peak reduction of  $q$  to a critical state, but no peak in the  $q:\varepsilon_s$  curve is predicted for Test A100(-1). In contrast, the isotropic model predicts a monotonic increase of  $q$  to the critical state in all of these simulations. The peak deviator stress predicted by the anisotropic model for the probing at  $[\Delta q/\Delta \bar{p}] = -1$  is a good match to the experimental peak deviator stress, whereas the anisotropic model slightly over-predicts the peak deviator stress for the probing stage at  $[\Delta q/\Delta \bar{p}] = -1.5$  and for the shearing stage at  $[\Delta q/\Delta \bar{p}] = 3$  (in Test A100(-0.5)) However, the critical state values of  $q$  predicted by the model match very well the experimental peak values of  $q$ .

Figure 8.9a shows that the anisotropic model captures very well the generation of shear strain during the probing stage at  $[\Delta q/\Delta \bar{p}] = -0.5$ . Figures 8.10a and 8.11a show that the anisotropic model does reasonably well in predicting the development of shear strains during the probing stages at  $[\Delta q/\Delta \bar{p}] = -1$  and  $-1.5$  (shear strains are slightly under-predicted). In contrast, the generation of shear strains is considerably over-predicted by the isotropic model during the probing stages at  $[\Delta q/\Delta \bar{p}] = -0.5, -1$  and  $-1.5$  (see Figures 8.9a, 8.10a and 8.11a). The over-prediction of shear strain by the isotropic model suggests that the combination of an associated flow rule with an isotropic yield curve (with  $\alpha^*$  remaining at zero) does not work well.

In general, Figures 8.5 to 8.11 indicate that predictions of the anisotropic model are significantly better than those of the isotropic model in capturing the soil behaviour observed in the experimental tests, even for isotropically compacted samples. This supports the argument that it is important to represent the evolution of anisotropy during plastic straining. Figure 8.12 combines the results for three tests in Test Series A100 (Tests A100(0), A100(1) and A100(-1), previously shown in Figures 8.5, 8.6 and 8.10 respectively), to illustrate the overall performance of the anisotropic model over a wide range of stress paths. Setting aside strain localisation effects in the experimental results, it is clear that the anisotropic model does a satisfactory overall job in predicting the soil behaviour, with the only significant mismatches being under-prediction of the peak value of deviator stress in Test A100(1) (attributed to the very acute angle of approach to the critical state line in the  $q:p^*$  plane) and over-prediction of the volumetric strain in the final shearing stage of Test A100(0).

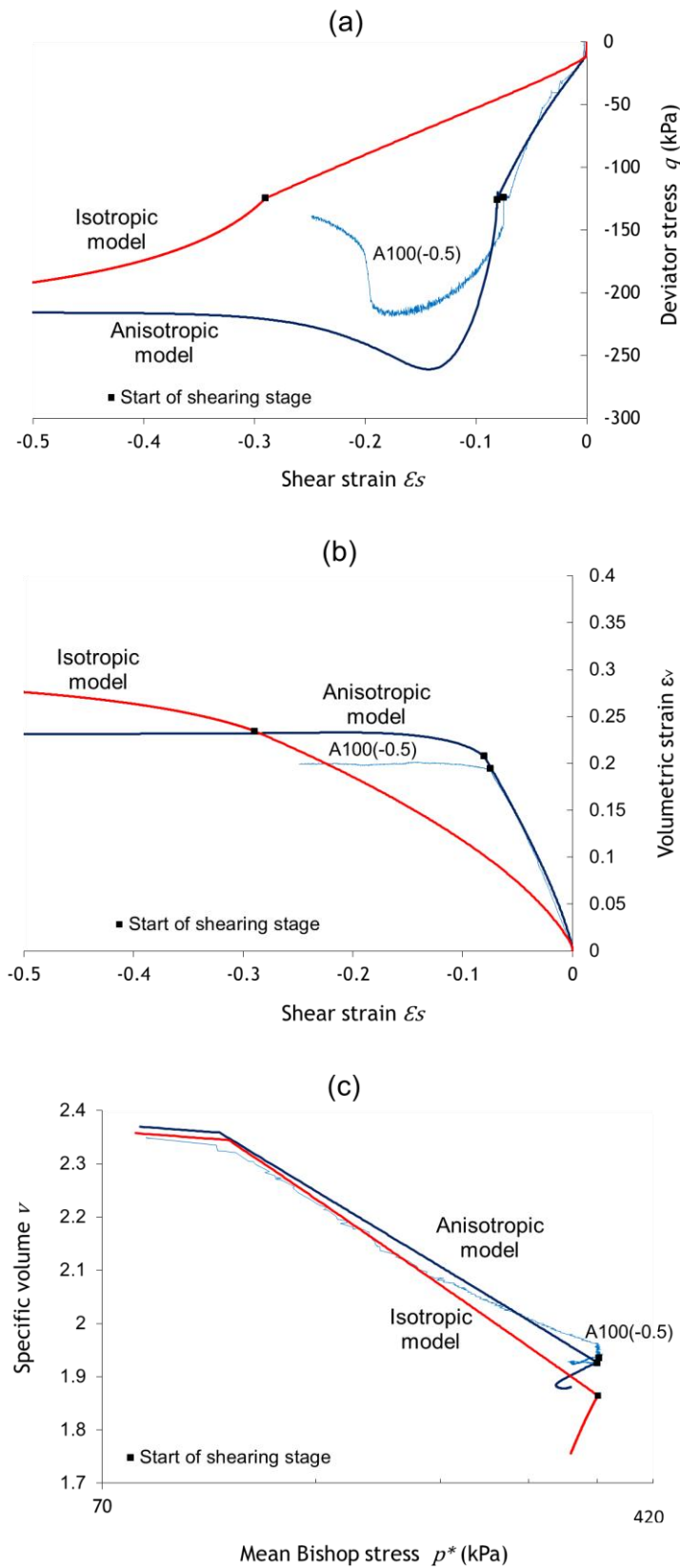


Figure 8.9 Model simulations and experimental results for Test A100(-0.5)

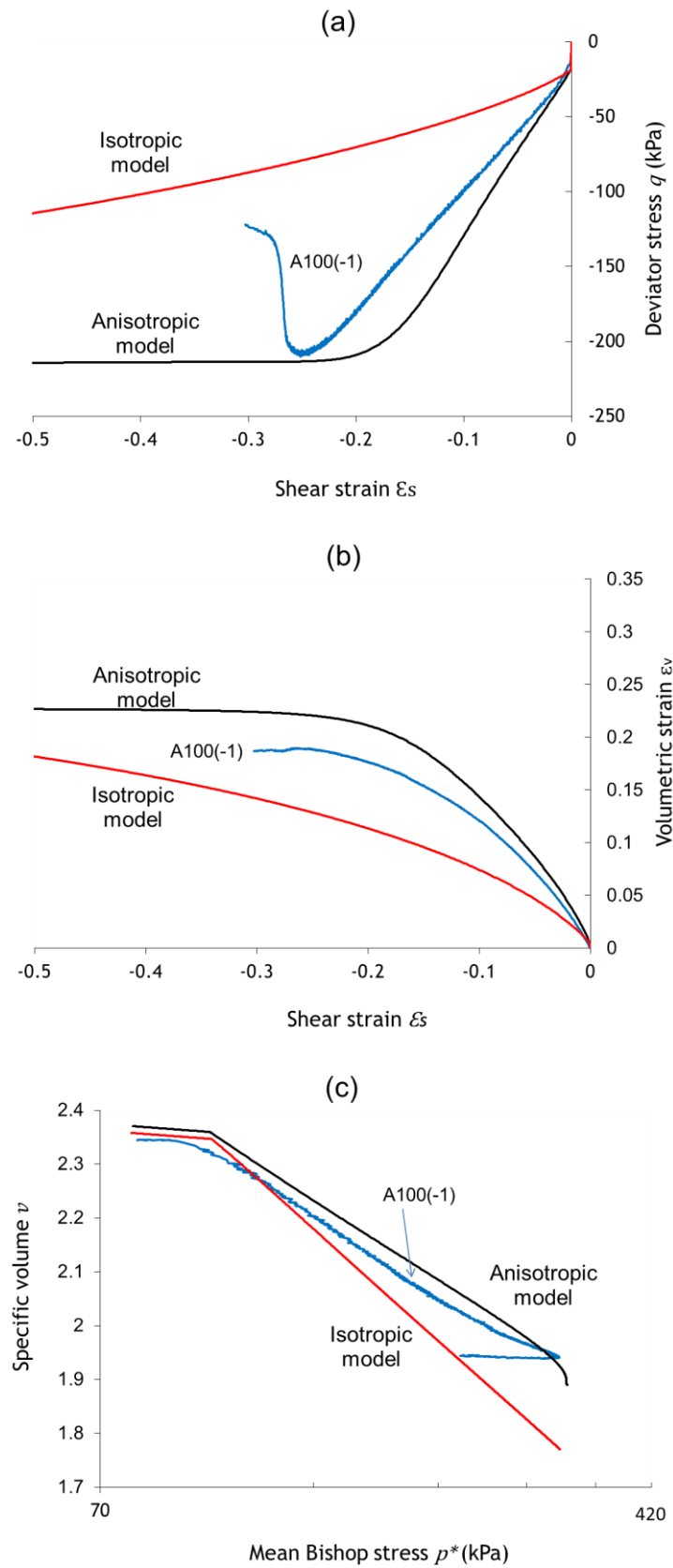


Figure 8.10 Model simulations and experimental results for Test A100(-1)

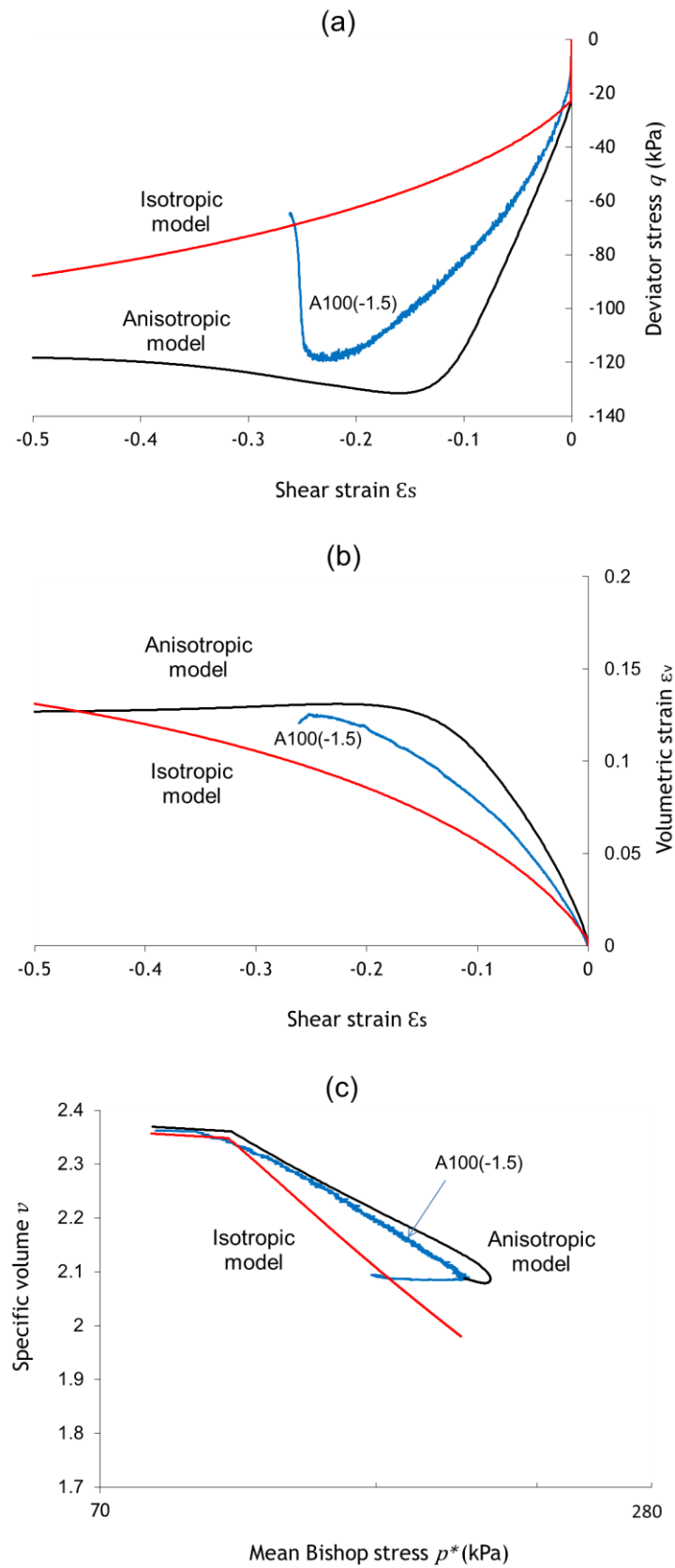


Figure 8.11 Model simulations and experimental results for Test A100(-1.5)

Many of the anisotropic model simulations in Figures 8.5 to 8.11 show a peak value of deviator stress and then a modest post-peak reduction of  $q$  to a critical state. Anisotropic model simulations for these tests show that the stress path in the  $q:p^*$  plane initially progresses beyond the critical state line, before returning to a final state on the critical state line. This occurs because when the stress path first crosses the critical state line in the  $q:p^*$  plane, the inclination  $\alpha^*$  and aspect ratio  $m^*$  of the  $LC$  yield surface have not yet attained their critical state values (see Sections 7.7 and 7.8 respectively). As a consequence, when the stress path first crosses the critical state line in the  $q:p^*$  plane, positive plastic volumetric strains are still being predicted, and hence the  $LC$  yield surface continues to increase in size and the stress path is temporarily able to continue beyond the critical state line in the  $q:p^*$  plane.

This type of anisotropic model simulation is illustrated in Figure 8.13, which shows simulation of Test A100(3). Figure 8.13a show the stress path in the  $q:p^*$  plane, and Figures 8.13b, 8.13c and 8.13d show the predicted variations of  $\alpha^*$ ,  $m^*$  and  $p_m^*$  respectively. Yielding on the  $SD$  surface is predicted from the start of the test, with simultaneous yielding on the  $LC$  surface commencing at Point  $a$ . From Point  $a$  onwards significant increases of  $\alpha^*$  are predicted (see Figure 8.13b). However, when the stress path first crosses the critical state line in the  $q:p^*$  plane at Point  $b$  (see Figure 8.13a), the value of  $\alpha^*$  is still significantly below its final critical state value (see Figure 8.13b).

As a consequence, at Point  $b$ , the aspect ratio  $m^*$  of the  $LC$  surface is still much greater than the final critical state value (see Figure 8.13c) (this is particularly marked because the expression selected for the variation of  $m^*$  with  $\alpha^*$  (see Equation 7.22) means that  $m^*$  only begins to decrease significantly once  $\alpha^*$  gets relatively close to its critical state value). With  $\alpha^*$  below its critical state value and  $m^*$  above its critical state value, the cross-section of the  $LC$  yield surface does not have a horizontal tangent at Point  $b$  and hence positive plastic volumetric strains are still predicted, together with corresponding continuing increase in the size of the  $LC$  surface (see the variation of  $p_m^*$  in Figure 8.13d). The increase of  $p_m^*$  finally ceases at Point  $c$ , when the value of  $\alpha^*$  and  $m^*$  have become relatively close to their respective critical state values. The final part of the simulation shows a post-peak reduction of  $q$  to a final critical state at  $d$ . During this part of the simulation, negative plastic volumetric strains are predicted,  $p_m^*$  decreases (see Figure 8.13d) and hence coupled downward movement of the  $SD$  yield surface is predicted. This means that the  $SD$  surface moves away from the current stress point and no yielding on the  $SD$  surface is predicted for this final part  $c - d$  of the test.

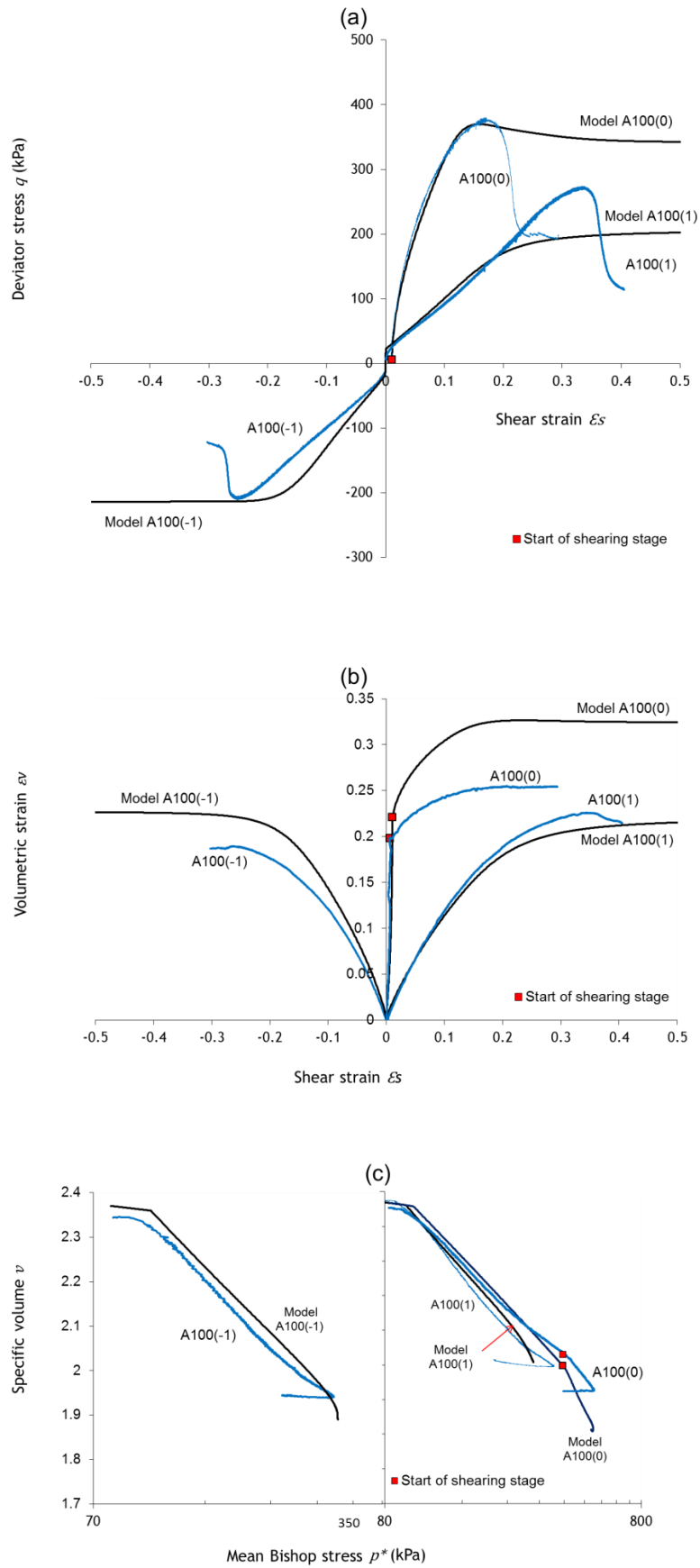


Figure 8.12 Anisotropic model simulations and experimental results for Tests A100(1), A100(0) and A100(-1)

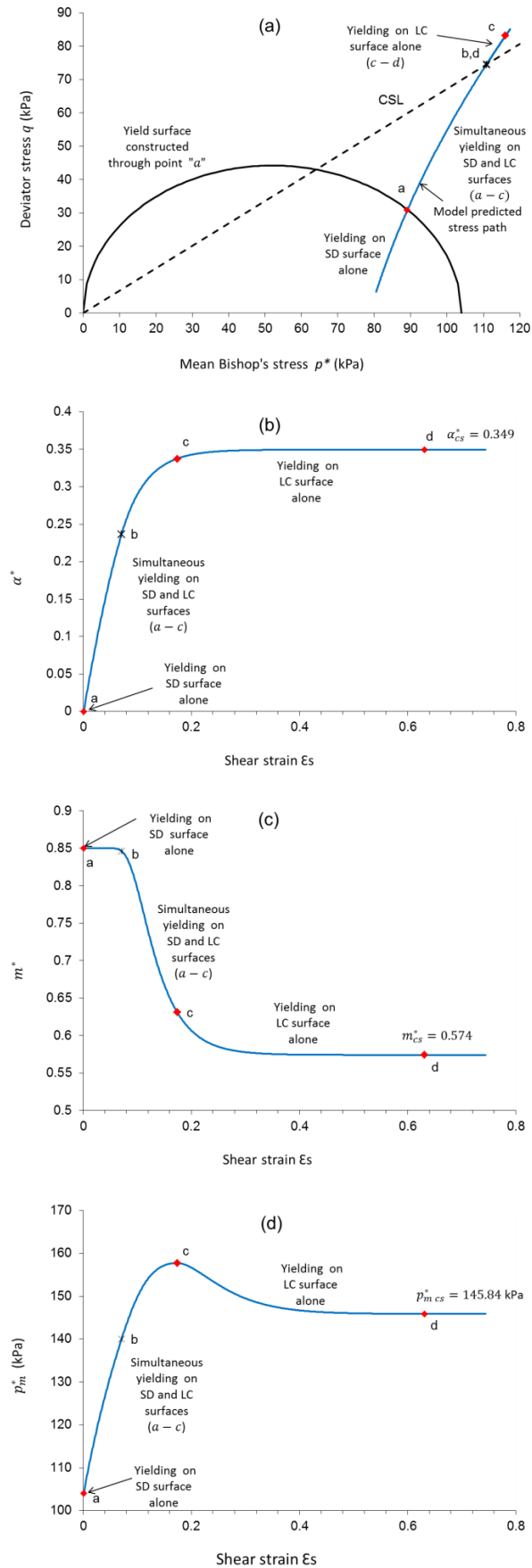


Figure 8.13 Evolution of  $\alpha^*$  and  $p_m^*$  during anisotropic model simulation of Test A100(3)

In those tests where the magnitude of the stress gradient  $[\Delta q/\Delta \bar{p}]$  was relatively low, the anisotropic model did not predict the occurrence of a peak deviator stress and a post-peak reduction to a critical state. In these tests, where the critical state line was approached at a relatively acute angle in the  $q:p^*$  plane, there was a much greater length of stress path before the critical state line was reached for the first time. This gave much more opportunity for the values of  $\alpha^*$  and  $m^*$  to attain their critical state values before the critical state line in the  $q:p^*$  plane was reached for the first time.

The isotropic variant of the model does not predict the occurrence of a peak value of deviator stress and a subsequent post-peak reduction of  $q$  to a critical state in any of the simulations because in this isotropic variant of the model the values of  $\alpha^*$  and  $m^*$  are always at their critical state values of zero and  $M^*$  respectively.

### 8.6.2 Influence of suction (at one value of $[\Delta q/\Delta \bar{p}]$ )

The anisotropic model simulations for the probing stages of Tests A100(2), A300(2) and A0(2) are shown together with the experimental results in Figure 8.14, to illustrate the influence of suction on tests with the same stress path in the  $[\Delta q/\Delta \bar{p}]$  plane.

Inspection of Figure 8.14a shows that the model accurately predicts the failure value of deviator stress at suction of 100 kPa (in Test A100(2)), but significantly over-predicts the failure value of  $q$  at a suction of  $s = 300$  kPa (Test A300(2)) and under-predicts the failure value of  $q$  at zero suction (Test A0(2)). This is a consequence of assuming a unique critical state line in the  $q:\bar{p}$  plane, which is clearly not entirely correct (see Section 6.3.3).

Figure 8.14 shows that the anisotropic model accurately predicts the yield value of  $q$  in Test A0(2) but tends to over-predict the yield values of  $q$  in Tests A100(2) and A300(2). This is also clear in Figure 8.14c, where close inspection shows that yield value of  $p^*$  is well-predicted in Test A0(2) but over-predicted in Tests A100(2) and A300(2).

Inspection of Figures 8.14b and 8.14c shows that final volumetric strains are under-predicted by the anisotropic model at all suction values and particularly for  $s = 0$  (this severe under-prediction of volumetric strain at  $s = 0$  occurs because of the under-prediction of the critical state values of  $q$  and  $p^*$  in the test at  $s = 0$ ). The predicted final value of volumetric strain (see Figure 8.14b) is bigger for the simulation at  $s = 300$  kPa than at  $s = 100$  kPa which contradicts the experimental observation. It is also clear in Figure 8.14c that pre-yield elastic volumetric strains are over-predicted in Test A0(2). This is because the model assumes a variable elastic bulk modulus of the form  $K^* =$

$vp^*/\kappa^*$ , and this bulk modulus takes very low values in Test A0(2) (because the range of  $p^*$  is very low). Inspection of Figure 8.14b shows that the ratio of shear strain to volumetric strain is well-predicted by the model for Tests A100(2) and A300(2). This suggests that for these unsaturated tests, the associated flow rule is working well, when combined with a yield curve with evolving anisotropy. It is not possible to draw the same conclusion for the saturated Test A0(2), because the predictions of volumetric strain is so poor.

A general conclusion that can be drawn from Figure 8.14 is that the model appears to be more successful in predicting the results of unsaturated tests (A100(2) and A300(2)) than in predicting the results of a saturated test (A0(2)).

## 8.7 SIMULATIONS OF TESTS ON ANISOTROPICALLY COMPACTED SAMPLES

The influence of the stress path slope  $[\Delta q/\Delta \bar{p}]$  and suction are investigated for the anisotropically compacted samples in Section 8.7.1. A comparison is made between model predictions for the isotropically and anisotropically compacted samples in Section 8.7.2 to investigate whether the model is able to capture the observed differences in the responses of isotropically and anisotropically compacted samples.

### 8.7.1 Influence of the value of $[\Delta q/\Delta \bar{p}]$ and suction

Figure 8.15 demonstrates the effect of stress path slope (i.e. the value of  $[\Delta q/\Delta \bar{p}]$ ) on model predictions for Tests B100(1), B100(0) and B100(-1). By the time the stress state arrived at the final critical state, the predicted  $\alpha^*$  value was +0.349 in Tests B100(1) and B100(0) and -0.349 in Test B100(-1). Knowing that the initial value of  $\alpha^*$  for the anisotropically compacted samples was 0.20, arriving at the final critical state required only a modest change to anisotropy (i.e. from 0.20 to 0.349) for  $[\Delta q/\Delta \bar{p}] = 1$  but required significant change to anisotropy (i.e. from 0.20 to -0.349) for  $[\Delta q/\Delta \bar{p}] = -1$ . The anisotropic model predicts that the isotropic loading of B100(0) (from the initial state to  $\bar{p} = 300$  kPa) causes erasure of anisotropy (i.e. a decrease of  $\alpha^*$ ) from 0.20 to 0.04, then during the shearing stage (performed at  $[\Delta q/\Delta \bar{p}] = 3$ ), the predicted value of  $\alpha^*$  increases to +0.349.

The anisotropic model captures very well the peak deviator stress in all tests and predicts a modest post-peak reduction of  $q$  during the shearing stage of B100(0). The anisotropic model over-predicts the generation of volumetric strains at  $[\Delta q/\Delta \bar{p}] = 1, 0$  and  $-1$  (see Figure 8.15c). A contributory factor in this is simply that the model over-predicts the initial values of  $v$  for anisotropic samples (see Figure 8.15c). It is also

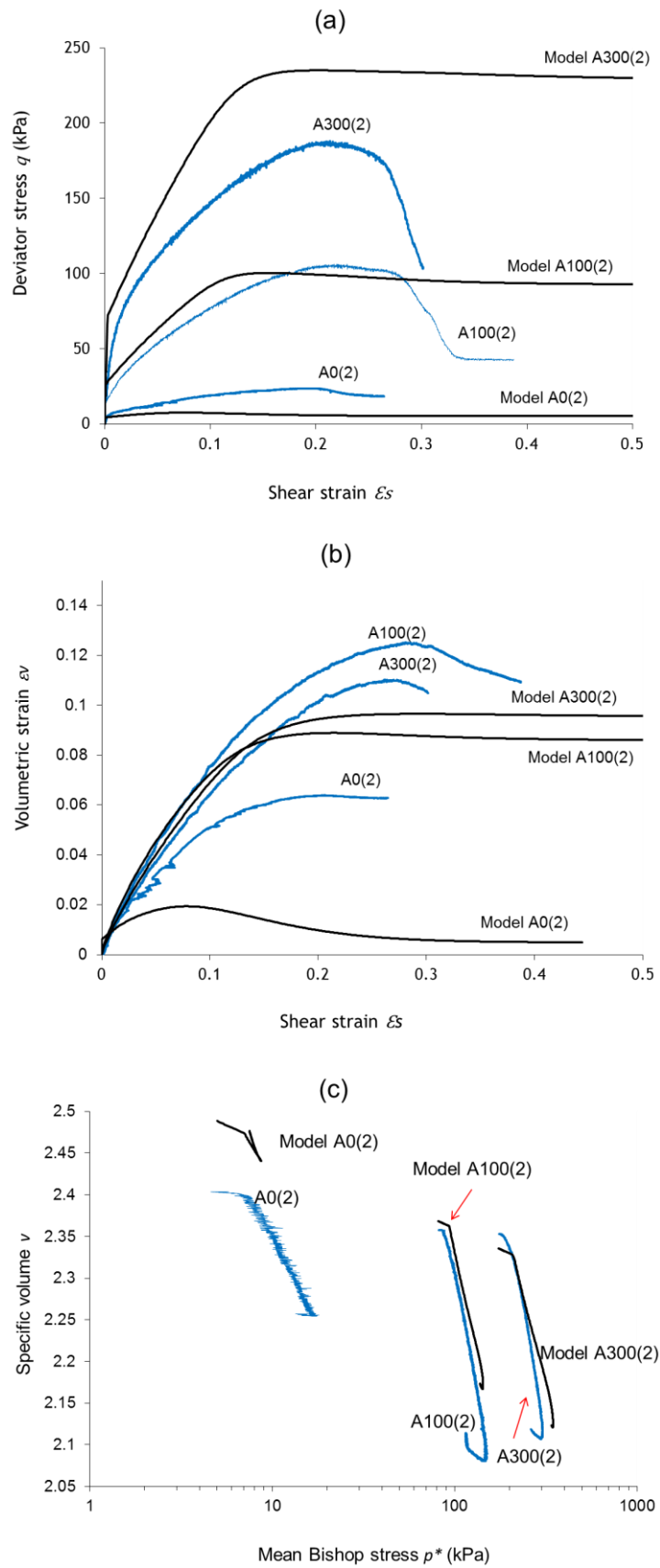


Figure 8.14 Anisotropic model simulations and experimental results for Tests A300(2), A100(2) and A0(2)

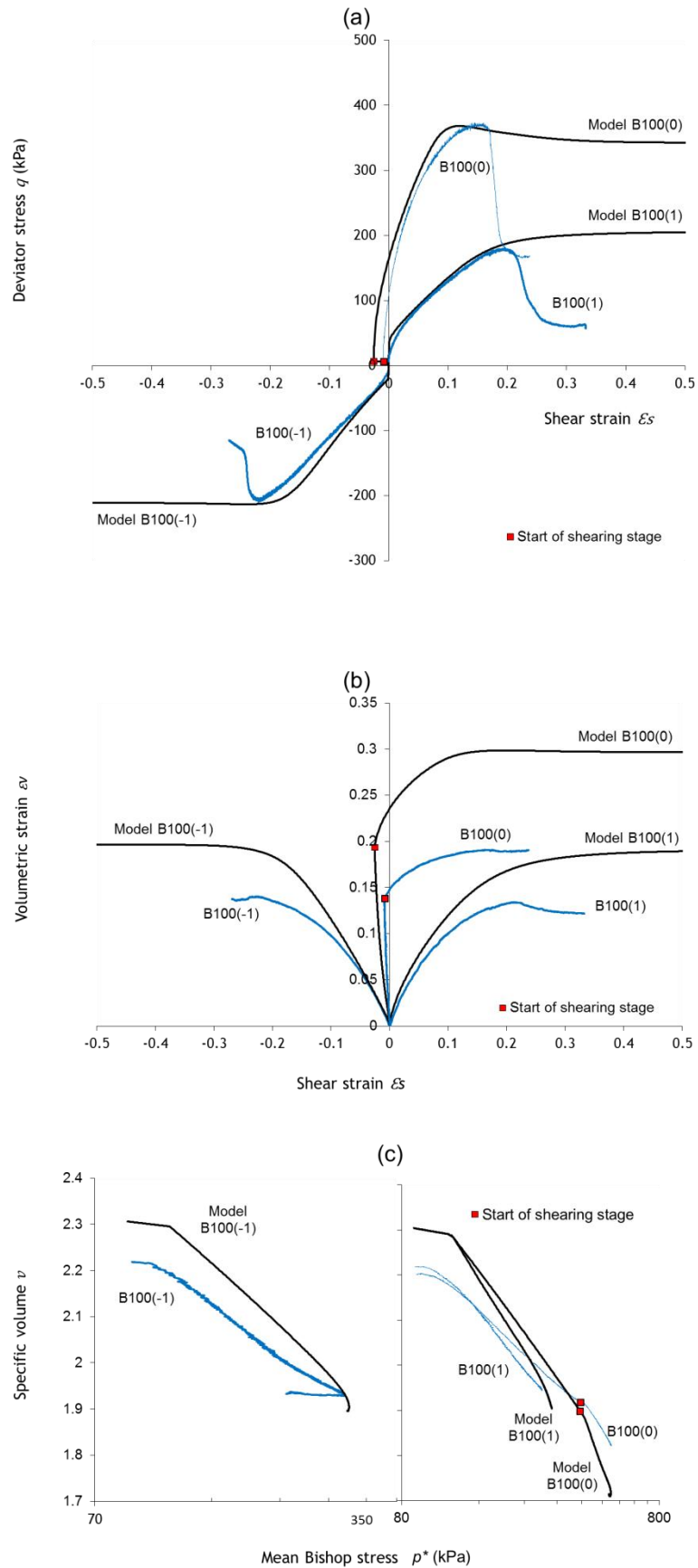


Figure 8.15 Anisotropic model simulations and experimental results for Tests B100(1), B100(0) and B100(-1)

clear however that the model over-predicts the volumetric strain during the final shearing stage of Test B100(0) because the critical state value of  $v$  is under-predicted.

Generally, the anisotropic model gives excellent predictions of the evolution of shear strains (see Figure 8.15a), suggesting that the combination of an associated flow rule and the anisotropic yield curve with evolving anisotropy works well (as observed in Section 8.6 for the isotropically compacted samples).

Generally, Figure 8.15 shows that the anisotropic model performs reasonably well in simulating the behaviour of anisotropically compacted samples over a wide range of stress paths.

The anisotropic model simulations for the probing stage of Tests B100(2), B300(2) and B0(2) (i.e. at  $s = 300$  kPa,  $s = 100$  kPa and  $s = 0$  respectively) are shown together with the experimental results in Figure 8.16.

Inspection of Figure 8.16a shows that the peak value of deviator stress  $q$  is reasonably well-predicted in the unsaturated tests (B100(2) and B300(2)) but significantly under-predicted (in percentage terms) in the saturated test (B0(2)). However, inspection of Figures 8.16a and 8.16c show that the yield values of  $q$  and  $p^*$  are well-predicted in Tests B0(2) and B300(2) but over-predicted in Test B100(2).

Inspection of Figure 8.16b and 8.16c shows that the final volumetric strain is reasonably well predicted in Test B300(2) but somewhat under-predicted in Test B100(2). However, the comparison is complicated by the fact that the model significantly over-predicts the initial values of  $v$  for these anisotropically compacted samples. The predicted volumetric strain in Test B0(2) is an extremely poor match to the observed behaviour, because the model predicts significant dilation after yielding, whereas the experimental results show compressive behaviour through the test (see Figure 8.16b and 8.16c).

### 8.7.2 Comparison of isotropically and anisotropically compacted samples

Figure 8.17 shows anisotropic model simulations for A100(2) and B100(2) (i.e. in triaxial compression) and for A100(-1) and B100(-1) (i.e. in triaxial extension) in order to investigate whether the anisotropic model captures the differences and similarities between isotropically compacted and anisotropically compacted samples.

For the tests in triaxial compression the model predicts the same final critical state value of deviator stress for both tests (A100(2) and B100(2)) (see Figure 8.17a), because the

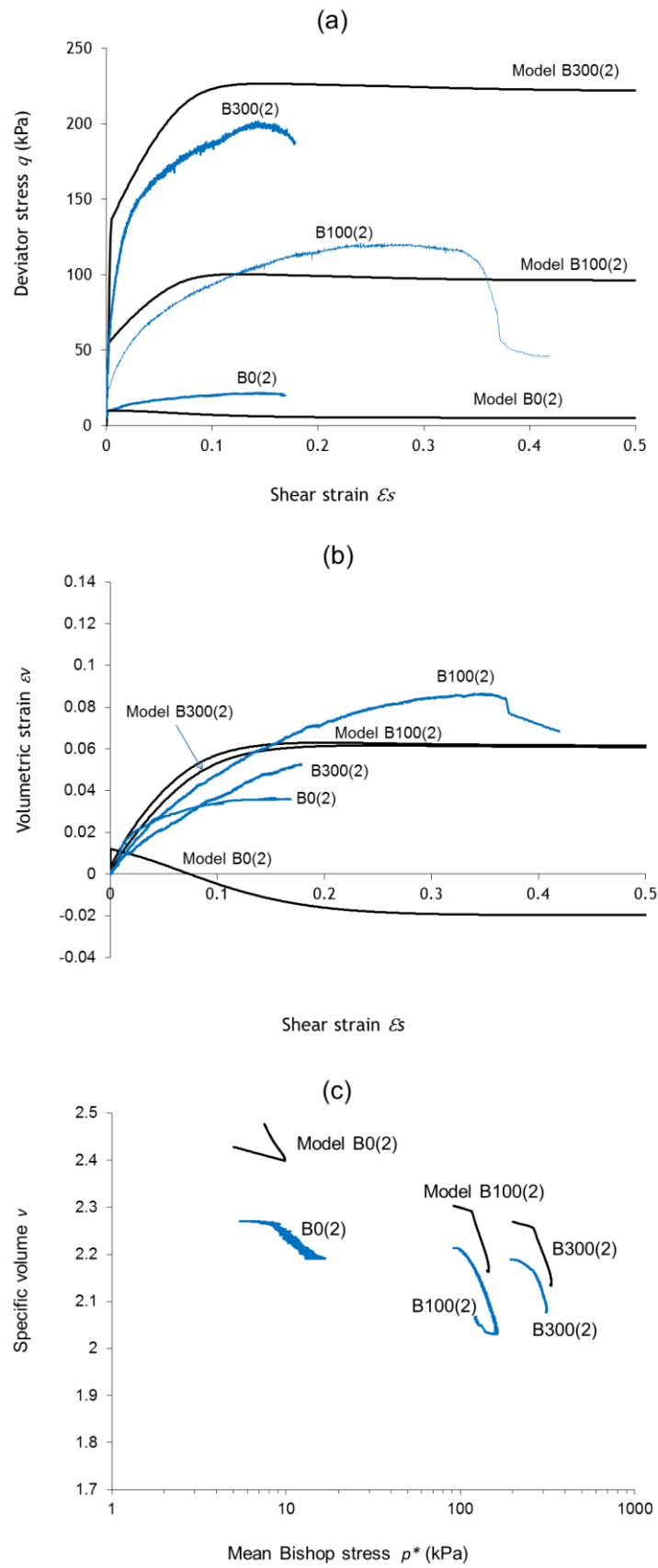


Figure 8.16 Anisotropic model simulations and experimental results for Tests B300(2), B100(2) and B0(2)

model predicts a unique critical state value of  $\alpha^*$ , which is independent of the initial value of  $\alpha^*$ . In contrast, the experimental results show a higher failure value of  $q$  for the anisotropically compacted sample than for the isotropically compacted sample. The model does however capture (at least qualitatively) the differences in pre-failure behaviour in the  $q:\varepsilon_s$  plot, where the model predicts a stiffer pre-failure response for the anisotropically compacted sample than for the isotropically compacted sample (because it predicts that yield will occur at a higher value of  $q$  for the anisotropically compacted sample).

In triaxial extension, the anisotropic model predicts not only that the final failure values of  $q$  will be the same for the two samples it also predicts that the pre-failure responses of the two samples will be indistinguishable in the  $q:\varepsilon_s$  plot (see Figure 8.17a). The experimental results show the same failure value of  $q$  for both samples, but a slightly stiffer pre-failure response for the anisotropically compacted sample than for the isotropically compacted sample.

In qualitative terms, the model correctly predicts that the volumetric strain will be greater for the isotropically compacted samples than for isotropically compacted samples (for tests in both triaxial compression and triaxial extension). In the model simulations this is simply attributed to the isotropically compacted samples starting at higher initial values of  $v$  than the anisotropically compacted samples, whereas the predicted final values of  $v$  are the same for both types of samples. The inability of the model to accurately predict the initial values of  $v$  for the anisotropically compacted samples (as discussed in Section 8.2) is again clear in Figure 8.17c. In absolute terms, the model under-predicts the volumetric strain for the tests in triaxial compression (for both samples) and over-predicts the volumetric strain for the tests in triaxial extension (for both samples) (see Figure 8.17b).

## 8.8 SIMULATING THE INFLUENCE OF A PREVIOUS LOADING OR WETTING STAGE

This section investigates the anisotropic model performance on simulating soil behaviour observed in the experimental work when the initial anisotropy is altered by stress paths including plastic straining (i.e. by the loading/wetting stages of Test Series Ba300, Bb300, Bc300 and Bd100, see Section 5.1.2). For comparison, simulations are also performed with the isotropic model in order to investigate whether incorporation of anisotropy in the model results in a significant improvement in the accuracy of the model simulations. Among a large number of model simulations performed with the anisotropic model and isotropic model, four representative simulations are presented, which are

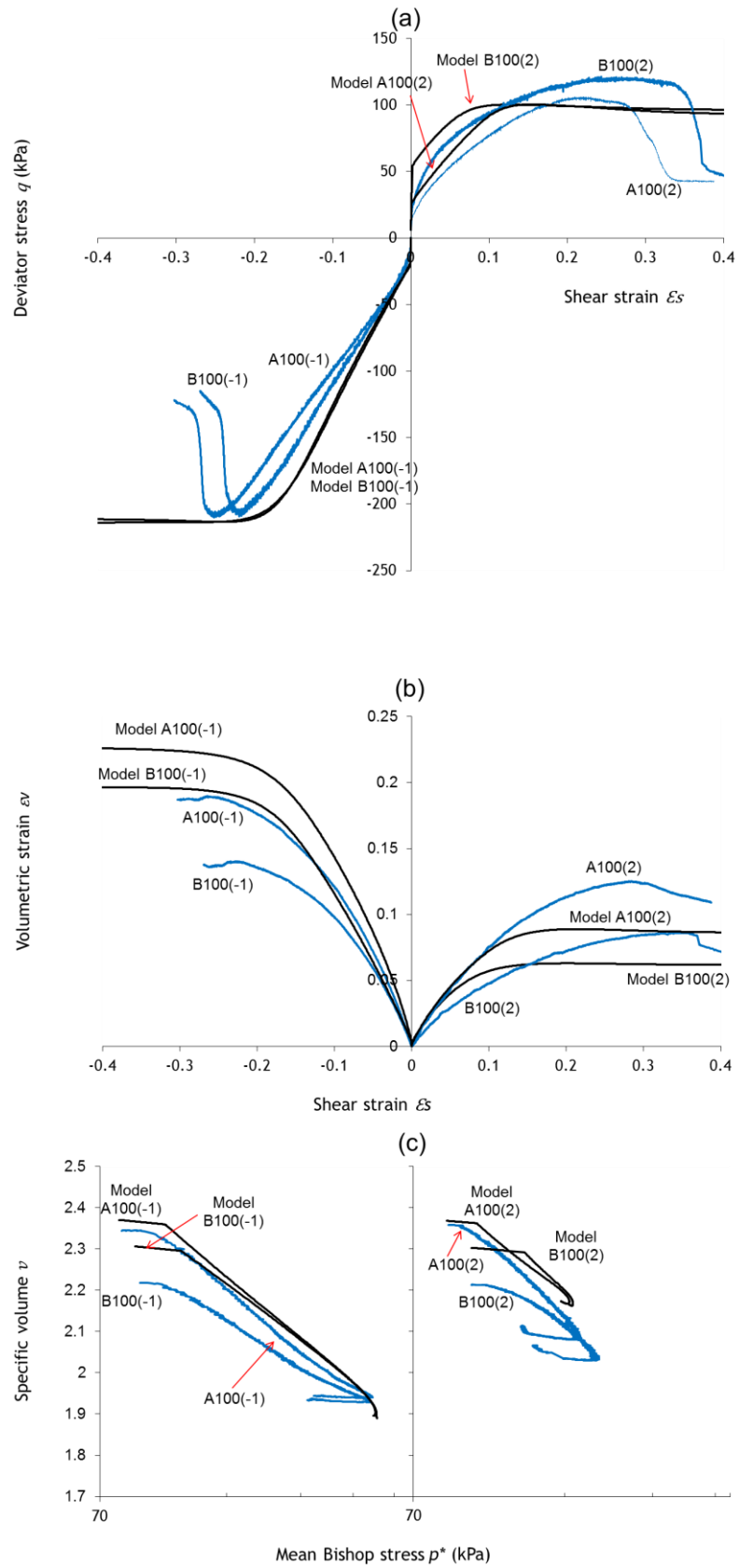


Figure 8.17 Anisotropic model simulations and experimental results for Tests A100(2), B100(2), A100(-1) and B100(-1)

those for Tests Ba300(-1.5), Bb300(-1.5), Bc300(-1.5) and Test Bd100(-1.5). Each of these involved a final probing stage in triaxial extension, with  $[\Delta q/\Delta \bar{p}] = -1.5$ , but preceded either by previous loading and unloading stages (at different values of  $[\Delta q/\Delta \bar{p}]$ ) or by a previous wetting stage (Test Bd100(-1.5)). In each case, the model simulations and experimental results are compared with those for an equivalent test without the preceding loading/unloading or wetting stages.

Figure 8.18 shows the model simulations and experimental results for Test Ba300(-1.5). This test involved initial loading and unloading stages at  $[\Delta q/\Delta \bar{p}] = 1.2$  followed by a final probing stage at  $[\Delta q/\Delta \bar{p}] = -1.5$ . Also shown for comparison are the results from Test B300(-1.5) which involved a probing stage at  $[\Delta q/\Delta \bar{p}] = -1.5$ , but without preceding loading and unloading stages. Anisotropic model simulations are presented for both tests with isotropic model simulations only for Test Ba300(-1.5). For simplicity the results are shown only in the  $q: \varepsilon_s$  plot.

Figure 8.18 shows that the anisotropic model captures well the development of positive shear strain during the initial loading stage of Test Ba300(-1.5), whereas the isotropic model grossly over-predicts the development of shear strain during this stage. The anisotropic model predicts a peak value of deviator stress and then a drop to a final critical state value of  $q$  for the final probing stages in triaxial extension of both Test Ba300(-1.5) and B300(-1.5), and the model predicts that the peak value of  $q$  is higher for Test Ba300(-1.5) than for Test B300(-1.5). This last feature seems to fit the experimentally observed behaviour (although the model does over-predict the peak values of  $q$  for both tests). In contrast, the isotropic model predicts a monotonic increase of  $q$  to a critical state (for both tests) and hence the same peak value of  $q$  for both tests. The isotropic model also predicts a relatively high yield value of  $q$  for the final probing stage of Test Ba300(-1.5), whereas the anisotropic model predicts a significantly lower yield value of  $q$ , which is a better match to the observed behaviour.

Figure 8.19 shows the corresponding results for Test Bb300(-1.5), where the final probing stage was preceded by loading and unloading stages at  $[\Delta q/\Delta \bar{p}] = 0$ . For the final probing stage, the anisotropic model predicts a higher peak value of  $q$  for Test Bb300(-1.5) than for the equivalent test without previous loading and unloading stages (Test B300(-1.5)). This feature is not seen in the experimental results. The anisotropic model also significantly over-predicts the peak value of  $q$  for both tests. The anisotropic model does predict the values of negative shear strain to peak  $q$  with reasonable accuracy, whereas the isotropic model grossly over-predicts the values of negative shear strain. Both

anisotropic and isotropic models predict yield values of  $q$  during the final probing stage of Test Bb300(-1.5) which over-predict the observed value.

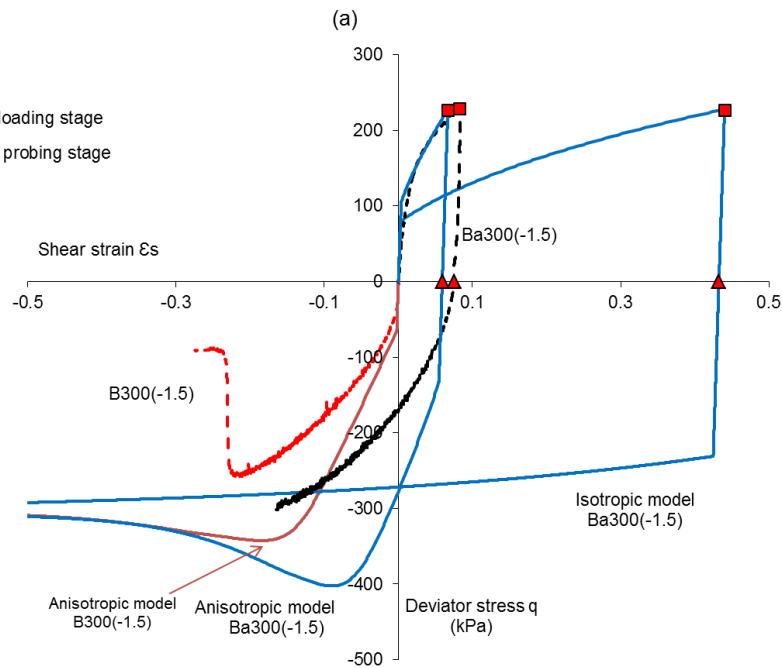


Figure 8.18 Model simulations and experimental results for Tests Ba300(-1.5) and B300(-1.5)

Figure 8.20 shows the results for Test Bc300(-1.5), where the final probing stage was preceded by loading and unloading stages at  $[\Delta q/\Delta \bar{p}] = -1$ . The results show that the anisotropic model slightly under-predicts the value of negative shear strain during the initial loading stage in triaxial extension, whereas the isotropic model grossly over-predicts this negative shear strain. During the final probing stage, the anisotropic model predicts a higher peak value of  $q$  for Test Bc300(-1.5) than for Test B300(-1.5). This feature matches the observed behaviour, although the peak values of  $q$  are over-estimated by the model in both tests. Figure 8.21 shows the results for Test Bd100(-1.5). This test involved an initial loading stage at  $s = 300$  kPa and  $[\Delta q/\Delta \bar{p}] = 0$  to  $\bar{p} = 90$  kPa, followed by a wetting stage at  $\bar{p} = 90$  kPa to  $s = 100$  kPa and then unloading at  $s = 100$  kPa before a final probing stage at  $s = 100$  kPa with  $[\Delta q/\Delta \bar{p}] = -1.5$ . Collapse-compression occurred during the wetting stage, so that there was the opportunity for this plastic straining during wetting to cause a change of anisotropy of the soil. Also, shown in Figure 8.21 are the corresponding results for Test B100(-1.5), which involved the same final probing stage, but without the preceding wetting and unloading stages. Inspection of the figure shows that the anisotropic model captures the observed behaviour reasonably well, including the negative shear strain during the wetting stage of Test Bd100(-1.5), the higher peak value of  $q$  in the final probing stage of Test Bd100(-1.5)

than in Test B100(-1.5) and the fact that the yield value of  $q$  in the final probing stage is higher in Test Bd100(-1.5) than in Test B100(-1.5). These features are not captured by the isotropic model, which also grossly over-predicts the negative value of shear strain required to reach peak  $q$  in the final probing stage.

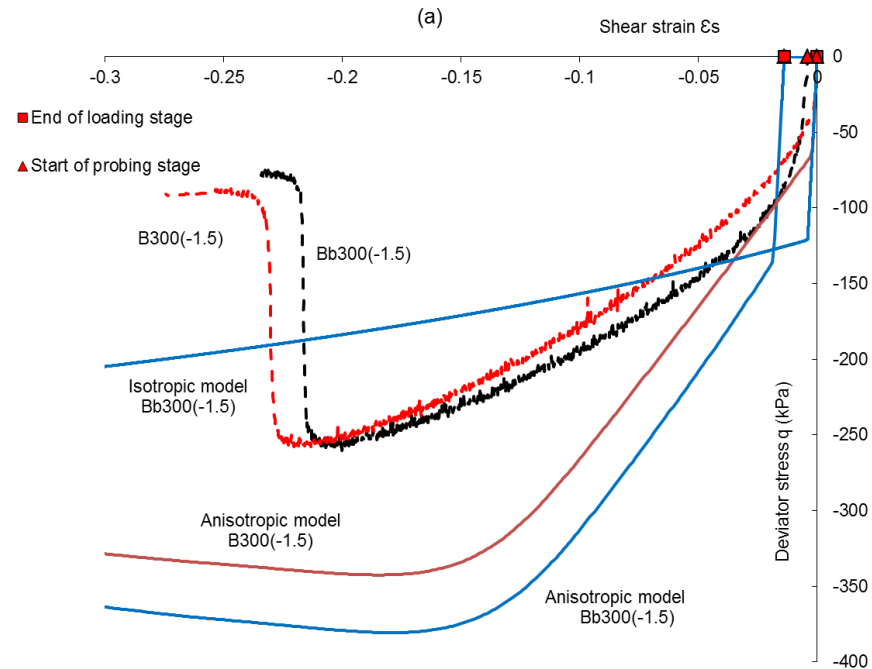


Figure 8.19 Model simulations and experimental results for Tests Bb300(-1.5) and B300(-1.5)

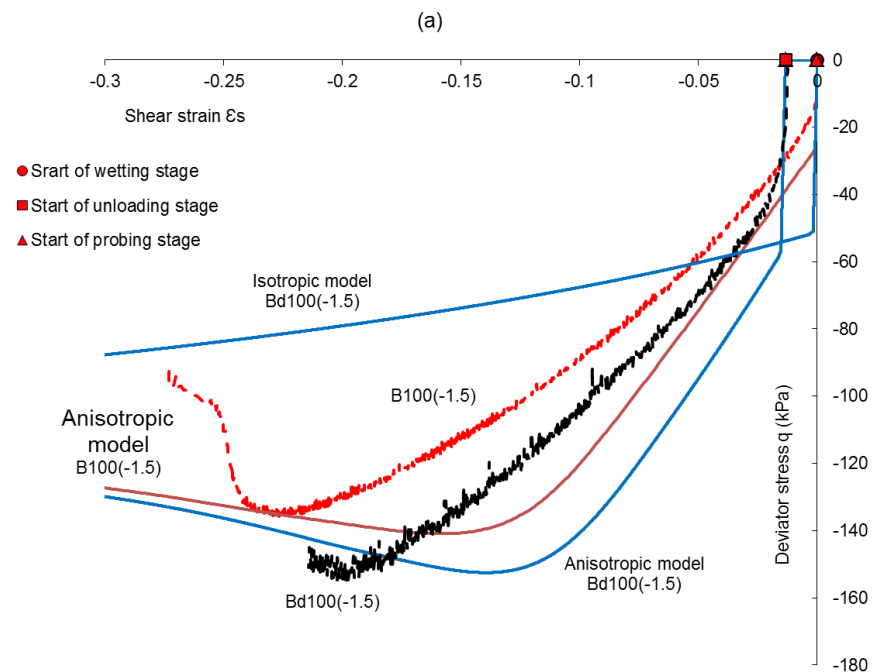


Figure 8.20 Model simulations and experimental results for Tests Bc300(-1.5) and B300(-1.5)

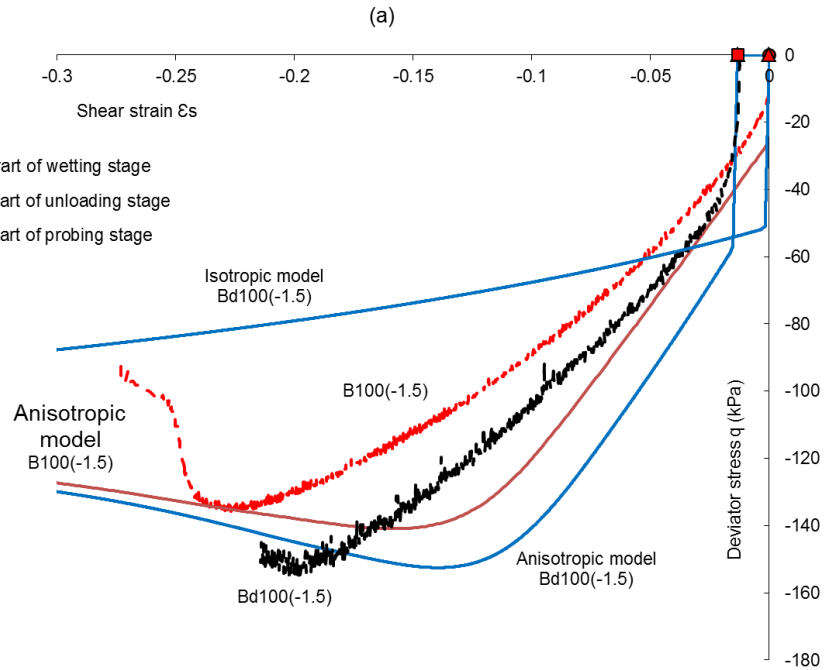


Figure 8.21 Model simulations and experimental results for Tests Bd100(-1.5) and B100(-1.5)

Overall, it is clear from Figures 8.18 to 8.21 that the anisotropic model provides a better qualitative match to the experimental results of Tests Ba300(-1.5), Bb300(-1.5), Bc300(-1.5) and Bd100(-1.5) than the isotropic model, although the anisotropic model does over-predict the peak values of  $q$  in the final probing stages in triaxial extension of many of these tests.

Table 8.8 compares average anisotropic model predicted and experimentally measured values of  $p_m^*$  and  $\alpha^*$  at the end of the loading/wetting stages for Test Series Ba300, Bb300, Bc300 and Bd100. The excellent match between the predicted and measured  $\alpha^*$  values for Test Series Ba300, Bb300 and Bc300 is expected because of the inclusion of these tests series in the calibration of  $\mu$  and  $c$  for the hardening law for changes of anisotropy (see Section 8.4). The excellent match between the predicted and measured  $\alpha^*$  values for Test Series Bd100 (which was not included in the calibration of  $\mu$  and  $c$ ) provides further validation to the proposed form of hardening law for changes of anisotropy.

Inspection of the predicted and experimentally observed values of  $p_m^*$  in Table 8.8 shows, again, that the anisotropic model gives excellent predictions of the size of the  $LC$  yield surface for all test series (remembering that values of  $p_m^*$  of these test series were not involved in any model calibration). In addition, the data presented in Table 8.8 and in Figures 8.18 to 8.21 suggest that the anisotropic model is capable of predicting

unsaturated soil behaviour under stress and strain paths where anisotropy is changing (increasing or decreasing) and when the plastic straining is caused by mechanical loading or by wetting.

**Table 8.6** Predicted and experimental values of  $p_m^*$  and  $\alpha^*$  at the end of the initial loading or wetting stages

Test Series	$\alpha^*$		$p_m^*$ (kPa)	
	Model predicted	Experimental	Model predicted	Experimental
Ba300	0.245	0.25	470	468
Bb300	0.115	0.12	407	398
Bc300	-0.107	-0.10	471	470
Bd100	0.115	0.12	175	179

## 8.9 COMPARISON OF VERSIONS 1 AND 2 OF THE ANISOTROPIC MODEL

This section compares predictions performed with Version 1 of the anisotropic model (which adopts an associated flow rule and a variable aspect ratio of the  $LC$  yield curve) and Version 2 (which adopts a non-associated flow rule with a constant aspect ratio of the  $LC$  yield curve).

### 8.9.1 Example simulations

Figures 8.22 and 8.23 show simulations for Tests A100(0) and Ba300(-1.5) respectively, to demonstrate the performance of Version 2 of the anisotropic model. Simulations of these test performed with Version 1 of the anisotropic model are shown also for comparison.

Figure 8.22b and 8.22c shows that both anisotropic model versions predict well the volumetric strains during the initial probing stage of Test A100(0) (at  $[\Delta q/\Delta \bar{p}] = 0$  with  $q = 6$  kPa). This is expected for an isotropic material loaded along an almost isotropic stress path, where almost no change of fabric anisotropy is expected. For this nearly isotropic stress path, the stress state remains almost on the isotropic normal compression planar surface once yielding is occurring on both the  $LC$  and  $SD$  surfaces. Figures 8.22b and 8.22c also show that both model versions over-predict volumetric strains during the final shearing stage, but the over-prediction is less for Version 2 than for Version 1.

In Figure 8.22a both model versions predict the same critical state value of deviator stress  $q$ . Version 1 of the anisotropic model predicts a peak in the  $q:\varepsilon_s$  curve and then a modest post-peak reduction of  $q$  to a critical state, whereas Version 2 of the anisotropic

model predicts a monotonic increase of  $q$  to the critical state. The peak deviator stress predicted by Version 1 is an excellent match to the peak deviator stress observed in the experimental results, whereas the match to the peak value of  $q$  is less good for Version 2. Figure 8.22a also show that Version 1 predicts the evolution of shear strain during the shear stage significantly better than Version 2, suggesting that the combination of an anisotropic  $LC$  yield curve (with evolving anisotropy and aspect ratio) and an associated flow rule is better than the combination of an anisotropic  $LC$  yield curve (with evolving anisotropy but with constant aspect ratio) and a non-associated flow rule.

Figures 8.23a and 8.23b show that for the initial loading stage of Test Ba300(-1.5) at  $\Delta q/\Delta \bar{p} = 1.2$ , both model versions provide a good prediction of the volumetric strains, but Version 1 predicts the generation of shear strain significantly better than Version 2. The over-prediction of shear strains in the initial loading stage by Version 2 of the model is because that the term  $(M^{*2} - \eta^{*2})$  which appears in the non-associated flow rule (see Equation 7.24) is much smaller than the term  $(m^{*2} + \alpha^{*2} - \eta^{*2})$  which appears in the associated flow rule (see Equation 7.21), which means that for a given plastic volumetric strain increment the non-associated flow rule predicts a larger increment of the plastic shear strain than the associated flow rule.

Figures 8.23b and 8.23c show that Version 1 of the anisotropic model predicts the volumetric strain during the final probing stage better than Version 2. In Figure 8.23a, both model versions predict the same critical state value of deviator stress  $q$ . Version 1 of the anisotropic model predicts a peak in the  $q:\varepsilon_s$  curve and then a modest post-peak reduction of  $q$  to a critical state, whereas Version 2 of the anisotropic model predicts a monotonic increase of  $q$  to the critical state. The peak deviator stress observed in the experimental results is over-predicted by Version 1 of the anisotropic model but well predicted by Version 2 of the model. Figure 8.23a also shows that Version 1 under-predicts the evolution of shear strain during the shear stage in contrast to Version 2 of the model.

Overall, it is clear from Figures 8.22 and 8.23 that Version 1 of the anisotropic model provides a rather better match to the experimental results of Tests A100(0) and Ba300(-1.5) than Version 2 of the model.

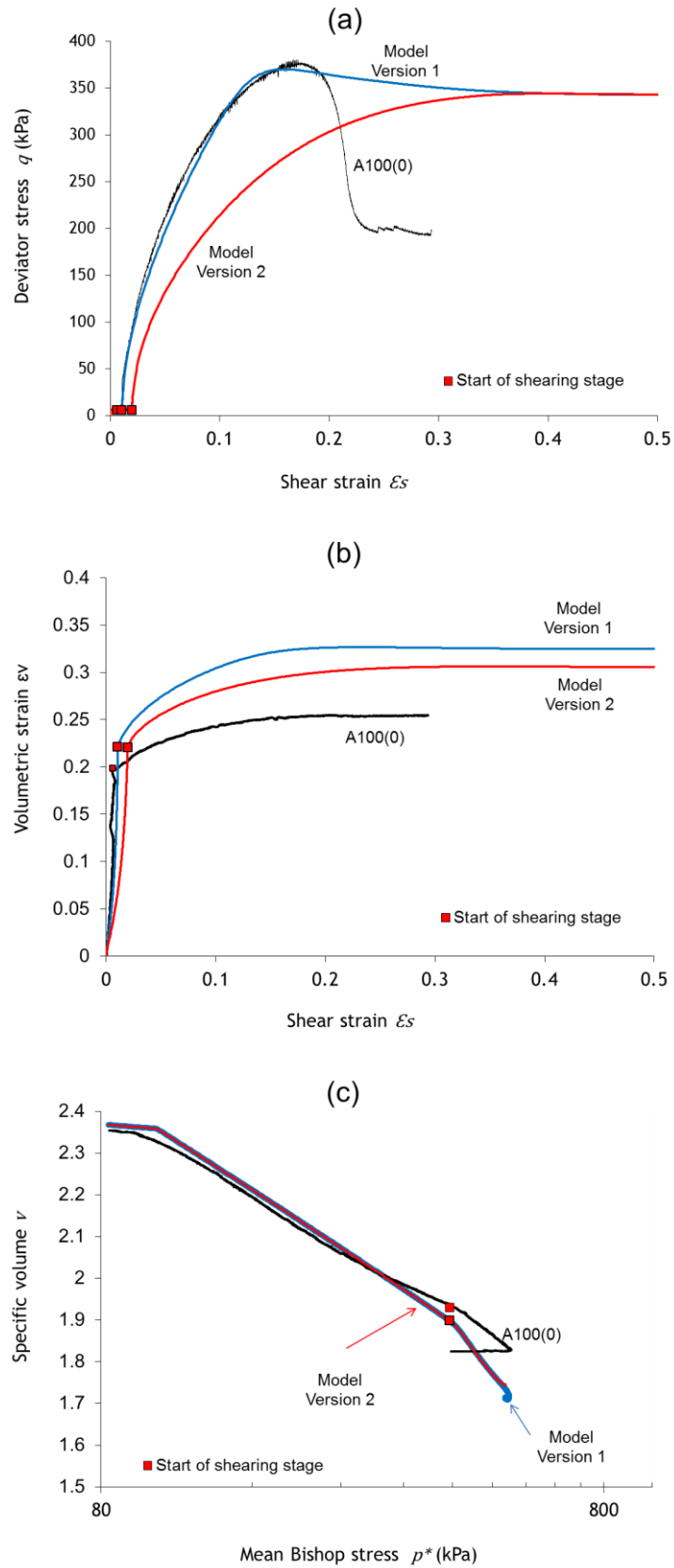


Figure 8.22 Version 1 and Version 2 model simulations and experimental results for Test A100(0)

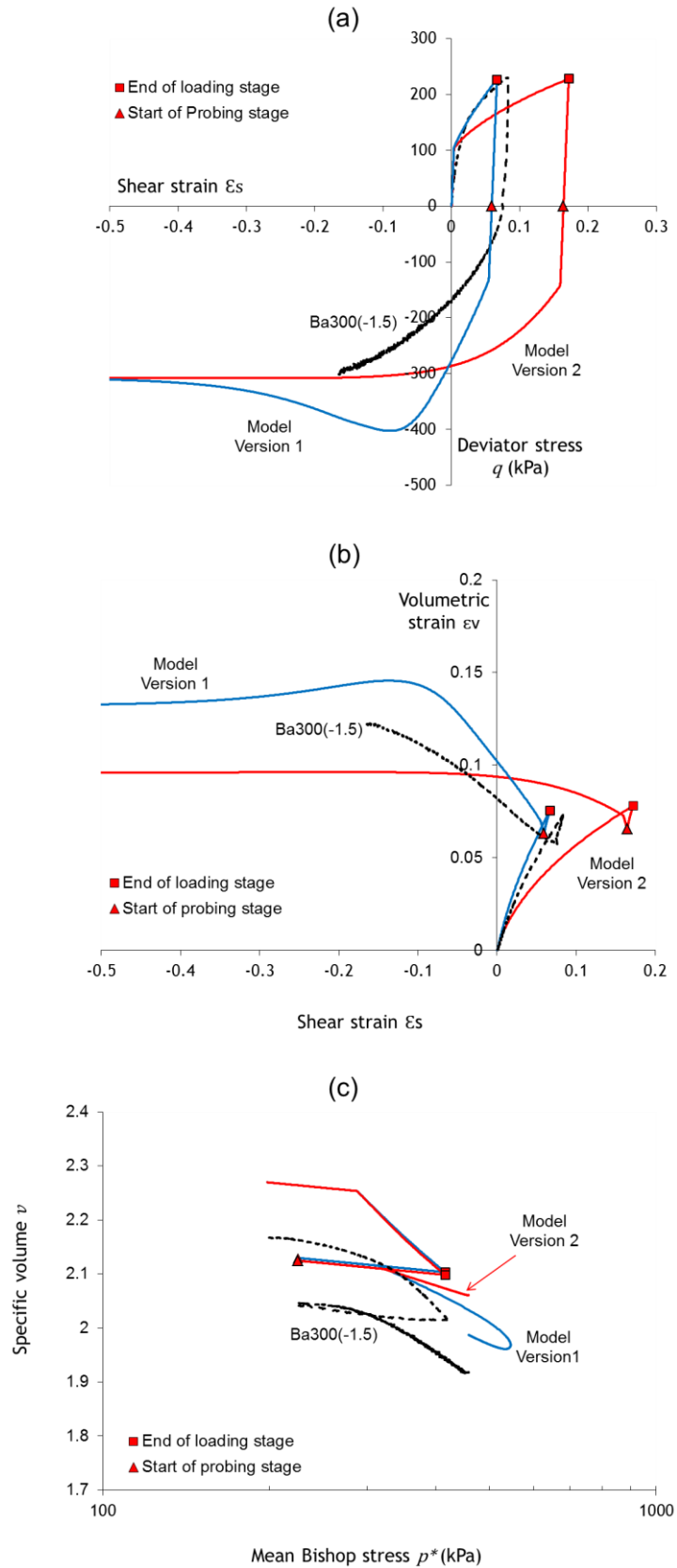


Figure 8.23 Version 1 and Version 2 model simulations and experimental results for Test Ba300(-1.5)

### 8.9.2 Critical state planar surface in $v:\ln p^*:\ln s^*$ space

Referring to Section 7.9, both versions of the model predict a unique critical state planar surface in  $v:\ln p^*:\ln s^*$  space (when critical states coincide with the intersection between  $LC$  and  $SD$  surfaces) that is parallel to the unique isotropic normal compression surface for an isotropic soil. The critical state planar surface is defined by Equation 7.29 for Version 1 of the anisotropic model and by Equation 7.30 for Version 2 of the anisotropic model.

The vertical spacing between the isotropic normal compression surface and critical state surface, depends on the value of  $c$  for Version 1 of the model (see Equation 7.29) and depends on the values of  $c$ ,  $M^*$  and  $m_0^*$  for Version 2 of the model (see Equation 7.30). For the latter, two unique planar surfaces can exist, one corresponds to triaxial compression (i.e. with  $m_0^* = m_{0c}^*$ ) and one corresponds to triaxial extension (i.e. with  $m_0^* = m_{0e}^*$ ). For the plots shown in Figure 8.24, the value of  $m_0^* = m_{0c}^* = 0.85$  is used to show the position of the critical state surface for Version 2 of the model, however, the planar surface with  $m_0^* = m_{0e}^* = 0.95$  was investigated and appeared slightly above the one shown in Figure 8.24.

The unique isotropic normal compression planar surface in  $v:\ln p^*:\ln s^*$  space, fitted to experimental data points, was already presented in Section 6.2.3. Figure 8.24 shows orthogonal two-dimensional views of the critical state planar surfaces in  $v:\ln p^*:\ln s^*$  space predicted by both anisotropic model versions as well as the critical state planar surface predicted by the isotropic model, together with critical state points obtained from the experimental work presented in Chapter 5.

There is considerable scatter in the experimental data, but on average Figure 8.24a shows that while the isotropic model over-predicts the spacing between the isotropic normal compression surface and the critical state surface, both anisotropic model versions under-predict the spacing, with Version 1 gives better prediction than Version 2.

In Figure 8.24b the experimental data appear in two groups, one corresponding to  $s = 300$  kPa (at high values of  $s^*$ ) and one corresponding to  $s = 100$  kPa (at low values of  $s^*$ ). Figure 8.24b shows that the isotropic model significantly over-predicts the spacing between the isotropic normal compression surface and the critical state surface for both values of  $s$ . Version 1 and Version 2 of the anisotropic model under-predict the spacing for those tests at  $s = 300$  kPa, but seem to match the correct average spacing at  $s = 100$  kPa. Overall, Figure 8.24 shows that the critical state surfaces, as predicted by the

anisotropic model versions, are shifted vertically in the right direction as compared as to the critical state surface predicted by the isotropic model.

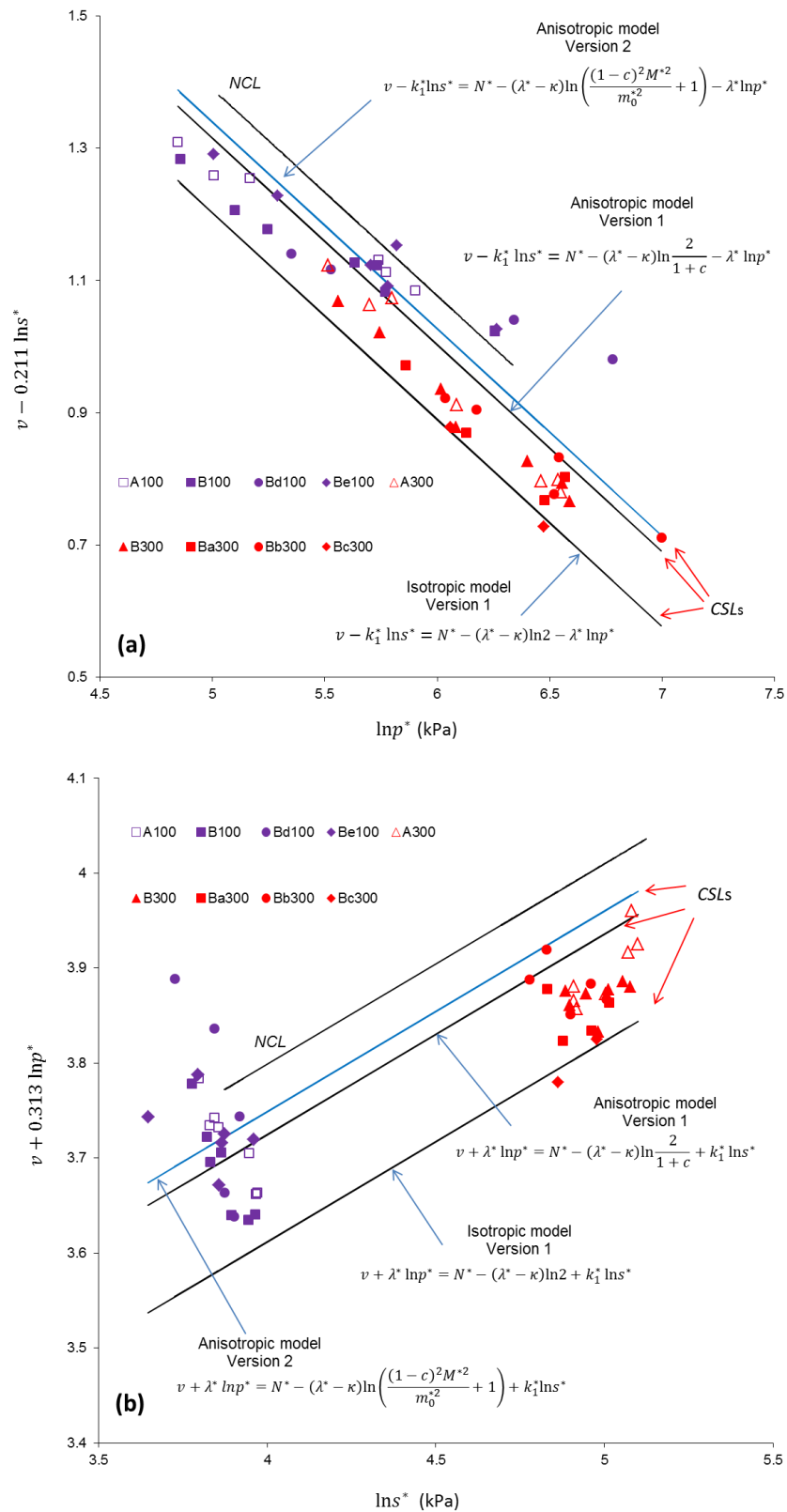


Figure 8.24 Orthogonal two-dimensional views of the unique critical state planar surface for Version 1 and Version 2 of the model with experimental critical state points

## CONCLUSIONS AND RECOMMENDATIONS

The influence of evolving anisotropy on unsaturated soil behaviour was investigated experimentally in this work. An extensive campaign of tests on isotropically and anisotropically compacted samples under a wide range of stress paths was conducted. Test data were interpreted to investigate the forms of yield surfaces and critical states for isotropically and anisotropically compacted samples at different suctions.

A new constitutive model incorporating the role of evolving anisotropy was also developed, based on concepts first put forward by Wheeler et al. (2003a) for isotropic unsaturated soils. The role of evolving anisotropy was incorporated in the new elastoplastic model through a kinematic hardening law that relates the value of the hardening parameter ( $\alpha^*$ ) to plastic straining. Two versions of the anisotropic model were presented; Version 1 assumes that the aspect ratio of the *LC* curve can evolve during plastic straining combined with an associated flow rule, while Version 2 assumes a *LC* curve with constant aspect ratio and a non-associated flow rule.

### 9.1 EXPERIMENTAL WORK

#### 9.1.1 Experimental equipment

- The use of a double wall triaxial cell (System 1 and System 2, see Section 3.1) with a glass inner cell allowed accurate measurement of the sample volume change under unsaturated conditions. Equipment was assembled under water to avoid trapping air in the system. Proof of the excellent quality and repeatability of volume change measurement was confirmed by the very close similarity of the volume change measurements of a saturated soil sample achieved by this technique and by conventional measurement of the pore water inflow or outflow (see Section 3.3.7).
- An effective design of the pore water drainage and flushing system was adopted (see Section 3.1), particularly the spiral shaped groove beneath the *HAE* filters, which provided sufficient contact area between the filter and the water in the drainage lines and a single flushing path. Moreover, any trapped air beneath the

filters could be easily removed as no corners exist in the water flow path during flushing.

- The capability to conduct tests with loading stages in triaxial extension as well as in triaxial compression (see Section 3.1), for unsaturated and saturated soil samples, allowed investigation of soil behaviour under a wide range of stress paths.
- The method of controlling radial net stress and suction (i.e. holding cell pressure constant while varying pore air pressure and pore water pressure as necessary, see Section 4.4) resulted in highly accurate measurements of sample volume change. This is because the imposition of a constant cell pressure eliminated the need of correcting changes of cell water volume caused by pressure variations. Furthermore, errors in the measurement of axial load by the load cell, due to varying cell pressure, were avoided by use of this procedure.

### 9.1.2 Compaction technique

- The compaction technique that was employed (see Section 4.1) allowed compaction along predefined stress path by controlling both the radial stress and deviator stress. Two methods of compaction were used: isotropic compaction (conducted at  $q/\bar{p} = 0$ ) and anisotropic compaction (conducted at  $q/\bar{p} = 1.2$ ).
- The isotropic compaction produced nearly isotropic samples (any very small anisotropy was due to unavoidable frictional behavior at the top and bottom of the sample), whereas the anisotropic compaction produced only moderately anisotropic samples (as shown in the subsequent experimental investigations).
- The relatively small amount of fabric anisotropy produced by the anisotropic compaction method can be explained by the high suction (more than 600 kPa, see Section 5.3) which provides high stability at inter-particle contacts during compaction.
- The post-compaction value of specific volume was noticeably lower for the anisotropically compacted samples than for the isotropically compacted ones (see Section 5.2). This indicates substantial rearrangement and reorientation of soil particles and aggregates during anisotropic compaction, to a form of fabric which gives a lower specific volume than isotropic compaction.
- The proposed compaction technique produced homogeneous samples in terms of soil fabric. The initial values of water content, specific volume and degree of saturation measured on a large set of samples reflected the high repeatability of the sample preparation technique and its suitability for triaxial testing (see Section 5.2).

- Compression curves showed reasonably large pre-yield and post-yield parts, so that the shape of the initial yield surface (i.e. the shape of the yield surface of the as-compacted material) could be clearly identified (see Section 6.4).

## 9.2 EXPERIMENTAL RESULTS

### 9.2.1 Wetting stages

- All samples showed an increase in water content, specific volume and degree of saturation during wetting to  $s = 300$  kPa, 100 kPa and 0. No collapse compression was observed during these stages (see Section 5.4).
- During wetting, both isotropically and anisotropically compacted samples showed the same pattern of increase of moisture content, specific volume and degree of saturation with time (see Section 5.4).
- The average increase of moisture content was nearly the same for the isotropically and the anisotropically compacted samples during wetting to  $s = 300$  kPa or  $s = 100$  kPa. The average increase of specific volume for a given suction was sometimes higher for isotropically compacted than the anisotropically compacted samples and vice versa. The average increase of degree of saturation was slightly higher for the anisotropically compacted samples than for the isotropically compacted samples during wetting to  $s = 300$  kPa or  $s = 100$  kPa (see Section 5.4). It was not clear whether the differences in the results of the wetting stage of isotropically and anisotropically compacted samples were due to the influence of anisotropy or due to slight lack of sample repeatability.
- During wetting, no apparent effect of small changes of the initial stress state (i.e.  $\bar{p} = 12$  kPa and  $q = 6$  kPa for tests with loading stages in triaxial compression or  $\bar{p} = 10$  kPa and  $q = 0$  kPa for tests with loading stages in triaxial extension) was observed on the change of moisture content, specific volume and degree of saturation.

### 9.2.2 Yielding behaviour

- Volumetric behaviour was contractant in all probing/shearing stages. However, in some cases, after strain localisation (causing the sample to split into two parts), an increase in specific volume was recorded and was therefore ignored.
- The curves in the  $q: \varepsilon_s$  plane showed that anisotropically compacted samples were stiffer than isotropically compacted samples at the beginning of loading and this was attributed to the lower initial specific volume of the former samples (see Sections 5.5 and 5.6).

- The elastic behaviour appears independent of fabric anisotropy, within the level of accuracy attainable with the equipment used in the current work. The values of the elastics soil constants (i.e.  $\kappa$ ,  $\kappa_s$  and  $G$  or  $\kappa^*$  and  $G$ ) obtained from different test series (i.e. from samples with different amounts of anisotropy) were relatively similar (see Section 6.1).
- Evolution of fabric anisotropy was evident from results of the probing stages plotted in the  $q:\varepsilon_s$  plane and  $v:\ln\bar{p}$  plane, especially when following different stress paths from those followed during previous loading stages. Evolution of fabric anisotropy was attributed to the reorientation of soil particles and aggregates (see Sections 5.5 and 5.6).
- The compression curves of isotropically and anisotropically compacted samples, when loaded along the same stress path, showed a tendency to merge in both the  $v:\ln\bar{p}$  plane and the  $v:\ln p^*$  plane as loading progressed. This suggested that any memory of the initial fabric had been almost entirely erased by the end of loading and that final anisotropy was controlled only by the most recent stress history (see Sections 5.5 and 5.6).
- The slopes of the isotropic normal compression curves of isotropically compacted samples increased with increasing suction (see Section 6.2).
- The degree of saturation increased in a consistent manner with decreasing specific volume, indicating the dominant influence of void compression on the change of degree of saturation.
- Several methods for identifying yield stresses were investigated, with the bi-linear method in the semi-log planes  $v:\ln\bar{p}$  or  $v:\ln p^*$  being the most satisfactory for both isotropically and anisotropically compacted samples. Moreover, it was found that the bi-linear method in the semi-log planes  $v:\ln\bar{p}$  or  $v:\ln p^*$  could be used systematically for any stress path, unlike other methods (e.g. strain energy method, see Section 6.4).
- Comparison of experimental results from tests on isotropically and anisotropically compacted samples at different suctions suggested that anisotropy is suction independent. This is supported by large number of observations showing that yielding of isotropically or anisotropically compacted samples tend to follow similar patterns of behaviour regardless of suction value.
- Comparison of results from probing stages in Test Series Bb300 and Test Series Bd100 shows very similar yielding patterns. This suggests that the mechanical properties induced by plastic collapse-compression during wetting at constant isotropic stress in Test Series Bd100 were very similar to those induced by isotropic loading at  $s = 300$  kPa in Test Series Bb300 (see Section 5.6).

- Post-yield data from tests on isotropically compacted samples isotropically loaded under constant suction confirmed the existence of two unique planar surfaces in  $v: \ln p^*: \ln s^*$  space and  $S_r: \ln p^*: \ln s^*$  space, respectively (see Section 6.2.3).

### 9.2.3 Critical states

- During shearing to failure, all samples showed very sharp post-peak reductions of deviator stress, which was attributed to strain localization, as confirmed by observation of shear bands at the end of the tests (see Sections 5.5 and 5.6).
- The peak deviator stress was taken as critical state, based on the observation that the specific volume had almost stopped changing when the peak deviator stress was reached.
- Inspection of critical state data in the  $q: \bar{p}$  plane and  $q: p^*$  plane shows no evident influence of differences of initial anisotropy on critical state behaviour. This is supported by the observation that results from tests on anisotropically compacted samples fall within the same scatter band as results from tests on isotropically compacted samples at the same suction (see Section 6.3).
- Critical states in triaxial compression or triaxial extension can be represented in the  $q: \bar{p}$  plane by a series of parallel lines corresponding to different suctions. Each pair of constant suction lines, describing critical states in triaxial compression and extension respectively, have the same intercept with the  $\bar{p}$  axis (see Section 6.3.2).
- Alternatively, critical states in triaxial compression or triaxial extension can be represented in the  $q: p^*$  plane by a single straight line (for all values of suction) passing through the origin, with the same slope in triaxial compression and triaxial extension (see Section 6.3.3).
- At a given suction, experimental critical state data for unsaturated samples can be adequately fitted by a single line in the  $v: \ln \bar{p}$  or  $v: \ln p^*$  plane, with no evident influence of anisotropy (see Section 6.3).
- In contrast, when experimental critical state data for saturated samples were plotted in the  $v: \ln \bar{p}$  plane, there was evidence of influence of initial anisotropy, with critical state values of  $v$  for anisotropically compacted samples falling below these for isotropically compacted samples (see Section 6.3).
- For probing/shearing stages at high stress ratio ( $[\Delta q/\Delta \bar{p}] = 2, 3$  and  $-1.5$ ), the isotropically and anisotropically compacted samples showed similar peak deviator stress at any given suction value. Conversely, for probing/shearing stages at lower stress ratio  $[\Delta q/\Delta \bar{p}] = \pm 1$ , in some cases the isotropically and anisotropically compacted samples showed different peak deviator stress. These differences in peak deviator stress are mainly due to slight lack of samples repeatability, which

is amplified when samples are sheared which approach sub-parallel to the critical state line at a very acute angle in the  $q:\bar{p}$  plane.

#### 9.2.4 Yield curves and plastic flow vectors

- Constant suction cross-sections of the anisotropic yield surface can be represented in the  $q:\bar{p}$  plane by distorted ellipses passing through the intersection of the corresponding critical state line with the negative mean net stress axis (at  $\bar{p} = -p_s(s)$ ).
- Alternatively, constant suction cross-sections of the anisotropic yield surface can be represented in the  $q:p^*$  plane by distorted ellipses of inclination  $\alpha^*$  passing through the origin.
- In the  $q:\bar{p}$  plane, different values of the aspect ratio  $m$  are necessary for the upper and lower sections of the constant suction yield curve (i.e.  $m = m_c$  for  $q/(\bar{p} + p_s(s)) > \alpha$  and  $m = m_e$  for  $q/(\bar{p} + p_s(s)) < \alpha$ ). The same values of  $m_c$  and  $m_e$  can be used for all yield curves at different values of suction, regardless of the current level of anisotropy. The fitted values of the aspect ratios  $m_c$  and  $m_e$  were greater than the critical state ratio  $M$ .
- In the  $q:p^*$  plane, as in the  $q:\bar{p}$  plane, different values of aspect ratio  $m^*$  were necessary for the upper and lower sections of each constant suction yield curve (i.e.  $m^* = m_c^*$  for  $q/p^* > \alpha^*$  and  $m^* = m_e^*$  for  $q/p^* < \alpha^*$ ). Again, the same values of  $m_c^*$  and  $m_e^*$  can be used for all constant-suction yield curves and regardless of the current level of anisotropy. The fitted values of the aspect ratios  $m_c^*$  and  $m_e^*$  were greater than the critical state ratio  $M^*$ .
- For isotropically compacted samples, the initial values of  $\alpha$  and  $\alpha^*$  were equal to zero in accordance with the isotropic nature of the compacted soil. For the anisotropically compacted samples, initial values of  $\alpha = 0.21$  and  $\alpha^* = 0.20$  were found adequate for all values of suction (see Section 9.2.2).
- The first loading stage in Test Series Ba300, Bb300 and Bc300 increased or decreased the values of  $\alpha$  and  $\alpha^*$ . In the former case, the initial value of  $\alpha = 0.21$  changed to  $\alpha = 0.29$ ,  $\alpha = 0.19$  or  $\alpha = -0.04$  at the end of probing/shearing, for Test Series Ba300, Bb300 and Bc300 respectively. In the latter case, the initial value of  $\alpha^* = 0.20$  changed to  $\alpha^* = 0.25$ ,  $\alpha^* = 0.12$  or  $\alpha^* = -0.10$  at the end of probing/shearing, for Test Series Ba300, Bb300 and Bc300 respectively. This confirms that fabric anisotropy can evolve during plastic straining.
- The wetting stage in Test Series Bd100 reduced the initial values of  $\alpha = 0.21$  and  $\alpha^* = 0.20$  to  $\alpha = 0.19$  and  $\alpha^* = 0.12$  at the end of probing/shearing. The reduction

of anisotropy indicates that plastic collapse-compression produces a change of the mechanical properties of the anisotropic soil, which is similar in nature to the change produced by external loading. Further confirmation of this is provided by the fact that the final values of  $\alpha$  (or the final values of  $\alpha^*$ ) were the same for Test Series Bb300 and Bd100, which fits the experimentally observed similarities between these two test series (see Section 9.2.2).

- At any suction level, the initial size of the yield curve, measured by the value of  $\bar{p}_m$  or  $p_m^*$ , was greater for the anisotropically compacted samples than for the isotropically compacted samples. This is qualitatively consistent with the fact that the initial values of specific volume  $v$  were lower for the anisotropically compacted samples than for the isotropically compacted samples. However, subsequent analysis indicated that the difference in initial  $v$  values was greater than could be explained simply by the difference in the initial size of the yield surface (see Section 9.3.3).
- No conclusive evidence of the normality of plastic flow vectors to the constant suction yield ellipses was obtained. Normality was evident in some cases (for example, Test Series Ba300, Bb300 and Bd100) but not in other cases (for example, Test Series A100, A0 and Be100).

### 9.3 DEVELOPMENT OF A CONSTITUTIVE MODEL FOR ANISOTROPIC UNSATURATED SOILS

The proposed anisotropic elasto-plastic constitutive model for unsaturated soils combines features from the isotropic model for unsaturated soils of Wheeler et al. (2003a) (see Section 2.9) with features from the anisotropic model for saturated soils *S – CLAY1* (see Section 2.7.2). The proposed constitutive model employs Bishop's stresses and modified suction as stress variables (rather than net stresses and suction) for the following reasons:

- Elastic strains can be solely related to changes of Bishop's stresses, i.e. there is no need to separately take into account elastic strains caused by changes of suction (as suction is already included in the Bishop's stress definition);
- Shear strength can be solely related to Bishop's stress (see Section 6.3);
- Formulation of yield curves (at constant  $s$ ) is simpler in the  $q:p^*$  plane (e.g. they always pass through the origin) than in the  $q:\bar{p}$  plane (see Section 6.5);
- Coupling between mechanical and water retention behaviour is easier if the constitutive model is formulated in terms of Bishop's stresses rather than net stresses and suction (see Section 2.9).

This project has developed an anisotropic version of the mechanical part of the Wheeler et al. (2003a) model (i.e. excluding the water retention part of that model). Experimental values of degree of saturation  $S_r$ , instead of predicted values, have therefore been used in the simulations presented in this work (see Section 8.3). By using experimental values of  $S_r$  it was possible to investigate the performance of the mechanical part of the model alone. If a fully coupled mechanical and water retention model had instead been used, it would have been unclear whether any inaccuracy in prediction of strains was attributable to the mechanical or water retention parts of the constitutive formulation.

### 9.3.1 Aspects of the new anisotropic constitutive model

The main aspects of the constitutive model can be summarised as follows (see Sections 7.2 to 7.9):

- Elastic volumetric and shear strains are given by the same equations as in the extended version of the Wheeler et al (2003a) model (see Section 7.2).
- The model includes three yield surfaces in  $q:p^*:s^*$  space, like the Wheeler et al. (2003a) model: the Loading Collapse (*LC*) yield surface to represent irreversible mechanical behaviour (onset of plastic volumetric strains and plastic shear strains) and the *SI* and *SD* yield surfaces to represent irreversible water retention behaviour (onset of plastic changes of degree of saturation) (see Section 7.3).
- The coupled movements of the *SD* and *SI* yield surfaces (caused by yielding on the *LC* surface) and the coupled movements of the *LC* yield surface (caused by yielding on the *SD* or *SI* surface) are governed by the same coupling relationships as in the Wheeler et al. (2003a) model (see Section 7.4).
- The general hardening law that links the occurrence of plastic volumetric strains to movements of the yield surfaces, takes the same form as in the model of Wheeler et al. (2003a) (see Section 7.5).
- Under unsaturated normal compression conditions, of an isotropic soil under isotropic loading, a unique planar surface is predicted in  $v:\ln p^*:\ln s^*$  space (see Section 7.6).
- Similarly, under saturated normal compression conditions, a unique planar surface exists in  $v:\ln p^*:\ln s^*$  space (see Section 7.10).
- The change of anisotropy, represented by the hardening parameter  $\alpha^*$ , is governed by a law that relates the change of  $\alpha^*$  to both plastic volumetric strains and plastic shear strains, with both types of plastic strain attempting to change  $\alpha^*$  to the same current target value. The current target value of  $\alpha^*$  (which is a

function of the current stress ratio  $\eta^*$ ) is for simplicity, governed by a tri-linear relationship between the target for  $\alpha^*$  and  $\eta^*$  (see Section 7.7).

- Over the experimentally investigated range of  $\alpha^*$  (i.e. from  $-0.10$  to  $+0.25$ , see Section 6.4), the aspect ratio  $m^*$  of the constant suction yield curves (i.e. constant suction cross-sections of the *LC* yield surface) is constant for both the upper and lower sections of the distorted elliptical yield curves and equal to  $m_c^* = m_{0c}^*$  and at  $m_e^* = m_{0e}^*$  respectively. No experimental information about the variation of  $m^*$  beyond the above range of  $\alpha^*$  and prior to arrive at critical states is available. Two possibilities were investigated for the variation of the aspect ratio  $m^*$  of the constant suction yield curves. The first possibility (Version 1 of the new model) assumes that  $m_c^*$  and  $m_e^*$  both remain constant at  $m_c^* = m_{0c}^*$  or at  $m_e^* = m_{0e}^*$  for  $\alpha^*$  ranging from  $-0.25$  to  $+0.25$  but then both decrease sharply towards a limiting critical state value. The second possibility (Version 2 of the new model) assumes that  $m_c^*$  and  $m_e^*$  both remain approximately constant over the full range of  $\alpha^*$ . Additional details regarding the variation of the yield curve aspect ratio  $m^*$  are given in Section 7.8.
- Version 1 of the model assumes an associated flow rule (the critical state aspect ratio of the yield curve is calculated to ensure zero plastic volumetric strains at critical state) while Version 2 of the model assumes a non-associated flow rule to satisfy zero plastic volumetric strains at critical state (see Section 7.8). For the latter case, the plastic potential takes the same form as the yield curve in the *S – CLAY1* model.
- Both versions of the model predict a unique critical state planar surface in  $v:\ln p^*:\ln s^*$  space that is parallel to the isotropic normal compression planar surface in the same space (see Section 7.9). The vertical spacing between the normal compression and critical state planar surfaces (i.e. the difference in specific volume at a given value of mean Bishop's stress and modified suction) is slightly different between the two versions. However, both versions predict a vertical spacing between the normal compression and critical state planar surfaces that is smaller than the spacing predicted by the isotropic model of Wheeler et al. (2003a) (see Section 2.9.6).

### 9.3.2 Model Calibration

- Version 1 of the anisotropic model involves 13 soil constants (see Section 7.11) including: 2 constants to describe elastic behaviour ( $\kappa^*$  and  $G$ ), 2 constants to describe saturated isotropic normal compression behaviour ( $\lambda$  and  $N$ ), 3 additional constants to describe unsaturated isotropic normal compression behaviour ( $k_1$ ,  $k_2$  and  $N^*$ ), 1 constant to describe shear strength ( $M^*$ ), 2 constants

to describe the aspect ratios of the upper and lower sections of constant suction yield curves at low values of  $\alpha^*$  ( $m_{0c}^*$  and  $m_{0e}^*$ ), 1 constant to describe the rate of change of this aspect ratio with  $\alpha^*$  ( $F$ ) and 2 constants to describe the variation of  $\alpha^*$  due to plastic straining ( $\mu$  and  $c$ ). Version 2 of the model involves one fewer soil constant, because parameter  $F$  is omitted.

- The values of the soil constants  $\kappa^*$ ,  $G$ ,  $\lambda$ ,  $N$ ,  $N^*$ ,  $M^*$ ,  $m_{0c}^*$  and  $m_{0e}^*$  were obtained by interpreting the soil behaviour observed during laboratory tests. The value of the constant  $F$  was selected to give the required variation of  $m_c^*$  and  $m_e^*$  with  $\alpha^*$ .
- The values of the constants  $k_1$  and  $k_2$  were worked out by knowing the values of  $k_1^*$ ,  $\lambda^*$ ,  $\lambda$  and  $\kappa^*$  where  $k_1^*$  and  $\lambda^*$  are the gradients of the isotropic normal compression planar surface in  $v:\ln p^*:\ln s^*$  space.
- The values of the constants  $\mu$  and  $c$  were worked out indirectly (independently for Version 1 and Version 2) by performing model simulations of Test Series Ba300, Bb300 and Bc300 using different values of  $\mu$  and  $c$  and comparing these simulations with the corresponding experimental results. Further details were given in Section 8.4.

### 9.3.3 Performance of Version 1 of the anisotropic model

The model (either Version 1 or Version 2) can be used to predict the soil response for any stress path in terms of  $q$ ,  $p^*$  and  $s^*$ . However, if the model is to be used to predict the soil response for a stress path specified in terms of  $q$ ,  $\bar{p}$  and  $s$ , it must either be combined with a separate water retention model (in order to predict the variation of  $S_r$  required to calculate  $p^*$ ) or experimental values of  $S_r$  must be used. The latter approach was used in the model simulations presented in Sections 8.6 to 8.9.

The following conclusions regarding model performance were drawn from a large number of laboratory test simulations conducted with Version 1 of the anisotropic model and with the isotropic variation of the model (corresponding to the anisotropic model but with the value of the soil constant  $\mu$  and the initial value of  $\alpha^*$  both set to zero):

- Incorporation of the effect of evolving anisotropy results in significant improvement of model predictions.
- The anisotropic model predicts with almost the same precision the behaviour of isotropically and anisotropically compacted soils. This confirms that the quality of model predictions is independent of the initial soil state (i.e. initial anisotropy).
- The predictions of unsaturated soil behaviour by the anisotropic model are equally good at  $s = 300$  kPa and  $s = 100$  kPa and better than under saturated conditions.

- The anisotropic model captures well the small positive or negative shear strains generated during isotropic loading of isotropically and anisotropically compacted samples under a nominal positive deviator stress.
- In the majority of simulations, the anisotropic model predicts well volumetric strains, in contrast to the isotropic model which over-predicts plastic volumetric strains.
- The development of shear strain during probing, wetting and shearing is well predicted by the anisotropic model in the majority of simulations. This suggests that the associated flow rule performs well when combined with an anisotropic yield surface (with constant suction cross-sections in the form of distorted ellipses), the inclination of which evolves during plastic straining.
- In contrast, the isotropic model grossly over-predicts the shear strains during the various loading stages. This indicates that the combination of an associated flow rule with an isotropic yield surface (with elliptical constant suction cross-sections) does not produce accurate predictions.
- The anisotropic model performs reasonably well in simulating the behaviour of isotropically and anisotropically compacted samples over a wide range of stress paths.
- In some cases, Version 1 of the anisotropic model predicts a peak deviator stress in the  $q:\varepsilon_s$  plane, followed by a modest post-peak reduction to critical state. In contrast, the isotropic model predicts, for the same cases, a monotonic increase of deviator stress to critical state.
- The peak deviator stress observed in the experiments is in some cases well matched by the anisotropic model, although it is over-predicted in other cases. The experimentally observed post-peak reduction of deviator stress caused by strain localisation cannot be captured by the model. It is therefore not possible to confirm the accuracy of the prediction of peak and post-peak deviator stress.

Despite the significant improvement of predictions by the anisotropic model compared to the isotropic model, some weaknesses were also found and these are detailed below:

- The anisotropic model under-predicts the differences in initial specific volume between isotropically compacted and anisotropically compacted samples. The model predicts that initial values of  $v$  for anisotropically compacted samples should be slightly lower than those for corresponding isotropically compacted samples, because experimental results indicate that the anisotropic compaction results in slightly greater expansion of the yield surface than isotropic

compaction. However, the initial value of  $v$  were actually substantially lower for anisotropically compacted samples than for isotropically compacted samples.

- The anisotropic model predictions under saturated conditions are less precise than under unsaturated conditions and the transition from unsaturated to saturated conditions is not well-matched by the anisotropic model. One clear shortcoming is the assumption of unique critical state line in the  $q:p^*$  plane, regardless of suction. Under saturated conditions, the experimental critical state values of deviator stress were always greater than those predicted by the model relationship  $q = M^* p^*$ , which also leads to significant under-prediction of the final volumetric strains during shearing of saturated samples to critical states.

### 9.3.4 Performance of Version 2 of the anisotropic model

- Although both versions of the model predict the same values of deviator stress at critical state, Version 2 of the model requires larger values of shear strain before critical state is attained during probing/shearing.
- The peak values of deviator stress are predicted less accurately by Version 2 than by Version 1 of the anisotropic model.
- Version 2 of the anisotropic model predicts similar amounts of volumetric strains during loading, wetting, probing and shearing stages as Version 1.
- Version 2 of the model grossly over-predicts shear strains during loading, wetting, probing and shearing stages. This suggests that the proposed form of non-associated flow rule is less accurate than an associated flow rule.
- Both versions of the model predict a unique critical state planar surface in  $v:\ln p^*:\ln s^*$  space that is parallel to the unique planar normal compression surface for an isotropic soil (as mentioned in Section 9.3.1). However, both versions of the anisotropic model under-predict the difference in specific volume between normal compression and critical state surfaces.

## 9.4 RECOMMENDATIONS FOR FUTURE WORK

### 9.4.1 Experimental equipment

- For the unsaturated triaxial cells (i.e. System 1 and System 2), original calibrations of pressure, volume, force and displacement gauges were done by the manufacturer and stored in the data logger without being visible to the user (see Section 3.3). Subsequent calibrations performed within this project indicated the need to adjust these calibrations. After consulting the manufacturer (who advised that pressure and volume would be more stable if controlled directly from the controller), it was decided to conduct the tests by applying a correction

to the raw readings of pressure and volume from the controller panel (the correction was however not significant). A better way would be to define pressure, volume, and other variables inside the software based on the calibration of voltage outputs from the transducers.

#### 9.4.2 Compaction technique

- During compaction, a double-layer rubber sheet (with silicon lubricant in-between) was used at the top and bottom of the wet kaolin (see Section 4.1.3) but unfortunately this did not completely eliminate friction. Although all samples for triaxial tests were obtained from the middle part of the compacted material, the presence of end friction might slightly affect homogeneity of the compacted material. In particular, for isotropic compaction, it is recommended that the compaction arrangement is modified in such a way that a confining all-round pressure can be applied on the soil without friction at either end.
- Experimental results from anisotropically compacted samples showed that initial anisotropy was modest (see Section 6.5) which was attributed to the high suction levels present in the material during compaction. The creation of anisotropic samples consolidated from slurry would be a better way to develop a soil fabric with significant amount of anisotropy. However, this might result in a fabric with very low valued of unsaturated water permeability, which would mean that very long test durations would be required in order to achieve satisfactory suction equalisation during unsaturated tests (especially for tests at high suction levels).

#### 9.4.3 Experimental testing

- This experimental programme investigated the influence of anisotropy on the mechanical behaviour of unsaturated soils. Further experimental work should however be conducted to study the effects of anisotropy on water retention behaviour. This could include performing drying and wetting cycles at different levels of stress and void ratio.
- The current study assumed an isotropic elastic law while, in reality, fabric anisotropy can manifest itself through both the elastic and plastic behaviour of the soil. However, it is likely that different aspects of fabric anisotropy control the elastic and plastic response. In addition, the study of elastic anisotropy requires additional instrumentation to measure small strain stiffness such as, for example, bender elements.
- The current study performed a phenomenological investigation of anisotropy in unsaturated soils based on the mechanical aspects of macroscopic material behaviour as observed in the laboratory. Future research might also investigate

the effects of mechanical loading on evolving fabric anisotropy from a microstructural level by using techniques such as scanning electron microscopy (*SEM*) and mercury intrusion porosimetry (*MIP*). This type of study provides better insight into the physical changes of soil fabric in terms of orientation of particles and aggregates, which can further add to knowledge at macrostructural level.

#### 9.4.4 Constitutive modelling

- The proposed constitutive modelling approach employs Bishop's stresses and modified suction as constitutive variables. An alternative mechanical constitutive model could, however, be developed by using net stresses and suction. The results from this study suggest that experimental yield points at constant suction can be fitted with similar ease and precision in both the  $q:p^*$  and  $q:\bar{p}$  planes (see Section 6.5).
- The anisotropic model developed in this study is solely a mechanical model, but it cannot be employed in isolation for Class A predictions because it requires values of degree of saturation in the definition of Bishop's stress (as explained in Section 8.1). It is therefore necessary either to combine the proposed mechanical model with a separate water retention model or to extend the model to a fully coupled mechanical and water retention model, as in the original isotropic model of Wheeler et al. (2003a). The latter development is recommended.
- For anisotropically compacted samples, the predicted initial specific volume was substantially greater than the experimentally observed value, which reflected a weakness in the hardening law of the *LC* curve (see Section 7.5). Addressing this weakness would result in significantly better predictions of initial states (in terms of both  $v$  and  $s^*$ ) for anisotropic soils.
- The predictions of the proposed anisotropic model are less satisfactory under saturated conditions than unsaturated conditions. Therefore, further work is required to improve modelling of the transition from unsaturated to saturated states or vice versa.
- For Version 1 of the anisotropic model, the proposed variation of aspect ratio  $m^*$  with inclination  $\alpha^*$  for the constant suction yield curves (see Section 7.8.1) is not simple. However, simulations with this version of the model have showed good predictions of soil behaviour. It would therefore be useful to look for alternative, and mathematically simpler, expressions describing the variation of aspect ratio  $m^*$  with inclination  $\alpha^*$ .
- Predictions by Version 2 of the model were not as good as predictions by Version 1, especially with respect to the prediction of shear strains during plastic loading.

This is partly attributable to the chosen form of plastic potential, and investigation of the alternative forms of plastic potential might solve this problem.

- Both Versions 1 and 2 of the anisotropic model under-predict the spacing between the normal compression planar surface and the critical state planar surface in  $v: \ln p^*: \ln s^*$  space. This is because both versions of the model predict a relatively high critical state value of  $\alpha^*$ . A lower critical state value of  $\alpha^*$  could be predicted by employing a suitable non-linear expression for the target function  $f(\eta^*)$  (see Section 7.7). This would produce a lower critical state value of  $\alpha^*$ , more similar to that predicted by the saturated anisotropic model *S – CLAY1* (see Figure 7.3). This point would be worth exploring, in order to try to improve the prediction of volumetric strains during shearing.

## REFERENCES

- AITCHISON, G. D. 1961. Relationship of moisture and effective stress functions in unsaturated soils. *Proceedings of the Conference on Pore Pressure and Suction in Soils*. Butterworths, London, 47-52.
- ALONSO, E. E., GENS, A. & JOSA, A. 1990 A constitutive model for partially saturated soils. *Géotechnique*, 40(3), 405-430.
- ALONSO, E. E., PEREIRA, J. M. , VAUNAT, J. & OLIVELLA, S. 2010. A microstructurally based effective stress for unsaturated soils *Géotechnique*, 60(12), 913-925.
- ALONSO, E. E., GENS, A. & GEHLING, W. Y. Y. 1994. Elastoplastic model for unsaturated expansive soils. *Proceedings of the 3rd European Conference on Numerical Mathematics in Geotechnological Engineering*. Manchester, Balkema, 11-18.
- ALONSO, E. E., GENS, A. & HIGHT, D. W. 1987. Special problem soils. *Proceedings of the 9th European Conference on Soil Mechanics and Foundation Engineering*. Dublin,3, 1087-1146.
- ALONSO, E. E., VAUNAT, J. & GENS, A. 1999. Modelling the mechanical behaviour of expansive clays. *Engineering Geology*, 54(1-2), 173-183.
- BAI, X. & SMART, R. 1997. Change in microstructure of kaolin in consolidation and undrained shear. *Géotechnique*, 47(5), 1009-1017.
- BAKER, R. & FRYDMAN, S. 2009. Unsaturated soil mechanics: Critical review of physical foundations. *Engineering Geology*, 106 (1-2), 26-139.
- BANERJEE, P. K., KUMBHOJKAR, A. S. & YOUSIF, N. B. 1988. Finite element analysis of the stability of a vertical cut using an anisotropic soil model. *Canadian Geotechnical Journal*, 25(1), 119-127.
- BANERJEE, P. K. & YOUSIF, N. B. 1986. A plasticity model for the mechanical behaviour of anisotropically consolidated clay. *International Journal for Numerical and Analytical Methods in Geomechanics*, 10(5), 521-541.
- BECKER, D. E., CROOKS, J. H. A., BEEN, K. & JEFFERIES, M. G. 1987. Work as a criterion for determining in situ and yield stresses in clays. *Canadian Geotechnical Journal*, 24(4), 549-564.
- BISHOP, A. W. 1959. The principle of effective stress. *Teknisk Ukeblad*, 39, 859-863.
- BISHOP, A. W. & BLIGHT, G. E. 1963. Some aspects of effective stress in saturated and partly saturated soils. *Géotechnique*, 13(3), 177-197.
- BISHOP, A. W. & DONALD, I. B. 1961. The experimental study of partly saturated soil in the triaxial apparatus. *Proceedings of the 5th International Conference on Soil Mechanics and Foundation Engineering*. Paris,1, 13-22.

- BLATZ, J., CUI, Y. J. & OLDECOP, L. 2008. Vapour equilibrium and osmotic technique for suction control. *Geotechnical and Geological Engineering*, 26(6), 661-673.
- BOLZON, G., SCHREFLER, B. A. & ZIENKIEWICZ, O. C. 1996. Elastoplastic soil constitutive laws generalized to partially saturated states. *Géotechnique*, 46(2), 279-289.
- BOONE, S. J. 2010. A critical reappraisal of “preconsolidation pressure” interpretations using the oedometer test. *Canadian Geotechnical Journal*, 47(3), 281-296.
- BROOKS, R. H. & COREY, A. T. 1964. Hydraulic properties of porous media. *Hydrology Paper No.3, Colorado State Univ., Fort Collins*.
- BUCKINGHAM, E. 1907. Water retention in soil. *Soil Bulletin (U.S. Department of Agriculture)*, 38.
- BURLAND, J. B. 1965. Some aspects of the mechanical behaviour of partly saturated soils. *Proceedings of the Conference on Moisture Equilibria and Moisture Changes in Soil Beneath Covered Areas*. London, Butterworths, 270-278.
- BURLAND, J. B. 1990. On the compressibility and shear strength of natural clays. *Géotechnique*, 40(3), 329-378.
- BUTTERFIELD, R. 1979. A natural compression law for soils (an advance on  $e$ -log  $p'$ ) *Géotechnique*, 29, 469-480.
- CAMPBELL, G. S. 1974. A simple method for determining unsaturated hydraulic conductivity from moisture retention data. *Soil Science*, 117(6), 311-314.
- CASAGRANDE, A. 1936. The determination of the preconsolidation load and its practical significance. *Proceedings of the 1st International Conference on Soil Mechanics and Foundation Engineering*. Cambridge, Mass,3, 60-64.
- CHIU, C. F. & NG, C. W. W. 2003. A state-dependent elasto-plastic model for saturated and unsaturated soils. *Géotechnique*, 53(9), 809-829.
- COLLINS, I. F. & HOULSBY, G. T. 1997. Application of thermomechanical principles to the modelling of geotechnical materials. *Proceedings of the Royal Society of London*, A 453,1975-2001.
- COLLINS, K. 1984. Characterisation of expansive soil microfabric. *Proceedings of the International Conference on Expansive Soils*. Adelaide, 1, 37-43.
- CRONEY, D., COLEMAN, J. D. & BLACK, W. P. M. 1958. Movement and distribution of water in relation to highway design and performance. *Special Report*. Washington, D.C: Highway Research Board, 40, 226-252.
- CUI, Y. J. & DELAGE, P. 1996. Yielding and plastic behaviour of an unsaturated compacted silt. *Géotechnique*, 46(2), 291-311.
- CUISINIER, O. & LALOUI, L. 2004. Fabric evolution during hydromechanical loading of a compacted silt. *International Journal for Numerical and Analytical Methods in Geomechanics*, 28(6), 483-499.

- D'ONZA, F., GALLIPOLI, D. & WHEELER, S. J. 2011. Effect of anisotropy on the prediction of unsaturated soil response under triaxial and oedometric conditions. *Proceedings of the 5th International Conference on Unsaturated Soils*. Barcelona, Spain, 2, 787-794.
- DAFALIAS, Y. F. 1987. Anisotropic critical state clay plasticity model. *2nd International Conference on Constitutive Laws for Engineering Materials*. Tucson, Arizona, 1, 513-521.
- DAFALIAS, Y. F. 1986. An anisotropic critical state soil plasticity model. *Mechanics Research Communications*, 13(6), 341-347.
- DAFALIAS, Y. F., MANZARI, M. T. & PAPADIMITRIOU, A. G. 2006. SANICLAY: simple anisotropic clay plasticity model. *International Journal for Numerical and Analytical Methods in Geomechanics*, 30(12), 1231-1257.
- DAVIES, M. C. R. & NEWSON, T. A. 1993. A critical state constitutive model for anisotropic soils. *Proceedings of the Worth memorial Symposium*. Oxford, Thomas Telford, London, 219-229.
- DELAGE, P., AUDIGUIER, M., CUI, Y. J. & HOWAT, M. D. 1996. Microstructure of a compacted silt. *Canadian Geotechnical Journal*, 33(1), 150-158.
- DELAGE, P. & GRAHAM, J. 1996. Mechanical behaviour of unsaturated soils: understanding the behaviour of unsaturated soils requires reliable conceptual models. *proceedings of the 1st International Conference on Unsaturated Soils*. Paris, Balkema, 3, 1223-1256.
- DELAGE, P. & LEFEBVRE, G. 1984. Study of the structure of a sensitive Champlain clay and of its evolution during consolidation. *Canadian Geotechnical Journal*, 21(1), 21-35.
- DELLA VECCHIA, G., JOMMI, C. & ROMERO, E. 2012. A fully coupled elastic-plastic hydromechanical model for compacted soils accounting for clay activity. *International Journal for Numerical and Analytical Methods in Geomechanics*, DOI: 10.1002/nag.1116.
- ESCARIO, V. & SÁEZ, J. 1986. The shear strength of partly saturated soils. *Géotechnique*, 36(3), 453-456.
- FREDLUND, D. G. & MORGENSTERN, N. R. 1977. Stress state variables for unsaturated soils. *ASCE Journal of Geotechnical Engineering*, 103(5), 447-466.
- FREDLUND, D. G., MORGENSTERN, N. R. & WIDGER, R. A. 1978. The shear strength of unsaturated soils. *Canadian Geotechnical Journal*, 15(3), 313-321.
- FREDLUND, D. G., RAHARDJO, H. & GAN, J. K. M. 1987. Nonlinearity of strength envelope for unsaturated soils. *Proceedings of the 6th International Conference on Expansive Soils*. New Delhi, India, 49-54.

- FREDLUND, D. G. & RAHARDJO, H. 1993. *Soil Mechanics for Unsaturated Soils*. New York, John Wiley & Sons.
- FREDLUND, D. G. & XING, A. 1994. Equations for the soil-water characteristic curve. *Canadian Geotechnical Journal*, 31(4), 521-532.
- GALLIPOLI, D. 2000. *Constitutive and numerical modelling of unsaturated soils*. PhD thesis, University of Glasgow, UK.
- GALLIPOLI, D., D'ONZA, F. & WHEELER, S. J. 2010. A sequential method for selecting parameter values in the Barcelona basic model. *Canadian Geotechnical Journal*, 47(11), 1175-1186.
- GALLIPOLI, D., GENS, A., CHEN, G. & D'ONZA, F. 2008. Modelling unsaturated soil behaviour during normal consolidation and at critical state. *Computers and Geotechnics*, 35(6), 825-834.
- GALLIPOLI, D., GENS, A., SHARMA, R. & VAUNAT, J. 2003a. An elasto-plastic model for unsaturated soil incorporating the effects of suction and degree of saturation on mechanical behaviour. *Géotechnique*, 53(1), 123-135.
- GALLIPOLI, D., WHEELER, S. J. & KARSTUNEN, M. 2003b. Modelling the variation of degree of saturation in a deformable unsaturated soil. *Géotechnique*, 53(1), 105-112.
- GAN, J. K. M., FREDLUND, D. G. & RAHARDJO, H. 1988. Determination of the shear strength parameters of an unsaturated soil using the direct shear test. *Canadian Geotechnical Journal*, 25(3), 500-510.
- GENS, A. & ALONSO, E. E. 1992. A framework for the behaviour of unsaturated expansive clays. *Canadian Geotechnical Journal*, 29(6), 1013-1032.
- GENS, A., SÁNCHEZ, M. & SHENG, D. 2006. On constitutive modelling of unsaturated soils. *Acta Geotechnica*, 1(3), 137-147.
- GRAHAM, J. 2006. The 2003 R.M. Hardy Lecture: Soil parameters for numerical analysis in clay. *Canadian Geotechnical Journal*, 43(2), 187-209.
- GRAHAM, J., CROOKS, J. H. A. & LAU, S. L. K. 1988. Yield envelopes: identification and geometric properties. *Géotechnique*, 38(1), 125-134.
- GRAHAM, J. & HOULSBY, G. T. 1983. Anisotropic elasticity of a natural clay. *Géotechnique*, 33(2), 165-180.
- GRAHAM, J., NOONAN, M. L. & LEW, K. V. 1983. Yield states and stress-strain relationships in a natural plastic clay. *Canadian Geotechnical Journal*, 20(3), 502-516.
- GRAHAM, J., PINKNEY, R. B., LEW, K. V. & TRAINOR, P. G. S. 1982. Curve-fitting and laboratory data. *Canadian Geotechnical Journal*, 19(3), 201-205.
- GRIFFITHS, F. J. & JOSHI, R. C. 1989. Change in pore size distribution due to consolidation of clays. *Géotechnique*, 39(1), 159-167.

- GROZIC, J. L. H., LUNNE, T. & PANDE, S. 2003. An oedometer test study on the preconsolidation stress of glaciomarine clays. *Canadian Geotechnical Journal*, 40(5), 857-872.
- HATTAB, M. & FLEUREAU, J. M. 2011. Experimental analysis of kaolinite particle orientation during triaxial path. *International Journal for Numerical and Analytical Methods in Geomechanics*, 35(8), 947-968.
- HICHER, P. Y., WAHYUDI, H. & TESSIER, D. 2000. Microstructural analysis of inherent and induced anisotropy in clay. *Mechanics of Cohesive-Frictional Materials*, 5(5), 341-371.
- HONG, Z., TATEISHI, Y. & HAN, J. 2006. Experimental study of macro- and micro-behavior of natural diatomite. *Journal of Geotechnical and Geoenvironmental Engineering*, 132(5), 603-610.
- HOULSBY, G. T. 1997. The work input to an unsaturated granular material. *Géotechnique*, 47(1), 193-196.
- JAKY, J. 1948. Pressure in silos. *Proceedings of the 2nd International Conference on Soil Mechanics and Foundations Engineering*. Rotterdam, 1, 103-107.
- JENNINGS, J. E. 1960. A revised effective stress law for use in the prediction of the behaviour of unsaturated soils. *Proceedings of the Conference on Pore Pressure and Suction in Soils*. Butterworths, London, 26-30.
- JENNINGS, J. E., B. & BURLAND, J. B. 1962. Limitations to the use of effective stresses in partly saturated soils. *Géotechnique*, 12(2), 125-144.
- JIANG, J. & LING, H. I. 2010. A framework of an anisotropic elastoplastic model for clays. *Mechanics Research Communications*, 37(4), 394-398.
- JOMMI, C. 2000. Remarks on the constitutive modelling of unsaturated soils. In: TARANTINO & MANCUSO, eds. *Experimentat Evidence and theoretical Approaches in Unsaturated Soils*, 2000. Balkema, Rotterdam, 139-153.
- JOMMI, C. & DI PRISCO, C. 1994. A simple theoretical approach for modelling the mechanical behaviour of unsaturated granular soils (in Italian). *Il Ruolo dei Fluidi nei Problemi di Ingegneria Geotecnica*. Mondovi, 167-188.
- KARSTUNEN, M. & KOSKINEN, M. 2008. Plastic anisotropy of soft reconstituted clays. *Canadian Geotechnical Journal*, 45(3), 314-328.
- KARSTUNEN, M., KRENN, H., WHEELER, S. J., KOSKINEN, M. & ZENTAR, R. 2005. Effect of anisotropy and destructuration on the behaviour of of Murro test embankment. *ASCE International Journal of Geomechanics*, 5(2), 87-97.
- KARSTUNEN, M. & WHEELER, S. 2002. Discussion of "Finite Strain, Anisotropic Modified Cam Clay Model with Plastic Spin. I: Theory" by George Z. Voyiadjis and Chung R. Song. *Journal of Engineering Mechanics*, 128(4), 497-498.

- KHALILI, N., GEISER, F. & BLIGHT, G. E. 2004. Effective stress in unsaturated soils: review with new evidence. *International Journal of Geomechanics*, 4(2), 115-126.
- KHALILI, N. & KHABBAZ, M. H. 1998. A unique relationship for  $\chi$  for the determination of the shear strength of unsaturated soils. *Géotechnique* 48(5), 681-687.
- KOHGO, Y., NAKANO, M. & MIYAZAKI, T. 1993a. Theoretical aspects of constitutive modelling for unsaturated soils. *Soils and Foundations*, 33(4), 49-63.
- KOHGO, Y., NAKANO, M. & MIYAZAKI, T. 1993b. Verification of the generalized elastoplastic model for unsaturated soils. *Soils and Foundations*, 33(4), 64-73.
- KORHONEN, K. H. & LOJANDER, M. 1987. Yielding of Perno clay. Proceedings of the 2nd International Conference on Constitutive Laws for Engineering Materials. Tucson, Arizona, 2, 1249-1255.
- KOSKINEN, M., KARSTUNEN, M. & LOJANDER, M. Yielding of "ideal" and natural anisotropic clays. In: VERMEER, P. A., SCHWEIGER, H. F., KARSTUNEN, M. & CUDNY, M., eds. *International Workshop on Geotechnics of Soft Soils-Theory and Practice*. Noordwijkerhout, Netherlands, 197-204.
- LAGIOIA, R., PUZRIN, A. M. & POTTS, D. M. 1996. A new versatile expression for yield and plastic potential surfaces. *Computers and Geotechnics*, 19(3), 171-191.
- LAMBE, T. W. & WHITMAN, R. V. 1969. *Soil Mechanics*. New York, John Wiley & Sons.
- LEONG, E. C. & RAHARDJO, H. 1997. Review of soil-water characteristic curve equations. *Journal of Geotechnical and Geoenvironmental Engineering*, 123(12), 1106-1117.
- LLORET, M. 2011. Numerical modelling of coupled behaviour in unsaturated soils. *PhD thesis*, Strathclyde University, UK.
- LLORET, M., SÁNCHEZ, M., WHEELER, S. J. & KARSTUNEN, M. 2008. Generalised elastoplastic stress-strain relations of a fully coupled hydro-mechanical model. *Proceedings of the 1st European Conference on Unsaturated Soils*. Durham, UK, 567-573.
- LORET, B. & KHALILI, N. 2000. A three-phase model for unsaturated soils. *International Journal for Numerical and Analytical Methods in Geomechanics*, 24(11), 893-927.
- LORET, B. & KHALILI, N. 2002. An effective stress elastic-plastic model for unsaturated porous media. *Mechanics of Materials*, 34(2), 97-116.
- LU, N. & LIKOS, W. J. 2004. *Unsaturated Soil Mechanics*, New York, John Wiley & Sons.
- MATYAS, E. L. & RADHAKRISHNA, H. S. 1968. Volume change characteristics of partially saturated soils. *Géotechnique*, 18(4), 432-448.
- MCGOWN, A. & COLLINS, K. 1975. The microfabrics of some expansive and collapsing soils. Proceedings of the 5th Panamerican Conference on Soil Mechanics and Foundation Engineering. Buenos Aires, 1, 323-332.
- MODARESSI, A. & ABOU-BEKR, N. 1994. A unified approach to model the behavior of saturated and unsaturated soils. *Proceedings of the 8th International Conference*

- on *Computer Methods and Advances in Geomechanics*. Morgantown, USA, Balkema, Rotterdam, 1507-1513.
- MONROY, R., ZDRAVKOVIC, L. & RIDLEY, A. 2010. Evolution of microstructure in compacted London Clay during wetting and loading. *Géotechnique*, 60(2), 105-119.
- MOURATIDIS, A. & MAGNAN, J. P. 1983. Un modèle élasto-plastique anisotrope avec écrouissage pour le calcul des ouvrages sur sols compressibles. *Rapport de Recherche des Laboratoires des Ponts et Chaussées*, 121.
- MUIR WOOD, D. 2004. Experimental inspiration for kinematic hardening soil models. *Journal of Engineering Mechanics*, 130(6), 656-664.
- PACHECO S. F. 1970. A new graphical construction for determination of the preconsolidation stress of a soil sample. *Proceedings of the 4th Brazilian Conference on Soil Mechanics and Foundation Engineering*, 2, 225-232.
- RAVEENDIRARAJ, A. 2009. Coupling of mechanical behaviour and water retention behaviour in unsaturated soils. *PhD thesis*, University of Glasgow, UK.
- RICHARDS, B. G. 1965. The significance of moisture flow and equilibria in unsaturated soils in relation to the design of engineering structures built on shallow foundations in Australia. *Proceedings of the Symposium on Permeability and Capillarity*. Butterworths, Sydney, Australia, 39-46.
- ROMERO, E. & JOMMI, C. 2008. An insight into the role of hydraulic history on the volume changes of anisotropic clayey soils. *Water Resources Research*, 44, W12412, 1-16.
- ROMERO, E. & VAUNAT, J. 2000. Retention curves of deformable clays. *Proceedings of the International Workshop on Unsaturated Soils: Experimental evidence and theoretical approaches in unsaturated soils*. Trento, Italy, Rotterdam: Balkema, 91-106.
- ROMERO, E., VECCHIA, G. D. & JOMMI, C. 2011. An insight into the water retention properties of compacted clayey soils. *Géotechnique* 61(4), 313-328.
- ROSCOE, K. H. & BURLAND J. B. 1968. On the generalised stress-strain behaviour of wet clay, Cambridge University Press, Cambridge, Engineering Plasticity, 535-609,
- ROSCOE, K. H., SCHOFIELD, A. N. & WROTH, C. P. 1958. On The Yielding of Soils. *Géotechnique*, 8(1), 22-53.
- SÁNCHEZ, M., GENS, A., DO NASCIMENTO GUIMARÃES, L. & OLIVELLA, S. 2005. A double structure generalized plasticity model for expansive materials. *International Journal for Numerical and Analytical Methods in Geomechanics*, 29(8), 751-787.
- SANTAGIULIANA, R. & SCHREFLER, B. 2006. Enhancing the Bolzon-Schrefler-Zienkiewicz constitutive model for partially saturated soil. *Transport in Porous Media*, 65(1), 1-30.

- SHARMA, R. S. 1998. Mechanical behaviour of unsaturated highly expansive clays. *PhD thesis*, University of Oxford, UK.
- SHENG, D., FREDLUND, D. G. & GENS, A. 2008. A new modelling approach for unsaturated soils using independent stress variables. *Canadian Geotechnical Journal*, 45(4), 511-534.
- SHENG, D., SLOAN, S. W. & GENS, A. 2004. A constitutive model for unsaturated soils: thermomechanical and computational aspects. *Computational Mechanics*, 33(6), 453-465.
- SIVAKUMAR, R. 2005. Effects of anisotropy on the behaviour of unsaturated compacted clay. *PhD. thesis*, Queen's University of Belfast, UK.
- SIVAKUMAR, R., SIVAKUMAR, V., BLATZ, J. & VIMALAN, J. 2006. Twin-cell stress path apparatus for testing unsaturated soils. *Geotechnical Testing Journal*, 29(2), 1-5.
- SIVAKUMAR, V. 1993. A critical state framework for unsaturated soil. *PhD thesis*, University of Sheffield, UK.
- SIVAKUMAR, V., DORAN, I. G., GRAHAM, J. & JOHNSON, A. 2001. The effect of anisotropic elasticity on the yielding characteristics of overconsolidated natural clay. *Canadian Geotechnical Journal*, 38(1), 125-137.
- SIVAKUMAR, V., SIVAKUMAR, R., BOYD, J. & MACKINNON, P. 2010b. Mechanical behaviour of unsaturated kaolin (with isotropic and anisotropic stress history). Part 2: performance under shear loading. *Géotechnique*, 60(8), 595-609.
- SIVAKUMAR, V., SIVAKUMAR, R., MURRAY, E. J., MACKINNON, P. & BOYD, J. 2010a. Mechanical behaviour of unsaturated kaolin (with isotropic and anisotropic stress history). Part 1: wetting and compression behaviour. *Géotechnique*, 60(8), 581-594.
- SMITH, P. R., JARDINE, R. J. & HIGHT, D. W. 1992. The yielding of Bothkennar clay. *Géotechnique*, 42(2), 359-362.
- SPOSITO, G. 1981. *The Thermodynamics of Soil Solutions*. London, Oxford Clarendon Press.
- STROPEIT, K., WHEELER, S. J. & CUI, Y. J. 2008. An anisotropic elasto-plastic model for unsaturated soils. *Proceedings of 1st European Conference on Unsaturated Soils*. Durham, Balkema, 625-631.
- SULTAN, N., CUI, Y.-J. & DELAGE, P. 2010. Yielding and plastic behaviour of Boom clay *Géotechnique*, 60(9), 657-666.
- TAIEBAT, M. & DAFALIAS, Y. F. 2010. Simple yield surface expressions appropriate for soil plasticity. *International Journal of Geomechanics*, 10(4), 161-169.
- TAVENAS, F., ROSIERS, J. P. D., LEROUEIL, S., ROCHELLE, P. L. & ROY, M. 1979. The use of strain energy as a yield and creep criterion for lightly overconsolidated clays. *Géotechnique*, 29(3), 285-303.

- TERZAGHI, K. 1936. The shearing resistance of saturated soils and the angle between the planes of shear. *Proceedings of the 1st International Conference on Soil Mechanics and Foundation Engineering*, Cambridge, 1, 54-56.
- TOLL, D. G. 2010. "Triax 5.1.8" user manual. Geotechnical System Research.
- VAN GENUCHTEN, M. T. 1980. A closed-form equation for predicting the hydraulic conductivity of unsaturated soils. *Soil Science Society of America Journal*, 44(5), 892-898.
- VANAPALLI, S. K., FREDLUND, D. G., PUFAHL, D. E. & CLIFTON, A. W. 1996. Model for the prediction of shear strength with respect to soil suction. *Canadian Geotechnical Journal*, 33(3), 379-392.
- VAUNAT, J., ROMERO, E. & JOMMI, C. 2000. An elasto-plastic hydromechanical model for unsaturated soils. *Proceedings of the International Workshop on Unsaturated Soils: Experimental evidence and theoretical approaches in unsaturated soils*. Trento, Italy, Rotterdam, Balkema, 121-138.
- WHEELER, S. J. & KARUBE, D. 1996. Constitutive modelling. *Proceedings of the 1st International Conference on Unsaturated Soils*. Balkema, Rotterdam, 3, 1323-1356.
- WHEELER, S. J. 1986. The stress-strain behaviour of soils containing gas bubbles. *D Phil Thesis*, University of Oxford, UK.
- WHEELER, S. J. 1997. A rotational hardening elasto-plastic model for clays. *Proceedings of the 14th International Conference on Soil Mechanics and Foundation Engineering*. Hamburg, A. A., Balkema, Rotterdam, 1, 431-434.
- WHEELER, S. J., GALLIPOLI, D. & KARSTUNEN, M. 2002. Comments on use of the Barcelona Basic Model for unsaturated soils. *International Journal for Numerical and Analytical Methods in Geomechanics*, 26, 15, 1561-1571.
- WHEELER, S. J., NÄÄTÄNEN, A., KARSTUNEN, M. & LOJANDER, M. 2003b. An anisotropic elastoplastic model for soft clays. *Canadian Geotechnical Journal*, 40(2), 403-418.
- WHEELER, S. J., SHARMA, R. S. & BUISSON, M. S. R. 2003a. Coupling of hydraulic hysteresis and stress-strain behaviour in unsaturated soils. *Géotechnique*, 53(1), 41-54.
- WHEELER, S. J. & SIVAKUMAR, V. 1995. An elasto-plastic critical state framework for unsaturated soil. *Géotechnique*, 45(1), 35-53.
- WHEELER, S. J. & SIVAKUMAR, V. 2000. Influence of compaction procedure on the mechanical behaviour of an unsaturated compacted clay. Part 2: Shearing and constitutive modelling. *Géotechnique*, 50(4), 369-376.
- WHITTLE, A. J. & KAVVADAS, M. J. 1994. Formulation of MIT-E3 constitutive model for overconsolidated clays. *Journal of Geotechnical Engineering*, 120(1), 173-198.
- YU, H. S. 2006. Plasticity and geotechnics. Springer, New York.

- ZAKARIA, I., WHEELER, S. J. & ANDERSON, W. F. 1995. Yielding of unsaturated compacted kaolin. *Proceedings of the 1st International Conference on Unsaturated Soils*. Paris, Rotterdam, Balkema, 1, 223-228.
- ZHOU, A. & SHENG, D. 2009. Yield stress, volume change, and shear strength behaviour of unsaturated soils: validation of the SFG model. *Canadian Geotechnical Journal*, 46(9), 1034-1045.